# Seismic Performance of CLT Core-Wall Systems and Connections

Ph.D. Thesis submitted in partial fulfilment

of the requirements for the degree of

DOCTOR OF PHILOSOPHY

in

EARTHQUAKE ENGINEERING

by

Justin Robert Brown

Supervised by:

Associate Professor Minghao Li, University of Canterbury

Professor Alessandro Palermo, University of Canterbury

Professor Stefano Pampanin, Sapienza University of Roma

Dr. Francesco Sarti, PTL | Structural Consultants


Department of Civil and Natural Resources Engineering

University of Canterbury

Christchurch, New Zealand

http:// www.civil.canterbury.ac.nz

# Executive Summary

The Ph.D. research reported explores the seismic performance of cross-laminated timber (CLT) core-wall systems and their connections. While there is a renewed interest and implementation of timber buildings globally, many of these structures are hybrid solutions with reinforced concrete or steel systems utilized to resist lateral loading. This in part motivated the research, with the main objective to quantify the increase in strength and stiffness when multiple CLT shear walls are connected together to transform a planar CLT lateral load resisting system (LLRS) to a CLT core-wall LLRS.

The research first comprised of experimental and analytical investigations of three critical connections for a CLT core-wall LLRS. The testing of dowelled hold-downs found that increased row spacing and end distance increased connection displacement capacity and ductility when compared to current spacing recommendations in literature. To provide an orthogonal connection between CLT walls, screws were installed with mixed angles, i.e. different installation angles between the screw axis and the plane of the CLT surface. An optimum ratio of two inclined screws to one screw installed at 90° to the CLT surface was found. The average experimental overstrength was 1.7 for these dowelled hold-downs and screwed orthogonal connections. Through testing, it was found that the shear strength and stiffness of castellated connections were 2.5 and 7 times greater than the specimens using commercial angle brackets. A simplified stiffness-based load sharing analytical model was developed to predict castellated connection strength.

A three phase CLT shear wall testing programme was executed to study the contribution of each component (wall and joint) to a CLT core-wall system. The programme consisted of 4 post-tensioned (PT) single wall tests, 5 PT double wall tests, 7 PT core-wall tests and one conventional core-wall test for comparison purposes. The highest CLT core-wall composite action of approximately two-thirds was achieved. The core-wall stiffness was greater than eight times a single CLT wall for an approximate 3.5 times increase in CLT wall area. Mixed angle screwed connections were implemented along the vertical joints to provide strong, stiff, and energy dissipative connections.

Analytical investigations sought to modify and develop the existing sectional analysis method for PT wall systems using the Modified Monolithic Beam Analogy. Through the use of Particle Tracking Technology, it was found that a strain amplification factor of 1.3 was required for CLT walls which is non edge glued and whose lamella are not machine stress graded. Analytical models were developed for PT double wall and core-wall systems based on a nonlinear curve fitting screwed connection model. Different kinematic modes could occur such as Flange Wall uplift and simultaneous Web and Flange Wall uplift depending on the relative strength and stiffness of the screwed connection s to the PT and dissipater elements. It was found that for the PT core-wall, the compression Flange Wall could be neglected during strong axis loading if screwed orthogonal joints are employed. The analytical model well predicted the instance when kinematic modes change due to the nonlinear behaviour of the screwed connections. The analytical model captured the behaviour of the tested PT double wall and PT core-wall systems within 10% error.

# Dedication

To my late grandmother, my mother and father.

# Acknowledgements

The Ph.D. research reported in this thesis was carried out at the University of Canterbury and was primarily funded by the Speciality Wood Products Partnership, New Zealand Douglas-Fir Association, Australian Research Council Future Timber Hub, and the New Zealand Commonwealth Scholarship and Fellowship Plan. Furthermore, there was industry sponsorship from SPAX Pacific and BBR Contech towards experimental testing. Support from XLam NZ Ltd. and Timber-Connect is also gratefully acknowledged.

I had the pleasure to work with most of the Structures Lab technicians throughout my experimental testing which had many of my most enjoyable Ph.D. moments. In particular, I would like to thank Peter Coursey, Gavin Keats, Russell McConchie, Alan Poynter and Alan Thirwell for their immense amount of support, good humour, and lasting memories. The experimental programme was supported by past University of Canterbury 3rd pro project students Wiaan Botha, Ben Karalus, Chris Ravn, Ben Scott, Sam Stanton, and Andrew Steel and their enthusiasm, ideas, and support is greatly appreciated.

I feel fortunate to have had the opportunity to undertake this Ph.D. under the primary supervision of Minghao Li. Minghao's guidance, trust, continual support, and endless availability have been truly appreciated. Under the mentorship of Minghao I have learned and grown an immense amount technically, professionally, and personally. I would also like to acknowledge the rest of my supervisory team Alessandro Palermo, Stefano Pampanin, and Francesco Sarti for their support especially at the early stages to form the Ph.D. story. In particular I would like to thank Francesco for his technical support, guidance, and friendship throughout these years. I would like to thank Roger Nokes, who developed Streams particle tracking software, for his enthusiasm and availability to help support the processing of my experimental results. I would also like to acknowledge Daniel Moroder, Tobias Smith, and Andy Buchanan from PTL | Structural Consultants. We had numerous fruitful discussions which significantly improved the quality of the research.

Lastly, I would like to thank some individuals who have supported me and inspired me to pursue a Ph.D. I would like to thank my Mom and Dad, sisters Alison and Melissa and brother-in-law Brent for their continuous support from afar, especially during the last years when the pandemic has kept us physically distant. To my late grandmother, who has inspired me to – *pursue your passion and in doing so you would feel like you never worked a day in your life* – I am so grateful for the time we had together. I am very appreciative for my formative years working at StructureCraft prior to my Ph.D. In particular I would like to thank Gerry Epp and Lucas Epp whose passion for timber design and enthusiasm and belief in my abilities sparked a curiosity in me that led me to pursue this Ph.D. Throughout my Ph.D. I have made many lifelong friendships and in particular I would like to acknowledge my timber Ph.D. colleague Wenchen – I feel so fortunate that we had each other to discuss ideas, give support, and push each other to succeed. Finally, I would like to acknowledge my partner, Ana. Thank you for your endless support throughout this Ph.D. journey.

# List of Publications

The following journal articles were published during the Ph.D. study:

[1] J. Brown, M. Li, B. Karalus, S. Stanton, Withdrawal Behaviour of Self-tapping Screws in New Zealand Cross-Laminated Timber, New Zeal. Timber Design Society Journal. 28 (2020).

[2] J.R. Brown, M. Li, A. Palermo, S. Pampanin, F. Sarti, Experimental Testing of a Low-Damage post-tensioned C-Shaped CLT Core-Wall, ASCE Journal of Structural Engineering. 147 (2021) 1–16. https://doi.org/10.1061/(ASCE)ST.1943-541X.0002926.

[3] J.R. Brown, M. Li, T. Tannert, D. Moroder, Experimental study on orthogonal joints in cross-laminated timber with self-tapping screws installed with mixed angles, Engineering Structures. 228 (2021) 111560. https://doi.org/10.1016/j.engstruct.2020.111560.

[4] J.R. Brown, M. Li, Structural performance of dowelled cross-laminated timber hold-down connections with increased row spacing and end distance, Construction and Building Materials. 271 (2021) 121595. https://doi.org/10.1016/j.conbuildmat.2020.121595.

[5] J.R. Brown, M. Li, F. Sarti, Structural performance of CLT shear connections with castellations and angle brackets, Engineering Structures. 240 (2021) 112346. https://doi.org/10.1016/j.engstruct.2021.112346.

The following conference papers were published during the Ph.D. study:

[1] J. Brown, M. Li, L.M. Ottenhaus, C. Ravn, B. Scott, Ductility of dowelled New Zealand Douglas-Fir CLT connections under monotonic and cyclic loading, in: Pacific Conference on Earthquake Engineering. Auckland, 2019.

[2] J. Brown, M. Li, R. Nokes, A. Palermo, S. Pampanin, F. Sarti, Investigating the compressive toe of pos-tensioned CLT core-walls use Particle Tracking Technology, in: 17th World Conference on Earthquake Engineering. 17WCEE, Sendai, Japan, 2020.

[3] J. Brown, M. Li, A. Palermo, S. Pampanin, F. Sarti, Bi-Directional Seismic Testing of Post-Tensioned Rocking CLT Walls and Core-Walls, in: World Conference on Timber Engineering. WCTE 2021, Santiago, Chile, 2021.

[4] J.R. Brown, M. Li, A. Palermo, S. Pampanin, F. Sarti, Investigating CLT lateral load resisting systems for taller timber buildings, in: New Zeal. Society for Earthquake Engineering Conference. NZSEE, Christchurch, N.Z, 2021.

# Contents

# List of Acronyms

| | |
|---|---|
| CA | Composite action. |
| CCMC | Canadian Construction Materials Centre. |
| CCW | Conventional core-wall. |
| CDW | Coupled double wall. |
| CLT | Cross-Laminated Timber. |
| CLT3 | Three-layer CLT. |
| CLT5 | Five-layer CLT. |
| CLT7 | Seven-layer CLT. |
| CNC | Computer numerical control. |
| CSA | Canadian standards association. |
| DW | Double wall. |
| EA | Equal angle. |
| ETA | European technical approval. |
| EYM | European yield model. |
| FT | Fully threaded. |
| HCA | High composite action. |
| ICC | International Code Council. |
| LLRS | Lateral load resisting system. |
| LCA | Low composite action. |
| LVL | Laminated veneer lumber. |
| LVDT | Linear variable displacement transducer. |
| MCA | Medium composite action. |
| MMBA | Modified monolithic beam analogy. |
| MBA | Monolithic beam analogy. |
| NA | National annex. |
| NDS | National design specification. |
| NZ | New Zealand. |
| PD | Peak drift. |
| PT | Post-tensioned. |
| PTH | Partially threaded. |

| | |
|---|---|
| PTT | Particle tracking technology. |
| RGB | Red green blue. |
| SC | Shear-compression self-tapping screw. |
| SCW | Single-coupled wall. |
| ST | Shear-tension self-tapping screw. |
| STS | Self-tapping screw. |
| SLS | Serviceability limit state. |
| SW | Single wall. |
| UFP | U-shaped flexural plate. |
| WSA | Winkler spring analogy. |

# List of Notations

| | |
|---|---|
| $a$ | Average width of the CLT lamella |
| $a_i$ | Distance between the centroid of the composite section and geometric centre. |
| $a_1$ | Dowel spacing within a dowel row. |
| $a_2$ | Dowel spacing between dowel rows. |
| $a_3$ | Dowel spacing loaded end distance. |
| $b_{eff}$ | Sum of the longitudinal board thickness. |
| $A_{eff,wi}$ | Effective cross-sectional area of the applicable CLT wall. |
| $A_{\text{Flange}}$ | Flange wall area to Winkler Spring Analogy. |
| $A_{PT,i}$ | Cross-section area of the i-th post-tensioning bar. |
| $b_{eff,Flange}$ | Flange wall effective width to Winkler Spring Analogy. |
| $b_u$ | UFP width. |
| $c_{i,j}$ | Wall 'i' neutral axis length for $\theta_j$ imposed base rotation angle. |
| $\text{C}_{\text{T,i,j}}$ | Timber compression force for the i-th Wall for $\theta_j$ imposed base rotation angle. |
| $CV$ | Co-efficient of variation. |
| $d$ | Dowel diameter, outer thread diameter for STS. |
| $d_c$ | Self-tapping screw core diameter. |
| $d_{ef}$ | Self-tapping screw effective diameter = 1.1$d_c$. |
| $d_{PT,i}$ | Edge distance of the i-th post-tensioning bar. |
| $d_{PT,W3,i}$ | Edge distance of the i-th post-tensioning bar in Wall 3. |
| $d_{UFP,i}$ | Edge distance of the i-th UFP element. |
| $d_{UFP,W1i}$ | Edge distance of the i-th UFP element in Wall 1. |
| $d_{UFP,W2i}$ | Edge distance of the i-th UFP element in Wall 2. |
| $d_{UFP,W3i}$ | Edge distance of the i-th UFP element in Wall 3. |
| $d_{2,j}$ | Relative in-plane joint displacement for $\theta_j$ imposed base rotation angle. |
| $d_{3,j}$ | Relative orthogonal joint displacement between Wall 1 and Wall 3 for $\theta_j$ imposed base rotation angle. |
| $d_{4,j}$ | Relative orthogonal joint displacement between Wall 2 and Wall 4 for $\theta_j$ imposed base rotation angle. |
| $D_u$ | Average radius of the UFP. |
| $E_{conn}$ | Timber connection elastic modulus. |

| | |
|---|---|
| $E_D$ | Total energy dissipation. |
| $E_0$ | Modulus of elasticity parallel to the timber grain. |
| $E_{o-End}$ | Modulus of elasticity considering end effect of timber fibers. |
| $E_0 I_{eff,\gamma}$ | The effective flexural stiffness considering the 'gamma method'. |
| $E_{PT}$ | Post-tensioning bar modulus of elasticity. |
| $E_s$ | Mild steel modulus of elasticity. |
| F | Force. |
| $F_{PD}$ | Force at peak drift. |
| $f_{ax}$ | Withdrawal strength. |
| $F_{ax}$ | Self-tapping screw withdrawal capacity. |
| $F_A$ | Analytical strength prediction. |
| $F_{A,S,i}$ | Analytical strength prediction for a self-tapping screw installed at 90° to the timber grain. |
| $F_{A,SC,i}$ | Analytical strength prediction for a shear-compression self-tapping screw. |
| $F_{A,ST,i}$ | Analytical strength prediction for a shear-tension self-tapping screw. |
| $F_{A,X,i}$ | Analytical strength prediction for a self-tapping screw pair arranged in 'X' arrangement. |
| $F_{A,X+S,i}$ | Analytical strength prediction for a self-tapping screws installed in 'X' and at 90° arrangements to the timber grain. |
| $f_c$ | Compression strength parallel to grain. |
| $f_{c,90}$ | Compression strength perpendicular to grain. |
| $F_d$ | Design strength. |
| $F_{est}$ | Estimated maximum connection strength. |
| $f_{h,\varphi}$ | Embedment strength with angle $\varphi$ between embedment force and timber grain. |
| $f_{h,k}$ | Characteristic embedment strength. |
| $f_{h,0.05}$ | 5$^{th}$ percentile embedment strength. |
| $f_{h,0.95}$ | 95$^{th}$ percentile embedment strength. |
| $F_k$ | Characteristic strength. |
| $F_{max}$ | Maximum strength. |
| $F_{max,theo,k}$ | Theoretical maximum strength. |
| $f_{rs}$ | Rolling shear strength. |
| $f_y$ | Steel yield strength. |
| $f_{y,pt}$ | Post-tensioning bar yield stress. |

| | |
|---|---|
| $f_{y,s}$ | Mild steel yield stress. |
| $f_{y,UFP}$ | Yield stress of the UFP. |
| $f_{u,pt}$ | Post-tensioning bar ultimate stress. |
| $f_v$ | Longitudinal shear strength stress. |
| $F_v$ | Longitudinal shear strength force. |
| $F_{rs,out}$ | Rolling shear strength force for an outer CLT layer. |
| $F_{rs,in}$ | Rolling shear strength force for an inner CLT layer. |
| $F_c$ | Compression parallel to grain strength force. |
| $F_{fr,2,j}$ | Friction force at in-plane joint for $\theta_j$ imposed base rotation angle. |
| $F_J$ | Castellated joint strength. |
| $\mathrm{F_{y,UFP}}$ | Yield force of the UFP. |
| $F_{100\%,\delta}$ | Theoretical force for a fully composite section at wall drift $\delta$. |
| $F_{0\%,\delta}$ | Theoretical force for a fully non-composite section at wall drift $\delta$. |
| $F_{Test,\delta}$ | The measured force at a wall drift $\delta$. |
| $F_{STS,2,j}$ | Self-tapping screw coupling force at the in-plane joint for $\theta_j$ imposed base rotation angle. |
| $F_{STS,3,j}$ | Self-tapping screw coupling force at the orthogonal joint between Wall 1 and Wall 3 for $\theta_j$ imposed base rotation angle. |
| $F_{STS,4,j}$ | Self-tapping screw coupling force at the orthogonal joint between Wall 2 and Wall 4 for $\theta_j$ imposed base rotation angle. |
| $F_u$ | Ultimate strength defined as post-peak 80% $F_{max}$. |
| $\mathrm{F_{UFP,Wk,i,j}}$ | Yield force of UFP 'i' on Wall 'k' for $\theta_j$ imposed base rotation angle. |
| $F_y$ | Yield strength. |
| $F_0$ | Foschi model parameter for force. |
| $f_1$ | Withdrawal parameter. |
| $f_{1,EC5}$ | Withdrawal parameter as per Eurocode 5. |
| $f_{1,SPAX}$ | Withdrawal parameter as per SPAX European Technical Approval. |
| $f_{1,U\&B}$ | Withdrawal parameter as per Uibel and Blaβ model. |
| $f_{1,R}$ | Withdrawal parameter as per Ringhofer model. |
| $F_{10}$ | 10% maximum force. |
| $F_{40}$ | 40% maximum force. |
| $F_{0.05}$ | 5$^{th}$ percentile of strength distribution. |
| $F_{0.95}$ | 95$^{th}$ percentile of strength distribution. |

| | |
|---|---|
| $G_0$ | Modulus of shear rigidity. |
| $G_{eff}$ | Effective shear modulus. |
| $G_{RS}$ | Modulus of rolling shear. |
| $G_{RS,out,i}$ | Tenon rolling shear strength for the applicable outer CLT layer 'i'. |
| $G_{RS,in,i}$ | Tenon rolling shear strength for the applicable inner CLT layer 'i'. |
| h | Wall length. |
| $H_T$ | Tenon height. |
| $I_{eff}$ | Effective second moment of inertia for the CLT wall section. |
| k | Stiffness. |
| $k_{sec}$ | Secant stiffness. |
| $k_{SLS,sec}$ | Secant stiffness at SLS drift |
| $K_{PD,sec}$ | Secant stiffness at peak drift |
| $k_{ax,k}$ | Withdrawal parameter as per Ringhofer model to account for screw angle. |
| $k_{ax,gap}$ | Withdrawal parameter as per Ringhofer model to account for lamination gap. |
| $K_A$ | Tenon combined stiffness for failure plane A. |
| $K_B$ | Tenon combined stiffness for failure plane B. |
| $K_C$ | Tenon combined stiffness for failure plane C. |
| $K_{A,S}$ | Analytical stiffness prediction for shear self-tapping screw. |
| $K_{A,ST}$ | Analytical stiffness prediction for shear-tension self-tapping screw. |
| $K_{A,SC}$ | Analytical stiffness prediction for shear-compression self-tapping screw. |
| $k_{ax,sp}$ | Analytical axial stiffness prediction for threaded portion of the self-tapping screw on the side panel side. |
| $k_{ax,mp}$ | Analytical axial stiffness prediction for threaded portion of the self-tapping screw on the middle panel side. |
| $K_{A,STS}$ | Analytical stiffness prediction of self-tapping screw group using empirical lateral and axial stiffness equations as input components. |
| $K_{A/EXP.}$ | Analytical stiffness prediction of self-tapping screw group using experimental lateral and axial stiffness values as input components. |
| $k_{el,exp.}$ | Experimental elastic stiffness. |
| $k_{el,pred}$ | Eurocode 5 predicted stiffness, $k_{ser}$. |
| $K_{E_0}$ | Tenon parallel to grain stiffness. |
| $K_{E_{0,Flange,j}}$ | Flange wall stiffness parallel to grain to Winkler Spring Analogy. |
| $K_{E,o,WSA}$ | Parallel to grain stiffness according to Winkler Spring Analogy. |

| | |
|---|---|
| $\mathrm{K_{Flange,j}}$ | Flange wall stiffness to Winkler Spring Analogy for $\theta_j$ imposed base rotation angle. |
| $K_{G_0}$ | Tenon longitudinal shear stiffness. |
| $k_{gap}$ | Modulus of elasticity adjustment factor to account for end-effect. |
| $K_{G_{RS,in,i}}$ | Tenon rolling shear stiffness for the applicable inner CLT layer 'i'. |
| $K_{G_{RS,out,i}}$ | Tenon rolling shear stiffness for the applicable outer CLT layer 'i'. |
| $k_{mod}$ | Load duration factor according to Eurocode 5. |
| $k_{PT,i,j}$ | Stiffness of the 'i-th' PT bar for $\theta_j$ imposed base rotation angle. |
| $k_{ser}$ | Stiffness at serviceability limit state. |
| $k_{STS,2,j}$ | The stiffness of a single self-tapping screw fastener for a given displacement, $\mathrm{d_{2,j}}$. |
| $K_{STS,2,j}$ | The total stiffness of the in-plane joint for a given displacement, $\mathrm{d_{2,j}}$. |
| $k_{STS,3,j}$ | The stiffness of a single self-tapping screw fastener for a given displacement, $\mathrm{d_{3,j}}$. |
| $K_{STS,3,j}$ | The total stiffness of the orthogonal joint for a given displacement, $\mathrm{d_{3,j}}$. |
| $k_{STS,4,j}$ | The stiffness of a single self-tapping screw fastener for a given displacement, $\mathrm{d_{4,j}}$. |
| $K_{STS,4,j}$ | The total stiffness of the orthogonal joint for a given displacement, $\mathrm{d_{4,j}}$. |
| $\mathrm{K_{STS,j}}$ | Orthogonal joint stiffness to Winkler Spring Analogy. |
| $k_{sys,k}$ | Withdrawal parameter as per Ringhofer model to account for system effects. |
| $k_{UFP,i,j}$ | Stiffness of the 'i-th' UFP element for $\theta_j$ imposed base rotation angle. |
| $\mathrm{K_{Web,j}}$ | Web wall stiffness parallel to grain to Winkler Spring Analogy for $\theta_j$ imposed base rotation angle. |
| $K_0$ | Foschi model parameter for initial stiffness. |
| $k_{\perp}$ | Lateral self-tapping screw stiffness. |
| $k_{\parallel}$ | Axial withdrawal self-tapping screw stiffness. |
| $k_{\rho}$ | Withdrawal parameter as per Ringhofer model to account for screw angle. |
| $k_{13}$ | End grain factor. |
| $k_{15}$ | In service moisture condition factor. |
| $L$ | Dowel length. |
| $L_{cant}$ | Cantilever wall length. |
| $l_{nom}$ | Nominal self-tapping screw installation length. |
| $l_{ef}$ | Effective thread embedment length. |
| $\mathrm{L_{eff,j}}$ | Effective length of timber parallel to grain for Winkler Spring Analogy. |
| $l_{emb}$ | Embedment length of the unthreaded portion of a partially threaded screw. |
| $l_{tip}$ | STS tip length. |

| | |
|---|---|
| $L_T$ | Tenon length. |
| $l_{ub,i}$ | Unbonded length of the i-th post-tensioning bar. |
| $\mathrm{M}_{conn,\mathrm{j}}$ | Total base connection moment for $\theta_j$ imposed base rotation angle. |
| $M_{dec}$ | Decompression moment. |
| $M_{pt}$ | Base connection moment due to the post-tensioning bars. |
| $M_s$ | Base connection moment due to the dissipative elements. |
| $M_T$ | Total base connection moment. |
| $M_{y,k}$ | Characteristic yield moment. |
| $M_{y,mean}$ | Mean yield moment. |
| $\mathrm{M}_{\mathrm{y,eff}}$ | Effective yield moment. |
| $M_{y,p}$ | Plastic yield moment. |
| $\mathrm{M}_{\mathrm{y,UFP}}$ | UFP yield moment. |
| $\mathrm{M}_{\mathrm{w,i,j}}$ | Base connection moment of the i-th wall for $\theta_j$ imposed base rotation angle. |
| $n_A$ | Number of instances of $K_A$ failure plane. |
| $n_B$ | Number of instances of $K_B$ failure plane. |
| $n_C$ | Number of instances of $K_C$ failure plane. |
| $n_d$ | Number of dowels. |
| $n_{L,0}$ | Number of CLT layers oriented parallel to the loading direction. |
| $n_{s,in}$ | Number of inner rolling shear planes. |
| $n_{s,out}$ | Number of outer rolling shear planes. |
| $n_S$ | Number of shear self-tapping screws. |
| $n_{sp}$ | Number of shear planes. |
| $n_{ST}$ | Number of shear-tension self-tapping screws. |
| $n_{SC}$ | Number of shear-compression self-tapping screws. |
| $n_{STS,2}$ | The number of self-tapping screws along the in-plane joint. |
| $n_{STS,3}$ | The number of self-tapping screws along the orthogonal joint. |
| $n_{STS,4}$ | The number of self-tapping screws along the orthogonal joint. |
| $N$ | Axial force from gravity loading. |
| $R_{a,i}$ | Self-tapping screw axial strength for panel side 'i'. |
| $R^*_{a,i}$ | Shear-compression self-tapping screw axial strength for panel side 'i'. |
| $R_{v,i}$ | Self-tapping screw shear strength for panel side 'i'. |
| $R^*_{v,i}$ | Shear-compression self-tapping screw shear strength for panel side 'i'. |
| $r_1$ | Foschi model parameter for ascending branch |

| | |
|---|---|
| $r_2$ | Foschi model parameter for descending branch stiffness. |
| $s_i$ | Spacing of the fastener for 'Gamma Method'. |
| t | The time step identification of each image frame in particle tracking technology. |
| $t_b$ | Average thickness of the CLT lamella. |
| $t_{CLT}$ | Thickness of CLT panel. |
| $t_L$ | Thickness of individual CLT layer. |
| $T_{L,0}$ | Thickness of the outer / longitudinal CLT layer. |
| $T_{L,90}$ | Thickness of the cross CLT layer. |
| $T_{PT,Wk,i,j}$ | Post-tensioning force in the i-th bar on Wall 'k' for $\theta_j$ imposed base rotation angle. |
| $T_{PT,0,i}$ | Initial post-tensioning force in the i-th bar. |
| $t_u$ | UFP thickness. |
| $w_{GAP}$ | Width of gap between CLT lamella. |
| $w_L$ | Width of individual CLT lamella. |
| $X_m$ | Mean joint performance parameter. |
| x | Cartesian coordinate system horizontal axis. |
| $x_1$ | Length of zero stress zone for self-tapping screw joints with angle to the timber grain. |
| y | Cartesian coordinate system vertical axis. |
| $Z$ | Elastic section modulus. |
| | |
| $\alpha$ | Primary self-tapping screw installation angle. |
| $\beta$ | Recentering parameter for post-tensioned systems. |
| $\chi$ | Ratio of middle panel and side panel embedment strength. |
| $\Delta\epsilon_{pt,i}$ | Change in strain of the i-th post-tensioning bar. |
| $\Delta T_{pt,i}$ | Change in force of the i-th post-tensioning bar. |
| $\Delta_{PT,i,j}$ | Elongation of the i-th post-tensioning bar for $\theta_j$ imposed base rotation angle. |
| $\Delta_{UFP,i,j}$ | Elongation of the i-th UFP element for $\theta_j$ imposed base rotation angle. |
| $\Delta\theta$ | Incremental wall base rotation. |
| $\Delta_y$ | Yield displacement. |
| $\Delta_{Fmax}$ | Displacement at maximum strength. |
| $\Delta_{Fu}$ | Displacement at ultimate strength. |
| $\Delta_{F_{40}}$ | Connection slip at 40% maximum strength. |

| | |
|---|---|
| $\Delta_{F_{10}}$ | Connection slip at 10% maximum strength. |
| $\delta$ | Wall drift. |
| $\delta_r$ | Rocking deformation component. |
| $\delta_b$ | Bending deformation component. |
| $\delta_s$ | Shear deformation component. |
| $\delta_T$ | Total deformation. |
| $\delta_{r,w1}$ | Rocking deformation percentage of total Wall 1 drift. |
| $\delta_{sl,w1}$ | Sliding deformation percentage of total Wall 1 drift. |
| $\delta_{b+s,w1}$ | Bending and shear deformation percentage of total Wall 1 drift. |
| $\varepsilon$ | Secondary self-tapping screw installation angle. |
| $\varepsilon_t$ | Timber strain. |
| $\eta$ | The ratio between inclined self-tapping screw and self-tapping screw installed at 90°. |
| $\gamma$ | Gamma factor for composite sections. |
| $\gamma_l$ | Longitudinal shear strain. |
| $\gamma_{s-t}$ | Stiffness factor which is 2 for steel-timber connections and 1 for timber-timber connections. |
| $\gamma_{Rd}$ | Experimental overstrength. |
| $\gamma_{Rd,theo}$ | Theoretical overstrength. |
| $\gamma_M$ | Material safety factor. |
| $\gamma_{0.95}$ | Overstrength attributed to the strength distribution. |
| $\gamma_{an}$ | Overstrength attributed to differences between analytical models and 5-th percentile strength. |
| $\gamma_{an,My}$ | Analytical overstrength attributed to the yield moment determination. |
| $\gamma_{0.95,My}$ | Overstrength attributed to the strength distribution of the yield moment. |
| $\gamma_{an,fh}$ | Analytical overstrength attributed to the embedment strength determination. |
| $\gamma_{0.95,fh}$ | Overstrength attributed to the strength distribution of the embedment strength. |
| $\lambda$ | STS slenderness ratio ($L / d_c$). |
| $\varphi$ | Angle between the screw axis and timber grain direction. |
| $\varphi_{\|\|}$ | Angle between the screw axis and outer CLT layer timber grain direction. |
| $\varphi_{\perp}$ | Angle between the screw axis and cross CLT layer timber grain direction. |
| $\varphi_{RS}$ | Rolling shear strain. |
| $\varphi_{out}$ | Rolling shear strain for the outer CLT layers. |

| | |
|---|---|
| $\varphi_{in}$ | Rolling shear strain for the inner CLT layers. |
| $\phi$ | Diameter. |
| $\phi_{dec}$ | Decompression curvature. |
| $\phi_t$ | Timber strain amplification factor. |
| $\psi$ | Friction co-efficient for wood-wood surfaces. |
| $\mu$ | Connection ductility. |
| $\nu_{PT}$ | Yield percentage of the extreme PT bar. |
| $\nu_T$ | Yield strain percentage of the extreme timber fibre value. |
| $\nu_{PT,web}$ | Yield percentage of the extreme PT bar in a Web Wall. |
| $\nu_{PT,fl}$ | Yield percentage of the extreme PT bar in a Flange Wall. |
| $\omega_u$ | Displacement at maximum force as per Foschi model. |
| $\omega_f$ | Final displacement as per Foschi model. |
| $\rho_k$ | Characteristic density. |
| $\rho_m$ | Mean density. |
| $\rho_{ref}$ | Reference timber density. |
| $\tau_l$ | Longitudinal shear stress. |
| $\tau_{RS}$ | Rolling shear stress. |
| $\theta$ | Angle between the embedment force and timber grain direction. |
| $\theta_{\|\|}$ | Angle between the embedment force and outer CLT layer timber grain direction. |
| $\theta_{\perp}$ | Angle between the embedment force and cross CLT layer timber grain direction. |
| $\theta_j$ | Imposed base connection rotation. |
| $\theta_{j+1}$ | Following wall base rotation. |
| $\emptyset_{ax,w}$ | Screw withdrawal reduction factor. |
| $sgn(\omega)$ | Signum function to extract the sign of the displacement, $\omega$. |
| $\xi$ | Equivalent viscous damping. |
| $\sum T_{PT,wi}$ | Sum of post-tensioning bar force for the applicable wall, i. |
| $\sum T_{PT,o,wi}$ | Sum of the initial post-tensioning bar force for the applicable wall,i. |

# 1 Introduction

## 1.1 RESEARCH MOTIVATION

Timber is experiencing a renaissance as a building material. There is a renewed interest in utilizing timber as a primary construction material due in part to its positive environmental, aesthetic, and biophilic effects (Kotradyova et al., 2019). Recent technological advancements and socio-economic factors have generated an interest in timber buildings globally (Dangel, 2016). Recent taller timber buildings worldwide have often utilized the hybrid solutions of mixed materials where reinforced concrete (RC) or steel systems are used to resist lateral loads, and timber to resist gravity loads. A lack of experimental evidence and prescriptive guidelines and design methods which reflect state-of-the-art possibilities in timber are in part limiting further application of timber as a lateral load resisting system (LLRS), especially for taller timber buildings in seismic regions.

### 1.1.1 History of Timber Design and Construction

In the early 1900s in North America, the first mass timber buildings which have resemblance to what we call mass timber construction today were built. It was a system of choice due to the vast availability of large dimensional sawn timber sourced from old growth forests. Figure 1-1a shows the 9 storey Butler Building constructed in 1906 and still in use today, which has solid sawn Douglas-Fir (610mm x 610mm) columns at the ground level. These solid timber 'tooth picks', as advertised and shown in Figure 1-1b, could reach dimensions as large as 900mm x 900mm x 18m long, and were a primary construction material in many mass timber warehouse buildings across North America (Square, 2021).

(a) (b)

*Figure 1-1: (a) Butler Building* (Square, 2021)*, and (b) old growth forest logging* (Vancouver Public Library, n.d.)

Due in part to the diminished availability of old growth forests and large cross section timber, timber construction primarily shifted to residential housing, generally referred to as light timber frame (LTF)

construction. LTF construction uses small dimension lumber as vertical framing members to resist gravity loads with wood-based structural panels, which is used for the LLRS (Li et al., 2009). Nowadays, LTF construction is very popular in North America and Oceania. Design codes today allow LTF construction up to 3 stories in New Zealand and up to 6 stories in jurisdictions such as Canada as shown in Figure 1-2a (Canadian Wood Council, 2021). Figure 1-2b shows a logging photo of 25-30 year old New Zealand Radiata Pine logs with diameter of approximately 600mm. These logs could be sawn to small dimensional lumber for LTF construction. Because many walls are generally required, LTFs are unsuitable for commercial buildings which require larger open spaces.

(a) (b)

*Figure 1-2: (a) 6-storey LTF in Canada* (On-Site, 2015)*, and (b) logging photo of New Zealand Radiata Pine c/o Andy Buchanan*

The advancement of Engineered Wood Products (EWPs), wherein smaller lamella or veneers are glued together to make large solid timber members, has dramatically changed the landscape in which timber can be used. With EWPs, large dimension solid timber members can be produced, which has in part facilitated a shift back to traditional heavy timber construction, but now with new design and construction methodologies. Figure 1-3 shows some EWPs which include glulam, laminated veneer lumber (LVL), cross-laminated timber (CLT), and parallel strand lumber (PSL).

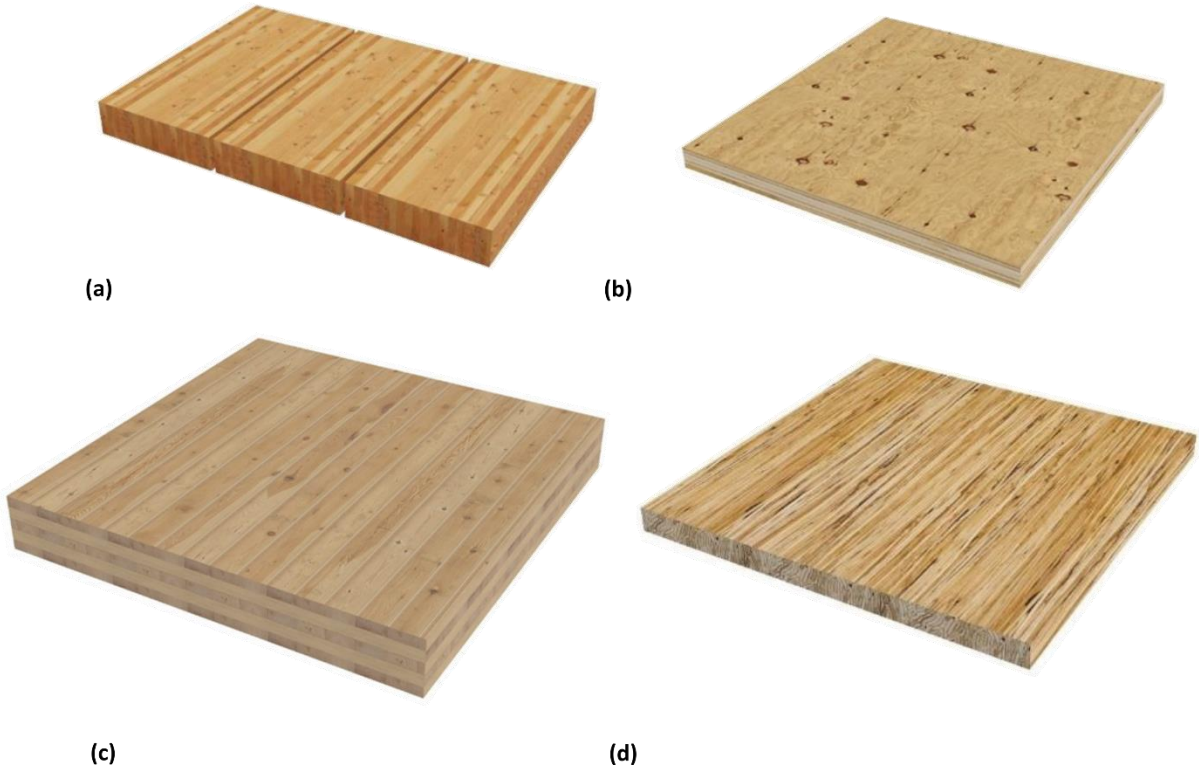


*Figure 1-3: Engineered wood products: (a) glulam, (b) laminated veneer lumber, (c) cross-laminated timber, (d) parallel strand lumber (c/o of StructureCraft Builders Inc.)*

### 1.1.2 Rise of Mass Timber Buildings Using EWPs

In the last few decades, mass timber construction has gained popularity globally due in part to the increased availability and cost efficiency of EWPs and in particular CLT (Green & Taggart, 2017). While an initial lack of awareness of CLT hindered its implementation in regions outside Europe (Laguarda Mallo & Espinoza, 2015), CLT is now a global product with exponential growth forecasted throughout the 2020s (Muszynski, 2020). Figure 1-4 shows the 9 storey Murray Grove CLT mass timber building which was constructed in the United Kingdom in 2009 and one of the early built examples of this construction type which implements a CLT LLRS.

*Figure 1-4 Murray Grove* (KLH, 2009)

Under seismic loads, conventional and planar CLT shear walls with properly designed connection systems are able to provide adequate capacity as a LLRS for multi-storey buildings. However, in the cases of open commercial floor plans or taller buildings, conventional CLT shear walls may struggle to achieve the required strength and stiffness performance with current design methodologies. Further, the inherent timber material properties such as relatively low stiffness (approximately ¼ of reinforced concrete) and possible brittle behaviour make it more challenging for ductile lateral design of taller timber building, especially in high seismic regions.

To overcome these challenges, one possibility is to adopt hybrid systems with steel or RC. This is now a commonly implemented building typology. Mass timber members are used for the gravity load system while RC shear walls or steel-bracing are implemented for the LLRS. Figure 1-5a and Figure 1-5b show recently completed examples of hybrid buildings which employed RC and steel-braced LLRS respectively.


**(a)** **(b)**

*Figure 1-5 (a) T3 Minneapolis building with RC core-wall LLRS modified from* (StructureCraft, 2016)*, and (b) T3 Atlanta building with steel-braced LLRS modified from* (StructureCraft, 2019)

To overcome the inherent flexibility of timber structures, Buchanan (2016) stated that another possible solution is to introduce flanged core-walls that can develop composite action among in-plane and orthogonal walls to enhance lateral strength and stiffness. As such, there have been recent explorations and few rare built examples of CLT core-wall LLRS systems. Figure 1-6a shows the floor plan for the conceptual design of Cathedral Hill II project which utilized an I-shaped mass timber core-wall LLRS. Figure 1-6b shows the recently completed Catalyst building (Katerra, 2021) which is believed to be the first implementation of a CLT core-wall as the LLRS.


*Figure 1-6: (a) Cathedral Hill II concept design* (Below & Sarti, 2016)*, and (b) Catalyst building modified from* (Katerra, 2021)

In New Zealand and starting in 2005, post-tensioned (PT) timber technology (called Pres-Lam) has been developed and tested (Palermo et al., 2005). Pres-Lam buildings can provide a low-damage seismic design solution for multi-storey mass timber buildings. By adopting similar concepts and principles originally developed for precast concrete structures (Priestley, 1991), it uses unbonded PT tendons to provide moment capacity at the wall base through clamping action and desirable re-centering properties. Energy dissipation devices allow adequate energy dissipation and provide increased moment capacity under lateral loading. Figure 1-7 shows the controlled rocking mechanism of a Pres-Lam wall with the post-tensioning element shown in blue and energy dissipaters shown in red.

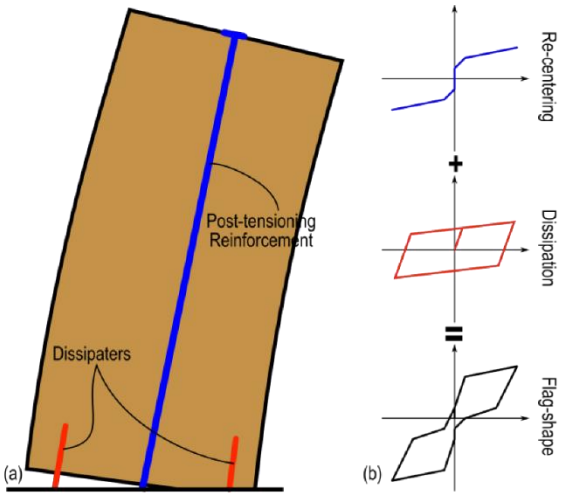


*Figure 1-7: Pres-Lam wall controlled rocking with flag-shaped hysteresis loop* (Sarti, 2015)

Completed in 2016, the Kaikōura Civic Centre shown in Figure 1-8 was the first building to use Pres-Lam CLT walls. The building had its lateral strength tested directly by the 2016 Kaikōura Earthquake as the building location is very close to the epicentre. The Pres-Lam CLT LLRS system worked successfully and the building was used as a post-disaster headquarter for military, police and hospital staff (XLam NZ Limited, 2017).


**(a)** **(b)**

*Figure 1-8: Kaikōura Civic Centre Pres-Lam CLT wall building (image (a) c/o Andy Buchanan and (b) Pres-Lam* (2018)

### 1.1.3 Research Focus

The main focus of this research is on the development of a PT CLT core-wall system as a LLRS. While the flanged core-wall concept is common and well-developed for reinforced concrete structures (Beyer et al., 2008; Khan & Sbarounis, 1964), few studies for mass timber core-wall buildings were reported. There has been a recently built CLT core-wall LLRS example (Katerra, 2021); however, in general a lack of design guidelines and the challenge of forming enhanced connections between orthogonal walls to achieve composite action are hindrances to further application of this system. A PT CLT core-wall system could provide one effective LLRS which is also a low-damage seismic design solution. Experimental testing of critical CLT core-wall connections and large scale CLT core-wall subassembly testing is required to further validate this type of new mass timber wall structures. Then, the development of practical analytical modelling validated by experimental results can serve as a fundamental first step for its application in mass timber buildings.

## 1.2 RESEARCH OBJECTIVES

The main objective of this Ph.D. research was to define the structural performance of a CLT core-wall LLRS based on its connection details. To address this objective, three main sections were defined which were then broken down into the following specific research objectives and tasks.

### Objective I: To evaluate the behaviour of critical connections for CLT core-wall systems.

I.I. Prerequisite: Determine critical joint and possible connection solutions.

Figure 1-9 shows a C-shaped core-wall system with vertical orthogonal and in-plane joints and horizontal joints. The three critical connections to investigate included: (1) dowelled hold-down joints between lower wall panels and upper wall panels, (2) screwed orthogonal joints, and (3) castellated timber-timber connections for horizontal shear joints.

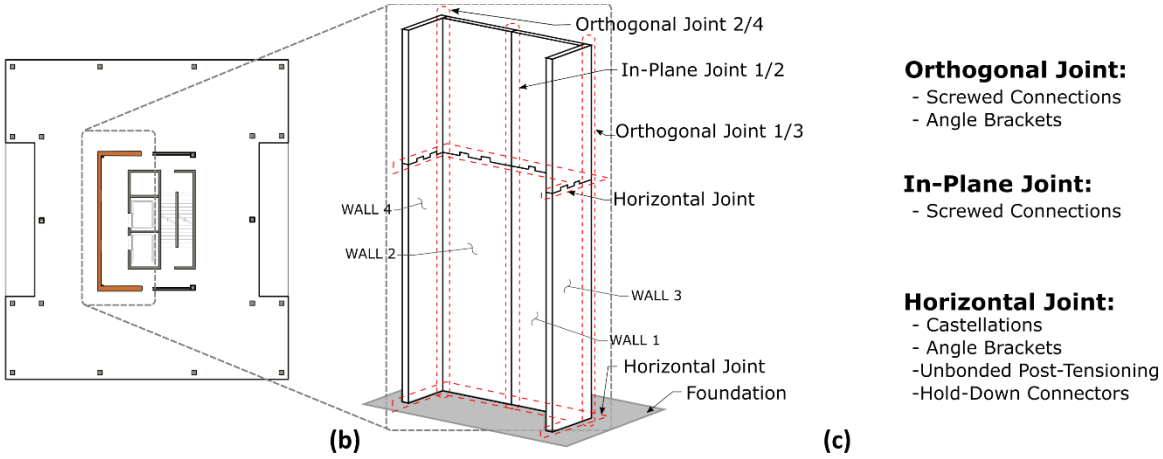


*Figure 1-9: Core-wall system research plan: (a) plan view building adopted from* (Green, 2017)*, (b) isometric of four wall core-wall system with key joints, and (c) joint options investigated*

I.II. Assessment of dowelled hold-down connections.

The following research tasks were defined to achieve this objective:

- Investigate the influence of increased fastener row spacing and end distance on strength, stiffness, ductility, and overstrength.
- Investigate benefits of applying reinforcement techniques to delay onset of brittle failure.
- Perform embedment testing and dowel bending tests to inform analytical connection strength prediction models.
- Derive experimental overstrength factors for the Douglas-Fir CLT hold-down connections and compare results to past research.

I.III. Assessment of orthogonal CLT panel joints with varying mixed angle self-tapping screws (STS) combination ratios, η.

The following research tasks were defined to achieve this objective:

- Investigate through experiments the influence of η ratio to determine which STS combinations could provide enhanced seismic performance.
- Evaluation of STS withdrawal testing to inform analytical prediction models and sources of overstrength.
- Assess applicability of state-of-art analytical strength and stiffness models for orthogonal CLT joints with mixed angle STS.

I.IV. Evaluation of mortise and tenon castellated CLT joints.

The following research tasks were defined to achieve this objective:

- Compare experimental strength and stiffness of castellated CLT joints to commercial angle shear brackets.
- Develop an analytical method to predict the load-carrying capacity of CLT castellated joints.
- Perform material property testing of New Zealand Douglas-Fir to verify the analytical strength method.

## Objective II: To experimentally assess the structural performance of post-tensioned CLT core-wall systems

The following research tasks were defined to achieve this objective:

- Design three phase PT wall testing programme to decouple core-wall system. The phases included: (1) single wall testing, (2) double wall testing, and (3) core-wall testing.
- Implement Particle Tracking Technology (PTT) in order to capture complex displacement and strain fields of PT CLT shear wall systems.
- Quantify and optimize core-wall system performance when changing STS vertical joint details.
- Experimentally compare the performance between PT CLT core-wall systems and conventional CLT core-wall systems.

### Objective III: To develop analytical prediction models for post-tensioned CLT wall systems

The following research tasks were defined to achieve this objective:

- Refine PT CLT single wall analytical model through PTT results of compressive strain fields at the wall base.
- Develop PT CLT double wall analytical models to capture different possible kinematic modes which depend on STS vertical joint details.
- Develop PT CLT core-wall analytical models to capture different possible kinematic modes which depend on STS orthogonal and in-plane joint details.

## 1.3 THESIS STRUCTURE

A visual representative of the thesis structure and its objectives is shown in Figure 1-10.

In Chapter 2, a comprehensive literature review of relevant CLT connections and CLT LLRS is provided. Chapters 3, 4 and 5 present the experimental testing of three different types of CLT connections. Chapter 3 presents the assessment of CLT dowelled hold-down connections with one slotted-in steel plate. Experimental tests are compared with existing design equations. In Chapter 4, experimental testing of CLT orthogonal connections with STS installed at mixed angles is presented. STS withdrawal tests are also presented and compared to existing design equations. The STS connection test results are compared to existing analytical models in literature. Chapter 5 presents the experimental testing of CLT shear connections with mortise and tenon castellated joints in comparison to commercial angle brackets. Material property testing are performed to verify a proposed component-based analytical model to predict castellation strength.

In Chapter 6, the experimental design and testing of PT and conventional CLT shear walls and core-walls are presented. The experimental results of 17 experimental wall specimen tests are discussed.

In Chapter 7, updates on the existing analytical models for PT CLT single walls are presented. In Chapters 8 and 9, analytical models are proposed to capture the behaviour of PT CLT double wall and core-wall systems coupled with STS along the vertical in-plane and orthogonal joints. The analytical models are validated by the experimental wall testing results presented in Chapter 6.

Finally, in Chapter 10 the key research findings and summary of contributions from each research phase are presented. Future research needs are also outlined for CLT connections and CLT shear wall and core-wall systems as a LLRS in mass timber buildings.

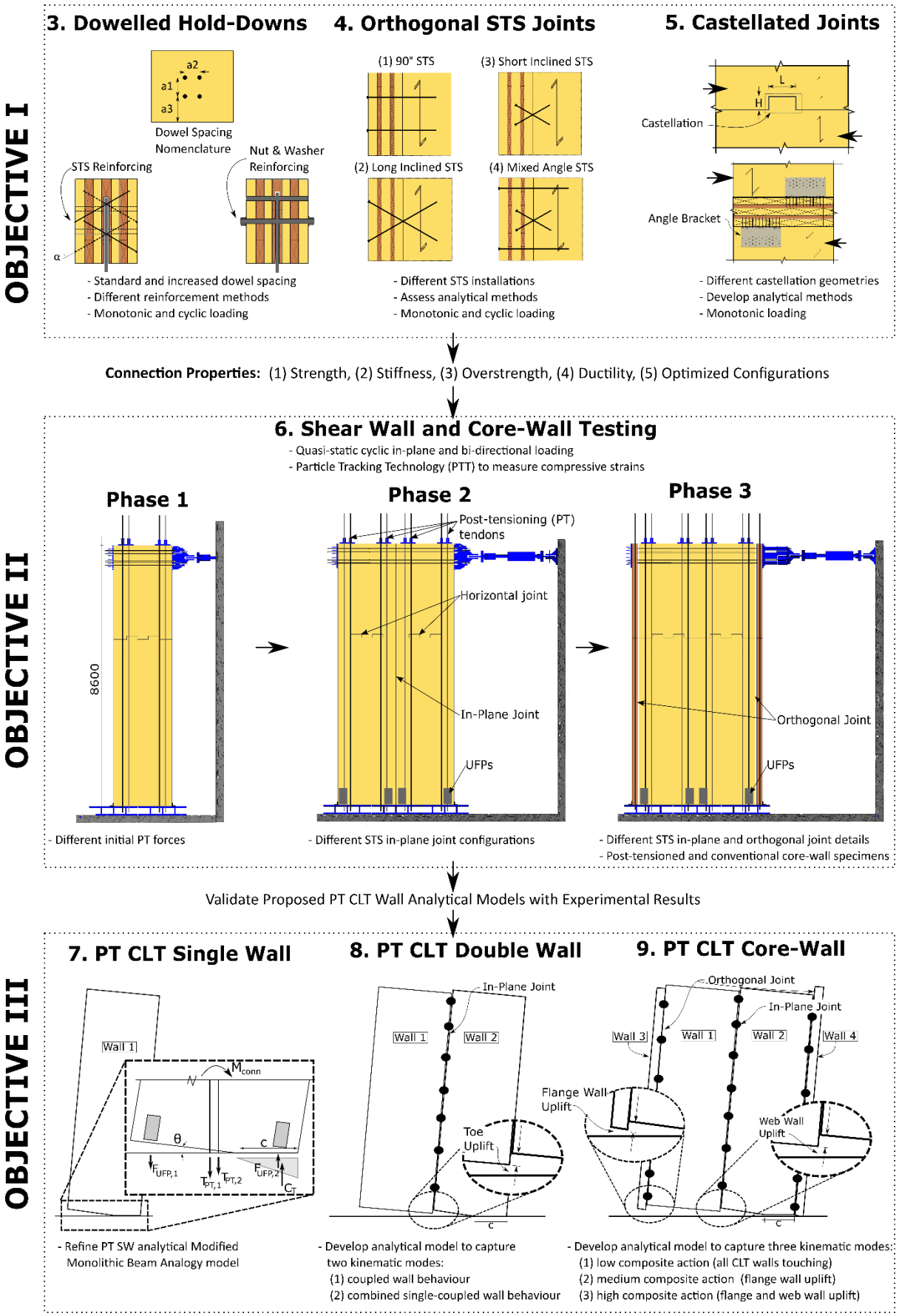


*Figure 1-10: Visual representation of thesis structure and objectives*

## 1.4 REFERENCES

Below, K., & Sarti, F. (2016). Cathedral hill 2: Challenges in the design of a tall all-timber building. *WCTE 2016 - World Conference on Timber Engineering*.

Beyer, K., Dazio, A., & Priestley, M. J. N. (2008). Quasi-Static Cyclic Tests of Two U-Shaped Reinforced Concrete Walls. *Journal of Earthquake Engineering*, *12*(7), 1023–1053. https://doi.org/10.1080/13632460802003272

Buchanan, A. (2016). The challenges for designers of tall timber buildings. *WCTE 2016 - World Conference on Timber Engineering*.

Canadian Wood Council. (2021). *Mid-Rise Building*. https://cwc.ca/how-to-build-with-wood/building-systems/mid-rise-buildings/

Dangel, U. (2016). *Turning Point In Timber Construction: A New Economy* (1st ed.). Birkhauser.

Green, M. (2017). *The case for tall wood buildings: how mass timber offers a safe, economical, and environmentally friendly alternative for tall building structures* (2nd ed., Issue Book, Whole). MGA.

Green, M., & Taggart, J. (2017). *Tall wood buildings: design, construction and performance*. Birkhauser.

Katerra. (2021). *Catalyst*. https://katerra.com/projects/catalyst-building/

Khan, F. R., & Sbarounis, J. A. (1964). Interaction of shear walls and frames in concrete structures under lateral loads. *American Society of Civil Engineers*, *90*.

KLH. (2009). *Murray Grove*. https://www.klh.at/en/references/murray-grove/

Kotradyova, V., Vavrinsky, E., Kalinakova, B., Petro, D., Jansakova, K., Boles, M., & Svobodova, H. (2019). Wood and its impact on humans and environment quality in health care facilities. *International Journal of Environmental Research and Public Health*, *16*(18). https://doi.org/10.3390/ijerph16183496

Laguarda Mallo, M. F., & Espinoza, O. (2015). Awareness, perceptions and willingness to adopt Cross-Laminated Timber by the architecture community in the United States. *Journal of Cleaner Production*, *94*, 198–210. https://doi.org/10.1016/j.jclepro.2015.01.090

Li, M., Lam, F., & Foschi, R. O. (2009). Seismic reliability analysis of diagonal-braced and structural-panel- sheathed wood shear walls. *Journal of Structural Engineering*, *135*(5), 587–596. https://doi.org/10.1061/(ASCE)ST.1943-541X.0000008

Muszynski, L. (2020). Global CLT industry in 2020 : Growth beyond the Alpine Region. *Proc. 63rd Int.*

*Conv. Soc. Wood Sci. Technol., 2020: Pp. 1–8. International Convention of Society of Wood Science and Technology*, *July*, 1–8.

On-Site. (2015). *Quebec launches 12-storey wood building construction guide*. https://www.on-sitemag.com/construction/quebec-launches-12-storey-wood-building-construction-guide/1003764735/

Palermo, A., Pampanin, S., Buchanan, A. H., & Newcombe, M. P. (2005). Seismic design of multi-storey buildings using laminated veneer lumber (LVL). *New Zealand Society for Earthquake Engineering Conference*.

Pres-Lam. (2018). *Kaikoura Civil Centre*. http://pres-lam.com/projects/kaikoura-civic/

Priestley, M. J. N. (1991). Overview of PRESSS research program. *PCI JOURNAL*, *36*(4), 50–57.

Sarti, F. (2015). *Seismic design of low-damage post-tensioned timber wall systems* (Issue PhD Thesis). University of Canterbury.

Square, B. (2021). *Butler Square*. https://www.butlersquare.com/photos.html

StructureCraft. (2016). *T3 Minneapolis Office Building*. https://structurecraft.com/projects/t3-minneapolis

StructureCraft. (2019). *T3 Atlanta Office Building*. https://structurecraft.com/projects/t3-atlanta

Vancouver Public Library. (n.d.). *British Columbia Tooth Picks*. Retrieved from: Vancouver Public Library Archives.

XLam NZ Limited. (2017). *Xlam Rocking Shear Walls Withstand Kaikoura Earthquake*. https://www.eboss.co.nz/ebossnow/xlam-cross-laminated-timber-panels-rocking-shear-walls-seismic-performance

# 2 Literature review

## 2.1 INTRODUCTION

Chapter 2 provides a comprehensive overview of past research relevant to CLT core-wall lateral load resisting systems (LLRS). In Section 2.2, an overview of timber LLRS is presented covering light timber frame (LTF) and then CLT construction. In Section 2.3, relevant research on post-tensioned (PT) timber shear walls is presented and discussed. Section 2.4 discusses the principles of capacity design and ductility which are critical for the implementation of CLT core-wall LLRS in seismic regions. Sections 2.5, 2.6, and 2.7 summarize relevant CLT connection research on dowelled hold-downs, self-tapping screw joints, and then carpentry joints respectively. The relevant literature on core-wall LLRS systems with a focus on CLT core-wall research is presented in Section 2.8.

## 2.2 CROSS-LAMINATED TIMBER LATERAL LOAD RESISTING SYSTEMS

Light timber frame (LTF) construction is very popular in North America and Oceania for low- and mid-rise residential buildings up to 6 storeys (Canadian Wood Council, 2021). In LTF construction, shear walls consisting of light timber framing elements braced by wood-based panels are typically used as the lateral load resisting system (LLRS) against wind and seismic loads. The nailed panel-frame connections are critical components in LTF shear walls and provide the main source of ductility and energy dissipation (Li et al., 2009). Post and beam timber frame construction is widely used in Japan for residential buildings up to 3 storeys in which diagonally braced or panel-sheathed shear walls are typically used as LLRS (Li et al., 2012b, 2012a). In post-and-beam timber buildings, diagonally braced walls can also be used as LLRS and the braces and the associated connections are the critical components that govern the shear wall behaviour (Li et al., 2012b, 2012a). Figure 2-1 shows schematics of these different LTF arrangements.

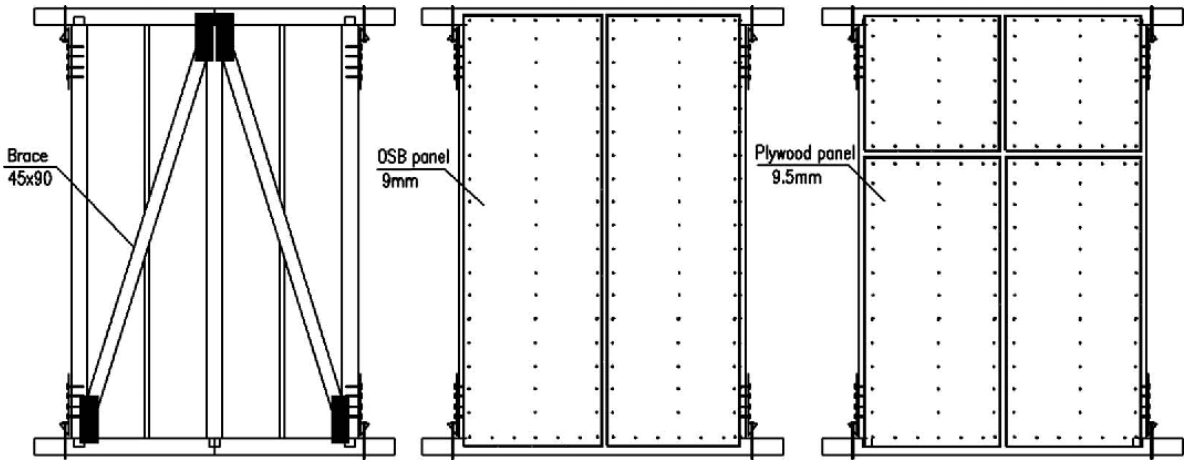


*Figure 2-1: Schematics of double-bracked, oriented strand board (OSB) and plywood sheathed LTF shear walls (photo taken from Li et al.* (2009)*)*

Mass timber construction is gaining popularity globally due to the increased availability and cost efficiency of engineered timber products and the increased demand of using more sustainable construction materials in the built environment (Green & Taggart, 2017). In the last two decades, cross-laminated timber (CLT), manufactured as a mass timber panel product, has attracted great attention and offers a competitive solution for multi-storey residential, commercial and public buildings (Dangel, 2016). Compared to LTF, CLT structures have higher in-plane strength and stiffness (Izzi et al., 2018). CLT is commonly composed of an odd number of layers of timber boards laminated in a crosswise pattern to create large solid timber panels as shown in Figure 2-2 (Brandner et al., 2016).

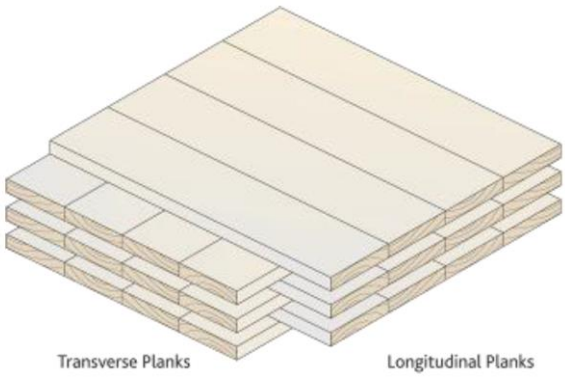


*Figure 2-2: Schematic of cross-laminated timber (CLT) (photo taken from CLT Handbook* (2019)*)*

Performance of CLT shear walls is often governed by connection systems that are designed to transfer shear loads and resist overturning moments under seismic loads (Pei et al., 2016). Dujic et al. (2004) tested the in-plane behaviour of CLT panels; and subsequent research mainly focused on CLT shear walls using commercial LTF connectors (Amini et al., 2018; Flatscher et al., 2015; Gavric et al., 2014, 2015b; Popovski et al., 2010). These standard connectors, shown in Figure 2-3, include commercially available hold-downs and angle brackets which are connected to CLT wall panels mainly with nails and screws. Research has reported that CLT wall panels behave relatively rigid in low- to medium-rise

buildings and that the connections are critical and govern the wall behaviour, typically limiting wall ductility/drift capacity (Izzi et al., 2018).

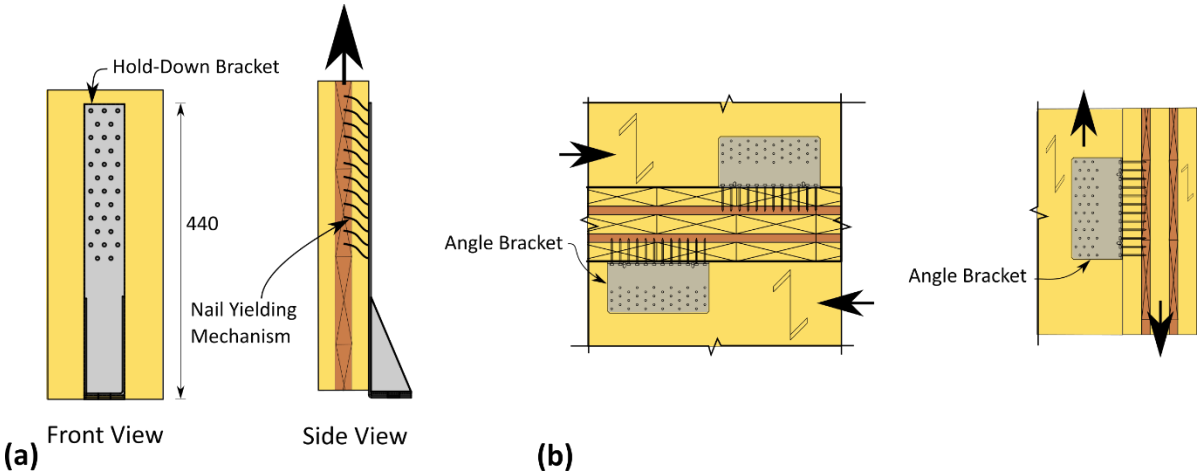


*Figure 2-3: Commercial connectors with CLT walls (a) hold-downs, and (b) angle brakets*

After a decade of intense research, the design and construction of CLT structures 'is no longer a domain for early adopters, but is becoming a part of regular timber engineering practice, also in earthquake-prone regions' (Tannert et al., 2018). Globally, updates to buildings codes will allow mass timber constructions up to 8-, 12-, and 18-storeys in Australia, Canada, and the United States, respectively (Breneman & Richardson, 2019; NRC, 2018; Wood Solutions, 2019). In New Zealand, policies such as the "Zero Carbon" Act (*Climate Change Response (Zero Carbon) Amendment Act 2019*, 2019), and Wood First (*Wood First Policy for Gisborne District Council*, 2018; *Wood First Policy*, 2015) are also promoting the use of mass timber construction. More recently, seismic performance factors for platform framed CLT shear walls systems in the United States were determined by van de Lindt et al. (2020) following the FEMA P695 (2009) methodology for inclusion in the 2021 AWC Special Design Provisions for Wind & Seismic. In CLT platform construction, connections with self-tapping screws (STS) are commonly used. This is increasingly the case for vertical joints between CLT wall panels with recent aspect ratio (height-to-length) limitations between 1:1 and 4:1 in the Canadian standard (CSA O86, 2019; Tannert, 2019). This coupling effect provides increased system displacement capacity and energy dissipation. Depending on the vertical joint details between adjacent CLT wall panels, single, coupled, or combined wall behaviour was observed (Gavric et al., 2015). There are numerous analytical approaches for the design of conventional and in-plane CLT shear walls (Lukacs et al., 2019). The analytical model presented by Gavric et al. (2015) is one rare approach which accounts for the nonlinear behaviour of the CLT shear wall connections. Chen & Popovski (2020) developed mechanics-based analytical models for balloon type CLT shear walls. In the balloon type wall configuration, shear walls are continuous and floor panels are attached at each floor. The resistance of the system was governed by the hold-downs, shear keys, and vertical in-plane joint. Another recent analytical model

can also account for the influence of orthogonal CLT shear walls, and CLT floors above and below in CLT platform construction (Shahnewaz et al., 2020). This model, however, is only valid within the elastic range.

The load carrying capacity of CLT shear walls is only partially exploited when standard commercial connectors are used, which often have only limited capacity (Flatscher et al., 2015). In order to realize taller CLT structures, enhanced connection solutions are required that meet increased strength and stiffness demands. Thus, high performance hold-downs with energy dissipating and recentering capability have been investigated (Hashemi et al., 2020). The inherent timber material properties such as relatively low stiffness (approximately ¼ reinforced concrete) and possible brittle behaviour make it more challenging for ductile design of taller timber building, especially in high seismic regions. Within this lies the displacement paradox, because while a designer needs to control lateral displacements to meet the code prescribed drift criteria, one also needs to provide displacement capacity to ensure the assumed system ductility is achieved (Smith et al., 2015). To overcome the inherent flexibility of timber structures, Buchanan (2016) stated transforming conventional planar shear walls to core-walls using efficient connections including post-tensioning could meet the increased strength and stiffness demands for taller timber buildings.

## 2.3 POST-TENSIONED TIMBER SHEAR WALL LATERAL LOAD RESISTING SYSTEMS

Adopting concepts and principles originally developed for precast concrete construction (Priestley et al., 1999), PT timber systems, also called Pres-Lam technology (Pre-Stressed Laminated Timber), have been developed and tested since 2005 at the University of Canterbury (UC) (Palermo et al., 2005). In PT timber shear walls, conventional hold-downs are not used and the moment capacity at the wall base is provided by the clamping action of the PT tendons and/or by special ductile "hold-downs", consisting of axially loaded internally epoxied or external and replaceable rebars/dissipaters (Palermo et al., 2006). This system can maximize the stiffness achievable in mass timber structures, minimize damage, and have strong re-centering capabilities. Figure 2-4 shows the first key subassembly tests which included exterior PT beam-column joints, PT interior beam column joints, PT single walls, PT double walls, and PT columns.

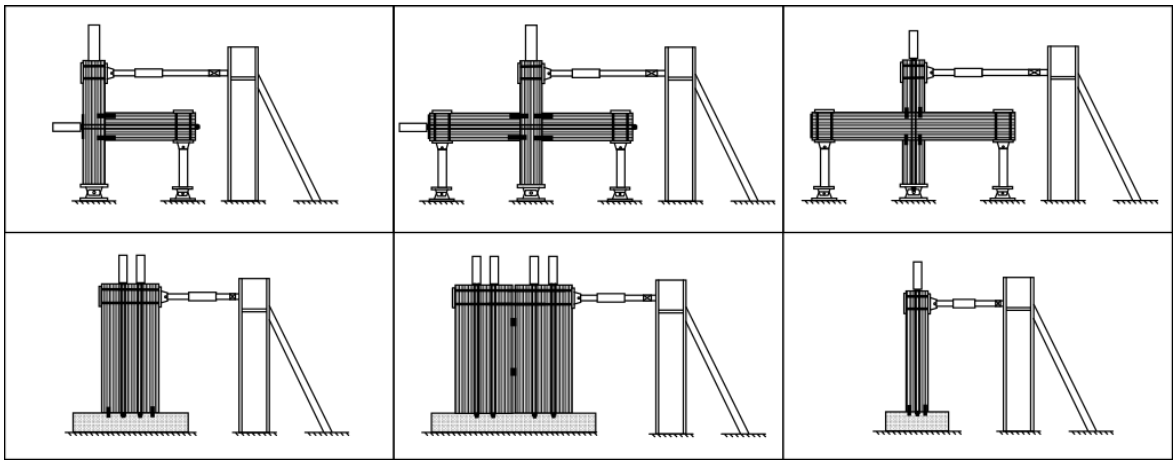

*Figure 2-4: Overview of post-tensioned timber subassembly testing programme at University of Canterbury (photo taken from Palermo et al.* (2005)*)*

An extensive testing programme at UC included PT laminated veneer lumber (LVL) single wall testing (Palermo et al., 2005), hybrid wall systems with internal epoxied and external replaceable energy dissipating devices (Sarti et al., 2016), U-shaped flexural plates (UFPs) in coupled walls (Iqbal et al., 2015; Kelly et al., 1972), or simply coupled walls with nailed plywood sheets (Iqbal et al., 2015). Sarti et al. (2016a; 2016b) studied the in-plane performance of PT LVL hybrid walls and the PT column-wall-column system. Figure 2-5 shows the experimental test setups for each subassembly test. The main objectives of the study included investigating larger scale PT LVL wall subassemblies with a particular focus on connection detailing. As such, PT anchorage details, internal and external axial dissipaters, and UFP dissipater details were investigated. The results show that PT LVL wall subassemblies can provide a high level of energy dissipation with minimal damage to the wall element and minimal residual drifts.

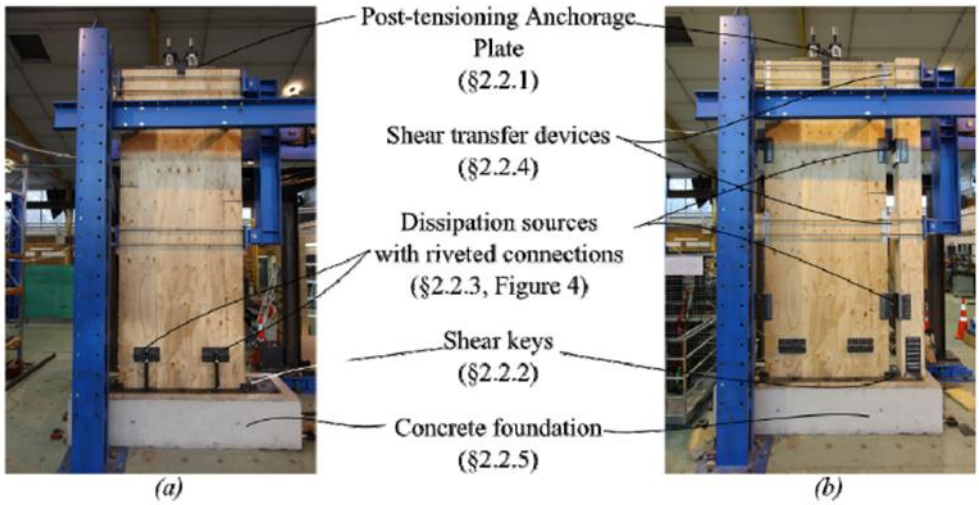


*Figure 2-5: (a) Post-tensioned hybrid LVL walls, and (b) post-tensioned column-wall-column LVL walls with UFPs (photo taken from Sarti* (2015)*)*

Adopting principles from precast concrete wall systems, Iqbal et al. (2015) studied PT LVL double walls coupled with UFPs through quasi-static cyclic and pseudo-dynamic tests and the UFPs showed stable performance while PT bars provided desirable recentering hysteretic capability. Analytical methods were presented including the lumped plasticity and multi-spring methods for numerical modelling of PT wall systems. A step-by-step design procedure for PT double walls coupled with UFPs which includes the iterative Modified Monolithic Beam Analogy (MMBA) was also presented. The experimental test set-ups are shown in Figure 2-6. Since then, other experimental works have also focussed on UFPs as energy dissipating elements for PT DW timber systems (Chen et al., 2020; Ganey et al., 2017; Shiling Pei, Van De Lindt, et al., 2019; Sun et al., 2020).

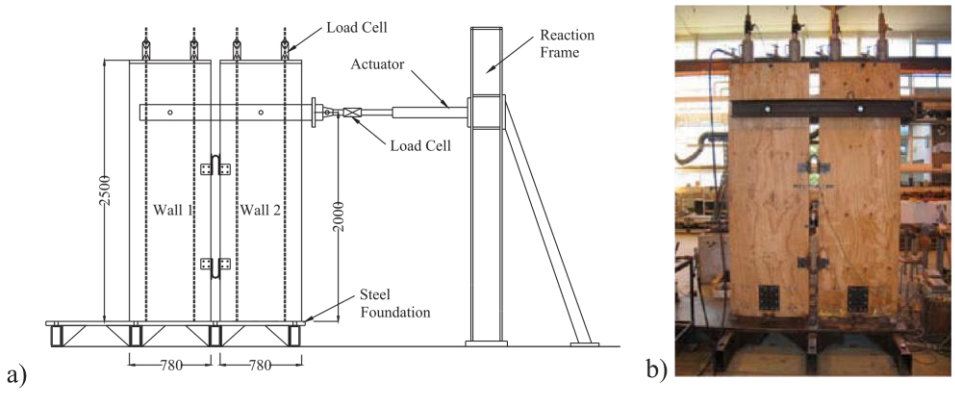


*Figure 2-6 Post-tensioned double LVL walls coupled with UFPs. (a) schematic of test, and (b) experimental test set-up (photo taken from Iqbal et al.* (2015)*)*

Iqbal et al. (2015; 2018) experimentally tested PT LVL DW systems coupled with plywood and nails and developed an analytical model assuming a constant nail yield force equal to the design capacity for prediction at design drift. The model was able to adequately capture the moment-rotation response. Figure 2-7 shows the experimental set-up for the PT LVL DW tests with plywood.

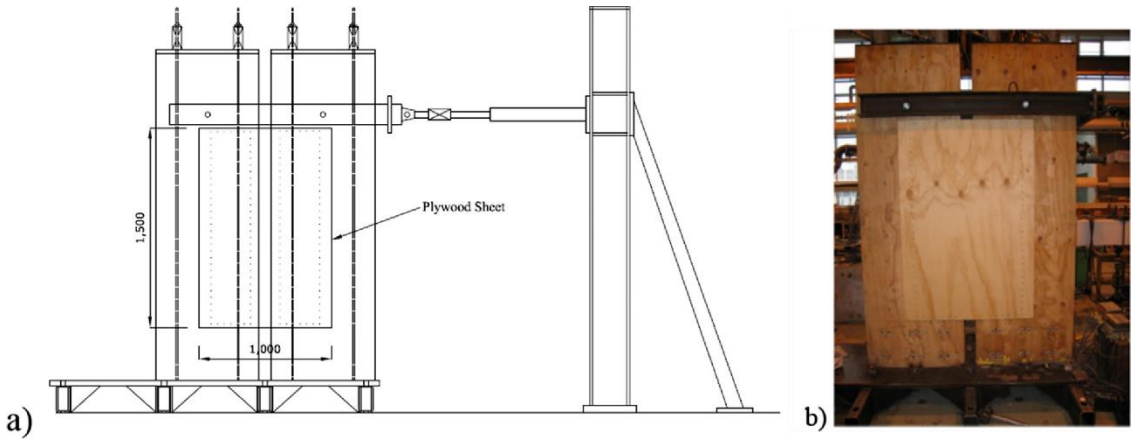


*Figure 2-7: Post-tensioned double LVL walls coupled with nails and plywood. (a) schematic of test, and (b) experimental test set-up (photo taken from article published in Engineering Structures, Vol 167, Iqbal A., Fragiacomo, M., Pampanin, S., & Buchanan, A., Seismic resilience of plywood-coupled LVL wall panels, 750-759, Copyright Elsevier* (2018)*.)*

The importance of connection detailing between the diaphragm and the lateral load resisting system was highlighted during a two-storey frame and wall building experimental test by (Newcombe et al., 2010) and in-plane experimental testing of Timber-Concrete-Composite diaphragms (Newcombe et al., 2010). This was subsequently extensively researched by Moroder et al. (2017). Careful detailing is required to resolve the wall-floor displacement incompatibilities. The extensive research programme at UC is summarized in the Pres-Lam design guide which is targeted for designers (Pampanin et al., 2013).

While initial research with PT mass timber systems focussed on using LVL for its inherent higher mechanical properties, recent work has also confirmed its usability with other engineered wood products such as Glulam (Di Cesare et al., 2017; Mancini & Pampanin, 2018; Smith et al., 2014) and CLT (Chen et al., 2020; Dunbar et al., 2014; Ganey et al., 2017; Ho et al., 2017; Pilon et al., 2019). Under the multiyear Natural Hazards Engineering Research Infrastructure (NHERI) research project (Pei et al., 2017), Ganey et al. (2017) tested configurations of single and double PT CLT walls on both steel and CLT bases. In 2017, Pei et al. (2019) conducted a series of shake table tests of a full-scale 2-storey mass timber building with PT CLT walls. Figure 2-8 shows the full-scale 2-storey mass timber building on the outdoor shake table at the NHERI at University of California, San Diego. At the end of the NHERI project, a ten-storey full scale PT CLT wall building shake table test is planned (Pei et al., 2019). A current state-of-the-art in Pres-Lam concept, testing and implementation is provided by Granello et al. (2020).

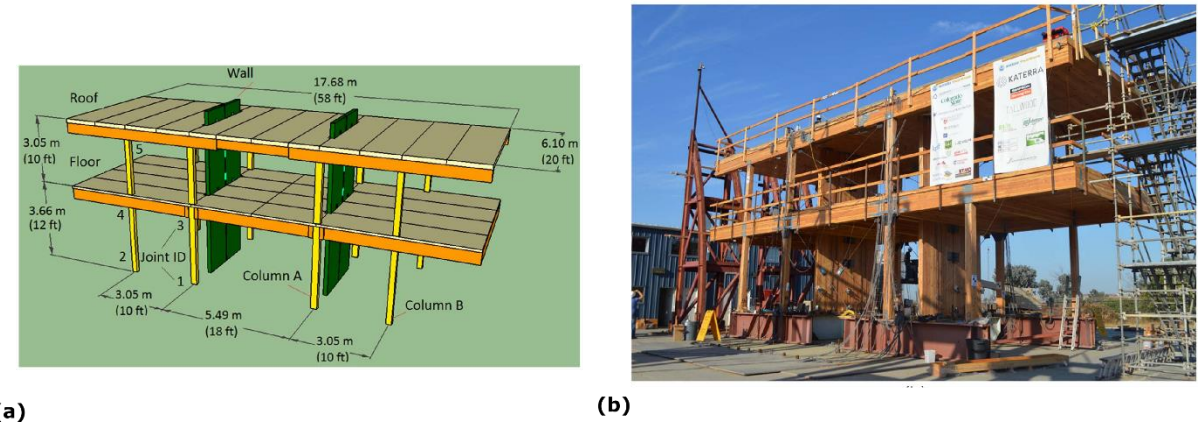


*Figure 2-8: 2-storey mass timber building shake table test. (a) schematic of test set-up, and (b) experimental test set-up (photo adopted from Pei et al. (2019))*

In past PT DW tests, the primary purpose of the in-plane vertical joint between adjacent panel walls was to provide increased energy dissipation during the rocking motion (Chen et al., 2020; Ganey et al., 2017; Iqbal et al., 2015). There are few examples using the in-plane vertical joint or orthogonal vertical joint as a method to provide increased strength and stiffness through partial composite action between the panels to create a C-, I-, or tube-shaped LLRS. However, with proper connection detailing

accounting for capacity design principles this method could meet increased lateral stiffness demands for taller timber buildings, even in high seismic regions.

## 2.4 CAPACITY DESIGN AND OVERSTRENGTH

The uptake of CLT buildings in earthquake-prone regions requires a deep understanding of the strength hierarchy among building elements to ensure seismic safety through capacity design (Casagrande et al., 2019). Capacity design (Paulay & Park, 1975) aims to ensure ductile system behaviour and protect all brittle elements (or less ductile parts) from failure. The strength demand of the brittle elements needs to consider the overstrength of the ductile elements (Smith et al., 2015).

As CLT wall elements behave relatively rigid, joints are often designed as ductile elements and then their overstrength needs to be well understood to protect all non-ductile elements and guarantee system ductility. For timber buildings, well-detailed connections with dowel-type fasteners are often used as ductile elements through the yielding of fasteners to provide system ductility (Buchanan, 2016). In this regard, for CLT shear walls, the connection ductility and overstrength properties need to be well understood so that they can sustain loads even at large displacement. In addition, the onset of brittle failure modes in ductile elements must be avoided until large displacements to ensure ductile system behaviour. Further, while it is important to know the true strength of ductile connections along the load path, a good understanding of the strength of elastic/non-ductile connections is also important. This is increasingly the case for taller timber buildings with increased strength and stiffness demands (Buchanan, 2016; Smith et al., 2015).

Connection ductility, $\mu$, is commonly defined as the ratio of the ultimate displacement over the yield displacement, as shown in Equation (2-1) (CEN, 2005):

$$\mu = \frac{\Delta_{Fu}}{\Delta_y} \tag{2-1}$$

where $\Delta_{Fu}$ = ultimate displacement corresponding to the post-peak deformation at 80% of the maximum load; $\Delta_y$ = displacement at yield point.

Connection overstrength can be defined as the discrepancy between analytically calculated design strength based on code provisions and the 95th-percentile of the true strength distribution. Jorissen and Fragiacomo (2011) defined the overstrength factor for timber connections, $\gamma_{Rd}$, as shown in Figure 2-9 as:

$$\gamma_{Rd} = \gamma_M \cdot \gamma_{an} \cdot \gamma_{0.95} = \frac{F_k}{F_d} \cdot \frac{F_{0.05}}{F_k} \cdot \frac{F_{0.95}}{F_{0.05}} \tag{2-2}$$

where $\gamma_M$ = overstrength attributed to material safety factor; $\gamma_{an}$ = overstrength attributed to conservatism of analytical models; $\gamma_{0.95}$ = overstrength attributed to difference between 5th and 95th percentile of strength distribution; $F_k$ = characteristic strength; $F_d$ = design strength; $F_{0.05}$ = 5th percentile of strength distribution; $F_{0.95}$ = 95th percentile of strength distribution.

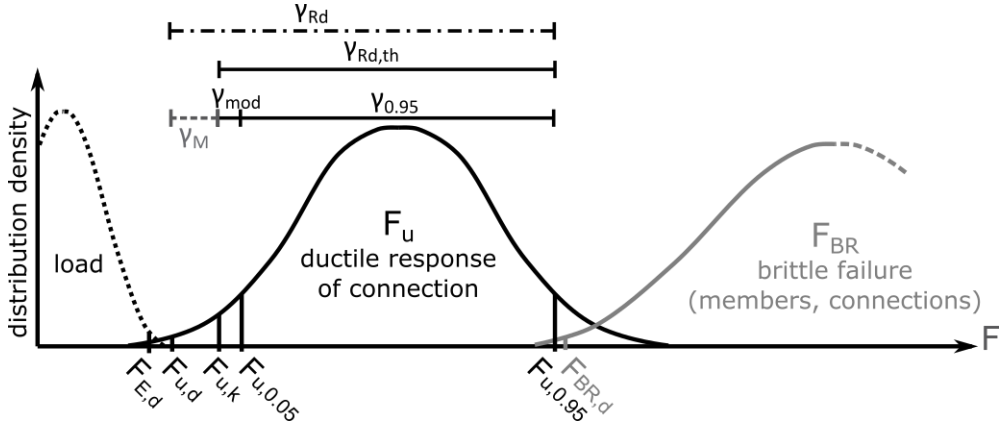


*Figure 2-9: Theoretical overstrength components (figure taken from Ottenhaus et al.* (2020)*, modified from Jorissen and Fragiacomo* (2011)*)*

So far, most timber design standards do not provide overstrength factors of ductile connections for capacity design. Only a limited number of studies have been conducted to establish overstrength factors for certain connection types as ductile elements in timber shear walls (Bruhl et al., 2014; Dong et al., 2020; Ottenhaus, Li, & Smith, 2018; Ottenhaus et al., 2018; Trutalli et al., 2019). In Canada, a supplement to CSA-O86 (2019) now stipulates capacity design principles; however, overstrength factors for ductile elements are not provided. Thus, designers may need to rely on the limited available test data or assume overstrength factors for commercial or fit-for-purpose connectors designed as ductile elements. One rare example is the New Zealand Timber Structures Standard NZS 3603 (1993) that explicitly stipulates an overstrength factor of 1.6 for nailed connections in plywood shear walls. Timber joints often contain groups of fasteners, and design codes such as Eurocode 5 (2014) introduce an effective number of fasteners to account for the group effect. For ductile joints with dowels, these reductions can lead to conservative strength predictions, making it difficult to quantify overstrength (Dorn et al., 2013; Ottenhaus et al., 2018). For STS joints, Tomasi et al. (2010) reported no group effect on strength while Hossain et al. (2019) provided a conservative recommendation for group effects on both strength and stiffness. In these studies, the possible non-conservative implication of group effect on overstrength was not considered.

A lack of prescriptive design guidance in timber design standards on the aspects including capacity design has required performance-based engineering as a path to code compliance, which can add significant project time, cost and uncertainty and ultimately limit implementation (McDonnell & Jones, 2020). In the research presented herein, dowelled CLT hold-downs with one slotted-in steel plate and

mixed angle STS orthogonal CLT connections were investigated as ductile links for a core-wall system. In addition, mortise and tenon castellated carpentry joints were investigated as strong and stiff non-ductile shear connections protected by capacity design. Of critical importance for design guidance was to verify and/or develop analytical methods to predict the connection strength and secondly to derive overstrength and ductility of the ductile connections.

## 2.5 HOLD-DOWN CONNECTION RESEARCH

In current CLT shear wall design for platform construction, off-the-shelf connectors adapted from LTF construction are widely used for hold-downs and shear keys. Past and current examples of this construction include the 9-storey Stadthaus (Green & Taggart, 2017) and the recently completed Aveo Norwest 10-storey CLT building in Sydney (Moroder et al., 2018). These connectors typically use small diameter nails or screws and thin steel brackets. Having limited strength and stiffness, the connectors limit the structural efficiency of CLT shear walls (Flatscher et al., 2015) as they are often limited to axial capacity of 100kN (Rothoblaas, 2019; Simpson Strong-Tie, 2019), or less if ductile behaviour characterized by yielding of the nails is required (Benedetti et al., 2019; Dong et al., 2020; Flatscher et al., 2015). Due to the higher load demand in multi-storey CLT buildings, CLT shear walls need to incorporate stronger and stiffer hold-downs and shear keys which often require a fit-for-purpose project specific solution by the designer.

Recent research has thus also focussed on high capacity hold-downs to resist high overturning moments (Hashemi et al., 2020; Schneider et al., 2018; Zhang et al., 2018). One such high capacity hold-down type which has been used on numerous projects in New Zealand and other countries is the dowelled connection with slotted-in steel plates. Large scale experimental tests confirmed their high capacity and ductile behaviour (Ottenhaus et al., 2018a). As an example, Figure 2-10 shows the application of a dowelled connection with slotted-in steel plate in CLT shear walls. Current design approaches for dowel-type joints in CLT are summarized by Mohammad et al. (2018) and Ringhofer et al. (2018).

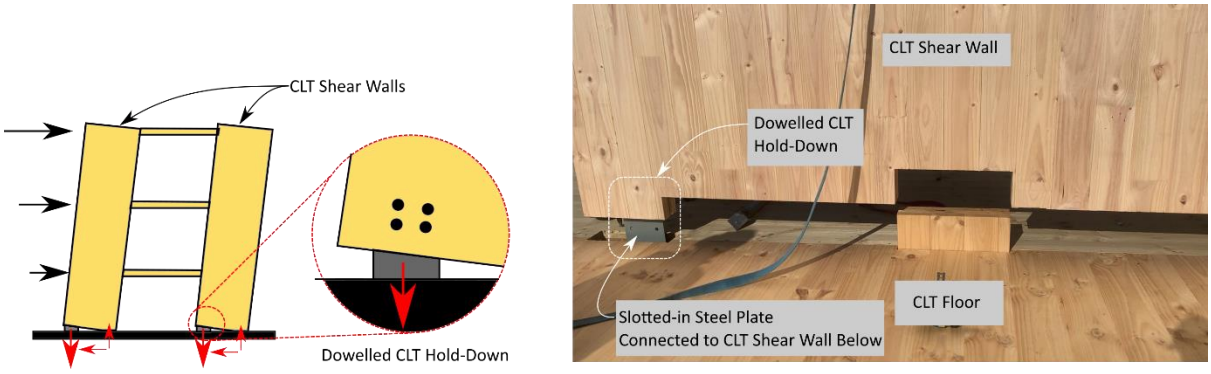


*Figure 2-10: Hold-down systems in CLT buildings. (a) schematic, and (b) slotted-in steel plate dowelled hold-down connection. Photo by ENGCO is courtesy of Arvida Group - Living Well Apartments, Christchurch, New Zealand (image taken from* (Brown & Li, 2021)*)*

A comparison of selected research on dowelled hold-downs, commercial connectors, and other high capacity hold-downs is provided in Table 2-1.

*Table 2-1: Comparison of selected experimental research of hold-down connections*

| Research Study | Connection Description | Fastener Type | Fastener Quantity | Peak Load kN |
|---|---|---|---|---|
| Gavric et al. (2015b) | Rothoblaas WHT540 (2019)[1] | ø4x60mm nails | 12 | 48 |
| Flatscher et al. (2015) | Simpson StrongTie HTT22 (2019) [1] | ø4x60mm nails | 15 | 51 |
| Dong et al. (2020) | Rothoblaas WHT440 (2019) [1] | ø4x60mm nails | 30 | 70 |
| Polastri et al. (2019) | Rothoblaas WHT620 (2019) [1] | ø4x60mm nails | 52 | 107 |
| Schneider et al. (2018) | Novel tube connector with steel rod | Steel rod | n/a | 58 |
| Zhang et al. (2018) | Internal perforated steel plates | Adhesive | n/a | 180 |
| Hashemi et al. (2020) | Resilient Slip Friction Joint (RSFJ) | n/a | n/a | 350 |
| Ottenhaus et al. (2018) | Slotted-in steel plate[2] | ø20mm dowels | 4 | 188 |
| Ottenhaus et al. (2018) | Slotted-in steel plate[2] | ø20mm dowels | 16 | 1164 |

[1]Commerical connector

[2]Dowelled hold-downs with slotted-in steel plates

Brittle failure modes such as row shear (RS), group tear-out (GT) and net tensile failure (TF) are checked and explicitly adopted in the Canadian standard CSA-O86 (2019), or implicitly in others such as Eurocode 5 (2014). Generally, the requirements of using the effective number of fasteners, minimum fastener spacing, row spacing, end and edge distances in dowel-type connections aim to ensure ductile response will occur as per Figure 2-11e rather than brittle failure modes shown in Figure 2-11a - Figure 2-11d. These were based on experience as well as comprehensive experimental investigations (Blaß & Sandhaas, 2017).

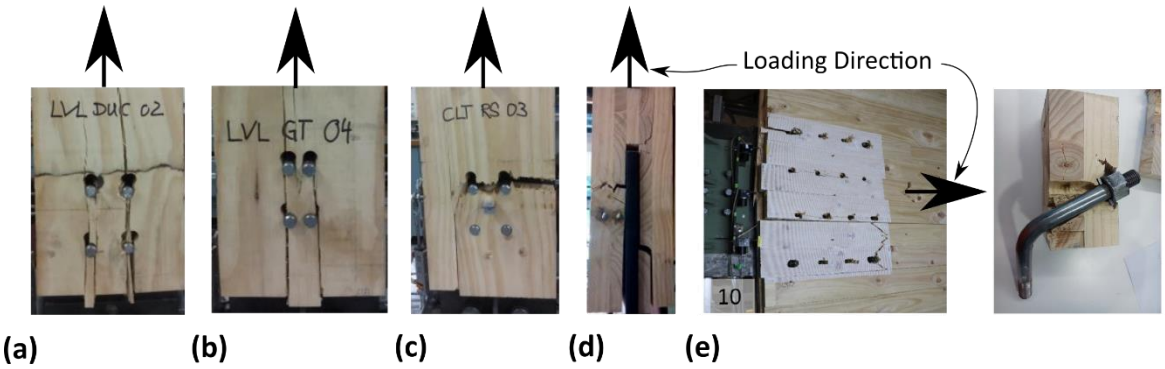


*Figure 2-11: Brittle failure modes. (a) row shear failure, (b) group tear-out failure, (c) and (d) net tensile failure from Ottenhaus et al.* (2018)*& (e) ductile failure with significant dowel yielding and timber embedment from Ottenhaus et. al* (2018)

Currently, few timber standards provide minimum fastener spacing requirements for dowel type connections in CLT. The Canadian standard CSA-O86 (2019) is one rare example which currently considers minimum fastener spacing to be the same as solid sawn timber or engineered timber products such as glulam in which wood fibres are oriented along one major direction. Uibel and Blaß (2007, 2006) have conducted a comprehensive test campaign on minimum fastener spacing in dowel type connections in CLT and their findings are summarized in Ringhofer et al. (2018). Although these minimum spacing requirements were satisfied, Ottenhaus et al. (2018; 2018), however, observed cross-over failure modes with a three stage response of dowelled CLT connections: (1) onset of dowel bending and yielding (2) continued dowel yielding, out-of-plane bending of wood laminations and onset of crack growth (e.g., initiating row shear) (3) final brittle rupture in wood laminations. It was also found through dowelled connection tests in 5-ply 130mm thick CLT that cross-layers are able to provide a reinforcing effect but the brittle failures described above could still occur if dowel spacing was not sufficient (Ottenhaus et al., 2018). CLT has a different configuration with crosswise fibre directions when compared to sawn timber or glulam and it is mostly manufactured without edge gluing, leaving small gaps between laminations. Therefore, the fastener spacing requirements in current design standards might not be fully applicable to CLT. More research is needed to assess the influence of fastener spacing on CLT connection performance and with different CLT manufacturers and timber species.

Based on large scale experimental results, Ottenhaus et al. (2018) suggested that increased dowel spacing will increase connection ductility and strength by delaying the onset of mode cross-over to brittle failure (Ottenhaus et al., 2018). Through further experimental studies, this finding could be validated as it is important for the design of ductile link dowelled hold-down elements in a CLT LLRS.

## 2.6 SELF-TAPPING SCREW CONNECTION RESEARCH

Joints with self-tapping screws (STS) can offer superior performance when compared to standardized dowel-type connectors such as nails, bolts or wood screws. STS, manufactured by hardened steel with yield strength up to 1,000 MPa, are the most popular fastener type used in mass timber construction, in part due to their ease of installation and flexibility in design (Brandner et al., 2016). STS -while optimized primarily for axial loading- can offer one reliable solution to meet strength and stiffness demands (Dietsch & Brandner, 2015). Bejtka & Blaß (2002) tested STS joints in glued laminated timber (glulam) by installing inclined STS and developed an analytical strength model that accounts not only for the embedding strength of the timber member and the bending capacity of the STS, but also the withdrawal capacity of the STS and the friction between the members. Figure 2-12 shows the test set-ups and assumed force/stress distribution for their analytical model. Their tests showed the increase in strength and stiffness potential with inclined fully threaded (FT) STS.

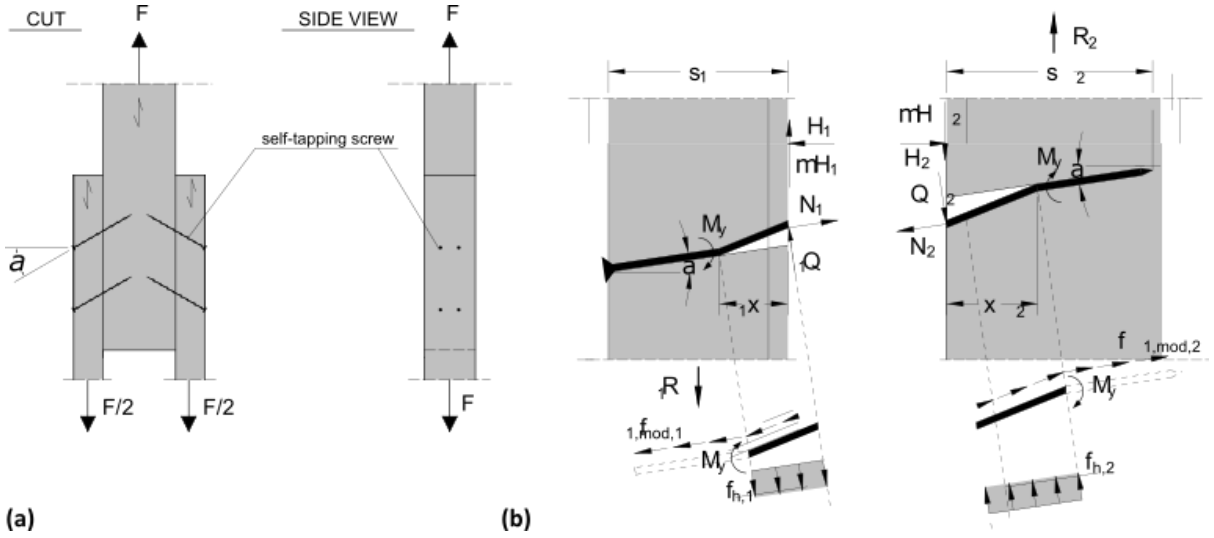


*Figure 2-12: Inclined STS testing by Bejtka & Blaß (2002). (a) test set-up, and (b) forces and stresses in inclined STS timber-timber joint (photo taken from Bejtka & Blaß (2002))*

The stiffness of inclined STS was studied by Kevarinmaki (2002) and a stiffness model was proposed for STS installed at 45° in a shear-tension and cross-wise pattern. Subsequent work by Tomasi et al. (2010) extended the existing strength model and developed a stiffness model appropriate for any installation angle. The models were compared against experimental monotonic tests in glued laminated timber. The results showed that the strength model was appropriate and the stiffness model worked if a "single stiffness" approach was adopted, contrary to the system of springs in series approach proposed by Kevarinmaki (2002). Tomasi et al. (2006) also tested combinations of STS installed inclined and STS installed at 90° to the timber grain, simply called 90° STS, in glulam and reported promising cyclic performance with mixed angle installations.

The crosswise layup of CLT introduces complexities for joint design. Current design approaches for dowel-type joints in CLT including STS are summarized by Mohammad et al. (2018) and Ringhofer et al. (2018). Gavric et al. (2015a) studied the cyclic performance of 12 different common platform construction STS joints between CLT walls and floor panels. Figure 2-13 shows some tests which included in-plane STS spline and lap joints and orthogonal 90° STS joints. It was found that 90° STS joints provided ductile performance in dowel action if recommended spacing and edge distances were followed. The design parameters proposed by Uibel and Blaß (2006, 2007) were appropriate and an overstrength of 1.6 was suggested for the tested STS joints in CLT.

**(a)** **(b)**

*Figure 2-13: Experimental STS testing by Gavric et al.* (2015a). *(a) in-plane joints with plywood splines and 90° STS, and (b) orthogonal joints with 90° STS (photos adopted from Gavric et al.* (2015a)*)*

Hossain et al. (2016) tested butt joints with doubly inclined STS between in-plane CLT panels. The results showed that butt joints, which have a low machining cost, could achieve moderate ductility with a displacement capacity of 8mm under cyclic loading. In-plane CLT lap joints with STS were also studied by considering 90° STS joints, inclined STS joints, and joints with an equal combination of STS in shear and withdrawal (Hossain et al., 2018; Sullivan et al., 2018). The η ratio, i.e. the ratio of STS installed inclined and STS installed at 90° to the timber grain, of 1:1 reported similar findings to Tomasi et al. (2006). Figure 2-14 shows different installation arrangements for STS in-plane joints.

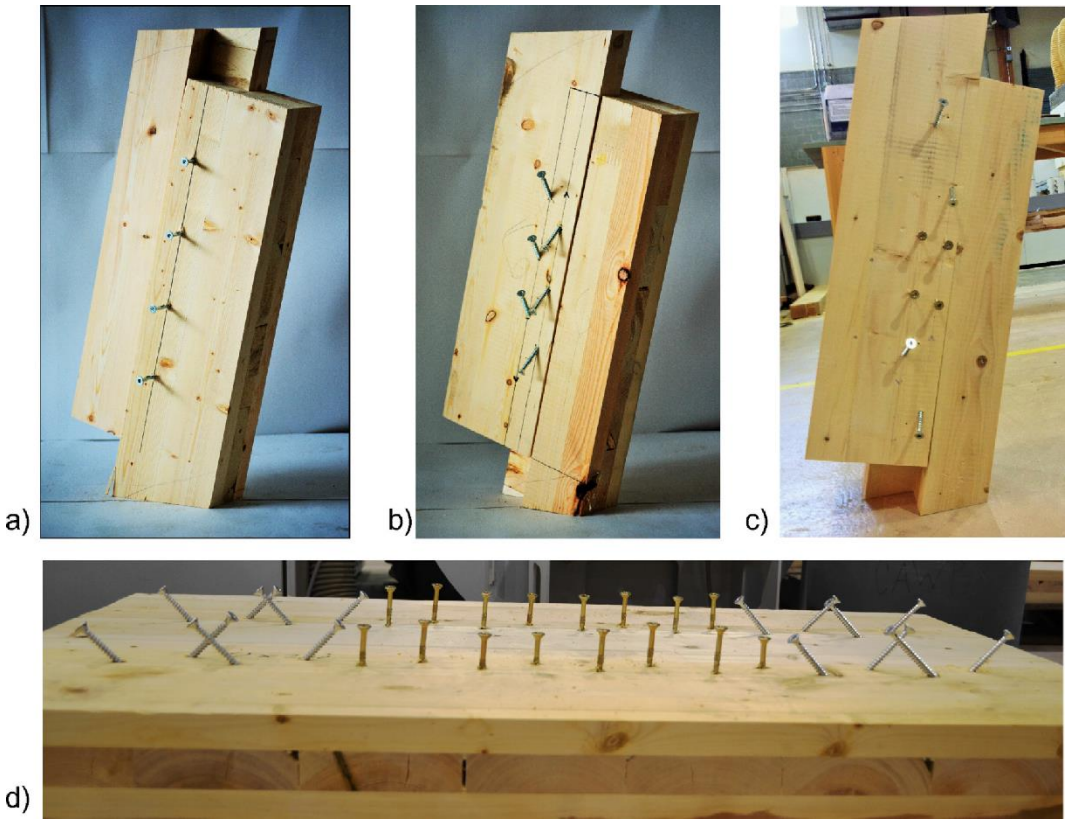


*Figure 2-14: In-Plane STS joint configurations tested by Hossain et al.* (2018). *(a) 90° STS, (b) inclined STS, (c) and (d) mixed angle STS with η ratio of 1:1 (photo taken from Hossain et al.* (2018)*)*

With the objective to show that the spatial insertion angle chosen for STS in-plane CLT joints significantly affects the strength, stiffness, and displacement capacity, Loss et al. (2018) studied STS in-plane CLT joints and compared experimental results to current analytical design models. Satisfactory experimental-analytical agreement was shown for spatially arranged STS strength models but the stiffness models were found inaccurate due to the assumptions on individual lateral and axial stiffness components. Increased energy dissipation with increased STS slenderness was also reported (Loss et al., 2018). Past research reported that 90° STS act through timber embedment and fastener yielding mechanisms and provide limited stiffness but high displacement capacity, ductility, and energy dissipation. Inclined STS act primarily in withdrawal and provide high strength and stiffness but limited displacement capacity, ductility and energy dissipation. STS joints with η ratio of 1:1 provided promising performance combining high strength, stiffness, ductility, and displacement capacity (Hossain et al., 2018; Loss et al., 2018; Sullivan et al., 2018; Tomasi et al., 2006).

Past experimental work on STS joints in CLT has focussed on common in-plane joints with relatively smaller fasteners (up to ø10mm x 200mm) and thin 3- or 5-ply CLT panels. Past orthogonal CLT panel joint tests with STS were limited to 90° installation angles (Gavric et al., 2015a). As taller timber buildings will require thicker (5-, 7-ply or greater) CLT panels with larger diameter STS, experimental testing to verify performance is required. While the use of mixed angle STS with an η of 1:1 has shown

promising performance for seismic design (Hossain et al., 2018; Sullivan et al., 2018; Tomasi et al., 2006), little work has quantified the impact of inclined to 90° STS η ratio on the joint performance.

CLT orthogonal joints with STS introduce complexities such as different STS axis angles to timber grain on each STS head side and tip side and also the increased variability when installing STS into the narrow face of CLT. It appears appropriate to investigate orthogonal joints with mixed angle STS configurations due to their potential to develop composite action between orthogonal CLT wall panels, which could transform conventional in-plane CLT shear wall to a core-wall structure with enhanced lateral strength and stiffness. Further, these joints could serve as ductile links if an appropriate mixed angle STS η ratio was implemented. If STS orthogonal joints are to be implemented in CLT core-wall structures, there is further research need to quantify the differences between orthogonal and in-plane joint configurations, quantify connection ductility, determine an optimum η ratio, and finally verify existing analytical methods to determine overstrength.

## 2.7 CARPENTRY JOINTS

In timber structures, members are generally connected together by the use of direct wood-wood contact (carpentry joints), mechanical fasteners, and/or adhesive bonding (Tannert, 2016). Carpentry joints are the most traditional connection methodology. In ancient timber structures the most common carpentry joints include dovetail joints, mortise and tenon joints, notched/step joints, lap joints and scarf joints (Siem & Jorissen, 2015). Figure 2-15 shows some of these carpentry joints. These joints were used widely across Asia (Ssu-Ch'eng, 1984; Sumiyoshi & Matsui, 1989), Europe (Karolak et al., 2020) and North America (Sobon, 2004) but highly skilled and costly labour rendered them uncompetitive to modernized timber buildings with mechanical fasteners. Because many historical timber buildings now require refurbishment, recent work has also aimed to provide analysis and strengthening methods for existing carpentry joints (Branco et al., 2018; Branco & Descamps, 2015; Branco et al., 2011; Parisi & Piazza, 2000, 2015; Verbist et al., 2017). Significant work has focussed on the step joints or similar variations to determine shear and compressive stress distributions (Siem & Jorissen, 2015) and analytical methods have been presented for certain joint types (Branco & Descamps, 2015; Wald et al., 2000).

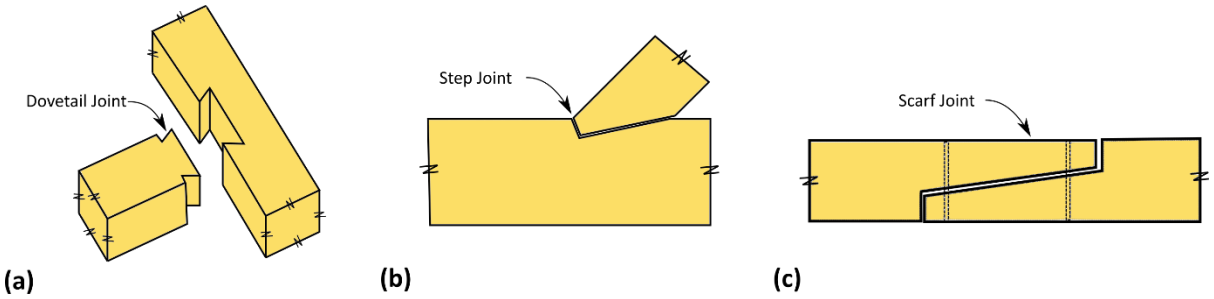


*Figure 2-15: Examples of carpentry joints. (a) dovetail joint, (b) step joint, and (c) scarf joint (image taken from Brown et al. (2021))*

Mechanical fasteners are now the most common connection method and timber design standards such as Eurocode 5 (2014) cover their design in detail. Their behaviour has been well researched and the failure modes focus on the bending yielding of mechanical fasteners which is more easily predicted than timber brittle failure. CLT structures are commonly connected using mechanical connectors/fasteners adapted from LTF construction. Figure 2-16 shows an example of commercial angle brackets used in a recently completed 10-storey Aveo Norwest CLT building in Sydney (Moroder et al., 2018). Because CLT panels have higher in-plane strength and stiffness than LTF (Izzi et al., 2018), their in-plane performance is generally governed by the mechanical connection systems (Pei et al., 2016). With commercial brackets, Flatscher et al. (2015) reported that the performance of CLT LLRS was underutilized.


*Figure 2-16: Photos of Aveo Norwest 10-storey CLT building c/o Andy Buchanan of PTL | Structural Consultants. (a) CLT wall to floor below angle bracket detail, (b) CLT wall to floor above angle bracket detail (image taken from Brown et al. (2021))*

Recent advances in computer numerically controlled (CNC) machining technologies have facilitated CLT structures to be designed with increasing levels of prefabrication and complexity (Dangel, 2016). The ability of CNC machining with high precision and efficiency (Robeller, 2019) has led to some carpentry joints being revisited (Chapman et al., 2016; Tannert, 2016). Siem (2017) stated that while further research is necessary to understand the combination of shear and compression stress distributions, design rules should be developed so these joints can be fully exploited and incorporated

in upcoming design codes. Accordingly, Schmidt and Blaß (2016) explored ten different interlocking CNC carpentry joints for in-plane CLT shear connections loaded parallel to the outer CLT layer and then further investigated Beech LVL shear keys (Schmidt & Blaß, 2018). Some of those CNC carpentry joints are shown in Figure 2-17.

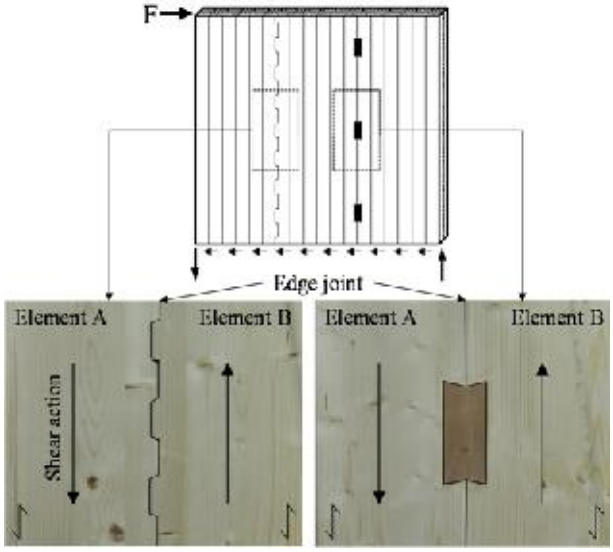


*Figure 2-17: CLT shear wall in-plane joint contact joints (Photo taken from Schmidt and Blaß (2016))*

Claus et al. (2018) also investigated interlocking CNC carpentry joints to connect glulam, CLT, or glulam and CLT with concrete. Though the joints were not suitable as energy dissipating ductile links, increased characteristic load-carrying capacities as a percentage of the characteristic CLT panel shear capacity were reported when compared to mechanically fastened commerical steel brackets (Claus et al., 2018; Schmidt & Blaß, 2016). The load carrying capacity of small scale digitally produced mortise and tenon joints were experimentally investigated by Gamerro et al. (2020) and the failure modes depended on the geometrical parameters including tenon length (L), tenon height (H), tenon or mortise thickness, and mortise length. The different failure modes could be (1) longitudinal shear failure of the tenon, (2) compression failure of the tenon, (3) shear failure of the mortise, and (4) compression failure of the mortise.

Previous mortise and tenon castellated joint studies have focussed on loading parallel to the outer CLT layer and analytical models have not been developed to determine the load carrying capacity of a single mortise and tenon castellated CLT joint. However, the castellated joints can also be loaded perpendicular to the outer CLT layer when transferring horizontal shear loads between CLT panels. For example, Figure 2-18 shows a castellated mortise and tenon joint in two recently completed CLT buildings in New Zealand. In both cases, the castellated joints were designed as capacity protected joints with high strength and stiffness. An experimental study of castellated joints to understand

strength, stiffness and failure modes in large CLT panels and strength prediction models is required for further implementation of this joint type.

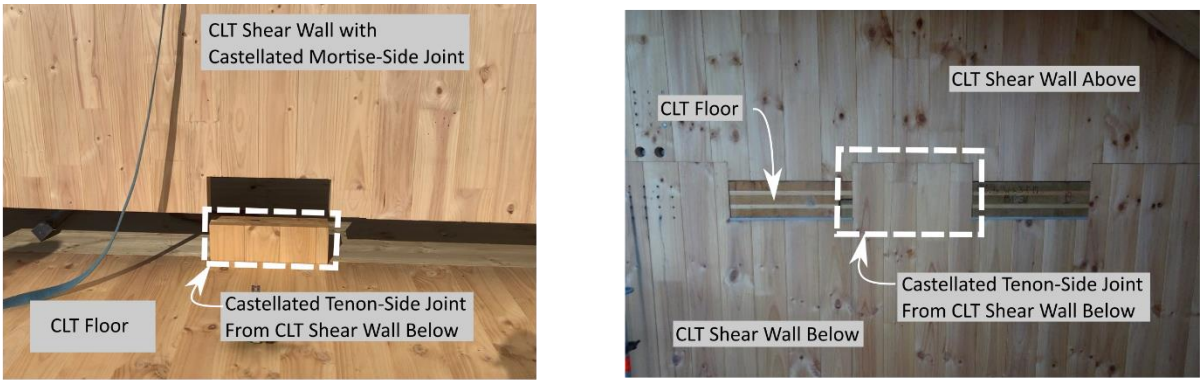


**(a)** **(b)**

*Figure 2-18: Castellated joints in CLT structures. (a) platform construction. Photo by ENGCO is courtesy of Arvida Group – Living Well Apartments. Christchurch, New Zealand, (b) Otago polytechnic (photo courtesy of Sam Leslie)*

## 2.8 CORE-WALL LATERAL LOAD RESISTING SYSTEMS

Cast in-situ reinforced concrete (RC) core-walls are popular for commercial construction to resist lateral loads. Core-wall structures provide advantages architecturally by allowing for open floor plans, and structurally by developing a tube-like behaviour with high lateral stiffness and strength. Core-wall structures can also provide torsional stiffness which is important for centrally located LLRS on floor plans. The ACI318-11 (2011) in the U.S. provides a design guide for a RC core-wall section to consider an effective flange width depending on the flange to web wall length ratio and total wall height and plastic hinging at the foundation level. A summary of experimental works on various flanged-type RC walls by Constantin & Beyer (2014) highlighted the complex behaviour of flanged walls and the importance of understanding bi-directional loading (Beyer et al., 2008). Figure 2-19 shows the experimental test set-up for a C-shaped reinforced concrete core-wall.

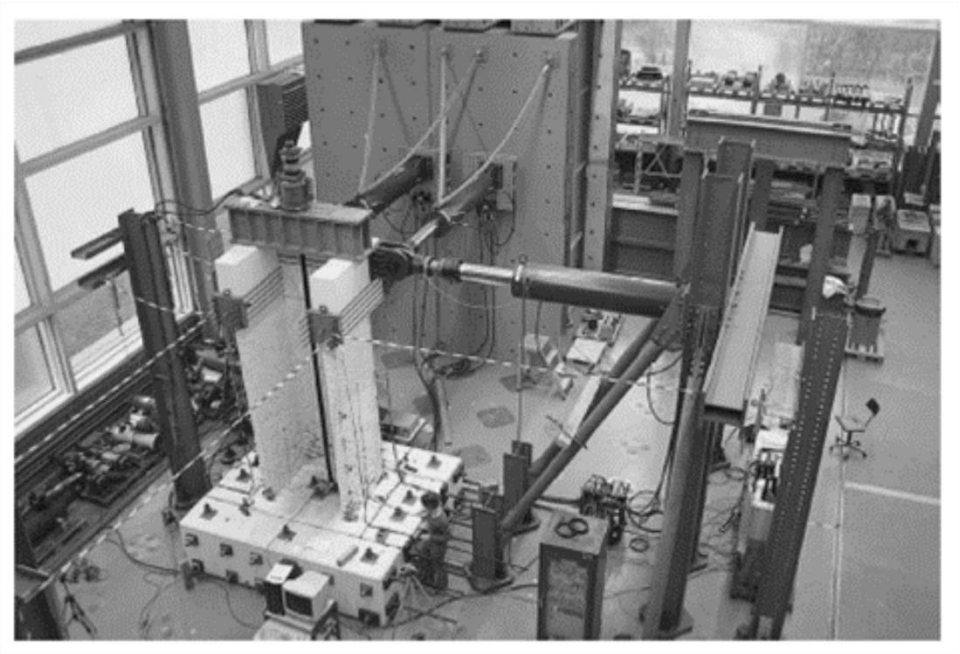

*Figure 2-19: Experimental test set-up for C-shaped reinforced concrete core-wall (photo taken from Beyer et al.* (2008)*)*

In Australia and New Zealand (NZ) precast concrete core-walls are also used and recent precast concrete core-wall experimental work by Menegon et al. (2020a) suggested that typical connections used between precast concrete panels are too flexible, and that typical grout tube connections to the foundation can result in unintended stress / strain concentrations. Thus, only partial composite core-wall behaviour is developed and ductility is limited. Figure 2-20 shows the connections with enhanced strength and stiffness for precast concrete core-walls were subsequently developed and tested to provide increased composite action (Menegon et al., 2020b).

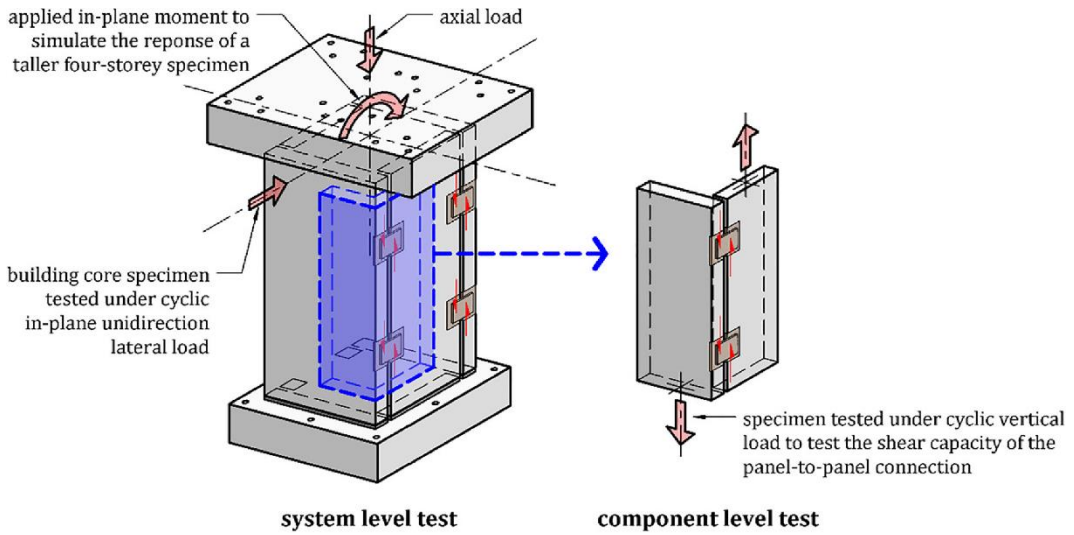


*Figure 2-20: Precast concrete core-wall research schematics: (a) system level testing, and (b) orthogonal joint testing (photo taken from article published in Engineering Structures, Vol 207, Menegon, Scott J., Wilson, John L., Lam, Nelson T.K., Gad, Emad F., Experimental testing of innovative panel-to-panel connections for precast concrete building cores, 1-15, Copyright Elsevier* (2020b)*.)*

Under seismic loads, in-plane CLT shear walls with properly designed connection systems are able to provide adequate lateral capacity for multi-storey buildings. However, in the cases of open commercial floor plans or taller buildings, conventional CLT shear walls may struggle to achieve the required strength and stiffness with current design methodologies. One possible improvement is to adopt hybrid systems with steel or concrete. Another possible solution is to introduce flanged core-walls which is common in RC structures (Beyer et al., 2008; Khan & Sbarounis, 1964). Few studies for mass timber core-wall buildings were reported. One rare recent example of mass timber core-walls is the Catalyst building (2018) in Spokane, WA shown in Figure 2-21. Catalyst required performance based engineering for code compliance through project specific testing (McDonnell & Jones, 2020). However, in general the lack of design guides and the challenge of forming enhanced connections between orthogonal walls to achieve composite action are hindrances to further application of this system type in timber.

*Figure 2-21: Catalyst Building with CLT core-walls as LLRS (figure courtesy of Hans-Erik Blomgren, Katerra* (Katerra, 2021)*)*

Mass timber core-wall construction is similar to precast concrete construction in that connections are required to connect prefabricated panels together and also to the foundation. In contrast to a cast in-situ RC core-wall, base connection stiffness of a PT mass timber core-wall is controlled by the stiffness of the post-tensioning elements and any supplementary energy dissipation devices at the base. Figure 2-22 shows one of the two PT CLT stair-case core-walls with box configuration which were experimentally tested by Dunbar et al. (2014) with a small number of STS installed at 90° to connect the CLT panels together. It was demonstrated that PT CLT core-walls were a viable LLRS with increased strength and stiffness (Moroder et al., 2018). While this work demonstrated the feasibility of PT timber

core-walls, there is a lack of comprehensive research to quantify the increase in stiffness and strength achievable when considering the composite action of orthogonal walls. By engaging the post-tensioning elements of the flange walls, a PT timber core-wall base connection stiffness can be increased when compared to in-plane PT timber walls.

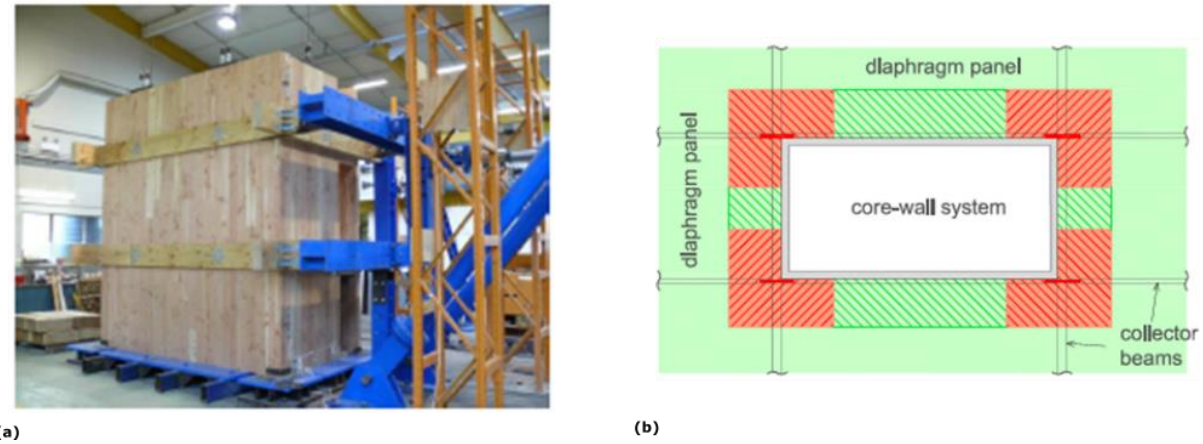


*Figure 2-22: (a) Post-tensioned CLT core-wall test set-up (A. J. M. Dunbar, 2014), and (b) recommended and prohibited diaphragm force transfer areas to core-wall ( photo taken from article published in Engineering Structures, Vol 167, Moroder, D., Smith, T., Dunbar, A., Pampanin, S., Buchanan, A., Seismic testing of post-tensioned Pres-Lam core walls using cross laminated timber, 639-654, Copyright Elsevier* (2018)*.)*

Mass timber flanged core-wall structures can also be achieved without post-tensioning, named herein as conventional core-wall structures. The orthogonal wall hold-downs, which could for example be dowelled hold-downs with one slotted-in steel plate, could be engaged by implementing strong and stiff orthogonal joints. Similar to precast concrete construction, mass timber core-wall structures require enhanced high-strength and high-stiffness connections to maximise the composite action. The feasibility of mass timber conventional core-wall structures has been numerically investigated, either by assuming an orthogonal joint stiffness for a feasibility study (Connolly et al., 2018), or by using small scale inclined STS experimental data as input for orthogonal joint stiffness (Polastri et al., 2019). The previously mentioned Catalyst building (2018) is one rare conventional CLT core-wall built example which utilized a project specific capacity protected STS orthogonal joint to activate hold-down connectors which were buckling restrained braces (BRBs) (Wakabayashi et al., 1973; Yoshino & Karino, 1971). The project specific orthogonal joint was studied experimentally through an industry-university collaboration prior to implementation (McDonnell & Jones, 2020). Further, while there are analytical design methods for planar conventional PT wall systems (Lukacs et al., 2019; Pampanin et al., 2013), currently there is no method to predict the strength and stiffness of a CLT core-wall system.

## 2.9 SUMMARY

In-plane CLT shear walls as LLRS are increasing in popularity globally. Research has reported that CLT shear wall performance is generally governed by the connection systems, especially if ductile behaviour is required under seismic loading. Most current timber building codes are behind state-of-the-art timber design possibilities. Besides, the inherent timber material properties such as relatively low stiffness and possible brittle behaviour make it more challenging for timber systems to resist high lateral loads, especially for taller buildings in high seismic regions. As such, recent research has focussed on high performance connections for CLT shear walls. Some connections which have shown high stiffness, strength and energy dissipation capacity include dowelled hold-downs with slotted-in steel plates or mixed angle combinations of STS. Appropriate capacity design measures could target some joints as ductile links and others joints as capacity protected and therefore remain elastic. One such capacity protected joint could be carpentry joints for horizontal shear transfer. To overcome the inherent flexibility of timber structures, Buchanan (2016) stated flanged timber core-walls could provide one effective solution. Whether the core-wall system is PT or uses conventional hold-downs, its system level behaviour will depend on its connections between CLT wall panels. Certain joints will be required as ductile links to dissipate energy when subjected to earthquake loading.

Further study on CLT core-wall systems is required to facilitate their implementation, and analytical methods are required for practical design. There is a lack of comprehensive studies on CLT orthogonal joints with STS, but STS could provide one effective solution to transform in-plane CLT shear walls to more structurally efficient CLT core-wall systems. Critical core-wall connection research and system-level testing is required. Then, analytical models could be proposed and validated against the experimental results.

## 2.10 REFERENCES

ACI. (2011). *Building code requirements for structural concrete and commentary. Technical Report ACI 318M-11*. American Concrete Institute.

Amini, M. O., van de Lindt, J. W., Rammer, D., Pei, S., Line, P., & Popovski, M. (2018). Systematic experimental investigation to support the development of seismic performance factors for cross laminated timber shear wall systems. *Engineering Structures*, *172*, 392–404. https://doi.org/10.1016/j.engstruct.2018.06.021

Bejtka, I., & Blaß, H. J. (2002). Joints with inclined screws. *CIB-W18 Timber Structures, Meeting 35*, *35-7–4*, 141.

Benedetti, F., Rosales, V., Opazo-Vega, A., Norambuena-Contreras, J., & Jara-Cisterna, A. (2019). Experimental and numerical evaluation of hold-down connections on radiata pine Cross-Laminated-Timber shear walls: a case study in Chile. *European Journal of Wood and Wood Products*, *77*(1), 79–92. https://doi.org/10.1007/s00107-018-1365-1

Beyer, K., Dazio, A., & Priestley, M. J. N. (2008). Quasi-Static Cyclic Tests of Two U-Shaped Reinforced Concrete Walls. *Journal of Earthquake Engineering*, *12*(7), 1023–1053. https://doi.org/10.1080/13632460802003272

Blaß, H. J., & Sandhaas, C. (2017). *Timber Engineering: Principles for Design*. KIT Scientific Publishing. https://doi.org/10.5445/KSP/1000069616

Branco, Jorge M., & Descamps, T. (2015). Analysis and strengthening of carpentry joints. *Construction and Building Materials*, *97*, 34–47. https://doi.org/10.1016/j.conbuildmat.2015.05.089

Branco, Jorge M., Verbist, M., & Descamps, T. (2018). Design of three Step Joint typologies: Review of European standardized approaches. *Engineering Structures*, *174*(February), 573–585. https://doi.org/10.1016/j.engstruct.2018.06.073

Branco, Jorge Manuel, Piazza, M., & Cruz, P. J. S. (2011). Experimental evaluation of different strengthening techniques of traditional timber connections. *Engineering Structures*, *33*(8), 2259–2270. https://doi.org/10.1016/j.engstruct.2011.04.002

Brandner, R., Flatscher, G., Ringhofer, A., Schickhofer, G., & Thiel, A. (2016). Cross laminated timber (CLT): overview and development. *European Journal of Wood and Wood Products*, *74*(3), 331–351.

Breneman, S., & Richardson, D. (2019). Tall Wood Buildings and the 2021 IBC: Up to 18 Stories of Mass Timber. *WoodWorks*.

Brown, J. R., & Li, M. (2021). Structural performance of dowelled cross-laminated timber hold-down connections with increased row spacing and end distance. *Construction and Building Materials*, *271*, 121595. https://doi.org/10.1016/j.conbuildmat.2020.121595

Brown, J. R., Li, M., & Sarti, F. (2021). Structural performance of CLT shear connections with castellations and angle brackets. *Engineering Structures*, *240*(August), 112346. https://doi.org/10.1016/j.engstruct.2021.112346

Bruhl, F., Schanzlin, J., & Kuhlmann, U. (2014). Ductility in Timber Structures: Investigations on Over-Strength Factors. In *Materials and Joints in Timber Structures: Recent Developments of Technology*. Springer. https://doi.org/10.1007/978-94-007-7811-5

Buchanan, A. (2016). The challenges for designers of tall timber buildings. *WCTE 2016 - World Conference on Timber Engineering*.

Canadian Wood Council. (2021). *Mid-Rise Building*. https://cwc.ca/how-to-build-with-wood/building-systems/mid-rise-buildings/

Casagrande, D., Doudak, G., & Polastri, A. (2019). A proposal for the capacity-design at wall- and building-level in light-frame and cross-laminated timber buildings. *Bulletin of Earthquake Engineering*, *17*(6), 3139–3167. https://doi.org/10.1007/s10518-019-00578-4

Catalyst. (2018). *Catalyst Spokane*. http://www.catalystspokane.com/

CEN. (2005). *EN12512: Timber structures: test methods : cyclic testing of joints made with mechanical fasteners : [including amendment A1:2005]* (Issue Book, Whole). European Committee for Standardization.

CEN. (2014). Eurocode 5: Design of timber structures-Part 1-1: General-Common rules and rules for buildings. In *EN1995-1-1:2004-11 + AC2006-06 + A1:2008-06 + A2:2014-05 Eurocode 5*. European Committee for Standardization.

Chapman, J., Ma, Q., Pham, V., & Whitehead, J. (2016). Integrating CLT panels for building cores: Introduction. Rocking response, and foundation connection testing. *WCTE 2016 - World Conference on Timber Engineering*.

Chen, Z., & Popovski, M. (2020). Mechanics-based analytical models for balloon-type cross-laminated timber (CLT) shear walls under lateral loads. *Engineering Structures*, *208*(January 2019), 109916. https://doi.org/10.1016/j.engstruct.2019.109916

Chen, Z., Popovski, M., & Iqbal, A. (2020). Structural Performance of Post-Tensioned CLT Shear Walls with Energy Dissipators. *Journal of Structural Engineering*, *146*(4).

https://doi.org/10.1061/(asce)st.1943-541x.0002569

Claus, T., Riehle, T., Seim, W., & Götz, T. (2018). Interlocking shear wall connections. *WCTE 2018 - World Conference on Timber Engineering*, 3–8.

Connolly, T., Loss, C., Iqbal, A., & Tannert, T. (2018). Feasibility study of mass-timber cores for the UBC tall wood building. *Buildings*, *8*(8). https://doi.org/10.3390/buildings8080098

Constantin, R., & Beyer, K. (2014). Non-Rectangular RC Walls : A Review on Experimental Investigations. *Proc Second European Conference on Earthquake Engineering*, 1–12.

CSA 086. (2019). *Engineering design in wood*. Canadian Standards Association, Mississauga, ON.

Dangel, U. (2016). *Turning Point In Timber Construction: A New Economy* (1st ed.). Birkhauser.

Di Cesare, A., Ponzo, F. C., Nigro, D., Pampanin, S., & Smith, T. (2017). Shaking table testing of post-tensioned timber frame building with passive energy dissipation systems. *Bulletin of Earthquake Engineering*, *15*(10), 4475–4498. https://doi.org/10.1007/s10518-017-0115-9

Dietsch, P., & Brandner, R. (2015). Self-tapping screws and threaded rods as reinforcement for structural timber elements-A state-of-the-art report. *Construction and Building Materials*, *97*, 78–89. https://doi.org/10.1016/j.conbuildmat.2015.04.028

Dong, W., Li, M., Ottenhaus, L. M., & Lim, H. (2020). Ductility and overstrength of nailed CLT hold-down connections. *Engineering Structures*, *215*(February), 110667. https://doi.org/10.1016/j.engstruct.2020.110667

Dorn, M., de Borst, K., & Eberhardsteiner, J. (2013). Experiments on dowel-type timber connections. *Engineering Structures*, *47*, 67–80. https://doi.org/10.1016/j.engstruct.2012.09.010

Dujic, B., Pucelj, J., & Zarnic, R. (2004). Testing of racking behavior of massive wooden wall panels. *Proceedings of CIB W18 Meeting Thirty-Seven*.

Dunbar, A. J. M. (2014). *Seismic design of core-wall systems for multi-storey timber buildings*. Master's thesis, University of Canterbury.

Dunbar, A., Moroder, D., Pampanin, S., & Buchanan, A. (2014). Timber core-walls for lateral load resistance of multi-storey timber buildings. *World Conference on Timber Engineering*.

FEMA. (2009). *Quantification of building seismic performance factors. FEMA P695*. FEMA.

Flatscher, G., Bratulic, K., & Schickhofer, G. (2015). Experimental tests on cross-laminated timber joints and walls. *Proceedings of the Institution of Civil Engineers - Structures and Buildings*, *168*(11), 868–877. https://doi.org/10.1680/stbu.13.00085

FPInnovations. (2019). *CLT Handbook* (E. Karacabeyli & S. Gagnon (eds.)). FPInnovations.

Gamerro, J., Bocquet, J. F., & Weinand, Y. (2020). Experimental investigations on the load-carrying capacity of digitally produced wood-wood connections. *Engineering Structures*, *213*(April), 110576. https://doi.org/10.1016/j.engstruct.2020.110576

Ganey, R., Berman, J., Akbas, T., Loftus, S., Daniel Dolan, J., Sause, R., Ricles, J., Pei, S., Lindt, J. V. D., & Blomgren, H. E. (2017). Experimental investigation of self-centering Cross-Laminated Timber walls. *Journal of Structural Engineering*, *143*(10).

Gavric, I, Fragiacomo, M., & Ceccotti, A. (2015). Cyclic behavior of CLT wall systems: experimental tests and analytical prediction models. *Journal of Structural Engineering*, *141*(11), 4015034. https://doi.org/doi:10.1061/(ASCE)ST.1943-541X.0001246

Gavric, Igor, Ceccotti, A., Fragiacomo, M., & Popovski, M. (2014). Behaviour of Cross-Laminated Timber Panels under Cyclic Loads. *Materials and Joints in Timber Structures: Recent Developments of Technology*, 689–702.

Gavric, Igor, Fragiacomo, M., & Ceccotti, A. (2015a). Cyclic behavior of typical screwed connections for cross-laminated (CLT) structures. *European Journal of Wood and Wood Products*, *73*(2), 179–191.

Gavric, Igor, Fragiacomo, M., & Ceccotti, A. (2015b). Cyclic behaviour of typical metal connectors for cross-laminated (CLT) structures. *Materials and Structures/Materiaux et Constructions*, *48*(6), 1841–1857. https://doi.org/10.1617/s11527-014-0278-7

*Wood first policy for Gisborne District Council*, (2018) (testimony of Gisborne District Council).

Granello, G., Palermo, A., Pampanin, S., Pei, S., & Lindt, J. Van De. (2020). Pres-Lam Buildings : State-of-the-Art. *Journal of Structural Engineering*, *146*(6), 1–16. https://doi.org/10.1061/(ASCE)ST.1943-541X.0002603

Green, M., & Taggart, J. (2017). *Tall wood buildings: design, construction and performance*. Birkhauser.

Hashemi, A., Bagheri, H., Yousef-Beik, S. M. M., Darani, F. M., Valadbeigi, A., Zarnani, P., & Quenneville, P. (2020). Enhanced Seismic Performance of Timber Structures Using Resilient Connections: Full-Scale Testing and Design Procedure. *Journal of Structural Engineering*, *146*(9), 04020180. https://doi.org/10.1061/(asce)st.1943-541x.0002749

Hashemi, A., Zarnani, P., & Quenneville, P. (2020). Seismic assessment of rocking timber walls with energy dissipation devices. *Engineering Structures*, *221*(June), 111053. https://doi.org/10.1016/j.engstruct.2020.111053

Ho, T. X., Dao, T. N., Aaleti, S., Van De Lindt, J. W., & Rammer, D. R. (2017). Hybrid System of Unbonded

Post-Tensioned CLT Panels and Light-Frame Wood Shear Walls. *Journal of Structural Engineering*, *143*(2), 1–12. https://doi.org/10.1061/(ASCE)ST.1943-541X.0001665

Hossain, A., Danzig, I., & Tannert, T. (2016). Cross-laminated timber shear connections with double-angled self-tapping screw assemblies. *Journal of Structural Engineering*, *142*(11).

Hossain, A., Popovski, M., & Tannert, T. (2018). Cross-laminated timber connections assembled with a combination of screws in withdrawal and screws in shear. *Engineering Structures*, *168*, 1–11. https://doi.org/10.1016/j.engstruct.2018.04.052

Hossain, A., Popovski, M., & Tannert, T. (2019). Group Effects for Shear Connections with Self-Tapping Screws in CLT. *Journal of Structural Engineering (United States)*, *145*(8), 1–9. https://doi.org/10.1061/(ASCE)ST.1943-541X.0002357

Iqbal, A, Pampanin, S., Palermo, A., & Buchanan, A. H. (2015). Performance and design of LVL walls coupled with UFP dissipaters. *Journal of Earthquake Engineering*, *19*(3), 383–409. https://doi.org/10.1080/13632469.2014.987406

Iqbal, A, Smith, T., Pampanin, S., Fragiacomo, M., Palermo, A., & Buchanan, A. H. (2015). Experimental performance and structural analysis of plywood-coupled LVL walls. *Journal of Structural Engineering*, *142*(2).

Iqbal, Asif, Fragiacomo, M., Pampanin, S., & Buchanan, A. (2018). Seismic resilience of plywood-coupled LVL wall panels. *Engineering Structures*, *167*, 750–759. https://doi.org/10.1016/j.engstruct.2017.09.053

Izzi, M., Casagrande, D., Bezzi, S., Pasca, D., Follesa, M., & Tomasi, R. (2018). Seismic behaviour of Cross-Laminated Timber structures: A state-of-the-art review. *Engineering Structures*, *170*, 42–52. https://doi.org/10.1016/j.engstruct.2018.05.060

Jorissen, A., & Fragiacomo, M. (2011). General notes on ductility in timber structures. *Engineering Structures*, *33*(11), 2987–2997. https://doi.org/10.1016/j.engstruct.2011.07.024

Karolak, A., Jasieńko, J., & Raszczuk, K. (2020). Historical scarf and splice carpentry joints: state of the art. *Heritage Science*, *8*(1), 1–19. https://doi.org/10.1186/s40494-020-00448-2

Katerra. (2021). *Catalyst*. https://katerra.com/projects/catalyst-building/

Kelly, J. M., Skinner, R. I., & Heine, A. J. (1972). Mechanisms of energy absorption in special devices for use in earthquake resistant structures. *Bulletin of the New Zealand Society for Earthquake Engineering*, *5*(3), 63–73.

Kevarinmaki, A. (2002). Joints with Inclined Screws. *CIB-W18 Timber Structures, Meeting 35*, *35-7–3*.

Khan, F. R., & Sbarounis, J. A. (1964). Interaction of shear walls and frames in concrete structures under lateral loads. *American Society of Civil Engineers*, *90*.

Li, M., Lam, F., & Foschi, R. O. (2009). Seismic reliability analysis of diagonal-braced and structural-panel- sheathed wood shear walls. *Journal of Structural Engineering*, *135*(5), 587–596. https://doi.org/10.1061/(ASCE)ST.1943-541X.0000008

Li, M., Lam, F., Foschi, R. O., Nakajima, S., & Nakagawa, T. (2012a). Seismic performance of post-and-beam timber buildings II: Reliability evaluations. *Journal of Wood Science*, *58*(2), 135–143. https://doi.org/10.1007/s10086-011-1232-8

Li, M., Lam, F., Foschi, R. O., Nakajima, S., & Nakagawa, T. (2012b). Seismic performance of post and beam timber buildings I: Model development and verification. *Journal of Wood Science*, *58*(1), 20–30. https://doi.org/10.1007/s10086-011-1219-5

Loss, C., Hossain, A., & Tannert, T. (2018). Simple cross-laminated timber shear connections with spatially arranged screws. *Engineering Structures*, *173*, 340–356. https://doi.org/10.1016/j.engstruct.2018.07.004

Lukacs, I., Björnfot, A., & Tomasi, R. (2019). Strength and stiffness of cross-laminated timber (CLT) shear walls: State-of-the-art of analytical approaches. *Engineering Structures*, *178*(October 2018), 136–147. https://doi.org/10.1016/j.engstruct.2018.05.126

Mancini, M. J., & Pampanin, S. (2018). Numerical and Experimental Investigation on Low Damage Steel-Timber Post-Tensioned Beam-Column Connection. *16th European Conference on Earthquake Engineering*, 1–12.

McDonnell, E., & Jones, B. (2020). Performance-Based Engineering Provides Path to More Compelling Mass Timber Projects. *Technology Architecture and Design*, *4*(1), 9–13. https://doi.org/10.1080/24751448.2020.1705709

Menegon, S. J., Wilson, J. L., Lam, N. T. K., & Gad, E. F. (2020a). Experimental assessment of the ultimate performance and lateral drift behaviour of precast concrete building cores. *Advances in Structural Engineering*, *23*(12). https://doi.org/10.1177/1369433220919077

Menegon, S. J., Wilson, J. L., Lam, N. T. K., & Gad, E. F. (2020b). Experimental testing of innovative panel-to-panel connections for precast concrete building cores. *Engineering Structures*, *207*. https://doi.org/10.1016/j.engstruct.2020.110239

Mohammad, M., Blaß, H. J., Salenikovich, A., Ringhofer, A., Line, P., Rammer, D., Smith, T., & Li, M. (2018). Design Approaches for CLT Connections. *Wood and Fiber Science*, *50*, 27–47.

Moroder, D., Pampanin, S., Palermo, A., Smith, T., Sarti, F., & Buchanan, A. (2017). Diaphragm Connections in Structures with Rocking Timber Walls. *Structural Engineering International*, *27*(2), 165–174.

Moroder, D., Smith, T., Dunbar, A., Pampanin, S., & Buchanan, A. (2018). Seismic testing of post-tensioned Pres-Lam core walls using cross laminated timber. *Engineering Structures*, *167*, 639–654. https://doi.org/10.1016/j.engstruct.2018.02.075

Moroder, D., Smith, T., Sarti, F., Armstrong, J., Young, B., & Buchanan, A. (2018). Challenges and solutions in the design of a 10 storey CLT building. *SESOC Journal*.

*Climate Change Response (Zero Carbon) Amendment Act 2019*, (2019) (testimony of New Zealand Government).

Newcombe, M. P., Pampanin, S., & Buchanan, A. H. (2010). Global response of a two storey Pres-Lam timber building. *New Zealand Society for Earthquake Engineering Conference*, *8*(28), 8.

Newcombe, M. P., Van Beerschoten, W. A., Carradine, D., Pampanin, S., & Buchanan, A. H. (2010). In-plane experimental testing of timber-concrete composite floor diaphragms. *Journal of Structural Engineering*, *136*(11), 1461–1468. https://doi.org/10.1061/(ASCE)ST.1943-541X.0000239

NRC. (2018). *Proposed Changes to 2020 NBCC*.

Ottenhaus, L.-M., Li, M., & Smith, T. (2018). Structural performance of large-scale dowelled CLT connections under monotonic and cyclic loading. *Engineering Structures*, *176*(Lvl), 41–48. https://doi.org/10.1016/j.engstruct.2018.09.002

Ottenhaus, L.-M., Li, M., Smith, T., & Quenneville, P. (2018). Mode Cross-Over and Ductility of Dowelled LVL and CLT Connections under Monotonic and Cyclic Loading. *Journal of Structural Engineering (United States)*, *144*(7), 4018074. https://doi.org/10.1061/(ASCE)ST.1943-541X.0002074

Ottenhaus, L., Li, M., & Smith, T. (2020). Analytical Derivation and Experimental Verification of Overstrength Factors of Dowel-type Timber Connections for Capacity Design. *Journal of Earthquake Engineering*, 1–15. https://doi.org/10.1080/13632469.2020.1781711

Ottenhaus, L. M., Li, M., Smith, T., & Quenneville, P. (2018). Overstrength of dowelled CLT connections under monotonic and cyclic loading. *Bulletin of Earthquake Engineering*, 1–21. https://doi.org/10.1007/s10518-017-0221-8

Palermo, A, Pampanin, S., Fragiacomo, M., Buchanan, A. H., & Deam, B. L. (2006). Innovative seismic solutions for multi-storey LVL timber buildings. *WCTE 2006 - World Conference on Timber*

*Engineering*.

Palermo, Alessandro, Pampanin, S., Buchanan, A. H., & Newcombe, M. P. (2005). Seismic design of multi-storey buildings using laminated veneer lumber (LVL). *New Zealand Society for Earthquake Engineering Conference*.

Pampanin, S., Palermo, A., & Buchanan, A. (2013). *Post-Tensioned Timber Buildings - Design Guide Australia and New Zealand*. Structural Timber Innovation Company.

Parisi, M. A., & Piazza, M. (2000). *Mechanics of plain and retrofitted traditional timber connections*. *126*(December), 1395–1403.

Parisi, M. A., & Piazza, M. (2015). Seismic strengthening and seismic improvement of timber structures. *Construction and Building Materials*, *97*, 55–66. https://doi.org/10.1016/j.conbuildmat.2015.05.093

Paulay, T., & Park, R. (1975). *Reinforced concrete structures*. Wiley.

Pei, S, Van De Lindt, J. W., Popovski, M., Berman, J. W., Dolan, J. D., Ricles, J., Sause, R., Blomgren, H., & Rammer, D. R. (2016). Cross-Laminated Timber for Seismic Regions: Progress and Challenges for Research and Implementation. *Journal of Structural Engineering*, *142*(4).

Pei, S, van de Lindt, J. W., Ricles, J., Sause, R., Berman, J., Ryan, K., Dolan, J. D., Buchanan, A., Robinson, T., & McDonnell, E. (2017). Development and Full-Scale Validation of Resilience-Based Seismic Design of Tall Wood Buildings: The NHERI Tallwood Project. *Proceedings of the New Zealand Society for Earthquake Engineering Annual Conference, April 27-29, Wellington, New Zealand, 2017*.

Pei, Shiling, Dolan, J. D., Zimmerman, R. B., Mcdonnell, E., Line, P., & Popovski, M. (2019). From Testing to Codification : Post-tensioned Cross Laminated Timber Rocking Post-tensioned Rocking Wall System. *International Network on Timber Engineering Research (INTER) - Meeting Fifty-Two*, 1–14.

Pei, Shiling, Van De Lindt, J. W., Barbosa, A. R., Berman, J. W., McDonnell, E., Daniel Dolan, J., Blomgren, H. E., Zimmerman, R. B., Huang, D., & Wichman, S. (2019). Experimental seismic response of a resilient 2-story mass-timber building with post-tensioned rocking walls. *Journal of Structural Engineering*, *145*(11), 1–15.

Pilon, D. S., Palermo, A., Sarti, F., & Salenikovich, A. (2019). Benefits of multiple rocking segments for CLT and LVL Pres-Lam wall systems. *Soil Dynamics and Earthquake Engineering*, *117*, 234–244. https://doi.org/10.1016/j.soildyn.2018.11.026

Polastri, A., Izzi, M., Pozza, L., Loss, C., & Smith, I. (2019). Seismic analysis of multi-storey timber buildings braced with a CLT core and perimeter shear-walls. *Bulletin of Earthquake Engineering*, *17*(2), 1009–1028. https://doi.org/10.1007/s10518-018-0467-9

Popovski, M., Schneider, J., & Schweinsteiger, M. (2010). Lateral load resistance of cross-laminated wood panels. *WCTE 2010*, *4*, 3394–3403.

Priestley, M. J. N., Sritharan, S. S., Conley, J. R., & Pampanin, S. (1999). Preliminary results and conclusions from the PRESSS five-story precast concrete test building. *PCI Journal*, *44*(6), 42–67. https://doi.org/10.15554/pcij.11011999.42.67

Ringhofer, A., Brandner, R., & Blaß, H. J. (2018). Cross laminated timber (CLT): Design approaches for dowel-type fasteners and connections. *Engineering Structures*. https://doi.org/10.1016/j.engstruct.2018.05.032

Robeller, C. (2019). Timber plate shell structures: a digital resurgence of traditional joining methods. *Springer International Publishing*, 1117–1133.

Rothoblaas. (2019). *WHT Angle bracket for tensile loads*. Rothoblaas design manual.

*Wood First Policy*, (2015) (testimony of Rotorua Lakes Council).

Sarti, F, Palermo, A., & Pampanin, S. (2016). Development and testing of an alternative dissipative post-tensioned rocking timber wall with boundary columns. *Journal of Structural Engineering*. https://doi.org/10.1061/(ASCE)ST.1943-541X.0001390

Sarti, Francesco. (2015). *Seismic design of low-damage post-tensioned timber wall systems* (Issue PhD Thesis). University of Canterbury.

Sarti, Francesco, Palermo, A., & Pampanin, S. (2016). Quasi-static cyclic testing of two-thirds scale unbonded post-tensioned rocking dissipative timber walls. *Journal of Structural Engineering*, *142*(4), 1–14. https://doi.org/10.1061/(ASCE)ST.1943-541X.0001291

Schmidt, T, & Blaß, H. J. (2016). Contact joints in engineered wood products. *WCTE 2016 - World Conference on Timber Engineering*.

Schmidt, Tobias, & Blaß, H. J. (2018). In-plane shear connection for CLT diaphragms. *International Network on Timber Engineering Research (INTER)*, *51-07–4*, 1–12.

Schneider, J., Tannert, T., Tesfamariam, S., & Stiemer, S. F. (2018). Experimental assessment of a novel steel tube connector in cross-laminated timber. *Engineering Structures*, *177*(September), 283–290. https://doi.org/10.1016/j.engstruct.2018.09.058

Shahnewaz, M., Popovski, M., & Tannert, T. (2020). Deflection of cross-laminated timber shear walls

for platform-type construction. *Engineering Structures*, *221*(July), 111091. https://doi.org/10.1016/j.engstruct.2020.111091

Siem, J. (2017). The single-step joint–a traditional carpentry joint with new possibilities. *International Wood Products Journal*, *8*, 45–49. https://doi.org/10.1080/20426445.2017.1302148

Siem, J., & Jorissen, A. (2015). Can taditional carpentry joints be assessed and designed using modern standards. *Structural Health Assessment of Timber Structures*.

Simpson Strong-Tie. (2019). *Structural connector & fasteners solutions for CLT & Engineered Wood Products*. Simpson Strong-Tie Company Inc.

Smith, T, Moroder, D., Sarti, F., Pampanin, S., & Buchanan, A. (2015). The Reality of Seismic Engineering in a Modern Timber World. *Proceedings of the INTER Meeting Forty-Eight*, *48-102–03*.

Smith, Tobias, Ponzo, F. C., Di Cesare, A., Pampanin, S., Carradine, D., Buchanan, A. H., & Nigro, D. (2014). Post-tensioned glulam beam-column joints with advanced damping systems: Testing and numerical analysis. *Journal of Earthquake Engineering*, *18*(1), 147–167. https://doi.org/10.1080/13632469.2013.835291

Sobon, J. A. (2004). *Historic American Timber Joinery A Graphic Guide*. Timber Framers Guild.

Ssu-Ch'eng, L. (1984). *A Pictorial History of Chinese Architecture: A Study of the Development of its Structural System and the Evolution of its Types* (W. Fairbank (ed.)). The MIT Press. https://doi.org/10.1017/S0305741000033567

Standards New Zealand. (1993). *NZS 3603: Timber structures standard*. Standards New Zealand.

Sullivan, K., Miller, T. H., & Gupta, R. (2018). Behavior of cross-laminated timber diaphragm connections with self-tapping screws. *Engineering Structures*, *168*, 505–524.

Sumiyoshi, T., & Matsui, G. (1989). *Wood Joints in Classical Japanese Architecture*. Kajima Institute Publishing Co., Ltd.

Sun, X., He, M., Li, Z., & Lam, F. (2020). Seismic performance of energy-dissipating post-tensioned CLT shear wall structures I: Shear wall modeling and design procedure. *Soil Dynamics and Earthquake Engineering*, *131*(January), 106022. https://doi.org/10.1016/j.soildyn.2019.106022

Tannert, T. (2019). Design provisions for cross-laminated timber structures. *Structures Congress 2019*, 127–136.

Tannert, Thomas. (2016). Improved performance of reinforced rounded dovetail joints. *Construction and Building Materials*, *118*, 262–267. https://doi.org/10.1016/j.conbuildmat.2016.05.038

Tannert, Thomas, Follesa, M., Fragiacomo, M., González, P., Isoda, H., Moroder, D., Xiong, H., & Van De Lindt, J. W. (2018). Seismic design of cross-laminated timber buildings. *Wood and Fiber Science*, *50*, 3–26.

Tomasi, R, Piazza, M., Angeli, A., & Mores, M. (2006). A new ductile approach design of joints assembled with screw connectors. *WCTE 2006*.

Tomasi, Roberto, Crosatti, A., & Piazza, M. (2010). Theoretical and experimental analysis of timber-to-timber joints connected with inclined screws. *Construction and Building Materials*, *24*(9), 1560–1571. https://doi.org/https://doi.org/10.1016/j.conbuildmat.2010.03.007

Trutalli, D., Marchi, L., Scotta, R., & Pozza, L. (2019). Capacity design of traditional and innovative ductile connections for earthquake-resistant CLT structures. *Bulletin of Earthquake Engineering*, *17*(4), 2115–2136. https://doi.org/10.1007/s10518-018-00536-6

Uibel, T., & Blaß, H. J. (2007). Edge joints with dowel type fasteners in cross laminated timber. *Proceedings of CIB W18 Meeting Forty*, *40-7–2*.

Uibel, T., & Blaß, H. J. (2006). Load carrying capacity of joints with dowel type fasteners in solid wood panels. *Proceedings of CIB W18 Meeting Thirty-Nine*, *39-7–5*, 191–202.

van de Lindt, J. W., Amini, M. O., Rammer, D., Line, P., Pei, S., & Popovski, M. (2020). Seismic Performance Factors for Cross-Laminated Timber Shear Wall Systems in the United States. *Journal of Structural Engineering*, *146*(9), 1–16. https://doi.org/10.1061/(ASCE)ST.1943-541X.0002718

Verbist, M., Branco, J. M., Poletti, E., Descamps, T., & Lourenço, P. B. (2017). Single Step Joint: overview of European standardized approaches and experimentations. *Materials and Structures/Materiaux et Constructions*, *50*(2). https://doi.org/10.1617/s11527-017-1028-4

Wakabayashi, M., Nakamura, T., Katagihara, A., Yogoyama, H., & Morisono, T. (1973). Experimental study on the elasto-plastic behavior of braces enclosed by precast concrete panels under horizontal cyclic loading - Parts 1 &2. Summaries of technical papers of annual meeting. *Architectural Institue of Japan, Structural Engineering SEction*, *10*.

Wald, F., Mareš, J., Sokol, Z., & Drdácký, M. (2000). Component Method for Historical Timber Joints. *The Paramount Role of Joints into the Reliable Response of Structures*, 417–424. https://doi.org/10.1007/978-94-010-0950-8_36

Wood Solutions. (2019). *2019 changes to the National Construction Code (NCC)*. https://www.woodsolutions.com.au/blog/2019-changes-national-construction-code-ncc

Yoshino, T., & Karino, Y. (1971). Experimental study on shear wall with braces: Part 2. Summaries of technical papers of annual meeting. *Architectural Institue of Japan, Structural Engineering SEction*, *11*.

Zhang, X., Popovski, M., & Tannert, T. (2018). High-capacity hold-down for mass-timber buildings. *Construction and Building Materials*, *164*, 688–703. https://doi.org/10.1016/j.conbuildmat.2018.01.019

# 3 Structural performance of dowelled CLT hold-down connections with increased row spacing and end distance

*The work presented herein is based on the published articles cited below:*

*J.R. Brown, M. Li, Structural performance of dowelled cross-laminated timber hold-down connections with increased row spacing and end distance, Constr. Build. Mater. 271 (2021) 121595. https://doi.org/10.1016/j.conbuildmat.2020.121595.*

*J. Brown, M. Li, L.M. Ottenhaus, C. Ravn, B. Scott, Ductility of dowelled New Zealand Douglas-Fir CLT connections under monotonic and cyclic loading, in: Pacific Conf. Earthq. Eng., Auckland, 2019.*

*Key Findings / Outputs:*

- 47 dowelled CLT connections were tested under monotonic and cyclic loading.
- Increased row spacing and end distance significantly increased ductility.
- Reinforcement by screws or threaded dowels with nuts enhanced performance.
- 3-ply (135 mm), 5-ply (175 mm), and 7-ply (275 mm) CLT panels were employed.
- The maximum connection overstrength factor was 1.70 and the average was 1.61.
- 215 half hole dowel embedment tests were compared against existing analytical embedment strength equations and used to determine theoretical overstrength.

## 3.1 INTRODUCTION

This study is to assess the structural performance of dowelled CLT hold-down connections under monotonic and cyclic loading. The focus is to study the influence of increased fastener row spacing and end distance on strength, stiffness, ductility and overstrength of the connections. The study also investigates the benefits of applying screw reinforcement to deter the onset of potential brittle failure modes or mode cross-over. The experimental results are compared with analytical calculations to validate the design equations and derive connection overstrength. Meanwhile, embedment testing on the CLT materials and fastener bending testing are also carried out to check against the embedment strength prediction models and fastener bending yielding moments which are critical input for the prediction accuracy of the analytical calculations of the connection strength.

The experimental test programme is introduced in Section 3.2 and connection strength and overstrength predictions are described in Section 3.3 which included 215 dowel embedment tests. In Section 3.4, the connection test results, failure modes, and discussion are presented.

## 3.2 EXPERIMENTAL PROGRAMME

### 3.2.1 Specimen Description

As shown in Table 3-1, 47 hold-down specimens were tested in 17 series. Three different CLT layups (3-ply 135mm thick; 5-ply 175mm thick; and 7-ply 275mm thick) were used, herein simply referred to as CLT3, CLT5 and CLT7, respectively. The Douglas-Fir lamella were graded SG8 with average Modulus of Elasticity of 8 GPa according to NZS3603 (1993). The CLT panels were not edge glued. After testing, a small piece was cut from each specimen and oven dried to determine density and moisture content. The average moisture content was 11%, and the mean and characteristic densities are listed in Table 3-2. The characteristic density was determined assuming a normal distribution as per EN 14358 (2016) and combining hold-down and dowel embedment samples with the same CLT layup. $\phi$12mm dowels were used in the CLT3 panels and $\phi$20mm dowels were used for the CLT5 and CLT7 specimens. The dowels were Grade 300E according to AS/NZS4671 (2001), which specifies a yield strength in the range of 300 MPa – 380 MPa.

In the test series labelling with the format of XXX-YYY-Z-V, XXX refers to the CLT type (CLT3, CLT5, or CLT7), YYY refers to the dowel spacing type (Std indicates the standard spacing following Eurocode 5 (2014) and CLT Handbook (2011), or Inc indicates the increased spacing), Z refers to unreinforced (U) or reinforced specimens R1 and R2 (R1 indicates reinforcement by inclined self-tapping screw and R2 indicates reinforcement by threaded dowels with nut and washer), and V refers to monotonic loading (M) or cyclic loading (C). For all unreinforced test series, the number of samples for monotonic loading

was three and for cyclic loading was five. Testing standard EN 14358 (2016) specifies a minimum sample size of three to determine the 5th and 95th percentile value with a 75% confidence interval. This was the main reason for choosing a sample size of three for the monotonic tests. For the cyclic tests, a sample size of five was chosen as it was the next suggested sample size increment in EN 14358 (2016) which would reduce the $k_s$ multiplication factor on the standard deviation. Increased sample sizes could further reduce the $k_s$ factor as discussed in Section 3.4.4. The sample size for the reinforced specimens was limited to one which provided qualitative comparison to the unreinforced series' results.

*Table 3-1: Dowelled hold-down test matrix*

| Panel | Layup | Thickness | Dowel Diameter | Load Type | Series | Sample Size |
|---|---|---|---|---|---|---|
| - | mm | mm | mm | - | - | - |
| CLT3 | 45/45/45 | 135 | 12 | M | CLT3-Std-U-M | 3 |
| | | | | | CLT3-Std-R1-M | 1 |
| | | | | C | CLT3-Std-U-C | 5 |
| | | | | | CLT3-Inc-U-C | 5 |
| | | | | | CLT3-Inc-R1-C | 1 |
| CLT5 | 45/20/45/20/45 | 175 | 20 | M | CLT5-Std-U-M | 3 |
| | | | | | CLT5-Std-R1-M | 1 |
| | | | | C | CLT5-Std-U-C | 5 |
| | | | | | CLT5-Std-R2-C | 1 |
| | | | | | CLT5-Inc-U-C | 5 |
| | | | | | CLT5-Inc-R1-C | 1 |
| CLT7 | 45/35/35/45/35/35/45 | 275 | 20 | M | CLT7-Std-U-M | 3 |
| | | | | | CLT7-Std-R1-M | 1 |
| | | | | C | CLT7-Std-U-C | 5 |
| | | | | | CLT7-Std-R1-C | 1 |
| | | | | | CLT7-Inc-U-C | 5 |
| | | | | | CLT7-Inc-R2-C | 1 |

*Table 3-2: Density of specimens*

| Panel | Layup | Thickness | $\rho_m$ | $\rho_k$ |
|---|---|---|---|---|
| - | mm | mm | kg/m$^3$ | kg/m$^3$ |
| CLT3 | 45/4545 | 135 | 478 | 426 |
| CLT5 | 45/20/45/20/45 | 175 | 462 | 422 |
| CLT7 | 45/35/35/45/35/35/45 | 275 | 457 | 417 |

Figure 3-2a - Figure 3-2c show isometric views of the CLT3, CLT5, and CLT7 specimens with the dimensions. The top dowel group of 6-7 dowels was the overdesigned connection to connect the actuator. The lower group of four dowels formed the hold-down connections tested to failure. The predrilled holes in CLT had the same diameter as the dowel. Dowel spacing parameters $a_2$ and $a_3$ in the hold-down connections (shown in Table 3-3 and Figure 3-2d) were varied. Figure 3-2e - Figure 3-2m show the specific dowel size, spacing and the reinforcement if used for each test series. An internal slot was in the middle of each CLT specimen for the internal steel plate with 2mm tolerance. Thus, a 14mm wide slot was used for a 12mm thick steel plate for the CLT3 specimens and a 22mm wide slot was used for the 20mm thick steel plate for the CLT5 and CLT7 specimens. The diameter of the holes on the steel plates was 2mm larger than the dowel diameter as per NZS 3404 (Standards New Zealand, 1992) which accounted for the approximately 1mm initial connection slip discussed later.

Type 1 (R1) reinforcement was implemented on each of the CLT3, CLT5 and CLT7 specimens with standard or increased fastener spacing. Four fully threaded (FT) self-tapping screws (STS) were installed at $\alpha = 30°$ and at a spacing of 3 times the dowel diameter as indicated in Figure 3-2i, Figure 3-2j, and Figure 3-2l. These inclined FT STS aimed to delay the onset of the potential side wood member opening/splitting by prying action. The FT $\phi$7mm STS were installed into $\phi$4mm predrilled holes to 70% of the screw length with jigs to ensure correct alignment. The STS were 140mm, 180mm, and 260mm long for the CLT3, CLT5 and CLT7 panels respectively. Type 2 reinforcement (R2) was implemented only on the test series CLT5-Std-R2 and CLT7-Inc-R2 by replacing the lower two smooth dowels with dowels with threaded ends for a washer and nut (R2). The new draft of the New Zealand timber design standard DZ NZS/AS 1720.1/V6.0 (2018) requires the designer to take measures to ensure joint cohesion at large deformations and one possible solution to prevent timber member splitting/separation in dowelled connections is to replace some dowels with fitted bolts (Hans Joachim Blaß & Sandhaas, 2017). By implementing both R1 and R2 reinforcement in different test series, the effectiveness of using FT STS instead of end threaded dowels with nuts and washers was evaluated, which could also provide a more aesthetically appealing solution.

Timber design standards specify minimum fastener spacing for dowel-type connections including row spacing ($a_2$) and end distance ($a_3$). Table 3-3 provides a summary of minimum fastener spacing requirements in different design standards as well as the two types of fastener spacing (Std and Inc) used in this study. The current NZS3603 (1993), and Eurocode 5 (2014), other than German and Austrian National Annex's (NAs), do not specifically mention CLT. Dowel spacing in CLT in the NAs and the CLT Handbook (2011) are predominantly adopted from previous work by Uibel and Blaß (2007, 2006). The new CSA-O86 Supplement (2019) and NDS (2015) provide spacing and adjustment factors

for joints in CLT. Previous studies on dowelled CLT hold-downs by Ottenhaus et al. (2018) implemented denser dowel spacing to investigate brittle failure modes and hypothesized that by increasing dowel row spacing ($a_2$) and dowel end distance ($a_3$), increased ductility could be achieved. As such, in this test programme, the Std dowel spacing represents the spacing close to and representative of current design standards and the Inc dowel spacing represents increased $a_2$ and $a_3$ such that the impact of dowel spacing on connection ductility could be assessed. It should be noted that some of the spacing's listed below are minimum values, and that to compare similar behaviours, one should compare the relevant design equations as well.

*Table 3-3: Dowel spacing in design codes and test programme*

| Spacing | Design Codes and Handbooks | | | | | Test Programme | |
|---|---|---|---|---|---|---|---|
| | NZS3603[1] (Standards New Zealand, 1993) | Eurocode 5[1] (CEN, 2014) | CLT Handbook (Gagnon et al., 2011) | CSA-O86 (Canada) (CSA 086, 2019) | NDS (USA) (AWC, 2015) | Std | Inc |
| $a_1$ | 5d | 5d | 4d | 4d | 4d | 5d | 5d |
| $a_2$ | 2.5d[2] | 3d | 4d | 3d | 3d | 4d | 6d |
| $a_3$ | 8d | 7d | 5d | 5d | 7d | 7d | 9d |

[1]Dowel spacing is not specific to CLT, but to general timber connection design

[2]$a_2$ = 2.5d is calculated following Eq. 4.10 in NZS 3603

The locations of the predrilled holes for the dowels were random with regard to the gaps between CLT laminations, as shown in Figure 3-1a - Figure 3-1f. The test specimens with dowel locations coinciding with the gaps are highlighted in the results. Figure 3-1b and Figure 3-1d show R1 reinforcement with STS and R2 reinforcement with end-threaded dowels with nuts and washers, respectively.

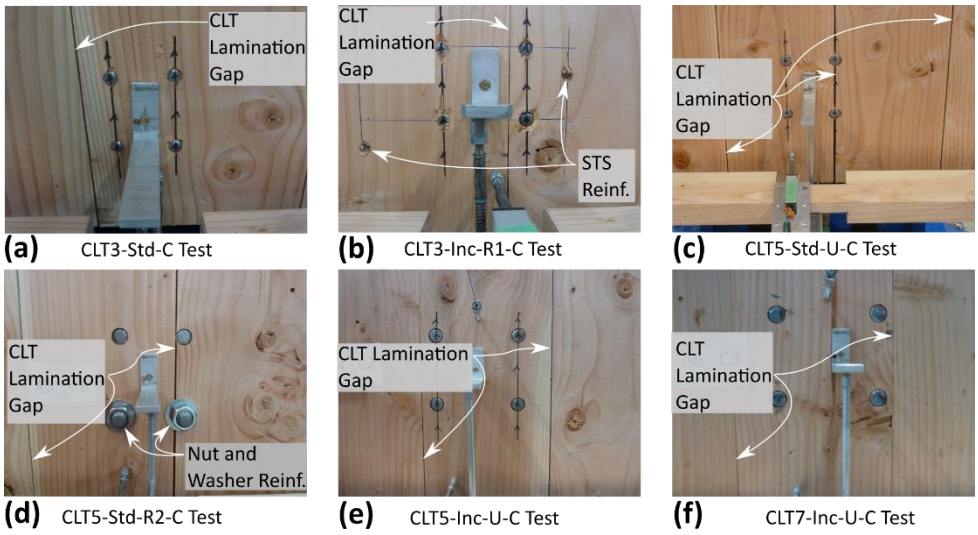


*Figure 3-1: Random location of dowel group with reference to CLT lamination gaps*

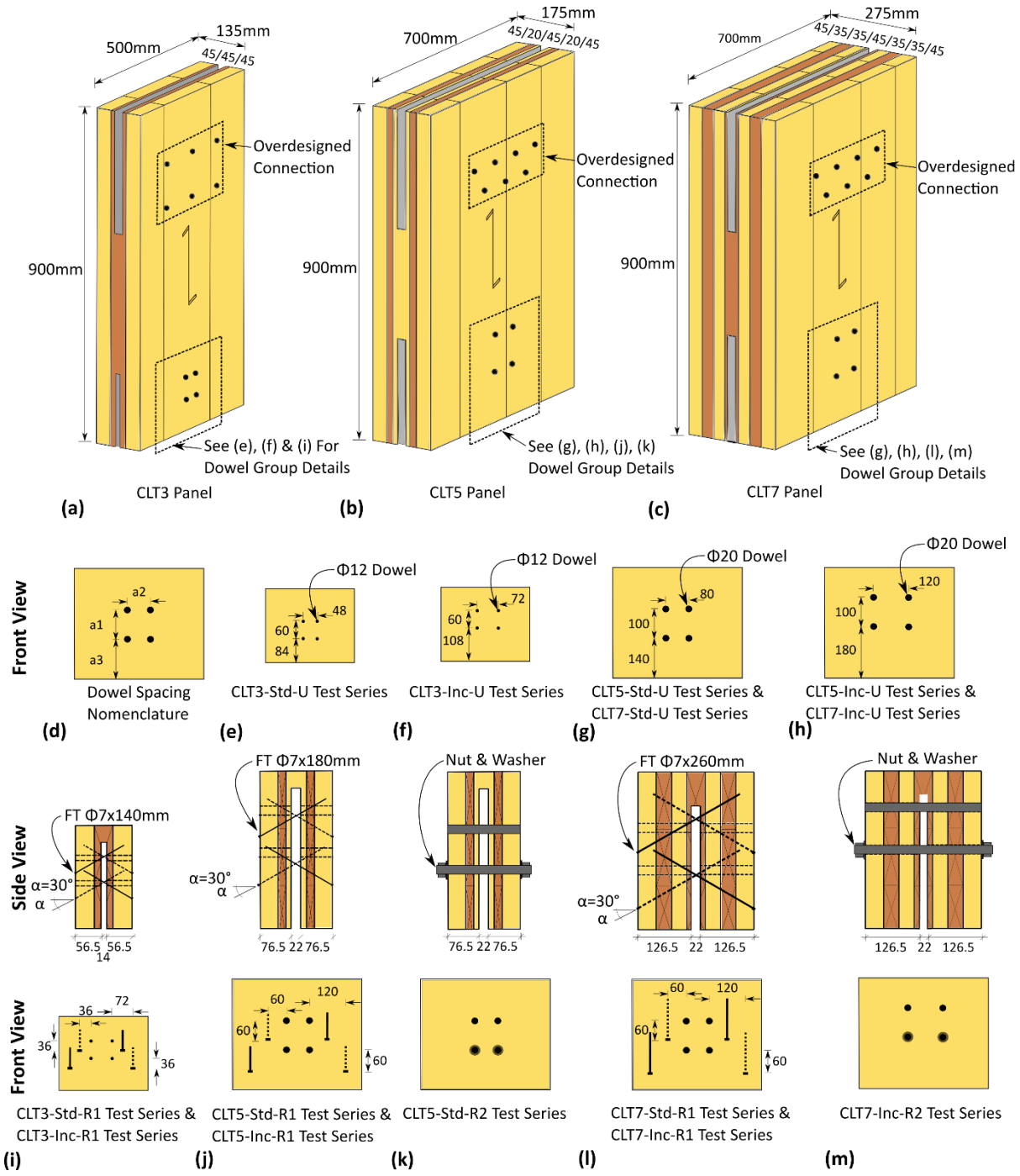


*Figure 3-2: (a) CLT3 isometric (b) CLT5 isometric (c) CLT7 isometric (d) dowel spacing nomenclature (e) CLT3-Std-U (f) CLT3-Inc-U (g) CLT5-Std-U & CLT7-Std-U (h) CLT5-Inc-U & CLT7-Inc-U (i) CLT3-Std-R1 & CLT3-Inc-R1 (j) CLT5-Std-R1 & CLT5-Inc-R1 (k) CLT5-Std-R2 (l) CLT7-Std-R1 & CLT7-Inc-R1 (m) CLT7-Inc-R2*

### 3.2.2 Methods

Figure 3-3 shows a photo of the test setup. A 700kN hydraulic ram with a load cell was attached to the reaction frame on one end and the 20mm thick steel plate in the overdesigned connection. Parallel flange channel (PFC) steel beams (Standards New Zealand, 1992) were installed on either side of the custom connector plate for the hydraulic ram and overstrength connection in order to guide the

loading head and provide out-of-plane restraint for the test specimen. Plastic shims were installed between PFCs and the loading head connector plate to minimize friction. The overdesigned connection consisted of six $\phi$20mm dowels for the CLT3 specimens and seven $\phi$25mm dowels for the CLT5 and CLT7 specimens. Grade 4140 (2007) high strength steel dowels with minimum 0.2% proof stress of 655 MPa were implemented, and the connection design strength was significantly stronger than the lower hold-down connection with a group of 4 dowels.

Figure 3-4 shows the instrumentation used in the testing. 50mm linear variable displacement transducers (LVDTs) were used throughout except at positions 1 and 2 where 100mm LVDTs were used. The key measurements were the relative displacement of the lower dowel group measured on each side of the specimen by positions 1 and 2, and the displacement of the lower internal steel plate measured by positions 3 and 4. The relative displacement was determined by subtracting the average measurement of position 3 and position 4 from the average measurement of position 1 and position 2. LVDTs at positions 5 and 6 monitored out-of-plane rotation, and at positions 7 and 8 monitored the overdesigned connection.

The average of three monotonic test results was used to determine the ultimate displacement of the specimen, which was the displacement at which the post-peak load reached 80% of the maximum load. The average ultimate displacement was used to define the displacement amplitudes of the modified half cyclic loading protocol based on ISO 16670 (2003). One half cycle amplitude at 1.25, 2.5, 5, 7.5, and 10% $\Delta_{Fu}$ were performed followed by three half cycle amplitudes at 20, 40, and 60% $\Delta_{Fu}$, and then increasing increments of 20% $\Delta_{Fu}$ (80, 100% $\Delta_{Fu}$ etc.) until failure as defined by ISO 16670 (2003) and explained later. This loading protocol was chosen to match previous similar testing by Ottenhaus et al. (2018) for comparison purposes. The loading rate was 0.5mm/s and within the specified limits of ISO 16670 (2003). The test results were analysed as per EN 12512 (2005a) to determine the yield strength, $F_y$, maximum strength, $F_{max}$, and ultimate displacement, $F_u$, and the corresponding yield displacement, $\Delta_y$, displacement at maximum strength, $\Delta_{Fmax}$, ultimate displacement, $\Delta_{Fu}$, and the elastic stiffness, $k$. The elastic stiffness was calculated for the range of the load-slip curve between 10% and 40% $F_{max}$. Herein, the displacement capacity is synonymous to the ultimate displacement. While EN 12512 (2005a) limits the ultimate displacement to the minimum of 30mm connection slip or the displacement at which post-peak 80% $F_{max}$ is reached, connection slips greater than 30mm were recorded and they are presented to illustrate the impact of increased dowel spacing on connection ductility. In the CLT7-Inc-C test series the test was stopped due to reaching the displacement limits of the test setup before the post-peak load dropped to 80% $F_{max}$. In these instances, the minimum $\Delta_{Fu}$ and ductility are reported. Connection ductility, $\mu$, is reported as the ratio

of $\Delta_{Fu}$ to $\Delta_y$ as shown in Equation (3-1) and the connection ductility was defined as ductile for $\mu > 6$ (Smith et al., 2006).

$$\mu = \frac{\Delta_{Fu}}{\Delta_y} \tag{3-1}$$

where $\Delta_{Fu}$ = ultimate displacement corresponding to the post-peak deformation at 80% of the maximum load; $\Delta_y$ = displacement at yield point. It should be noted that connection ductility is not the same a building / system level ductility/drift capacity. In this context and depending on the relation of the connection to the lateral load resisting system and building, $\mu = 6$ may not be sufficient to provide target system level ductility/drift capacity. System level ductility/drift capacity relation to connection ductility was beyond the scope of the study presented herein.

Connection overstrength can be defined as the discrepancy between analytically calculated design strength in code provisions and the 95th-percentile of the true strength distribution. Jorissen and Fragiacomo (2011) defined the overstrength factor for timber connections, $\gamma_{Rd}$, as:

$$\gamma_{Rd} = \gamma_M \cdot \gamma_{an} \cdot \gamma_{0.95} = \frac{F_k}{F_d} \cdot \frac{F_{0.05}}{F_k} \cdot \frac{F_{0.95}}{F_{0.05}} \tag{3-2}$$

where $\gamma_M$ = overstrength attributed to material safety factor; $\gamma_{an}$ = overstrength attributed to conservatism of analytical models; $\gamma_{0.95}$ = overstrength attributed to difference between 5$^{th}$ and 95$^{th}$ percentile of strength distribution; $F_k$ = characteristic strength; $F_d$ = design strength; $F_{0.05}$ = 5$^{th}$ percentile of strength distribution; $F_{0.95}$ = 95$^{th}$ percentile of strength distribution.

The observed experimental overstrength factors for the maximum strength, $\gamma_{Rd,i}$, were determined as per Equation (3-3) whereas the overstrength factors for each hold-down group with the same dowel spacing were determined as per Equation (3-4).

$$\gamma_{Rd,i} = \frac{F_{max,i}}{F_{max,theo,k}} \tag{3-3}$$

$$\gamma_{Rd} = \frac{F_{max,0.95}}{F_{max,theo,k}} \tag{3-4}$$

where Equation (3-3) and Equation (3-4) were derived from Equation (3-2) assuming that $\gamma_M = 1.0$ according to Eurocode 8 (2005b). $F_{max,i}$ was the observed experimental maximum strength, and $F_{max,theo,k}$ was the characteristic value of the theoretical maximum strength prediction which will be discussed further in Section 3.3.4. $F_{max,0.95}$ was the 95$^{th}$ percentile of the strength distribution for each hold-down series which was determined as per EN 14358 (2016) assuming that the data were log-normally distributed. Energy dissipation was calculated by determining the total area enclosed by the hysteretic loops.

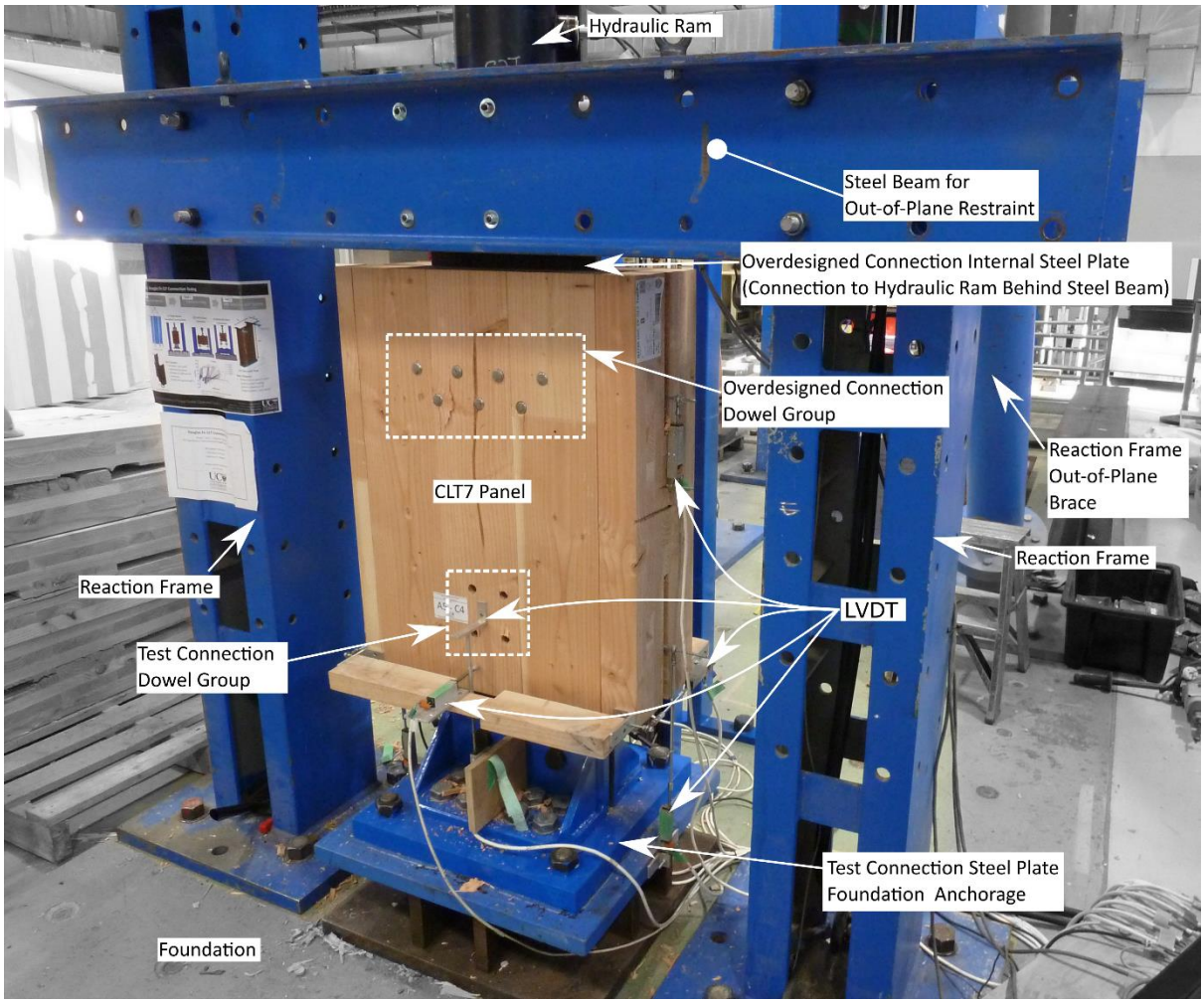


*Figure 3-3: Experimental test set-up*

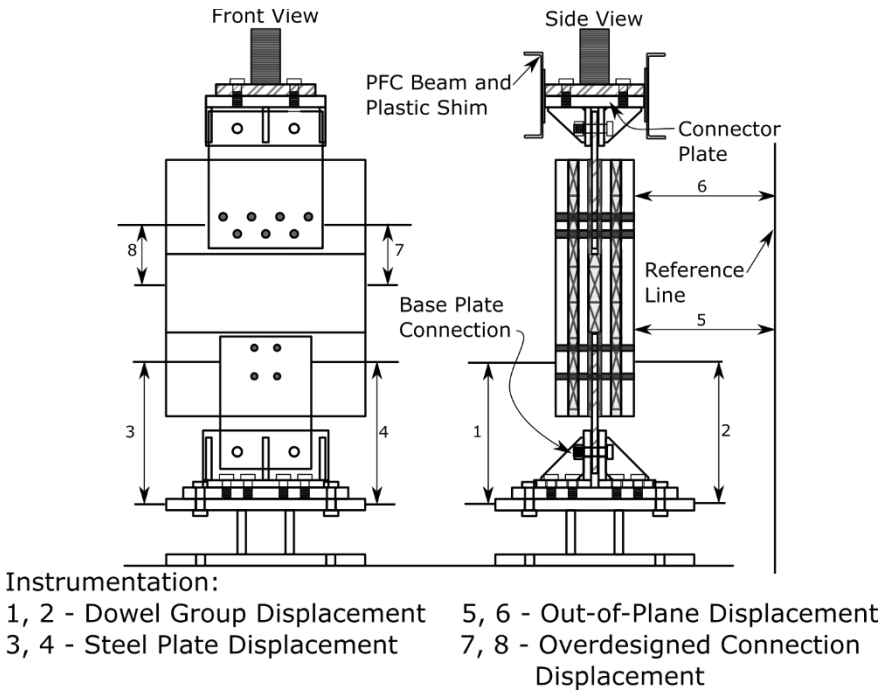


*Figure 3-4: Specimen instrumentation – CLT7 joint specimen shown*

## 3.3 PREDICTIONS OF CONNECTION STRENGTH AND OVERSTRENGTH FACTORS

### 3.3.1 Theoretical Considerations

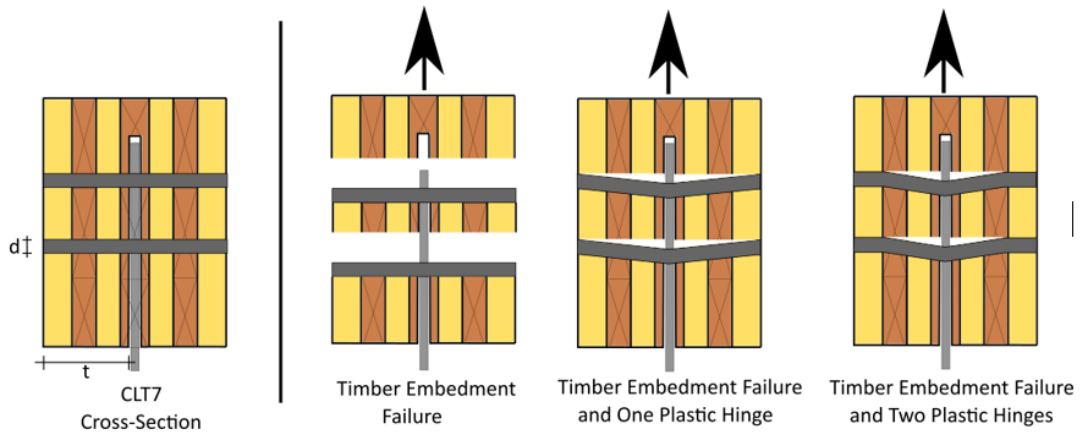


*Figure 3-5: European yield model ductile failure modes* (CEN, 2014)*, CLT7 panel shown*

Within the EYM, the characteristic embedment strength, $f_{h,k}$, and fastener yield moment, $M_y$, are two critical influencing parameters. To determine the connection strength $f_{h,k}$ can be calculated by Eq. 5 as per CLT Handbook (2011) and Uibel and Blaß (2006) as:

$$f_{h,k} = \frac{0.031(1 - 0.015d)\rho_k^{1.16}}{1.1sin^2\varphi + cos^2\varphi} \quad (3\text{-}5)$$

where d = dowel diameter, $\rho_k$ was as per Table 3-2 and $\varphi$ was 0°. $M_y$ can be determined by Equation (3-6):

$$M_{y,p} = \frac{d^3}{6} f_y \quad (3\text{-}6)$$

where $f_y$ was for the ordered steel grade. In this instance $f_y$ was 300MPa and $f_y$ will be discussed further in Section 3.3.2. The effective plastic moment capacity ($M_{y,eff}$) as per Eurocode 5 (2014) was not used in this study. Blaβ et al. (2001) initially proposed $M_{y,eff}$ based on the experimental results for dowel-type fasteners at a maximum 15mm connection displacement as per EN 26891 (1991). Because the reported dowel rotation angles were significantly less that the required 45° dowel rotation angle for full plasticization as per EN 409 (2009), the $M_{y,eff}$ equation was proposed and later adopted in Eurocode 5 (2014). However, recent work by Ottenhaus et al. (2018) reported that for ductile dowel-type connections, close to full plasticisation of the fasteners occurred, and therefore implementing $M_{y,eff}$ would significantly under predict the connection strength and introduce additional overstrength. Therefore, in this study the full plastic yield moment was assumed similar to Ottenhaus et al. (2018) which will be verified based on experimental observations in Section 3.4.2. The strength predictions in this study were as per the EYM in Equation (3-7).

$$F_{max,theo,k} = min\begin{cases} n_s \cdot n \cdot f_{h,k} \cdot t \cdot d & (a) \\ n_s \cdot n \cdot f_{h,k} \cdot t \cdot d \left[\sqrt{2 + \frac{4M_{y,p}}{f_{h,k} d t^2}} - 1\right] & (b) \\ n_s \cdot n \cdot 2.3\sqrt{M_{y,p} f_{h,k} d} & (c) \end{cases} \quad (3\text{-}7)$$

where n = 4 for number of fasteners and $n_s$ = 2 for two shear planes, t = side member thickness, d = dowel diameter, $f_{h,k}$ and $M_{y,p}$ are as defined previously. Rope effect was only considered for specimens CLT5-Std-R2 and CLT7-Inc-R2 which had two dowels end-threaded with nuts and washers as per Eurocode 5 (2014). In all other specimens, rope effect was not considered. The side member thickness t was 56.5mm, 76.5mm, and 126.5mm and fastener diameter d = 12mm, 20mm, and 20mm for CLT3, CLT5, and CLT7 specimens respectively as shown in Figure 3-2. In all specimens, Equation (3-7) governed the connection strength.

Theoretical overstrength, $\gamma_{Rd,theo}$, can be evaluated on a component based approach. Ottenhaus et al. (2020; 2018) derived a generic theoretical evaluation of overstrength such that Equation (3-2) for dowelled hold-down connections becomes:

$$\gamma_{Rd,theo} = \gamma_M \cdot \gamma_{an} \cdot \gamma_{0.95} = \gamma_{an,My} \cdot \gamma_{0.95,My} \cdot \gamma_{an,fh} \cdot \gamma_{0.95,fh} \quad (3\text{-}8)$$

Where $\gamma_{an,My}$ = 1.0 when the plastic yield moment is assumed as per Ottenhaus et al. (2018), $\gamma_{0.95,My}$ = overstrength attributed to the strength distribution given in AS NZS 4671 (2001), $\gamma_{an,fh}$ = overstrength attributed to experimentally determined embedment strength and the CLT Handbook (2011), and $\gamma_{0.95,fh}$ = overstrength attributed to the strength distribution of the embedment tests performed.

In this study, dowel bending capacity $M_{y,p}$ and the CLT embedment strength $f_h$ were evaluated by experimental testing to validate the design specifications and to determine the theoretical overstrength.

### 3.3.2 Dowel Bending Tests

In the hold-down tests, $\phi$12mm and $\phi$20mm dowels with Grade 300E (2001) were used. According to AS/NZS 4671 (2001), the specified yield stress $f_y$ is in a range of 300MPa - 380MPa. To verify this, three replicates of three-point dowel bending tests were performed according to AS/NZS ISO 10984 (2015) as shown in Figure 3-6a. The dowels were 200mm long, the distance between the supports was 120mm, and the displacement was measured from the top of the dowel. The load displacement curves of the tests are shown in Figure 3-6b.

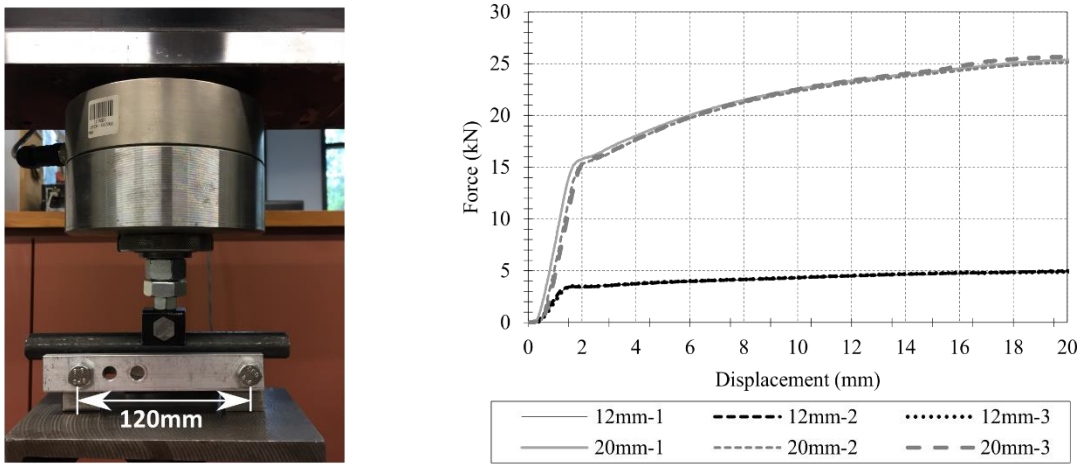


*Figure 3-6: (a) Dowel bending test set-up, ø20mm dowel shown, and (b) load displacement curves of ø12mm and ø20mm dowels*

Table 3-4 shows the mean results and the coefficients of variation (CV) of three replicates. The CV was less than 1% such that the mean yield moment, $M_{y,mean}$, was approximately equal to the characteristic $M_{y,k}$. The mean yield strength $f_y$ was determined to be 357 and 367MPa for $\phi$12mm and $\phi$20mm dowels, within the specified limits of AS/NZS 4671 (2001). From the tensile test data provided by the supplier, the mean $f_y$ was 343 and 330MPa.

*Table 3-4: Results of dowel bending tests*

| Dowel Diameter | $M_{y,mean}$ | CV | Panel | $\gamma_{95,My}$ |
|---|---|---|---|---|
| mm | Nmm | % | | - |
| 12 | 102,815 | 0.69 | CLT3 | 1.03 |
| 20 | 488,900 | 0.87 | CLT5 | 1.06 |
| | | | CLT7 | 1.03 |

Table 3-4 also lists the connection overstrength component $\gamma_{0.95,My}$ considering the contribution from the yield moment strength distribution of dowels. These overstrength components were calculated by using $f_y$ = 300MPa and $f_y$ = 357 and 367MPa for ø12mm and $\phi$20mm dowels in Equation (3-6) and then within the EYM Equation (3-7) b for the 4 dowel group connections described in Section 3.2.1. $\gamma_{an,My}$ = 1 is assumed when the plastic yield moment is used (Ottenhaus et al., 2018).

### 3.3.3 CLT Embedment Tests

In order to verify the applicability of the embedment strength equation of the CLT Handbook with commonly available CLT sizes and layups in New Zealand Douglas-fir, 215 embedment tests were performed as shown in Table 3-5. The half-hole embedment tests with $\phi$12, $\phi$16, and $\phi$20mm dowels were conducted according to ASTM D5764-97a (2013). CLT3, CLT5 and CLT7 panels with four different

layups were tested in two load-grain directions, i.e., parallel (Par.) and perpendicular (Perp.) to the grain of the outer CLT layer. The mean, $\rho_m$, and characteristic, $\rho_k$, density for each CLT layup are specified in Table 3-5. The minimum sample size was 30 in order to derive 5th and 95th percentile values with a 75% confidence level as per EN 14358 (2016).

*Table 3-5: CLT embedment test matrix*

| Panel | Layup | Thickness | $\rho_m$ | $\rho_k$ | Load Direction | Dowel Diameter | Series | Sample Size |
|---|---|---|---|---|---|---|---|---|
| - | mm | mm | kg/m³ | kg/m³ | - | mm | - | - |
| CLT3 | 35/35/35 | 105 | 467 | 424 | Par. | 12 | CLT3-105-Par-12 | 30 |
| | 45/4545 | 135 | 478 | 426 | Par. | 12 | CLT3-135-Par-12 | 30 |
| CLT5 | 45/20/45/20/45 | 175 | 462 | 422 | Par. | 20 | CLT5-175-Par-20 | 32 |
| | | | | | Perp. | 20 | CLT5-175-Perp-20 | 30 |
| CLT7 | 45/35/35/45/35/35/45 | 275 | 457 | 417 | Par. | 16 | CLT7-275-Par-16 | 32 |
| | | | | | Par. | 20 | CLT7-275-Par-20 | 31 |
| | | | | | Perp. | 20 | CLT7-275-Perp-20 | 30 |

Figure 3-7a shows the embedment test set-up and Figure 3-7b shows representative embedment load displacement curves for each test series. The samples were loaded at 1mm/min in order to reach the maximum load within 10 minutes as prescribed by ASTM D5764-97a (2013).

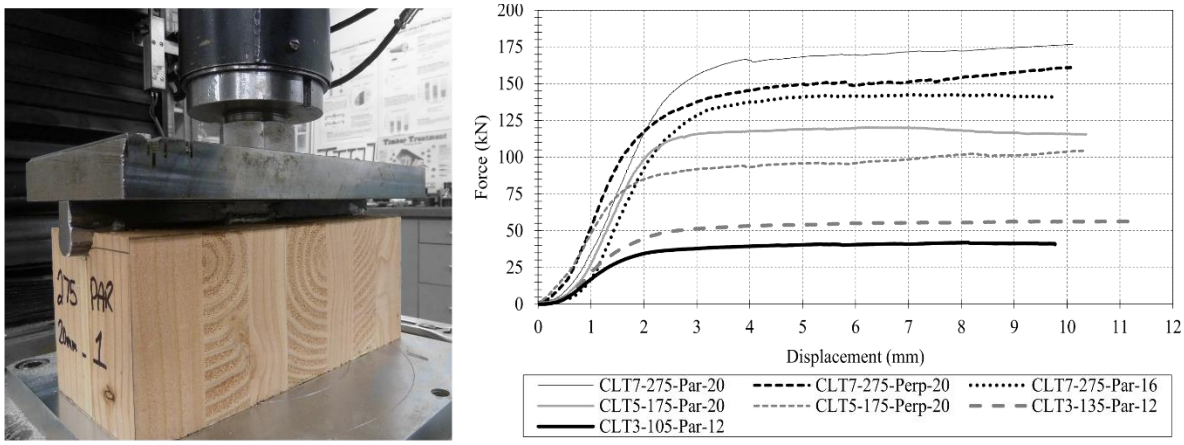


**(a)** **(b)**

*Figure 3-7: (a) Embedment test set-up, CLT275-Par-20 shown, and (b) load displacement curve of embedment tests*

Table 3-6 lists the results of the 7 embedment test series. The embedment strength, $f_h$, was determined following the 5th offset method as prescribed in ASTM D5764-97a (2013) and the mean, 5th percentile and 95th percentile and CV values are listed. It should be noted that the CLT Handbook characteristic embedment strength prediction by Equation (3-5) requires that a single CLT layer does not exceed 40mm thickness and the ratio of thicknesses of the longitudinal and cross laminate boards

is between 0.95 and 2.1. Under these restrictions only the 105mm thick CLT3 layup qualifies; however, in general, the CLT Handbook was able to give reasonably good predictions for the test series. The previously described embedment equation limits were based on the work from Blaß and Uibel (2007) where 15 different CLT layups from four different manufactures were used for dowel embedment tests. The validity of the developed regression model equation, which was then presented in the CLT Handbook (2011), was limited to the limits stated above. Further, the CLT Handbook (2011) embedment equation considers an experimental load duration (short-term). The updated 2019 CLT Handbook (2019) equation accounts for the load duration factor of 0.8 to convert from short-term to standard-term in line with the CSA 086 (2019) design procedure; however, this updated equation was not investigated within this study.

The ratios between the experimental 5$^{th}$ percentile results and the calculated characteristic embedment strength by the CLT handbook were from 0.88 to 1.20, with an average of 1.01. The ratio was less than one and therefore non conservative in CLT3-105-Par-12, CLT3-135-Par-12 and CLT5-175-Perp-20 test series. Similar dowel embedment strength work by Dong et al. (2020) mainly based on three-layer CLT also reported that in some instances the CLT Handbook embedment strength formulation was non conservative for Canadian spruce-pine-fir commercial species group, Douglas fir and southern pine species whose characteristic densities were 400, 540, and 480 kg/m$^3$ respectively. Dong el al. (2020) found that the ratio of the thicknesses of the longitudinal and cross laminate boards was statistically significant. Future research should determine a more generally applicable CLT embedment strength formulation which includes a broader range of CLT layup ratios and CLT with more than three layers such as commercially available layups tested herein.

*Table 3-6: Results of embedment tests*

| Test Series | $f_{h,mean}$ | $f_{h,0.05}$ | $f_{h,0.95}$ | CV | $f_h$ (Gagnon et al., 2011) | $f_{h,0.05}/f_h$ | $\gamma_{an,fh}$ | $\gamma_{95,fh}$ |
|---|---|---|---|---|---|---|---|---|
| | MPa | MPa | MPa | % | MPa | - | - | - |
| CLT3-105-Par-12 | 30.1 | 25.6 | 35.4 | 8.7 | 28.6 | 0.90 | 0.92 | 1.30 |
| CLT3-135-Par-12 | 30.9 | 25.0 | 38.2 | 11.5 | 28.6 | 0.88 | 0.90 | 1.41 |
| CLT5-175-Par-20 | 33.5 | 28.9 | 38.8 | 7.9 | 24.1 | 1.20 | 1.13 | 1.24 |
| CLT5-175-Perp-20 | 25.9 | 19.8 | 33.8 | 14.0 | 21.9 | 0.90 | 0.94 | 1.44 |
| CLT7-275-Par-16 | 30.1 | 27.4 | 33 | 4.9 | 25.8 | 1.06 | 1.06 | 1.18 |
| CLT7-275-Par-20 | 29.8 | 25.2 | 35.3 | 9.0 | 23.7 | 1.06 | 1.05 | 1.34 |
| CLT7-275-Perp-20 | 26 | 22.1 | 30.6 | 8.9 | 21.6 | 1.02 | 1.02 | 1.31 |

The differences between the experimental 5$^{th}$ percentile results and CLT Handbook equation, and the variation in experimental strength distribution (95$^{th}$ to 5$^{th}$ percentile) introduces analytical, $\gamma_{an,fh}$, and

strength distribution, $\gamma_{95,fh}$, overstrength, respectively. In the context of the four dowel hold-down connections described in Section 3.2.1, the component overstrength from $\gamma_{an,fh}$ and $\gamma_{95,fh}$ can be evaluated following Ottenhaus et al. (2018) where the different embedment strength results were implemented within the EYM Equation (3-7)b. For example, to determine $\gamma_{an,fh}$ the four dowel connection strength was determined using both the 5th percentile of embedment testing and the CLT Handbook (2011) equation results listed in Table 3-6. Then, $\gamma_{an,fh} = F_{Conn,f_{h,0.05}}/F_{Conn,f_h}$ where $F_{Conn,f_{h,0.05}}$ is the four dowel connection strength determined using the 5th percentile of embedment testing within the EYM Equation (3-7)b and $F_{Conn,f_h}$ is the four dowel connection strength determined using the CLT Handbook (2011) equation within the EYM Equation (3-7)b. The results of each theoretical overstrength component are listed in Table 3-6. $\gamma_{an,fh}$ can be greater than or less than 1.0 if $f_h$, shown in Equation (3-5), is less than or greater than the observed $f_{h,0.05}$ respectively. Increasing the sample size for each test series could decrease $\gamma_{95,fh}$. The results of the CLT3-135-Par-12, CLT5-175-Par-20, and CLT7-275-Par-20 were used in Section 3.3.4 to determine the theoretical component overstrength.

### 3.3.4 Theoretical Predictions

#### *3.3.4.1 Connection Strength Prediction*

Table 3-7 summarizes the dowel bending properties and embedment strength properties used to predict the theoretical maximum strength $F_{max,theo,k}$ of the dowelled hold-down connections following Equation (3-7)b. The theoretical strength predictions used the material design specifications $f_y$ = 300MPa for $\phi$ 12mm and $\phi$ 20mm dowels and $f_h$ calculated as per Equation (3-5) using the characteristic density of 440kg/m$^3$ as provided in the upcoming DZ NZS AS 1720.1/V6.0 (2018). Therefore, the theoretical strength is based on the material properties readily available to designers. Because the dowel tensile test data were obtained from the supplier and embedment tests were performed, an informed strength prediction could be made, which would eliminate overstrength due to analytical models, $\gamma_{an}$. The informed strength predictions were 79, 214 and 254kN respectively for the CLT3, CLT5 and CLT7 specimens.

*Table 3-7: Summary of hold-down strength predictions*

| CLT Specimen | Fastener Properties | | | CLT Embedment Strength | Hold-down capacity |
|---|---|---|---|---|---|
| | Diameter | $f_y$ | $M_{y,p}$ | $f_{h,k}$ | $F_{max,theo,k}$ |
| mm | mm | MPa | Nmm | MPa | kN |
| CLT3 (135) | 12 | 300 | 86,400 | 29.6 | 87 |
| CLT5 (175) | 20 | 300 | 400,000 | 25.3 | 184 (208[1]) |
| CLT7 (275) | 20 | 300 | 400,000 | 25.3 | 247 (278[1]) |

[1]Theorectical strength prediction for specimens with two dowels end-threaded with nuts and washers. The rope effect for bolts was considered as per Eurocode 5 (CEN, 2014) for two fasteners.

### *3.3.4.2 Connection Overstrength Prediction*

Table 3-8 summarizes the theoretical connection overstrength, $\gamma_{Rd,theo}$ based on the contribution of the components as per Equation (3-8). From Section 3.3.2, $\gamma_{an,My}$ is 1.0 and $\gamma_{0.95,My}$ was determined from the dowel bending tests. From Section 3.3.3 $\gamma_{an,fh}$ and $\gamma_{95,fh}$ were determined from embedment tests. The theoretical results will be compared to the observed overstrength, $\gamma_{Rd}$, determined by the experimental strength distribution of each dowelled hold-down test series in Section 3.4.4.

*Table 3-8: Summary of theoretical overstrength predictions*

| Panel (thickness) | Dowel Diameter | Embedment Test Series | My | | $f_h$ | | Overstrength |
|---|---|---|---|---|---|---|---|
| mm | mm | | $\gamma_{an,My}$ | $\gamma_{95,My}$ | $\gamma_{an,fh}$ | $\gamma_{95,fh}$ | $\gamma_{Rd,theo}$ |
| CLT3 (135) | 12 | CLT3-135-Par-12 | 1.0 | 1.03 | 0.90 | 1.41 | **1.31** |
| CLT5 (175) | 20 | CLT5-175-Par-20 | 1.0 | 1.06 | 1.13 | 1.24 | **1.50** |
| CLT7 (275) | 20 | CLT7-275-Par-20 | 1.0 | 1.03 | 1.05 | 1.34 | **1.45** |

## 3.4 CONNECTION TEST RESULTS AND DISCUSSION

### 3.4.1 Overview

Table 3-9, Table 3-10, and Table 3-11 provide a summary of the hold-down test results for the CLT3, CLT5 and CLT7 specimens respectively and the averages of each test series group. The test results were analysed as per EN 12512 (2005a) as discussed in Section 3.2.2. The experimental overstrength factor for the maximum strength of each connection type is reported as per Equation (3-3) using the strength predictions in Table 3-7. The instances where dowel groups were located on a CLT lamination gap as shown in Figure 3-1 are indicated in each table. In the CLT3-Std-U-C1 test, the loading protocol did not force the dowel group back to the initial position at the end of each amplitude cycle. As a consequence, the reported total energy dissipated was significantly less than tests C2-C5; however, the backbone curve was determined unaffected by this and all other connection performance parameters were deemed adequate for comparison. In the test series CLT7-Inc-U the minimum ultimate displacement and ductility are reported as the test was stopped before post-peak 80% of the maximum load was reached due to test set-up displacement limitations. The observed experimental overstrength factors for the maximum strength, $\gamma_{Rd,i}$, were on average within 4% to the theoretical overstrength factors determined through component testing in Section 3.3. This shows that the theoretical component overstrength method was valid in this instance.

*Table 3-9: Summary of CLT3 hold-down connections*

| Series | | $F_y$ | $F_{max}$ | $F_u$ | $\Delta_y$ | $\Delta_{Fmax}$ | $\Delta_{Fu}$ | k | μ | $\gamma_{Rd,i}$ | $E_D$ |
|---|---|---|---|---|---|---|---|---|---|---|---|
| | | kN | kN | kN | mm | mm | mm | kN/mm | | | kN mm |
| CLT3-Std-U | M1 | 53.5 | 109.6 | 87.3 | 1.9 | 20.5 | 28.0 | 28.0 | 14.6 | 1.26 | - |
| | M2 | 55.3 | 118.3 | 94.6 | 1.5 | 11.6 | 11.9 | 36.9 | 7.9 | 1.36 | - |
| | M3 | 57.0 | 96.3 | 77.1 | 2.0 | 12.5 | 18.0 | 28.6 | 9.0 | 1.11 | - |
| | *Avg* | *55.3* | *108.1* | *86.3* | *1.8* | *14.8* | *19.3* | *31.2* | *10.5* | *1.24* | - |
| CLT3-Std-R1 | M | 61.6 | 105.7 | 89.5 | 2.3 | 22.1 | 38.7 | 27.3 | 17.2 | 1.22 | - |
| CLT3-Std-U | C1 | 69.0 | 119.2 | 94.5 | 2.9 | 22.0 | 32.8 | 24.1 | 11.3 | 1.37 | 6,551[2] |
| | C2[1] | 60.3 | 84.5 | 68.1 | 4.9 | 15.9 | 30.0 | 12.4 | 6.2 | 0.97 | 11,741 |
| | C3 | 64.5 | 104.9 | 83.9 | 3.3 | 16.3 | 30.3 | 19.6 | 9.2 | 1.21 | 10,956 |
| | C4 | 66.0 | 108.1 | 86.5 | 3.3 | 19.6 | 33.3 | 19.9 | 10.0 | 1.24 | 13,228 |
| | C5 | 84.0 | 113.9 | 91.1 | 5.3 | 20.4 | 35.3 | 15.9 | 6.7 | 1.31 | 10,722 |
| | *Avg.* | *68.8* | *106.1* | *84.8* | *3.9* | *18.9* | *32.3* | *18.4* | *8.7* | *1.22* | *10,639* |
| CLT3-Inc-U | C1 | 62.8 | 120.6 | 96.5 | 2.4 | 20.1 | 27.7 | 29.8 | 11.4 | 1.39 | 10,504 |
| | C2[1] | 57.0 | 117.0 | 93.6 | 2.0 | 19.1 | 26.0 | 28.0 | 12.8 | 1.35 | 8,145 |
| | C3 | 56.2 | 118.6 | 94.9 | 2.2 | 15.9 | 29.7 | 26.1 | 13.8 | 1.36 | 10,767 |
| | C4 | 63.5 | 104.0 | 83.2 | 3.0 | 21.3 | 27.9 | 20.8 | 9.2 | 1.20 | 9,452 |
| | C5 | 55.0 | 110.8 | 88.6 | 2.3 | 21.7 | 29.7 | 23.6 | 12.7 | 1.27 | 10,283 |
| | *Avg.* | *58.9* | *114.2* | *91.4* | *2.4* | *19.6* | *28.2* | *25.6* | *12.0* | *1.31* | *9,830* |
| CLT3-Inc-R1 | C | 63.0 | 122.5 | 98.0 | 2.7 | 21.7 | 36.3 | 23.1 | 13.3 | 1.41 | 13,781 |

[1]Some or all dowels were located at CLT lamination gap

[2]Loading protocol did not capture complete full reversal of hold-down

*Table 3-10: Summary of CLT5 hold-down connections*

| Series | | $F_y$ | $F_{max}$ | $F_u$ | $\Delta_y$ | $\Delta_{Fmax}$ | $\Delta_{Fu}$ | k | μ | $\gamma_{Rd,i}$ | $E_D$ |
|---|---|---|---|---|---|---|---|---|---|---|---|
| | | kN | kN | kN | mm | mm | mm | kN/mm | | | kN mm |
| CLT5-Std-U | M1 | 135.0 | 292.8 | 234.2 | 1.5 | 27.4 | 34.9 | 90.9 | 23.5 | 1.59 | - |
| | M2 | 139.0 | 286.4 | 229.1 | 1.4 | 24.6 | 35.1 | 100.8 | 25.4 | 1.56 | - |
| | M3 | 135.5 | 276.7 | 221.4 | 1.4 | 24.6 | 37.8 | 95.7 | 26.7 | 1.51 | - |
| | *Avg.* | *136.5* | *285.3* | *228.2* | *1.4* | *25.5* | *35.9* | *95.8* | *25.2* | *1.55* | - |
| CLT5-Std-R1 | M | 137.5 | 289.8 | 231.8 | 1.2 | 22.8 | 40.5 | 117.0 | 34.4 | 1.58 | - |
| CLT5-Std-U | C1 | 155.0 | 268.7 | 213.4 | 2.1 | 17.8 | 34.3 | 74.0 | 16.4 | 1.46 | 35,545 |
| | C2[1] | 151.0 | 291.9 | 233.5 | 1.6 | 19.2 | 26.0 | 94.6 | 16.3 | 1.59 | 22,494 |
| | C3 | 160.0 | 295.3 | 236.2 | 2.0 | 17.8 | 29.8 | 78.8 | 14.7 | 1.61 | 32,568 |
| | C4 | 135.0 | 267.9 | 214.3 | 1.3 | 18.7 | 28.3 | 105.6 | 22.1 | 1.46 | 32,766 |
| | C5 | 135.0 | 268.5 | 214.8 | 1.6 | 16.8 | 30.9 | 83.1 | 19.0 | 1.46 | 34,591 |
| | *Avg.* | *147.2* | *278.5* | *222.4* | *1.7* | *18.1* | *29.9* | *87.2* | *17.7* | *1.51* | *31,593* |
| CLT5-Std-R2 | C | 150.0 | 319.2 | 255.4 | 1.7 | 25.0 | 50.3 | 90.4 | 30.3 | 1.54 | 52,104 |
| CLT5-Inc-U | C1 | 164.5 | 270.3 | 216.2 | 1.7 | 18.3 | 35.9 | 99.4 | 21.7 | 1.47 | 48,137 |
| | C2 | 161.0 | 267.1 | 213.7 | 2.2 | 31.4 | 42.8 | 72.4 | 19.2 | 1.45 | 46,146 |
| | C3 | 144.0 | 275.5 | 284.4 | 1.8 | 33.0 | 42.5 | 78.5 | 23.2 | 1.50 | 45,838 |
| | C4[1] | 193.5 | 265.5 | 253.8 | 3.1 | 17.2 | 39.4 | 61.9 | 12.6 | 1.44 | 44,175 |
| | C5 | 170.0 | 270.3 | 216.2 | 2.6 | 31.7 | 40.5 | 66.6 | 15.9 | 1.47 | 41,044 |
| | *Avg.* | *166.6* | *269.7* | *236.9* | *2.3* | *26.3* | *40.2* | *75.8* | *18.5* | *1.47* | *45,068* |
| CLT5-Inc-R1 | C | 150.0 | 282.4 | 225.9 | 1.7 | 16.4 | 45.8 | 86.8 | 26.5 | 1.54 | 50,735 |

[1]Some or all dowels were located at CLT lamination gap

*Table 3-11: Summary of CLT7 hold-down connections*

| Series | | $F_y$ | $F_{max}$ | $F_u$ | $\Delta_y$ | $\Delta_{Fmax}$ | $\Delta_{Fu}$ | k | μ | $\gamma_{Rd,i}$ | $E_D$ |
|---|---|---|---|---|---|---|---|---|---|---|---|
| | | kN | kN | kN | mm | mm | mm | kN/mm | | | kN mm |
| CLT7-Std-U | M1 | 180.0 | 308.5 | 246.8 | 2.0 | 52.2 | 67.3 | 92.2 | 34.5 | 1.25 | - |
| | M2 | 193.0 | 328.1 | 262.5 | 2.4 | 49.2 | 66.7 | 81.4 | 28.2 | 1.33 | - |
| | M3 | 217.0 | 354.2 | 283.4 | 3.0 | 44.5 | 69.5 | 73.1 | 23.4 | 1.43 | - |
| | *Avg.* | *196.7* | *330.3* | *264.2* | *2.4* | *48.6* | *67.8* | *82.2* | *28.7* | *1.34* | - |
| CLT7-Std-R1 | M | 176.0 | 352.9 | 328.7 | 1.8 | 45.5 | 70.0 | 100.2 | 39.9 | 1.43 | - |
| CLT7-Std-U | C1 | 235.5 | 351.3 | 295.5 | 3.3 | 36.8 | 63.4 | 70.5 | 19.0 | 1.42 | 71,393 |
| | C2 | 225.0 | 360.0 | 288.0 | 3.5 | 32.0 | 48.8 | 64.9 | 14.1 | 1.46 | 53,029 |
| | C3[1] | 224.3 | 362.1 | 306.0 | 4.0 | 30.8 | 55.1 | 56.2 | 13.8 | 1.47 | 67,969 |
| | C4 | 216.0 | 355.0 | 284.0 | 3.4 | 36.4 | 49.7 | 63.0 | 14.5 | 1.44 | 60,247 |
| | C5 | 236.0 | 325.8 | 260.6 | 4.1 | 18.8 | 58.4 | 57.3 | 14.2 | 1.32 | 71,558 |
| | *Avg.* | *227.4* | *350.8* | *286.8* | *3.7* | *31.0* | *55.1* | *62.4* | *15.1* | *1.42* | *64,839* |
| CLT7-Std-R1 | C | 177.5 | 337.9 | 270.3 | 2.9 | 45.4 | 63.4 | 60.5 | 21.6 | 1.37 | 69,409 |
| CLT7-Inc-U | C1 | 220.5 | 348.7 | 336.0 | 2.7 | 45.4 | ≥ 48.7 | 81.8 | ≥ 18.1 | 1.41 | 46,662[2] |
| | C2 | 217.0 | 363.6 | 363.6 | 3.8 | 42.8 | ≥ 42.8 | 56.8 | ≥ 11.2 | 1.47 | 63,249[2] |
| | C3 | 200.0 | 372.2 | 314.5 | 2.3 | 35.3 | ≥ 49.3 | 88.2 | ≥ 21.8 | 1.51 | 51,212[2] |
| | C4[1] | 206.8 | 350.2 | 341.3 | 2.3 | 50.3 | ≥ 64.0 | 89.2 | ≥ 27.6 | 1.42 | 78,020[2] |
| | C5 | 201.0 | 361.3 | 344.6 | 2.0 | 34.9 | ≥ 64.3 | 99.2 | ≥ 32.1 | 1.46 | 78,332[2] |
| | *Avg.* | *209.1* | *359.2* | *340.0* | *2.6* | *41.7* | *≥ 53.8* | *83.0* | *≥ 22.2* | *1.45* | *64,495*[2] |
| CLT7-Inc-R2 | C | 198.0 | 382.3 | 381.8 | 2.7 | 49.0 | ≥ 62.7 | 73.5 | ≥ 23.2 | 1.38 | 75,228[2] |

[1]Some or all dowels were located at CLT lamination gap

[2] Minimum total energy dissipation as failure was not captured due to test set-up displacement limitations

It was found that the curves of the replicates in each hold-down series were consistent. Therefore, for each test series, one representative monotonic load-displacement curve and one representative cyclic load-displacement curve are provided in Figure 3-8. Figure 3-8a, Figure 3-8c, and Figure 3-8e show that reinforcement increased connection displacement capacity. The cyclic load-slip curves showed typical pinching behaviour with a compression force required to bring the connection back to zero displacement. A further discussion on the effect of increased row spacing and end distance on key performance indicators is provided in Section 3.4.3.

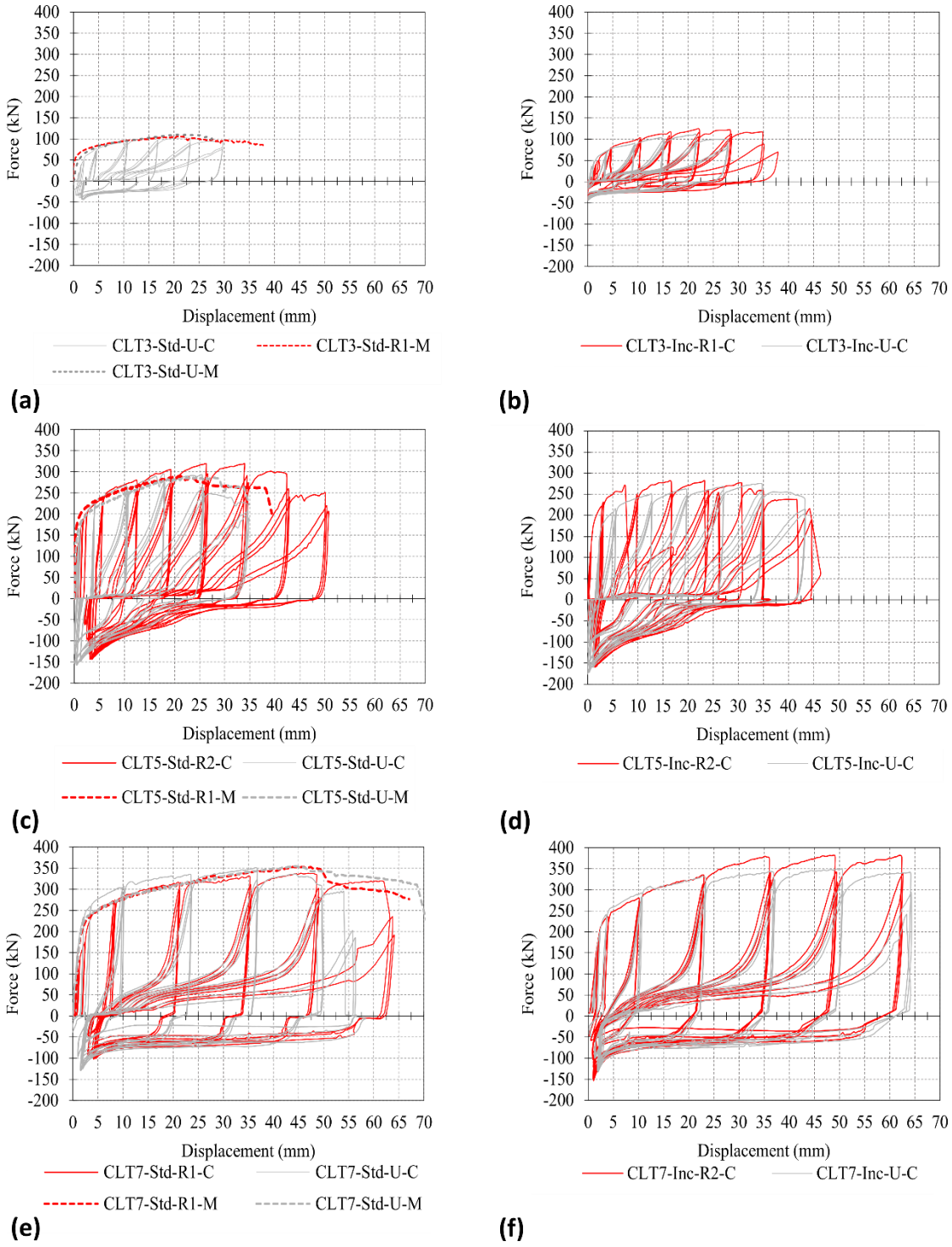


*Figure 3-8: Monotonic and cyclic load-slip curves by CLT panel size and dowel spacing; (a) CLT3 Std spacing, (b) CLT3 Inc spacing, (c) CLT5 Std spacing, (d) CLT5 Inc spacing, and (e) CLT7 Std spacing (f) CLT7 Inc spacing*

### 3.4.2 Failure Modes

Figure 3-9 shows typical failure modes for different test series. For the standard spacing specimens, a similar three-stage failure mechanism to Ottenhaus et al. (2018) was observed: onset of dowel yielding, continued yielding leading to the onset of crack growth aligned with the dowel group and cross-layers, and then final brittle failure which was panel splitting as the dowel bending action caused outward prying action. Brittle tensile or group tear-out was not observed in any instance as reported in past denser dowel spacing arrangements by Ottenhaus et al. (2018). As shown in Figure 3-9a, Figure 3-9b and Figure 3-9e, CLT3-Std and CLT5-Std specimens developed tension perpendicular-to-grain crack growth along dowel lines. This was partially mitigated by both STS and nut and washer reinforcement techniques as shown in Figure 3-9c and Figure 3-9f. For CLT3-Inc and CLT5-Inc specimens, Figure 3-9d and Figure 3-9f show that tension perpendicular-to-grain crack development along the dowel group lines was not observed; however, brittle panel splitting failure still occurred as shown in Figure 3-9h. In all CLT7 specimens, crack growth in the outer CLT layer was not observed. Significant displacement capacity was observed in both CLT7-Std and CLT7-Inc specimens. Figure 3-9i - Figure 3-9l show significant plastic embedment deformation and that the ø20x275mm dowels achieved minimum 35° dowel rotation angle. In proposing $M_{y,eff}$, Blaβ et al. (2001) developed a normalised moment-angle diagram and for a 35° dowel rotation angle, greater than 95% of the full plastic moment was achieved. Therefore, it was deemed appropriate to consider the full plastic yield moment in theoretical strength predictions as described in Section 3.3.1 in this study. Figure 3-9j shows that some $\phi$20x275mm dowels from CLT7 test series may have started to develop four plastic hinges as per EYM Equation (3-7)c. For CLT7 test series, the strength prediction of EYM Equation (3-7)c was within 5% of EYM Equation (3-7)b. It was observed that the reinforcement by STS provided a similar effect as the reinforcement by nut and washer in terms of prolonging the onset of brittle failure.

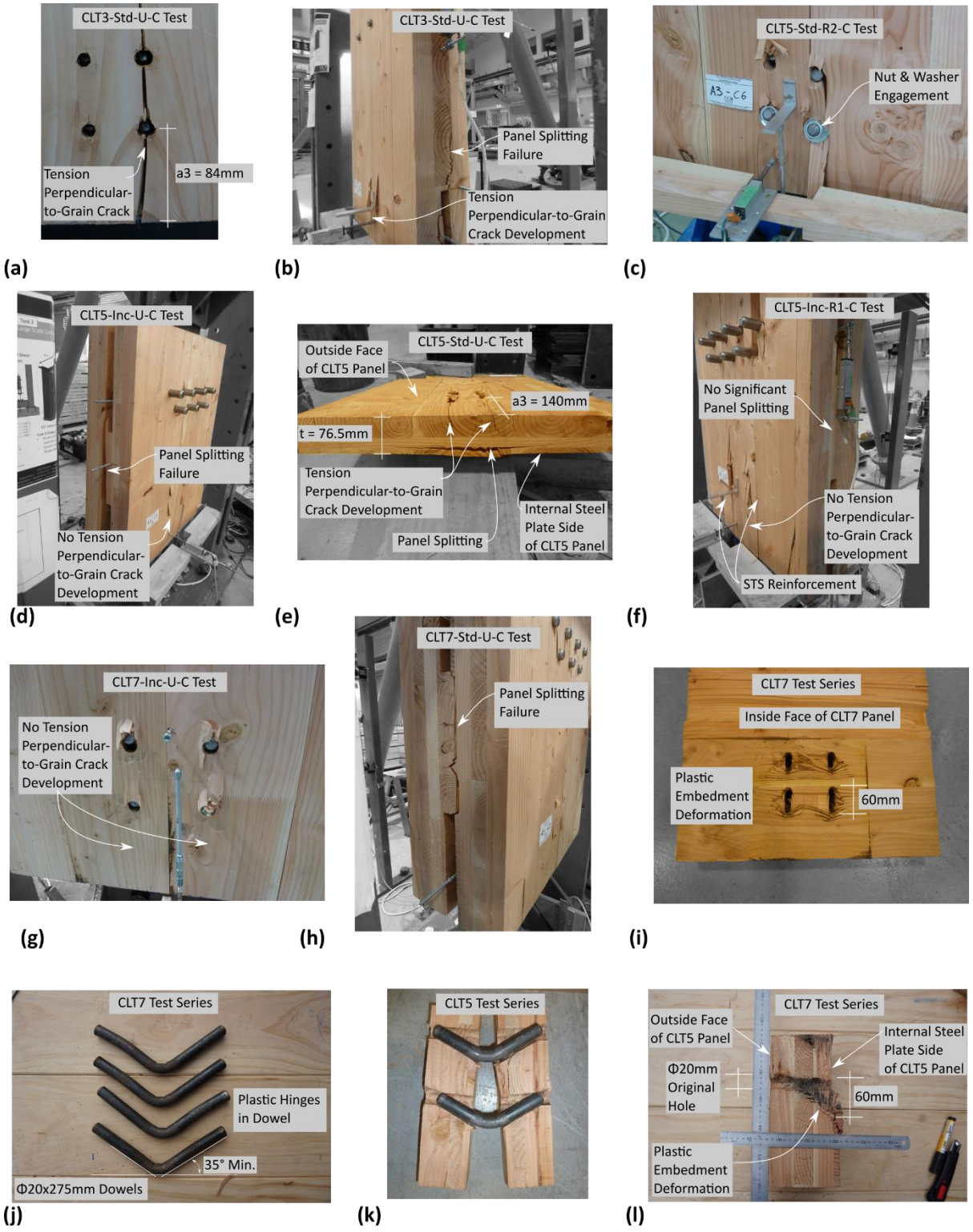


*Figure 3-9: Failure mode photos: (a) and (b) CLT3 specimens, (c)-(f) and (k) CLT5 specimens, (g)-(j) and (l) CLT7 specimens*

### 3.4.3 Discussion of Performance Indicators

#### *3.4.3.1 Strength*

On average, the increased row spacing by two dowel diameters (50% increase) and end distance by two dowel diameters (30% increase) of the dowel group led to increase in maximum strength of 5%. This increase was not significant and indicated that increased dowel row and end spacing did not affect strength significantly when the connections were ductile ( $\mu > 6$). The CV in the yield strength, $F_y$, was 8% and greater than the variation in maximum strength, $F_{max}$, with CV of 5%. The higher variability in yield strength can be attributed to the sensitivity of the method of determining the yield point on load-slip curves (Flatscher, 2017). Strength increased for reinforced specimens CLT5-Std-R2 and CLT7-Inc-R2 that had two dowels end-threaded with nuts and washers. This indicated that considering rope effect was appropriate in this instance. For CLT7 specimens, reinforcement only increased strength of the specimens with increased row spacing and end distance. It could not be determined whether or not the specimen density had a significant impact on strength and this was beyond the scope of the study. The cyclic yield strength was 20% higher on average than the monotonic yield strength but the maximum strength was not significantly affected by the loading patterns. The higher cyclic yield strength compared to the monotonic yield can be attributed to the sensitivity in the determination of the yield point as per EN 121512 (2005a). In the results presented herein, the cyclic stiffness was less than the monotonic stiffness on average. As per EN 12512 (2005a), this decreased cyclic initial stiffness line decreased the 1/6 "β-line" slope which then increased the determined yield strength. Yield strength was not a significant performance indicator in the study herein in comparison to the maximum strength, which was required to determine the connection overstrength.

#### *3.4.3.2 Displacement capacity and ductility*

Displacement capacity and ductility increased significantly with increased row spacing and end distance. In all instances, a 1mm correction for initial slip for the yield displacement, $\Delta_y$, was used to adequately account for the 2mm oversized steel plate holes. The yield displacement did not appear to be influenced by increased panel and dowel size, although the CV was high and 30% on average which might be attributed to the determination method described previously. The displacement capacity, synonymous to the ultimate displacement, $\Delta_{Fu}$, increased by 35% in CLT5-Std to CLT5-Inc test series. For CLT3 test series the onset of panel splitting was not changed with increased spacing which could be attributed to less cross-layer reinforcement when compared to CLT5 and CLT7 specimens. Although $\Delta_{Fu}$ was not observed in CLT7 test series, the load-displacement curves in Figure 3-8 indicated that increased displacement capacity could be achieved as no significant drop in load occurred. Reinforcement by STS or threaded dowels with nut and washer significantly improved displacement capacity in all instances as the onset of panel splitting was delayed. Displacement capacity was

increased by 64%, 32%, and 5% for CLT3, CLT5, and CLT7 specimens respectively which shows that reinforcement had a more significant impact on smaller CLT panels with less cross-layer reinforcement.

High ductility was achieved in all test series, and ductility increased by 20% on average with increased row spacing and end distance. Had the displacement capacity of CLT7-Inc-U test series been reached, the ductility would have increased further. It was also observed that reinforced specimens had 30% higher ductility than unreinforced specimens. In the study herein, cyclic ductility was 33% less on average than monotonic ductility. However, work by Ottenhaus et al. (2018) reported that cyclic ductility increased when compared to monotonic ductility. These differences could be attributed to loading protocols, loading rates, and perhaps the fact that Ottenahaus et al. (2018) primarily investigated specimens with decreased dowel spacing where brittle failure modes occurred. In connection groups with brittle failure modes, it is speculated that the monotonic loading protocol could in fact be more demanding. A detailed investigation on these differences was beyond the scope of work presented herein; however, this work shows the importance of conducting cyclic testing for these connections. Future work should study differences between monotonic and cyclic loading regimes, especially given that cyclic testing is often more complicated to implement.

Table 3-12 compares the five-layer CLT panel displacement capacity and ductility results to past 130mm thick five-layer CLT panel results of similar panel and dowel sizes. Both the standard and increased dowel spacing test series had significantly higher displacement capacity and ductility, which shows the importance of specifying proper row spacing ($a_2$) and end distance ($a_3$) to avoid brittle tensile and group tear-out failure modes in CLT. Mode-cross over to these brittle failure modes was not observed with increased spacing and end distance and the panel splitting at large displacement remained the dominant failure mode.

*Table 3-12: Displacement capacity and ductility comparison with past research*

| | **Ottenhaus et al.** (2018) | | | | **Experimental programme** | | | | | |
|---|---|---|---|---|---|---|---|---|---|---|
| **Series** | A-M | A-C | B-M | C-M | CLT5-Std-R1-M | CLT5-Std-U-M | CLT5-Std-R2-C | CLT5-Std-U-C | CLT5-Inc-R1-C | CLT5-Inc-U-C |
| **a1** | 5d | 5d | 4d | 4d | 5d | 5d | 5d | 5d | 5d | 5d |
| **a2** | 3d | 3d | 3d | 2d | 4d | 4d | 4d | 4d | 6d | 6d |
| **a3** | 5d | 5d | 7d | 7d | 7d | 7d | 7d | 7d | 9d | 9d |
| **$\Delta_u$ (mm)** | 7.7 | 5.7 | 7.9 | 12.9 | 40.5 | 35.9 | 50.3 | 29.9 | 45.8 | 40.2 |
| **μ** | 12.3 | 8.4 | 9.2 | 14.6 | 34.4 | 25.2 | 30.3 | 17.7 | 26.5 | 18.5 |

#### *3.4.3.3 Stiffness*

Stiffness increased by 35% and 25% with increased dowel spacing for CLT3 and CLT7 specimens but decreased by 13% for CLT5 specimens. Reinforcement also did not appear to affect stiffness and on average the results between unreinforced and reinforced specimens was within 5%. Zhang (2018) has reported that STS reinforcement installed perpendicular to the dowel axis in tensile connections did not significantly impact stiffness unless STS were installed directly underneath the dowel. STS reinforcement perpendicular to the dowel axis was previously studied by Bejtka and Blaβ (2005). The results herein showed that the Eurocode 5 (2014) stiffness prediction equation $k_{ser} = \rho_m^{1.5} \cdot \frac{d}{23} \cdot n_{sp} \cdot n \cdot \gamma_{s-t}$ where $\rho_m$ is the mean density, $d$ is the dowel diameter, $n_{sp}$ is the number of shear planes, $n$ is the number of dowels, and $\gamma_{s-t}$ = 2 for steel-timber connections significantly over predicted the experimental stiffness by a factor greater than two. The predicted stiffness for the CLT3, CLT5, and CLT7 specimens was 87, 138, and 136kN/mm respectively. The difference between the test results and the prediction equation was more significant in CLT3 and CLT7 specimens in which the thickness ratios between the longitudinal and the cross laminate boards were 90:45 and 160:115. In the CLT5 specimens the ratio was 135:40. Sandhaas et al. (2017), Rahim et al. (2018), and Dong et. al (2020) have also reported that the stiffness prediction equation overestimated the experimental stiffness considerably for dowelled and bolted connections in glulam timber and laminated veneer lumber. Jockwer et al. (2018) has reported that the current Eurocode 5 (2014) stiffness prediction equation does not consider the number and slenderness of the dowels or the influence of the cross laminate layer. Cyclic stiffness was more than 30% less than monotonic stiffness on average. A detailed discussion on connection stiffness is beyond the scope of this study, and further research should also

consider the impact of the number of dowels, slenderness of the dowels, orientation of the timber grain, and connection reinforcement.

#### *3.4.3.4 Energy dissipation*

Increased dowel spacing increased total energy dissipation when the onset of brittle panel splitting failure was delayed. For example, increased dowel spacing in CLT5 specimens increased average total energy dissipation by more than 40%, and reinforcement increased total energy dissipation by almost 30% on average. Increased dowel spacing did not impact total energy dissipation for CLT3 specimens as brittle panel splitting failure was not delayed due to less cross-layer reinforcement. The load-displacement curves of CLT7-Inc-U-C4 and C5 specimens indicated increased energy dissipation could be achieved with increased dowel spacing as their total energy dissipation was greater than 20% the average of CLT7-Std specimens. However, due to instrumentation limitation described previously the total energy dissipation increase for CLT7 specimens could not be accurately quantified. The results show that significant energy dissipation can be achieved with minimum dowel spacing which aligns with past research by Ottenhaus et al. (2018a).

### 3.4.4 Theoretical-Experimental Overstrength Comparisons

Table 3-13 compares the theoretical overstrength, $\gamma_{Rd,theo}$, determined in Section 3.3 to the experimental overstrength of each test series group, $\gamma_{Rd}$, determined by Equation (3-4). Reinforced specimens were not included in the strength distribution determination. Past work by Ottenhaus et al. (2018) indicated a positive correlation between overstrength and ductility when considering brittle to ductile dowelled connections. In this instance, overstrength did not change significantly with increased row spacing and end distance, although ductility increased. This may be attributed to the standard and increased dowel spacing specimens being highly ductile connections. Based on the test results, the recommended overstrength value for these dowelled connections is 1.70, which was the maximum experimental overstrength shown in bold and is comparable to 1.68 from the previous study on dowelled CLT connections by Ottenhaus et al. (2018). The maximum experimental overstrength 1.70 was higher than the maximum theoretical overstrength 1.50; however, further research with a larger sample size could reduce the experimental overstrength to a value closer to the theoretical. Further, it should be noted that the theoretical overstrength was derived from the density distribution determined from the relatively smaller sample size presented herein. If, for example, a larger density sample of ungraded New Zealand Douglas-fir was considered such as that reported from Kimberley et al. (2017), the maximum theoretical overstrength value became 1.88. A similar study by Ottenhaus et al. (2018b; 2020) showed the theoretical overstrength considering the full density distribution of

ungraded New Zealand Radiata Pine timber increased to 1.91 from 1.68. The analytical determination of overstrength used herein has been validated by Ottenhaus et al. (2020) with data from previous experiments and it was found to be sufficient when full timber density distributions are considered. Using relatively homogenous material with reduced variability such as Laminated Veneer Lumber (LVL) will lead to more consistent strength properties and less overstrength.

*Table 3-13: Theoretical-experimental overstrength comparison summary*

| **Series** | **Theoretical** | | **Experimental** | | | |
|---|---|---|---|---|---|---|
| - | $F_{max,theo,k}$ | $\gamma_{Rd,theo}$ | $F_{max,mean}$ | $F_{0.05}$ | $F_{0.95}$ | $\gamma_{Rd}$ |
| - | kN | - | kN | kN | kN | - |
| CLT3-Std-U | 87 | 1.31 | 106 | 83 | 137 | 1.57 |
| CLT3-Inc-U | 87 | | 114 | 98 | 133 | 1.52 |
| CLT5-Std-U | 184 | 1.50 | 281 | 252 | 313 | **1.70** |
| CLT5-Inc-U | 184 | | 270 | 238 | 305 | 1.66 |
| CLT7-Std-U | 247 | 1.45 | 343 | 302 | 389 | 1.58 |
| CLT7-Inc-U | 247 | | 359 | 317 | 407 | 1.65 |

## 3.5 CONCLUSIONS

This chapter investigated the performance of CLT dowelled hold-down connections with one slotted-in steel plate with standard fastener spacing as well as increased row spacing and end distance. A total of 47 experimental tests were performed on the dowelled CLT connections with three different CLT sizes, two different dowel spacing layouts, and with the addition of reinforcing elements. Dowel bending and CLT embedment tests were also performed to derive the theoretical connection overstrength in comparison of observed experimental overstrength results. The key findings are:

- Increased dowel row spacing and end distance increased connection displacement capacity and ductility. This effect was most pronounced in five-layer CLT specimens, where increased row spacing and end distance eliminated tension perpendicular-to-grain crack development which could initiate mode-cross over to brittle failure. Ductile connections with $\mu \geq 6$, were achieved in all instances. In seven-layer CLT specimens, displacement capacity ≥ 60mm and $\mu \geq 30$ was achieved with increased row spacing and end distance. Meanwhile, increased dowel row spacing and end distance did not affect connection strength as significantly as connection ductility and it also did not affect the connection stiffness. It was found that the stiffness prediction equation within Eurocode 5 was inadequate and significantly over predicted the observed stiffness. Further research should investigate the impact of the number and

slenderness of the dowels, the influence of the timber grain orientation, and the reinforcement effect on connection stiffness.

- The maximum experimental overstrength was 1.70 which was higher than the theoretical component overstrength of 1.50. However, the higher experimental overstrength can be attributed to the relatively small sample size and the variable density distribution of CLT. Using more homogenous timber materials such as LVL would reduce the overstrength and variability.
- Reinforcement by inclined self-tapping screws or replacing the lower two dowels with threaded dowels with nut and washer significantly increased displacement capacity and ductility by delaying the onset of brittle panel splitting failure. The observations made from a total of eight reinforced specimens (six with inclined STS reinforcement and two with nuts and washers reinforcement) indicated that both methods were effective. Reinforcement had a greater impact on smaller three-layer CLT specimens with less cross-layer reinforcement than five- and seven-layer CLT specimens. It was found to be appropriate to consider rope effect for the two dowels that had reinforcement with nuts and washer. Due to the limited number of specimens with reinforcement, further study is needed to quantify the effect of the reinforcement.
- Embedment testing results indicated that the 2011 CLT Handbook equation was generally applicable to the CLT layups tested herein, and that the applicability of the CLT Handbook may be extendable beyond the 40mm maximum layer thickness and longitudinal to cross-layer thickness ratio of 0.95 to 2.1. Further research should determine a more generally applicable CLT embedment strength formulation which includes current commercial CLT layups and the impact of density on CLT embedment strength formulation and then dowelled hold-down connection strength.

## 3.6 REFERENCES

American Society for Testing and Materials. (2013). *ASTM D5764-97a - Standard test method for evaluating dowel-bearing strength of wood and wood-based prducts*.

Australian / New Zealand Standard. (2001). *AS/NZS 4671: Steel reinforcing materials*.

Australian / New Zealand Standard. (2015). *AS/NZS ISO 10984.1: Timber Structures -Dowel-type fasteners*.

AWC. (2015). *AWC, National Design Specifications for Wood Construction(ANSI/AWC NDS-2015)*.

American Wood Council.

Bejtka, I., & Blaß, H. J. (2005). Self-tapping Screws as Reinforcements in Connections with Dowel-type Fasteners. *Working Commission W18 on Timber Structures*, *August*, 19.

Blaß, H J, & Uibel, T. (2007). *Tragfähigkeit von stiftförmigen Verbindungsmitteln in Brettsperrholz (In German)* (number 8). Karlsruher Berichte zum Ingenieurholzbau Universitätsverlag Karlsruhe.

Blaß, Hans Joachim, Bienhaus, A., & Krämer, V. (2001). Effective bending capacity of dowel-type fasteners. *Proceedings of the International RILEM Symposium Joints in Timber Structures*, *22*, 71–88.

Blaß, Hans Joachim, & Sandhaas, C. (2017). *Timber Engineering: Principles for Design*. KIT Scientific Publishing. https://doi.org/10.5445/KSP/1000069616

CEN. (1991). *EN 26891 - Joints made with mechanical fasteners. General principles for the determination of strength and deformation characteristics*. European Committee for Standardization (CEN).

CEN. (2005a). *EN12512: Timber structures: test methods : cyclic testing of joints made with mechanical fasteners : [including amendment A1:2005]* (Issue Book, Whole). European Committee for Standardization.

CEN. (2005b). *Eurocode 8: Design of structures for earthquake resistance* (Issue Book, Whole). European Committee for Standardization (CEN).

CEN. (2009). *EN 409 - Timber structures - Test methods - Determination of the yield moment of dowel type fasteners*. European Committee for Standardization (CEN).

CEN. (2014). Eurocode 5: Design of timber structures-Part 1-1: General-Common rules and rules for buildings. In *EN1995-1-1:2004-11 + AC2006-06 + A1:2008-06 + A2:2014-05 Eurocode 5*. European Committee for Standardization.

CEN. (2016). *EN 14358:2016 - Timber structures - Calculation and verification of characteristic values*. European Committee for Standardization (CEN).

CSA 086. (2019). *Engineering design in wood*. Canadian Standards Association, Mississauga, ON.

Dong, Weiqun, Li, Q., Wang, Z., Zhang, H., Lu, X., & Gong, M. (2020). Effects of embedment side and loading direction on embedment strength of cross-laminated timber for smooth dowels. *European Journal of Wood and Wood Products*, *78*(1), 17–25. https://doi.org/10.1007/s00107-019-01490-z

Dong, Weiqun, Wang, Z., Zhou, J., Zhang, H., Yao, Y., Zheng, W., Gong, M., & Shi, X. (2020). Embedment

strength of smooth dowel-type fasteners in cross-laminated timber. *Construction and Building Materials*, *233*, 117243. https://doi.org/10.1016/j.conbuildmat.2019.117243

Dong, Wenchen, Li, M., Lee, C. L., MacRae, G., & Abu, A. (2020). Experimental testing of full-scale glulam frames with buckling restrained braces. *Engineering Structures*, *222*(July), 111081. https://doi.org/10.1016/j.engstruct.2020.111081

Flatscher, G. (2017). *Evaluation and approximation of timber connection properties for displacement-based analysis of CLT wall systems*.

FPInnovations. (2019). *CLT Handbook* (E. Karacabeyli & S. Gagnon (eds.)). FPInnovations.

Gagnon, S., Pirvu, C., & Fpinnovations. (2011). *CLT handbook: cross-laminated timber: Vol. SP-528E.;S* (Canadian, Issue Book, Whole). FPInnovations.

ISO16670:2003. (2003). *Timber Structures - joints made with mechanical fasteners - quasi-static reversed-cyclic test method*. The International Organization for Standardization.

Jockwer, R., & Jorissen, A. (2018). Stiffness and deformation of connections with dowel-type fasteners. In *Design of Connections in Timber Structures* (COST Action FP1402 / WG3).

Jorissen, A., & Fragiacomo, M. (2011). General notes on ductility in timber structures. *Engineering Structures*, *33*(11), 2987–2997. https://doi.org/10.1016/j.engstruct.2011.07.024

Kimberley, M. O., McKinley, R. B., Cown, D. J., & Moore, J. R. (2017). Modelling the variation in wood density of New Zealand-grown Douglas-fir. *New Zealand Journal of Forestry Science*, *47*(1), 0–15. https://doi.org/10.1186/s40490-017-0096-0

Ottenhaus, L.-M., Li, M., & Smith, T. (2018a). Structural performance of large-scale dowelled CLT connections under monotonic and cyclic loading. *Engineering Structures*, *176*(Lvl), 41–48. https://doi.org/10.1016/j.engstruct.2018.09.002

Ottenhaus, L.-M., Li, M., & Smith, T. (2018b). Analytical Method to Derive Overstrength of Dowel-Type Connections Overstrength components. *Proceedings of the INTER Meeting Fifty-One*, *05*, 1–12.

Ottenhaus, L.-M., Li, M., Smith, T., & Quenneville, P. (2018). Mode Cross-Over and Ductility of Dowelled LVL and CLT Connections under Monotonic and Cyclic Loading. *Journal of Structural Engineering (United States)*, *144*(7), 4018074. https://doi.org/10.1061/(ASCE)ST.1943-541X.0002074

Ottenhaus, L., Li, M., & Smith, T. (2020). Analytical Derivation and Experimental Verification of Overstrength Factors of Dowel-type Timber Connections for Capacity Design. *Journal of Earthquake Engineering*, 1–15. https://doi.org/10.1080/13632469.2020.1781711

Ottenhaus, L. M., Li, M., Smith, T., & Quenneville, P. (2018). Overstrength of dowelled CLT connections under monotonic and cyclic loading. *Bulletin of Earthquake Engineering*, 1–21. https://doi.org/10.1007/s10518-017-0221-8

Rahim, N. L., Raftery, G. M., & Quenneville, P. (2018). Stiffness of Bolted Timber Connection. *WCTE 2018 - World Conference on Timber Engineering*.

Sandhaas, C., & van de Kuilen, J.-W. G. (2017). Strength and stiffness of timber joints with very high strength steel dowels. *Engineering Structures*, *131*, 394–404. https://doi.org/https://doi.org/10.1016/j.engstruct.2016.10.046

Smith, I., Asiz, A., Snow, M., & Chui, Y. H. (2006). Possible Canadian / ISO Approach to Deriving Design Values From Test Data. *Proceedings of the CIB W18 Meeting Thirty-Nine*.

Standards Australia. (2007). *AS 1444-2007: Wrought alloy steels-standard hardenability (H) series and hardened and tempered to designated mechanical properties*. Standards Australia.

Standards New Zealand. (1992). *NZS 3404: Steel Structures Standard*. Standards New Zealand.

Standards New Zealand. (1993). *NZS 3603: Timber structures standard*. Standards New Zealand.

Standards New Zealand. (2018). *DZ NZS AS 1720.1/V6.0 Timber Structures - Part 1: Design Methods (draft out for public consultation)*. Standards Australia/Standards New Zealand.

Uibel, T., & Blaß, H. J. (2007). Edge joints with dowel type fasteners in cross laminated timber. *Proceedings of CIB W18 Meeting Forty*, *40-7–2*.

Uibel, T., & Blaß, H. J. (2006). Load carrying capacity of joints with dowel type fasteners in solid wood panels. *Proceedings of CIB W18 Meeting Thirty-Nine*, *39-7–5*, 191–202.

Zhang, C. (2018). *Reinforcement of Timber Dowel-Type Connections Using Self-Tapping Screws*. University of Bath.

# 4 Structural performance of orthogonal joints in CLT with self-tapping screws installed with mixed angles

*The work presented herein is based on the published articles cited below:*

*J.R. Brown, M. Li, T. Tannert, D. Moroder, Experimental study on orthogonal joints in cross-laminated timber with self-tapping screws installed with mixed angles, Eng. Struct. 228 (2021) 111560. https://doi.org/10.1016/j.engstruct.2020.111560.*

*J. Brown, M. Li, B. Karalus, S. Stanton, Withdrawal Behaviour of Self-tapping Screws in New Zealand Cross-Laminated Timber, New Zeal. Timber Des. J. 28 (2020).*

---

*Key Findings / Outputs:*

- 59 orthogonal joints in CLT with self-tapping screws (STS) were tested under monotonic and cyclic loading.
- 202 STS withdrawal tests were performed to verify existing withdrawal strength and stiffness models.
- The ratio of two inclined STS to one 90° STS led to a significant increase in ductility and displacement capacity, approximately three times of the specimens using inclined STS only.
- The average experimental overstrength was 1.7. Existing analytical strength models were found to be adequate.
- Analytical models for estimating joint stiffness were found to be inadequate.
- To avoid brittle steel failure of STS, embedment length of the threaded portion should not be greater than 12d under the condition of axial load only.

## 4.1 INTRODUCTION

The primary objective of this study is to evaluate the performance of orthogonal CLT panel joints with varying mixed angle self-tapping screw (STS) combination ratios, η. These joints are of particular interest for their potential to develop composite action between orthogonal CLT wall panels, which could transform conventional in-plane CLT LLRS to a core-wall structure with enhanced lateral strength and stiffness. In this study, a total of 59 CLT orthogonal joint tests were performed in 9 different configurations with varying STS η ratio under monotonic and cyclic loading. The different joint configurations were chosen to evaluate which mixed angle STS joint combination could provide enhanced seismic performance and efficiency as shown in Figure 4-1. Figure 4-1 shows the Cathedral Hill II (Below & Sarti, 2016) concept design building plan with a potential core-wall LLRS, to a the 8.6m high C-shaped CLT core-wall test presented in Chapter 6, and to four options for orthogonal CLT panel joints with STS. The secondary objectives are to compare current analytical strength and stiffness models with the experimental results and to evaluate overstrength. Input parameters for the analytical models are based on both current STS design documents and experimental data from baseline STS withdrawal and lateral load tests.

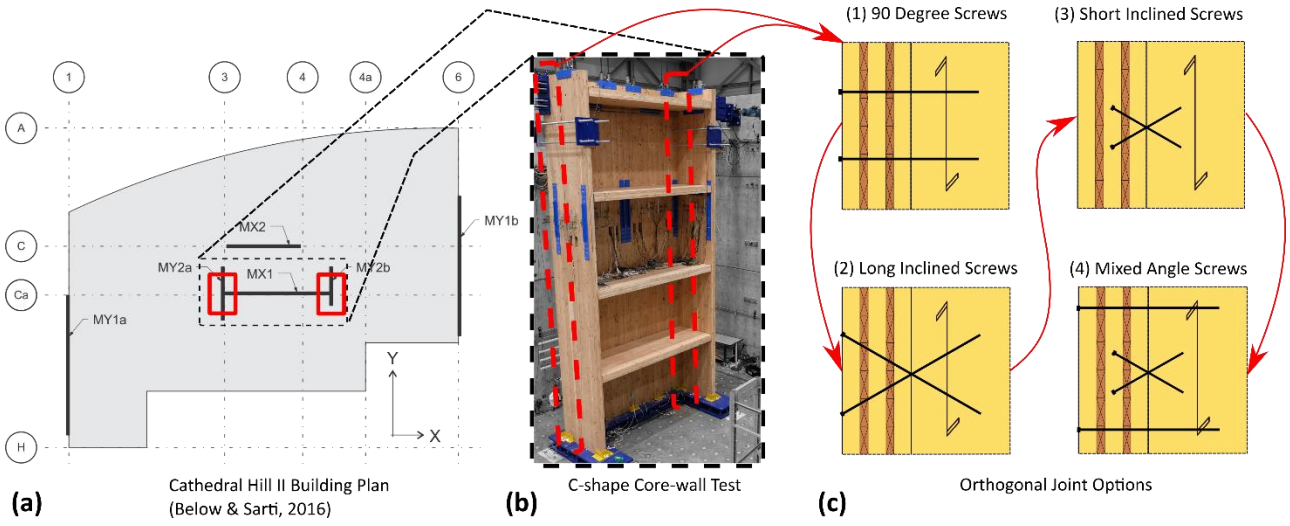


*Figure 4-1: (a) Cathedral Hill II concept design* (Below & Sarti, 2016), *(b) C-shape core-wall test (See Chapter 6), and (c) orthogonal joint options with STS*

STS withdrawal testing results are presented in Section 4.2 with comparison to design standards. Section 4.3 described the orthogonal joint test programme and Section 4.4 presents the STS joint experimental results. In Section 4.5, existing analytical strength and stiffness models are compared to experimental results and experimental overstrength values are derived.

## 4.2 SELF-TAPPING SCREW WITHDRAWAL TESTING

STS are the most popular fastener type used in CLT construction, in part due to their ease of installation and flexibility in design (Brandner et al., 2016). For common wood screws and coach screws, New Zealand Timber Structures Standard NZS 3603 (1993) and Australian Timber Structures Standard AS 1720.1 (2010) provide tabular values for characteristic withdrawal capacity per millimetre of thread penetration for each timber species group. The recently proposed draft standard DZ NZS AS 1720.1/V6 (2018) to supersede NZS 3603 (1993) only covers wood screws with $\phi$6.3mm or less. Design methods for the withdrawal capacity of STS are not covered by any of these standards.

The benefit of utilizing the high withdrawal strength of inclined STS was first presented by Bejtka & Blaß (2002). Since then, Uibel & Blaß (2007) developed a predictive analytical model for the withdrawal capacity of STS in CLT. Numerous subsequent studies in Europe, summarized within Ringhofer et al. (2015b), have investigated the influence of gaps between timber boards in laminated timber products, the influence of the number of timber laminations penetrated, and the influence of the moisture content on the withdrawal capacity of STS in CLT. Figure 4-2 shows a typical layout of non-edge-glued CLT with some definitions such as small gaps, $w_{GAP}$, between adjacent laminated boards. Most recently, Ringhofer et al. (2015b) proposed a universal analytical approach to calculate the withdrawal capacity for STS in solid timber and laminated timber products. European STS suppliers, such as Rothoblaas (2019), SPAX (2017), and Würth (2018) among others, also provide European Technical Approvals (ETAs) to guide the design of their proprietary products. Meanwhile, Eurocode 5 (2014) provides analytical design equations based on the previous research on STS.

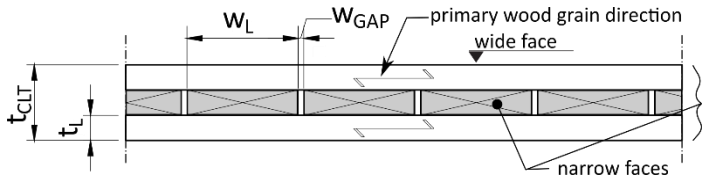


*Figure 4-2: CLT layup with definitions*

In North America, many STS suppliers provide designers with Canadian Construction Materials Centre (CCMC) or International Code Council (ICC) reports which in principal are similar to ETAs in Europe. In contrast to NZS 3603 (1993) or AS 1720.1 (2010), these CCMC and ICC reports are sufficient to allow designers to use STS within the Canadian Timber Standard (2019) and American National Design Standard (2015). Currently, designers in New Zealand and Australia may use a STS supplier ETA with New Zealand and Australian timber characteristic densities.

In this study, the withdrawal strength of STS in New Zealand Radiata Pine and Douglas-fir CLT was experimentally investigated with SPAX STS. The results were compared to the STS design equations in

literature, which have generally been derived from European softwood species which typically have lower density than New Zealand grown Radiata Pine and Douglas-Fir. As an extensive recent study comparing 65 ETAs by Ringhofer (2017) has reported meaningful differences in withdrawal strength parameters, the experimental results are compared with the SPAX ETA (2017) only and not ETAs in general. The effect of embedding the threaded portion of the partially threaded screw was also investigated.

### 4.2.1 Withdrawal Strength Formulas

Eurocode 5 (2014), SPAX ETA (2017), Uibel & Blaß (2007), and Ringhofer et al. (2015b) provide methods for determining the withdrawal capacity of screws in solid and laminated timber products. EN 1382 (2016) specifies the formulation of the withdrawal parameter, $f_1$ in Equation (4-1), to determine the fastener withdrawal capacity, $F_{ax}$. The key STS parameters to determine $F_{ax}$ are shown in Figure 4-3. Following recent work by Ringhofer et al. (2018) and Westermayr & van de Kuilen (2019), the results presented herein are for the withdrawal strength, $f_{ax}$, defined in Equation (4-2).

$$f_1 = \frac{F_{ax}}{l_{ef} d} \ (N/mm^2) \tag{4-1}$$

$$f_{ax} = \frac{f_1}{\pi} \ (N/mm^2) \tag{4-2}$$

$$l_{ef} = l_{nom} - xd; \tag{4-3}$$

$x = 1$ (Westermayr & van de Kuilen, 2019)

where $d$ is the screw diameter; $l_{nom}$ is the nominal screw installation length; $l_{ef}$ is the effective thread embedment length excluding the length of the screw tip; and $l_{emb}$ is the embedment length of unthreaded portion for a partially threaded screw.

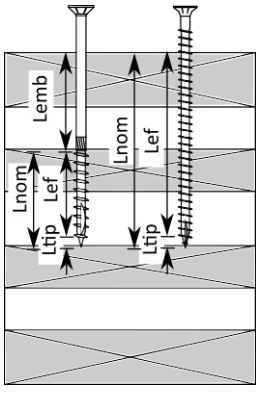


*Figure 4-3: STS key parameters (partially threaded vs. fully threaded)*

SPAX ETA (2017) and the method presented by Ringhofer et al. (2015b) do not include $l_{ef}$ in the calculation of $f_1$ whereas Eurocode 5 (2014) and Uibel & Blaß (2007) include $l_{ef}$ as an influencing parameter. Further, Eurocode 5 (2014), SPAX ETA (2017), and Uibel & Blasß (2007) consider the screw

tip length, $l_{tip}$, within $l_{ef}$ for the calculation of $f_1$ whereas the Ringhofer et al. (2015b) and the proposed draft DZ NZS AS 1720.1/V6 (2018) specifically state to neglect $l_{tip}$ in the calculation of $f_1$ or $l_{ef}$. While the current NZS 3603 (1993) and AS 1720.1 (2010) do not explicitly feature STS withdrawal equations, tables based on the joint group provide the characteristic capacity per millimetre penetration of the threaded portion for wood screws and coach screws. It is not clear if $l_{tip}$ is considered or not. The embedment length of unthreaded portion, $l_{emb}$ shown in Figure 4-3, is not considered as an influencing parameter in any design equations. The following lists the Eurocode 5 (2014), the SPAX ETA (2017), Uibel & Blaß (2007), Ringhofer et al. (2015b), and DZ NZS AS 1720.1/V6 (2018) equations to determine the characteristic withdrawal capacity. For simplicity, the analytical design methods are referred to as EC5, SPAX, U&B and Ringhofer in the following context.

EC5 (2014):

$$F_{ax,\alpha,k} = \frac{f_{1,EC5}\, d l_{ef} k_d}{1.2cos^2\varphi + sin^2\varphi}\ (N) \tag{4-4}$$

$$f_{1,\mathrm{EC5}} = 0.52\mathrm{d}^{-0.5}{\mathrm{l_{ef}}}^{-0.1}{\rho_\mathrm{k}}^{(0.8)}\left(\frac{N}{mm^2}\right), \mathrm{k_d} = \min\left\{\frac{\mathrm{d}}{8}, 1\right\}$$

SPAX (2017)

$$\mathrm{F_{ax,\alpha,k}} = \frac{f_{1,\mathrm{SPAX}}\mathrm{dl_{ef}k_d}}{1.2\cos^2\varphi + \sin^2\varphi}\left(\frac{\rho_\mathrm{k}}{350}\right)^{0.8}(\mathrm{N}) \tag{4-5}$$

$$f_{1,SPAX} = 12.0\ (\phi 8mm); 11.0\ (\phi 12mm)\left(\frac{N}{mm^2}\right)$$

U&B (Blaß & Uibel, 2007; Uibel & Blaß, 2007):

$$F_{ax,\alpha,k} = \frac{f_{1,U\&B} d l_{ef}}{1.5cos^2\varphi + sin^2\varphi}\left(\frac{\rho_k}{400}\right)^{0.75}(N) \tag{4-6}$$

$$f_{1,U\&B} = 0.35 d^{-0.2} l_{ef}^{-0.1} {\rho_{ref}}^{0.75}\pi\ \left(\frac{N}{mm^2}\right),\ \rho_{ref} = 400\frac{kg}{m^3}$$

Ringhofer (2015b):

$$F_{ax,\alpha,k} = \mathrm{d} l_{ef} k_{ax,k} k_{sys,k} f_{1,R}\left(\frac{\rho_k}{350}\right)^{k_\rho}(N) \tag{4-7}$$

$$f_{1,R} = 0.013 d^{-0.33}{\rho_{ref}}^{1.11}\pi\ \left(\frac{N}{mm^2}\right),\ \rho_{ref} = 350\,\frac{kg}{m^3},$$

$$k_{ax,k} = \begin{cases} 1.00 & 45° \le \varphi \le 90° \\ 0.64k_{gap} + \dfrac{1 - 0.64k_{gap}}{45}\varphi & 0° \le \varphi \le 45° \end{cases}$$

$$k_{gap} = \begin{cases} 0.90 & CLT\ narrow\ face \\ 1.00 & other \end{cases}, k_{\rho} = \begin{cases} 1.10 & 0° \leq \varphi \leq 90° \\ 1.25 - 0.05d & \varphi = 0° \end{cases}$$

$$k_{sys,k} = \begin{cases} 1.00, solid\ timber \\ 1.10, CLT, if\ N \geq 3 \\ 1.13, Glulam \end{cases}$$

where in all instances φ is the angle between the screw axis and the timber grain direction. In the Ringhofer et al. (2015b) analytical method $k_{ax,k}$ accounts for STS installation angles, $k_{gap}$ accounts for STS installed in the CLT narrow face, $k_{\rho}$ considers the influence of density, and $k_{sys,k}$ accounts for increased homogeneity when a screw penetrates multiple layers of laminated timber products. Following Eurocode 5 (2014), the design withdrawal capacity of a single screw is then:

$$F_{ax,\alpha,d} = \frac{k_{mod}}{\gamma_m} F_{ax,\alpha,k} \quad (4\text{-}8)$$

where $k_{mod}$ = load duration factor similar to $k_1$ of NZS 3603 or AS 1720.1 and $\gamma_m$ = 1.3 and is the connection partial factor similar to the inverse of the strength reduction factor ∅ of NZS 3603 or AS 1720. Within DZ NZS AS 1720.1/V6.0 (2018), the design withdrawal capacity of wood screws or coach screws is:

$$N_{ax,w} = n_{ax,w} n k_{15} k_{13}\ (N) \quad (4\text{-}9)$$

$$n_{ax,w} = \emptyset_{ax,w} d^{0.82} \rho'^{1.77} \frac{t_p}{2770}, n = number\ of\ screws$$

$$k_{15} = in\ service\ moisture\ factor, k_{13} = end\ grain\ factor$$

$$\emptyset_{ax,w} = 0.6, t_p = penetration\ length\ less\ the\ tip\ length\ (mm)$$

This study will focus on the characteristic withdrawal strength instead of the design withdrawal strength. Thus, $k_{mod}$, $\gamma_m$, ∅, and $k_1$ are not considered in comparing the test results with the analytical design equations.

### 4.2.2 Withdrawal Test Programme

A total of 202 screw withdrawal tests were performed using $\phi$8mm and $\phi$12mm SPAX Delta Seal flat countersunk head screws. The CLT specimens were fabricated by XLAM Ltd. The Radiata Pine (RP) and Douglas-Fir (DF) lamella were graded SG8 with an average Modulus of Elasticity of 8 GPa according to NZS 3603 (1993). The CLT specimens tested were 3-layer (CLT3) 5-layer (CLT5) and 7-layer (CLT7) as shown in Figure 4-4. The STS were installed on either the wide face or narrow face of CLT. Figure 4-5 shows the screw installation angles and possible screw location in the CLT wide or narrow face. The primary thread-grain angle α is shown as per Figure 4-5 and the secondary angle $\varepsilon$ is out-of-plane of

the primary wood grain (see Figure 4-2 and Figure 4-5b) direction. In this testing programme, screws installed in the CLT narrow face were only installed in position 4 of Figure 4-5b. The other possible STS positions shown in Figure 4-5b were not investigated in this study. When a single install angle α was used, $\alpha = \varphi$ for design equations. In some instances, a compound α°+ε° angle was used and then $\cos(\varphi) = \cos(\varepsilon)\sin(90^\circ - \alpha)$. The CLT specimens had an average moisture content of 11% and the mean and characteristic densities as per EN 14358 (2016) are provided in Table 4-1.

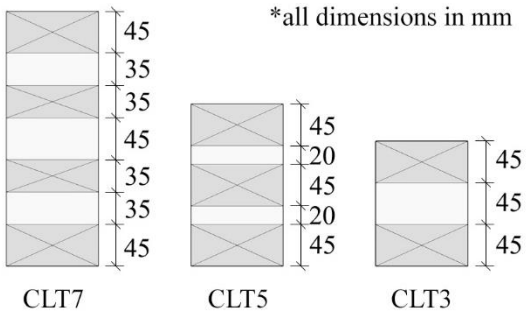


*Figure 4-4: CLT types used in test programme*

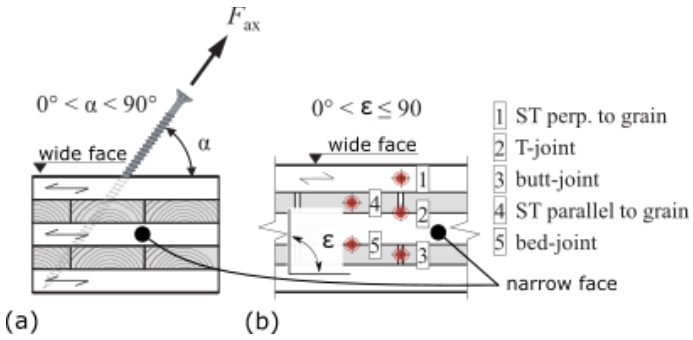


*Figure 4-5: Screw installation angle: (a) relative to outer wood grain, and (b) possible positions in CLT narrow face (adopted from Ringhofer et al.* (2018)*)*

*Table 4-1: CLT specimen and individual layer density (kg/m3)*

| **Species** | **Radiata Pine (RP)** | **Douglas-Fir (DF)** | | | | | |
|---|---|---|---|---|---|---|---|
| **CLT** | CLT3 | CLT3 | CLT5 | | | CLT7 | |
| **Sample** | specimen | specimen | specimen | 45mm lamella | 20mm lamella | specimen | 35mm lamella |
| **$\rho_m$ (kg/m³)** | 470.5 | 478.4 | 463.7 | 461.8 | 538.6 | 457.4 | 464.5 |
| **$\rho_k$ (kg/m³)** | 430.2 | 426.4 | 421.8 | 413.3 | 487.3 | 416.5 | 420.5 |

Group 1 test series consisted of 187 withdrawal tests with varied CLT types, CLT installation faces, timber species (Radiata Pine and Douglas-Fir), fastener diameters, screw installation angles as per Figure 4-5 ($\alpha + \varepsilon$), and $l_{nom}$ with a constant $l_{emb}$=0. Group 2 test series consisted of 15 withdrawal tests with varied $l_{emb}$ and a constant $l_{nom}$. Generally, five replicates were performed at each of the 8d, 10d, 12d, and 16d nominal installation lengths, $l_{nom}$. With reference to Figure 4-3, $l_{nom}$=8d resulted in $l_{ef}$=56mm (excluding the screw tip of 1d) for a $\phi$8mm STS. For the $l_{emb}$ test series, partially threaded screws were used to embed the threaded portion with various distances (0, 50mm, 100mm) from the timber surface. The full experimental test programme is outlined in Table 4-2 and Table 4-3.

*Table 4-2: Test matrix for group 1: STS withdrawal series*

| Test ID | CLT Type | CLT Installation Face | Timber Species | Screw Diameter, $\phi$ (mm) | Angle to grain (α°+ε°) | Number of tests at each $l_{nom}$ | | | |
|---|---|---|---|---|---|---|---|---|---|
| | | | | | | 8d | 10d | 12d | 16d |
| **CLT3-8-90-RP** | CLT3 | Wide | RP | 8 | 90 | 5 | 5 | 5 | 5 |
| **CLT3-8-90** | | | | 8 | 90 | 5 | 5 | 5 | 5 |
| **CLT5-8-90** | CLT5 | | DF | 8 | 90 | 6 | 5 | 6 | 5 |
| **CLT5-8-60** | | | | 8 | 60 | 5 | 5 | 5 | - |
| **CLT5-8-60+15** | | | | 8 | 60+15 | 5 | 5 | - | - |
| **CLT5-8-0** | | | | 8 | 0 | 5 | 5 | 5 | 1 |
| **CLT5-8-30** | | Narrow | | 8 | 30 | 8 | 5 | 6 | - |
| **CLT5-8-30+15** | | | | 8 | 30+15 | 5 | 5 | 5 | - |
| **CLT7-12-90** | CLT7 | Wide | | 12 | 90 | 5 | 5 | 5 | 5 |
| **CLT7-12-60** | | | | 12 | 30 | 5 | 5 | - | - |
| **CLT7-12-0** | | Narrow | | 12 | 0 | 5 | 5 | - | - |
| **CLT7-8-0** | | | | 8 | 0 | - | - | 5 | 5 |

*Table 4-3: Test matrix for group 2: STS withdrawal embedment length, $l_{emb}$, series*

| Test ID | CLT Type | Timber | Screw Diameter, $\phi$ (mm) | Angle to grain (α °) | Embedment Length $l_{emb}$ (mm) | Number of Tests |
|---|---|---|---|---|---|---|
| **CLT7-12-90-0** | CLT7 | DF | 12 | 90 | 0 | 5 |
| **CLT7-12-90-50** | | | | | 50 | 5 |
| **CLT7-12-90-100** | | | | | 100 | 5 |

All tests were performed in a displacement controlled manner following EN 1382 (2016). The test set-up for the 90° and inclined screw withdrawal tests are shown in Figure 4-6.


(a) (b)

*Figure 4-6: (a) 90 degree STS withdrawal test setup, and (b) inclined STS withdrawal test setup*

### 4.2.3 Self-Tapping Screw Withdrawal Test Results and Discussion

Figure 4-7 shows the summary of the withdrawal strength for each test series of Group 1. The experimental results combine the $l_{nom}$ tests of 8d, 10d and 12d assuming $l_{ef}$ is not an influencing parameter on withdrawal strength as per Ringhofer et al. (2015b). As expected, the withdrawal strength (MPa) as per Equation (4-2) was higher for the $\phi$8mm series compared to the $\phi$12mm screw series. However, a $\phi$12mm screw will have a higher withdrawal capacity (kN) than an $\phi$8mm screw for the same $l_{ef}$. Further, an increasing strength and homogenization was observed with increasing number of CLT layers penetrated as previously reported by Ringhofer et al. (2015b). Withdrawal strengths for the CLT5 test series on the narrow face, which included the installation angles of 0°, 30°, and 30°+15°, had high strength but also high variability. This higher withdrawal strength is in part due to the higher density of the 20mm lamella layer as reported in Table 4-1. The compound installation angle ($\alpha + \varepsilon$) on the CLT narrow face had a lower coefficient of variation (CV) when compared to the single angle. Therefore, engaging more CLT layers with a compound angle installation increased homogenization. The benefit of lower dispersion was not observed in compound angle withdrawal tests on the CLT wide face.

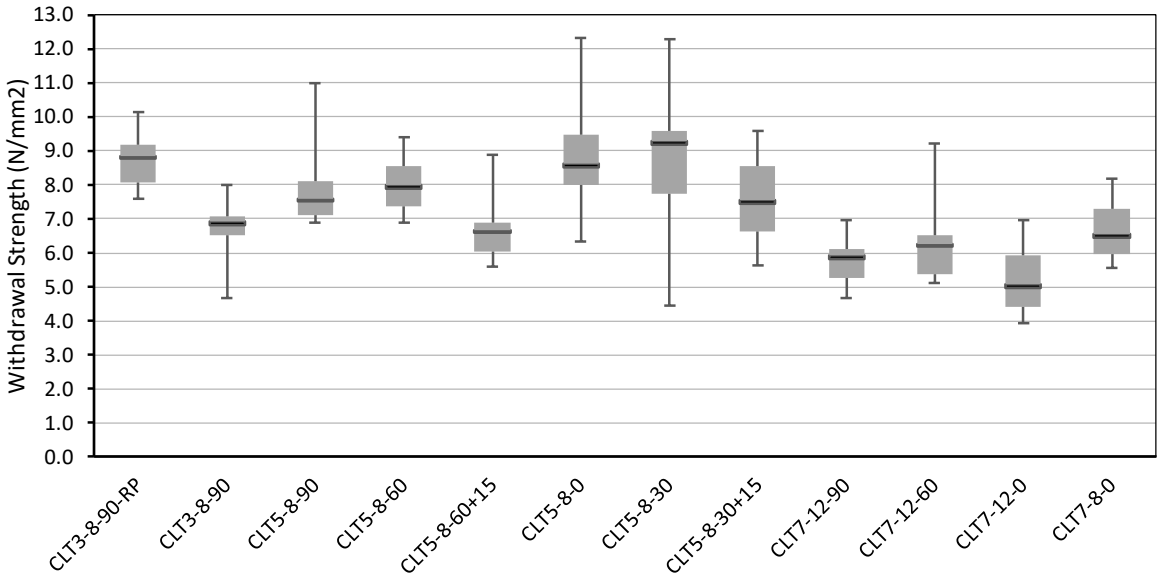


*Figure 4-7: Withdrawal strength of various test series*

In all test series, the 16d embedment length reached the steel tensile capacity of the screws. In this instance, the 5$^{th}$ percentile steel tensile results were determined as per EN 14358 (2016). Table 4-4 provides a comparison of the experimental results to the provided SPAX ETA (2017) characteristic tensile values.

*Table 4-4: Tensile capacity of screw with comparison to ETA*

| Screw | $F_{tens,SPAX,k}$ (kN) | $F_{tens,exp,0.05}$ (kN) | $F_{tens,exp,mean}$ (kN) | Samples |
|---|---|---|---|---|
| $\phi$8mm | 17 | 19.2 | 21.4 | 16 |
| $\phi$12mm | 38 | 41.8 | 49.0 | 3 |

Typical failure modes in the CLT wide face and CLT narrow face testing are shown in Figure 4-8.

(a) (b)

*Figure 4-8: (a) Timber splitting in CLT wide face 90° screw withdrawal test, and (b) Shear cylinder failure in CLT narrow face 0° screw withdrawal test*

#### *4.2.3.1 Comparison to design standards*

Table 4-5 compares the 5th percentile withdrawal strength determined as per EN 14358 (2016) with the calculations by the SPAX and Ringhofer analytical methods. The SPAX ETA and Ringhofer methods were compared because they do not include $l_{ef}$ as an influencing parameter on $f_{ax}$. In general, there is good agreement between the analytical methods and the experimental results given the relatively small sample size of each test series. The higher characteristic withdrawal strength predicted by the Ringhofer method when compared to the SPAX ETA is in part due to the higher density correction factor used by Ringhofer. The experimental results of the narrow face 0° installation are significantly higher than the analytical methods. With reference to Figure 4-5, this result is expected as all experimental tests were installed in location 4 (screws driven in end grain) whereas both SPAX ETA and Ringhofer methods account for all possible installation locations. If a screw was installed in location 3 of Figure 4-5 the withdrawal strength would be lower. It is important to note that currently Eurocode 5 (2014) requires screw axis-grain angles $\alpha \geq 30°$ while more recent STS ETAs require $\alpha \geq 15°$ (ETA-12/0114, 2017), or allow $\alpha = 0°$ but with significant reduction (ETA-11/0030, 2019; ETA-11/0190, 2018). Allowable withdrawal STS axis-grain angles is an area of current research.

*Table 4-5: Comparison of full experimental characteristic withdrawal strength, $f_{ax,k,i}$ (N/mm²)*

| Test ID | CLT3-8-90-RP | CLT3-8-90 | CLT5-8-90 | CLT5-8-60 | CLT5-8-60+15 | CLT5-8-0 |
|---|---|---|---|---|---|---|
| $f_{ax,0.05,exp}$ | 7.3 | 5.2 | 5.9 | 6.6 | 4.9 | 5.9 |
| $CV_{exp}$(%) | 8.7 | 12.2 | 16.6 | 9.6 | 15.2 | 18.5 |
| $f_{ax,k,SPAX}$ | 4.5 | 4.5 | 4.4 | 4.2 | 4.2 | 4.1 |
| $f_{ax,k,Ringhofer}$ | 6.0 | 6.0 | 5.9 | 5.9 | 5.9 | 3.3 |

| Test ID | CLT5-8-30 | CLT5-8-30+15 | CLT7-12-90 | CLT7-12-60 | CLT7-12-0 | CLT7-8-0 |
|---|---|---|---|---|---|---|
| $f_{ax,0.05,exp}$ | 5.3 | 5.5 | 4.6 | 4.2 | 3.4 | 4.9 |
| $CV_{exp}$(%) | 21.5 | 15.4 | 11.2 | 20.0 | 19.2 | 14.2 |
| $f_{ax,k,SPAX}$ | 4.3 | 4.3 | 4.0 | 3.8 | 3.4 | 3.7 |
| $f_{ax,k,Ringhofer}$ | 5.4 | 5.4 | 5.1 | 5.1 | 2.5 | 2.9 |

Based on the experimental results presented, the average ratio of $f_{ax,0.05,exp}$ to $f_{ax,k,SPAX}$, defined as $\gamma_{an}$, is 1.3 excluding test series with $\alpha$=0°. This means that the SPAX ETA equation was appropriate as similar analytical model conservativism has been reported for laterally loaded dowelled connections (Jorissen & Fragiacomo, 2011). If $\rho_k$= 440 kg/m$^3$ for SG8 New Zealand timber in DZ NZS AS 1720.1/V6 was used in lieu of reported experimental densities in Table 4-1 with SPAX ETA analytical equations, the average $\gamma_{an}$ was 1.3 excluding test series with $\alpha$=0° as well. Therefore, the proposed characteristic density in DZ NZS AS 1720.1/V6 was appropriate in this instance as well.

Figure 4-9 shows the comparison between the seven analytical design methods, $f_{ax,i}$, described in Section 4.2.1 and the characteristic withdrawal strength of test series CLT3-8-90 and CLT7-12-90. Most methods under-predicted the withdrawal strength except for the Ringhofer method. U&B, EC5, and SPAX all provide similar strength predictions with the inclusion of $l_{tip}$ having a larger impact on the $\phi$12mm screw size for U&B and EC5. It should be pointed out that NZS 3603 and AS 1720.1 tabular values and the proposed design method in DZ NZS AS 1720.1/V6.0 for coach screws were used and they are not representative of STS as expected.

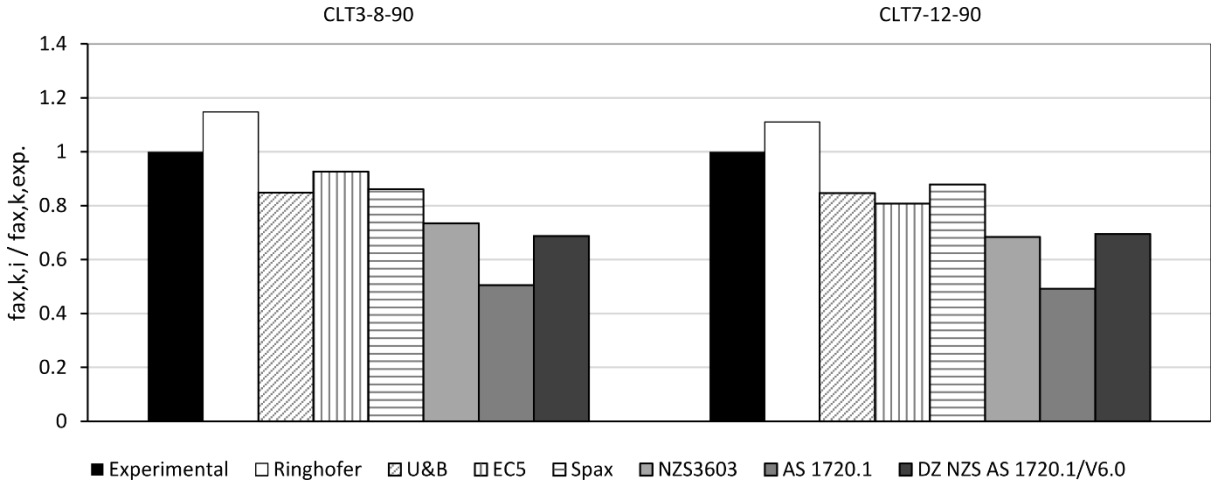


*Figure 4-9: Comparison of characteristic withdrawal strength according to experimental results for Ø8mm and Ø12mm screws at constant 10d length and 90° installation*

#### 4.2.3.2 *Embedment length test series results*

The load slip curves of Group 2 test series are shown in Figure 4-10 and the strength results are given in Table 4-6. With increased $l_{emb,}$ no significant effect on the displacement capacity was observed. However, the withdrawal strength in this instance increased by 15% and 10% for $l_{emb}$ = 50mm and 100mm, respectively. A larger parametric study is required to further quantify this behaviour. Once localized shear failure at the timber-thread interface occurred, the withdrawal capacity decreased in a similar manner. Figure 4-10b shows that increased $l_{emb}$ prevented timber surface splitting which had also been observed by Westermayr & van de Kuilen (2019).

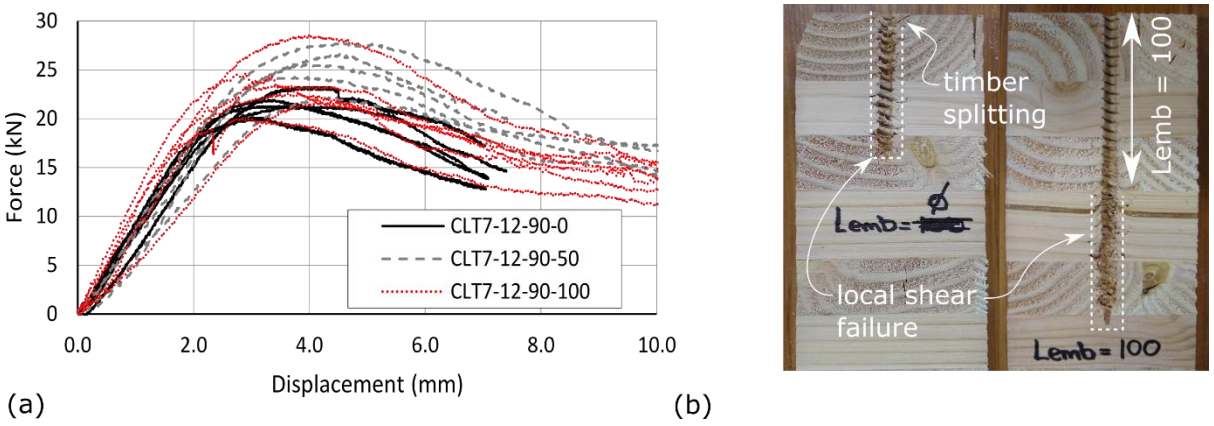


*Figure 4-10: (a) $l_{emb}$ test series load-slip curves, (b) comparison of $l_{emb}$=0 and 100mm*

*Table 4-6: $l_{emb}$ test series experimental results*

| Test ID | CLT7-12-90-0 | CLT7-12-90-50 | CLT7-12-90-100 |
|---|---|---|---|
| $f_{ax,mean,exp}$ (N/mm²) | 6.5 | 7.4 | 7.1 |
| CV (%) | 5.3 | 8.9 | 12.6 |

### 4.2.4 Withdrawal Testing Summary

A total of 202 STS withdrawal tests of $\phi$8mm and $\phi$12mm screws in three-, five- and seven-layer New Zealand Radiata Pine and Douglas-Fir CLT were performed. Experimental results were compared with seven analytical design methods in literature. Because the STS from one supplier were used in the study, some of the following experimental findings cannot be assumed for all other STS suppliers as meaningful withdrawal strength differences within ETAs have been reported recently by Ringhofer & Schickhofer (2019).

- While the current NZS 3603 (Standards New Zealand, 1993), AS 1720.1 (Standards Australia, 2010) do not specify STS, using their design values for coach screws significantly under-predicted the withdrawal strength of STS. The proposed DZ NZS AS 1720.1/V6 (2018)

analytical equation for screws with $\phi$6.3mm or less and coach screws significantly under-predicted the withdrawal strength.

- The ratio of the average experimental 5$^{th}$ percentile withdrawal strength to the ETA analytical model calculation, $\gamma_{an}$, was 1.3 using both experimental and AS 1720 timber densities. Therefore, the SPAX ETA provided reasonably good predictions for the New Zealand Radiata pine and Douglas-Fir CLT.
- To avoid brittle steel tensile failure of STS, embedment length of the threaded portion should not be greater than 12d.
- Increased embedment length of unthreaded portion of partially threaded screws, $l_{emb}$, was able to increase the average withdrawal strength by 10%~15% by eliminating timber surface splitting. However, it did not significantly affect the displacement capacity.

## 4.3 CONNECTION TESTING EXPERIMENTAL PROGRAMME

### 4.3.1 Specimen Description

The orthogonal joint test programme is shown in Table 4-7. A total of 59 joint specimens were tested in nine series with different connection configurations. In labelling each test series, the number indicates the quantity of screws installed in the joints and S, ST, SC, and X indicate different installations: S = 90° STS; ST = shear-tension STS; SC = shear-compression STS, and X = cross-pattern STS (i.e., a combination of shear-tension and shear-compression STS), respectively. Note the test series 16X-400 label is unique and used 16 STS 400mm long, installed in cross-pattern. Three series (2S, 8ST, 8SC) were tested under monotonic (M) loading only, the other six series were tested under both M and reversed cyclic (C) loading. The number of replicates for monotonic tests was three except for the 2S test series which had five replicates; the number of the replicates for cyclic tests was five.

Each test series was designed to verify current design models for mixed angle STS as applicable to orthogonal CLT joints. The test programme allowed to assess the performance of orthogonal CLT panel joints with varying mixed angle STS combination ratios. With series 2S, 8ST, 8SC, and 16X, the applicability of existing analytical models to estimate the load-carrying capacity was assessed. By comparing series 16X-400 and 16X, the influence of STS embedment length on strength, stiffness, and failure mode was investigated. Comparing series 16X and 16X+16S (combination of 90° STS and inclined STS) allowed for verification of the increase in displacement capacity and ductility. Finally, series 12X, 12X+4S, and 12X+6S aimed to determine the impact of 90° STS on strength, displacement capacity, ductility, stiffness, and energy dissipation. STS slenderness, $\lambda = L/d_c$, where L and $d_c$ are the

STS length and core diameter, varied from 40 to 80 by considering STS of different L and $d_c$.

The specimens consisted of 5-ply 175mm thick CLT with a layup of 45/20/45/20/45 and 7-ply 275mm thick CLT with a layup of 45/35/35/45/35/35/45, herein simply referred to as CLT5 and CLT7, respectively. The Douglas-Fir lamella were graded SG8 with average Modulus of Elasticity of 8 GPa according to NZS3603 (1993). After testing, a small piece was removed from each specimen and oven dried to determine density and moisture content. The CLT specimens had an average moisture content of 11%, and the mean and characteristic densities were $\rho_m$ = 462 kg/m$^3$ and $\rho_k$ = 422 kg/m$^3$ for CLT5 specimens and $\rho_m$ = 457 kg/m$^3$ and $\rho_k$ = 417 kg/m$^3$ for CLT7 specimens respectively.

SPAX (2017) fully threaded (FT) $\phi$8mm STS were used for the CLT5 specimens and FT $\phi$12mm STS were used for the CLT7 specimens. The STS length varied for inclined STS and STS installed at 90°. In series 16X-400 the inclined STS length was longer than 90° STS in a similar manner as past research (Hossain et al., 2018; Sullivan et al., 2018; Roberto Tomasi et al., 2010). However, in all other series to ensure screw withdrawal failure occurred the inclined STS were shorter than 90° STS. The η ratio, i.e. the ratio between inclined STS and STS installed at 90°, varied from 1:0, 3:1, 2:1, 1:1, and 0:1 in the joints. Shear-tension and shear-compression screws were both considered inclined STS. The η ratio of 0:1 indicated that only 90° STS were used and the η ratio of 1:0 indicated that only inclined STS were used. The η ratios of 3:1, 2:1 and 1:1 indicated the inclined STS to 90° STS ratio. For example, an η ratio of 3:1 meant that for three inclined STS there was one 90° STS. Changing the η ratio accordingly from 1:0, 3:1, 2:1 to 1:1 was defined as decreasing the η ratio, and hence increasing the amount of 90° STS in the joint.

*Table 4-7: Experimental test programme*

| Series | Load Type | Repl. | CLT | Inclined STS Type | λ | Qty. | 90° STS Type | λ | Qty. | Mixed Angle STS Ratio (η) |
|---|---|---|---|---|---|---|---|---|---|---|
| 2S | M | 5 | CLT5 | - | - | - | $\phi$8x350 | 70 | 2 | 0:1 |
| 8ST | M | 3 | CLT5 | $\phi$8x200 | 40 | 8 | - | - | - | 1:0 |
| 8SC | M | 3 | CLT5 | $\phi$8x200 | 40 | 8 | - | - | - | 1:0 |
| 16X-400 | M | 3 | CLT5 | $\phi$8x400 | 80 | 16 | - | - | - | 1:0 |
| | C | 5 | CLT5 | $\phi$8x400 | 80 | 16 | - | - | - | 1:0 |
| 16X | M | 3 | CLT5 | $\phi$8x200 | 40 | 16 | - | - | - | 1:0 |
| | C | 5 | CLT5 | $\phi$8x200 | 40 | 16 | - | - | - | 1:0 |
| 16X+16S | M | 3 | CLT5 | $\phi$8x200 | 40 | 16 | $\phi$8x350 | 70 | 16 | 1:1 |
| | C | 5 | CLT5 | $\phi$8x200 | 40 | 16 | $\phi$8x350 | 70 | 16 | 1:1 |
| 12X | M | 3 | CLT7 | $\phi$12x350 | 47 | 12 | - | - | - | 1:0 |
| | C | 5 | CLT7 | $\phi$12x350 | 47 | 12 | - | - | - | 1:0 |
| 12X+4S | M | 3 | CLT7 | $\phi$12x350 | 47 | 12 | $\phi$12x550 | 74 | 4 | 3:1 |
| | C | 5 | CLT7 | $\phi$12x350 | 47 | 12 | $\phi$12x550 | 74 | 4 | 3:1 |
| 12X+6S | M | 3 | CLT7 | $\phi$12x350 | 47 | 12 | $\phi$12x550 | 74 | 6 | 2:1 |
| | C | 5 | CLT7 | $\phi$12x350 | 47 | 12 | $\phi$12x550 | 74 | 6 | 2:1 |

Figure 4-11 shows the test specimens and joint details of all test series. Figure 4-11a and Figure 4-11b provide isometric views and the dimensions for the CLT5 and CLT7 specimens. The $\phi$8mm and $\phi$12mm STS were installed into $\phi$5mm and $\phi$7mm predrilled holes, respectively, to 70% of the STS length with jigs to ensure correct alignment. Each joint specimen had three CLT panels: two side panels and one middle panel. The two side panels were connected to the middle panel with STS installed in a symmetrical layout such that each specimen had two orthogonal joints. Figure 4-11c - Figure 4-11k show one joint and half of a test specimen to provide details for each STS layout including the η ratio. The monotonic loading direction is indicated for the 8ST and 8SC test series to show the shear-tension and shear-compression STS respectively. The fastener spacing followed the product ETA (2017). In all test series except 16X-400, the inclined STS were countersunk into the side panels to ensure equal embedment length of the screw into the side panel and the middle panel.

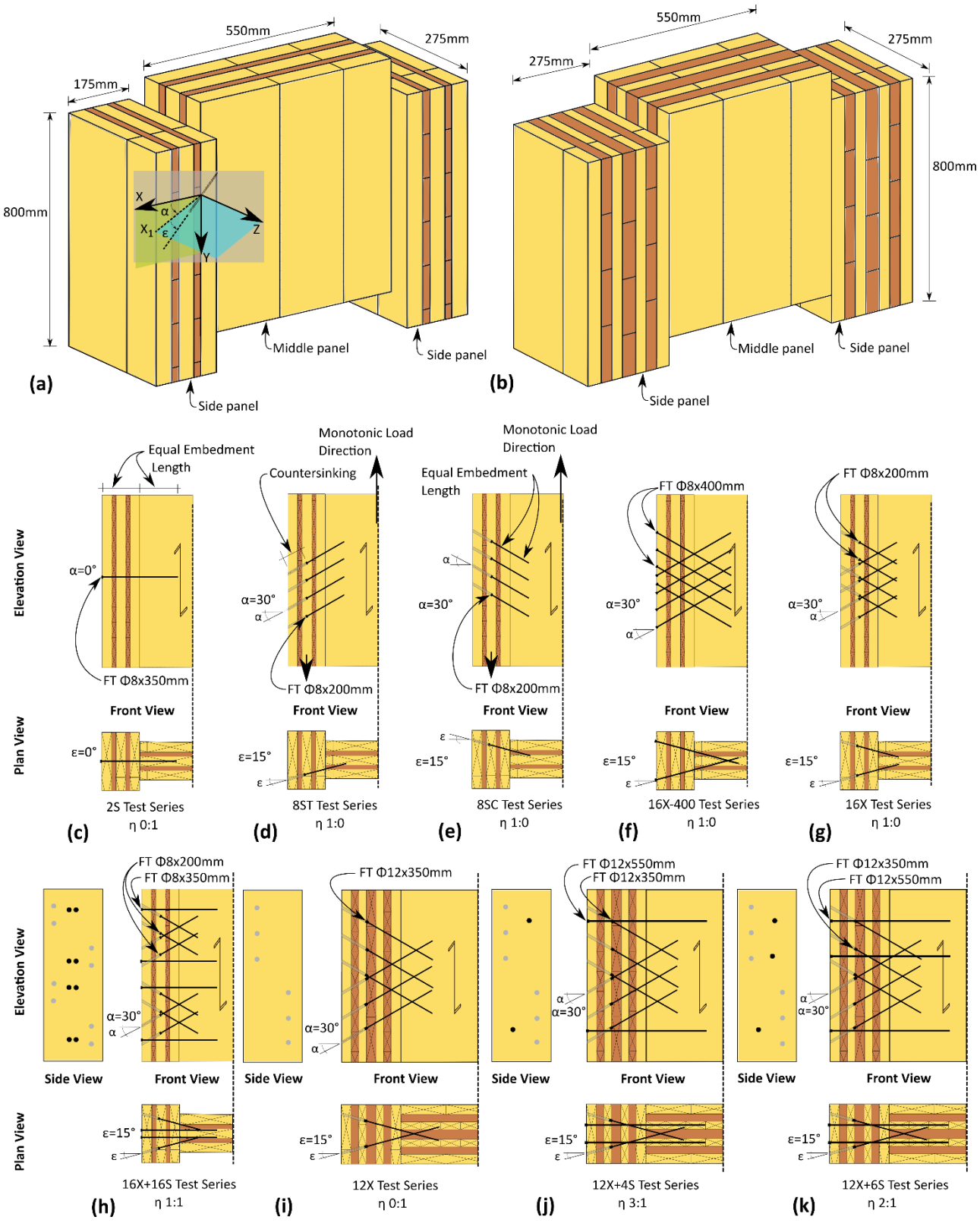


*Figure 4-11: (a) CLT5 isometric, (b) CLT7 isometric, (c) 2S test series, (d) 8ST test series, (e) 8SC test series, (f) 16X-400 test series, (g) 16X test series, (h) 16X+16S test series, (i) 12X test series, (j) 12X+4S test series, and (k) 12X test series*

In these test series, the inclined STS embedment length was chosen based on single STS withdrawal studies presented in Section 4.2 so that the withdrawal strength was sufficiently greater than the STS

tensile strength to promote STS withdrawal failure and minimize brittle STS tensile failure. All inclined STS were installed at α = 30° and ε = 15° to create a double angle. 90° STS did not have a double angle. For inclined STS, a double angle was implemented for the following reasons: (1) the product ETA (2017) requires a minimum angle to the grain of 15° for withdrawal capacity; (2) the general embedding strength formulation could be used which is significantly higher than the reduced formulation for STS installed parallel to the CLT plane as per product ETA (2017); (3) significant homogenization is found when STS penetrate more layers (Ringhofer et al., 2015a); and (4) for an actual core-wall application, the orthogonal joint would be subjected to bi-directional loading and a double angle would provide optimized axial STS loading in either direction.

### 4.3.2 Methods

Figure 4-12 shows the test setup. A 700 kN capacity hydraulic ram with a load cell was clamped to the middle CLT panel of the joint specimen. The two side CLT panels were fully restrained by steel plates and 4-M20 Grade 8.8 threaded rods (Standards New Zealand, 1992). Horizontal in-plane movement was also restrained by two sets of steel plates with 4-M36 Grade 8.8 threaded rods placed at the top and bottom of the specimen. Out-of-plane translation and rotation was prevented by a horizontal steel beam with rectangular hollow section that was bolted to the reaction frame.

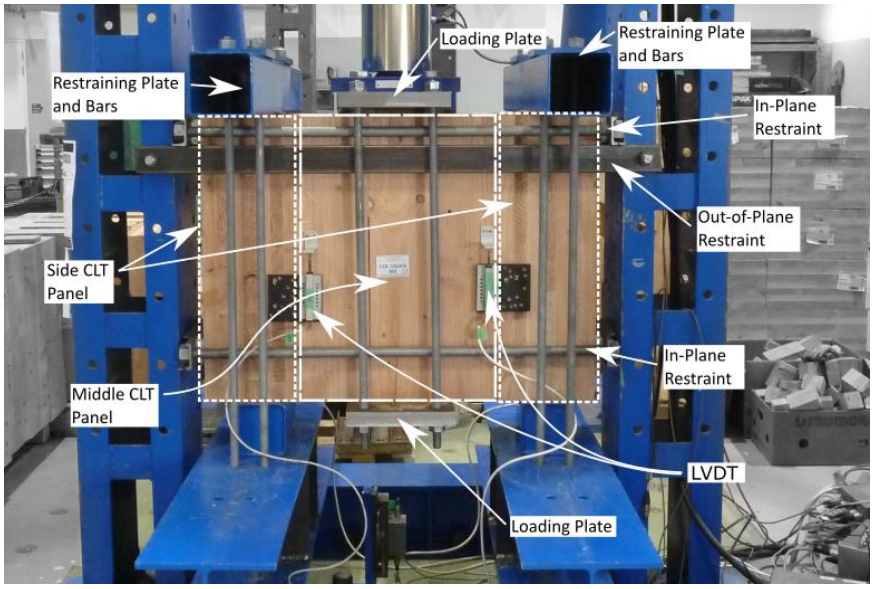


*Figure 4-12: Overall test set-up*

Figure 4-13 shows the instrumentation used in the testing. Relative displacement between the middle and outer CLT panels was measured with 100mm linear variable displacement transducers (LVDTs) at two points on each shear plane for a total of four measurements. The average joint slip was

determined from the four measurements. Out-of-plane displacement was also measured at two points.

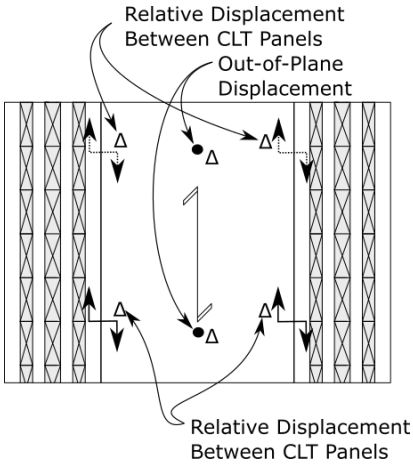


*Figure 4-13: Specimen instrumentation - CLT7 joint specimen shown*

Test series 2S, 8ST and 8SC were tested under monotonic loading only following EN 26891 (1991). For these test series if a maximum strength was not reached the joint slip was limited to 15mm following EN 26891 (1991). For the remaining test series, three monotonic tests were performed first to determine the average yield displacement, $\Delta_y$, that was used as the reference displacement to define the cyclic loading protocol as per EN 12512 (2005a). One cycle amplitude at $0.25\Delta_y$ and $0.5\Delta_y$ were performed followed by three cycle amplitudes at $0.75\Delta_y$, $1.0\Delta_y$ $2.0\Delta_y$, $4.0\Delta_y$, and then increasing multiples of $2.0\Delta_y$ ($6.0\Delta_y$, $8.0\Delta_y$, etc.) until failure as defined by EN 12512 (2005a) and explained later. The monotonic loading rate was between 3-6mm/min for a total test time of 10 to 15min as per EN 26891 (1991) and the cyclic loading rate was between 12-18mm/min as per EN 12512 (2005a). The results were analysed as per EN 12512 (2005a) to determine the yield strength $F_y$, maximum strength $F_{max}$, and ultimate strength $F_u$, the corresponding yield displacement $\Delta_y$, displacement at maximum strength $\Delta_{Fmax}$, ultimate displacement $\Delta_{Fu}$, and the elastic stiffness, k. The elastic stiffness was calculated for the range of the load-slip curve between 10% and 40% $F_{max}$ as per EN 26891 (1991). Herein, the displacement capacity is synonymous to the ultimate displacement defined as the displacement at which $F_u$ occurred, which is the post-peak load at 80% of $F_{max}$. While EN 12512 (2005a) assesses the ultimate strength $F_u$ to a maximum slip of 30mm, in 16X+16S, 12X+4S and 12X+6S test series slips greater than 30mm were recorded and they are presented to illustrate the impact of the η ratio on joint performance. Energy dissipation properties were derived in terms of equivalent viscous damping following EN 12512 (2005a). Ductility, μ, is reported as it is often defined as a ratio of $\Delta_{Fu}$ to $\Delta_y$, as shown in Equation (4-10) (Jorissen & Fragiacomo, 2011).

$$\mu = \frac{\Delta_{Fu}}{\Delta_y} \quad (4\text{-}10)$$

Following the recommendations by Smith et al. (2006), the joint was defined as low ductility (LD) for μ<4, as moderate ductility (MD) for 4≤μ≤6, and as Ductile (D) for μ> 6. It should be noted that connection ductility is not the same a building / system level ductility/drift capacity. In this context and depending on the relation of the connection to the lateral load resisting system and building, $\mu$ = 6 may not be sufficient to provide target system level ductility/drift capacity. System level ductility/drift capacity relation to connection ductility was beyond the scope of the study presented herein.

Connection overstrength can be defined as the discrepancy between analytically calculated design strength in code provisions and the 95th-percentile of the true strength distribution. Jorissen and Fragiacomo (2011) defined the overstrength factor for timber connections, $\gamma_{Rd}$, as:

$$\gamma_{Rd} = \gamma_M \cdot \gamma_{an} \cdot \gamma_{0.95} = \frac{F_k}{F_d} \cdot \frac{F_{0.05}}{F_k} \cdot \frac{F_{0.95}}{F_{0.05}} \quad (4\text{-}11)$$

where $\gamma_M$ = overstrength attributed to material safety factor; $\gamma_{an}$ = overstrength attributed to conservatism of analytical models; $\gamma_{0.95}$ = overstrength attributed to difference between 5$^{th}$ and 95$^{th}$ percentile of strength distribution; $F_k$ = characteristic strength; $F_d$ = design strength; $F_{0.05}$ = 5$^{th}$ percentile of strength distribution; $F_{0.95}$ = 95$^{th}$ percentile of strength distribution. The observed $\gamma_{Rd}$ will be discussed in Section 4.5.

## 4.4 CONNECTION TESTING RESULTS AND DISCUSSION

### 4.4.1 Overview

Table 4-8 provides a summary of joint performance parameters as mean, $X_m$, with coefficient of variation (CV), for each test series. Similar to the results reported by Tomasi et al. (2010), ultimate loads were not observed in both 2S and 8SC test series groups even at large joint slips. Thus, as per EN 26891 (1991) the ultimate slip was limited to 15mm. For the 16X+16S, 12X+4S, and 12X+6S monotonic test series, $F_{max}$ is reported as the average load at the first peak on the load-slip curve. In the mixed angle test series under monotonic loading, the load kept increasing after an initial drop at the first peak and even surpassed the first peak load. The load at the first peak is required in Section 4.5 for comparison to analytical models and to derive cyclic overstrength.

*Table 4-8: Test summary of joint performance factors*

| Series | | Fy | | Fmax | | Fu | | Δy | | Δmax | | Δu | | K | | μ | |
|---|---|---|---|---|---|---|---|---|---|---|---|---|---|---|---|---|---|
| | | $X_m$ | CV | $X_m$ | CV | $X_m$ | CV | $X_m$ | CV | $X_m$ | CV | $X_m$ | CV | $X_m$ | CV | $X_m$ | CV |
| | | kN | % | kN | % | kN | % | mm | % | mm | % | mm | % | kN/mm | % | - | % |
| 2S | M | 7 | 12 | 7[1] | - | 18 | 15 | 6.0 | 20 | 6[1] | - | 15[2] | - | 0.8 | 14 | -[2] | - |
| 8ST | M | 121 | 3 | 138 | 2 | 110 | 1 | 2.7 | 30 | 5.8 | 10 | 11.0 | 16 | 45 | 24 | 4.2 | 13 |
| 8SC | M | 24 | 13 | 34[1] | - | 34 | 6 | 0.7 | 22 | 6[1] | - | 15[2] | - | 33 | 23 | -[2] | - |
| 16X-400 | M | 191 | 2 | 208 | 4 | 167 | 4 | 3.8 | 23 | 5.9 | 10 | 7.1 | 19 | 49 | 19 | 1.9 | 15 |
| | C | 177 | 9 | 202 | 4 | 169 | 7 | 2.6 | 15 | 5.0 | 7 | 5.6 | 11 | 69 | 16 | 2.3 | 30 |
| 16X | M | 120 | 30 | 153 | 20 | 122 | 20 | 1.7 | 35 | 6.3 | 29 | 11.1 | 16 | 69 | 26 | 7.3 | 52 |
| | C | 134 | 8 | 165 | 5 | 132 | 5 | 1.6 | 27 | 5.0 | 9 | 7.3 | 12 | 83 | 21 | 4.9 | 18 |
| 16X+16S | M | 190 | 2 | 244[1] | 4 | 251 | 4 | 1.9 | 12 | 6[1] | 4 | 26.9 | 14 | 92 | 18 | 14.4 | 10 |
| | C | 179 | 6 | 238 | 3 | 190 | 3 | 1.7 | 14 | 11.0 | 65 | 21.8 | 27 | 107 | 15 | 14.4 | 24 |
| 12X | M | 188 | 4 | 219 | 6 | 176 | 6 | 2.4 | 36 | 5.8 | 18 | 16 | 18 | 75 | 27 | 7 | 16 |
| | C | 186 | 11 | 243 | 7 | 195 | 7 | 1.6 | 13 | 5.7 | 12 | 11.6 | 21 | 110 | 8 | 7.9 | 33 |
| 12X+4S | M | 226 | 11 | 290[1] | 8 | 277 | 20 | 2 | 8 | 8[1] | 7 | 50.2 | 32 | 103 | 3 | 25 | 37 |
| | C | 236 | 7 | 309 | 5 | 247 | 5 | 1.7 | 7 | 6.6 | 11 | 13 | 9 | 126 | 5 | 7.8 | 16 |
| 12X+6S | M | 246 | 8 | 314[1] | 6 | 308 | 6 | 2.2 | 32 | 8[1] | 4 | 49.3 | 4 | 102 | 25 | 23.5 | 29 |
| | C | 215 | 6 | 314 | 5 | 251 | 5 | 1.3 | 18 | 9.4 | 13 | 24.1 | 29 | 151 | 12 | 20.2 | 41 |

Notes: 1 indicates $F_{max}$ chosen as load at first peak for analytical comparison

2 as per EN 26891, Δu = 15mm and μ not stated as a maximum load was not reached

Figure 4-14 shows the experimental monotonic and hysteresis curves for all test specimens which included two joints. The force represented the total applied load and the relative joint displacement, slip, was derived by averaging the data measured from four LVDTs. It was found that the curves of the replicates in each series were consistent. Therefore, for each test series, one representative monotonic load-slip and one representative cyclic load-slip curve are provided. The monotonic-load slip curves for the inclined STS show that when tensile screw failure was avoided, the joint had stable post-peak performance that varied between test series due to the η ratio. With only inclined STS (η of 1:0), limited displacement capacity was observed. However, the post-peak displacement capacity was significantly increased by adding 90° STS with the η ratio reduced.

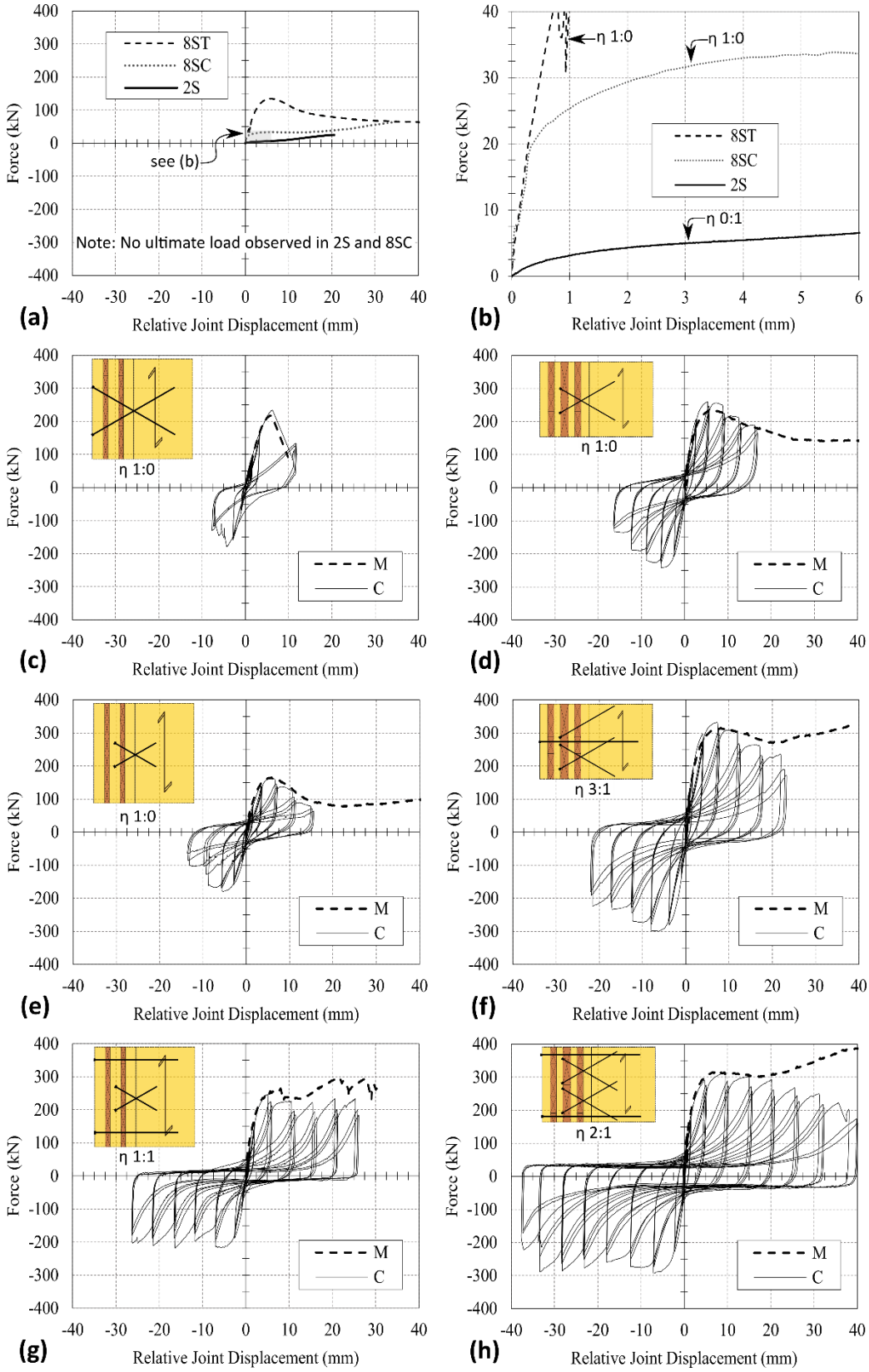


*Figure 4-14: Monotonic and cyclic load-slip curves by test series; (a) and (b) 2S, 8ST, 8SC, (c) 16X-400, (d) 12X, (e) 16X, (f) 12X+4S, (g) 16X+16S, and (h) 12X+6S*

The cyclic load-slip curves showed typical pinching behaviour and stable response in all series other than 16X-400, when brittle screw tensile failure occurred. With the addition of 90° STS the displacement capacity increased and the pinching behaviour was more pronounced. Other than for series 16X-400, $F_{max}$ was within 10% on average between the positive and negative cycles. The displacement capacity was less consistent between positive and negative cycles of each test.

### 4.4.2 Failure Modes

Figure 4-15 shows typical failure modes for series 16X, 16X+16S and 12X after testing by showing the side and middle panel respectively. Figure 4-15a - Figure 4-15f show plastic embedment deformation and the length is indicated at each STS location in mm. Figure 4-15c and Figure 4-15d show the longest plastic embedment deformation lengths, indicative of the test series large displacement capacity and the most STS tensile failure as well. Significant plastic embedment deformation is shown by the pronounced pinching behaviour in Figure 4-14g and Figure 4-14h. Figure 4-15e shows STS yielding that occurred with each STS removed from the joint specimen. Series 16X-400 had brittle tensile failure of the screws on one shear plane which propagated in a zipper like effect. This is shown by the sudden load drop in Figure 4-14c. These tests were characterised with low ductility in both monotonic and cyclic loading. The reduced embedment length in series 16X compared to 16X-400 led to a more gradual screw withdrawal as the dominating failure mode, as shown in Figure 4-14e (series 16X) and Figure 4-14d (series 16X-400). For the remaining test series, the shortened length of the inclined STS ensured gradual STS withdrawal failure mode. Under monotonic loading tensile screw failure was avoided in most instances and the load increased at larger slips due to the significant rope effect as observed by Tomasi et al. (2010). Under cyclic loading, in some instances tensile screw failure occurred at larger slips but a sudden load drop was avoided. In the mixed angle screw test series, a more complex failure mode similar to that reported by Hossain et al. (2018) was observed. The inclined screws provided high initial stiffness. Once screw withdrawal started, a small load drop was observed but the 90° screws became more engaged to carry the load. Under cyclic loading with increased slips, STS tensile failure occurred and the load dropped significantly. However, a progressive zipper-like failure as observed in series 16X-400 did not occur with mixed angle screws and the joint continued to sustain the load. The η ratio influenced the shape of the load slip-curve and failure mode. Figure 4-14f with η of 3:1 had similar behaviour to the test series in Figure 4-14d and Figure 4-14e with η of 1:0. However, Figure 4-14h with η of 2:1 had similar behaviour to the test series in Figure 4-14g with η of 1:1, which had been studied for in-plane CLT joints (Hossain et al., 2018; Sullivan et al., 2018).

With both decreasing η and increased quantity of screws in the joint, the tensile failure of an individual screw had a lesser effect on the overall joint behaviour.

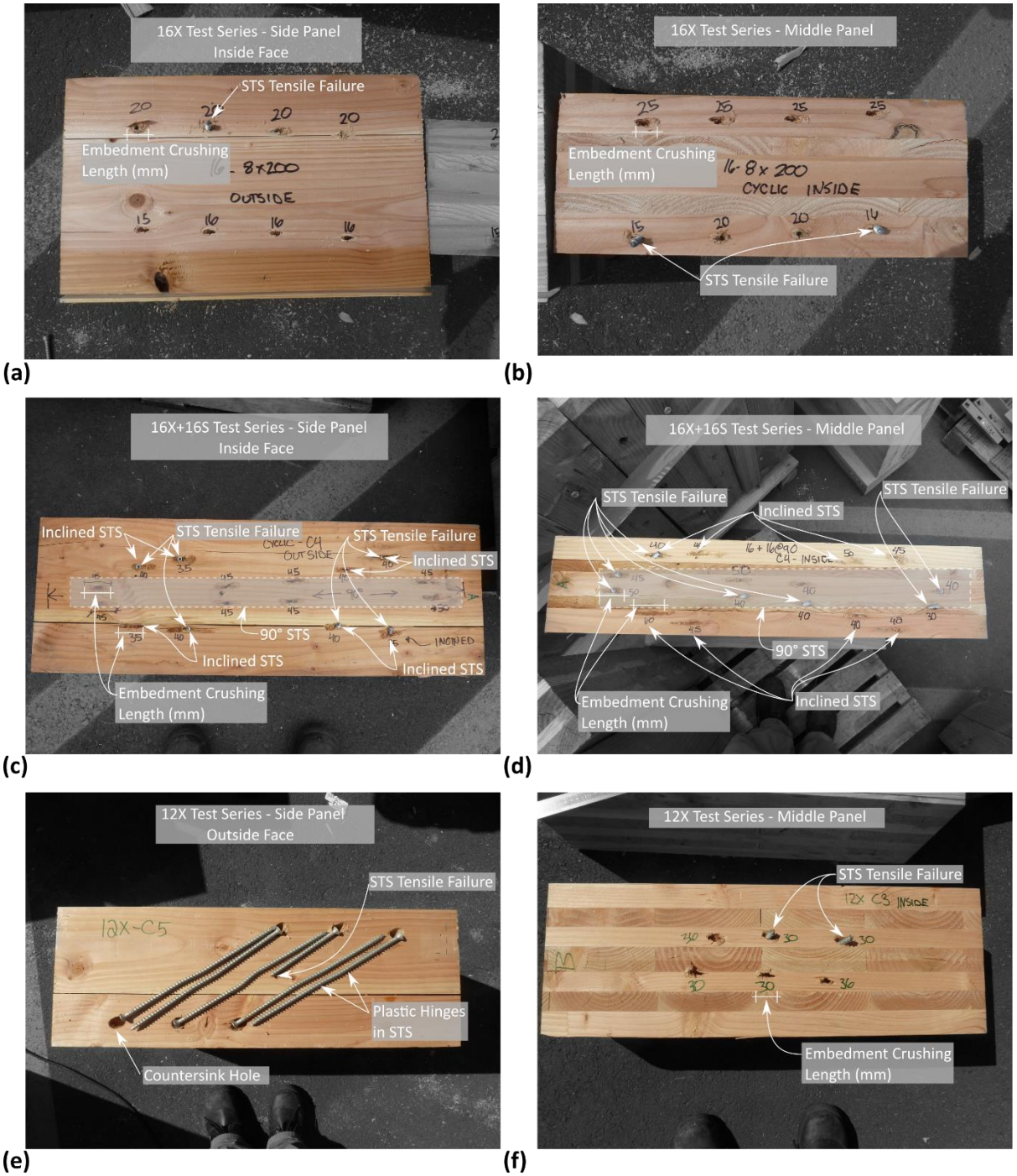


*Figure 4-15: After test specimen photos: (a) 16X side panel (b) 16X middle panel (c) 16X+16S side panel (d) 16X+16S middle panel (e) 12X side panel (f) 12X middle panel*

### 4.4.3 Strength

As shown in Table 4-8, inclined STS joints had significantly higher maximum strength, $F_{max}$, than 90° STS joints given the specific parameters tested. On a per screw basis and neglecting a possible group effect, $F_{max}$ was approximately five times higher in 8ST test series than 2S test series when considered at the 15mm slip limit. This agrees with past reported research which indicated inclined STS can provide increased strength (Hossain et al., 2018b; Loss et al., 2018; Sullivan et al., 2018; Tomasi et al., 2010). $F_{max}$ in test series 16X was less than 16X-400 due to shorter embedment length. The load-carrying capacity was also less than the superposition of 8ST and 8SC, which indicated that assuming the friction term balanced and was zero in a cross-wise configuration as per Bejtka & Blaß (2002) was appropriate in this instance. A progressive increase in $F_{max}$ was observed from series 12X, to 12X+4S, and then to 12X+6S, indicating that the 90° screws contributed to the strength. In all test series except 16X, the CV was notably small (< 8%) and decreased with decreased η and increased screw quantity. The higher CV for $F_y$ (around 9%) when compared to the CV for $F_{max}$ (around 5%) can be attributed to the sensitivity of the method to analyse the load-slip curve (Flatscher, 2017). That the CV decreased with decreased η and increased screw quantity indicated the effectiveness of using mixed angle screw combinations, and the importance of testing large multi-fastener joints (up to 16 screws per joint and 32 screws per specimen) to represent actual applications. On average, the ratio of cyclic $F_{max}$ to monotonic $F_{max}$ was 1.04 which was contrary to previous findings by Hossain et al. (2018).

### 4.4.4 Displacement Capacity and Ductility

The displacement capacity, synonymous to the ultimate displacement or 15mm limit for monotonic specimens which did not reach maximum load, and ductility increased significantly with a maximum η ratio of 2:1. Firstly, the displacement capacity of series 16X+16S with η=1:1 was three times larger than for series 16X, which confirmed previous findings for in-plane mixed angle STS CLT joints (Hossain et al., 2018; Sullivan et al., 2018). It was found that a minimum number of 90° STS, herein half the number of inclined STS, were required to provide significant influence on joint behaviour. Cyclic ductility was unchanged between series 12X and 12X+4S which indicated that the η ratio of 3:1 was too large and the influence of 90° screws was not significant. However, the series with η of 2:1 (12X+6S) and 1:1 (16X+16S) had high displacement capacity greater than 20mm and cyclic ductility greater than 14, respectively, demonstrating that 90° screws significantly contributed for such ratios. This indicated that a maximum η of 2:1 could be recommended to achieve enhanced joint behaviour. It should be noted that if gradual screw withdrawal of inclined STS was the governing failure mode, moderate ductility was achieved, in agreement with past studies (Hossain et al., 2016; Loss et al., 2018). Though, with an η of 1:0 the cyclic displacement capacity is limited and less than 12mm. STS

slenderness, $\lambda = L/d_c$, impacted displacement capacity and ductility. When comparing series 12X to 16X, cyclic displacement capacity and ductility increased by a factor of 1.5 with increased λ to 47 from 40 even with larger diameter and fewer STS in the 12X series. Past work by Loss et al. (2018) and Sullivan et al. (2018) also had increased ductility with increased λ. STS slenderness as an influencing parameter on STS joint performance will be discussed further and the results indicated that slenderness may be a more representative parameter irrespective of STS diameter which had been reported in past work (Sullivan et al., 2018). In all test series, the displacement capacity and ductility were lower under cyclic loading compared to monotonic loading. Displacement capacity and ductility were 35% and 15% lower on average respectively. The yield displacement was also 20% smaller on average under cyclic loading, but was minimally affected by changing η.

### 4.4.5 Stiffness

The stiffness of inclined STS in ST, SC and X configuration test series was significantly higher than the 90° screws as expected. For series 2S, upon evaluating the elastic portion of the curve in a similar manner to Gavric et al. (2015), the derived elastic stiffness was 1.8kN/mm/screw and almost 5 times less than series 16X. While this comparison neglects a possible group effect, it agrees with past reported research which indicated inclined STS provide increased stiffness (Hossain et al., 2018b; Loss et al., 2018; Sullivan et al., 2018; Tomasi et al., 2010). It should be noted that as per EN 12512 (2005a), the stiffness for 2S was only 0.4kN/mm/screw, but this was significantly influenced by the shape of the load-slip curve and deemed not representative for comparative purposes in this instance. The joint stiffness also increased with decreasing η which indicated that 90° screws impact stiffness. For instance, the progressive increase in cyclic stiffness from series 12X, to 12X+4S, and then to 12X+6S was 110, 126, and 151 kN/mm. Increased STS slenderness, λ, appeared to influence and decrease joint stiffness. The stiffness of series 16X (λ=40) was 1.2 times higher than that of series 16X-400 (λ=80) which is contrary to the values calculated by the product approval (ETA-12/0114, 2017), as the STS embedment length in 16X was approximately half that in 16X-400. In the product approval (ETA-12/0114, 2017) stiffness increases linearly with embedment length. A comparison between series 8ST and 8SC with 16X indicated that there was a contribution from friction to stiffness for shear-tension STS in agreement with past reported work (Loss et al., 2018;Tomasi et al., 2010). The cyclic stiffness was on average 1.3 times higher than the monotonic stiffness, which could in part be due to the faster cyclic loading rate.

### 4.4.6 Energy Dissipation

Energy dissipation was evaluated in terms of equivalent viscous damping, $\xi$, for the first and third cycle of the load-slip curve at each displacement amplitude. The results are presented as the averages of the replicates of the test series. Figure 4-16 reports $\xi$ for each displacement amplitude cycle up to the limit of post-peak load at 80% of $F_{max}$ in a similar manner to Loss et al. (2018). The results indicated that $\xi$ was directly linked to the associated failure mode. In all test series, the initial increase in $\xi$ at early displacement cycles is indicative of ST and SC screws loaded in withdrawal which have low initial energy dissipation capacity due to high elastic stiffness (Hossain et al., 2016). Steel tensile failure in 16X-400 resulted in the lowest $\xi$ as expected. For the remaining test series, $\xi$ reached its peak in the two or four times yield displacement amplitude cycles. The increased $\xi$ was due to gradual withdrawal of STS, timber embedment deformation, and STS bending yielding deformation. With decreased η, at large displacement $\xi$ gradually decreased and the difference between $\xi_{1st}$ and $\xi_{3rd}$ was more significant which is typical in dowelled joints or STS installed at 90° with pinched hysteresis loops (Gavric et al., 2015).

Previous testing by Loss et al. (2018) reported increased $\xi$ to 8% with increased λ from 23 to 30 and noted this positive correlation. In this instance, the average $\xi$ at maximum load was 10% with λ of 40 and 47, which is 1.25 times higher than $\xi$ reported by Loss et al. (2018) with lower λ. The $\xi$ was found to be similar to values reported by Tomasi et al. (2006) with a mixed angle STS installation joint and λ of 41. While increased λ may increase energy dissipation capacity, λ of inclined screws should be limited to avoid STS tensile failure.

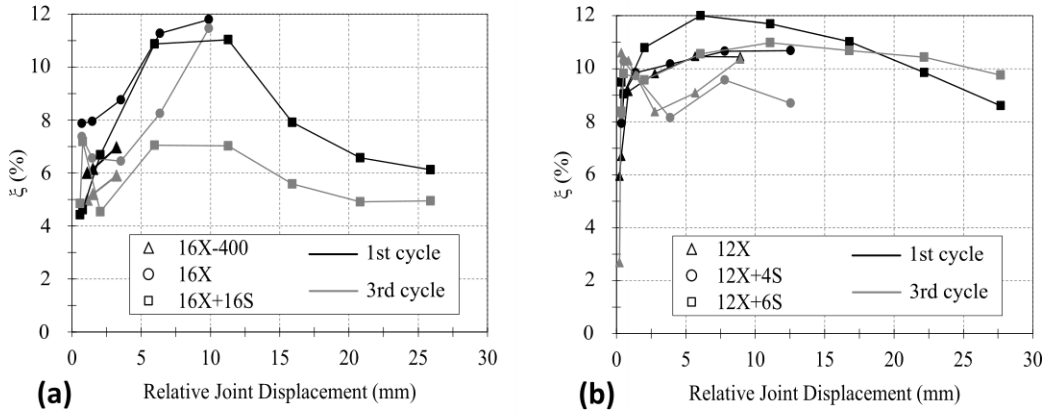


*Figure 4-16: Equivalent viscous damping of each test series: (a) CLT5 specimens (b) CLT7 specimens*

## 4.5 ANALYTICAL MODELS AND COMPARISONS WITH EXPERIMENTAL RESULTS

### 4.5.1 Experimental Considerations for Models

For all inclined STS test series, the angle $\varphi_{/\!/}=\varphi$ between the screw axis and the grain of the longitudinal CLT layer is related to the screw installation angles $\alpha = 30°$ and $\varepsilon = 15°$, calculated by Equation (4-12).

$$\cos\varphi = \cos\varepsilon \sin\alpha \tag{4-12}$$

The angle between the screw axis and the grain of the longitudinal and cross CLT layer is $\varphi_{/\!/}$ and $\varphi_{\perp}$ respectively. The angle between the embedment force and the grain of the longitudinal and cross layer is $\theta_{\|}$ and $\theta_{\perp}$ respectively. As such, for design purpose the middle panel design angles for the longitudinal and cross layer were $\varphi_{/\!/}=\varphi = 61°$, $\varphi_{\perp} = 33°$, and $\theta_{\|} = 29°$ for all test series, as shown in Figure 4-17. For the side panel, $\varphi_{\perp} = 75°$ and all other design angles were as per the middle panel. Table 4-9 provides a summary of key STS properties required for analytical models.

*Table 4-9: Test series STS details*

| Series | STS Name | d<br>mm | L<br>mm | $d_c$<br>mm | $l_t$ (min)<br>mm |
|---|---|---|---|---|---|
| 16X-400 | $\phi$8x400 | 8 | 400 | 5 | 375 |
| 2S, 16X+16S | $\phi$8x350 | 8 | 350 | 5 | 325 |
| 8ST, 8SC, 16X, 16X+16S | $\phi$8x200 | 8 | 200 | 5 | 185 |
| 12X+4S, 12X+6S | $\phi$12x550 | 12 | 550 | 7.4 | 525 |
| 12X, 12X+4S, 12X+6S | $\phi$12x350 | 12 | 350 | 7.4 | 325 |

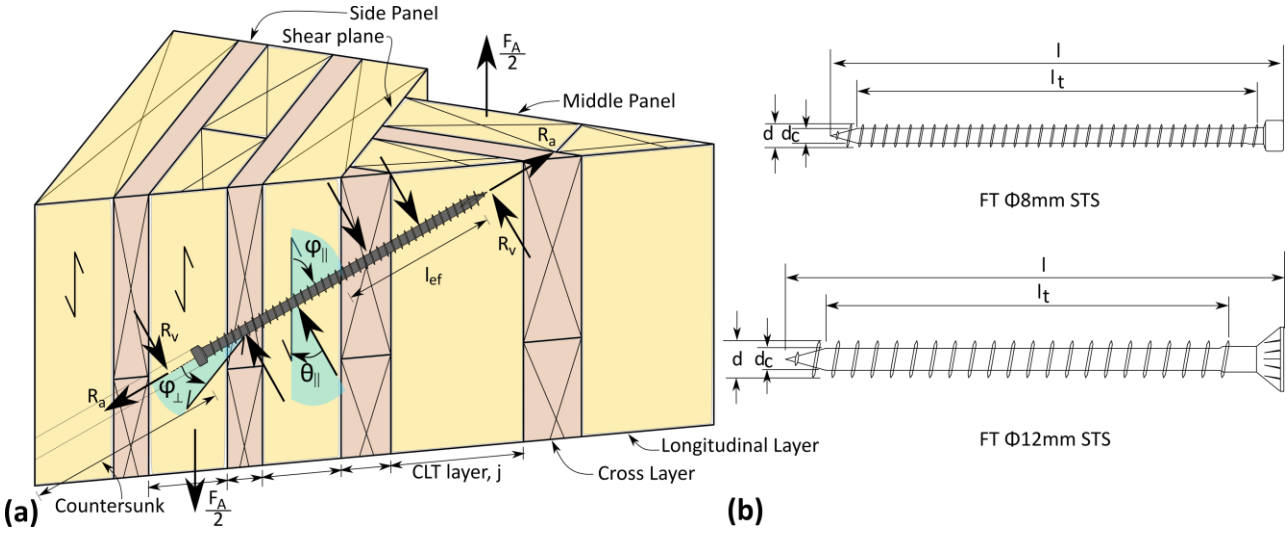


*Figure 4-17: (a) Isometric of shear-tension ϕ8mm STS in CLT5 (b) key parameters for STS*

### 4.5.2 Strength Model

The analytical strength model developed by Bejtka & Blaß (2002) with extensions by Jockwer et al. (2014) was adapted herein for orthogonal joint design. As STS joint design is not covered by many design standards including New Zealand Timber Structures Standard NZS3603 (1993), design guidance within the SPAX ETA (2017) was used to determine the withdrawal strength, fastener bending yield moment, and embedment strength component properties for the analytical model because there are differences between different STS ETAs (Dietsch & Brandner, 2015). While current design codes guide designers to a ductile joint by introducing certain factors such as an effective number of fasteners, $n_{ef}$, Dorn et al. (2013) reported this can lead to conservative strength predictions for ductile joints. This makes it hard to quantify the overstrength due to conservatism in analytical models, $\gamma_{an}$, and was therefore not considered herein. Accordingly, the withdrawal strength parameter, $f_1$, is 12.0 and 11.0MPa for the $\phi$8mm and $\phi$12mm STS respectively, and the bending yield moment, $M_y$, and embedment strength, $f_{h,\varphi}$, are calculated by Equation (4-13) and Equation (4-14).

$$M_y = 0.15(600)d^{2.6} \tag{4-13}$$

where d is the outer thread diameter. The embedment strength for inclined screws, $f_{h,\varphi}$, is determined as:

$$f_{h,\varphi} = \frac{0.082\rho_k(1-0.01d)}{(2.5\ cos^2\varphi + sin^2\varphi)(k_{90}sin^2\theta_{\parallel} + cos^2\theta_{\parallel})} \tag{4-14}$$

where $\rho_k$ is the characteristic CLT density, $k_{90} = 1.35\text{-}0.015d$, and $\varphi = \varphi_{//}$ and $\theta_{//}$ as defined above as the angles to longitudinal CLT layer grain direction. For $90^o$ STS in all test series, the embedment strength was $f_{h,S}=20d^{-0.5}$ in the middle panel as the STS was installed parallel to the plane of CLT. With reference to Figure 4-18, for the orthogonal joint specimen, the side and middle panel, *i = sp or mp*, strengths are determined separately and the minimum governs the specimen capacity as per Equation (4-15).

$$F_{A,specimen} = 2 * min\begin{cases} F_{A,SIDE\ PANEL} \\ F_{A,MIDDLE\ PANEL} \end{cases} \tag{4-15}$$

where the factor 2 accounts for both sides of the symmetrical specimen to determine the overall specimen capacity. In all instances, the side panel strength governed the capacity due to the lower rolling shear strength of the 45mm layer required for Equation (4-21), which will be discussed further.

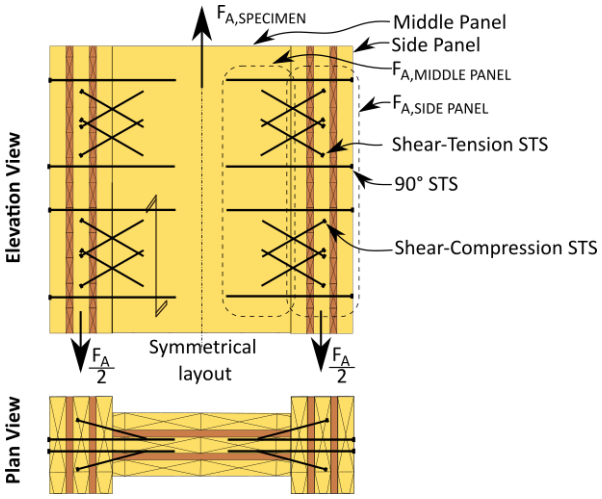


*Figure 4-18: Strength calculation illustrated by 16X+16S specimen*

For a 90° STS acting in dowel action as in the 2S series, the Johansen equations of Eurocode 5 (2014) with consideration for the rope effect are considered as:

$$F_{A,S,i} = R_{v,i} + \min\begin{cases} R_{a,i}/4 \\ R_{v,i} \end{cases} \tag{4-16}$$

where $R_{v,i}$ is shear strength in dowel action and $R_{a,i}$ is the axial strength determined in Equation (4-18). The slenderness of the STS ensures plastic hinges will develop such that $R_{v,i}$ is:

$$R_{v,i} = \sqrt{\frac{2\chi}{1+\chi}}\sqrt{2M_y d_{ef} f_{h,\varphi,i}} \tag{4-17}$$

with $M_y$ as defined before, $d_{ef} = 1.1d_c$ where $d_c$ is the screw core diameter and $f_{h,\varphi,i}$ as defined before. $\chi = f_{h,\varphi,mp}/f_{h,\varphi,sp}$, is the ratio between embedment strengths on the screw middle panel side and screw side panel side. In the instance of ST and SC STS $\chi = 1$. The determination of $R_{a,i}$ was as per ETA (2017) as the minimum of either the withdrawal strength or the STS tensile strength:

$$R_{a,i} = min\left(\frac{f_1 d l_{ef}}{1.2cos^2\varphi + sin^2\varphi}\left(\frac{\rho_k}{350}\right)^{0.8};\ 17{,}000\ (\phi 8mm), 38{,}000\ (\phi 12mm)\right) \tag{4-18}$$

where $f_1$, $d$, and $\varphi = \varphi_{//}$ are as defined before, and $l_{ef}$ is the screw thread length (mm) in each CLT panel side, which was half the screw thread length ($l_t/2$). For each side and middle panel the withdrawal strength determination, $R_{a,i}$, is the sum of each component determined for each CLT layer, $j$, penetrated considering both $l_{ef}$, $\varphi_{\parallel}$ and $\varphi_{\perp}$ with reference to Figure 4-17. For the shear-tension (ST) STS, the strength is determined as:

$$F_{A,ST,i} = R_{a,i}\,(\psi\ sin\varphi + cos\,\varphi) + R_{v,i}(sin\,\varphi - \psi\ cos\,\varphi) \tag{4-19}$$

where $R_{a,i}$ and $R_{v,i}$ are the screw axial and shear resistance respectively, $\varphi = \varphi_{//}$ and $\psi$ is the coefficient of friction, taken as 0.25 for wood-wood surfaces as per Eurocode 5 (2014). For a shear-compression (SC) STS, the strength is determined similar to a ST STS without the contribution due to friction as:

$$F_{A,SC,i} = R^*_{a,i} cos\ \varphi + R^*_{v,i}\ sin\varphi \tag{4-20}$$

where $R_{a,i}^*$ was calculated similar to $R_{a,i}$ but included the consideration for "edge effect". Jockwer et al. (2014) observed that an area from the surface of the timber member was affected by splitting / compression failures such that a zero stress zone exists up until a certain length, $x_1$. In this way $l_{ef}$ is reduced by $x_1$, which is defined as the length from the CLT face with zero embedment and withdrawal capacity and determined as:

$$x_1 = f_{h,\varphi} d_{ef} / 2\, tan\, \varphi\, f_{rs} \tag{4-21}$$

where $f_{rs}$ is the rolling shear strength of the applicable layer. In this instance, $f_{rs}$ is 2.2, 1.1 or 0.9MPa considering the 20, 35, and 45mm layers of the CLT specimens respectively as previously reported by Li et al. (2019). $R_{v,i}^*$ is determined as per Jockwer et al. (2014) as:

$$R^*_{v,i} = \sqrt{2M_y d_{ef} f_{h,\varphi} + \left(f_{h,\varphi} d_{ef} x_1\right)^2} - f_{h,\varphi} d_{ef} x_1 \tag{4-22}$$

When ST and SC STS are used together in a X configuration, the strength of a cross-pattern (X) pair of screws is defined similar to Tomasi et al. (2010) as:

$$F_{A,X,i} = (R_{a,i} cos\, \varphi + R_{v,i} sin\, \varphi) + (R^*_{a,i} cos\, \varphi + R^*_{v,i}\, sin\, \varphi) \tag{4-23}$$

where $\varphi = \varphi_{\|}$ and the contribution from friction from the ST and SC screw are opposite and balance each other. For a X + S configuration, in a similar manner to Tomasi et al. (2006), by superposition the strength is determined as:

$$F_{A,X+S,i} = n_x F_{A,X,i} + n_s F_{A,S,i} \tag{4-24}$$

where $F_{A,X,i}$ and $F_{A,S,i}$ are defined above and $n_x$ and $n_s$ are the number of X pair and S STS respectively.

### 4.5.3 Stiffness Model

The analytical stiffness model developed by Tomasi et al. (2010) and shown in Equation (4-25) with work by Kevarinmaki (2002) was adapted herein for orthogonal joint design.

$$K_{STS} = k_{\perp} sin^2\varphi + k_{\parallel} cos^2\varphi \tag{4-25}$$

where $K_{STS} = K_{A,S}$, $K_{A,ST}$, *or* $K_{A,SC}$ for a 90°, ST, or SC STS respectively, $\varphi = \varphi_{\parallel}$ as defined before and $k_{\perp}$ is the lateral stiffness component and provided in Eurocode 5 (2014) as:

$$k_{\perp} = \frac{\rho_m^{1.5} d_{ef}}{23} \tag{4-26}$$

where $\rho_m$ is the mean characteristic density and $d_{ef}$ is defined previously. The axial stiffness component, $k_{\parallel}$, is determined following the model proposed by Kevarinmaki (2002) which considered the axial stiffness of a screw as a function of the thread stiffness on the middle and side panel side of the screw, similar to a system of two springs in series as:

$$k_{\parallel} = \frac{1}{\frac{1}{k_{ax,sp}} + \frac{1}{k_{ax,mp}}} \tag{4-27}$$

where $k_{ax,sp}$ and $k_{ax,mp}$ are the axial slip modulus of the side and middle panel of the joint respectively, determined by SPAX ETA (2017) as:

$$k_{ax} = 25 d l_{ef} \tag{4-28}$$

where $d$ and $l_{ef}$ are defined previously. For a 90° STS, $\varphi = 90°$ and the axial component in Equation (4-25) reduces to 0. For a SC STS, $l_{ef}$ is reduced by $x_1$ as defined before. The overall specimen stiffness is determined as per Equation (4-29).

$$K_{A,STS} = n_S K_{A,S} + n_{ST} K_{A,ST} + n_{SC} K_{A,SC} \tag{4-29}$$

where $n_S$, $n_{ST}$, and $n_{SC}$ are the number of S, ST, and SC STS respectively. $k_{\perp}$ and $k_{\parallel}$ can also be determined from experimental tests as suggested by Blaß et al. (2006) instead of empirical component equations. In this way, the overall specimen stiffness could be determined using experimental STS stiffness for $k_{\perp}$ and $k_{\parallel}$ in Equation (4-25) and then in Equation (4-29) to determine $K_{A/EXP}$.

### 4.5.4 Experimental-Analytical Comparison and Discussion

Table 4-10 summarizes the experimental-analytical comparison results. Using EN 14358 (2016) and assuming a log-normal strength distribution, the 5th and 95th percentile strength, $F_{0.05}$ and $F_{0.95}$, were determined from the cyclic test $F_y$ results. The $F_{0.05}$ was compared to the analytical strength $F_A$, $\gamma_{an}$= $F_{0.05}/F_A$, and the experimental overstrength, $\gamma_{Rd}$, was derived. The average monotonic stiffness, $k$, was compared to both analytical stiffness $K_{A,STS}$, which was derived from empirical component equations and $K_{A/EXP.}$, which was derived from experimental component stiffness results.

*Table 4-10: Experimental-analytical comparisons summary*

| Series | $F_{0.05}$ | $F_{0.95}$ | k | $F_A$ | $K_{A,STS}$ | $\gamma_{an}$ | $\gamma_{0.95}$ | $\gamma_{Rd}$ | $k/K_{A,STS}$ | $k/K_{A/Exp.}$ |
|---|---|---|---|---|---|---|---|---|---|---|
| | kN | kN | kN/mm | kN | kN/mm | - | - | - | - | - |
| 2S | - | - | 0.8 | 6 | 5 | - | - | - | 0.2 | 1.0 |
| 8ST | - | - | 45 | 68 | 38 | - | - | - | 1.2 | 2.0 |
| 8SC | - | - | 33 | 27 | 25 | - | - | - | 1.3 | 1.7 |
| 16X-400 | 140 | 222 | 49 | 150 | 104 | 0.9 | 1.6 | - | 0.5 | - |
| 16X | 108 | 164 | 69 | 81 | 57 | 1.3 | 1.5 | 2.0 | 1.2 | 1.7 |
| 16X+16S | 154 | 208 | 92 | 132 | 96 | 1.2 | 1.4 | 1.6 | 1.0 | 1.3 |
| 12X | 139 | 247 | 75 | 140 | 90 | 1.0 | 1.8 | 1.8 | 0.8 | - |
| 12X+4S | 196 | 284 | 103 | 170 | 104 | 1.2 | 1.4 | 1.7 | 1.0 | - |
| 12X+6S | 184 | 250 | 102 | 184 | 110 | 1.0 | 1.4 | 1.4 | 0.9 | - |

The average $\gamma_{an}$, which is the ratio between the experimental 5th percentile strength and analytical strength, was 1.1. This shows that the analytical strength model considered in Section 4.5.2 and used herein was acceptable. The appropriateness of using superposition in Equation (4-24) to determine for example $F_{A,16X+16S}$ was calculated considering the 16X and 2S test series average monotonic results. $F_{2S}$ = 7kN was considered at 6mm joint slip because for series 16X and 16X+16S, peak load occurred at approximately 6mm joint slip. For comparison, $F_{max,16X-M} + 8F_{2S} = 209kN$ which is within 15% of $F_{max,16X+16-M}$. Therefore, superposition of mixed angle screws provided reasonable predictions in this instance, as was reported by Tomasi et al. (2006). However, a strength prediction model which can account for the significantly different stiffness of inclined STS and $90^o$ STS is needed to give more accurate prediction results.

The experimental stiffness, $k$, was compared to analytical stiffness, as per Equation (4-29), considering both empirical component equations to determine $K_{A,STS}$ and experimental component test results for $k_\perp$ and $k_{ax}$ to determine $K_{A/EXP.}$. In general, the analytical stiffness model was inadequate. Although the $k/K_{A,STS}$ ratio showed that the analytical model appeared to be working well, as noted by Loss et al. (2018), the model is very sensitive to the components $k_\perp$ and $k_{ax}$. In determining $K_{A,STS}$, $k_\perp$ was

determined as per Eurocode 5 (2014) which had been derived for a traditional wood screw and does not consider the screw type, insertion angle and length of the STS (Loss et al., 2018). Reported results herein of $k_{2S}/K_{A,STS}$ = 0.2, which were similar to past reported lateral stiffness (Loss et al., 2018; Sullivan et al., 2018), indicated that Equation (4-26) from Eurocode 5 (2014) is not appropriate for STS. As $k_{\perp}$ contributed to both inclined STS and 90° STS this affected the analytical stiffness model. Further, it has been reported that the axial slip modulus, $k_{ax}$, equations used can provide significant differences up to 500% depending on the screw diameter and insertion length (Ringhofer, 2017). For example, the Ø12x350mm screws could have $k_{ax}$ = 48.9kN/mm or 9.8kN/mm if Equation (4-28) or if the equation used in Loss et al. (2018) of $k_{ax} = 780 d^{0.2} l_{ef}^{0.4}$ was used. As recommended by Blaß et al. (2006), as a second comparison, $K_{A/Exp.}$ was determined using experimental STS stiffness for $k_{\perp}$ and $k_{ax}$ and it was compared to experimental results as $k/K_{A/Exp.}$ in Table 4-10. To determine $K_{A/Exp.}$, $k_{\perp}$ was 1.8kN/mm as reported in Section 3.5 and $k_{ax}$ was 9.5 kN/mm as per Figure 4-19 to determine $k_{//}$ as per Equation (4-27). Figure 4-19 shows the reported experimental $k_{ax}$ results of 187 STS withdrawal tests with Ø8mm and Ø12mm STS (presented in Section 4.2) at various angles to the grain and penetration lengths in comparison to Equation (4-28). The average $k/K_{A/Exp.}$ ratio of 1.7 indicated that the analytical stiffness model of Tomasi et al. (2010) underestimated the observed experimental stiffness. That Tomasi et al. (2010) observed similar findings with $k/K_{A,STS}$ ≈ up to 2.0 when $k_{//}$ was determined as per Kevarinmaki (2002) suggests that further research is required to capture the joint stiffness of STS installed at varying inclinations to grain.

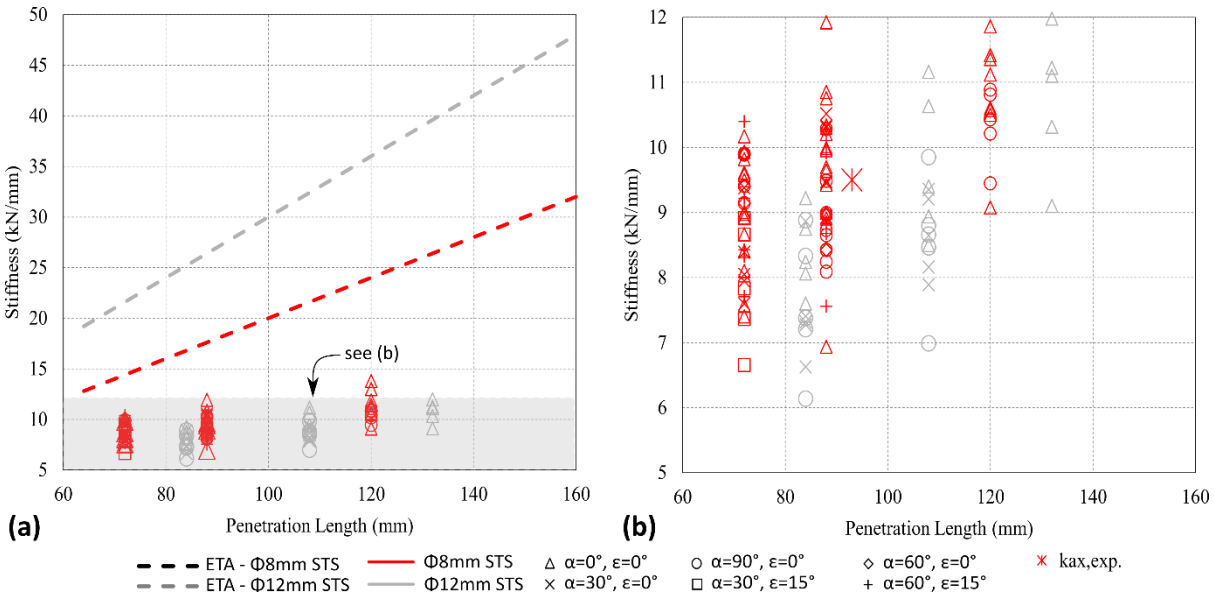


*Figure 4-19: Experimental STS withdrawal stiffness with comparison to empirical equation (see Section 4.2)*

### 4.5.5 Overstrength Discussion

The overstrength of each test series was calculated as per Equation (4-11) assuming $\gamma_m$ = 1.0 as per Eurocode 8 (2005b). As per Table 4-10, the average cyclic experimental $\gamma_{Rd}$ was 1.7 excluding the 16X-400 test series as brittle STS tensile failure occurred. This $\gamma_{Rd}$ was comparable to past experimental overstrength factors for timber joints (Bruhl et al., 2014; Dong et al., 2020; Gavric et al., 2015; Ottenhaus et al., 2018; Ottenhaus et al., 2018). The slightly higher experimental overstrength reported herein could in part be due to the relatively small sample size as the average $\gamma_{0.95}$ was 1.5. The average $\gamma_{an}$ was 1.1 which is comparable to $\gamma_{an}$ = 1.18 (Jorissen & Fragiacomo, 2011) and $\gamma_{an}$ = 1.06 (Ottenhaus et al., 2018). In a similar manner to Ottenhaus et al. (2018), the analytical component overstrength component can be determined as per Equation (4-30).

$$\gamma_{an} = \gamma_{an,cyc}\ \gamma_{fh}\ \gamma_{an,f1}\gamma_{an,My} \quad (4\text{-}30)$$

where $\gamma_{an,cyc.}$ is the ratio of cyclic loading to monotonic loading, $\gamma_{an,fh}$ is overstrength from embedment strength formulation, $\gamma_{an,f1}$ is overstrength from the withdrawal strength parameter, and $\gamma_{an,My}$ is the overstrength from the STS yield moment formulation. The average overstrength observed under cyclic loading, $\gamma_{an,cyc.,}$ was 0.98. For instance, the 16X test series $\gamma_{an,f1}$ was 1.5 when considering the experimental withdrawal strength parameter reported in Section 4.2.3. A parametric component study of embedment strength and yield moment determination could also define $\gamma_{an,fh}$ and $\gamma_{an,My}$ respectively. It is important to note that the experimentally determined overstrength of this study should only be used for this particular tested joint. A generic analytical component strength overstrength approach such as that developed by Ottenhaus et al. (2018) was beyond the scope of this study, though it could provide a strong alternative to costly experimental testing.

## 4.6 CONCLUSIONS

This chapter investigated the performance of orthogonal joints between CLT panels with varying mixed angle STS combination ratios, η, for the purpose of developing enhanced joints between CLT wall panels. A total of 59 specimens consisting of two CLT layups and different STS sizes were tested under monotonic and cyclic loading to determine strength, displacement capacity, ductility, stiffness and overstrength and to compare to analytical predictions. In addition, 202 STS withdrawal tests of $\phi$8mm and $\phi$12mm STS in three-, five- and seven-layer New Zealand Radiata Pine and Douglas-Fir CLT were performed. Withdrawal testing results were compared with seven analytical design methods in literature. The key findings are summarized as follows:

- Mixed angle STS joints had increased joint displacement capacity, ductility and energy dissipation when compared to inclined only STS joints.
- Based on the test results, a maximum inclined STS to 90° STS η ratio of 2:1 led to more efficient design than the η ratio of 1:1. The 2:1 η ratio ensured high displacement capacity exceeding 20mm, whereas a larger 3:1 or 1:0 η ratio had displacement capacity limited to 13mm or less respectively. Displacement capacity is critical to develop ductility and hysteretic damping under seismic loading. The 2:1 η ratio ensured rope effect by 90° STS at increased joint displacement was significant enough to maintain post-peak strength above 80% $F_{max}$.
- Strength and stiffness of the mixed angle STS joints were affected by 90° STS. For example, in cyclic series 12X, 12X+4S, and 12X+6S, $F_{max}$ was 195, 247, and 251kN and k was 110, 126 and 151kN/mm respectively. Peak strength in inclined only and mixed angle test series occurred at similar displacements, which can provide one reason for using superposition to estimate the joint strength.
- The average experimental overstrength, $\gamma_{Rd}$, was 1.7 excluding 16X-400 where brittle tensile failure occurred. Existing analytical models were found to be adequate in estimating the joint yield strength using superposition to determine the strength of joints with STS of mixed angles with different stiffness. Further work should verify the suitability of such method.
- Analytical models for estimating joint stiffness were found to be inadequate, especially when considering experimental results for $k_{\perp}$ and $k_{ax}$ from $90^{o}$ STS and single STS withdrawal tests.
- The preferred failure mode for inclined STS joints is gradual screw withdrawal. It is critical to limit the STS thread embedment such that progressive zipper-like tensile failure is avoided. Except for series 16X-400, screw withdrawal failure was the dominant failure mode which led to moderate to high ductility, $\mu \geq 4$, even in the test series with only inclined STS. However, the displacement capacity is limited in joints with inclined only STS and significantly less than joints with η ratio of 0:1, 1:1 and 2:1.
- STS slenderness ratio, λ, was found to influence the joint displacement capacity, ductility, stiffness and energy dissipation capacity. $\phi$12mm STS with higher λ had increased displacement capacity, ductility, and energy dissipation capacity in terms of equivalent viscous damping than $\phi$8mm STS. This highlighted the importance of testing larger diameter STS with various λ in larger 7-ply (275mm thick) CLT panels which may be required in taller timber buildings.
- While the current NZS 3603 (Standards New Zealand, 1993), AS 1720.1 (Standards Australia, 2010) do not specify STS, using their design values for coach screws significantly under-

predicted the withdrawal strength of STS. The proposed DZ NZS AS 1720.1/V6 (2018) analytical equation for screws with $\phi$6.3mm or less and coach screws significantly under-predicted the withdrawal strength.

- The ratio of the average experimental 5$^{th}$ percentile STS withdrawal strength to the ETA analytical model calculation, $\gamma_{an}$, was 1.3 using both experimental and AS 1720 timber densities. Therefore, the SPAX ETA provided reasonably good predictions for the New Zealand Radiata Pine and Douglas-Fir CLT.
- To avoid brittle steel tensile failure of STS, embedment length of the threaded portion should not be greater than 12d under the condition of axial load only.
- The experimental withdrawal strength from CLT narrow face installation generally was higher than all predictions. However, this study only considered one screw installation location without considering all possible locations on the narrow face. It should also be noted that current design standards generally do not recommend parallel to grain screw installation.
- Increased embedment length of unthreaded portion of partially threaded screws, $l_{emb}$, was able to increase the average withdrawal strength by 10%~15% by eliminating timber surface splitting. However, it did not significantly affect the displacement capacity.

While the results presented herein showed mixed angle STS installations could provide enhanced displacement capacity, ductility and energy dissipation, further work is needed to optimize design. Inclined STS without countersinking but with controlled thread embedment length on the STS tip side member could be investigated for similar enhanced performance. A possible group effect for ductile STS joint design should be further investigated. This study provided fundamental information for a better understanding of mixed angle STS joints in orthogonal CLT panels such that in-plane CLT LLRS could transform to core-wall structures with enhanced strength, stiffness and energy dissipation capacity.

## 4.7 REFERENCES

AWC. (2015). *AWC, National Design Specifications for Wood Construction(ANSI/AWC NDS-2015)*. American Wood Council.

Bejtka, I., & Blaß, H. J. (2002). Joints with inclined screws. *CIB-W18 Timber Structures, Meeting 35*, *35-7–4*, 141.

Below, K., & Sarti, F. (2016). Cathedral hill 2: Challenges in the design of a tall all-timber building. *WCTE 2016 - World Conference on Timber Engineering*.

Blaß, H. J., Bejtka, I., & Uibel, T. (2006). *Tragfähigkeit von Verbindungen mit selbstbohrenden Holzschrauben mit Vollgewinde(In German)* (number 4). Karlsruher Berichte zum Ingenieurholzbau Universitätsverlag Karlsruhe.

Blaß, H. J., & Uibel, T. (2007). *Tragfähigkeit von stiftförmigen Verbindungsmitteln in Brettsperrholz (In German)* (number 8). Karlsruher Berichte zum Ingenieurholzbau Universitätsverlag Karlsruhe.

Brandner, R., Flatscher, G., Ringhofer, A., Schickhofer, G., & Thiel, A. (2016). Cross laminated timber (CLT): overview and development. *European Journal of Wood and Wood Products*, *74*(3), 331–351.

Bruhl, F., Schanzlin, J., & Kuhlmann, U. (2014). Ductility in Timber Structures: Investigations on Over-Strength Factors. In *Materials and Joints in Timber Structures: Recent Developments of Technology*. Springer. https://doi.org/10.1007/978-94-007-7811-5

CEN. (1991). *EN 26891 - Joints made with mechanical fasteners. General principles for the determination of strength and deformation characteristics*. European Committee for Standardization (CEN).

CEN. (2005a). *EN12512: Timber structures: test methods : cyclic testing of joints made with mechanical fasteners : [including amendment A1:2005]* (Issue Book, Whole). European Committee for Standardization.

CEN. (2005b). *Eurocode 8: Design of structures for earthquake resistance* (Issue Book, Whole). European Committee for Standardization (CEN).

CEN. (2014). Eurocode 5: Design of timber structures-Part 1-1: General-Common rules and rules for buildings. In *EN1995-1-1:2004-11 + AC2006-06 + A1:2008-06 + A2:2014-05 Eurocode 5*. European Committee for Standardization.

CEN. (2016). *EN 14358:2016 - Timber structures - Calculation and verification of characteristic values*.

European Committee for Standardization (CEN).

CSA 086. (2019). *Engineering design in wood*. Canadian Standards Association, Mississauga, ON.

Dietsch, P., & Brandner, R. (2015). Self-tapping screws and threaded rods as reinforcement for structural timber elements-A state-of-the-art report. *Construction and Building Materials*, *97*, 78–89. https://doi.org/10.1016/j.conbuildmat.2015.04.028

Dong, W., Li, M., Ottenhaus, L. M., & Lim, H. (2020). Ductility and overstrength of nailed CLT hold-down connections. *Engineering Structures*, *215*(February), 110667. https://doi.org/10.1016/j.engstruct.2020.110667

Dorn, M., de Borst, K., & Eberhardsteiner, J. (2013). Experiments on dowel-type timber connections. *Engineering Structures*, *47*, 67–80. https://doi.org/10.1016/j.engstruct.2012.09.010

EN 1382. (2016). *Timber structures - test methods - withdrawal capacity of timber fasteners*. European Committee for Standardization (CEN).

ETA-11/0030. (2019). *Rotho Blass Self-tapping screws and threaded rods*. ETA-Danmark A/S.

ETA-11/0190. (2018). *Würth self-tapping screws*. DIBt-Berlin.

ETA-12/0114. (2017). *SPAX self-tapping screws- screws for use in timber constructions* (Issue 305). ETA-Danmark A/S.

Flatscher, G. (2017). *Evaluation and approximation of timber connection properties for displacement-based analysis of CLT wall systems*.

Gavric, I., Fragiacomo, M., & Ceccotti, A. (2015). Cyclic behavior of typical screwed connections for cross-laminated (CLT) structures. *European Journal of Wood and Wood Products*, *73*(2), 179–191.

Hossain, A., Danzig, I., & Tannert, T. (2016). Cross-laminated timber shear connections with double-angled self-tapping screw assemblies. *Journal of Structural Engineering*, *142*(11).

Hossain, A., Popovski, M., & Tannert, T. (2018). Cross-laminated timber connections assembled with a combination of screws in withdrawal and screws in shear. *Engineering Structures*, *168*, 1–11. https://doi.org/10.1016/j.engstruct.2018.04.052

Jockwer, R., Steiger, R., & Frangi, A. (2014). Design model for inclined screws under varying load to grain angles. *International Network on Timber Engineering Research (INTER) - Meeting 47*, 141–154.

Jorissen, A., & Fragiacomo, M. (2011). General notes on ductility in timber structures. *Engineering*

*Structures*, *33*(11), 2987–2997. https://doi.org/10.1016/j.engstruct.2011.07.024

Kevarinmaki, A. (2002). Joints with Inclined Screws. *CIB-W18 Timber Structures, Meeting 35*, *35-7–3*.

Li, M., Dong, W., & Lim, H. (2019). Influence of lamination aspect ratios and test methods on rolling shear strength evaluation of Cross-Laminated Timber. *Journal of Materials in Civil Engineering*, *31*(12), 1–11. https://doi.org/10.1061/(ASCE)MT.1943-5533.0002977

Loss, C., Hossain, A., & Tannert, T. (2018). Simple cross-laminated timber shear connections with spatially arranged screws. *Engineering Structures*, *173*, 340–356. https://doi.org/10.1016/j.engstruct.2018.07.004

Ottenhaus, L.-M., Li, M., & Smith, T. (2018). Structural performance of large-scale dowelled CLT connections under monotonic and cyclic loading. *Engineering Structures*, *176*(Lvl), 41–48. https://doi.org/10.1016/j.engstruct.2018.09.002

Ottenhaus, L. M., Li, M., Smith, T., & Quenneville, P. (2018). Overstrength of dowelled CLT connections under monotonic and cyclic loading. *Bulletin of Earthquake Engineering*, 1–21. https://doi.org/10.1007/s10518-017-0221-8

Ringhofer, A, Brandner, R., & Schickhofer, G. (2015a). Withdrawal resistance of self-tapping screws in unidirectional and orthogonal layered timber products. *Materials and Structures*, *48*(5), 1435–1447. https://doi.org/10.1617/s11527-013-0244-9

Ringhofer, A, Brandner, R., & Schickhofer, G. (2015b). A universal approach for withdrawal properties of self-tapping screws in solid timber and laminated timber products. *International Network on Timber Engineering Research (INTER)*, *48-07–01*, 79–96.

Ringhofer, Andreas. (2017). Axially Loaded Self-Tapping Screws in Solid Timber and Laminated Timber Products. In *Graz University of Technology*. Timber Engineering & Technology, TET 5, Verlag der Technischen Universität Graz. https://doi.org/10.3217/978-3-85125-555-3

Ringhofer, Andreas, Brandner, R., & Blaß, H. J. (2018). Cross laminated timber (CLT): Design approaches for dowel-type fasteners and connections. *Engineering Structures*. https://doi.org/10.1016/j.engstruct.2018.05.032

Ringhofer, Andreas, & Schickhofer, G. (2019). 52-07-1 - Product Characteristics of Self-Tapping Timber Screws. *International Network on Timber Engineering Research (INTER)*.

Smith, I., Asiz, A., Snow, M., & Chui, Y. H. (2006). Possible Canadian / ISO Approach to Deriving Design Values From Test Data. *Proceedings of the CIB W18 Meeting Thirty-Nine*.

Standards Australia. (2010). *AS 1720.1-2010 Timber Structures Part 1 Design Methods.pdf*. Standards Australia.

Standards New Zealand. (1992). *NZS 3404: Steel Structures Standard*. Standards New Zealand.

Standards New Zealand. (1993). *NZS 3603: Timber structures standard*. Standards New Zealand.

Sullivan, K., Miller, T. H., & Gupta, R. (2018). Behavior of cross-laminated timber diaphragm connections with self-tapping screws. *Engineering Structures*, *168*, 505–524.

Tomasi, R, Piazza, M., Angeli, A., & Mores, M. (2006). A new ductile approach design of joints assembled with screw connectors. *WCTE 2006*.

Tomasi, Roberto, Crosatti, A., & Piazza, M. (2010). Theoretical and experimental analysis of timber-to-timber joints connected with inclined screws. *Construction and Building Materials*, *24*(9), 1560–1571. https://doi.org/https://doi.org/10.1016/j.conbuildmat.2010.03.007

Uibel, T., & Blaß, H. J. (2007). Edge joints with dowel type fasteners in cross laminated timber. *Proceedings of CIB W18 Meeting Forty*, *40-7–2*.

Westermayr, M., & van de Kuilen, J.-W. G. (2019). 57-07-2- Withdrawal strength of screws and screw groups in European beech (Fagus s.) parallel to the grain. *6th International Network on Timber Engineering Research (INTER)*.

# 5 Structural performance of CLT shear connections with castellations and angle brackets

*The work presented herein is based on the published article cited below:*

*J.R. Brown, M. Li, F. Sarti, Structural performance of CLT shear connection with castellations and angle brackets, Eng. Struct. (2021) 112346. https://doi.org/10.1016/j.engstruct.2021.112346.*

---

*Key Findings / Outputs:*

- Twenty-nine cross-laminated timber (CLT) castellated joints and six angle bracket joints were tested with large 5-ply (175mm thick) and 7-ply (275mm thick) CLT panels.
- Castellated joints shear strength and stiffness were 2.5 and 7 times greater than angle bracket joints.
- Castellated joints did not experience sudden load drops once longitudinal or rolling shear failure occurred mainly due to the cross-layer reinforcement. This effect was more pronounced with thicker seven-layer CLT specimens than five-layer CLT specimens.
- A stiffness based analytical component model was developed to predict castellated joint strength with reasonable accuracy.
- The commercial angle brackets tested herein had significantly lower experimental stiffness, more than 2.5 times lower than the Eurocode 5 prediction equation. The steel angle bracket underwent significant in-plane and out-of-plane deformation. Further, peak strength was limited due to timber failure and not a more favourable nail yielding and timber embedment crushing mechanism. The increased angle bracket size, nail geometry, and CLT size meant that loading eccentricities were increased and the nail primarily penetrated only the outer layer of the CLT specimen. Reduced nail patterns and penetrating the nail through more than one CLT layer could help avoid unfavourable timber failure mechanisms.

## 5.1 INTRODUCTION

The primary objective of this study is to assess shear strength and stiffness of mortise and tenon castellated CLT joints in comparison with the connections using commercial angle brackets. The secondary objective is to develop an analytical method to predict the load-carrying capacity of CLT castellated joints such that these connections can provide one efficient shear transfer mechanism for CLT structures.

Carpentry joints were historically employed based on tradition, skilled craftsmen, and proven good performance based on experience (Siem, 2017). Taller CLT buildings will have increased load and stiffness demands and therefore will require connections with enhanced performance (Buchanan, 2016). The CNC machining technology has positioned CLT carpentry joints as a viable connection type which could be capacity design protected and implemented even in seismic regions. Figure 5-1 shows different building locations where either castellated or angle bracket joints could be implemented.

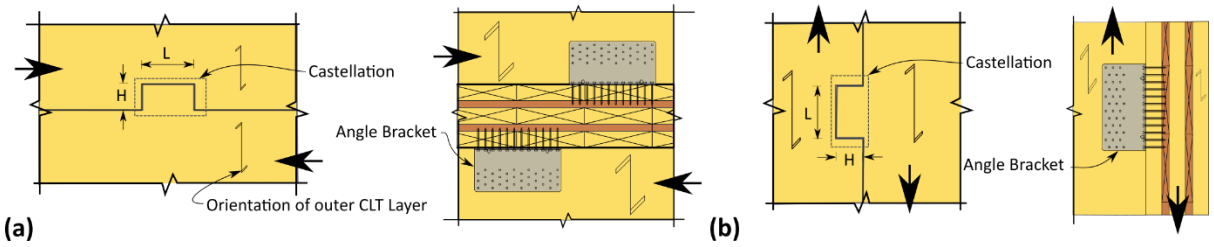


*Figure 5-1: Castellated and angle bracket joint configuration for (a) perpendicular to the outer CLT face loading, and (b) parallel to the outer CLT face loading.*

The experimental test programme is presented in Section 5.2. Section 5.3 evaluates the castellated and angle bracket joint strength and stiffness performance and discusses their associated failure modes. In Section 5.4, the proposed stiffness based analytical model is presented and compared to the castellated joint experimental results.

## 5.2 EXPERIMENTAL PROGRAMME

### 5.2.1 Specimen Description

The test programmes for the castellated joints and angle bracket joints are shown in Table 5-1 and Table 5-2 respectively. A total of 29 castellated joints and 6 angle bracket joints were tested in 15 series with different configurations. Two different CLT layups (5-ply 175mm thick and 7-ply 275mm thick) were used, herein simply referred to as CLT5 and CLT7, respectively. The Douglas-Fir lamella were graded SG8 with average Modulus of Elasticity of 8 GPa according to NZS3603 (Standards New Zealand, 1993). The CLT panels were not edge glued. After testing, a small piece was cut from each specimen and oven dried to determine density and moisture content. The average moisture content

was 11%, and the average density was 462 and 457 kg/m$^3$ for the CLT5 and CLT7 specimens respectively.

In the test series labelling with the format of XXX-YY-ZZZZ-V, XXX refers to the CLT type (CLT5 or CLT7), YY refers to the tenon or bracket label, ZZZZ refers to the loading direction relative to the CLT outer layer, and V refers to specimens unreinforced (U) or reinforced (R) with inclined self-tapping screws. The sample size was three for all unreinforced test series. The sample size for the reinforced specimens was limited to one which provided qualitative comparison to the unreinforced specimens.

Due to the stiffness differences between layers in CLT, rolling shear failure in either the tenon or the mortise can also occur. The castellation test programme was designed such that either longitudinal or rolling shear failure of the tenon would occur in all test series except for tenon label C4. With tenon labels C1 and C2, the impact of tenon length on the load-carrying capacity was assessed. Tenon labels C1 and C2 with loading perpendicular to the outer CLT layer are also similar to the situations shown in Figure 5-1. In the test series with tenon label C3, loads parallel to the outer CLT layer were applied. These joints could be used to provide in-plane shear transfer for CLT walls or floors diaphragms (T Schmidt & Blaß, 2016). The C4 tenon label test series was unique in that the tenon length (L) to tenon height (H) ratio was significantly changed in an attempt to trigger bending in the tenon and tensile perpendicular to the grain failure in the corner of the notch might occur. This is important to investigate, because in CLT platform frame construction, a large tenon height (H) could be required to be greater than the CLT floor thickness and provide wall-wall shear transfer. There was no lamination gap in the tenon for test series C1, C2, and C3. However, a lamination gap existed in at least one of the two tenons for test series C4 and its location was random. Failure in the mortise part was avoided by ensuring the mortise shear length was two times the tenon shear length.

Angle bracket shear connections are currently commonly used in platform CLT construction as shown in Figure 5-1. In this study, the angle bracket joints were tested mainly to compare their load-carrying capacity and stiffness to the castellated joints. As such, loading both parallel and perpendicular to the outer CLT layer were considered.

*Table 5-1: Castellation test programme*

| Test Series | Panel | Layup | Thickness | Tenon Label | $L_T$ | $H_T$ | Loading Direction | Sample Size |
|---|---|---|---|---|---|---|---|---|
| - | - | mm | mm | | mm | mm | - | - |
| CLT5-C1-Perp-U | CLT5 | 45/20/45/20/45 | 175 | C1 | 150 | 50 | Perp | 3 |
| CLT7-C1-Perp-U | CLT7 | 45/35/35/45/35/35/45 | 275 | C1 | 150 | 50 | Perp | 3 |
| CLT7-C1-Perp-R | CLT7 | 45/35/35/45/35/35/45 | 275 | C1 | 150 | 50 | Perp | 1 |
| CLT5-C2-Perp-U | CLT5 | 45/20/45/20/45 | 175 | C2 | 100 | 50 | Perp | 3 |
| CLT5-C2-Perp-R | CLT5 | 45/20/45/20/45 | 175 | C2 | 100 | 50 | Perp | 1 |
| CLT7-C2-Perp-U | CLT7 | 45/35/35/45/35/35/45 | 275 | C2 | 100 | 50 | Perp | 3 |
| CLT7-C2-Perp-R | CLT7 | 45/35/35/45/35/35/45 | 275 | C2 | 100 | 50 | Perp | 1 |
| CLT5-C3-Para-U | CLT5 | 45/20/45/20/45 | 175 | C3 | 105 | 35 | Para | 3 |
| CLT5-C3-Para-R | CLT5 | 45/20/45/20/45 | 175 | C3 | 105 | 35 | Para | 1 |
| CLT7-C3-Para-U | CLT7 | 45/35/35/45/35/35/45 | 275 | C3 | 105 | 35 | Para | 3 |
| CLT5-C4-Para-U | CLT5 | 45/20/45/20/45 | 175 | C4 | 75 | 100 | Para | 3 |
| CLT5-C4-Para-R | CLT5 | 45/20/45/20/45 | 175 | C4 | 75 | 100 | Para | 1 |
| CLT7-C4-Para-U | CLT7 | 45/35/35/45/35/35/45 | 275 | C4 | 75 | 100 | Para | 3 |

*Table 5-2: Angle bracket test programme*

| Test Series | Panel | Layup | Thickness | Bracket | Loading Direction | Fastener | Nailing Pattern | Sample Size |
|---|---|---|---|---|---|---|---|---|
| - | - | mm | mm | - | - | - | - | - |
| CLT5-B1-Perp-U | CLT5 | 45/20/45/20/45 | 175 | Titan TTN240 | Perp | LBA ϕ4x60 | Full | 3 |
| CLT5-B1-Para-U | CLT5 | 45/20/45/20/45 | 175 | Titan TTN240 | Para | LBA ϕ4x60 | Full | 3 |

The connection configurations of the different test series are shown in Figure 5-2. Figure 5-2a - Figure 5-2c show the key nomenclature and details for the tenon and the angle bracket, respectively. The mortise was made with 3mm tolerance relative to the tenon to allow for ease of assembly. The thickness of the mortise and tenon was the same as the CLT panel thickness. Figure 5-2d - Figure 5-2g show one half of each specimen with the specific dimensions of each tenon C1 through C4. The reinforcement details are shown in Figure 5-2h. $\phi$7x140mm fully threaded (FT) self-tapping screws (STS) (ETA-11/0030, 2019) were installed in the tenon at installation angles $\alpha$ = 45° and $\varepsilon$ = 15° in a cross-wise pattern. The number of STS was six and eight for the CLT5 and CLT7 specimens respectively and the STS were installed following minimum spacing ($a_2$=4d) as per STS product approval (ETA-11/0030, 2019). These inclined FT STS aimed to provide reinforcement along each rolling shear plane. As such, they were positioned to have equal threaded length on each side of the rolling shear plane. The FT $\phi$7mm STS were installed into $\phi$4mm predrilled holes to 70% of the screw length with jigs to ensure correct alignment. Figure 5-2i and Figure 5-2j show the elevation and plan views of the angle bracket specimens with the dimensions. To ensure the loads were kept within the limit of the test machine, two commercial Titan TTN240 brackets (ETA-11/0496, 2018) were installed symmetrically and on opposite sides of the middle CLT panel and loaded in a similar manner to past bracket testing (Gavric et al., 2015). Then, L-shaped brackets were installed to provide torsional restraints as shown in Figure 5-2j and they are discussed in Section 5.2.2. LBA $\phi$4x60mm annular-ringed shanked nails (ETA-11/0496, 2018) were installed in every hole of each side of the bracket for a full nailing pattern. Due to the nail specifications, bracket thickness, and CLT5 layup, most of the LBA $\phi$4x60mm was installed into the outer 45mm thick CLT layer and the impact of this will be discussed later in Section 5.3. The locations of the mortise and tenon and placement of brackets were random with regard to the gaps between CLT laminations.

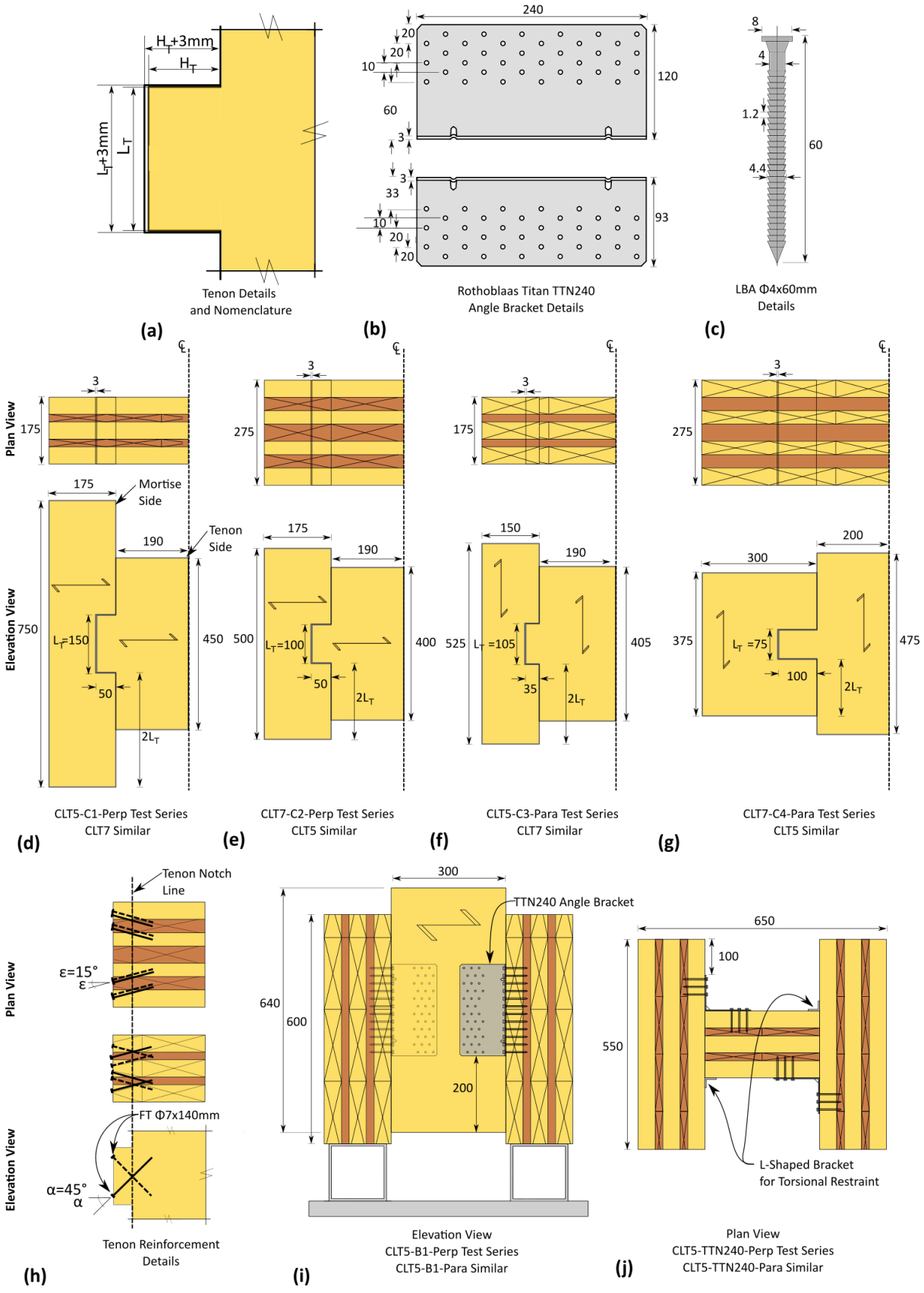


*Figure 5-2: (a) tenon details, (b) angle bracket details, (c) nail details, (d) C1 test series, (e) C2 test series, (f) C3 test series, (g) C4 test series, (h) tenon reinforcement details, (i) elevation view angle bracket test series, (j) plan view angle bracket test series*

### 5.2.2 Methods

Figure 5-3 shows a photo of the castellation and angle bracket test setup. For the castellation testing, a 700kN hydraulic ram with a load cell was attached to the beam of the reaction frame which consisted of two vertical columns and two out of plane steel braces. The other side of the hydraulic ram contained a load cell with 350x300x40mm thick steel loading plate which was in contact bearing with the middle CLT panel. Horizontal in-plane restraint was provided with 4-M36 Grade 8.8 threaded rods placed at the top and bottom of the specimen. The threaded rods were installed through steel parallel flange sections which then clamped the specimen and the reaction frame together with hand tightened bolts. A load cell monitored out-of-plane forces in the threaded rods and the impact of any clamping force will be discussed in Section 5.3.1. Out-of-plane translation and rotation was prevented by a horizontal steel beam with rectangular hollow section that was bolted to the reaction frame. A similar test setup was used for the bracket testing but they were conducted using a 250kN Instron Universal Test Machine (UTM) with a load cell mounted on the crosshead. In-plane restraint was provided on the bottom by 2-M20 Grade 8.8 threaded rods placed through holes in the side CLT panel with end bearing plates and on the top by 2x2 wood braces graded SG8 (Standards New Zealand, 1993) installed with $\phi$10x100mm partially threaded washer head screws (ETA-12/0114, 2017). Torsional restraint was provided by two L-shaped brackets fastened to the side CLT panels with wood screws as shown in Figure 5-3b. The L-shaped bracket prevented any rotation of the middle CLT panel while allowing it to move vertically downwards during loading.

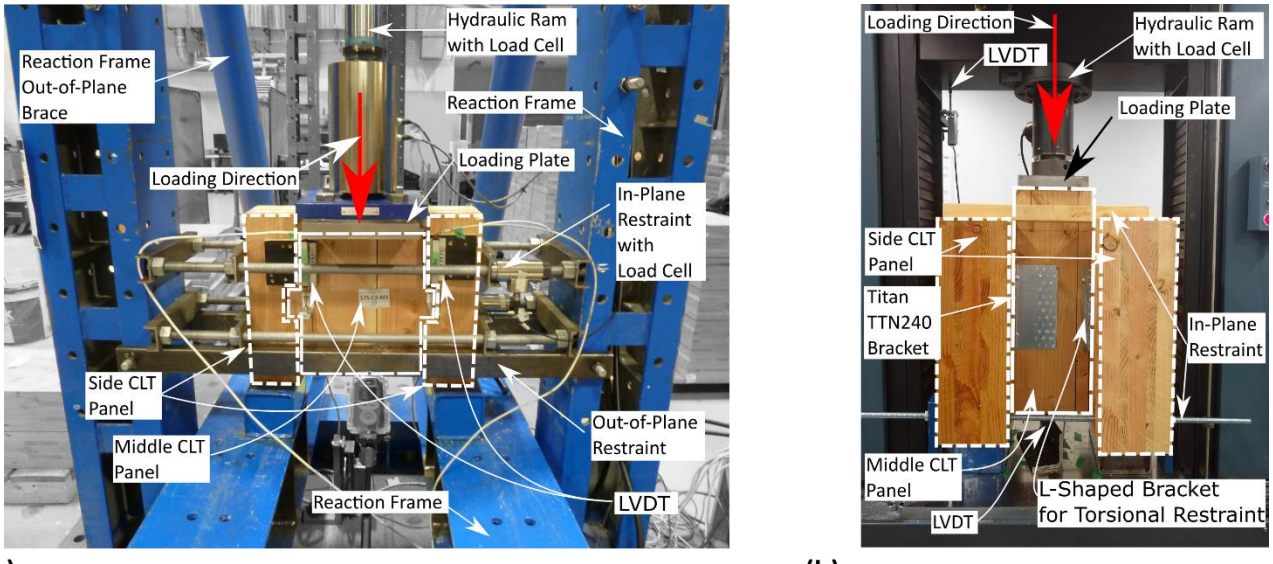


*Figure 5-3: (a) Castellation test set-up, and (b) bracket test set-up*

Figure 5-4 shows the instrumentation of the testing. For the castellation specimens, the relative displacement between the middle and outer CLT panels was measured with 50mm linear variable

displacement transducers (LVDTs) which were fastened to the outer CLT layer with small wood screws. Two LVDTs were placed to record the relative displacement both outside and inside the tenon for a total of four measurements. The average of the two LVDTs measuring relative displacement outside the tenon was presented so that the global behaviour after peak load could be captured. For test series CLT5-C1, the LVDTs were incorrectly fastened on the mortise side of the joint such that mortise deformation was not captured. The implication of this will be discussed in Section 5.3.1. For the angle bracket specimens, the global relative joint displacement was recorded in a similar manner as past research (Casagrande et al., 2020; Gavric et al., 2015). While past research has reported angle bracket connectors may have deformation contributions on each side of the bracket due to timber embedment deformation, nail yielding and in-plane and out-of-plane steel plate deformations (Izzi et al., 2018), a detailed investigation was beyond the scope of the study. The primary purpose was to compare an angle bracket's global strength and stiffness to a castellated joint.

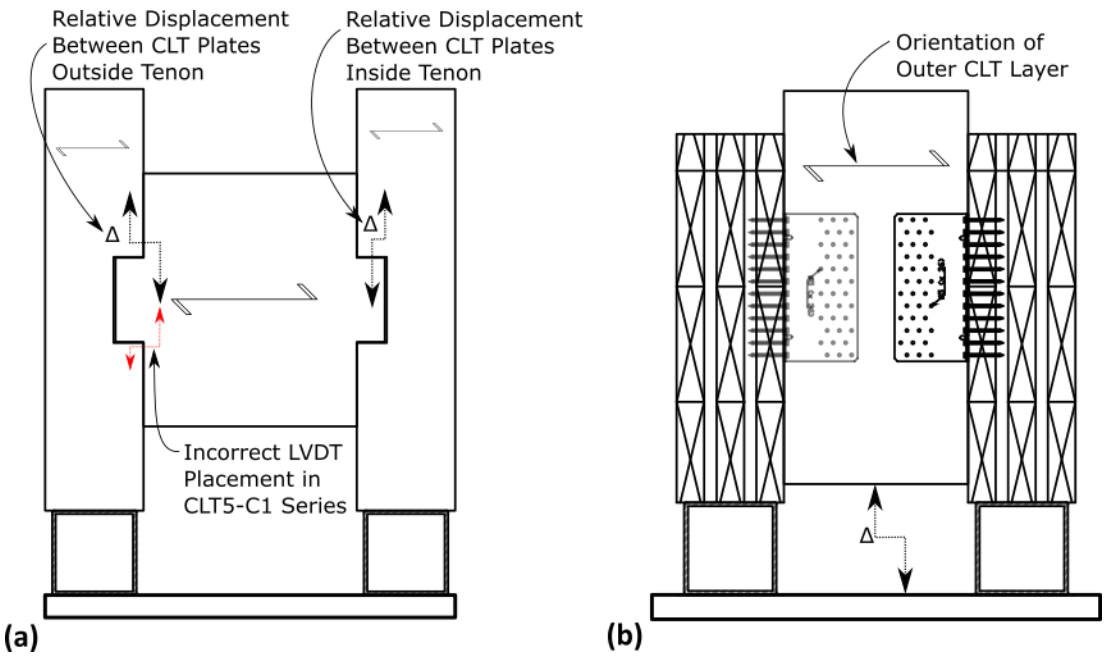


*Figure 5-4: Specimen instrumentation - (a) castellation specimen, and (b) CLT5-TTN240-Perp specimen shown*

The specimens were tested under monotonic loading following EN 26891 (1991). The estimated maximum load, $F_{est}$, was determined on the basis of a first trial test. Then, for each test specimen the load was applied to $0.4F_{est}$, maintained for 30s, reduced to $0.1F_{est}$, maintained for 30s, and then the loaded until failure, $F_u$, which was defined as post-peak load of 80% maximum strength, $F_{max}$, as per EN 12512 (2005). The monotonic loading rate was between 2-4mm/min for a total test time of 10 to 15min as per EN 26891 (1991). While EN 26891 (1991) assesses the ultimate strength to a maximum slip of 15mm, for the bracket specimens joint slips greater than 15mm were recorded as $F_{max}$ was not

reached at the limit of 15mm. For the castellation specimens, $F_{max}$ was always reached within 15mm joint slip. In some castellation specimens $F_u$ was not reached at 15mm joint slip, and the total joint slip is reported to provide a comparison to the bracket specimens.

The load-slip curves were analysed in order to assess the maximum strength $F_{max}$, ultimate strength $F_u$, and the displacement at maximum strength $\Delta_{Fmax}$, ultimate displacement $\Delta_{Fu}$, and the elastic stiffness, $k_{el,exp}$. The elastic stiffness was calculated for the range of the load-slip curve between 10% and 40% $F_{max}$ as per:

$$k_{el,exp} = \frac{F_{40} - F_{10}}{\Delta_{F40} - \Delta_{F10}} \quad (5\text{-}1)$$

where $F_{40}$ and $F_{10}$ are the load at $0.4F_{max}$ and $0.1F_{max}$ and $\Delta_{F40}$ and $\Delta_{F10}$ are the corresponding connection slips.

## 5.3 CONNECTION TEST RESULTS AND DISCUSSION

### 5.3.1 Joint Performance

Table 5-3 provides a summary of the castellation experimental results. The results are reported for one mortise and tenon castellated joint. Tenon series C1, C2, and C3 reached maximum strength, $F_{max}$, at an average joint displacement less than 4mm. $F_{max}$ of series C2 was on average 22% less than series C1 due to the reduced tenon L by 33%. $F_{max}$ of series C4 was reached at an average joint displacement of 7mm, significantly different from the other test series. This was due to a differing dominant failure mode which will be discussed further in Section 5.3.2. The strength did not increase proportionally to the increase in longitudinal shear area when comparing CLT5 and CLT7 specimens. For series C1 and C2, the longitudinal shear area increased by a factor of 2.8 when comparing CLT5 and CLT7, but $F_{max}$ only increased by a factor of 1.6 on average. For series C3 the longitudinal shear area increased by a factor of 1.2 when comparing CLT5 and CLT7, while $F_{max}$ increased by a factor of 1.3 on average. The results suggested that $F_{max}$ was not only dependent on the longitudinal shear area, but also the thickness ratio of the CLT panel layers and therefore the influence of other load paths such as rolling shear. This will be discussed further in Section 5.4. Reinforcement increased $F_{max}$ in CLT5 series by 35% on average but did not impact CLT7 series. This qualitative observation suggested that not enough STS were installed in CLT7 series to have significant impact. The in-plane restraint clamping force did not change significantly throughout the loading sequence. A low initial clamping pressure of approximately 0.1 MPa changed +/-0.03 MPa until joint failure occurred. During loading, the force in the lower threaded rod slightly increased and the force in the upper threaded rod slightly decreased. Claus et al. (2018) studied the impact of initial clamping pressure on interlocking CNC carpentry joints

by applying a clamping pressure of 1.0 and 0.4 MPa. Claus et al. (2018) showed that while the initial clamping pressure influenced the first instance of connection slip due to friction, it did not influence the ultimate load and failure mode. In the experimental results reported herein, it was found that the low initial clamping force did not appear to influence the ultimate load and failure mode. A further detailed study on initial clamping pressure was beyond the scope of the study presented.

The stiffness, $k_{el,exp}$, of the joint was also dependent on the geometry and loading direction with respect to the outer CLT layer. It should be noted that the reported $k_{el,exp}$ of series CLT5-C1 should not be directly compared to those of series C2, C3, and C4 due to the differences of the LVDT placement described in Section 5.2.2. In series CLT5-C1, the global joint deformation was slightly under reported and thus increased $k_{el,exp}$. The LVDT placement was corrected and fastened above the tenon in all other series. Reinforcement did not appear to influence joint stiffness as the results were on average within 10% difference. In almost all test series except for C4 series, the ultimate load $F_u$ occurred at a joint slip less than 15mm. In C4 series, the last recorded measurement was reported for $F_u$ as the test was stopped before 80% post-peak load was reached. In general, the STS reinforcement did not appear to influence joint displacement capacity as the results were too variable.

*Table 5-3: Castellation experimental results summary*

| Series | | $F_{max}$ kN | $\Delta_{Fmax}$ mm | $k_{el,exp}$ kN/mm | $F_u$ kN | $\Delta_{Fu}$ mm |
|---|---|---|---|---|---|---|
| CLT5-C1-Perp-U | M1 | 107 | 2.9 | 45[1] | 75 | 13.1 |
| | M2 | 101 | 3.0 | 44[1] | 81 | 7.4 |
| | M3 | 106 | 1.8 | 67[1] | 84 | 5.0 |
| | *Avg.* | *104* | *2.6* | *52[1]* | *80* | *8.5* |
| CLT7-C1-Perp-U | M1 | 152 | 2.4 | 72 | 121 | 7.0 |
| | M2 | 170 | 2.6 | 46 | 135 | 3.5 |
| | M3 | 151 | 3.2 | 68 | 121 | 4.9 |
| | *Avg.* | *157* | *2.7* | *62* | *126* | *5.1* |
| CLT7-C1-Perp-R | M1 | 151 | 3.8 | 71 | 125 | 17.7 |
| CLT5-C2-Perp-U | M1 | 66 | 6.6 | 14 | 59[2] | 23.8[2] |
| | M2 | 89 | 3.0 | 31 | 71 | 10.3 |
| | M3 | 73 | 4.9 | 16 | 59 | 12.8 |
| | *Avg.* | *76* | *4.8* | *20* | *63* | *15.6* |
| CLT5-C2-Perp-R | M1 | 98 | 3.4 | 22 | 78 | 7.9 |
| CLT7-C2-Perp-U | M1 | 127 | 4.6 | 45 | 102 | 8.3 |
| | M2 | 125 | 5.3 | 59 | 117[2] | 20.0[2] |
| | M3 | 145 | 2.9 | 77 | 116 | 9.8 |
| | *Avg.* | *132* | *4.3* | *60* | *112* | *12.7* |
| CLT7-C2-Perp-R | M1 | 139 | 3.4 | 80 | 111 | 8.2 |
| CLT5-C3-Par-U | M1 | 95 | 5.1 | 31 | 76 | 5.9 |
| | M2 | 85 | 3.5 | 22 | 57 | 4.6 |
| | M3 | 100 | 3.0 | 29 | 80 | 4.7 |
| | *Avg.* | 93 | 3.9 | 27 | 71 | 5.1 |
| CLT5-C3-Par-R | M1 | 116 | 3.1 | 25 | 93 | 5.7 |
| CLT7-C3-Par-U | M1 | 135 | 1.7 | 75 | 108 | 3.6 |
| | M2 | 117 | 4.9 | 53 | 93 | 20.8 |
| | M3 | 119 | 3.3 | 61 | 95 | 5.0 |
| | *Avg.* | *123* | *3.3* | *63* | *98* | *9.8* |
| CLT5-C4-Par-U | M1 | 62 | 5.0 | 21 | 49 | 25.3 |
| | M2 | 63 | 3.2 | 20 | 50 | 24.4 |
| | M3 | 70 | 12.8 | 22 | 56 | 26.7 |
| | *Avg.* | *65* | *7.0* | *21* | *52* | *25.4* |
| CLT5-C4-Par-R | M1 | 97 | 6.7 | 20 | 78 | 11.1 |
| CLT7-C4-Par-U | M1 | 100 | 6.2 | 23 | 89[2] | 30.4[2] |
| | M2 | 100 | 8.5 | 37 | 85[2] | 33.9[2] |
| | M3 | 87 | 5.9 | 27 | 74[2] | 28.9[2] |
| | *Avg.* | *95* | *6.8* | *29* | *83* | *31.1* |

Note: [1]Incorrect placement of LVDT increased reported stiffness

[2]Test was stopped before 80% post-peak load was reached

Table 5-4 provides a summary of the specimens using angle brackets. The results are reported for one angle bracket. The maximum strength $F_{max}$ was reached on average at a joint slip of 20mm, which was more than 5 times the joint slip at $F_{max}$ for series C1, C2, and C3. $F_{max}$ was on average 25% greater in the Perp test series than that of the Para test series. This trend agreed with the previous study by Izzi

et al. (2016). The experimental elastic stiffness, $k_{el,exp}$, was consistent and on average 7kN/mm for both Perp and Para specimens and more than 2.5 times lower than the predicted elastic stiffness following the modified Eurocode 5 (2014) method where Izzi et al. (2016) suggested to neglect the factor 2 used for steel-to-timber joints. The reported stiffness herein with larger brackets and 36 nails per side was also less than the 8.3kN/mm stiffness reported by Polastri et al. (2019) with smaller brackets and 30 nails per side. The results suggested that the deformability of the brackets themselves have a significant influence on the angle bracket connection stiffness which has also been previously reported (Gavric et al., 2015; Izzi et al., 2018; Tomasi & Smith, 2015; Tomasi & Sartori, 2013). However, the angle bracket deformability is not accounted for in the general stiffness equation provided in Eurocode 5 (2014).

*Table 5-4: Angle bracket experimental results summary*

| Series | | $F_{max}$ kN | $\Delta_{Fmax}$ mm | $k_{el,exp}$ kN/mm | $F_u$ kN | $\Delta_{Fu}$ mm |
|---|---|---|---|---|---|---|
| CLT5-TTN240-Perp | M1 | 88 | 22.8 | 6 | 88 | 24.5 |
| | M2 | 82 | 18.8 | 6 | 66 | 27.5 |
| | M3 | 100 | 25.0 | 8 | 77 | 42.3 |
| | *Avg.* | *90* | *22.2* | *7* | *77* | *31.4* |
| CLT5-TTN240-Par | M1 | 79 | 20.7 | 8 | 67 | 26.8 |
| | M2 | 68 | 20.2 | 5 | 54 | 36.9 |
| | M3 | 68 | 14.3 | 8 | 55 | 35.0 |
| | *Avg.* | *72* | *18.4* | *7* | *59* | *32.9* |

It was found that the load-slip curves of the replicates were relatively consistent. Therefore, for each test series one representative curve is plotted in Figure 5-5 and Figure 5-6 for the castellated joints and the angle bracket joints respectively. In the castellation series, the load drops occurred due to longitudinal and rolling shear failure. Figure 5-5 shows that after peak load, the cross-wise layup of CLT ensured post-peak displacement capacity. This reinforcing effect was more pronounced in CLT7 specimens and allowed load redistribution to the less stiff layers loaded perpendicular to the grain such that sudden failure was avoided. Figure 5-6 shows the difference between the Eurocode 5 (2014) predicted stiffness, $K_{el,pred}$, and the load-displacement test curve, and the load drops which occurred when timber splitting failure occurred.

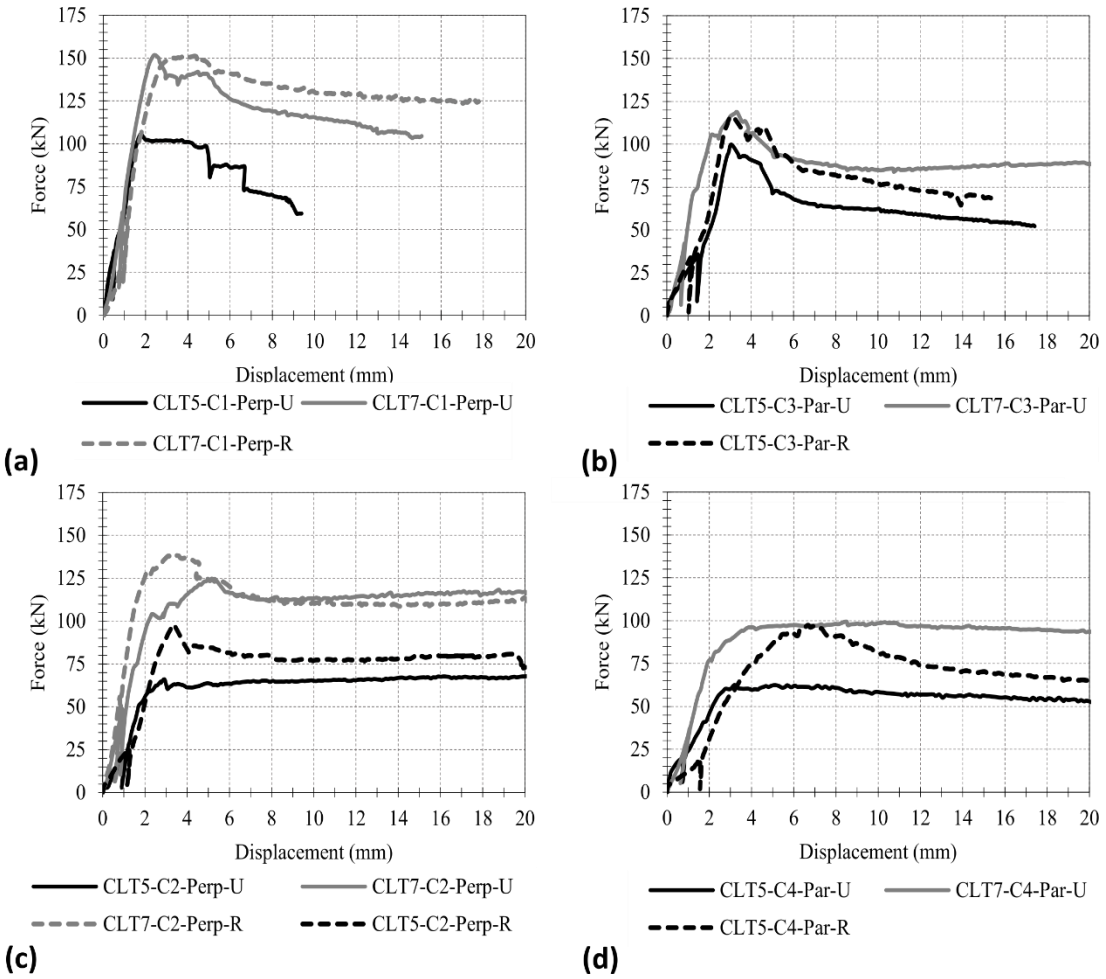


*Figure 5-5: Load-slip curves: (a) C1 test series, (b) C3 test series, (c) C2 test series, and (d) C4 test series*

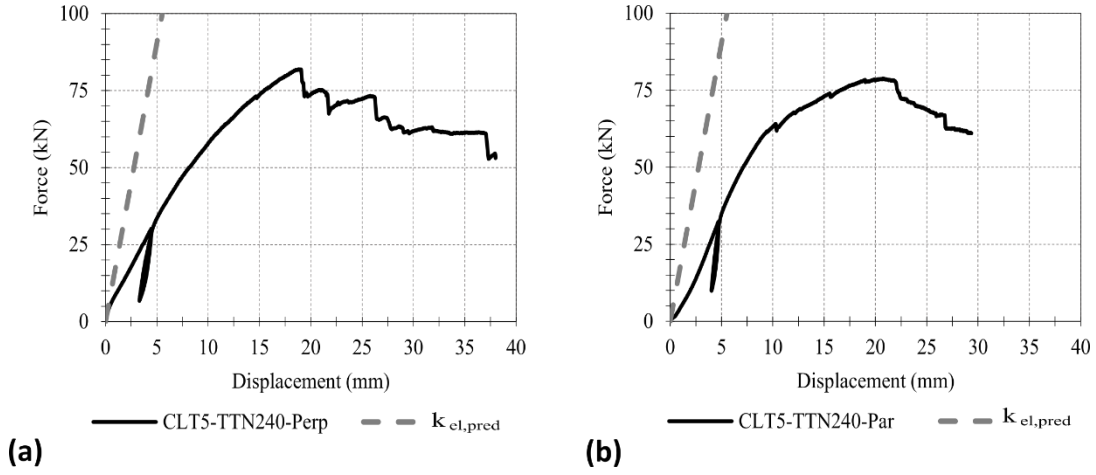


*Figure 5-6: Load-slip curves: (a) TTN240 bracket perpendicular-to-outer CLT layer, and (b) TTN240 bracket parallel-to-outer CLT layer*

### 5.3.2 Failure Modes

Figure 5-7 shows the typical failure modes for each test series. In the castellation test series with tenon geometry C1 to C3, the dominant failure modes were a combination of longitudinal shear failure and rolling shear failure on the tenon side. Deformation on the mortise side also occurred as shown in Figure 5-7c and Figure 5-7g. Figure 5-7f and Figure 5-7h show that a similar failure mode occurred in the reinforced specimens as in the unreinforced specimens. In all specimens, a relative displacement was observed between the CLT layers. The layers loaded parallel to the grain had greater displacement than the layers loaded perpendicular to the grain. This behaviour was also observed in contact joint testing by Schmidt (2018) and illustrated that rolling shear load transfer occurred. The castellation test series with tenon geometry C4 had a unique failure mode due to the increased tenon height and the presence of a lamination gap within the tenon. Figure 5-8 shows the tension perpendicular to grain crack progression throughout tests CLT5-C4-Par-U M1 and M2. The presence of a lamination gap also reduced the load-carrying capacity of the joint, but more work is needed in future to conduct a thorough investigation on lamination gap location effect. As with tenon geometries C1 to C3, the cross-wise layup of CLT provided reinforcing effect and stable post-peak behaviour.

Figure 5-7j - Figure 5-7m show the angle bracket failure modes. The angle brackets exhibited a three phase failure mechanism: initial slip and small bending deformation of the nails, significant in-plane and out-of-plane deformation of the angle bracket, and finally tensile perpendicular-to-grain and rolling shear crack propagation to ultimate failure. Past research has reported these commercial angle brackets are generally governed by fastener yielding and withdrawal and timber embedment crushing failure modes (Amini et al., 2018; Benedetti et al., 2019; Cao et al., 2020; Gavric et al., 2015; Polastri et al., 2019). In many of these past studies, the angle bracket geometries were relatively smaller, which reduced eccentricities; fewer nails were installed, which reduced loads; and in some instances smooth shanked nails were used, which decreased the rope effect. However, Tomasi et al. (2015) has also reported that brittle timber failure can occur in angle brackets if the nail primarily penetrates one layer of the CLT and if the loading eccentricities are significant. In this study, the increased size of the bracket, the CLT5 layer layup, and the nail size and type contributed to a predominantly timber failure mode. The CLT5 layup of 45/20/45/20/45 and nail and bracket geometry meant that only 7mm of nail, excluding the nail tip, penetrated into the second layer of the CLT5 panel. Further, the ETA (2018) for the annular-ringed shank nail considers the shear capacity as having contribution from the lateral dowel capacity ($R_v$) and rope effect. The rope effect contribution is equal to $0.5F_{ax}$, where $F_{ax}$ is the withdrawal capacity, due to their higher withdrawal capacity as described by Izzi et al. (2018). This is different from Eurocode 5 (2014) where the rope effect is set to $0.25F_{ax}$ in general and for smooth shanked nails it is also limited to $0.15R_v$. The increased rope effect contribution promoted rolling shear

and tension perpendicular to grain failure. It is interesting to note that Li et al. (2019) has also reported the Douglas-Fir CLT with 45mm thick layer had lower rolling shear capacity when compared to the CLT with 20mm or 35mm thick layers. Figure 5-7k and Figure 5-7l show that minimal timber embedment deformation and nail bending deformation occurred during testing.

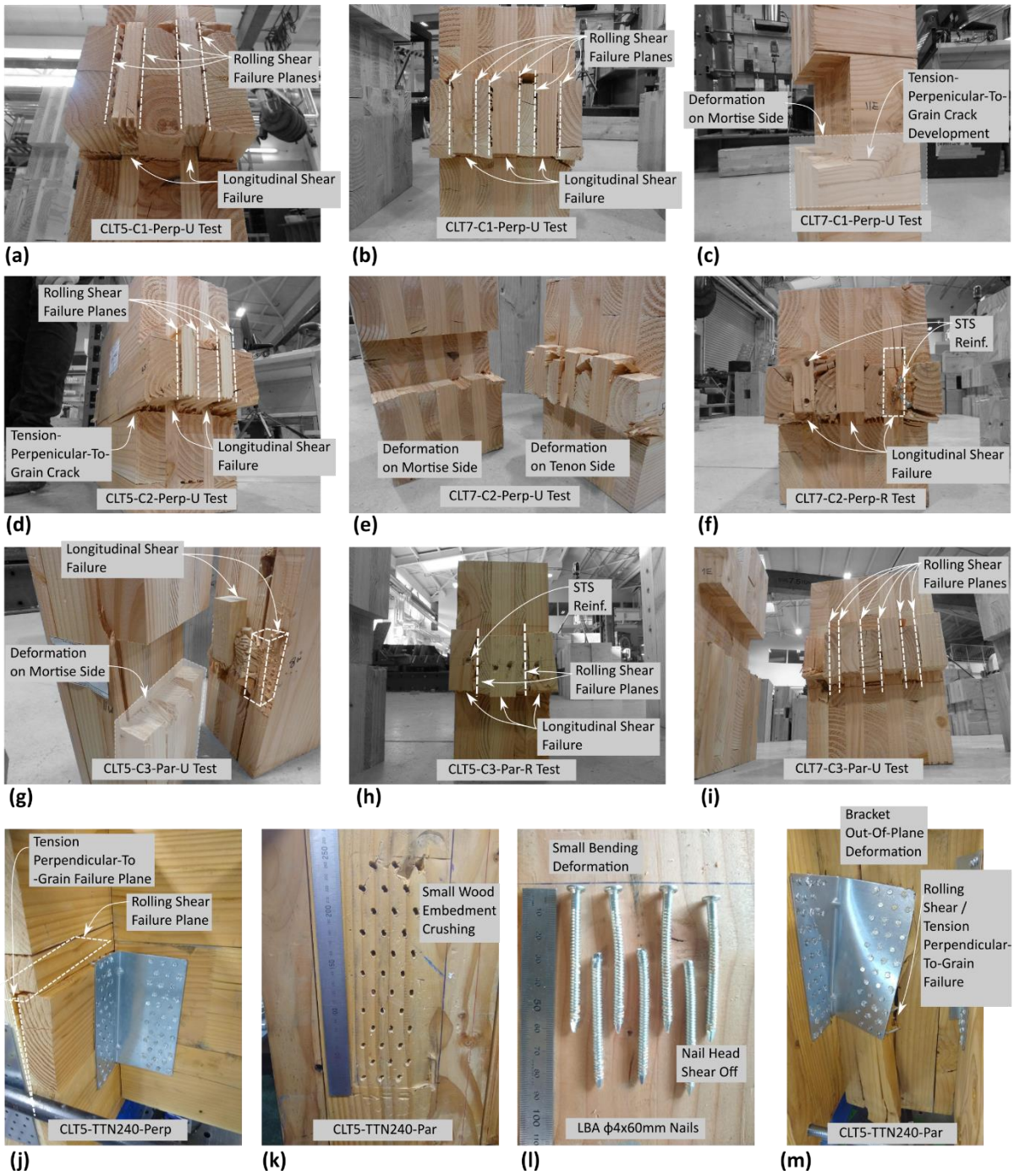


*Figure 5-7: After test specimen photos*

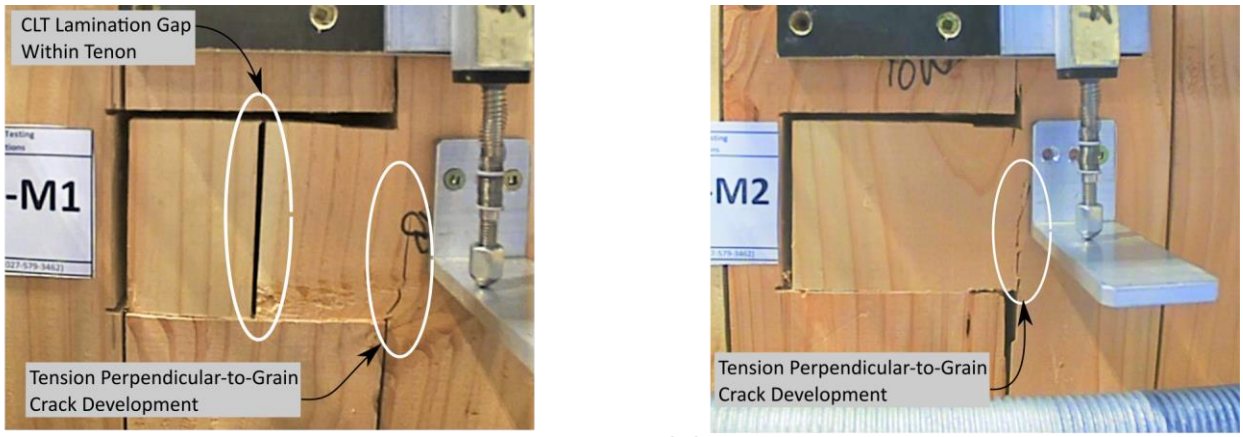


*Figure 5-8: During testing photos of C4 specimens showing tension perpendicular-to-grain crack development and a CLT lamination gap within the tenon.*

### 5.3.3 Joint Strength and Stiffness Comparison

Table 5-5 provides a strength and stiffness comparison of the castellated and angle bracket connections per meter of CLT length. The average experimental strength and stiffness results were used. Castellated joints provided greater than 2.5 times the strength and greater than seven times the stiffness, which highlights the castellated joints significantly improved connection efficiency. Past research has reported commercial angle brackets have limited strength and stiffness thus limiting the efficiency of CLT shear walls (Flatscher et al., 2015). Schmidt & Blaß (2016; 2018) presented different variations of contact joint connections which have characteristic load-carrying capacities closer to the gross shear capacity of the CLT wall. The work presented herein showed contact joints loaded parallel and perpendicular to the outer CLT layer could also provide connections with increased efficiency. It is important to note that in design, the actual load-carrying capacity and stiffness per meter wall will be less as adequate spacing between castellations and brackets is required in addition to possible group effects. This was beyond the scope of the study.

*Table 5-5: Summary of strength and stiffness parameter comparisons*

| Connection Type | Test Series | Load Direction Relative to the Outer CLT Layer | $F_{max}$ per meter wall | Stiffness per meter wall |
|---|---|---|---|---|
| | | | kN/m | kN/mm/m |
| Castellation | CLT5-C2-Perp-U | Perp. | 760 | 203 |
| | CLT5-C3-Par-U | Par. | 887 | 257 |
| Angle Bracket | CLT5-TTN240-Perp | Perp. | 375 | 28 |
| | CLT5-TTN240-Par | Par. | 298 | 30 |

## 5.4 CASTELLATION ANALYTICAL MODEL AND COMPARISON WITH EXPERIMENTAL RESULTS

A component-based elastic spring model was developed in order to predict the strength of castellated joints loaded parallel and perpendicular to the outer CLT layer. Component-based analytical models have been implemented for carpentry joints (Branco & Descamps, 2015) where all timber fibres are aligned and also for wood brittle failure modes in dowelled connections (Quenneville & Zarnani, 2014; Yurrita & Cabrero, 2020). In this study, extensions were adopted to account for the increased complexity due to the cross-wise layup of CLT. As described in Section 5.2.1, the geometry of the castellation ensured that shear and compression failure of the mortise part did not occur. Furthermore, it was assumed that there were no lamination gaps within the tenon. Joints with lamination gaps within the tenon are beyond the scope of the model presented herein. While previous work (Branco et al., 2018; Siem & Jorissen, 2015; Verbist et al., 2017) considered a non-uniform shear stress distribution for the design of carpentry step joints, a uniform shear stress distribution was assumed herein due to the relatively small tenon length to height ratio of 3:1, 2:1, and 0.75:1 which Aira et al. (2015) has shown numerically has significantly lower peak stress concentrations than the tenons with length to height ratios greater than 3. Uniform contact bearing was also assumed along the tenon height with the mortise side, and the load was assumed to transfer only to the CLT layers loaded parallel to grain which was also assumed by Schmidt & Blaß (2018). The approach developed was similar to the stiffness-based load sharing approach by Zarnani & Quenneville (2014) to predict wood block tear out resistance based on three different possible failure planes with different stiffness properties.

### 5.4.1 Analytical Model Development

The analytical model was developed by assuming a global and interlayer deformed shape of the tenon side. Figure 5-9 shows the assumed regions of the specimen that are deformable followed by the uniform stress distribution at the contact surfaces and the assumed deformed shape of the tenon side. Figure 5-10 shows the tenon cross-section interlayer and the assumed deformation profile which imposes rolling shear strain, $\varphi_{RS}$ (i.e. $\varphi_{in}$ and $\varphi_{out}$ as shown in Figure 5-10b), due to the relative displacement between the CLT layers. It should be noted that this was a simplified displacement shape when compared to the complex inter-layer displaced shape shown in Figure 5-13b.

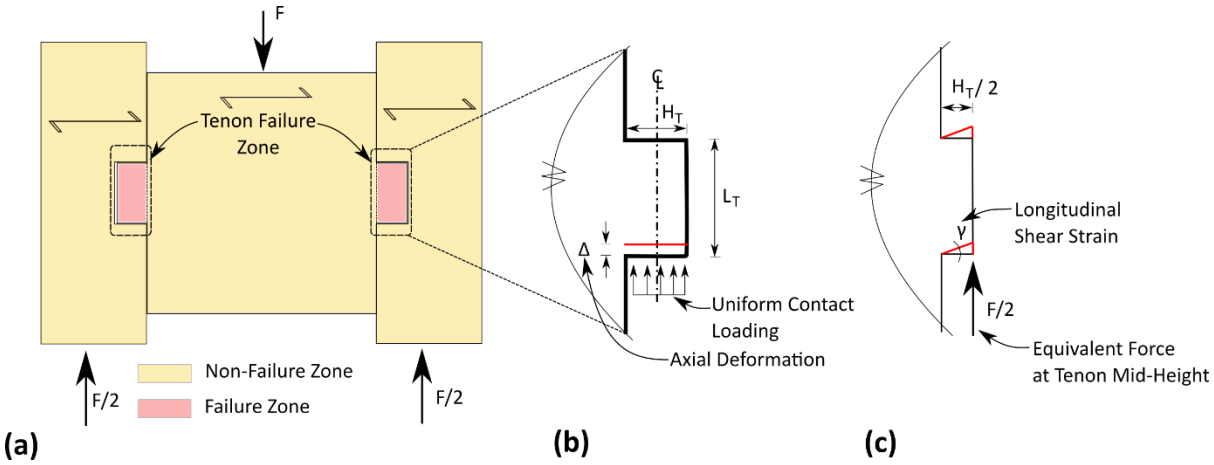


*Figure 5-9: Component model assumptions; (a) global deformation, (b) tenon axial deformation, (c) tenon longitudinal in-plane shear deformation*

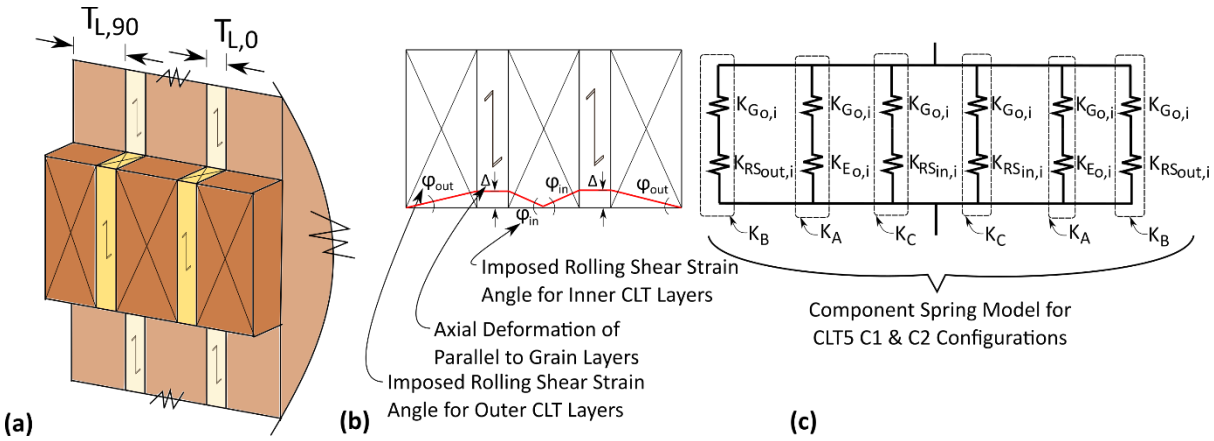


*Figure 5-10: (a) CLT5 C1 & C2 tenon isometric, (b) CLT5 C1 & C2 tenon rolling shear and axial deformation, (c) component spring model*

The axial stiffness of CLT layers loaded parallel to grain is derived from the constitutive equation $E_o = {}^{\sigma}/_{\varepsilon}$ and then from Figure 5-9b and Figure 5-10a as:

$$K_{E_{0,i}} = \frac{E_{o,i} H_T T_{L_{0,i}}}{L_T} \ (kN/mm) \qquad (5\text{-}2)$$

where $E_{o,i}$ is the modulus of elasticity for the applicable layer, and $H_T$, $T_{Lo,i}$, $L_T$ are the tenon height, the thickness of the CLT layer loaded parallel to grain, and the tenon length, respectively, as shown in Figure 5-9 and Figure 5-10. The tenon longitudinal shear stiffness is derived from $G_o = {}^{\tau_l}/_{\gamma_l}$, where $\tau_l$ is the longitudinal shear stress, and then from Figure 5-9c and Figure 5-10a as:

$$K_{G_{0,i}} = \frac{G_{0,i} L_T T_{L_{0,i}}}{\frac{H_{T,i}}{2}} \ (kN/mm) \qquad (5\text{-}3)$$

where $G_{o,i}$ is the longitudinal shear modulus for the applicable layer, and $L_T$, $T_{Lo,i}$, and $H_T$ are as defined previously.

The rolling shear stiffness of CLT layer loaded perpendicular to grain is derived from $G_{RS} = {}^{\tau_{RS}}/_{\varphi_{RS}}$ and then from Figure 5-10 as:

$$K_{G_{RS,out,i}} = \frac{G_{RS,out,i} L_T H_T}{T_{L_{90,i}}} \text{ (kN/mm)} \quad (5\text{-}4)$$

$$K_{G_{RS,in,i}} = \frac{G_{RS,in,i} L_T H_T}{\frac{T_{L_{90,i}}}{2}} \text{ (kN/mm)} \quad (5\text{-}5)$$

where $G_{RS,out,i}$ and $G_{RS,in,i}$ are the rolling shear modulus for the applicable outer and inner layer respectively, $L_T$, and $H_T$ are as defined previously, and $T_{L90,i}$ is the thickness of the CLT layer in rolling shear deformation.

Then, the appropriate spring combinations in series for different layers are made to determine the stiffness of each potential failure plane. The layer loaded parallel to grain is assumed to have parallel to grain compressive deformations and longitudinal shear deformations as shown in Figure 5-10b and Figure 5-10c. Therefore, it has the following combined stiffness $K_A$:

$$K_A = \frac{K_{E_{0,i}} K_{G_{0,i}}}{K_{E_{0,i}} + K_{G_{0,i}}} \text{ (kN/mm)} \quad (5\text{-}6)$$

The cross layers loaded perpendicular to grain are assumed to have both rolling shear and longitudinal shear deformations, as shown in Figure 5-10b and Figure 5-9c. The stiffness values of the outer and inner cross layers, referred to as $K_B$ and $K_C$, are determined as:

$$K_B = \frac{K_{RS_{out,i}} K_{G_{0,i}}}{K_{RS_{out,i}} + K_{G_{0,i}}} \text{ (kN/mm)} \quad (5\text{-}7)$$

$$K_C = \frac{K_{RS_{in,i}} K_{G_{0,i}}}{K_{RS_{in,i}} + K_{G_{0,i}}} \text{ (kN/mm)} \quad (5\text{-}8)$$

By knowing the stiffness contribution of each layer/failure plane within a tenon, the proportion of load associated to each failure plane can be predicted as $F_i = {}^{n_i K_i}/_{\sum nK'}$ where $n_i$ is $n_A$, $n_B$, and $n_C$ which represent the number of instances of each failure plane $K_A$, $K_B$, and $K_C$ respectively. For example, as shown in Figure 5-10c $n_A = 2$, $n_B = 2$, and $n_C = 2$ for CLT5 C1 and C2 series. The resistance of each failure plane can be determined as a function of the strength criterion similar to the method proposed by Zarnani & Quenneville (2014). In the component model, failure of the tenon occurred when either longitudinal shear strength, $f_v$, rolling shear strength, $f_{rs}$, or compression parallel to the grain strength, $f_c$, is reached. Tenon failure occurred due to overloading of one of the failure planes which is the minimum of $F_v$, $F_{rs,in}$, $F_{rs,out}$, or $F_c$ as shown in Equation (5-9). The failure load is then determined as the summation of the critical failure plane load plus the load carried by the other planes. The $f_v$, $f_{rs}$, and $f_c$,

can be as per timber design standard or derived from material property testing. Accordingly, the strength of the castellated joint, $F_J$, is determined as:

$$F_J = min \begin{cases} F_v = f_v T_{L,0} L_T n_{L,0} \left(1 + \frac{n_B K_B}{n_A K_A} + \frac{n_C K_C}{n_A K_A}\right) \\ F_{rs,out} = f_{rs,out} H_T L_T n_{s,out} \left(\frac{n_A K_A}{n_B K_B} + 1 + \frac{n_C K_C}{n_B K_B}\right) \\ F_{rs,in} = f_{rs,in} H_T L_T n_{s,in} \left(\frac{n_A K_A}{n_C K_C} + \frac{n_B K_B}{n_C K_C} + 1\right) \\ F_C = f_c H_T T_{L,0} n_{L,0} \end{cases} \quad (5\text{-}9)$$

where $n_{L,0}$, $n_{s,in}$ and $n_{s,out}$ are the number of CLT layers oriented parallel to the loading direction and rolling shear planes respectively. Equation (5-9) is valid for $H_T / T_{L,0} \leq 3$ and $L_T / H_T \leq 3$ and the failure plane stiffness's $K_A$, $K_B$, and $K_C$ can be determined for any CLT layup and loading direction.

### 5.4.2 Input Component Data

In order to verify the component model developed herein, the modulus of elasticity parallel to grain, $E_0$, compression strength parallel to grain, $f_c$, shear modulus, $G_o$, rolling shear modulus, $G_{rs}$, shear strength, $f_v$, and rolling shear strength, $f_{rs}$, are required. These material properties can be determined from design codes such as NZS 3603 (1993) and generally accepted empirical relationships found in the CLT Handbook (2019) or through material property testing. In order to verify the component model with mean material properties, small samples were cut from untested timber of the same batch and tested in compression parallel to grain following EN 408 (2012) and in shear parallel to grain following ASTM D143-09 (2009). As previous material testing shown in Chapter 3 and Chapter 4 showed large density differences between CLT layers of different thickness, material property testing were performed on 45mm, and 20mm layers individually. The 45mm and 35mm CLT layers were planed from rough sawn 50x200 boards and the 20mm layer was planed from rough sawn 25x150mm boards. Therefore, $E_0$, $f_c$, $G_o$, and $f_v$ properties for the 35mm layer were assumed equal to the 45mm layer. The number of samples for each series of the compression and shear tests were 5 and 30 respectively in order to derive mean values. $G_{rs}$ and $f_{rs}$ of each individual layer were used from past tests by Li et al. (2019), which reported differences between 45mm, 35mm, and 20mm layers. Figure 5-11 shows the test set-ups used. The cross-section dimensions for the compression tests were 100mm x 175mm x 600mm high for CLT5 specimens and 70mm x 60mm x 360mm for CLT3 specimens. Displacements were measured using Particle Tracking Technology (PTT). Refer to Chapter 6, Section 6.5 for further details on PTT setup, implementation, and data processing in timber material property testing. Table 5-6 lists the measured properties with coefficient of variation in parenthesis. The reported $E_{0\text{-}End}$ includes the full specimen deformation and not the gauge length as specified in EN 408 (2012). Past research (Flaig et al., 2019; Newcombe et al., 2008) has reported that end effects due to local timber fibre crushing should be considered if they are present in the timber section or joint detail.

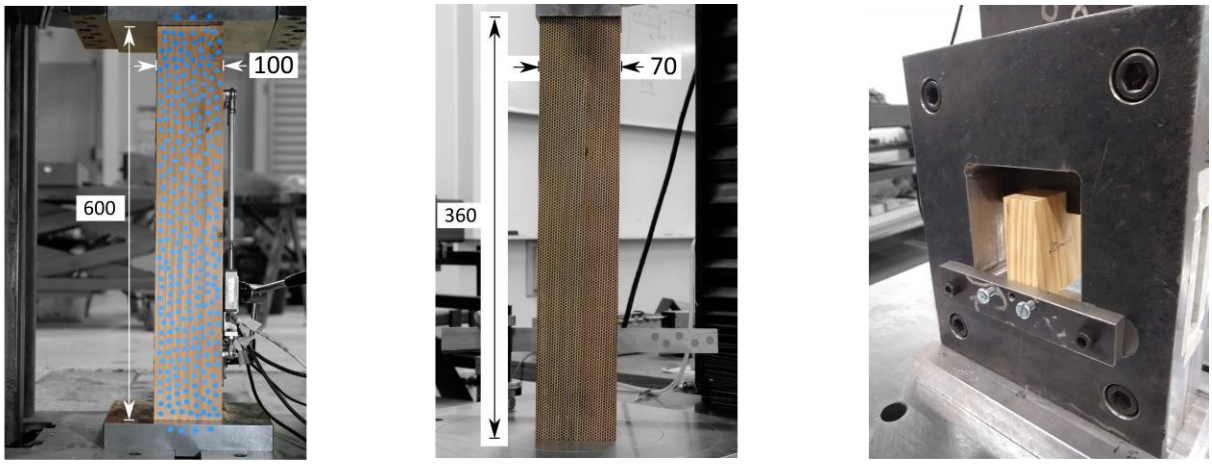


*Figure 5-11: (a) CLT5 compression parallel to grain testing; (b) CLT3 compression parallel to grain testing; (c) longitudinal shear testing*

*Table 5-6: Summary of mean material properties for input to component model*

| Layer thickness | $E_{0\text{-End}}$ | $f_c$ | $G_o$ | $G_{rs}$ (Li et al., 2019) | $f_v$ | $f_{rs}$ (Li et al., 2019) |
|---|---|---|---|---|---|---|
| | MPa | MPa | MPa | MPa | MPa | MPa |
| 45mm | 8,028 (4%) | 36.6 (9%) | 424 (13%) | 67 (21%) | 8.8 (10%) | 1.4 (22%) |
| 35mm | 8,028 (4%) | 36.6 (9%) | 424 (13%) | 78 (32%) | 8.8 (10%) | 1.7 (21%) |
| 20mm | 9,489 (4%) | 54.1 (7%) | 601 (18%) | 125 (22%) | 9.9 (14%) | 2.4 (23%) |

Table 5-7 lists the $E_0$, $f_c$, and $f_v$ material properties for Grade SG8 Douglas-Fir timber as per NZS3603 (1993). $G_o$, $G_{rs}$, and $f_{rs}$ were determined by empirical relationships given in the CLT Handbook (2019). By using Table 5-6 and Table 5-7, the component model could be assessed using experimentally determined mean material properties and material properties readily available to designers.

*Table 5-7: Summary of material properties using NZS 3603 and empirical relationships for input to component model*

| | $E_0$ | $f_c$ | $G_o$ | $G_{rs}$ | $f_v$ | $f_{rs}$ |
|---|---|---|---|---|---|---|
| | MPa | MPa | MPa | MPa | MPa | MPa |
| Relationship | Code | Code | $E_0$ / 15 | $G_0$ / 10 | Code | $f_v$ / 3 |
| Value | 8000 | 18 | 533 | 53 | 3 | 1 |

### 5.4.3 Analytical Prediction Comparison with Experimental Results

Figure 5-12 shows the ratios of the analytical model predictions to the average experimental results. In Figure 5-12, the governing strength failure criteria from Equation (5-9) is shown. The analytical model predictions used two sets of input data from Table 5-6 (informed) and Table 5-7 (code). It can be seen that series C4 was an outlier and as discussed, the model did not capture this failure mode due to the presence of a lamination gap and tension perpendicular to grain crack development as shown in Figure 5-8. Overall, the model was able to predict strength reasonably well with an average strength ratio of 0.92 excluding series C4. Using the informed material properties from Table 5-6, the average strength ratio for series C1 and C2, with loading perpendicular to the outer CLT layer, was 0.80. One possible reason for this strength under prediction is that bearing of the layer loaded perpendicular to grain is not considered in the model, and this area is more significant in series C1 and C2. This was chosen to simplify the component model to allow a relative displacement between the CLT layers to activate rolling shear load transfer. In reality the tenon deformed shape and inter layer deformed shape shown in Figure 5-13 is more complex than the simple triangles assumed in Figure 5-9 and Figure 5-10. The average ratio for tenon C3 with loading parallel to the outer CLT layer was 1.17. One possible reason for the analytical strength over prediction is that tenon C3 strength was more significantly governed by parallel to grain shear strength. Because the mean longitudinal shear strength from small shear block specimens is expected to be higher than the shear strength of larger specimens due to size effects (Foschi & Barrett, 1976), a higher strength prediction occurred. The average strength ratio using code material properties was 0.35 for series C1 and C2 and 0.56 for tenon C3, which highlights the higher strength under prediction when using code values. When code input values were used, the critical failure plane was the parallel to grain and longitudinal shear deformation failure plane, $K_A$. When informed values were used the critical failure plane depended on the geometry of the joint. This was primarily due to the strength and stiffness differences reported in Table 5-6 for different CLT layers.

Based on observed after test photos of the outer CLT layer as shown in Figure 5-13, deformation and rotation outside the tenon influence zone occurred. This implied that some bending deformation occurred. Future work should determine a true centre of rotation which accounts for additional deformation on the tenon and mortise side, and differences between the layers of CLT which could change load distribution and castellated joint deformation assumptions. However, the stiffness based analytical component model developed was able to predict the join strength with reasonable accuracy neglecting deformation due to bending given the tenon length to height maximum ratio limitation of 3:1 and ensuring there was no lamination gap within the tenon.

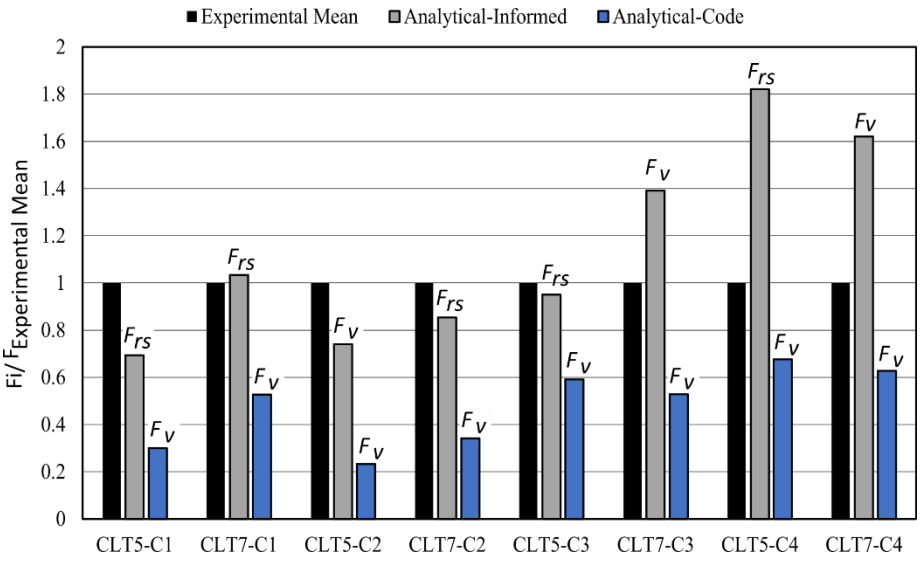


*Figure 5-12: Strength predictions summary*

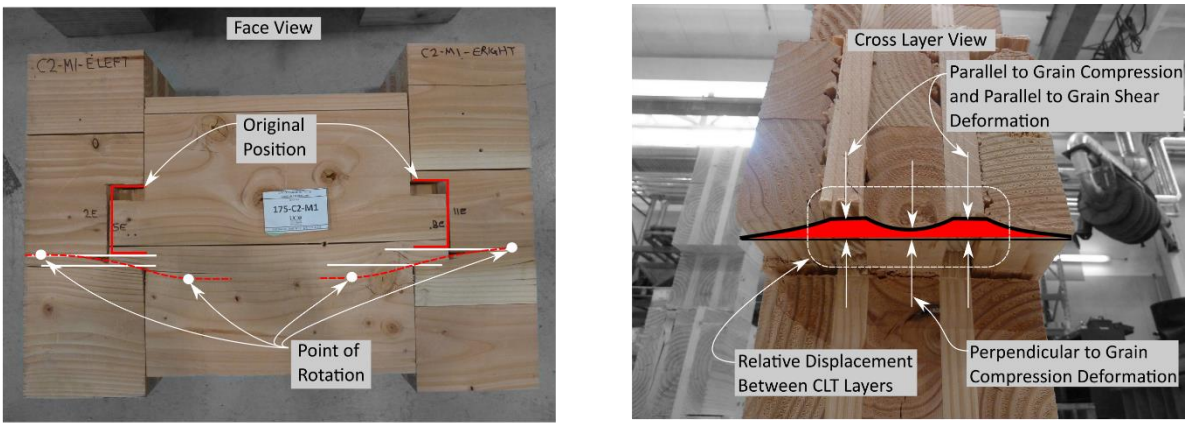


*Figure 5-13: Observed after test deformation; (a) face view, and (b) cross layer view*

## 5.5 CONCLUSIONS

The chapter mainly investigated CLT shear connections using castellated carpentry joints and compared their performance to commonly used commercial angle bracket connectors. A total of 29 castellations and 6 angle bracket joint specimens were tested use 5-layer and 7-layer CLT specimens. The castellation geometry was changed by varying the tenon length to height ratio. For both the castellated and angle bracket joints, shear loading perpendicular and parallel to the outer CLT layer were investigated. This study provided valuable information for a better understanding of the increased performance potential of castellated carpentry joints as capacity protected shear connections in CLT shear wall systems with increased strength and stiffness demands. The key findings are summarized as follows:

- Castellated joints were able to achieve high strength and stiffness. Their strength and stiffness values were 2.5 and more than 7 times greater when compared to the joints using the angle brackets.
- Castellated joints did not experience sudden load drops once longitudinal or rolling shear failure occurred mainly due to the cross-layer reinforcement. This effect was more pronounced with thicker seven-layer CLT specimens than five-layer CLT specimens.
- The presented stiffness-based analytical component model was found to be adequate to estimate joint strength with reasonable accuracy.
- The commercial angle brackets tested herein had significantly lower experimental stiffness, more than 2.5 times lower than the Eurocode 5 prediction equation. The steel angle bracket underwent significant in-plane and out-of-plane deformation. Further, peak strength was limited due to timber failure and not a more favourable nail yielding and timber embedment crushing mechanism. The increased angle bracket size, nail geometry, and CLT size meant that loading eccentricities were increased and the nail primarily penetrated only the outer layer of the CLT specimen. Reduced nail patterns and penetrating the nail through more than one CLT layer could help avoid unfavourable timber failure mechanisms.
- To overcome the limitations of the testing and analytical component method presented in this study, future work should study castellated joints with different tenon geometries, with increased tenon heights and with lamination gaps within the tenon. The analytical component method should be extended to account for the influence of lamination gaps within the tenon and to capture other timber failure modes such as tension perpendicular to grain failure.

## 5.6 REFERENCES

Aira, J. R., Descamps, T., Van Parys, L., & Léoskool, L. (2015). Study of stress distribution and stress concentration factor in notched wood pieces with cohesive surfaces. *European Journal of Wood and Wood Products*, *73*(3), 325–334. https://doi.org/10.1007/s00107-015-0891-3

Amini, M. O., van de Lindt, J. W., Rammer, D., Pei, S., Line, P., & Popovski, M. (2018). Systematic experimental investigation to support the development of seismic performance factors for cross laminated timber shear wall systems. *Engineering Structures*, *172*, 392–404. https://doi.org/10.1016/j.engstruct.2018.06.021

ASTM International. (2009). ASTM D143-09 - Standard Test Methods for Small Clear Specimens of Timber. In *ASTM International*. American Society for Testing and Materials. https://doi.org/10.1520/D0143-09.2

Benedetti, F., Rosales, V., Opazo-Vega, A., Norambuena-Contreras, J., & Jara-Cisterna, A. (2019). Experimental and numerical evaluation of hold-down connections on radiata pine Cross-Laminated-Timber shear walls: a case study in Chile. *European Journal of Wood and Wood Products*, *77*(1), 79–92. https://doi.org/10.1007/s00107-018-1365-1

Branco, J. M., & Descamps, T. (2015). Analysis and strengthening of carpentry joints. *Construction and Building Materials*, *97*, 34–47. https://doi.org/10.1016/j.conbuildmat.2015.05.089

Branco, J. M., Verbist, M., & Descamps, T. (2018). Design of three Step Joint typologies: Review of European standardized approaches. *Engineering Structures*, *174*(February), 573–585. https://doi.org/10.1016/j.engstruct.2018.06.073

Buchanan, A. (2016). The challenges for designers of tall timber buildings. *WCTE 2016 - World Conference on Timber Engineering*.

Cao, J., Xiong, H., Zhang, F. L., Chen, L., & Ramonell Cazador, C. (2020). Bayesian model selection for the nonlinear hysteretic model of CLT connections. *Engineering Structures*, *223*(July), 111118. https://doi.org/10.1016/j.engstruct.2020.111118

Casagrande, D., Bezzi, S., D'Arenzo, G., Schwendner, S., Polastri, A., Seim, W., & Piazza, M. (2020). A methodology to determine the seismic low-cycle fatigue strength of timber connections. *Construction and Building Materials*, *231*, 117026. https://doi.org/10.1016/j.conbuildmat.2019.117026

CEN. (1991). *EN 26891 - Joints made with mechanical fasteners. General principles for the determination of strength and deformation characteristics*. European Committee for Standardization (CEN).

CEN. (2005). *EN12512: Timber structures: test methods : cyclic testing of joints made with mechanical fasteners : [including amendment A1:2005]* (Issue Book, Whole). European Committee for Standardization.

CEN. (2012). *EN 408:2010+A1:2012*. European Committee for Standardization (CEN).

CEN. (2014). Eurocode 5: Design of timber structures-Part 1-1: General-Common rules and rules for buildings. In *EN1995-1-1:2004-11 + AC2006-06 + A1:2008-06 + A2:2014-05 Eurocode 5*. European Committee for Standardization.

Claus, T., Riehle, T., Seim, W., & Götz, T. (2018). Interlocking shear wall connections. *WCTE 2018 - World Conference on Timber Engineering*, 3–8.

ETA-11/0030. (2019). *Rotho Blass Self-tapping screws and threaded rods*. ETA-Danmark A/S.

ETA-11/0496. (2018). *Rotho Blaas Titan Angle Brackets*. ETA-Danmark A/S.

ETA-12/0114. (2017). *SPAX self-tapping screws- screws for use in timber constructions* (Issue 305). ETA-Danmark A/S.

ETA-13/0523. (2018). *Nails and screws for use in nailing plates in timber structures*. ETA-Danmark A/S.

Flaig, M., Schmidt, T., & Blaß, H. J. (2019). Compressive strength and stiffness of end grain contact joints in glulam and CLT. *International Network on Timber Engineering Research (INTER) - Meeting Fifty-Two, Tacoma (US)*, *Fig 1*, 1–13.

Flatscher, G., Bratulic, K., & Schickhofer, G. (2015). Experimental tests on cross-laminated timber joints and walls. *Proceedings of the Institution of Civil Engineers - Structures and Buildings*, *168*(11), 868–877. https://doi.org/10.1680/stbu.13.00085

Foschi, R. O., & Barrett, J. D. (1976). Longitudinal shear strength of Douglas-Fir. *1Canadian Journal of Civil Engineering*, *3*(2), 198–208.

FPInnovations. (2019). *CLT Handbook* (E. Karacabeyli & S. Gagnon (eds.)). FPInnovations.

Gavric, I., Fragiacomo, M., & Ceccotti, A. (2015). Cyclic behaviour of typical metal connectors for cross-laminated (CLT) structures. *Materials and Structures/Materiaux et Constructions*, *48*(6), 1841–1857. https://doi.org/10.1617/s11527-014-0278-7

Izzi, M., Flatscher, G., Fragiacomo, M., & Schickhofer, G. (2016). Experimental investigations and design provisions of steel-to-timber joints with annular-ringed shank nails for Cross-Laminated Timber structures. *Construction and Building Materials*, *122*, 446–457. https://doi.org/10.1016/j.conbuildmat.2016.06.072

Izzi, M., Polastri, A., & Fragiacomo, M. (2018). Modelling the mechanical behaviour of typical wall-to-floor connection systems for cross-laminated timber structures. *Engineering Structures*, *162*(February 2017), 270–282. https://doi.org/10.1016/j.engstruct.2018.02.045

Izzi, M., Rinaldin, G., Polastri, A., & Fragiacomo, M. (2018). A hysteresis model for timber joints with dowel-type fasteners. *Engineering Structures*, *157*(July 2017), 170–178. https://doi.org/10.1016/j.engstruct.2017.12.011

Li, M., Dong, W., & Lim, H. (2019). Influence of lamination aspect ratios and test methods on rolling shear strength evaluation of Cross-Laminated Timber. *Journal of Materials in Civil Engineering*, *31*(12), 1–11. https://doi.org/10.1061/(ASCE)MT.1943-5533.0002977

Newcombe, M. P., Pampanin, S., Buchanan, A., & Palermo, A. (2008). Section analysis and cyclic behavior of post-tensioned jointed ductile connections for multi-story timber buildings. *Journal of Earthquake Engineering*, *12*, 83–110. https://doi.org/10.1080/13632460801925632

Polastri, A., Izzi, M., Pozza, L., Loss, C., & Smith, I. (2019). Seismic analysis of multi-storey timber buildings braced with a CLT core and perimeter shear-walls. *Bulletin of Earthquake Engineering*, *17*(2), 1009–1028. https://doi.org/10.1007/s10518-018-0467-9

Quenneville, P., & Zarnani, P. (2014). Wood Block Tear-Out Resistance and Failure Modes of Timber Rivet Connections: A Stiffness-Based Approach. *Journal of Structural Engineering*, *140*(2), 4013055. https://doi.org/10.1061/(ASCE)ST.1943-541X.0000840

Schmidt, T. (2018). *Kontaktverbindungen für aussteifende Scheiben aus Brett sperrholz*. KIT Scientific Publishing.

Schmidt, T, & Blaß, H. J. (2016). Contact joints in engineered wood products. *WCTE 2016 - World Conference on Timber Engineering*.

Schmidt, Tobias, & Blaß, H. J. (2018). In-plane shear connection for CLT diaphragms. *International Network on Timber Engineering Research (INTER)*, *51-07–4*, 1–12.

Siem, J. (2017). The single-step joint–a traditional carpentry joint with new possibilities. *International Wood Products Journal*, *8*, 45–49. https://doi.org/10.1080/20426445.2017.1302148

Siem, J., & Jorissen, A. (2015). Can taditional carpentry joints be assessed and designed using modern standards. *Structural Health Assessment of Timber Structures*.

Standards New Zealand. (1993). *NZS 3603: Timber structures standard*. Standards New Zealand.

Tomasi, R, & Smith, I. (2015). Experimental characterization of monotonic and cyclic loading responses of CLT Panel-To-Foundation Angle Bracket Connections. *Journal of Materials in Civil Engineering*,

*27*(6). https://doi.org/10.1061/(ASCE)MT.1943-5533.0001144

Tomasi, Roberto, & Sartori, T. (2013). Mechanical behaviour of connections between wood framed shear walls and foundations under monotonic and cyclic load. *Construction and Building Materials*, *44*, 682–690. https://doi.org/10.1016/j.conbuildmat.2013.02.055

Verbist, M., Branco, J. M., Poletti, E., Descamps, T., & Lourenço, P. B. (2017). Single Step Joint: overview of European standardized approaches and experimentations. *Materials and Structures/Materiaux et Constructions*, *50*(2). https://doi.org/10.1617/s11527-017-1028-4

Yurrita, M., & Cabrero, J. M. (2020). New design model for brittle failure in the parallel-to-grain direction of timber connections with large diameter fasteners. *Engineering Structures*, *217*(September 2019), 110557. https://doi.org/10.1016/j.engstruct.2020.110557

# 6 Experimental design and testing of post-tensioned and conventional shear walls and core-walls

*Part of the work presented herein is based on the articles cited below:*

*J.R. Brown, M. Li, A. Palermo, S. Pampanin, F. Sarti, Experimental testing of a low-damage post-tensioned C-Shaped CLT core-wall, J. Struct. Eng. 147 (2021) 1–16. https://doi.org/10.1061/(ASCE)ST.1943-541X.0002926.*

*J. Brown, M. Li, A. Palermo, S. Pampanin, F. Sarti, Bi-directional seismic testing of post-tensioned rocking CLT walls and core-walls, in: WCTE 2021, Santiago, Chile, 2021.*

J. Brown, M. Li, R. Nokes, A. Palermo, S. Pampanin, F. Sarti, Investigating the compressive toe of post-tensioned CLT core-walls use Particle Tracking Technology, in: 17th World Conf. Earthq. Eng. 17WCEE, Sendai, Japan, 2021.

*Key Findings / Outputs:*

- A total of 17 CLT wall tests were performed. The wall configurations included post-tensioned (PT) single walls, PT double walls, PT core-wall, and one conventional core-wall.
- The mixed angle screwed connection solution was the most effective and was able to provide significant joint stiffness, displacement capacity, and energy dissipation.
- Significant system strength/stiffness and ductility/drift capacity were achieved in the PT C-shaped CLT core-wall with minimal damage through careful connection detailing. The highest core-wall composite action of approximately two-thirds was achieved and the core-wall stiffness at SLS drift level was greater than eight times that of a single wall for an approximate 3.5 times increase in wall area.
- Particle tracking technology implemented at the wall base confirmed approximately linear timber strain behaviour along the compressive toes throughout the wall testing. It was also found that the compression flange in the core-wall was not significantly engaged as low compressive timber strains and significant out-of-plane rotation at its base were observed.
- During some PT double wall and core-wall tests, a negative neutral axis wall depth occurred which indicated wall uplift (Web and/or Flange Walls) due to the significant strength and stiffness of the screwed connections implemented at the in-plane and orthogonal joints.

## 6.1 INTRODUCTION

This chapter presents a three-phase shear wall test programme including four post-tensioned (PT) CLT single wall (SW) tests in Phase I, five PT double wall (DW) tests in Phase II, and seven PT core-wall tests and one conventional core-wall test in Phase III. The primary objective of this study is to quantify the increase in system strength and system achievable when PT CLT walls are connected together primarily with self-tapping screws (STS) to create a partial composite double wall and C-shaped core-wall system. The key findings from STS connection testing reported in Chapter 4 were incorporated into the test specimen design. Secondary objectives include investigating the compression toe of PT CLT walls using Particle Tracking Technology (PTT) and comparing a PT core-wall to a benchmark conventional core-wall system.

In Section 6.2 an overview of the testing plan and its objectives is presented. Sections 6.3 and 6.4 discuss the test specimen detailing and the test programme. Section 6.5 presents the instrumentation including the use of PTT to evaluate the compressive toe behaviour at the base of each CLT wall. Section 6.6 presents the results of each testing phase.

## 6.2 TESTING PLAN

A total of 17 wall tests were performed in the shear wall testing programme: 4 PT SW tests, 5 PT DW tests, 7 PT core-wall tests and one conventional core-wall test. In order to understand the increased strength and stiffness contribution due to each component (wall and joint), the proposed core -wall system was decoupled and PT SW and DW tests were investigated first. The three-phase testing programme is shown in Figure 6-1.

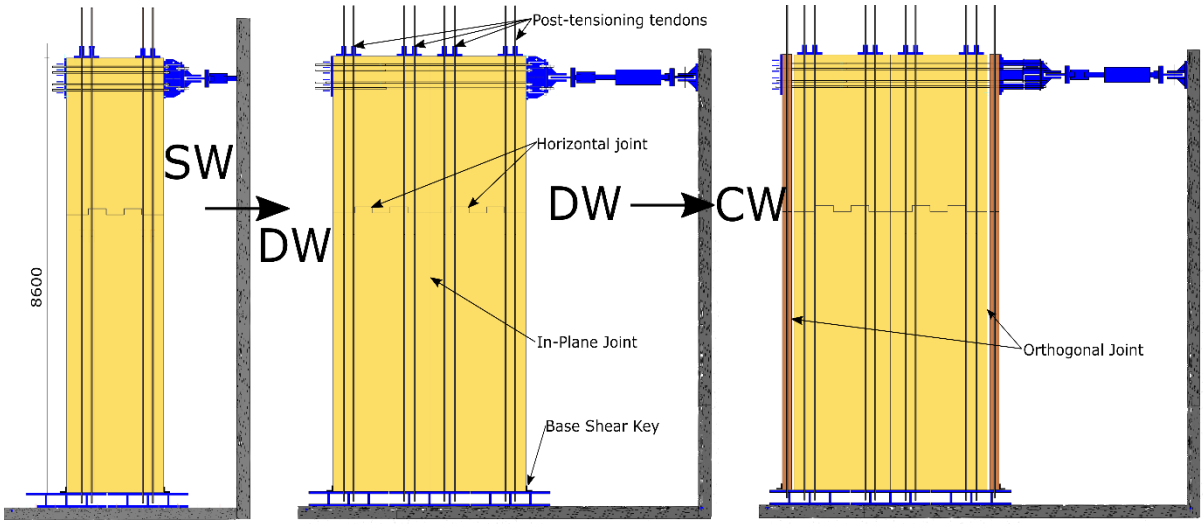


*Figure 6-1: Three phase shear wall testing plan programme: single wall, double wall, and core-wall*

Table 6-1 lists the key variables and objectives of each shear wall testing phase. By decoupling the four wall core-wall system into its individual components, the individual component behaviour and the overall composite effect could be quantified. The results of the SW and DW testing informed decisions made for the core-wall testing and then the development of analytical models.

*Table 6-1: Objectives of shear wall testing programme by testing phase*

| Phase | Key Variables | Objectives |
|---|---|---|
| SW | • Initial post-tensioning force | • Verify single wall analytical model behaviour<br>• Investigate compressive strains at the base and compare to analytical model |
| DW | • STS connection detail<br>• Use of UFPs at wall base | • Quantify influence of friction between two walls in quasi-static cyclic testing<br>• Quantify impact of in-plane screwed connection detail on system performance<br>• Provide experimental data to develop DW analytical models |
| Core-wall | • STS connection detail<br>• Use of UFPs at wall base<br>• Initial post-tensioning force<br>• Loading protocol | • Quantify increase in stiffness and strength achievable in core-wall systems<br>• Understand influence of orthogonal joints on core-wall system performance<br>• Quantify effect of tensile and compressive flanges on core-wall system performance<br>• Provide experimental data to develop core-wall analytical models<br>• Quantify the differences between PT and conventional CLT core-wall systems |

Figure 6-2 shows the critical components of the core-wall system for the PT and conventional core-wall specimens. The prior connection testing knowledge (Chapters 3-5) ensured stable connection behaviour under cyclic loading. The strength hierarchy among the wall components are described as follows. For the PT wall specimens, the un-bonded PT bars provided strong and stiff elastic base connections with wall recentering capability while the self-tapping screws (STS) connections provided the main source of energy dissipation as ductile links between the CLT wall panels at the orthogonal and in-plane joints. U-shaped Flexural Plate (UFP) devices also provided stable energy dissipation but they were primarily installed to investigate different connection details' performance under bi-directional loading. For the conventional core-wall specimen, ductile links with mixed angle STS hold-downs were detailed. In addition, the in-plane joint was detailed with mixed angle STS to ensure displacement capacity and energy dissipating capability. Figure 6-2 shows schematics of these ductile links. Commercial angle brackets (ETA-11/0496, 2018) were installed with a full nailing pattern of $\phi$4x60mm LBA nails (2018) at the orthogonal joint and designed to be capacity protected. At the horizontal joint, capacity protected dowelled and STS tie-down connections were designed as shown in Figure 6-2b to resist overturning moments. For both the PT and conventional core-wall specimens, capacity protected castellations at the horizontal joints provided shear transfer between the upper wall panels and the lower wall panels.

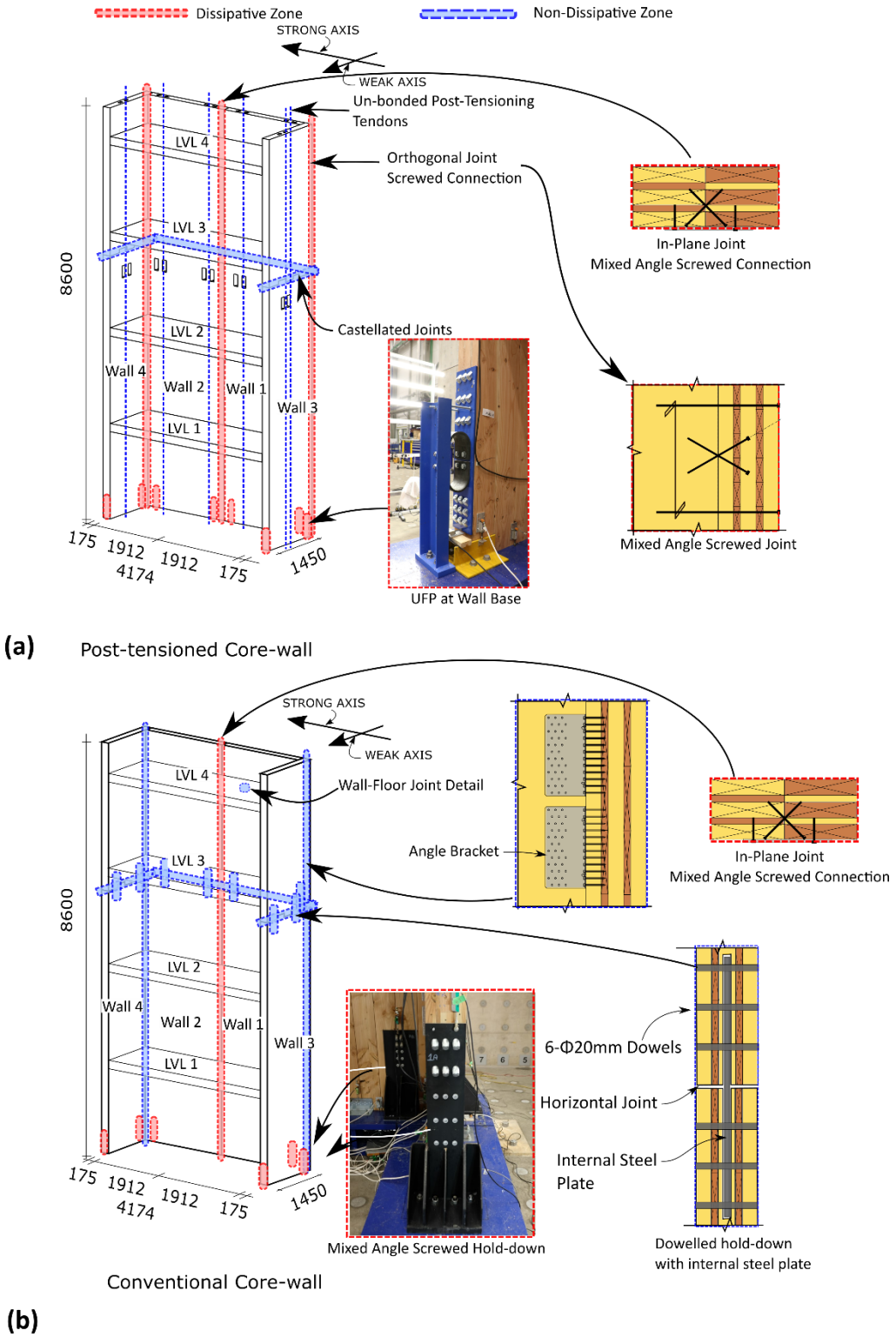


*Figure 6-2: Hierarchy of strength highlighting dissipative (in red) and non-dissipative (in blue) zones for (a) post-tensioned core-wall system, and (b) conventional core-wall system*

## 6.3 GENERAL TEST SPECIMEN DETAILING

### 6.3.1 Wall Section Design

The wall specimens were four-storey high (8.6m) with a 2/3 scale factor. The CLT wall panels were five-ply and 175mm thick (45/20/45/20/45), with visually graded SG8 grade Douglas-Fir laminations as specified in NZS3603 (1993). The CLT was fabricated by XLam NZ Ltd. (2017), face-glued with polyurethane adhesive and pressed by a vacuum press. To accommodate internal post-tensioning bars, 100mm x 45mm ducts were maintained in the middle layer of the CLT wall panels as shown in Figure 6-3. Table 6-2 lists the mechanical properties of the CLT, post-tensioning bars and steel dissipaters. Each wall had a horizontal castellated joint at 5.5m height which will be discussed further in the castellation design.

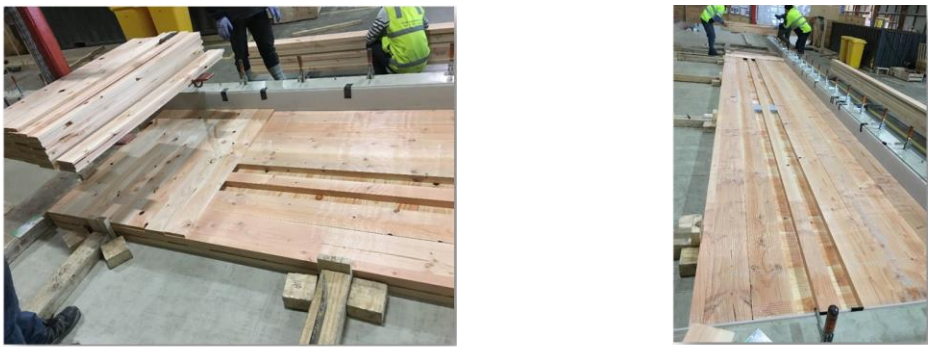

(a) (b)

*Figure 6-3: CLT fabrication with 100mm x 45mm void for unbonded post-tensioning bars*

*Table 6-2: Material properties*

| Material | Property | Value |
|---|---|---|
| Cross-laminated timber | Modulus of elasticity, $E_0$ (MPa) | 8,000 |
| | Characteristic compression strength parallel to grain, $f_c$ (MPa) | 18 |
| | Characteristic compression strength perpendicular to grain, $f_{c,90}$ (MPa) | 8.9 |
| Post-tensioning steel | Modulus of elasticity, $E_{pt}$ (GPa) | 170 |
| | Yield stress, $f_{y,pt}$ (MPa) | 835 |
| | Ultimate stress, $f_{u,pt}$ (MPa) | 1,030 |
| Mild steel (flat bar) | Modulus of elasticity, $E_s$ (GPa) | 200 |
| | Yield stress, $f_{y,s}$ (MPa) | 300 |

Figure 6-4 and Figure 6-5 shows the SW and DW test plan view. While each wall had a horizontal joint at 5.5m height with castellation, during SW and DW testing blue steel straps were installed (see Figure

6-23 and Figure 6-24) with self-tapping screws (STS) which prevented any significant movement during these testing phases. Figure 6-5 shows the location of the void within the CLT walls for internal post-tensioning bars (labelled PT).

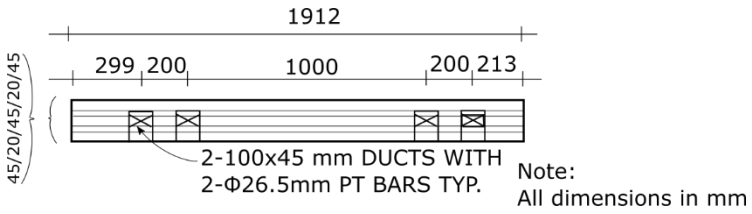


*Figure 6-4: Single wall test plan view*

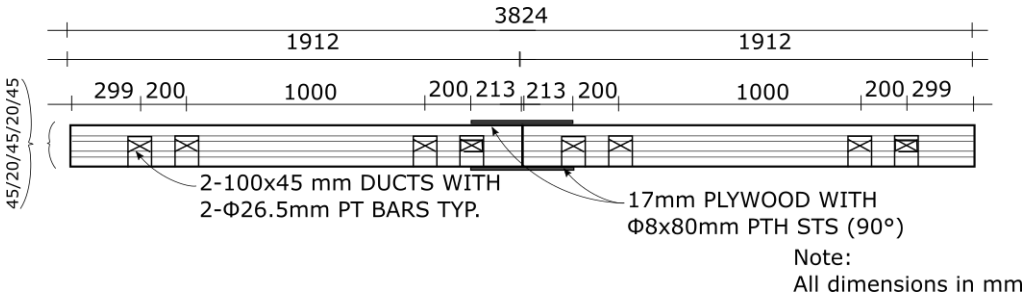


*Figure 6-5: Double wall test plan view*

Figure 6-6 shows the testing arrangement for the core-wall phase. The same walls which were used during the SW and DW testing phase were implemented in the core-wall phase and these walls were the Web Walls described herein. All the wall components were designed to be assembled with a 2mm tolerance. Figure 6-6a shows the orientation of the four panels with respect to each other and location of the PT bars. Web Walls 1 and 2 were 1912mm in length and Flange Walls 3 and 4 were 1450mm in length. The Flange Walls were overlapped with the Web Walls such that contact bearing would occur at the orthogonal joint during strong axis loading. The butt joint was maintained for the in-plane connection. Each wall had a horizontal joint at 5.5m height which will be discussed further in castellation design.

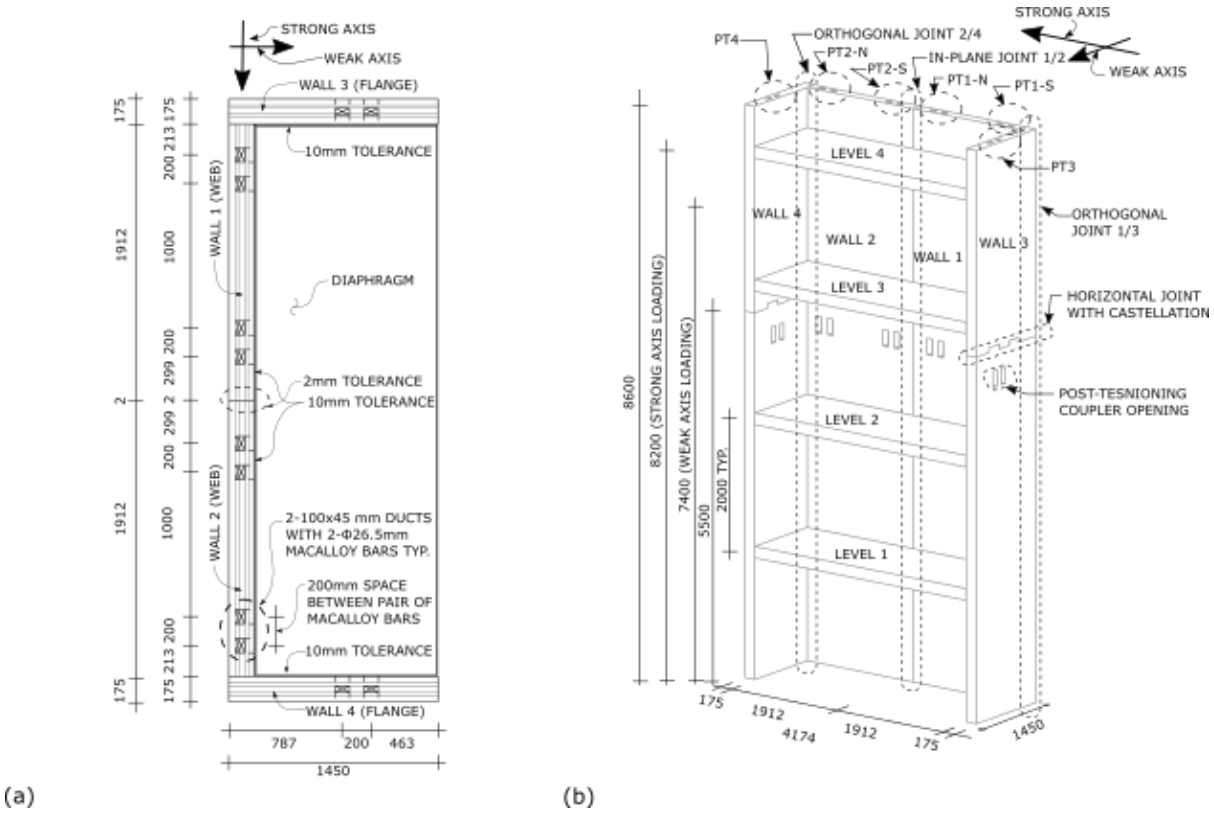


*Figure 6-6: Core-wall experimental design: (a) core-wall plan view arrangement, and (b) core-wall test isometric*

### 6.3.2 Self-Tapping Screw Connections

The in-plane and orthogonal joints employed self-tapping screws (STS) and during each test different details were employed. Past research has reported that depending on the STS installation angle, STS connections have significantly different behaviour in terms of strength, stiffness and displacement capacity (Loss et al., 2018). For example, Figure 6-7 compares the force-displacement curves of Chapter 4 STS connection testing with different installation angles and threaded embedment lengths. The results are shown as a group of four STS. When comparing the Long Inclined and the Short Indined tests, it is shown that the threaded embedment length should be limited to ensure gradual screw withdrawal failure instead of brittle screw tensile failure. As presented in Chapter 4, the threaded embedment length should be limited to 12d (12 times the screw diameter) to avoid screw tensile failure. When comparing different STS combination ratios, it was found that a ratio of one 90° STS for every two inclined STS ensured significant increase in connection displacement capacity. In the Mixed Angle test at 8mm displacement, some STS failed but this occurred gradually and was not a "zipper-like" failure of all STS as occurred in the Long Inclined test. Further, 90° STS contributed to both the strength and stiffness of the mixed angle STS joints. While 90° fully threaded (FT) STS experienced significant rope effect, Eurocode 5 (2014) limits the rope effect contribution to 100% of the lateral capacity, which is shown in blue in Figure 6-7.

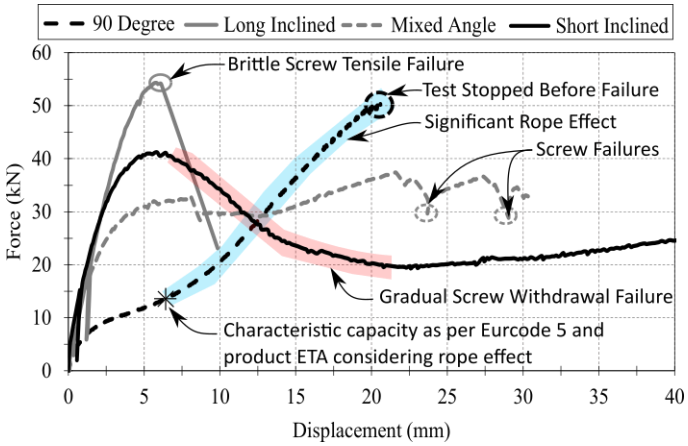


*Figure 6-7: Selection of force-displacement curves from STS connection testing in Chapter 4*

During the DW and core-wall testing, $\phi$8mm screws were installed into $\phi$5mm predrilled holes to 70% of the screw length with jigs to ensure correct alignment. Figure 6-8 shows a photo of the jig and screw install along the in-plane and orthogonal joints.

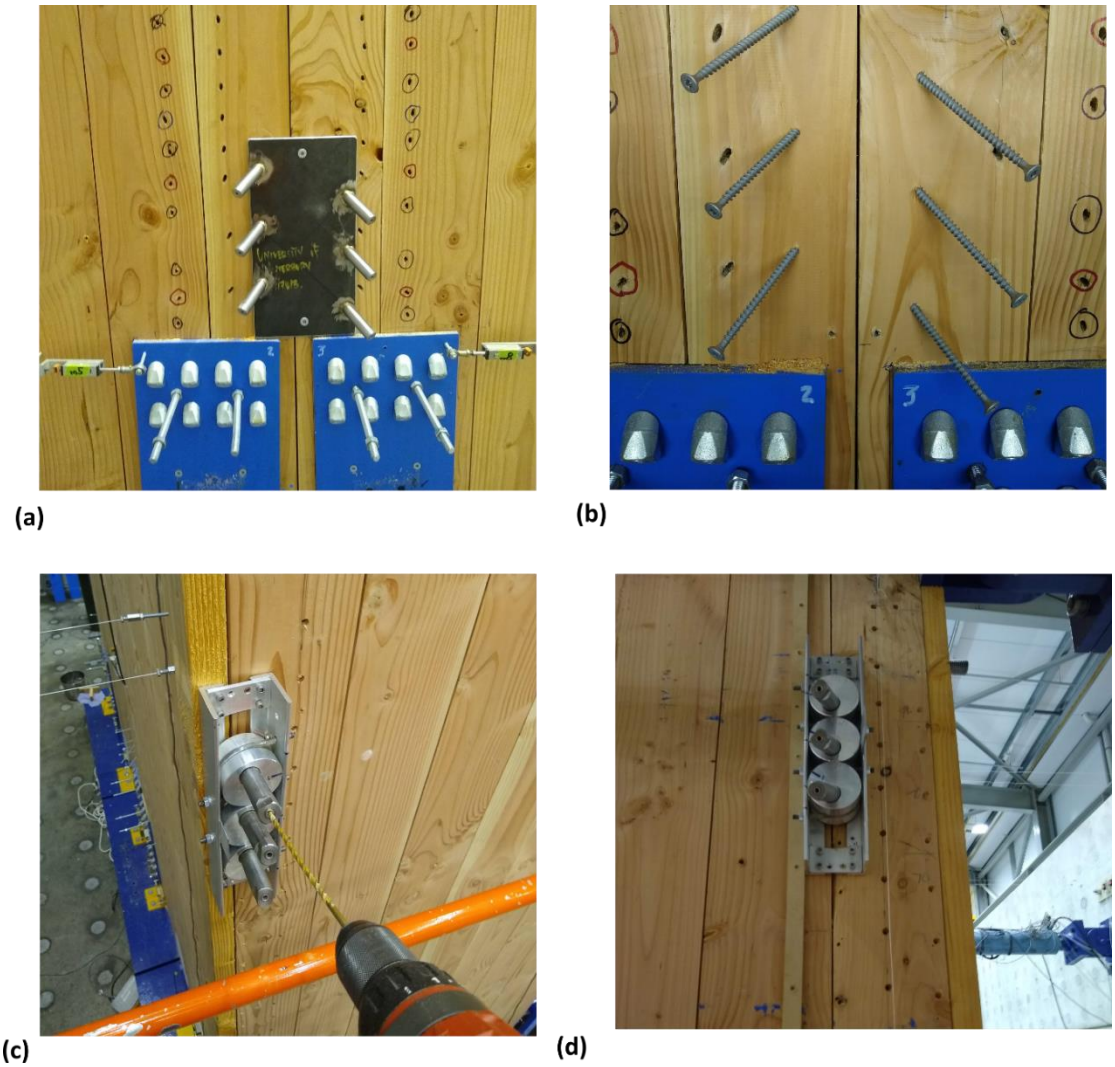


*Figure 6-8: STS installation methodology: (a) and (b) In-plane joint, (c) and (d) orthogonal joint*

After each test, all of the screws were removed from the specimen and new screws were installed in a different location following the minimum spacing requirement as per Eurocode 5 (2014). As the damage in the CLT walls was very localized, it was possible to run a number of tests by shifting the screw locations without impairing the connection behaviour significantly. This is also one advantage of using STS connections in mass timber products such as CLT to improve reparability. The specific screwed connection details employed during the DW and core-wall testing are discussed in Section 6.3.2.1 and Section 6.3.2.2.

### *6.3.2.1 STS connection details in double wall testing*

Figure 6-9 shows the STS connection detailing implemented at the in-plane joint. $\phi$8x80mm PTH STS (ETA-12/0114, 2017) were installed with 17mm thick plywood as per NZS 3603 (Standards New Zealand, 1993) with minimum $a_1$ spacing (=10d) as per Eurocode 5 (2014). The number of STS installed during each test is specified in Table 6-6.

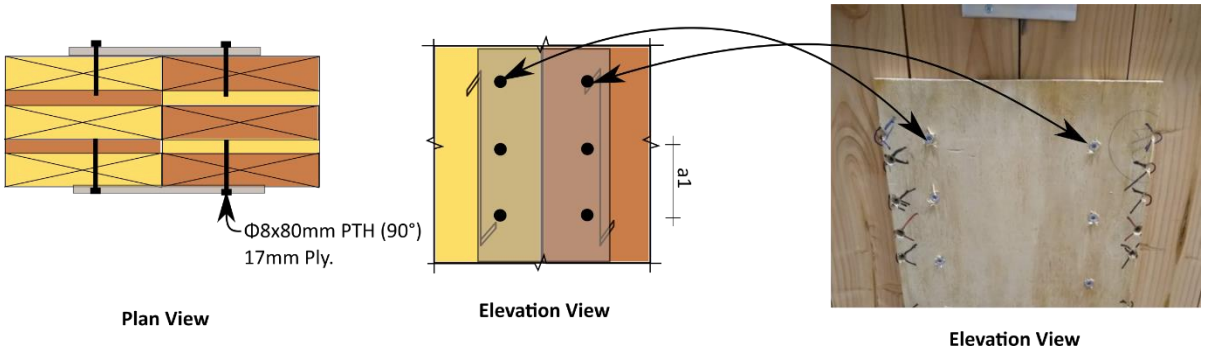


*Figure 6-9: STS connection detailing during double wall testing phase*

### *6.3.2.2 STS connection details in core-wall testing*

For core-wall testing, the different screw installations for the in-plane and orthogonal joint are shown in Figure 6-10. The screws were installed at 90°, inclined, or mixed inclinations which can provide different connection strength, stiffness and displacement capacity. The design summary of yield strength ($F_y$) and stiffness ($K_{ser}$) is provided in Table 6-3. The contribution from friction was neglected as reported by past research with 'X' pattern STS (Blaß & Bejtka, 2001; Loss et al., 2018). For the in-plane joint, PTH or FT screws were installed either at 90° with plywood or at a 45° + 45° double inclination. For the orthogonal joint, FT screws were installed either at 90° or at a 60° + 15° double inclination. All inclined STS were installed with the minimum spacing ($a_1$=10d) according to Eurocode 5 (2014) and European Technical Approval (ETA) (ETA-12/0114, 2017). There was equal screw threaded length in each timber side member, which meant that countersinking was required on the orthogonal joint. In addition to providing system stiffness through composite action (CA), the STS can provide a source of energy dissipation under large wall deformations (Lauriola & Sandhaas, 2006; Popovski et al., 2010).

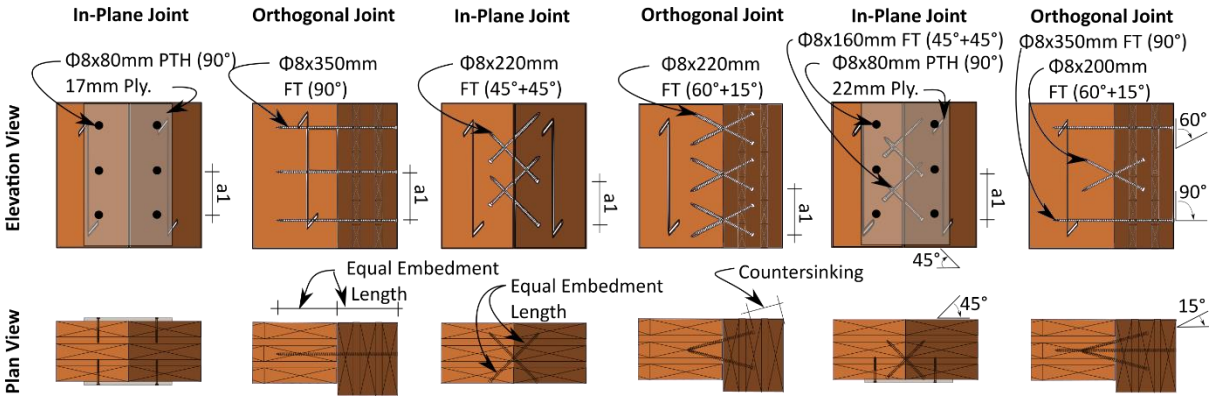


*Figure 6-10: STS connection detailing: (a) tests CW-2 and CW-7, (b) test CW-5, and (c) test CW-6*

*Table 6-3: Screwed connection design summary*

| Test | CW-2 & CW-7 | | CW-5 | | CW-6 | | |
|---|---|---|---|---|---|---|---|
| Joint | In-Plane | Orthogonal | In-Plane | Orthogonal | In-Plane | Orthogonal | |
| | | | | | | Wall 1/3 Joint | Wall 2/4 Joint |
| $F_y$ (kN/m) | 36 | 30 | 60 | 84 | 150 | 68 | 63 |
| $K_{ser}$ (kN/mm/m) | 18 | 23 | 45 | 67 | 121 | 55 | 51 |

Note: $F_y$ = yield strength prediction per meter of wall, where shear-tension and shear compression screws were determined as per analytical methods presented in Chapter 4 and Brown et al. (2021) and SPAX ETA-Danmark (ETA-12/0114, 2017), and 90° screws were considered as per Eurocode 5 (2014) and SPAX ETA-Danmark (ETA-12/0114, 2017); and $K_{ser}$ = stiffness prediction per meter of wall, which was considered as per analytical methods presented in Chapter 4 and Brown et al. (2021) and SPAX ETA-Danmark (ETA-12/0114, 2017).

### 6.3.3 Post-tensioning Bar and Anchorage Design

High strength PT threaded bars in diameter of $\phi$26.5mm (ETA-07/0046, 2018) were used to anchor the CLT walls to the foundation. Figure 6-11 shows the size and placement of the bars to ensure adequate load spreading in the CLT walls while satisfying the lab constraints. A 500mm long x 50mm thick steel anchorage plate was used to spread the load from a pair of $\phi$26.5mm high strength bars at the top of the CLT wall. The Web Walls contained four PT bars and the Flange Walls contained two PT bars per wall. Pairs of PT bars were spaced 200mm apart. Because the standard length of the PT bars is 5.6m, a mechanical coupler was required at the height of 5.1m to have continuous PT forces from the foundation to the wall top. To provide access to the mechanical coupler, a 250mm x 100mm opening was cut into the CLT. The PT anchorage details are shown in Figure 6-11. The specific placement of the PT bars for each CLT wall is shown in Figure 6-6.

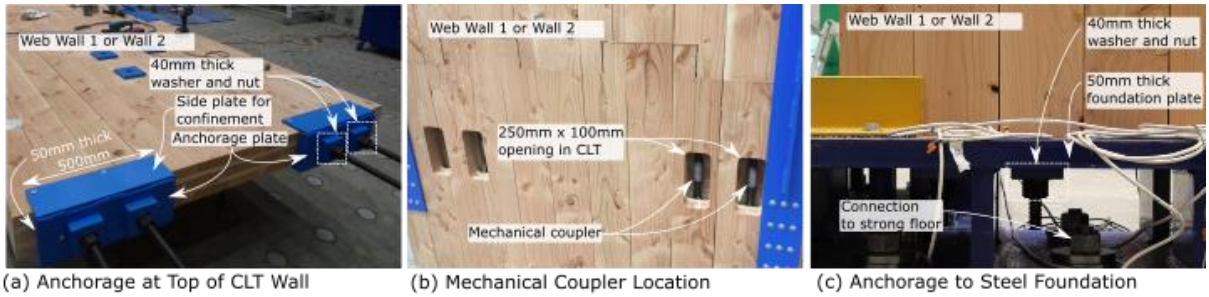


*Figure 6-11: Post-tensioning anchorage details: (a) anchorage at top of CLT wall, (b) mechanical coupler location, and (c) anchorage to steel foundation*

### 6.3.4 Castellation Design

Each CLT wall panel had a horizontal castellated joint located at a wall height of 5.5m to transfer horizontal shear load. The purpose of the horizontal joint was to evaluate the effectiveness of such joints transferring high shear loads, which had been previously verified through connection testing in Chapter 5. The castellation height location was chosen to ensure sufficient diaphragm restraint and the two diaphragms above the castellation provided out-of-plane restraint. The castellation only provided the in-plane restraint. Further, the location of the castellation was high enough to ensure that gap opening would not occur as the moment due to the applied lateral force was much smaller than the decompression moment provided by the post-tensioning. Though high friction could be expected due to the clamping effect caused by high post-tensioning forces, Appendix B of NZS3101 (2006) (NZ Concrete Standard covering jointed ductile connections for precast concrete) does not allow shear resistance to be taken fully by friction. Thus, the castellated joint was conservatively designed to resist all the horizontal shear load with rolling shear failure as the governing failure mode. The castellation was fabricated by a computer numerical control (CNC) machine with 2mm tolerance. Each wall had two castellations with an approximate 3:1 length to height ratio. The Web Wall castellations were 350mm long and 120mm high and the Flange Wall ones were 200mm or 250mm long and 70mm high. A Web Wall castellation is shown in Figure 6-12.

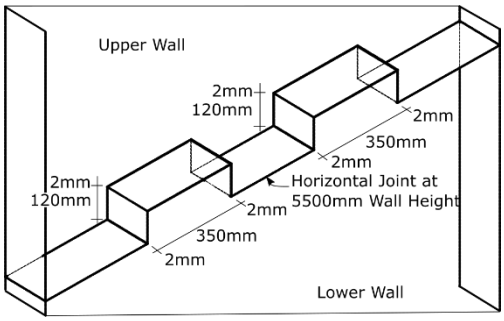


*Figure 6-12: Castellation design*

### 6.3.5 Diaphragm Design

CLT floor diaphragms provided out-of-plane restraint to the vertical wall components. Floors are generally constructed outside a core-wall system such that lift/elevator shafts, service shafts, or stairwells can be placed inside. However, in this study, by placing the diaphragms inside the core-wall, a self-contained test specimen with its own out-of-plane restraints was achieved without the necessity of additional structural members. The floors had a 10mm gap from the walls with the intention to eliminate the strut action potential which was observed by Newcombe et al. (2010). The floors were connected to each wall with a 700mm long steel Equal Angle (EA) 100mm x 100mm x 6mm as per AS/NZS 3679 (2016) with predrilled $\phi$11mm holes on the horizontal leg, and 11mm x 20mm slotted holes on the vertical leg. A similiar detail had previously been tested by Moroder et al. (2017). Following the NZ Steel Structure Standard (NZS3404 (1992)), the design out-of-plane force of 2.5% axial load required 16- $\phi$ 10x100mm partially threaded washer head screws with pre-drilled holes. This out-of-plane force demand was appropriate based on the results from Phase I and II testing. The STS on the vertical leg were unscrewed a ¼ turn after installation to accommodate global wall-floor displacement incompatibility through movement within the slotted hole connection. The steel angles were placed in the mid-length of each wall to minimize the displacement incompatibility as recommended by Moroder et al. (2018). A slotted hole diaphragm connection detail was also used in the NMIT building, which was the first PT timber building erected in 2011 (Holden et al., 2016). The diaphragm connection design is shown in Figure 6-13.

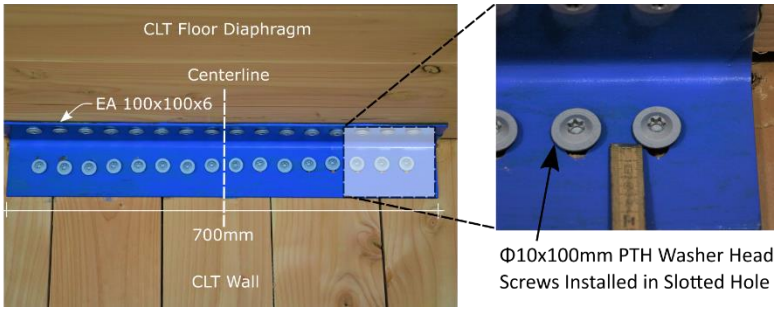


*Figure 6-13: Diaphragm connection*

### 6.3.6 UFP Dissipater Design

At the corners of each wall base, mild steel U-shaped flexural plates (UFPs) (Kelly et al., 1972) were installed. While past research (Chen et al., 2020; Ganey et al., 2017;Iqbal et al., 2015; Pei et al., 2019) and the NMIT building (Holden et al., 2016) used UFPs between PT walls to provide coupling effect and stable energy dissipation, in this study the primary focus was to investigate different connection details of the UFPs to CLT wall panels. Implications due to bi-directional loading would be investigated as well. Sarti et al. (2016) have shown the importance of providing stiff connections to engage the dissipaters. As such, three different connections were investigated which are shown in Figure 6-14:

(A) inclined STS installed in the face of CLT, (B) inclined STS installed in the edge of CLT, and (C) an epoxied steel plate on the face of CLT. Each inclined STS connection was designed to remain elastic with an overstrength factor of 1.8 neglecting friction and the contribution from STS under compression. Each UFP was connected by 2-M16 bolts to the steel plate and to the steel parallel flanged channel (PFC). 2-$\phi$ 12mm Grade 4.6 threaded rods (Standards New Zealand, 1992) were installed to connect the PFC and the steel plate to eliminate the induced force couple because UFPs were placed only on one side of the CLT wall. Tests with and without the $\phi$12mm threaded rod were implemented. The specific location of each UFP pair utilized is shown in Figure 6-14d.

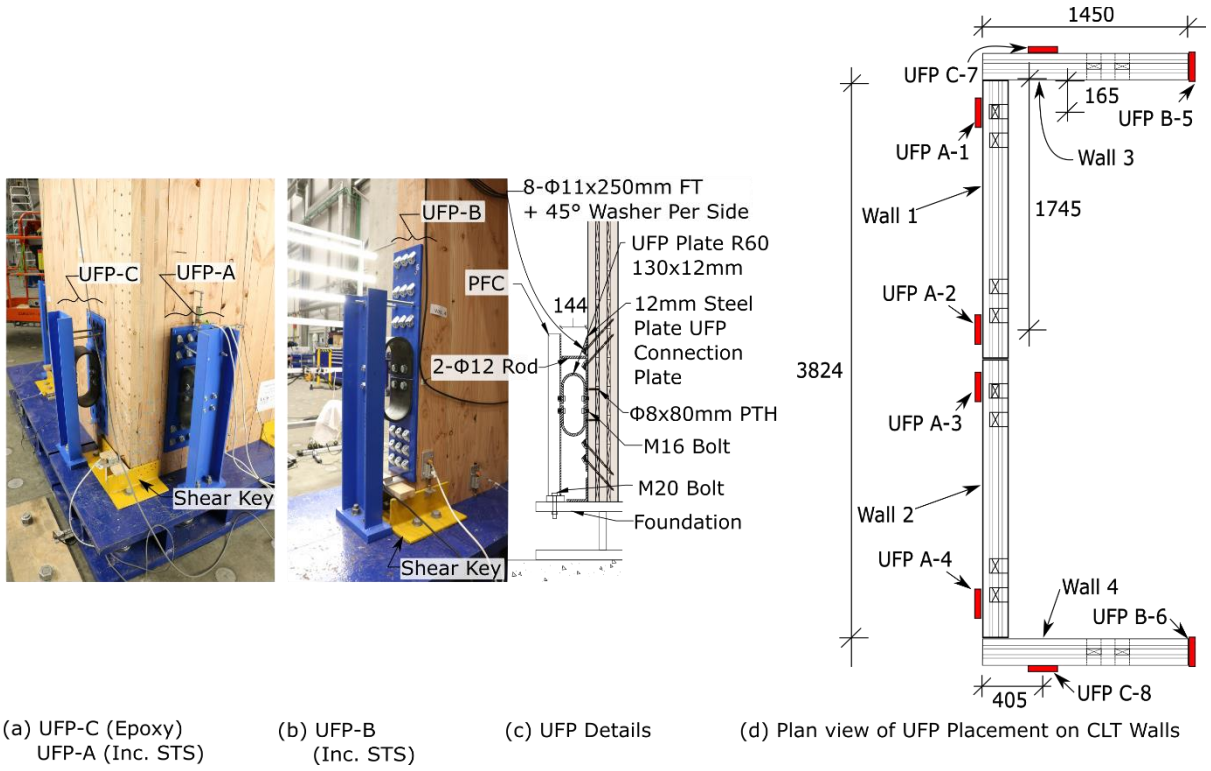


*Figure 6-14: UFP connection detailing: (a) UFP-A and UFP-C, (b) UFP-B, (c) UFP Details, and (d) plan view of the UFP placement on the CLT walls*

The UFPs were tested separately to better evaluate their cyclic performance. They were fabricated from 12mm thick Grade 300E (Australian / New Zealand Standard, 2001) steel plates and bent to the specified dimensions. The UFPs had a 60mm inner radius, a width of 130mm. The test set-up and the force-displacement curves are shown in Figure 6-15. The maximum force for the UFP pair was much larger than the analytical plastic capacity of 46kN based on the steel yield strength of 300MPa. However, this is within the overstrength of 145% - 215% found by Kelly et al. (1972) compared with the yield strength obtained from direct tension tests and further explained in Baird et al. (2014).

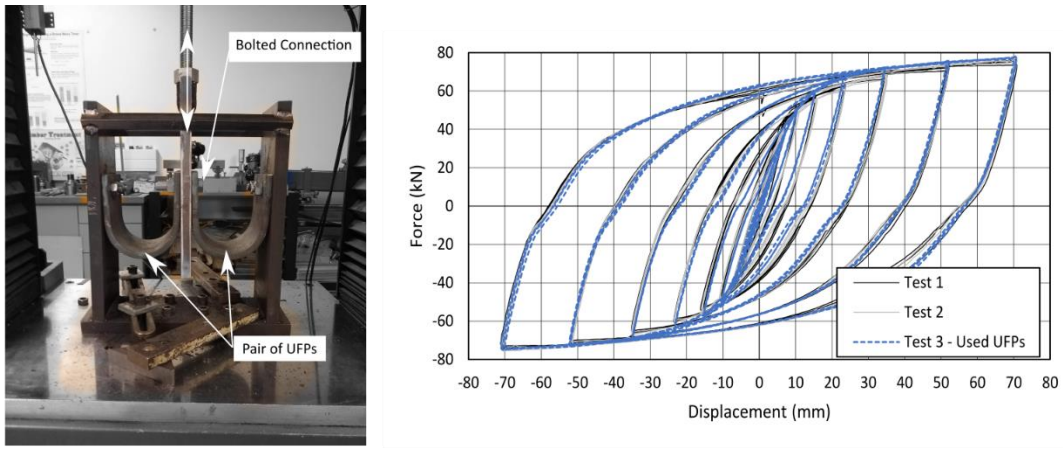


*Figure 6-15: UFP component testing: (a) test setup, and (b) UFP component testing force-displacement curves*

### 6.3.7 Foundation Details

Typically in PT timber buildings, large concrete pad foundations are used to transfer the concentrated loads from the PT bars while anchored steel plates can be used to transfer shear forces (Palermo et al., 2012). In this study, a custom fabricated steel foundation provided connection to the strong floor, anchorage to the PT bars and a shear key connection. Shear keys were installed to prevent both in-plane and out-of-plane movement. The shear keys were EA 125mm x 125mm x 12mm (Australian / New Zealand Standard, 2016) with welds on the bottom leg only so that the top leg could yield and bend to accommodate the wall rocking as reported by Moroder et al. (2018) and also detailed for the Carterton Events Centre building (Palermo et al., 2012). The various shear keys used are shown in Figure 6-16. The shear keys were bolted to the top flange of the steel foundation with Grade 8.8 M20 bolts (Australian / New Zealand Standard, 2016) with zero tolerance. However, because the actual CLT Web Wall length and Flange Wall thicknesses were closer to 1910mm and 173mm respectively, approximately 8mm tolerance occurred at the core-wall base during the strong axis loading.

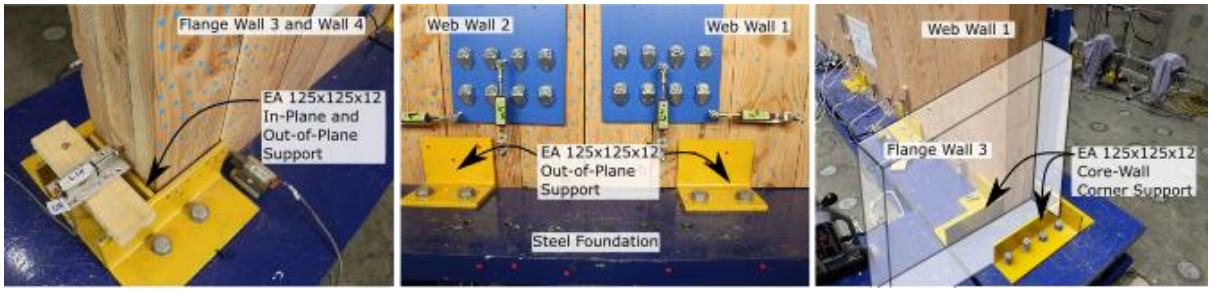


*Figure 6-16: Foundation details*

### 6.3.8 Conventional Core-Wall Test Specific Details

For the conventional core-wall test, CW-8, the PT bars were loosened and hold-down connectors were added to the specimen. Figure 6-17 shows the specimen with steel bracket hold-downs and shear keys installed at the base level and tie-downs installed at the horizontal joint.

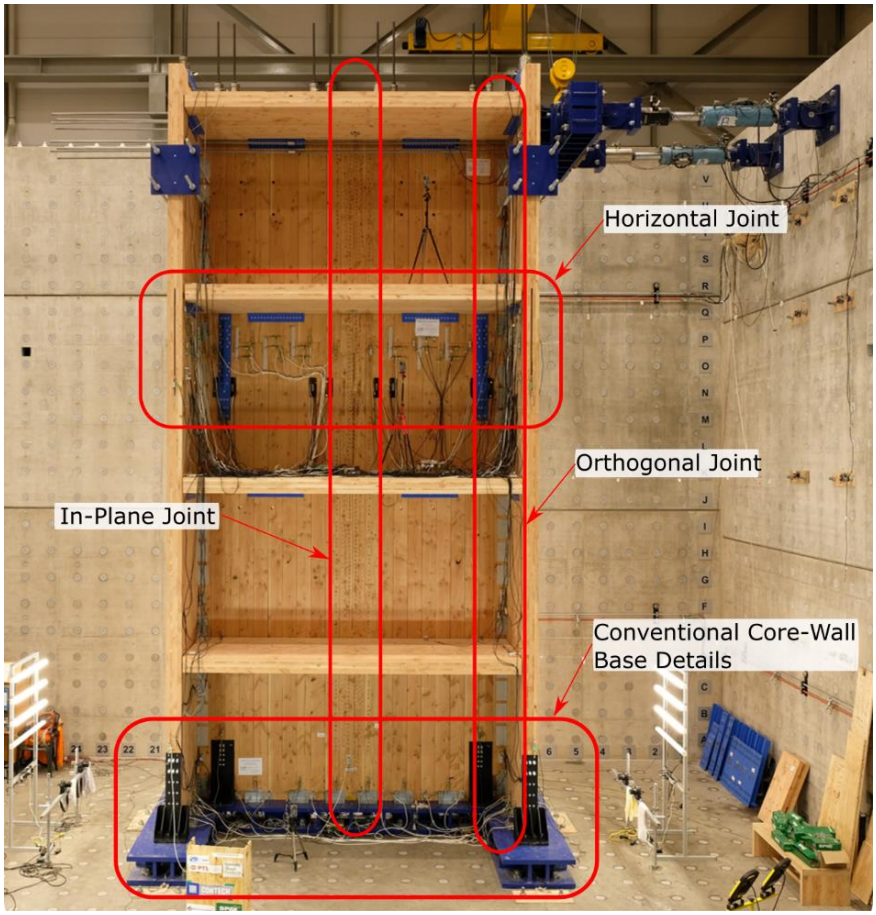


*Figure 6-17: Conventional core-wall test set-up*

As shown in Figure 6-2b, the base hold-downs and the in-plane joint were designed to be the ductile links. Figure 6-18 shows the placement of the hold-downs and angle brackets at the base level and horizontal joint level. In total, 16 hold-downs and 20 Rothoblaas Titan TCN240 angle brackets (ETA-11/0496, 2018) were installed.

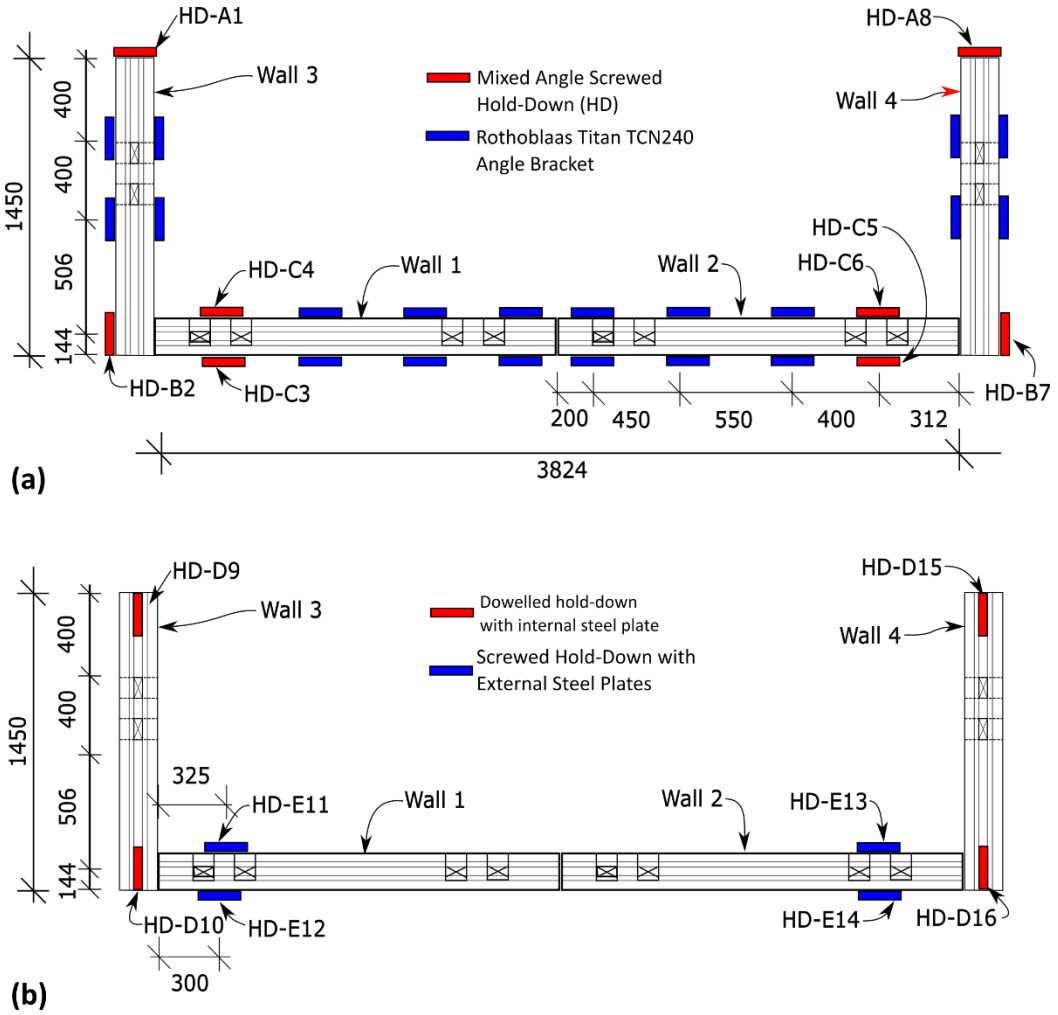


*Figure 6-18: Conventional core-wall test hold-down locations; (a) core-wall base, and (b) horizontal joint level*

Figure 6-19 shows the three different mixed angle screwed hold-downs that anchored the conventional core-wall to the foundation. In the hold-down (HD) type HD-A and HD-B, 6-$\phi$12 x 160mm long PTH STS (ETA-12/0114, 2017) and 9-$\phi$10 180mm long PTH STS (ETA-12/0114, 2017) were implemented. In HD-C, 4-$\phi$12 x 160mm long PTH STS (ETA-12/0114, 2017) and 6-$\phi$10 180mm long PTH STS (ETA-12/0114, 2017) were implemented and each HD-C was installed as a pair on each face of the CLT wall. All STS were installed into pre-drilled holes to 70% of the STS length with jigs to ensure correct alignment.

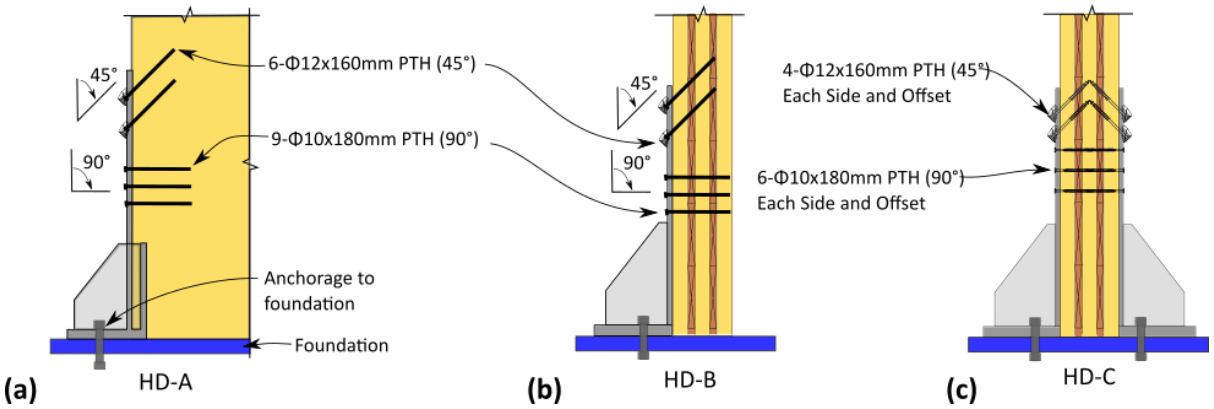


*Figure 6-19: Mixed angle screwed hold-down details*

Figure 6-20 shows the details for the orthogonal joint and the in-plane joint. At each orthogonal joint, 22 Rothoblaas Titan TTN240 angle brackets (ETA-11/0496, 2018) were installed. At the in-plane joint, 110--$\phi$8 x 160mm long FT STS were installed at 45° + 45° double inclination with 110—$\phi$8 x 80mm long PTH STS installed at 90° with 22mm thick plywood. Figure 6-21 provides details for the angle brackets (ETA-11/0496, 2018) and LBA $\phi$4 x 60mm ring shank nails (ETA-13/0523, 2018). In the TTN angle brackets, a full nailing pattern was implemented while for the TCN brackets, a half nailing pattern was used to ensure brittle failure did not occur.

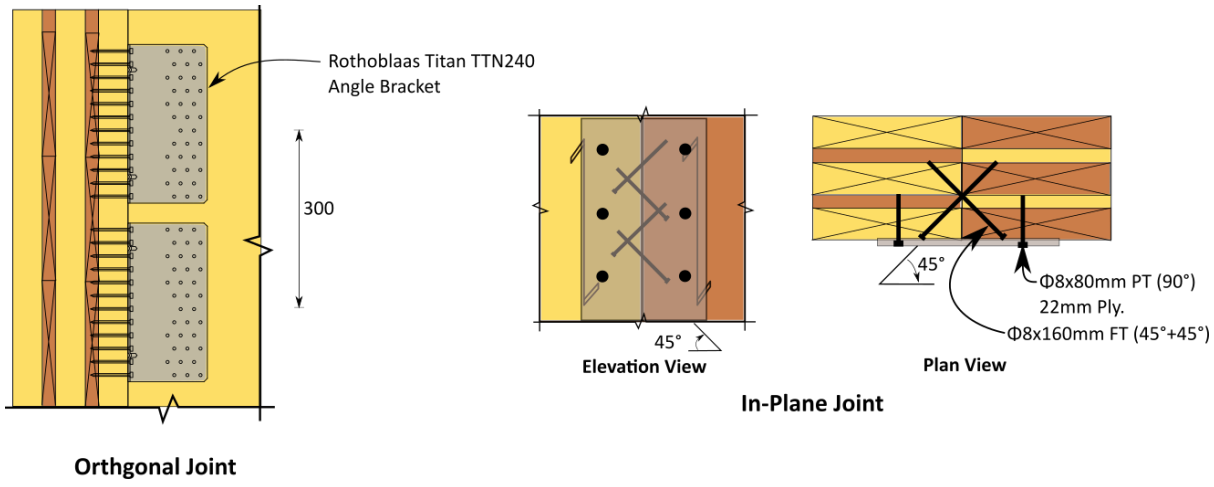


*Figure 6-20: Test CW-8 orthogonal and in-plane joint details*

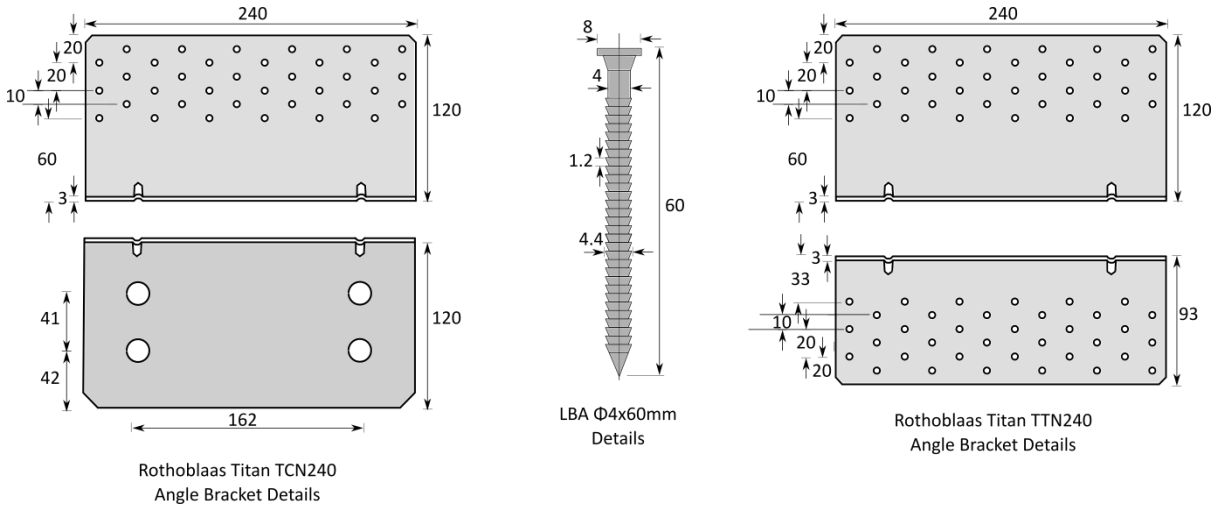


*Figure 6-21: Angle bracket details*

At the horizontal joint level at 5.5m wall height, two different HDs were implemented as shown in Figure 6-22 and Figure 6-18b. HD-D employed 6- $\phi$20 steel dowels Grade 300E (Australian / New Zealand Standard, 2001) with a 20mm thick internal steel plate. The appropriate dowel size, quantity and spacing was determined based on the dowelled hold-down test results presented in Chapter 3. HD-E employed 20- $\phi$10 x 100mm PTH STS per each side of the horizontal joint with a 10mm thick steel side plates. As per Figure 6-2b, both HD-D and HD-E were designed as non-dissipative elements and thus were capacity protected.

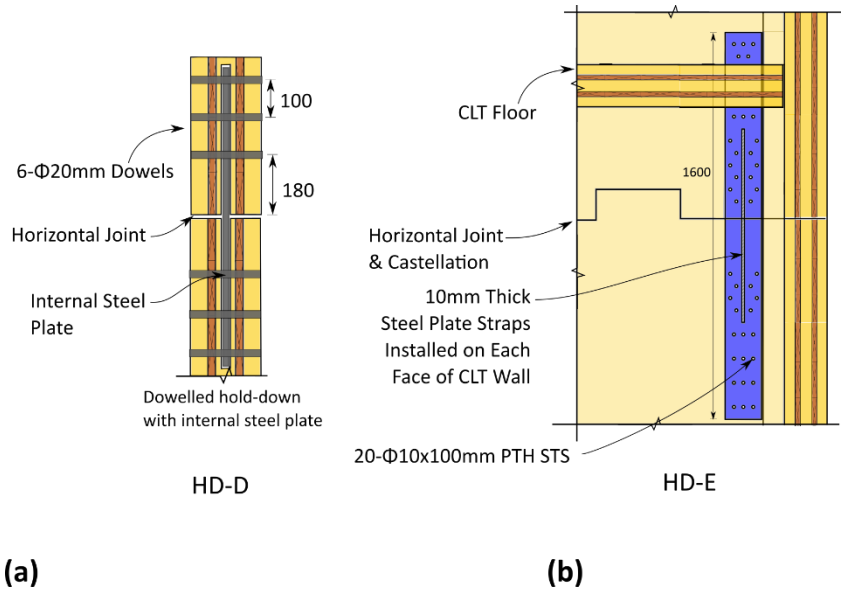


*Figure 6-22: Test CW-8 horizontal joint hold-down details: (a) HD-D, and (b) HD-E*

Table 6-4 summarizes each connection strength and stiffness for the conventional core-wall test. The yield strength, $F_y$, and stiffness, $k_{ser}$, of HD-A/B/C was determined considering inclined STS as shear-tension STS determined as per analytical methods presented in Chapter 4 and SPAX ETA-Danmark (ETA-12/0114, 2017), and 90° STS were considered as per Eurocode 5 (2014) and SPAX ETA-Danmark

(ETA-12/0114, 2017). HD-D yield strength and stiffness were determined following Eurocode 5 (2014) as presented in Chapter 3. HD-E yield strength and stiffness were determined as per SPAX ETA-Danmark (ETA-12/0114, 2017). Each angle bracket's strength and stiffness were determined following Eurocode 5 (2014). The in-plane joint yield strength and stiffness were determined as per the STS analytical model presented in Chapter 4. Table 6-4 shows that HD-A/B/C yield strengths were significantly lower than HD-D/E, especially considering that the load demand was approximately 3x higher for HD-A/B/C determined by the relative distance to the loading height. Further, the orthogonal joint was designed to be significantly stronger than the in-plane joint in order to maximize the CA from the flange walls. Table 6-8 provides a further summary of Test CW-8 details.

*Table 6-4 Summary of CW-8 connection strength and stiffness*

| **Component** | **HD-A/B** | **HD-C** | **TCN240** | **HD-D** | **HD-E** | **Orthogonal Joint (TTN240)** | **In-Plane Joint** |
|---|---|---|---|---|---|---|---|
| $F_y$ Units | kN | kN | kN | kN | kN | kN /m | kN /m |
| $K_{ser}$ Units | kN/mm | kN/mm | kN/mm | kN/mm | kN/m | kN/mm/m | kN/mm/m |
| $F_y$ | 180 | 240 | 384 (250[1]) | 250 | 400 | 165 | 80 |
| $K_{ser}$ | 131 | 175 | 216 (144[1]) | 102 | 95 | 46 | 56 |

[1] Weak axis loading strength and stiffness,

## 6.4 TEST PROGRAMME AND LOADING PROTOCOL

### 6.4.1 Single and Double Wall Testing Phases

The SW and DW testing programmes are provided in Table 6-5 and Table 6-6. In SW testing, the initial post-tensioning bar force was varied. In DW testing, the tests considered variations in terms of a) in-plane joint connection details, b) use of UFP dissipaters at the wall base, and c) self-centring ratio $\beta$ where $\beta = \frac{M_{pt}}{M_{tot}}$. $M_{pt}$ is the base moment contribution due to PT bars and $M_{tot}$ is the total base moment. The initial post-tensioning force, differing from traditional unbonded PT concrete applications, was limited to 5% yield force of the PT bar to avoid potential yielding due to wall uplifting in DW testing. Test DW-1 did not use STS or UFPs such that friction between the panels at the in-plane joint could be quantified. This also provided a baseline and lower bound performance. 17mm Plywood as per NZS 3603 (1993) was used at the in-plane joint to couple two PT CLT walls together. $\phi$8x80mm PTH STS were installed at 90° to the CLT wall face on each side of the in-plane joint. The experimental test setup for the SW and DW are shown in Figure 6-23 and Figure 6-24.

*Table 6-5: PT single wall testing programme*

| Test | - | SW-1 | SW-2 | SW-3 | SW-4 |
|---|---|---|---|---|---|
| Initial PT / bar (kN) | kN | 0 (0%[1]) | 25 (5%[1]) | 50 (11%[1]) | 75 (16%[1]) |

Note: [1] yield percentage of the post-tensioning bar

*Table 6-6: PT double wall testing programme*

| Test | | DW-1 | DW-2 | DW-3 | DW-4 | DW-5 |
|---|---|---|---|---|---|---|
| Initial PT / bar | kN | 25 (5%[1]) | 25 (5%[1]) | 25 (5%[1]) | 25 (5%[1]) | 25 (5%[1]) |
| In-plane Joint | Type | - | 8x80 PTH (17mm Ply.) | 8x80 PTH (17mm Ply.) | 8x80 PTH (17mm Ply.) | - |
| | Qty. | - | 64 (90°) | 220 (90°) | 64 (90°) | - |
| UFPs | - | No | No | No | Yes | Yes |
| Re-Centering Ratio ($\beta = M_{pt}/M_{tot}$) | - | 0.9 | 0.67 | 0.55 | 0.56 | 0.72 |

Note: [1] yield percentage of the post-tensioning bar

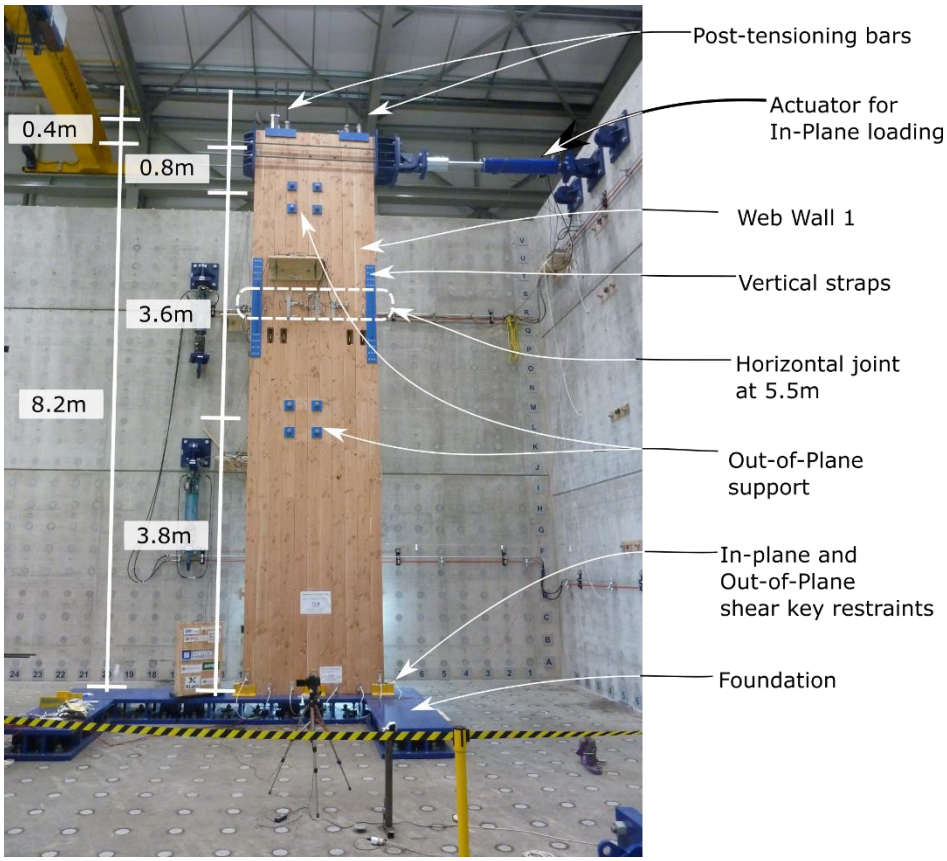


*Figure 6-23: Post-tensioned single-wall experimental design set-up*

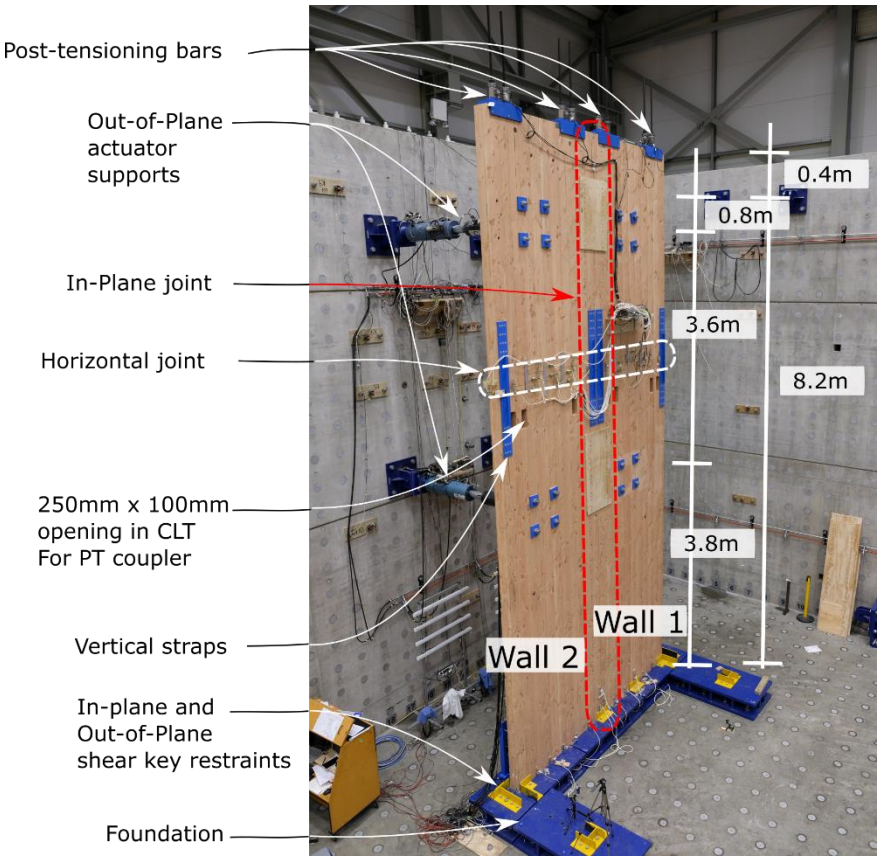


*Figure 6-24: Post-tensioned double wall test set-up*

Figure 6-23 and Figure 6-24 show how the wall specimens were loaded with actuators. One 700kN actuator with 4-M30 Grade 8.8 threaded rods were used to apply the lateral loads via a steel loading beam and bearing head at a wall height of 8.2m. Two actuators provided out-of-plane restraints at 3.8m and 7.4m wall height. At the base of the wall, in-plane and out-of-plane translational restraints were provided by EA 125mm x 125mm x 12mm shear keys. In DW testing, each wall had two out-of-plane restraints for a total of four actuators.

The displacement controlled loading followed the ACI ITG-5.1-07 special protocol for PT precast structural walls (ACI Innovation Task Group 5, 2008). Table 6-7 shows the amplitude of each cycle group with the amplitude of the subsequent cycle group 1.25 times that of the previous cycle group. Each cycle group had three identical cycles. The peak drift (PD) was chosen during each test upon evaluation of the actual CLT compression strains and visible damage at the wall base. During SW and DW testing phase, PD was determined once the non-linear elastic behaviour response due to the gap opening was observed sufficiently.

*Table 6-7: Single and double wall loading protocol cycle group summary*

| Cycle Group | 1 | 2 | 3 | 4 | 5 | 6 | 7 | 8 | 9 | 10 | 11 | 12 |
|---|---|---|---|---|---|---|---|---|---|---|---|---|
| Drift (%) | 0.10 | 0.13 | 0.16 | 0.20 | 0.24 | 0.31 | 0.38 | 0.48 | 0.60 | 0.75 | 0.93 | 1.2 |

There was non-zero displacement for the out-of-plane actuators to account for the arc that was induced by transverse displacement from the in-plane loading actuator. For example during unidirectional strong axis loading, the out-of-plane actuators connected to each wall at two points were required to extend during positive and negative strong axis drift to maintain in-plane movement of the wall.

### 6.4.2 Core-Wall Testing Phase

The core-wall testing schedule is provided in Table 6-8. The tests considered variations in terms of a) initial post-tensioning force, b) screwed connection detail, c) use of UFPs, and d) loading protocols. The initial post-tensioning force, differing from traditional unbonded PT concrete applications, was limited to 16% of yield strength of PT bars to avoid potential yielding due to wall uplifting. Figure 6-10 has provided the details on each screwed connection type for the in-plane and orthogonal joints. Tests CW-1, 3 and 4 did not use STS at the wall joints such that friction between the panels could be quantified. This also provided a baseline and lower bound performance. The experimental test setup for the core-wall is shown in Figure 6-25. Test CW-8 did not use post-tensioning but used tie-downs at each horizontal joint as discussed in Section 6.3.8. The connector quantities implemented for Test CW-8 are shown in Table 6-8.

*Table 6-8: Experimental core-wall test programme*

| Test | Initial Post-tensioning per bar (kN) | In-Plane Joint | | Orthogonal Joint | | | UFP |
|---|---|---|---|---|---|---|---|
| | | Screw | Screw Quantity | Screw | Screw Quantity | Screw Quantity | |
| | | | Wall 1/2 Joint | | Wall 1/3 Joint | Wall 2/4 Joint | |
| CW-1 | 25 (5%[1]) | Friction | n/a | Friction | n/a | n/a | No |
| CW-2 | 75 (16%[1]) | 8x80 PTH (17mm Ply.) | 220(90°) | 8x350 FT | 83(90°) | 83(90°) | No |
| CW-3 | 75 (16%[1]) | Friction | n/a | Friction | n/a | n/a | No |
| CW-4[3] | 75 (16%[1]) | Friction | n/a | Friction | n/a | n/a | No |
| CW-5 | 75 (16%[1]) | 8x220 FT | 110(Inc.) | 8x220 FT | 82(ST), 72(SC) | 82(ST), 72(SC) | Yes |
| CW-6 | 75 (16%[1]) | 8x160 FT, 8x80 PTH (22mm Ply.) | 248(Inc.), 206(90°) | 8x200 FT, 8x350 FT | 42(ST), 36(SC), 78(90°) | 34(ST), 36(SC), 78 (90°) | Yes |
| CW-7[3] | 25 (5%[1]) | 8x80 PTH (17mm Ply.) | 220(90°) | 8x350 FT | 83(90°) | 83(90°) | Yes |
| CW-8 | - | 8x160 FT, 8x80 PTH (22mm Ply.) | 110(Inc.), 110(90°) | Angle Bracket[2] | 22 | 22 | No |

Note: ST= shear-tension screw; SC = shear-compression screw; Inc. = inclined screw; and 90° = screw installed at 90°. [1] Yield percentage of post-tensioning bar, [2] Rothoblaas Titan TTN240 brackets (ETA-11/0496, 2018) with full LBA φ4x60 (ETA-13/0523, 2018) nailing pattern, [3] Bi-directional loading protocol

(a) (b)

*Figure 6-25: Overall test set-up: (a) specimen view, and (b) loading elevation view*

Figure 6-25b shows how the specimen was loaded with actuators. Along the strong axis, two 700kN actuators with 8-M30 Grade 8.8 threaded rods were used to apply the lateral loads via a steel loading beam and bearing head at a wall height of 8.2m. Along the weak axis, each Flange Wall was loaded by one 700kN actuator with 4-M36 Grade 8.8 threaded rods at a wall height of 7.4m. Figure 6-26 shows the two loading protocols. There was non-zero drift in the orthogonal direction for both loading protocols to account for the arc that was induced by transverse displacement to an orthogonal actuator. For example during unidirectional strong axis loading, the actuators connected to each Flange Wall were required to extend during positive and negative strong axis drift to maintain in-plane movement of the core-wall (Figure 6-26).

In all testing phases, the specimens were loaded in the strong axis at 8.2m wall height and at a single point instead of at each floor level. Recent balloon frame CLT shear wall testing by Shahnewaz et al. (2021) has tested a two storey wall with loading at each storey while Chen and Popovski (2020) loaded high aspect ratio CLT shear walls at near the top of the wall and at one point. In order to provide loading at each level, Shahnewaz et al. (2021) assumed a force distribution based on equivalent static elastic analysis and then the two loading rams were load controlled. On the other hand, Chen and Popovski (2020) did not assume a displaced shape but rather assessed the single- and coupled-panel CLT shear wall structural performance. The results reported that significant elastic deformation (bending and shear) occurred up to 30-60% of the total wall deformation which was significant and would have been difficult to report if the specimen was loaded/restrained to an assumed displaced shape at multiple loading points. In the testing presented herein and in particular for the core-wall testing phase, it was difficult to estimate a displacement shape due to the partial composite action between the CLT walls. This was made especially difficult given that we were targeting different levels of partial composite action in each test based on the connection details. Furthermore, performing a test with loading at one point is more demanding in term of base moment for a given base shear when compared to loading at each floor height. Given the reasons stated above, it was decided that loading at a single point would best suit the testing objective which was to assess the structural performance and partial composite action of CLT core-wall systems based on its connection details.

The displacement controlled loading followed the ACI ITG-5.1-07 special protocol for PT precast structural walls (ACI Innovation Task Group 5, 2008). The amplitude of each subsequent cycle group was 1.25 times the previous cycle group, and each cycle group had three identical cycles similar to the SW and DW testing. For Tests CW-4 and CW-7, one cycle group of uni-directional loading was followed by cloverleaf bi-directional loading. These drifts were chosen during each test upon evaluation of the actual CLT compression strains and visible damage at the wall base. For the final tests, the specimen

was tested until either connection failure occurred or the actuator stroke limit (i.e., 2.3% wall drift ratio) was reached.

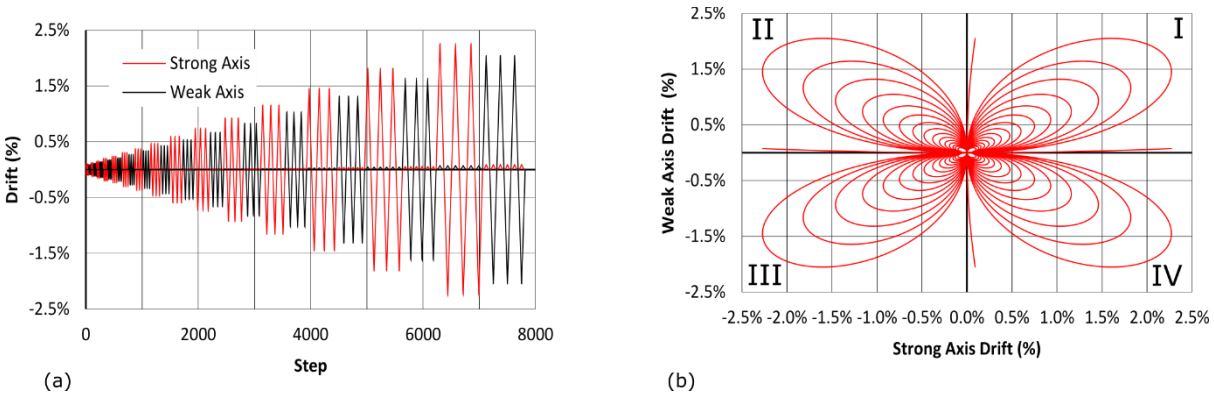


*Figure 6-26: Loading protocols; (a) uni-directional loading, and (b) bi-directional loading*

### 6.4.3 Torsional Restraints

The asymmetric "C" shape of the core-wall along the strong axis meant eccentricity and therefore torsional restraints were required when loading along the strong axis. Torsional restraints were then provided by shear keys at the base, vertical steel straps at the castellation level (shown in Figure 6-25a), and by the actuators on each flange along the weak axis. During CW testing, the vertical steel straps were fastened only to the section of wall below the castellation, and extended above the castellation to provide restraint. Further torsional restraints were provided by the floor diaphragms.

## 6.5 INSTRUMENTATION

### 6.5.1 General Instrumentation

In total, 220 linear variable differential transducers (LVDTs), load cells, and inclinometers were installed to measure the local and global responses of each specimen. Figure 6-27 shows the key instrumentation drawings for the core-wall testing. Instruments were placed on the specimen at 2m inter-storey heights when practicable. The actuators had 1000kN load cells to monitor the applied load, and the post-tensioning forces were monitored on each high strength bar with 500kN load cells. As the PT bars were placed in pairs, the results of each pair were combined. The potentiometers measured in-plane and out-of-plane wall movement, neutral axis depth (i.e., length of the compression zone) at the wall base, core-wall base sliding, wall joint relative slip, castellation movement, diaphragm connection movement, and UFP connection movement. Inclinometers measured wall and floor rotations.

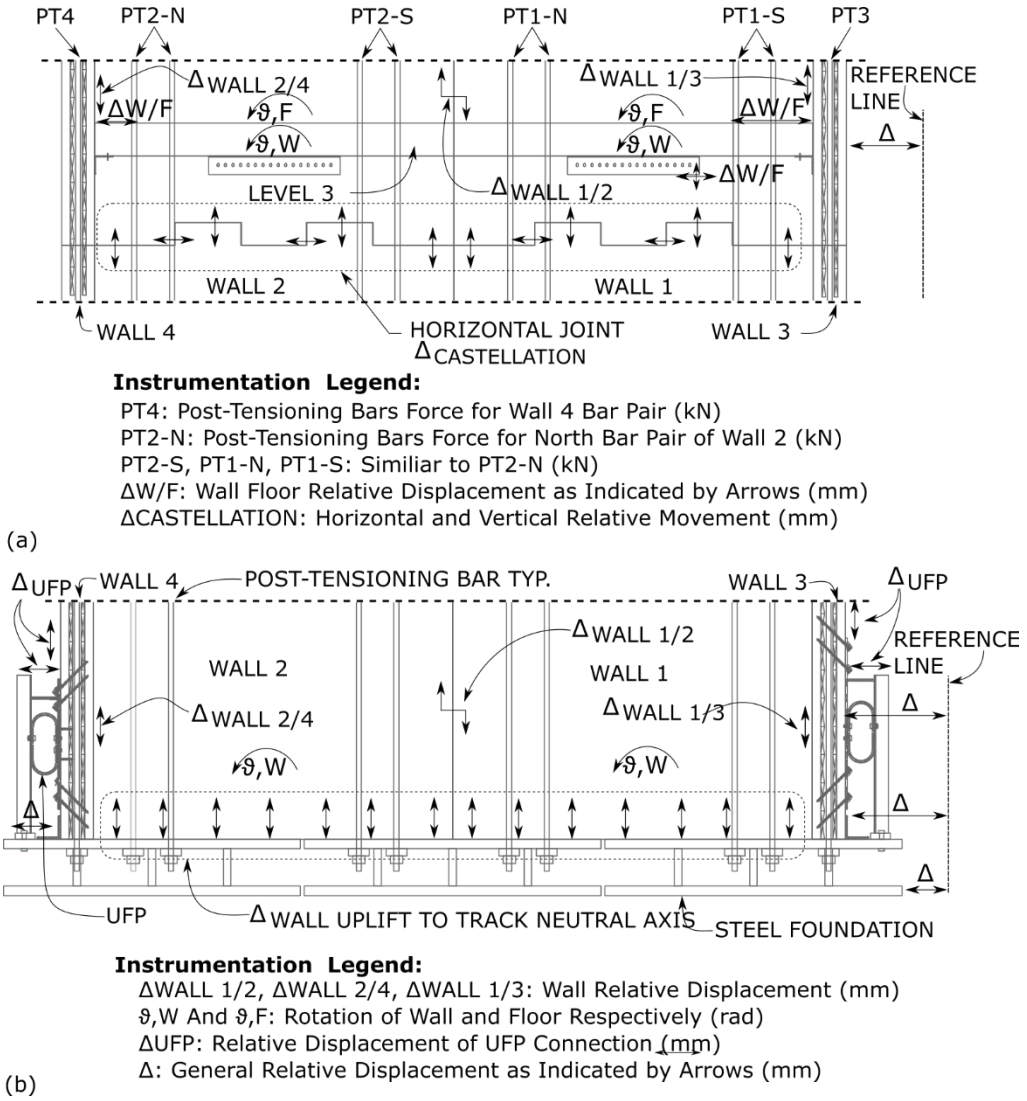


*Figure 6-27: Key test instrumentation: (a) floor level instrumentation, and (b) base level instrumentation*

Figure 6-28 shows different LVDT, and load cells positions for the test programme at various locations on the specimen.

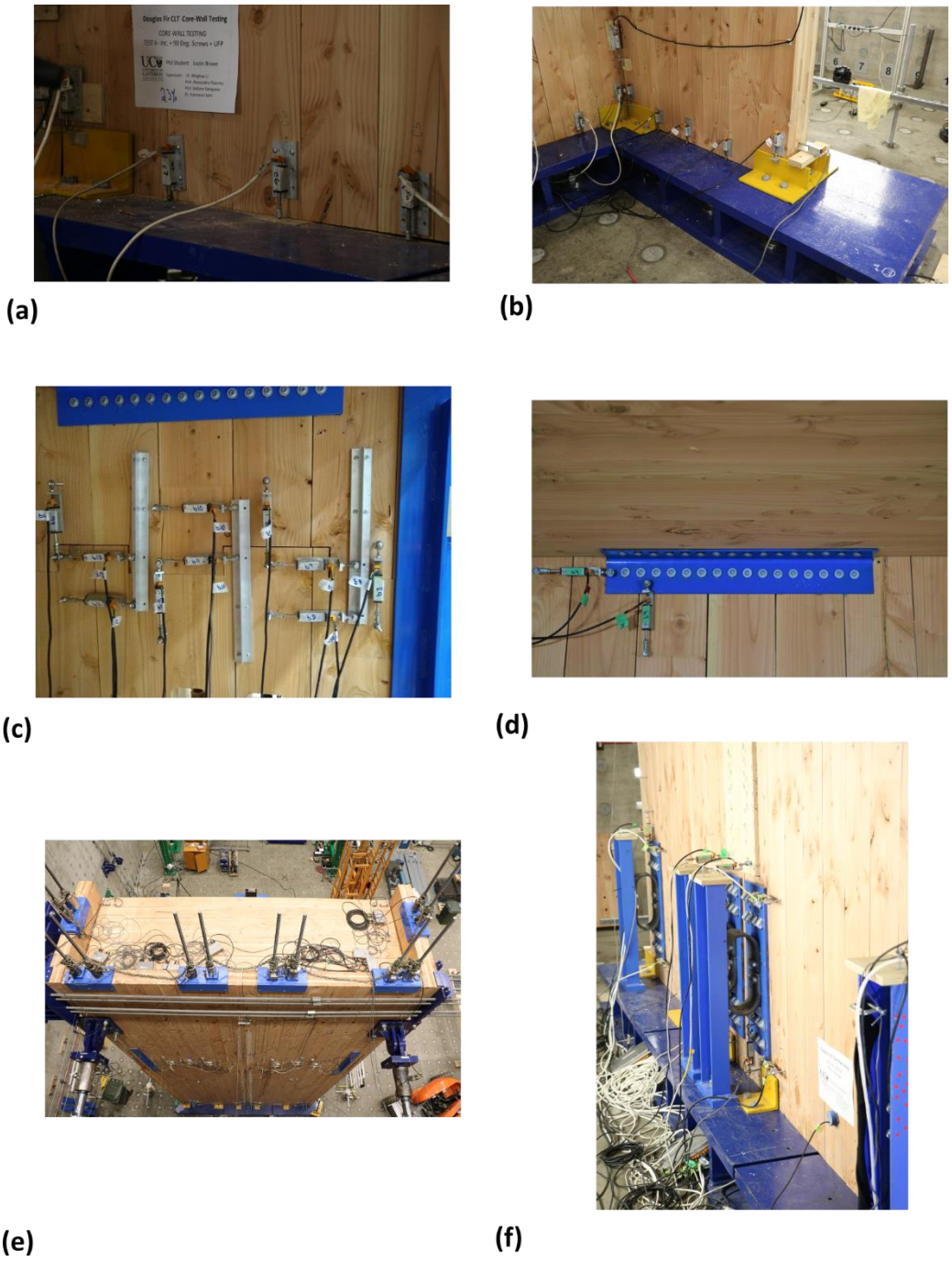


*Figure 6-28: Key test instrumentation: (a) and (b) wall base neutral axis tracking, (c) castellation tracking, (d) diaphragm connection tracking, (e) post-tensioning bar load cells and out-of-plane movement tracking ,and (f) UFP connection tracking*

### 6.5.2 Particle Tracking Technology Setup and Processing

Particle tracking technology (PTT) was implemented at the base of each CLT wall to better understand the base rocking interface and to monitor the UFP connection assembly movement. PTT is a contact-free quantitative field measuring technique originally developed to track individual particles in fluid flows (Nokes, 2019). The use of PTT has gained popularity in structural testing as displacement and strain fields can be generated while traditional LVDTs and strain gauges only provide one measurement per device. Within structural timber testing, Ottenhaus et al. (2019) have shown the

versatility of PTT with CLT testing in dowel embedment tests, large scale CLT connection tests and small scale material tests. It was shown that PTT could successfully capture displacements with increased accuracy compared with LVDTs, capture unexpected movements, and additionally capture strain fields. The software used to process the images and implement PTT algorithms was *Streams*, which was developed at University of Canterbury in the field of fluid mechanics (Nokes, 2019).

In this study, PTT was used for the first time in PT timber structures testing. In past research, the most common method for tracking the neutral axis depth at the base of a rocking timber wall is to linearly interpolate a number of single point measurements by LVDTs. If a detailed analysis of the rocking interface is desired, PTT has great advantages over LVDTs as the movement of a large number of particles can be tracked with digital cameras with high resolution. In this regard, PTT was implemented in order to verify and extend existing analytical models as well as to capture the complex and possibly unexpected behaviour of the 3-dimensional PT CLT core-wall system.

It is worth noting that there are some distinct material differences between LVL (Nelson Pine Industries Ltd., 2016) used in past PT timber testing (Sarti et al., 2016; Smith et al., 2006) and CLT (XLam NZ Limited, 2017) used in this testing campaign. Table 6-9 lists these material differences. The $E_0$, $f_c$, $f_{c,90}$, and lamella thickness, $t_L$, will all influence the behaviour of the rocking interface at the wall compression toe. In past research with PT LVL shear walls, investigation of the strain profile of the timber within the compression zone was performed and the linear profile was deemed suitable for design (Smith et al., 2007). By implementing PTT, this experimental research sought to verify whether or not a linear strain profile was also valid for PT CLT shear walls.

*Table 6-9: LVL and CLT material properties*

| Material | Modulus of Elasticity, $E_0$ (MPa) | Compression strength (MPa) | | Veneer / lamella thickness, $t_L$ (mm) |
|---|---|---|---|---|
| | | Parallel to grain, $f_c$ | Perpendicular to grain, $f_{c,90}$ | |
| LVL | 11 000 | 45 | n/a | 2.5 - 5.0 |
| CLT | 8 000 | 18 | 8.9 | 20.0 - 45mm |

The PTT methodology used in the testing was adopted from previous work by Ottenhaus et. al. (2019). For the experimental set-up, ten Fujifilm X-T2 cameras with XF 18-55 lens were positioned around the core-wall base on stiff supports. An additional two cameras monitored the UFP connection assembly response. The resolution of the images was 6000x4000 pixels, and the PTT resolution ranged from 0.145 mm/pix to 0.197 mm/pix. Artificial lighting was provided to ensure a consistent light intensity throughout each image frame. For particles, 8mm diameter blue or red circle stickers were attached to the CLT wall surface. As the particles were placed on the face of the CLT wall, all the measured displacement and strains represented the surface responses. An image was recorded at each

displacement step of the loading protocol such that each image could easily be correlated with the associated experimental data file. Figure 6-29 shows the PTT setup at the core-wall base and an image view of one camera.

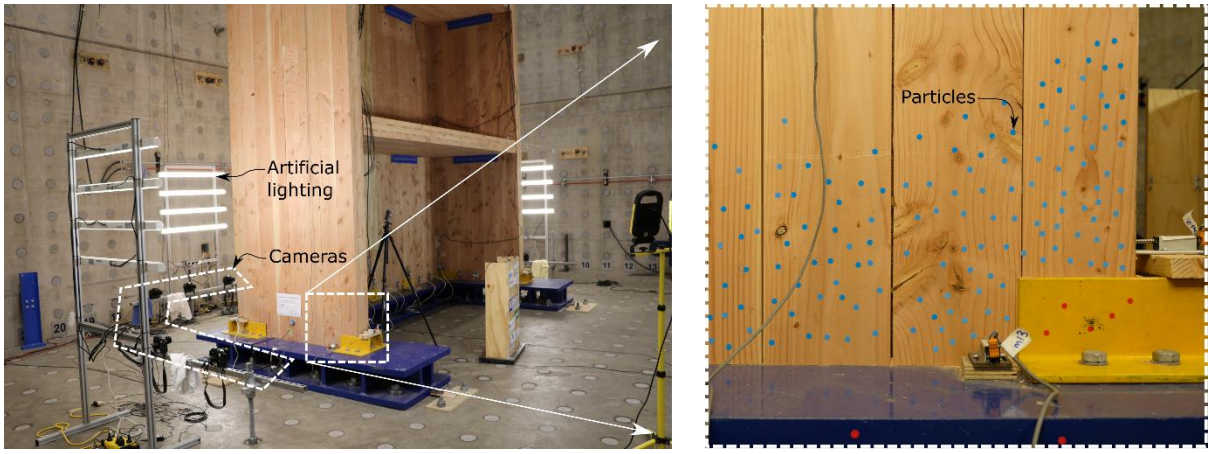


*Figure 6-29: PTT setup at core-wall base: general setup with image from a single camera*

Figure 6-30 shows a photo of each Wall 1 and Wall 2 toe. The yellow painted steel shear keys and UFP connectors interfered with PTT data collection in some instances.

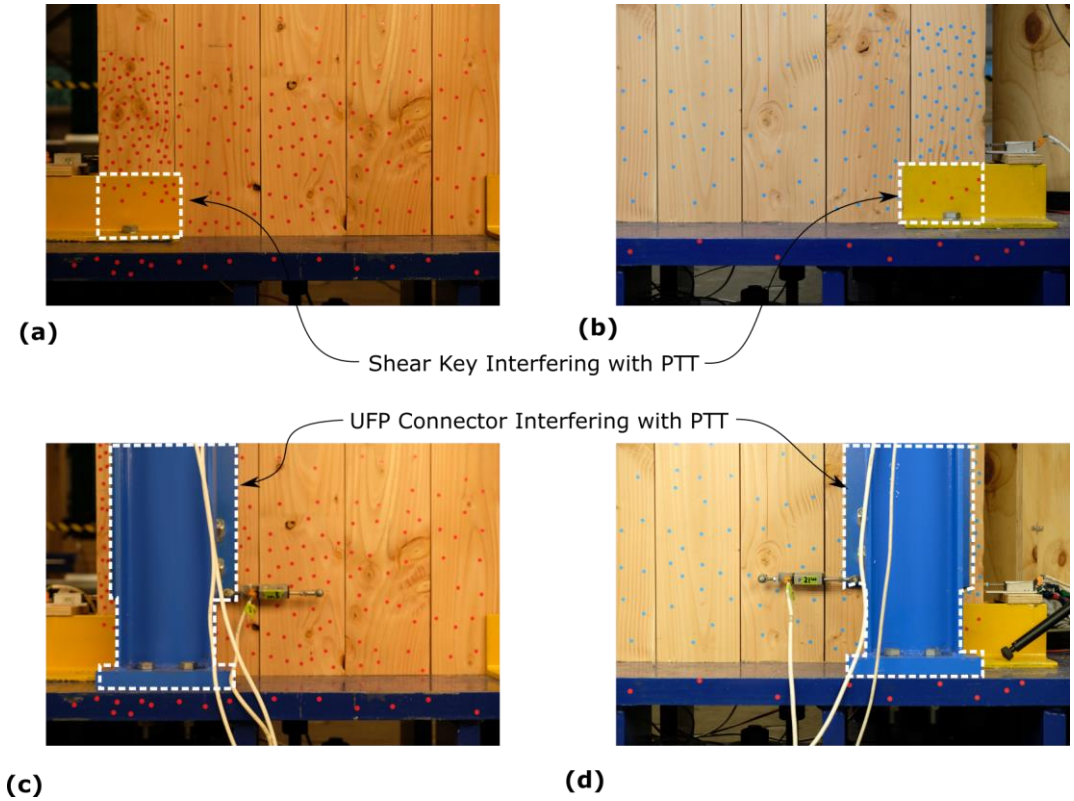


*Figure 6-30: PTT and interference by shear key and UFP connector: (a) and (c) Wall 1 base, (b) and (d) Wall 2 base*

*Streams* (Nokes, 2019) was used in image post processing and it has an extensive toolkit of processes to perform image filtering, particle identification, PTT analysis, and ultimately produce displacement

and strain fields. The particle identification algorithms within Streams require the ability to identify and distinguish the pixels that comprise the particles and differentiate them from the rest of the image frame. This is accomplished by a variation in light intensity on either a grey or RGB scale.

In the following, the processes performed to analyse this particular image set will be described with reference to Figure 6-31. The images were pre-processed and filtered by subtracting the red intensity from the blue. This accentuated the blue particles against the natural timber background. Particles were then identified as comprising the pixels whose blue intensity exceeded a user defined threshold. For example, the two particles shown in Figure 6-31c moved vertically approximately 30mm in one test. For Test CW-6, 7850 images were processed for each of the twelve cameras around the wall base which allowed the compression toe of each CLT wall and the UFPs to be assessed in great detail.

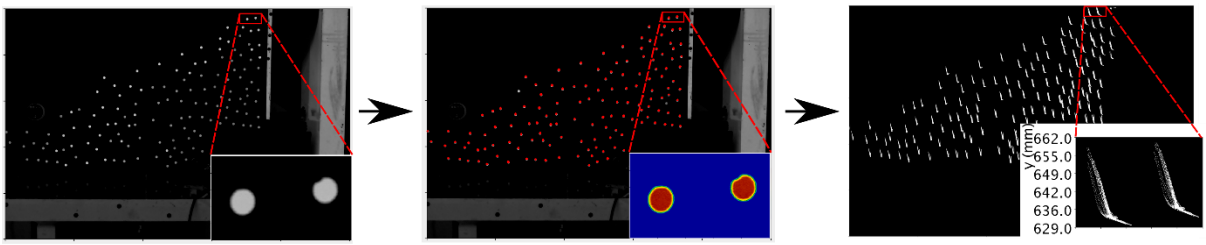


*Figure 6-31: PTT processes: (a) image filtering, (b) particle identification, (c) particle path*

In order to track the particles between each image frame, each particle in the image frame must be matched with the same particle in the next frame. *Streams* uses an optimisation process based on finding the particle in the next frame that is closest to the particle in the first frame. The collection of all distinct particles paths comprise the particle record. Particle records were combined together as required such that a displacement or strain field for a Phase I SW (three cameras), Phase II DW (six cameras) or Phase III core-wall (ten cameras + two cameras for UFPs) could be interpreted together.

With the particle records, *Streams* generated a material displacement field on a rectangular grid corresponding to x, y, and t (the time of each image). Particle displacements were interpolated onto the grid using a standard triangulation method similar to that used in a finite element analysis. Displacements were transformed into a material-based frame of reference such that displacements and strains were computed relative to the wall before testing began.

The PTT results are presented in Section 6.6.4 and Section 6.6.5.3 for the PT SW, PT DW and then PT core-wall tests respectively.

## 6.6 TESTING RESULTS

The experimental results of the three phase shear wall testing programme are discussed in each appropriate section. The key performance indicators are provided at two limit states, Serviceability Limit State (SLS) level, defined herein as 0.33% inter-storey drift ratio, and Peak Drift level. AS/NZS 1170.0 Appendix C (2002) specifies SLS of 0.33% for plaster/gypsum walls which are commonly used in NZ timber buildings. In order to quantify the increased system stiffness during DW and core-wall testing, the partial composite action of the DW and core-wall tests is presented by comparing test results with theoretical non-composite and fully composite systems in a similar manner to composite beams, as shown in Equation (6-1) (Gutkowski et al., 2008; Pault & Gutkowski, 1977).

$$\%CA = \frac{F_{Test,\delta} - F_{0\%,\delta}}{F_{100\%,\delta} - F_{0\%,\delta}} \quad (6\text{-}1)$$

where, for a given drift ($\delta$), $F_{0\%,\delta}$ is the theoretical force for a fully non-composite section, $F_{100\%,\delta}$ is the theoretical force for a fully composite section, and $F_{Test,\delta}$ is the measured force. The theoretical calculations are based on a PT rocking wall boundary condition following the Monolithic Beam Analogy (MBA) design procedure initially proposed by Pampanin et al. (2001) for precast concrete, extended by Palermo (2004) to capture the elastic range (called the Modified Monolithic Beam Analogy (MMBA)) and adopted by Newcombe et al. (2008) for timber. For DW and core-wall tests, $F_{0\%,\delta}$ was two in-plane PT CLT single walls with no composite action from friction or fasteners. For the DW tests, $F_{100\%,\delta}$ was a PT CLT wall with length of 3824mm, considering Wall 1 and Wall 2 with a rigid in-plane joint. For the core-wall tests, $F_{100\%,\delta}$ was determined by considering rigid connections between all Flange and Web Walls and the effective flange width was considered the full length of the Flange Wall. The theoretical calculations considered bending, shear, and rocking deformations. No sliding deformation was considered. The PT CLT walls were designed in accordance with the Pres-Lam design guide (Pampanin et al., 2013) which provides further details on the use of the MMBA with timber.

### 6.6.1 Post-Tensioned Single Wall Results Summary

For the SW tests, peak drift (PD) was limited to avoid significant damage to the compression toe at the wall base. As such, wall drifts were limited to 1.2%, 0.93%, 0.93%, and then 0.75% for Tests SW-1, SW-2, SW-3, and SW-4, respectively. These drifts were deemed sufficient to capture the SW behaviour while also minimizing compression toe damage for upcoming DW and core-wall tests. Table 6-10 list the key results from the SW tests.

*Table 6-10: Post-tensioned single wall key results summary*

| | Serviceability Limit State | | | | | Peak Drift | | | | | | |
|---|---|---|---|---|---|---|---|---|---|---|---|---|
| Test | CA (%) | F (kN) | $k_{sec}$ (kN/mm) | $\nu_{PT}$ (%) | $\nu_T$ (%) | Drift (%) | CA (%) | F (kN) | $k_{sec}$ (kN/mm) | $\nu_{PT}$ (%) | $\nu_T$ (%) | $E_D$ (kN-mm) |
| SW-1 | - | 16 | 0.6 | 7 | 26 | 1.2 | - | 53 | 0.6 | 30 | 66 | - |
| SW-2 | - | 29 | 1.1 | 14 | 29 | 0.93 | - | 57 | 0.7 | 31 | 69 | - |
| SW-3 | - | 32 | 1.2 | 17 | 37 | 0.93 | - | 63 | 0.8 | 33 | 64 | - |
| SW-4 | - | 38 | 1.4 | 23 | 32 | 0.75 | - | 64 | 1.1 | 34 | 64 | - |

Note: $\nu_{PT}$ is the yield percentage of the extreme post-tensioning bar; $\nu_T$ is the yield strain percentage of the extreme timber fibre value, determined by PTT and assuming $E_0$ = 9,700 MPa and $f_c$ = 37 MPa as per component testing in Chapter 7.

Figure 6-32 shows the base shear versus drift, moment versus rotation, and neutral axis depth versus rotation for the four SW tests. A typical non-linear elastic behaviour due to the gap opening at the wall base was observed. Increased initial post-tensioning forces delayed the onset of gap opening, and then the post gap opening wall stiffness was similar for all the tests as expected. The neutral axis depth ratio (c/h) was approximately 0.15 and slightly increased with increased initial post-tensioning forces. The minimum c/h ratio was also not exactly symmetrical due to the slightly non-symmetrical placement of the PT bars as shown in Figure 6-5. The PT force versus drift / rotation are not reported as only the outer PT bars were measured in most tests. In Test SW-2, all four post-tensioning bar forces were recorded and Test SW-2 will be used in Chapter 7, analytical design of PT CLT SW systems.

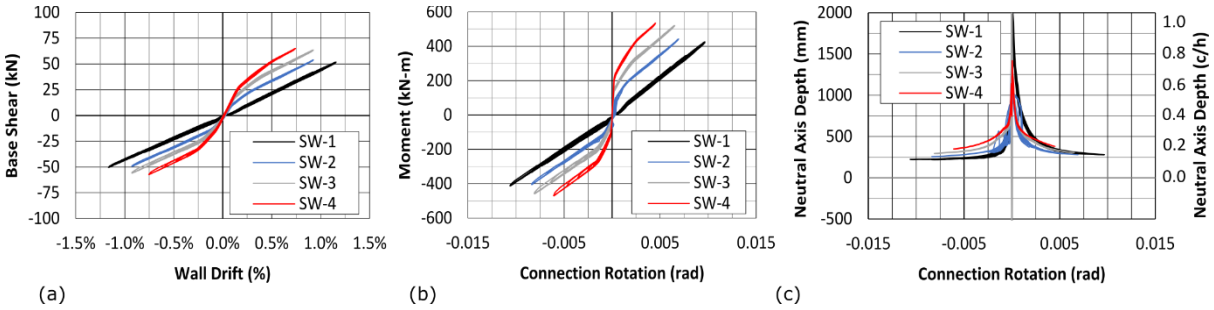


*Figure 6-32: SW test series summary: (a) base shear – drift, (b) moment – rotation, and (c) neutral axis depth – connection rotation*

Figure 6-33 shows a photo of the wall base with gap opening and tendon elongation on the left side of the wall and the compression toe on the right side with the assumed triangular stress/strain profile.

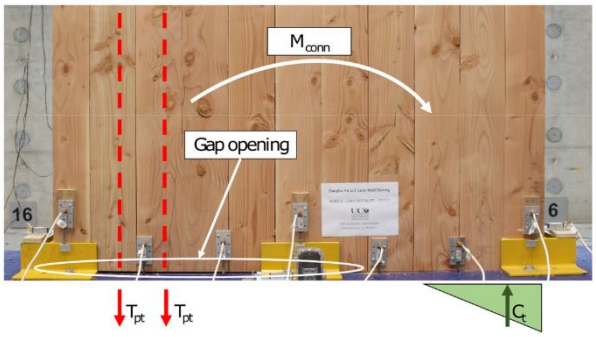


*Figure 6-33: During testing photo of single wall base*

## 6.6.2 Post-Tensioned Double Wall Results Summary

### *6.6.2.1 Global wall response*

The DW testing results summary is shown in Table 6-11. Table 6-11 shows that the composite action (CA) decreased at Peak Drift (PD) when compared to SLS drift. This was due to the gradual strength and stiffness degradation of the STS in-plane joint. The highest composite action was observed in Test DW-3, where composite action at SLS and PD were 70% and 38% respectively. The low composite action values reported in Test DW-1 are indicative of the friction contribution which had been noted previously by Moroder et al. (2018).

*Table 6-11: Double wall testing experimental results summary*

| | Serviceability Limit State | | | | | Peak Drift | | | | | | |
|---|---|---|---|---|---|---|---|---|---|---|---|---|
| Test | CA (%) | F (kN) | $k_{sec}$ (kN/mm) | $\nu_{PT}$ (%) | $\nu_T$ (%) | Drift (%) | CA (%) | F (kN) | $k_{sec}$ (kN/mm) | $\nu_{PT}$ (%) | $\nu_T$ (%) | $E_D$ (kN-mm) |
| DW-1 | 11 | 45 | 1.6 | 13 | 22 | 1.2 | 9 | 124 | 1.3 | 36 | 66 | 17,040 |
| DW-2 | 34 | 66 | 2.4 | 13 | 25 | 1.2 | 19 | 155 | 1.6 | 37 | 79 | 38,680 |
| DW-3 | 70 | 100 | 3.7 | 17 | 21 | 1.2 | 38 | 217 | 2.3 | 40 | 61 | 65,300 |
| DW-4 | 39 | 71 | 2.6 | 13 | 6 | 1.2 | 23 | 169 | 1.8 | 36 | 70 | 41,420 |
| DW-5 | 16 | 49 | 1.8 | 12 | 10 | 1.2 | 15 | 144 | 1.5 | 35 | 37 | 22,090 |

Note: F is the force, $k_{sec}$ is the secant stiffness, $\nu_{PT}$ is the yield percentage of the extreme post-tensioning bar; $\nu_T$ is the yield strain percentage of the extreme timber fibre value, determined by PTT and assuming $E_0$ = 9,700 MPa and $f_c$ = 37 MPa as per as per component testing in Chapter 4.

Figure 6-34 compares the key parameters of each test with the theoretical fully composite ($F_{100\%,\delta}$) and non-composite ($F_{0\%,\delta}$) PT walls. At low drift levels, Test DW-3 closely matched the theoretical fully composite curve. This was primarily due to the STS connection behaving within its elastic range and having higher stiffness as well as the higher friction while the wall panels align and initiate rocking as was reported by Moroder et al. (2018). However, with stiffness degradation of the STS joint the DW systems gradually tended away from the theoretical upper bound. The neutral axis behaviour was significantly different in Test DW-3. In this Test, a negative neutral axis was reported which indicated

one wall uplift due to the high strength and stiffness of the in-plane joint connection. This was unique behaviour not previously observed in past PT DW testing that used the in-plane joint slip to provide increased energy dissipation during the rocking motion (Chen et al., 2020; Ganey et al., 2017;Iqbal et al., 2015). Residual drift was negligible in all tests except DW-3 where it was 0.1%. The STS performed differently when compared to other mild steel dissipaters. The pinching behaviour of the STS dowel-type connections in timber reduces the required restoring force while the total energy dissipation could be reduced. This phenomenon has also been reported by Iqbal et al. (2018).

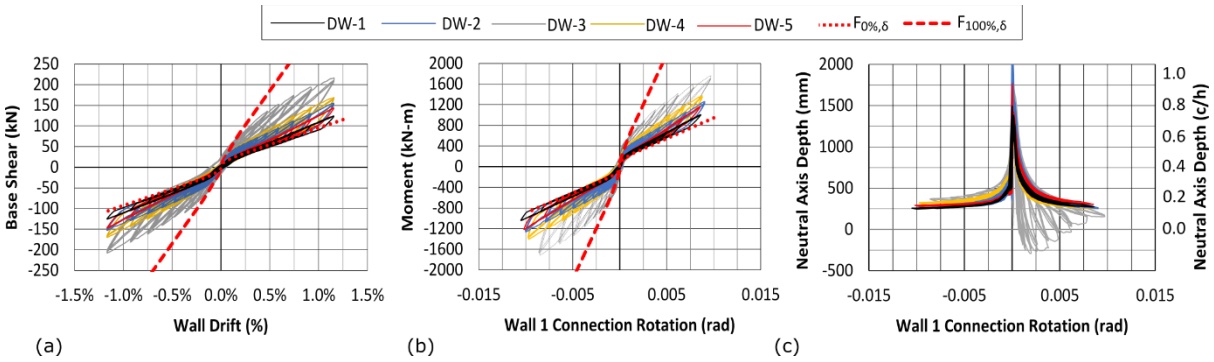


*Figure 6-34: DW Test Series Summary: (a) Moment - Drift, (b) Base Shear – Drift, and (c) Neutral Axis Depth – Connection Rotation*

The secant stiffness values at given drift levels include all possible slips and translational sliding due to the tolerances between the CLT wall panels. The SLS stiffness of 1.6 kN/mm achieved in Test DW-1, represents a lower bound for this PT CLT DW system. The significant change in stiffness for Tests DW-2, DW-3 and DW-4 indicated the impact of connection detailing on the system behaviour. In Test DW-3, the SLS stiffness was 3.7 kN/mm, more than two times of that achieved in Test DW-1. The yield percentage of the extreme PT bar is also reported in Table 6-11 and in test DW-3, 40% was reached at Peak Drift. Note that the initial post-tensioning forces were kept relatively low (5% of PT bar yield) to avoid significant crushing damage at the compression toe of the CLT wall for future core-wall testing. The yield strain percentage, $\gamma_T$, of the timber was determined by PTT. This was unique when compared to past experimental testing by Sarti et al. (2016), where timber strain values were back calculated assuming a triangular distribution, or not reported at all other than test observations (Chen et al., 2020; Ganey et al., 2017). The compression toe performance and PTT work will be discussed in Section 6.6.4 further and then in greater detail in Chapters 7-9 where it was used to inform and update analytical models for PT CLT walls.

#### *6.6.2.2 Energy dissipation comparison with STS and UFP dissipating elements*

The difference between using STS or UFPs as dissipating elements can be compared with Tests DW-2 and DW-5 in terms of total energy dissipation, $E_D$. Test DW-2 implemented STS while Test DW-5 implemented UFPs. The $\beta$ ratio was 0.67 and 0.72 in Tests DW-2 and DW-5 and therefore relatively

similar. $E_D$ of Test DW-2 was 1.75 times greater than that of Test DW-5. This was primarily due to the fact that the UFP requires a relatively large imposed displacement prior to yielding due to its lower stiffness, the fact that its rolling motion is not perfectly vertical, and with less significance but also due to its connection slips. It was found that an approximately 12mm imposed displacement was required for the UFPs to reach their yielding plateau, determined by the UFP component testing results (see Section 6.3.6). This was corresponding to approximately 0.8% wall drift. In contrast, the STS connections reached yielding at approximately 5mm connection displacement (Hossain, 2019); and significant energy dissipation could occur at even lower imposed displacements. The 5mm in-plane joint displacement occurred at approximately 0.25% wall drift. It should be noted this comparison is limited to relatively small wall drifts (1.2%) where the STS joint displacement reached 15mm. Work by Hossain (2019) showed that peak load of this type of STS connections occurs at approximately 19mm displacement. Therefore, the DW system displacement capacity with STS would be limited and significant strength and stiffness degradation would occur beyond 19mm connection displacement. The UFP energy dissipating devices have been shown to undergo displacements greater than 70mm (see Figure 6-15) which would provide stable performance even at very large wall drifts. This is an important consideration that should be distinguished for design. Currently, PT walls are generally designed to not have gap opening at SLS drift. In order to achieve this objective at SLS drift, the initial post-tensioning force should have been approximately 150kN/bar. Then, the connection displacement would be approximately 2mm and below the 5mm STS connection yield point previously described.

#### *6.6.2.3 Double wall selected tests detailed response*

Figure 6-35 shows the key plots summary for Tests DW-2, DW-3, and DW-4. All post-tensioning bar forces are reported as a pair as described in Section 6.3.3. In Test DW-3, the increase in PT1-N forces during positive drift cycles indicates tendon elongation due to wall uplift. The same behaviour occurred in PT2-S forces during negative drift cycles. The neutral axis behaviour was similar for Wall 1 and Wall 2 due to the symmetrical behaviour of the test setup as expected. In Test DW-3, the negative neutral axis depth which indicated wall uplift is shown for both Wall 1 and Wall 2 during positive and negative drift cycles respectively. At a base connection rotation of approximately 0.006 rad, the wall touched the ground, and a positive neutral axis is reported. The neutral axis depth ratio (c/h) was approximately 0.25 in Test DW-3, which was larger than Tests DW-2 and DW-4 where the c/h ratio was closer to 0.15 at Peak Drift. The relative connection slip at the in-plane joint varied in each test due to the different strength and stiffness of the STS connection details and UFP devices. At 1.2% wall drift, the connection slips were 17.1mm, 15.1mm, and 16.1mm for Tests DW-2, DW-3, and DW-4.

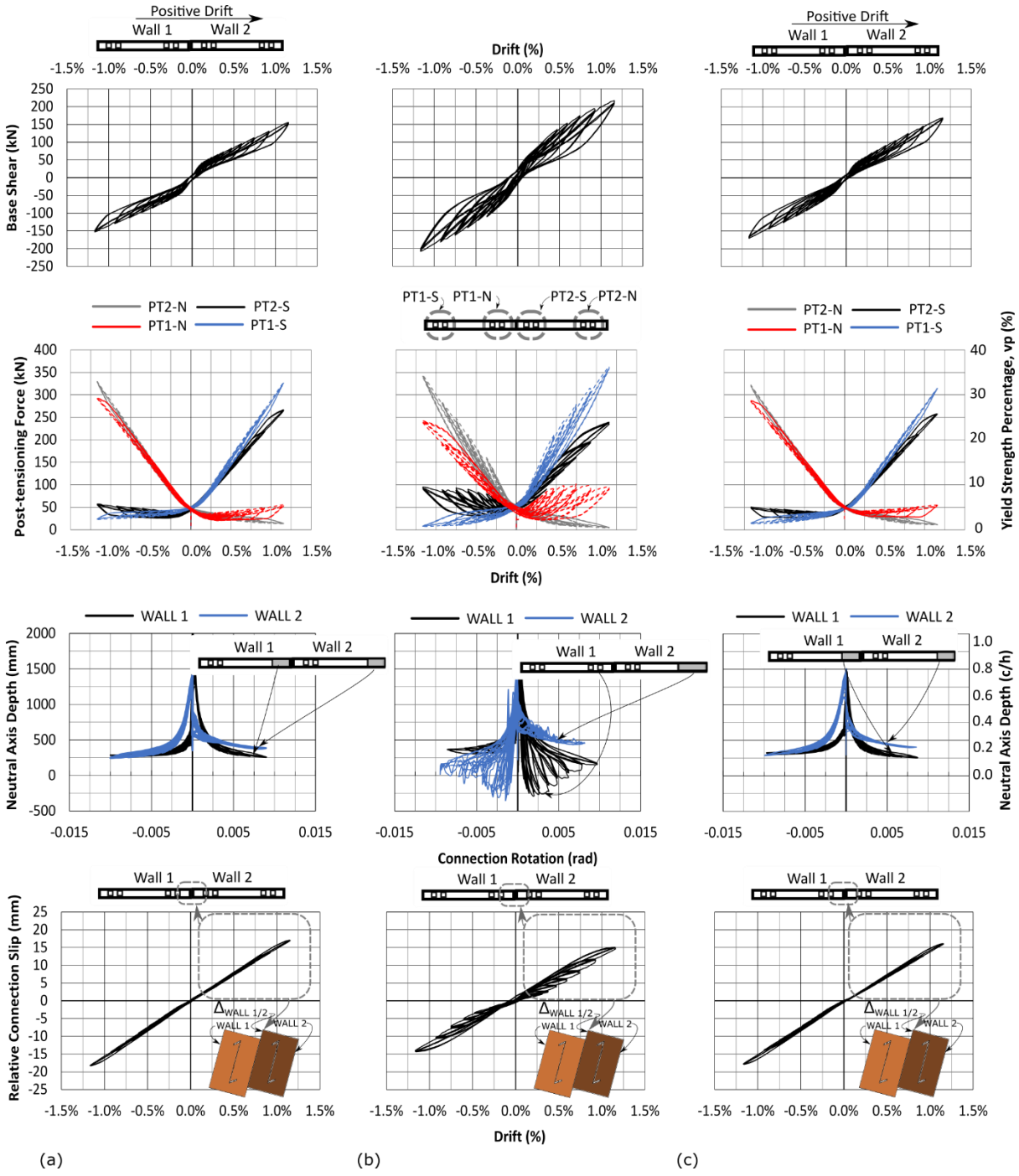


*Figure 6-35: DW testing Key Plots: (a) Test DW-2, (b) Test DW-3, and (c) Test DW-4*

### *6.6.2.4 Double wall connection response*

Figure 6-36 shows the after test photos of the in-plane joint. Figure 6-36b shows that the CLT damage due to embedment crushing was very localized to the STS location. STS in Test DW-3 (shown in black) were placed at 5d spacing apart from the original STS location in Test DW-2 (shown in red) and no negative impact was observed. The spacing requirements as per ETA (ETA-12/0114, 2017) is 10d. In Figure 6-36b, the after test photos of the $\phi$8x80mm PTH STS are shown. There was minor yielding of

the STS which could in part be due to the fact that the specimens were returned to 0% drift and also due to the relatively stockier nature of the STS which meant that primarily embedment crushing occurred. Figure 6-37 shows that the in-plane relative joint slip increased slightly with the increased wall height due to elastic deformation of the walls. However, the joint slip difference was less than 2mm over the wall height. At 1.2% wall drift, the relative slip was 15.1mm and 16.2mm at 0.4m and 4m wall height respectively. The in-plane joint slip at 7.6m wall height was less and 15.1mm due to the increased clamping effect that occurred in close proximity to the 8.2m wall height load application, though it was not significant in the double wall testing.

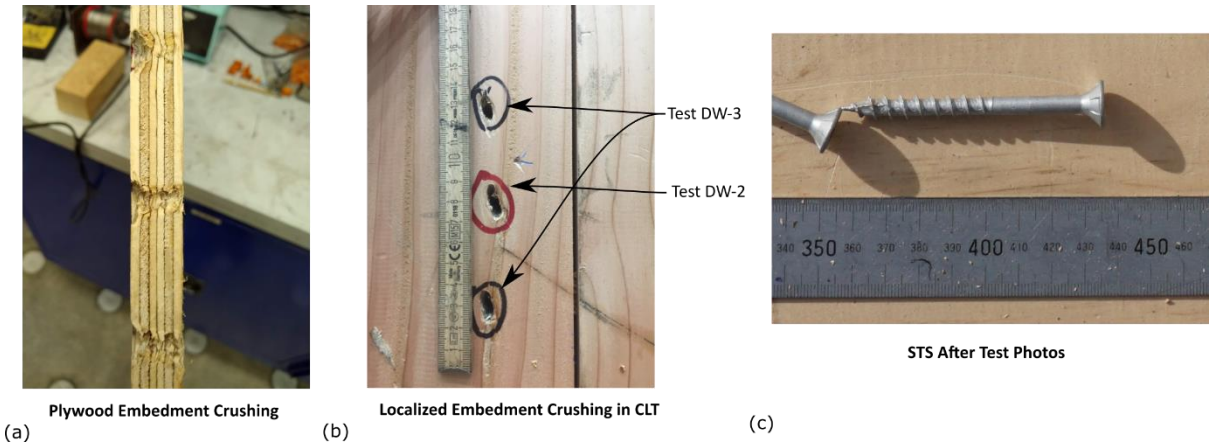


*Figure 6-36: After test photos of In-Plane joint: (a) Plywood, (b) CLT, and (c) STS*

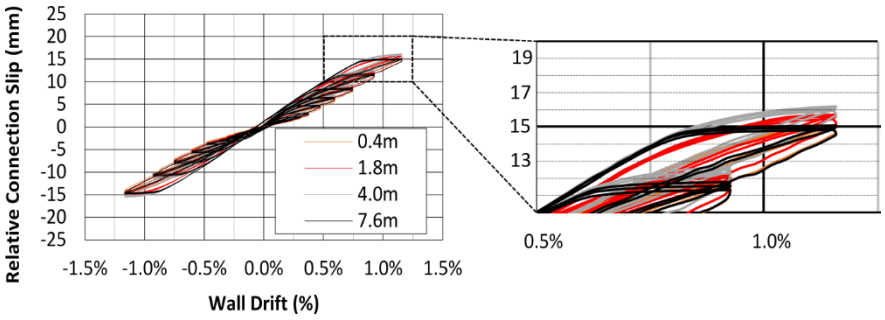


*Figure 6-37: In-plane joint relative connection slip at varying wall heights*

### 6.6.3 Post-Tensioned Single and Double Wall Out-of-Plane Twisting

Out-of-plane twisting occurred during both SW and DW testing. On the positive "push" wall drift cycles, the twisting was significant whereas on the negative "pull" wall drift cycles it was minimal. Figure 6-38 shows the SW twisting at 2m, 4m, 5m, 6m, and then 8m wall elevations. Greater than 50mm wall twist occurred at +0.93% drift cycle. The out-of-plane support rams were connected to the centre of the wall: however, the steel fittings for the rams have pin-pin detailing with spherical bearings which meant the wall could rotate around the support point as shown in Figure 6-38. Similarly for DW testing, Figure 6-39 shows the twisting of Wall 1 at 2m, 4m, 5m, 6m, and then 8m wall elevations. Greater than 50mm wall twisting occurred at +1.20% drift cycle. Consequently, on the

positive drift "push" cycles, additional force occurred to account for this twisting phenomenon which meant the curves in Figure 6-32 and Figure 6-34 were unbalanced. Table 6-12 provides a summary of the load differences on the push and pull cycles, and the maximum load difference was 18% in Test SW-4. This load difference was less significant in the DW testing which was attributed to the coupling from the plywood connection at the in-plane joint and the fact that the total loads were relatively larger. Nonetheless, in Chapters 7 and 8 the analytical models will be compared to the negative (pull) backbone curve only. Future work should install two rams at each restraint level per wall, provide out-of-plane guides, or provide continuous out-of-plane restraint as done in Hashemi et al. (2018).

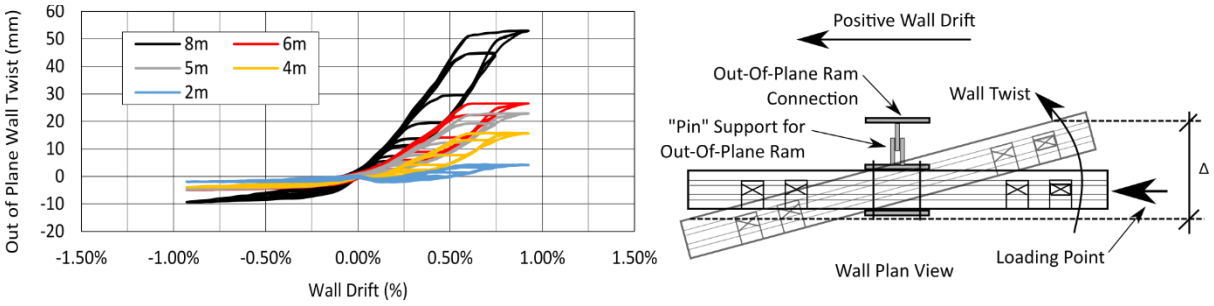


*Figure 6-38: SW testing wall twist at different wall heights for test SW-2*

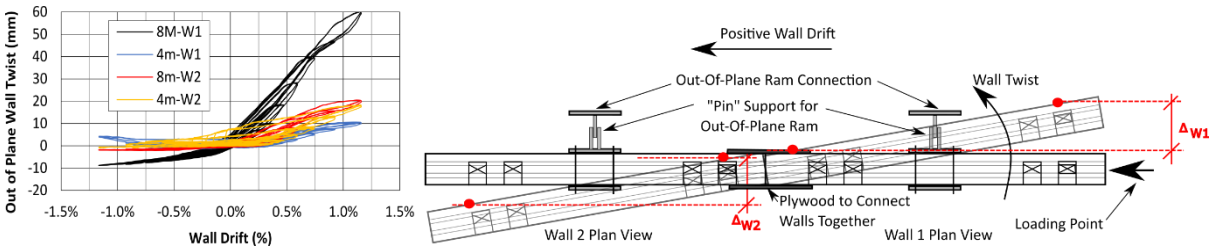


*Figure 6-39: DW testing wall twist at different wall heights for test DW-3*

*Table 6-12: SW and DW testing push and pull cycle load comparison*

| Test | Peak Drift | Push | Pull | Difference |
|---|---|---|---|---|
| - | % | kN | kN | % |
| SW-1 | 1.2 | 52 | -50 | 4 |
| SW-2 | 0.9 | 54 | -49 | 10 |
| SW-3 | 0.9 | 64 | -56 | 14 |
| SW-4 | 0.75 | 65 | -55 | 18 |
| DW-1 | 1.2 | 125 | -125 | 0 |
| DW-2 | 1.2 | 155 | -153 | 1 |
| DW-3 | 1.2 | 217 | -208 | 4 |
| DW-4 | 1.2 | 169 | -169 | 0 |
| DW-5 | 1.2 | 145 | 147 | -1 |

### 6.6.4 Post-Tensioned Single and Double Wall Compression Toe Performance

In Figure 6-40, the Test SW-2 displacement and strain field, generated with Particle Tracking Technology (PTT), is compared with MMBA predictions at wall drift of 0.9%. $Y_c$ represents vertical movement (mm), and x and y represent the material (i.e., particle) location along the wall with respect to its lower corner. At 0.9% drift, the MMBA over predicted the neutral axis depth, and thus under predicting the peak strain level. The MMBA prediction and experimental neutral axis depths are 325mm and 150mm respectively. The experimental results indicated that there was an initial disturbed region near the location of the neutral axis, and that throughout the neutral axis depth there was variation within the strain field. A thorough discussion of PTT and SW testing will be presented in Chapter 7 when discussing the extensions to the MMBA analytical model. It is worth noting that although the MMBA over predicted the neutral axis depth, the global system response was reasonably well predicted and within 15% error when characteristic material properties were used and only parallel-to-grain CLT layers were considered, which will be presented in Chapter 7.

Past research has primarily used LVL with the MMBA to predict the response. LVL is a relatively more homogenous material when compared to CLT, and Figure 6-40 shows two different neutral axis and strain predictions when the effective elastic modulus and wall width are varied within the MMBA calculation. With CLT, the impact of the cross-layer, the higher probability of imperfections due to knots and checks near the compression toe, and the fabrication process including being non-edge glued panels all add to the variability in strain that is reflected in Figure 6-40. This is significantly different than LVL, where thin veneers are glued together such that all fibres are aligned and the influence of knots and checks are significantly less.

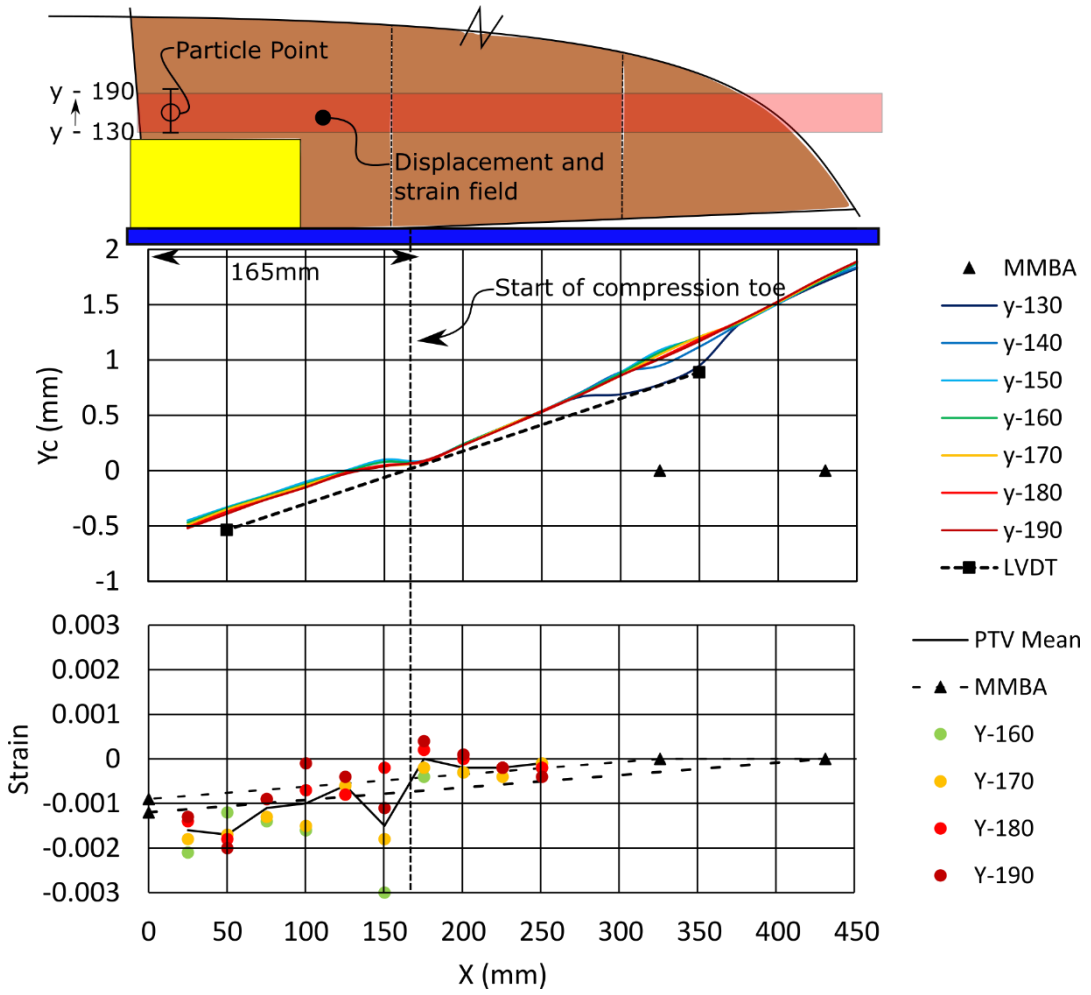


*Figure 6-40: Test SW-2 displacement and strain distribution with comparison to MMBA*

The displacement and strain at a point near the toes for Test SW-2 and Test DW-3 are shown in Figure 6-41a and Figure 6-41b respectively. In these figures, 't' represents a time step in the loading protocol. Refer to Figure 6-40 for the point location. The vertical displacement change from y=130 to y=200 during rocking to the toe indicates compression, which is reflected as compressive strain. The maximum compressive strain recorded was -2600 and -3000 με for Test SW-2 and DW-3 respectively. In Figure 6-41b, the three cycles at 1.2% drift are presented with compression strain occurring when the point is within the neutral axis and tension strain occurring during uplift. The measured strain of Test SW-3 shows a linearly increasing compression strain trend to peak at 1.2% wall drift at t=67.0, 72.5, and 78.0. This indicates that stable behaviour occurred at the point indicated in Figure 6-40.

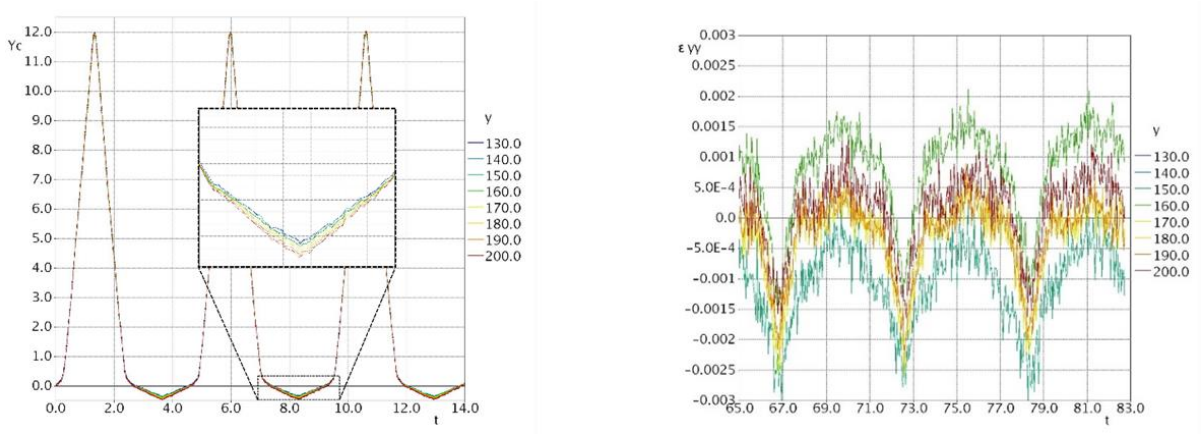


*Figure 6-41: (a) Test SW-2 displacement at 0.9% wall drift; and (b) Test DW-3 strain at 1.2% wall drift*

The displacement field at peak drift is shown for Test DW-3 in Figure 6-42. These displacement fields are generated from PTT. Agreeing with Test SW-2, there is a distinct disturbed region shown at x=1550mm in Figure 6-42 where more significant compression occurs. Following the disturbed region, the displacements over 250mm wall height, y, changed in a relatively similar manner.

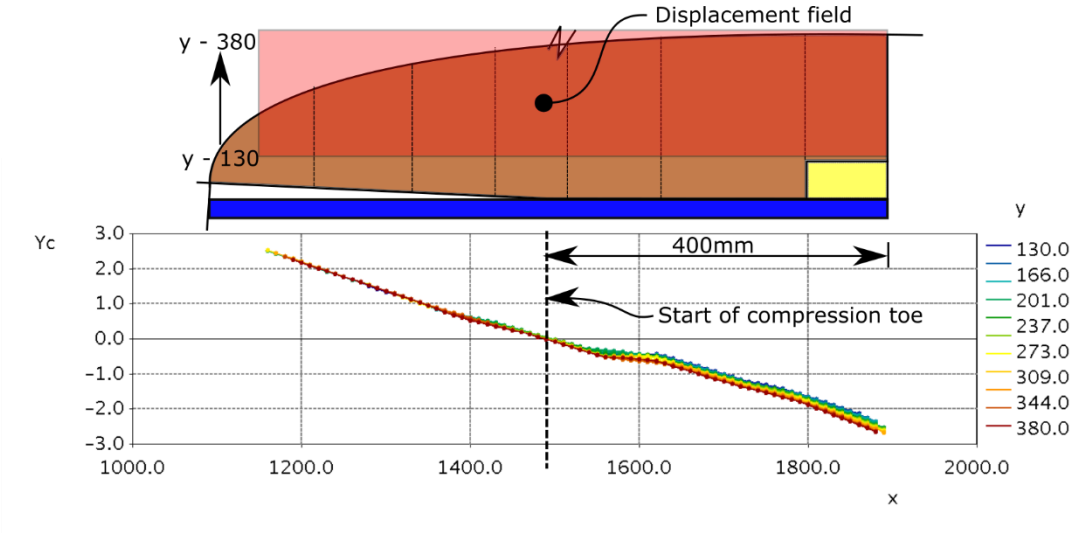


*Figure 6-42: Test DW-3 wall 2 compression toe performance at 1.2% wall drift*

Figure 6-43 shows the compression toe residual deformation after DW testing. As indicated by the Figure, residual deformation was minimal and less than a few millimetres. Further, damage was concentrated to the last 150mm of the compression toe. This minimal residual deformation was considered not to affect the performance of the subsequent core-wall testing.

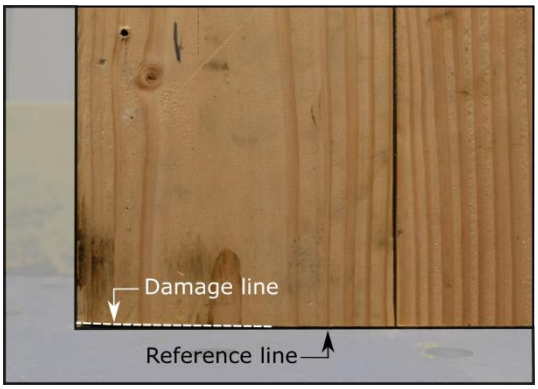


*Figure 6-43: Compression toe residual deformation after double wall testing*

### 6.6.5 Post-Tensioned Core-Wall Testing Results Summary

The key test results along the strong axis loading are reported in Table 6-13. In Tests CW-1, CW-3 and CW-4, peak drifts were limited to avoid significant damage to the compression toe at the wall base. During Test CW-2, a peak drift of 1.5% was deemed sufficient to capture the core-wall behaviour while also minimizing compression toe damage for upcoming tests. Test CW-5 peak drift was limited due to tensile failure of screws at the in-plane joint which will be discussed and Tests CW-6 and CW-7 peak drifts were limited by the actuator's stroke limit.

*Table 6-13: Experimental data results: summary of strong-axis loading*

| | Serviceability Limit State | | | | | Peak Drift | | | | | | | | | |
|---|---|---|---|---|---|---|---|---|---|---|---|---|---|---|---|
| Identifier | CA | F | $k_{sec}$ | $v_{PT,web}$ | $v_{PT,fl}$ | Drift | CA | F | $k_{sec}$ | $v_{PT,web}$ | $v_{PT,fl}$ | $E_D$ | $\delta_{r,w1}$ | $\delta_{sl,w1}$ | $\delta_{b+s,w1}$ |
| | % | kN | kN/mm | % | % | % | % | kN | kN/mm | % | % | kN-mm | % | % | % |
| CW-1 | 13 | 60 | 2.2 | 11 | 6 | 1.2 | 9 | 154 | 2.4 | 35 | 15 | 39,672 | 90 | 1 | 9 |
| CW-2 | 43 | 179 | 6.5 | 21 | 20 | 1.5 | 26 | 375 | 3.2 | 48 | 39 | 208,701 | 68 | 5 | 27 |
| CW-3 | 9 | 77 | 2.8 | 22 | 17 | 0.7 | 14 | 140 | 2.3 | 32 | 19 | 15,637 | 82 | 2 | 16 |
| CW-4 | 9 | 76 | 2.8 | 21 | 17 | 0.8 | 13 | 146 | 2.2 | 33 | 23 | 10,418 | 88 | 2 | 12 |
| CW-5 | 61 | 230 | 8.4 | 20 | 21 | 1.2 | 57 | 555 | 5.8 | 41 | 43 | 239,741 | 58 | 5 | 37 |
| CW-6 | 65 | 242 | 8.9 | 21 | 21 | 2.3 | 49 | 845 | 4.5 | 68 | 73 | 707,022 | 61 | 4 | 35 |
| CW-7 | 44 | 128 | 4.7 | 12 | 10 | 2.3 | 22 | 460 | 2.5 | 58 | 45 | 333,166 | 73 | 3 | 24 |

Note: CA= composite action as defined by; $k_{sec}$ = secant stiffness; $v_{PT,web}$ and $v_{PT,fl}$ = yield percentage of web and flange extreme post-tensioning bar, respectively; $E_D$ = total energy dissipation during full loading protocol; $\delta_{r,w1}$ = rocking deformation percentage of total Wall 1 deformation; $\delta_{sl,w1}$= sliding deformation percentage of total Wall 1 deformation; $\delta_{b+s,w1}$= bending and shear deformation percentage of total Wall 1 deformation.

Figure 6-44 shows the changing composite action (CA) at each drift level for each test. The highest CA was observed in Test CW-6, where composite action at 0.33%, 1.5%, and 2.3% drift were 65%, 62%, and 49% respectively. This gradual decrease in composite action with increased wall drift was also observed in Tests CW-2 and CW-7 and is indicative of the stiffness degradation of the screwed connections at the orthogonal and the in-plane joints. A sudden drop of composite action in Test CW-

5 occurred when tensile failure of screws at the in-plane joint occurred. This will be further discussed. The low composite action values reported in Tests CW-1, CW-3, and CW-4 are indicative of the friction contribution that occurred which had been noted previously by Moroder et al. (2018).

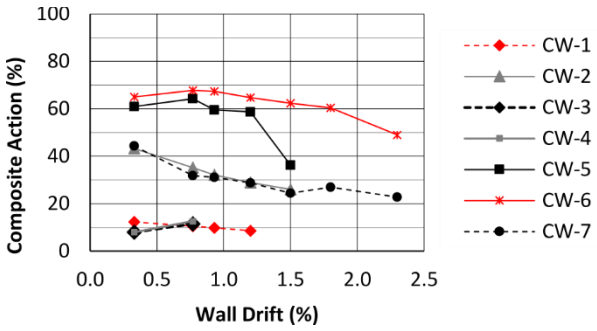


*Figure 6-44: Composite action summary*

The secant stiffness values at given drift levels in Table 6-13 include all possible slips and translational sliding due to the tolerances between the CLT wall panels. The SLS stiffness of 2.2, 2.8, and 2.8 kN/mm achieved in Tests CW-1, CW-3, and CW-4 respectively represent a lower bound for this PT CLT core-wall system. The significant change in stiffness for Tests CW-2, CW-5 and CW-6 indicated the impact connection detailing choice has on the system behaviour. In Test CW-6, the SLS stiffness was 8.9 kN/mm, almost four times of that achieved in Test CW-1.

The kinematics of the PT CLT core-wall was also dependent on the connection detailing chosen between the CLT wall panels. The deformation contributions listed are in reference to the displacement/drift at wall height 8.2m. For CW-6 using the mixed angle screwed connections, individual contributions to the total wall drift due to rocking, sliding, and shear and bending were 61%, 4% and 35% respectively. They were 82%, 2% and 16% respectively for the comparable Test CW-3. The observation was different from past conventional CLT shear wall testing by Gavric et al. (2015) where the combined contribution of in-plane shear and bending deformation was less than 5% and the wall drift was mainly caused by rigid body movement of CLT due to rocking and horizontal sliding. Therefore, this experimental study indicated that the PT CLT core-wall with careful connection detailing was able to provide much more efficient utilization of strong and stiff CLT panels when compared to conventional CLT shear walls. The bending and shear deformation contribution of 35% was comparable to that reported by Sarti et al. (2016) with post-tensioned LVL single wall testing.

#### *6.6.5.1 Global post-tensioned core-wall response*

All tests displayed non-linear geometric elastic behaviour, typical of PT rocking systems. In Tests CW-1, CW-3 and CW-4 very low energy dissipation was observed which was due to friction between the panels and minor post-tensioning losses. Residual drifts for Tests CW-1, CW-3, and CW-4 were

negligible. Post-tensioning losses at the end of each test were 5% (Web Walls) and 22% (Flange Walls) for Test CW-1, but negligible for Tests CW-3 and CW-4 respectively. The sequence of the testing and past peak post-tensioning forces observed in comparison to the current test influenced the amount of post-tensioning loss in the current test. For example, in Test CW-1 the Web Wall post-tensioning losses were significantly less than the Flange Wall post-tensioning losses because the Web Walls were previously used in SW and DW testing phases and had therefore been subject to similar or higher axial stresses. Then, In Tests CW-3, and CW-4, post-tensioning losses were negligible because the Web and Flange Walls had previously been subjected to high axial stresses in previous Test CW-2. The initial post-tensioning force was approximately 5% for Tests CW-1 and CW-7 versus 10% for Tests CW-2 through CW-6, respectively, axial load CLT wall ratio as per NZS3603 (1993).

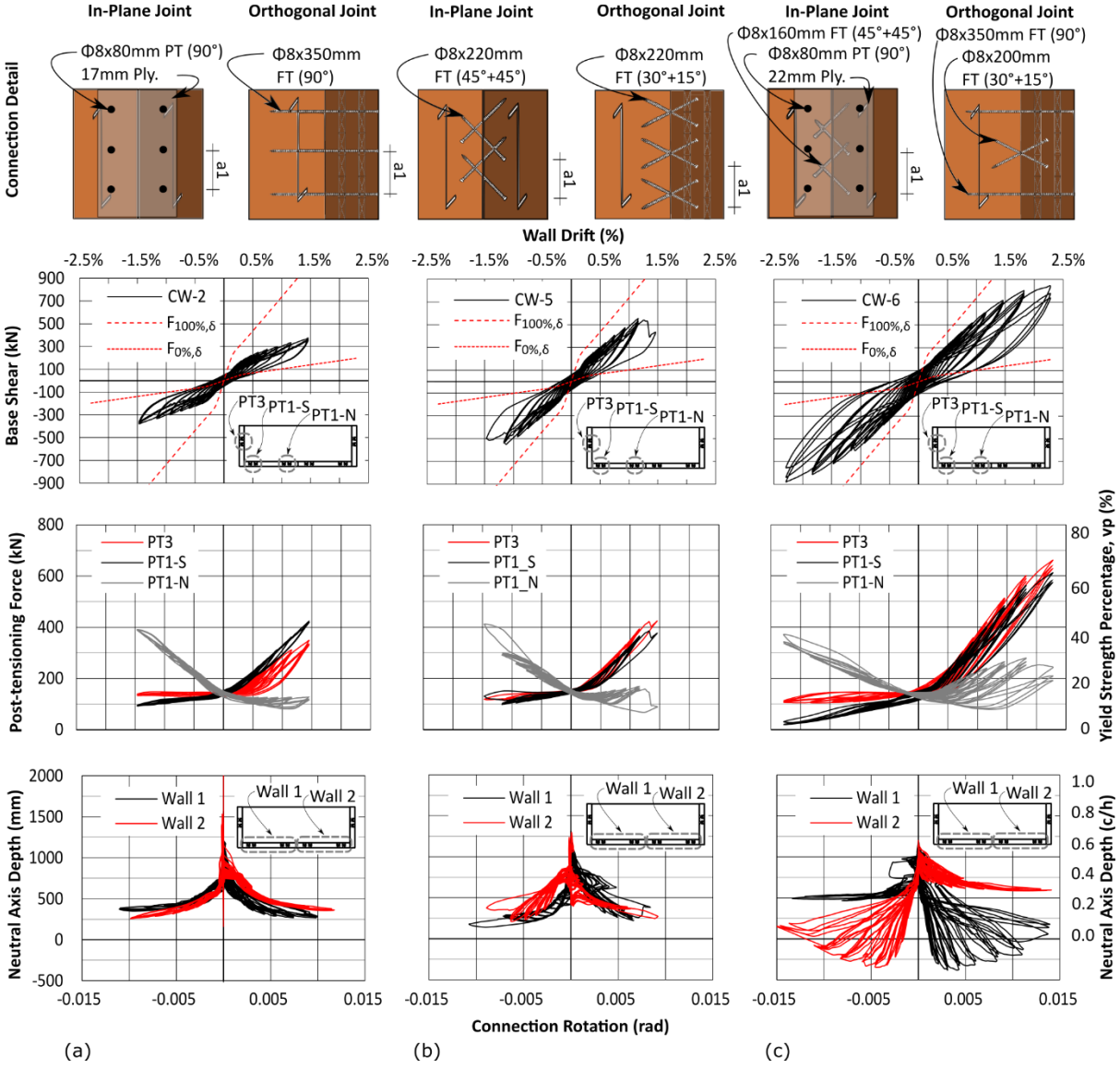


*Figure 6-45: Key strong-axis experimental results: (a) test CW-2, (b) test CW-5, and (c) test CW-6*

Figure 6-45 shows selected key plots from Tests CW-2, CW-5, and CW-6. The base shear-wall drift plots compare test results to the theoretical fully composite, $F_{100\%,\delta}$, and fully non-composite, $F_{0\%,\delta}$, core-wall. Similar to CW-1, CW-3 and CW-4, a typical non-linear elastic behaviour due to wall gap opening was observed. The initial slip in each test before yielding was observed because of the residual deformation developed at the wall bases, sliding, compression perpendicular to grain of the flange walls and the tolerances at the wall base. In Test CW-6, peak sliding was 24mm at $\pm$2.3% core-wall drift. With reduced screw spacing and the use of inclined screws, the core-wall strength, stiffness, and energy dissipation increased significantly. In particular, the use of mixed angle screws led to enhanced displacement capacity and energy dissipation. In Test CW-6 at 2.3% drift, a peak load of 845kN (≈7000kN-m overturning moment at the core-wall base) was achieved. At this drift level, a maximum load of 85kN was recorded in the actuators along the weak axis to provide torsional restraints. Investigating torsional response was beyond the scope of work presented herein. Though, the reported results indicated that torsional restraint would be required if a C-shaped CLT core-wall system connected together with STS was implemented in design. In order to investigate torsional response, a specifically designed experimental test set-up should be developed as was done by Beyer et al. (2008) for reinforced concrete U-shaped walls.

In Figure 6-45 the PT force-drift curves are shown for Walls 1 and 3 as similar responses in Walls 2 and 4 were observed due to the symmetrical wall layout, shown in Figure 6-25. The increase in post-tensioning forces in Wall 3 from Test CW-2 to CW-6 showed the increased stiffness and CA due to the enhanced orthogonal joint. In Test CW-6, the post-tensioning forces were higher in the Flange Wall 3 when compared to the Web Wall 1. The similar post-tensioning decrease in PT1-S and PT3 for each cycle at 2.3% drift in Test CW-6 indicated the stiffness degradation in the in-plane vertical joint. Average post-tensioning losses for each test considering all unbonded bars were 9% (CW-2), 2% (CW-5), and 9% (CW-6) of initial post-tensioning force respectively. The sequence of the testing and past peak post-tensioning forces observed in comparison to the current test influenced the amount of post-tensioning loss in the current test. There were increased post-tensioning in Test CW-6 because the walls were subject to the highest axials stresses from the PT bars.

The change of the neutral axis depth (c) compared to wall length (h) in Tests CW-2 and CW-5 showed that both Wall 1 and Wall 2 were in contact with foundation throughout the tests. In Test CW-6, the negative neutral axis depth indicated Web Wall uplift, which was unique behaviour when it was compared with past PT coupled wall testing. Wall uplift also occurred in Test DW-3. As illustrated in Figure 6-46, when the core-wall drift increased from the SLS level 0.33% to 1.8%, Web Wall 2 was completely lifted off the foundation. This was due to the high strength and stiffness of the in-plane joint. However, at 2.3% wall drift, the increased shear demand on the in-plane joint from increased

post-tensioning forces and shear flow due to composite action was greater than the capacity of the mixed angle STS connection. In the following second and third cycles at 2.3% wall drift, Wall 2 was in contact with the foundation. This is shown as a positive neutral axis and by the lower post-tensioning forces of PT1-S, PT1-N and PT3 of Figure 6-45c. At 2.3% wall drift, the in-plane deformation was greater than 20mm. The STS connection testing presented in Chapter 4 showed that significant energy dissipation occurs at joint slips less than 5mm. In all tests in general, the shifting of the neutral axis at each drift cycle and the differences between load and unload cycles were indicative of the STS connections with pinching behaviour and stiffness degradation. Though, the mixed angle STS connection ensured any behaviour was gradual and stable. Figure 6-46 is vertically exaggerated to show the wall base kinematics more clearly. In Chapter 9, three different core-wall kinematic modes to capture rocking deformation are derived: low composite action where all walls are in contact with the foundation, medium composite action (MCA) where Flange Wall uplift occurs, and high composite action (HCA) where both Flange and Web Wall uplift occur. In Test CW-6, the core-wall kinematics changed from HCA to MCA due to the aforementioned points which will be used to inform the proposed core-wall analytical model developed in Chapter 9.

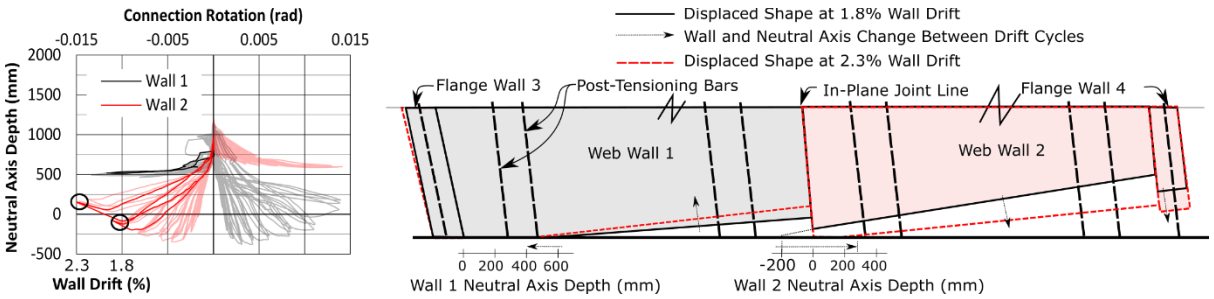


*Figure 6-46: Test CW-6: changing neutral axis*

At the end of each test, total residual drifts which included base sliding due to tolerances, relative joint slip, and timber crushing were 0.2% (CW-2), 0.2% (CW-5), and 0.5% (CW-6) respectively. The contribution of base sliding in total residual drift was 0.1% for Test CW-2 and CW-5, and 0.2% for Test CW-6. As residual drift is often associated with residual "tilt" and not sliding, the total residual drift in Test CW-6 could be reported as 0.3% and not 0.5%. The increased residual drift of Test CW-6 was primarily due to yielding of the STS connections along the orthogonal and in-plane joints where there was an average residual joint slip of more than 3mm. In Test CW-6, residual drift was negligible until the 1.8% drift cycle where it was 0.3%. Increasing the initial post-tensioning level might be able to reduce the residual drifts. However, the compressive stress level in wood should remain relatively low to avoid the long-term loaded timber creep effect (Ranta-Maunus, 1975). While a creep model has been developed for CLT (Nguyen et al., 2019) and a design approach to predict post-tensioning losses in a PT LVL or glulam frame building has been developed and quantified (Granello et al., 2018; Granello

et al., 2018), further research is required for PT CLT wall structures. A detailed investigation on residual drift was beyond the scope of the work presented herein; though, Clifton et al. (2011) have discussed 0.3% residual drift as a performance index based on the Christchurch 2010/2011 earthquake sequence.

#### 6.6.5.1.1 Bi-directional loading and global wall behaviour along the weak axis

Test CW-7 which followed the uni-directional (Uni-Dir.) and cloverleaf (Bi-Dir.) loading protocol is shown in Figure 6-47. During the loading along the strong axis, a similar response between uni-directional and bi-directional loading was found. For loading along the weak axis, differences between the hysteresis loop and strength were observed, especially during loading in quadrant I and II of Figure 6-26. Although the system level performance was stable and no significant differences were observed in the compressive behaviour of the Flange Walls, further research is required to quantify these effects. As expected, the stiffness was much lower and unsymmetrical under the uni-directional loading along the weak axis. Web Walls 1 and 2 were engaged accordingly to the orthogonal joint connection stiffness. Tests CW-5 and CW-6 reached similar peak loads of 300kN, however the mixed angle connection provided increased energy dissipation. When the Web Walls were engaged in tension, post-tensioning forces increased accordingly indicating the Web Wall uplift. The average post-tensioning loss for Test CW-7 was 6% of initial post-tensioning force.

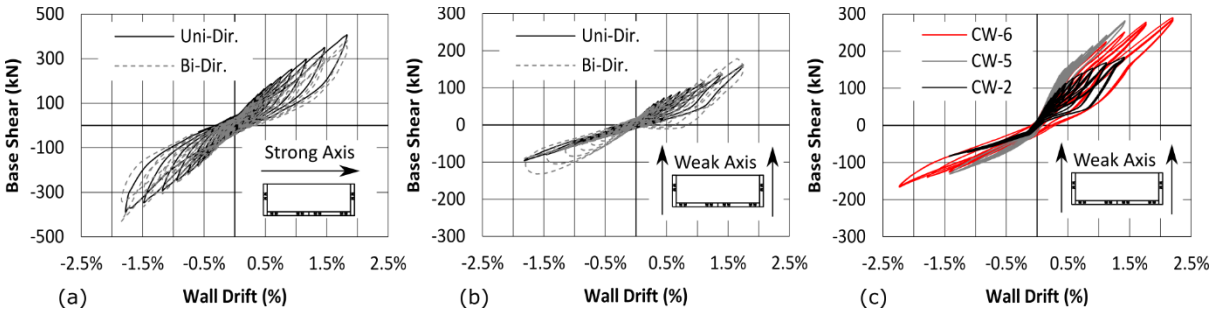


*Figure 6-47: Force-displacement: (a) Test CW-7 bi-directional strong axis, (b) Test CW-7 bi-directional weak axis, and (c) uni-directional weak axis*

### *6.6.5.2 Connection behaviour*

The STS connection details for the in-plane and orthogonal joints had primary influence on the core-wall system strength, stiffness, and displacement capacity. Other than STS connections, the castellations provided a strong and stiff horizontal joint, the diaphragm connection decoupled the wall-floor displacement incompatibility well, and each UFP connection performed well.

#### 6.6.5.2.1 STS connection behaviour

In the strong axis, Figure 6-48 shows the varying relative joint slips. At 0.75% drift, the relative slips in the in-plane joint were 13mm, 11mm, 6.6mm and 5mm for Tests CW-3, 2, 5 and 6 respectively. The relative slips in the orthogonal joints were 8.5mm, 4mm, 1mm and 1.5mm for Tests CW-3, 2, 5 and 6

respectively. In Test CW-5 in the 1.5% drift cycle group, the in-plane relative joint slip increased from 12mm to 20mm as a result of tensile failure in multiple inclined STS. The 12mm ultimate displacement capacity of the joint was similar to the findings from Hossain et al. (2016). By using the mixed angle STS connections in Test CW-6, the displacement capacity of the connections exceeded 20mm while sustaining high loads, which is shown in Figure 6-49a.

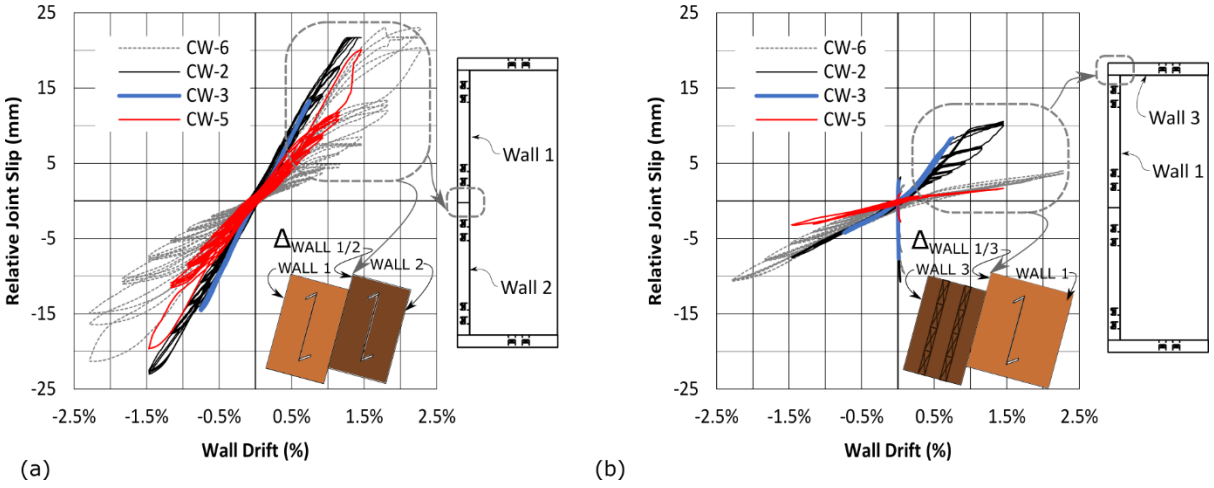


*Figure 6-48: Strong axis relative joint slip behaviour: (a) in-plane joint test comparison, and (b) orthogonal joint test comparison*

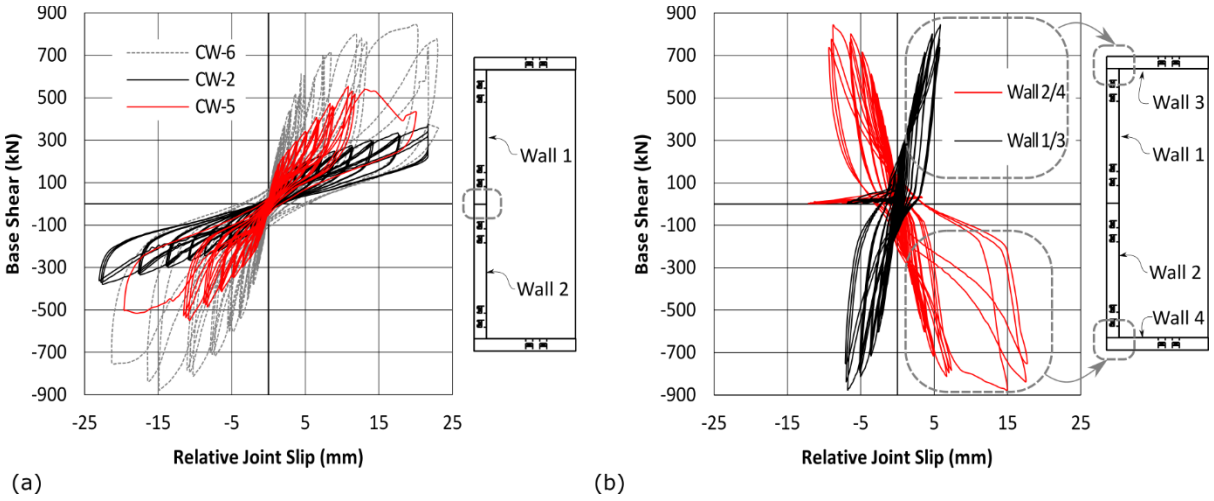


*Figure 6-49: Joint force-displacement behaviour: (a) in-plane joint slip behaviour, and (b) Test CW-6 orthogonal joint slip behaviour*

In all the tests, the in-plane joint was the weakest link in the system due to high shear demands. The inclined STS in Test CW-5 had limited displacement and energy dissipation capacity. In Test CW-6, the mixed angle STS connections were implemented for the orthogonal and in-plane joints. This resulted in significantly increased displacement capacity, energy dissipation capacity, and ultimately prevented a sudden loss in stiffness caused by brittle tensile failure of the STS. Table 6-14 provides the fraction of each STS type that failed in each test. As per Table 6-8, in Test CW-6 the orthogonal joint between Wall 2 and Wall 4 had 20% less inclined shear-tension STS than the joint between Wall 1 and Wall 3.

As a result, more shear-tension STS failed on the joint between Wall 2 and Wall 4, and Figure 6-49b shows the distinct difference in the positive joint displacement. Increased displacement and energy dissipation was shown for the orthogonal joint between Wall 2 and Wall 4 but there was no notable difference between the positive and negative cycles of the global hysteresis loop in Figure 6-45(c). In both orthogonal joints, the mixed angle STS connections provided stable connection and system performance. Figure 6-50 shows the images of wood crushing in CLT and STS bending in the in-plane and orthogonal joints after the tests.

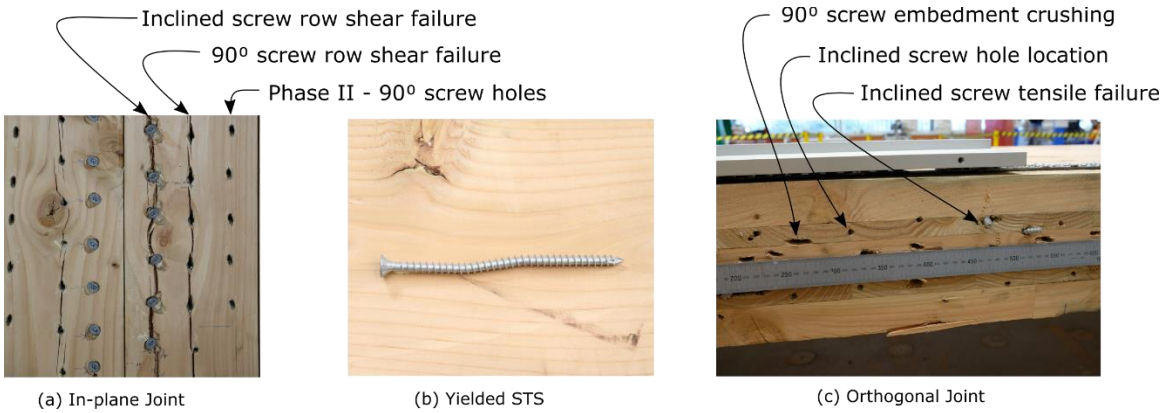


*Figure 6-50: Screw failure photos*

*Table 6-14: STS tensile failure summary as a ratio of failed STS / installed STS*

| Test | In-plane Joint Wall 1/2 Joint | Orthogonal Joint Wall 1/3 Joint | Orthogonal Joint Wall 2/4 Joint |
|---|---|---|---|
| CW-2 | 12/220 | 3/83 | 1/83 |
| CW-5 | 95/110 | 0/154 | 0/154 |
| CW-6 | 43/248 (inc.), 1/206 (90°) | 8/42 (ST), 0/36 (SC), 3/78 (90°) | 21/34 (ST), 2/36 (SC), 3/78 (90°) |
| CW-7* | 73/220 (90°) | 19/83 (90°) | 29/83 (90°) |

Note: ST= shear-tension STS; SC = shear-compression STS; inc. = inclined STS; and 90° = STS installed at 90°.
* Bi-directional loading protocol

#### 6.6.5.2.2 Castellation performance

The castellated joints provided a strong and stiff horizontal joint. Figure 6-51 shows the castellated joint slip during test CW-6 where the highest shear demands occurred. At 2.3% drift, the local deformation of the joint was less than 0.4mm. The global deformation was approximately 5mm which was primarily due to the installation construction tolerances as shown in Figure 6-51b. It should be noted that a large amount of friction provided by the PT clamped the panels together, and the vertical jumps in the global joint slip – drift curve indicate instances where instantaneous slips occurred.

Within Chapter 5, an analytical calculation method was developed which accounts for the increased complexity of cross-wise layup of CLT castellated joints.

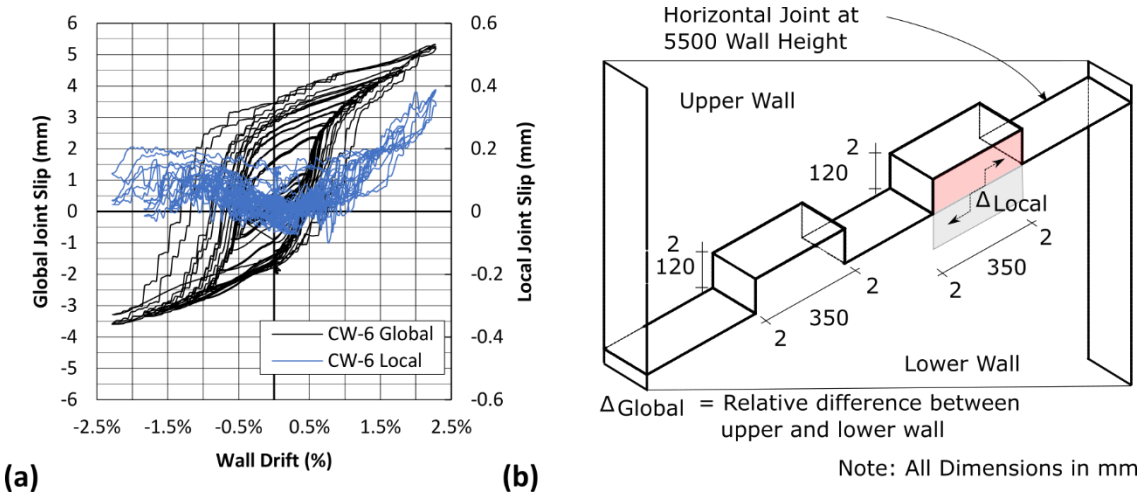


*Figure 6-51: Castellation CLT-CLT joint connection: (a) Test CW-6, and (b) castellation isometric*

### 6.6.5.2.3 Diaphragm performance

The CLT floors provided out-of-plane restraints in the core-wall testing. Figure 6-52b shows the L-shaped steel sections with slotted holes for partially threaded STS used which had been previously tested by Moroder et al. (2017). Though the loading was not applied through the CLT floors to represent real applications, Figure 6-52 shows that the connection detail performed well in decoupling floor rotations from wall rotations due to the rocking motion. At 2.3% wall drift, wall rotation was 0.9° while floor rotations were reduced to 0.3° based on the inclinometer measurements.

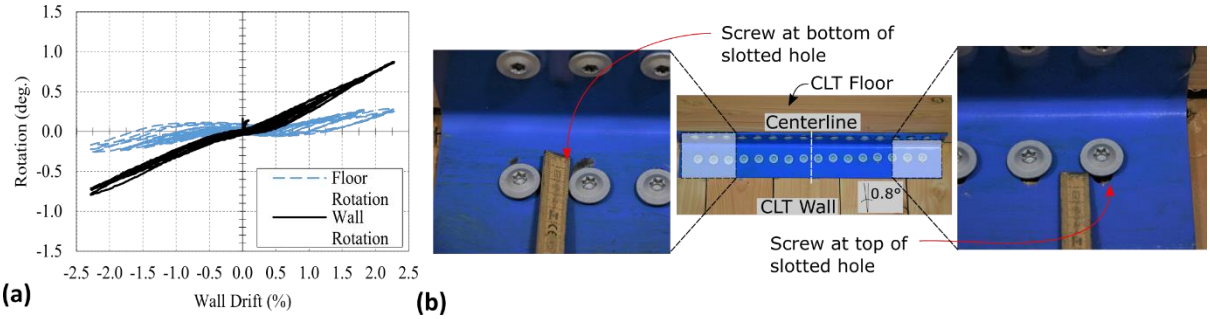


*Figure 6-52: Diaphragm connection performance: (a) wall and floor rotation versus wall drift, and (b) during testing photo at 1.8% wall drift ratio*

### 6.6.5.2.4 UFP connection performance

The UFP connection performance was evaluated with PTT by investigating the vertical, horizontal, and out-of-plane movement of a UFP-A and UFP-C connection type as shown in Figure 6-53a. UFP-B connection type had similar performance to UFP-A. Figure 6-53b shows UFP-A response in Test CW-6 at 1.8% drift under strong axis loading. The vertical displacement due to rocking of the CLT wall,

connection plate, UFP, and PFC were 20.6mm, 19.3mm, 17.4mm, and 0.3mm respectively. This indicated the inclined STS connection had 1.3mm slip, and that the UFP vertical movement was slightly less than the connection plate due to both the 1mm oversize holes for the M16 bolts and that the UFP rolling action was not perfectly vertical. In comparison the UFP-C epoxied connection plate had a maximum vertical connection slip of 0.4mm.

Figure 6-53c highlights that while the UFP-C had the least vertical connection slip, it could not provide decoupling effect as well as the inclined STS connection which behaved in dowel action when any wall movement other than vertical movement occurred (horizontal or out-of-plane). During the strong axis loading at 1.8% drift, total horizontal wall movement at the UFP-A connection plate location was greater than 45mm. The lower stiffness of the inclined screw connection in dowel action had greater than 8mm movement which would decrease torsional stresses on the UFP. Providing a slotted connection at the UFP-PFC interface or PFC-foundation interface could further decouple this behaviour. In contrast, the UFP-C epoxied plate connection in Test CW-7 had less than 0.5mm movement and thus negligible decoupling effect.

Figure 6-53d shows that when the $\phi$12mm threaded rods were implemented in Test CW-6, a stiff load path such that the connection plate and PFC had matching displacements occurred. In contrary, in Test CW-7 when the $\phi$12mm threaded rods were not implemented the PFC out-of-plane movement was approximately half the out-of-plane movement of the connection plate.

Providing horizontal and out-of-plane decoupling capability to connections for energy dissipating devices is critical to ensure stable performance under large deformations, especially if the energy dissipating devices provide major contributions to total system energy dissipation / moment capacity. The limited study herein highlighted the increased detailing complexities of energy dissipating devices with bi-directional loading for core-wall structures. Further, it was found that UFPs performed well and were also able to undergo twisting and out-of-plane movement without fracture. The limited study herein showed that inclined STS connections could provide targeted vertical connection stiffness while providing some decoupling effect to horizontal and out-of-plane wall movement.

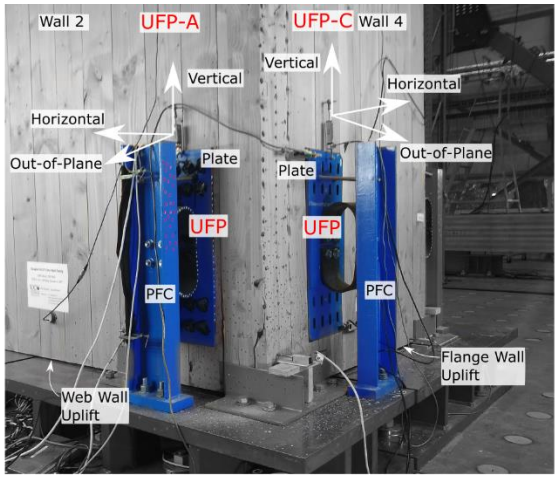


(a) Testing Photo During Negative Strong Axis Drift

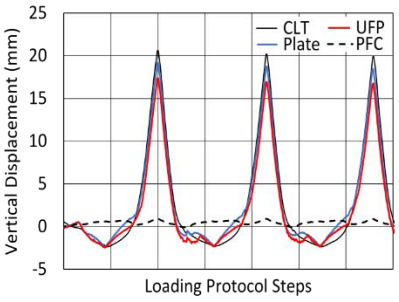


(b) UFP-A Vertical Displacement at Strong Axis 1.8% Drift

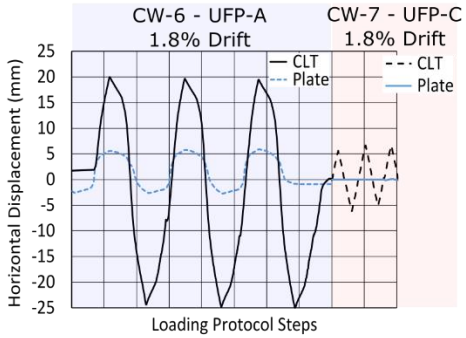


(c) UFP-A & UFP-C Horizontal Displacement Comparison

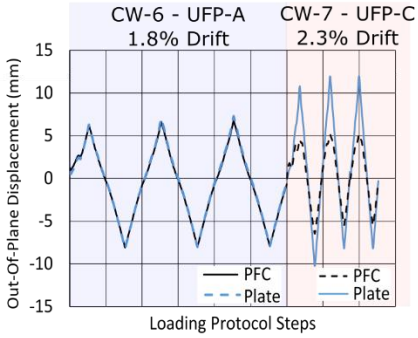


(d) UFP-A & UFP-C Out-of-Plane Displacement Comparison

*Figure 6-53: UFP performance*

### *6.6.5.3 Post-tensioned core-wall compression toe performance*

Figure 6-54 shows that damage was concentrated to the compression toes of the wall base. PTT was implemented at the core-wall base to capture displacement and strain fields and the results showed that the flange engagement decreased with increasing distance from the orthogonal joint.

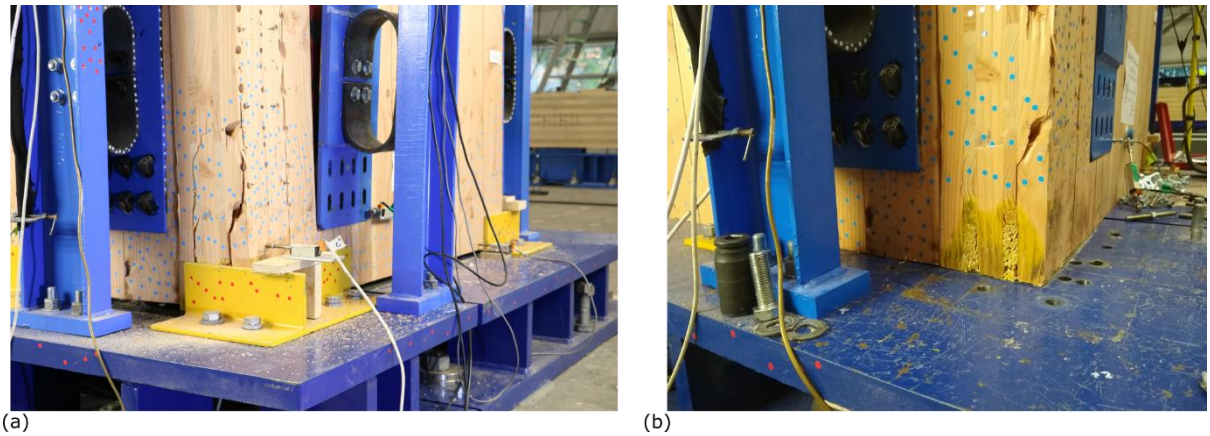

(a) (b)

*Figure 6-54: CLT wall base observed damage: (a) during testing, and (b) after testing*

Out-of-plane Flange Wall rotation occurred as shown in Figure 6-55. In Test CW-2, only 50mm of the 175mm Flange Wall thickness was in contact with the foundation at the orthogonal joint interface. As

such, it was observed that less flange engagement occurred than that assumed in the analytical fully composite section. Figure 6-56 shows the displacement profile of the compression flange at 1.5% drift in Test CW-2. A further discussion on wall base behaviour can be found in Chapter 9. It was found that the compressive flange was not engaged because very low compressive strains at the flange base were observed due to the relatively less stiff screwed connections between the Web and Flange Wall. At 2.3% drift in Test CW-6, local compression crushing and rippling occurred at the Web Wall corners, indicative of plastic strain behaviour. Though no significant load drop due to this was observed during its first incidence in the first 2.3% drift cycle, an increased neutral axis depth occurred in the second and third drift cycle as shown in Figure 6-45c which was partially attributed to the plastic compressive strain behaviour and connection slips. The plastic behaviour at the wall base also contributed to residual drift.

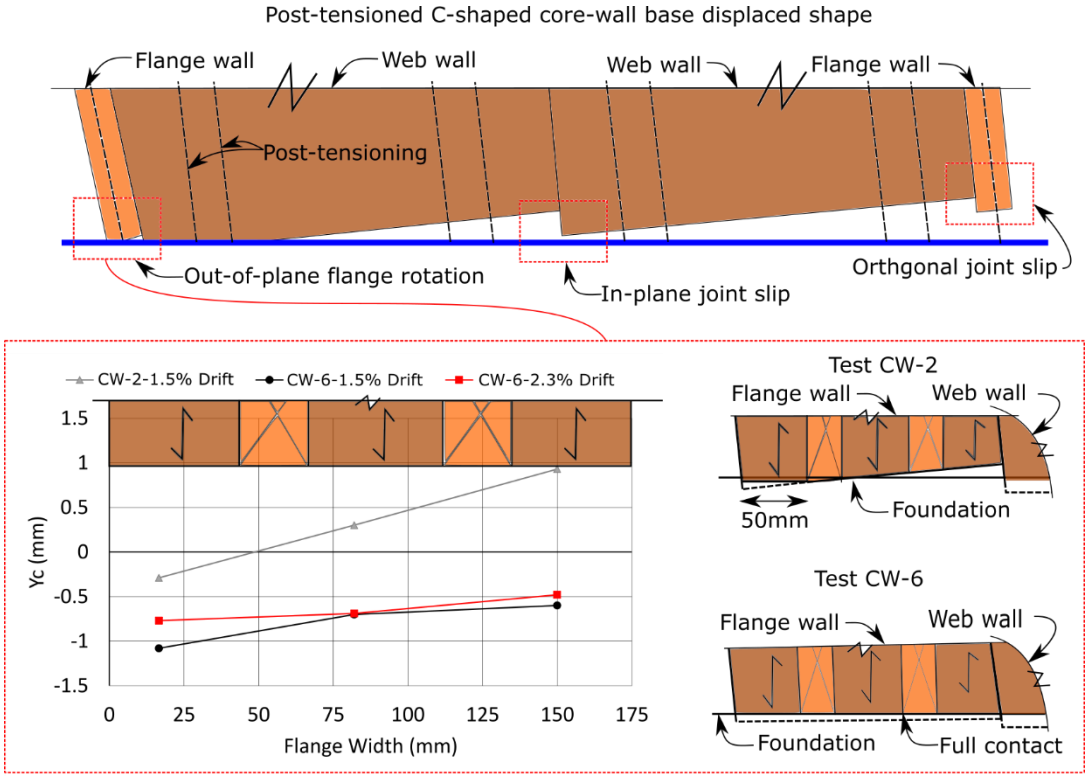


*Figure 6-55: Core-wall out-of-plane behaviour*

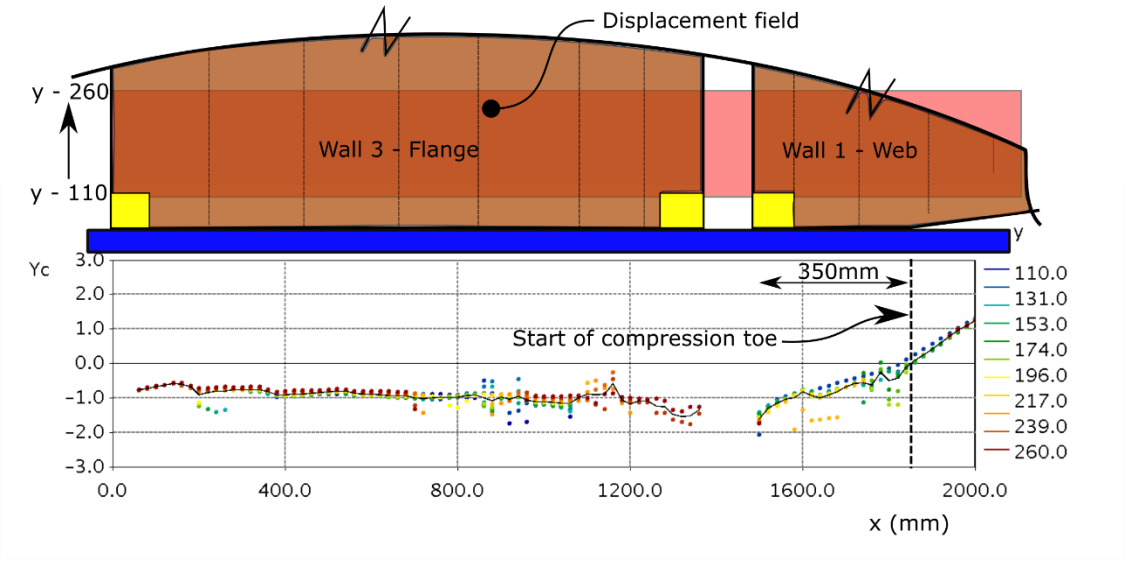


*Figure 6-56: Test CW-2 compression toe displacement profile at 1.5% drift*

### 6.6.6 Conventional Core-Wall Test (CW-8) Results

The purpose of the conventional core-wall Test CW-8 was to provide a performance benchmark against the previous PT core-wall tests. Figure 6-57 compares Test CW-8 to PT Tests CW-6 and CW-7. Test CW-8 base shear-wall drift hysteresis curve shows the typical pinching behaviour of connectors with yielding mechanical fasteners and timber embedment crushing mechanisms. It is interesting to note the CW-8 secant SLS stiffness was within the range of CW-6 and CW-7. This indicated that the connection stiffness between CLT panels at the in-plane and orthogonal joint has a significant influence on the system stiffness in addition to anchorage to the foundation (by post-tensioning or hold-down connector). In Test CW-8, PD was limited to 1.8% as the load drop in the 2.3% drift cycle exceeded 20%, typically defined as the ultimate drift in the testing standards (CEN, 2005). At peak drift, a peak load of 425 kN and secant stiffness of 2.8 kN/mm was achieved. Table 6-15 summarizes the comparison between Test CW-8 and Tests CW-6 and CW-7. In Test CW-6, residual drift was negligible until the 1.8% drift cycle, in which it was 0.3% and then 0.5% in the 2.3% drift cycle. In contrast, residual drift occurred throughout the conventional core-wall test. In Test CW-8 residual drifts continually increased from 0.5%, to 1.0%, and finally 1.4% in the 1.5%, 1.8% and 2.3% drift cycles respectively. This shows one significant difference between PT and conventional shear wall systems in terms of recentering capability.

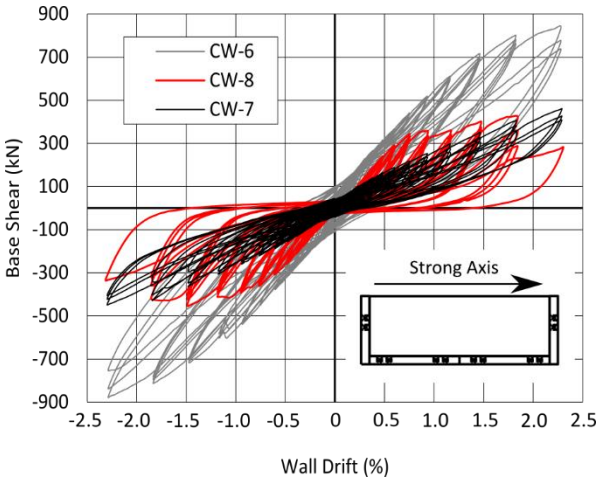


*Figure 6-57: Test CW-8 in comparison to selected PT CW tests*

*Table 6-15: Comparison of Test CW-8 to select post-tensioned core-wall tests*

| Phase<br>Test | Unit | CW<br>6 | CW<br>7 | CW<br>8 |
|---|---|---|---|---|
| $k_{SLS,sec}$ | kN/mm | 8.9 | 4.7 | 6.3 |
| **Peak Drift (PD)** | % | 2.3 | 2.3 | 1.8 |
| $F_{PD}$ | kN | 845 | 460 | 425 |
| $k_{PD,sec}$ | kN/mm | 4.5 | 2.5 | 2.8 |
| **Residual Drift** | % | 0.5 | n/a | 1.4 |

The 1.8% peak drift of Test CW-8 was primarily limited by the hold-down connections which had significant loss in load carrying capacity. Figure 6-58 shows that, at +/- 1.8% drift, the average slip of the in-plane joint was 19mm. Figure 6-59 shows the extreme hold-down slip was greater than 35mm. The mixed angle STS hold-downs were able to maintain the load at large displacements. In contrast, Figure 6-58 shows that the orthogonal joint remained relatively elastic as designed and at +/- 1.8% drift the tension flange joint slip was approximately 3mm while the compression flange joint slip was approximately -5mm. This affirmed the observation of the increased shear demand for compression flange engagement as occurred in the PT core-wall testing. Note that the vertical and abrupt slopes of the in-plane joint displacement (shown in red) are due to the LVDT reaching its displacement limits.

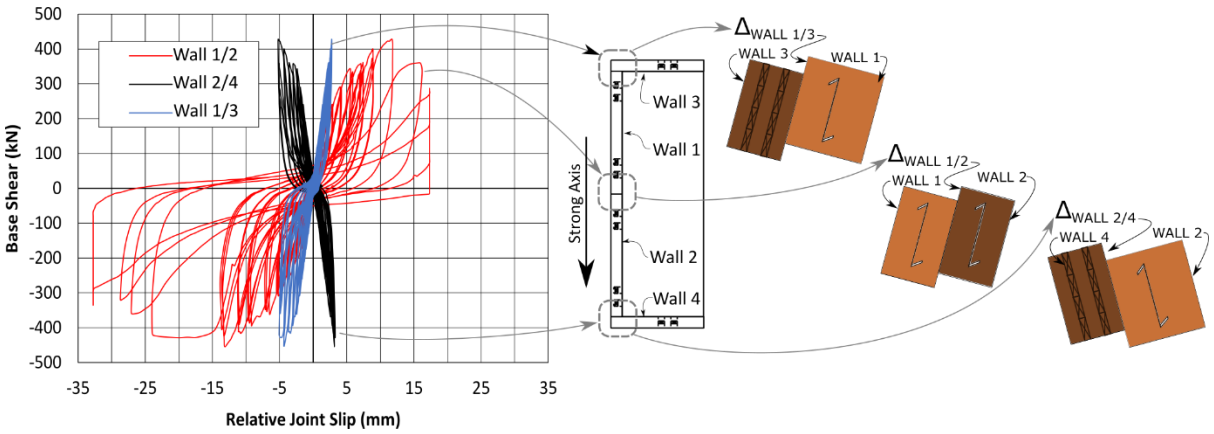


*Figure 6-58: Test CW-8 Relative joint displacement*

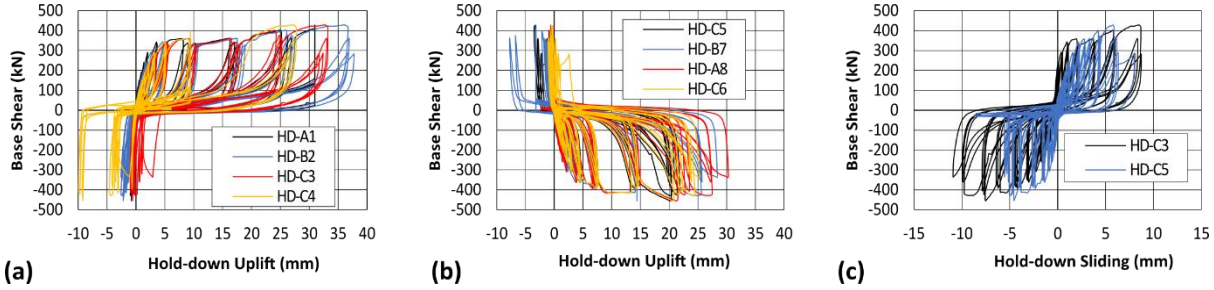


*Figure 6-59: Test CW-8 wall base hold-down slips*

Figure 6-60 shows that the hold-downs (or tie-downs) at 5.5m wall height level remained relatively elastic throughout the test due to the approximate linear relationship between the base force and the hold-down uplift. Further, Figure 6-60c shows that hold-down sliding (horizontal translation) was less than 1mm.

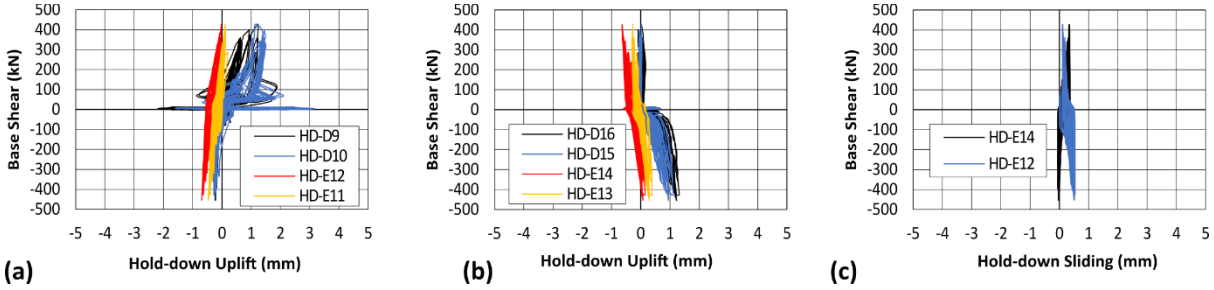


*Figure 6-60: Test CW-8 wall horizontal joint level hold-down slips*

Figure 6-61 shows the performance of the TTN and TCN angle brackets which were located at the orthogonal and base horizontal joints respectively. Figure 6-61a shows that the short leg SL and long leg LL of the TTN angle brackets had relatively similar relative displacement. Figure 6-61b shows that the TCN angle brackets primarily acted in uplift rather than resisting horizontal sliding. The TCN bracket plotted here was located closest to the in-plane joint on Wall 1.

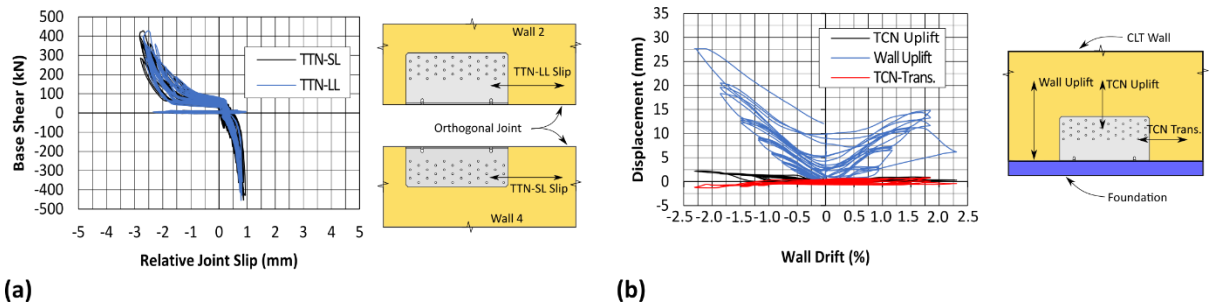


*Figure 6-61: Test CW-8 TTN and TCN performance*

Figure 6-62 shows after test photos of the hold-down and in-plane joint. The desired ductile failure modes in the STS hold-downs consisted of STS yielding, timber embedment crushing and gradual STS withdrawal. The research on this hold-down type with mixed angle STS is still ongoing (Wright et al., 2021). At the in-plane joint, timber embedment crushing and STS yielding also occurred.

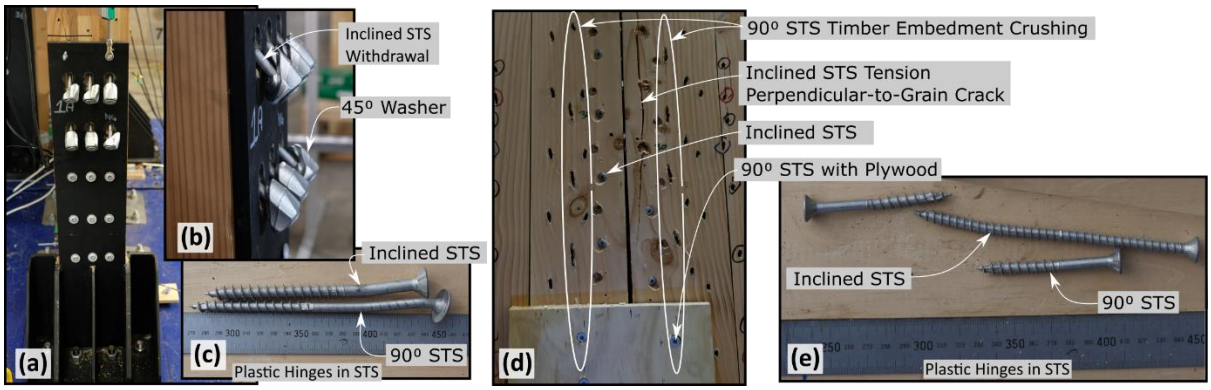


*Figure 6-62: Test CW-8 after test photos of ductile links: (a) – (c) mixed angle hold-down connector, (b) withdrawal failure of inclined STS, (c) yielding of inclined and 90° STS from hold-down connector, (d) after test photo of in-plane vertical joint, and (e) yielding of inclined and 90° STS from the in-plane joint*

## 6.7 CONCLUSIONS

The experimental results from the three phase shear wall testing programme were presented. Four single wall (SW), five double wall (DW), and eight core-wall tests were reported. The post-tensioned (PT) SW tests were performed primarily for comparison to the Modified Monolithic Beam Analogy analytical model and the PT DW tests showed that self-tapping screws (STS) with plywood could provide one effective coupling mechanism at the in-plane joint to increase system strength and stiffness while still providing a reliable source of energy dissipation. The PT C-shaped core-wall tests showed that the flanged walls formed a partial composite shear wall system and increased the lateral strength and stiffness. The conventional core-wall test (without post-tensioning) provided a performance benchmark against PT core-wall tests. The results confirmed that improved shear wall behaviour could be achieved through proper connection detailing between the walls. The STS connections with mixed angle installations for the in-plane and orthogonal joint offered one effective

connection solution for such a core-wall system. It was also found that different levels of partial composite action could be achieved based on the different connection methodologies.

The key findings are summarized as follows:

- Particle tracking technology (PTT) was implemented at the wall base. The results showed linear strain behaviour occurred throughout the wall testing. A thorough investigation of PTT in SW, DW, and core-wall testing will be presented in Chapters 7-9 to update and extend the current analytical models.
- The SW tests showed that increased initial post-tensioning force delayed the onset of gap opening, and then the post gap opening wall stiffness was similar for all the tests as expected.
- In Test DW-3, a negative neutral axis depth occurred in one of the two walls which indicated wall uplift. This occurred due to the high stiffness and strength of the STS coupling element at the in-plane joint.
- Test CW-6 showed that Flange and Web Wall uplift occurred during the rocking motion. This resulted in the highest core-wall composite action of approximately two-thirds and the SLS drift stiffness was almost four times when compared to the decoupled Test CW-1, or eight times when compared to Test SW-2.
- Mixed angle STS connections provided stable system performance for Test CW-6 at wall drift of 2.3%, which was at the stroke limit of the actuators. While inclined STS can provide high strength and stiffness, mixed angle STS connections on the in-plane and orthogonal joints provided the necessary high displacement and energy dissipation capacity. The partial composite action decreased with increasing core-wall drift and this behaviour was stable with either 90° or mixed angle STS connection details.
- Several tests were performed on the wall specimens with only minor damage occurring at the compression toes of the CLT wall panels and in proximity of each STS connection even at high levels of drift. At the end of each test, all STS were removed and new STS were installed in a different location following the minimum spacing requirement in an efficient manner. No significant impairment to the connection behaviour was observed.
- Though stable behaviour was observed in bi-directional loading, further analysis is required to quantify the differences in hysteresis loops and peak forces when compared to uni-directional loading.
- The combination of post-tensioning to provide moment capacity at the wall base and mixed angle STS connection details at the in-plane and orthogonal vertical joints to provide a C-shaped CLT core-wall composite behaviour can provide a viable solution to meet increased stiffness demands of taller timber buildings.

- While the conventional CLT core-wall system provided good performance to 1.8% wall drift, the PT CLT core-wall was able to minimize residual drift while having increased drift capacity.

In general, this experimental work provided fundamental knowledge for a better understanding of C-shaped PT rocking timber walls and very useful technical data for the extension of current analytical models for practical design.

## 6.8 REFERENCES

ACI Innovation Task Group 5. (2008). *Acceptance criteria for special unbonded post-tensioned precast structural walls based on validation testing and commentary : an ACI standard*. American Concrete Institute.

Australian / New Zealand Standard. (2001). *AS/NZS 4671: Steel reinforcing materials*.

Australian / New Zealand Standard. (2002). *AS/NZS 1170.0 Structural Design Actions Part 0: General Principles*.

Australian / New Zealand Standard. (2016). *AS/NZS 3679: Steel reinforcing materials*.

Baird, A., Smith, T., Palermo, A., & Pampanin, S. (2014). Experimental and numerical Study of U-shape Flexural Plate ( UFP ) dissipators. *NZSEE Conference*, 1–9.

Beyer, K., Dazio, A., & Priestley, M. J. N. (2008). Quasi-Static Cyclic Tests of Two U-Shaped Reinforced Concrete Walls. *Journal of Earthquake Engineering*, *12*(7), 1023–1053. https://doi.org/10.1080/13632460802003272

Blaß, H. J., & Bejtka, I. (2001). Screws with continuous threads in timber connections. *Joints in Timber Structures. Proceedings of the International RILEM Symposium*, 193–201.

Brown, J. R., Li, M., Tannert, T., & Moroder, D. (2021). Experimental study on orthogonal joints in cross-laminated timber with self-tapping screws installed with mixed angles. *Engineering Structures*, *228*(February 2021), 111560. https://doi.org/10.1016/j.engstruct.2020.111560

CEN. (2005). *EN12512: Timber structures: test methods : cyclic testing of joints made with mechanical fasteners : [including amendment A1:2005]* (Issue Book, Whole). European Committee for Standardization.

CEN. (2014). Eurocode 5: Design of timber structures-Part 1-1: General-Common rules and rules for buildings. In *EN1995-1-1:2004-11 + AC2006-06 + A1:2008-06 + A2:2014-05 Eurocode 5*. European Committee for Standardization.

Chen, Z., & Popovski, M. (2020). Mechanics-based analytical models for balloon-type cross-laminated timber (CLT) shear walls under lateral loads. *Engineering Structures*, *208*(January 2019), 109916. https://doi.org/10.1016/j.engstruct.2019.109916

Chen, Z., Popovski, M., & Iqbal, A. (2020). Structural Performance of Post-Tensioned CLT Shear Walls with Energy Dissipators. *Journal of Structural Engineering*, *146*(4). https://doi.org/10.1061/(asce)st.1943-541x.0002569

Clifton, G. C., Bruneau, M., MacRae, G., Leon, R., & Fussell, A. (2011). Steel building damage from the Christchurch earthquake series of 2010 and 2011. *Bulletin of the New Zealand Society for Earthquake Engineering*, *44*(4), 297–318.

ETA-07/0046. (2018). *ETA-07/0046: Macalloy 1030 post tensioning system*. European Technical Approval.

ETA-11/0496. (2018). *Rotho Blaas Titan Angle Brackets*. ETA-Danmark A/S.

ETA-12/0114. (2017). *SPAX self-tapping screws- screws for use in timber constructions* (Issue 305). ETA-Danmark A/S.

ETA-13/0523. (2018). *Nails and screws for use in nailing plates in timber structures*. ETA-Danmark A/S.

Ganey, R., Berman, J., Akbas, T., Loftus, S., Daniel Dolan, J., Sause, R., Ricles, J., Pei, S., Lindt, J. V. D., & Blomgren, H. E. (2017). Experimental investigation of self-centering Cross-Laminated Timber walls. *Journal of Structural Engineering*, *143*(10).

Gavric, I., Fragiacomo, M., & Ceccotti, A. (2015). Cyclic behavior of CLT wall systems: experimental tests and analytical prediction models. *Journal of Structural Engineering*, *141*(11), 4015034. https://doi.org/doi:10.1061/(ASCE)ST.1943-541X.0001246

Granello, G., Leyder, C., Palermo, A., Frangi, A., & Pampanin, S. (2018). Design Approach to Predict Post-Tensioning Losses in Post-Tensioned Timber Frames. *Journal of Structural Engineering*, *144*(8), 1–13. https://doi.org/10.1061/(ASCE)ST.1943-541X.0002101

Granello, G., Palermo, A., Pampanin, S., Smith, T., & Sarti, F. (2018). The implications of post-tensioning losses on the seismic response of pres-lam frames. *Bulletin of the New Zealand Society for Earthquake Engineering*, *51*(2), 57–69. https://doi.org/10.5459/bnzsee.51.2.57-69

Gutkowski, R., Brown, K., Shigidi, A., & Natterer, J. (2008). Laboratory tests of composite wood-concrete beams. *Construction and Building Materials*. https://doi.org/10.1016/j.conbuildmat.2007.03.013

Hashemi, A., Zarnani, P., Masoudnia, R., & Quenneville, P. (2018). Experimental Testing of Rocking

Cross-Laminated Timber Walls with Resilient Slip Friction Joints. *Journal of Structural Engineering (United States)*, *144*(1), 1–16. https://doi.org/10.1061/(ASCE)ST.1943-541X.0001931

Holden, T., Devereux, C., Haydon, S., Buchanan, A., & Pampanin, S. (2016). NMIT Arts and Media Building—Innovative structural design of a three storey post-tensioned timber building. *Case Studies in Structural Engineering*, *6*, 76–83. https://doi.org/10.1016/j.csse.2016.06.003

Hossain, A. (2019). *Experimental investigations of shear connection with STS for CLT panels* (Issue Phd Thesis) [University of British Columbia]. https://doi.org/.1037//0033-2909.I26.1.78

Hossain, A., Danzig, I., & Tannert, T. (2016). Cross-laminated timber shear connections with double-angled self-tapping screw assemblies. *Journal of Structural Engineering*, *142*(11).

Iqbal, A, Pampanin, S., Palermo, A., & Buchanan, A. H. (2015). Performance and design of LVL walls coupled with UFP dissipaters. *Journal of Earthquake Engineering*, *19*(3), 383–409. https://doi.org/10.1080/13632469.2014.987406

Iqbal, Asif, Fragiacomo, M., Pampanin, S., & Buchanan, A. (2018). Seismic resilience of plywood-coupled LVL wall panels. *Engineering Structures*, *167*, 750–759. https://doi.org/10.1016/j.engstruct.2017.09.053

Kelly, J. M., Skinner, R. I., & Heine, A. J. (1972). Mechanisms of energy absorption in special devices for use in earthquake resistant structures. *Bulletin of the New Zealand Society for Earthquake Engineering*, *5*(3), 63–73.

Lauriola, M. P., & Sandhaas, C. (2006). Quasi-static and pseudo-dynamic tests on XLAM walls and buildings. *Cost E29 Int. Worshop on Earthquake Engineering on Timber Structures, European Cooperation in Science and Technology*.

Loss, C., Hossain, A., & Tannert, T. (2018). Simple cross-laminated timber shear connections with spatially arranged screws. *Engineering Structures*, *173*, 340–356. https://doi.org/10.1016/j.engstruct.2018.07.004

Moroder, D., Pampanin, S., Palermo, A., Smith, T., Sarti, F., & Buchanan, A. (2017). Diaphragm Connections in Structures with Rocking Timber Walls. *Structural Engineering International*, *27*(2), 165–174.

Moroder, D., Smith, T., Dunbar, A., Pampanin, S., & Buchanan, A. (2018). Seismic testing of post-tensioned Pres-Lam core walls using cross laminated timber. *Engineering Structures*, *167*, 639–654. https://doi.org/10.1016/j.engstruct.2018.02.075

Nelson Pine Industries Ltd. (2016). *Nelson Pine LVL. Specific engineering design guide*.

Newcombe, M P, Pampanin, S., Buchanan, A., & Palermo, A. (2008). Section analysis and cyclic behavior of post-tensioned jointed ductile connections for multi-story timber buildings. *Journal of Earthquake Engineering*, *12*, 83–110. https://doi.org/10.1080/13632460801925632

Newcombe, Michael P., Pampanin, S., & Buchanan, A. H. (2010). Global response of a two storey Pres-Lam timber building. *New Zealand Society for Earthquake Engineering Conference*, *8*(28), 8.

Nguyen, T. T., Dao, T. N., Aaleti, S., Hossain, K., & Fridley, K. J. (2019). Numerical Model for Creep Behavior of Axially Loaded CLT Panels. *Journal of Structural Engineering*, *145*(1), 1–15. https://doi.org/10.1061/(ASCE)ST.1943-541X.0002219

Nokes, R. (2019). *Streams 3.02: System Theory and Design*.

Ottenhaus, L.-M., Li, M., Nokes, R., Cammock, P., & McInnes, B. (2019). Use of particle tracking velocimetry in timber material and connection testing. *European Journal of Wood and Wood Products*, *77*(2), 195–209. https://doi.org/10.1007/s00107-018-1376-y

Palermo, A. (2004). *Use of controlled rocking in the seismic design of bridges*. Technical University of Milan.

Palermo, A., Sarti, F., Baird, A., Bonardi, D., Dekker, D., & Chung, S. (2012). From theory to practice: Design, analysis and construction of dissipative timber rocking post-tensioning wall system for Carterton Events Centre, New Zealand. *Proceedings of the 15th World Conference on Earthquake Engineering, Lisbon, Portugal*, 24–28.

Pampanin, S., Nigel Priestley, M. J., & Sritharan, S. (2001). Analytical modelling of the seismic behaviour of precast concrete frames designed with ductile connections. *Journal of Earthquake Engineering*, *5*(3), 329–367. https://doi.org/10.1080/13632460109350397

Pampanin, S., Palermo, A., & Buchanan, A. (2013). *Post-Tensioned Timber Buildings - Design Guide Australia and New Zealand*. Structural Timber Innovation Company.

Pault, J., & Gutkowski, R. (1977). *Tests and analysis of composite action in glulam bridges', Structural Research report No. 17A* (No. 17A).

Pei, S., Van De Lindt, J. W., Barbosa, A. R., Berman, J. W., McDonnell, E., Daniel Dolan, J., Blomgren, H. E., Zimmerman, R. B., Huang, D., & Wichman, S. (2019). Experimental seismic response of a resilient 2-story mass-timber building with post-tensioned rocking walls. *Journal of Structural Engineering*, *145*(11), 1–15.

Popovski, M., Schneider, J., & Schweinsteiger, M. (2010). Lateral load resistance of cross-laminated wood panels. *WCTE 2010*, *4*, 3394–3403.

Ranta-Maunus, A. (1975). The viscoelasticity of wood at varying moisture content. *Wood Sci. Technol, 9 (3)*, 189–205.

Sarti, F., Palermo, A., & Pampanin, S. (2016). Quasi-static cyclic testing of two-thirds scale unbonded post-tensioned rocking dissipative timber walls. *Journal of Structural Engineering*, *142*(4), 1–14. https://doi.org/10.1061/(ASCE)ST.1943-541X.0001291

Shahnewaz, M., Dickof, C., & Tannert, T. (2021). Seismic Behavior of Balloon Frame CLT Shear Walls with Different Ledgers. *Journal of Structural Engineering*, *147*(9), 1–16. https://doi.org/10.1061/(ASCE)ST.1943-541X.0003106

Smith, T, Ludwig, F., Pampanin, S., Fragiacomo, M., Buchanan, A., Deam, B., & Palermo, A. (2007). Seismic response of hybrid-LVL coupled walls under quasi-static and pseudo-dynamic testing. *2007 New Zealand Society for Earthquake Engineering Conference, Palmerston North, New Zealand*, *8*.

Smith, Tobias, Pampanin, S., & Fragiacomo, M. (2006). *LVL Rocking Shear Walls: With external dissipater attachment - 3rd professional year project report*.

Standards New Zealand. (1992). *NZS 3404: Steel Structures Standard*. Standards New Zealand.

Standards New Zealand. (1993). *NZS 3603: Timber structures standard*. Standards New Zealand.

Standards New Zealand. (2006). *NZS 3101: Concrete structures standard*. Standards New Zealand.

Wright, T. D. W., Li, M., Moroder, D., & Carradine, D. (2021). Cyclic behvaiour of Douglas-Fir CLT hold-downs using self-tapping screws with mixed angle installations. *NZSEE Conference*.

XLam NZ Limited. (2017). *XLam design guide*.

# 7 Analytical modelling of post-tensioned CLT single wall systems

*Key Findings / Outputs:*

- The experimental results of four post-tensioned CLT single wall specimens were compared to analytical models.
- Particle tracking technology was used for the first time to investigate compressive toe strains in post-tensioned CLT wall specimen.
- The Modified Monolithic Beam Analogy (MMBA) and triangular strain distribution was verified for post-tensioned CLT Wall systems within elastic timber range.
- The test results show the MMBA could under-predict the peak strain response in the compression toe. A strain amplification factor of 1.3 was determined based on 37 analytical-experimental comparisons from the four wall tests presented. This amplification factor is preliminarily recommended for post-tensioned CLT wall systems where CLT is non-edge glued and whose timber lamella are not machine stress graded.

## 7.1 INTRODUCTION

The main objective of Chapter 7 is to refine current analytical models for post-tensioned (PT) CLT walls based on a detailed experimental study of the compressive toe behaviour of PT CLT wall systems. As described in Chapter 6, CLT has significantly different material properties than laminated veneer lumber (LVL) which has been researched extensively in past PT wall systems. Section 7.2 revisits the theory of PT wall systems. Section 7.3 evaluated the experimental compressive toe behaviour from the single wall testing presented in Chapter 6 and compares the results to the analytical model of Section 7.2. Finally, Section 7.4 provides an experimental-analytical parametric study with readily available material properties, material properties from CLT and post-tensioning bar testing, and finally with the suggested strain amplification factor.

### 7.1.1 Relevant Background Information

A brief literature review of relevant past work to investigate the compressive toe of PT timber wall systems is presented herein. Research on PT timber systems (Pres-Lam) started from 2005 at the University of Canterbury (Palermo et al., 2005). As part of that work, in order to verify the linear stress/strain distribution assumed by the analytical procedure, Smith et al. (2006) installed strain gauges along the base of PT laminated veneer lumber (LVL) walls. Figure 7-1 shows that a triangular and linear strain distribution was a valid assumption. Thus, the Pres-Lam design guide (Pampanin et al., 2013), which will be introduced in Section 7.2, implemented this assumption into the analytical design procedure. Further work by Newcombe (2011) suggested that the analytical procedure was valid up to a strain limit to 2 times the elastic timber strain.

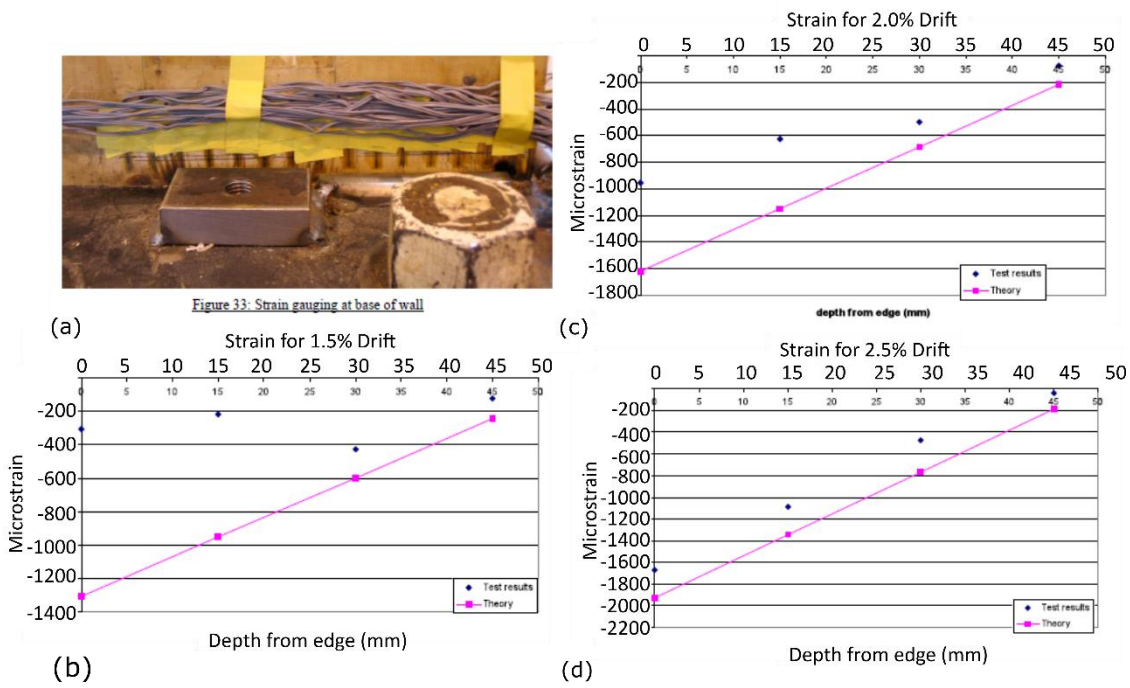


*Figure 7-1: Post-Tensioned LVL wall testing: (a) Strain gauges at base of wall, (b) Strain at 1.5% drift, (c) Strain at 2.0% drift, and (d) Strain at 2.5% drift (adopted from Smith et al. (2006))*

More recently, Nagashima et al. (2020) experimentally tested 3.5m high PT glulam walls anchored by $\phi$19mm high strength PT bars. The bar quantity and location changed for each specimen (H35C, H35EQ, and H35W). In order to capture timber strains, 70 strain gauges were installed on the specimen in a 7x10 grid. Figure 7-2 shows the strain contour plot of three different specimens and the compressive toe behaviour at the wall base. Through this work, a triangular stress/strain distribution was found appropriate within the elastic range of timber.

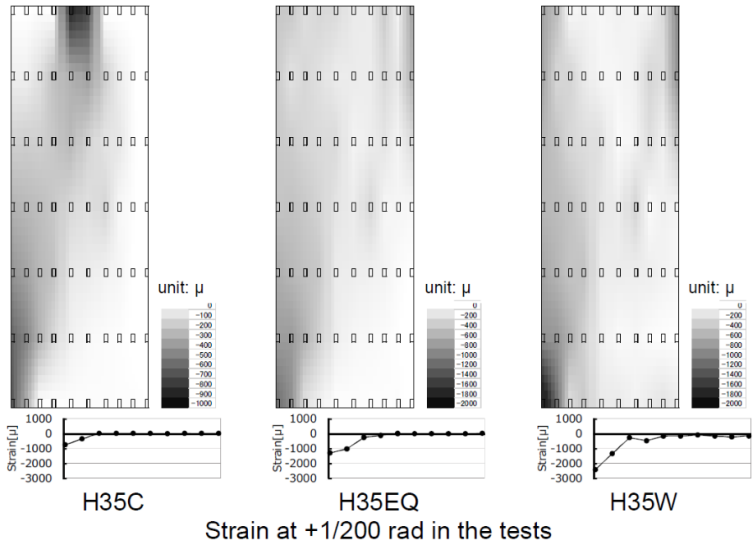


*Figure 7-2: Experimental test results of post-tensioned glulam wall at connection rotation of 1/200 = 0.005 rad (photo reproduced from Nagashima et al.* (2020)*)*

Wilson et al. (2019) numerically modelled PT CLT walls using shell elements in *SAP2000* (Computers and Structures, 2017). Figure 7-3 shows the results at 3% drift and the associated compressive toe stresses. While this work might be used to guide practical design, no experimental compression toe stress/strain data exists for further verifications.

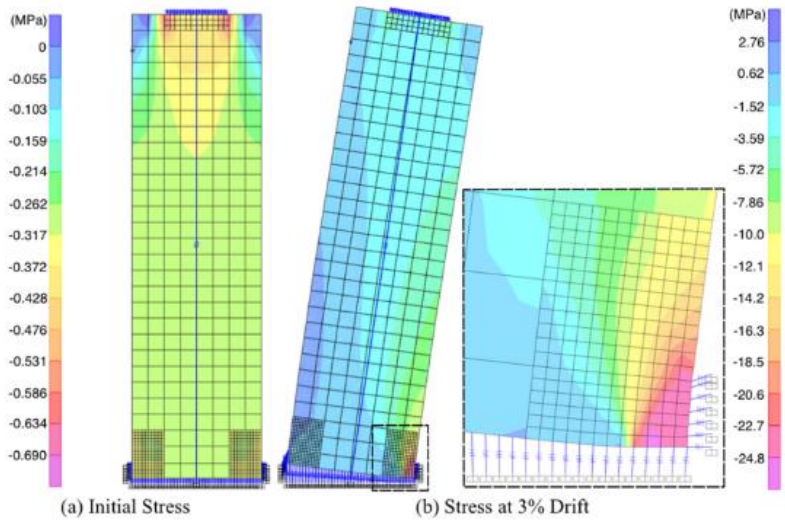


*Figure 7-3: Compressive toe stresses using shell elements in SAP2000 (photo reproduced from Wilson et al.* (2019)*)*

## 7.2 THEORY OF POST-TENSIONED TIMBER WALL SYSTEMS

The moment-rotation analysis is based on an unbonded PT rocking wall boundary condition following the Monolithic Beam Analogy (MBA) method initially proposed by Pampanin et al. (2001) for precast concrete, extended by Palermo (2004) to capture the elastic deformation of timber, and adopted by Newcombe et al. (2008) for PT wall research. The iterative procedure is referred to as the Modified Monolithic Beam Analogy (MMBA) developed for PT laminated veneer lumber (LVL) Pres-Lam systems first tested at the University of Canterbury in 2005 (Palermo et al., 2005). One of the outputs from the extensive research campaign was the Pres-Lam design guide (Pampanin et al., 2013), upon which the theory presented herein is based.

Figure 7-4 shows the predominant wall deformations present in a PT timber wall system which includes rocking, $\delta_r$, bending, $\delta_b$, and shear deformation, $\delta_s$. Sliding deformation is generally not considered in PT systems due to the presence of strong and stiff shear keys.

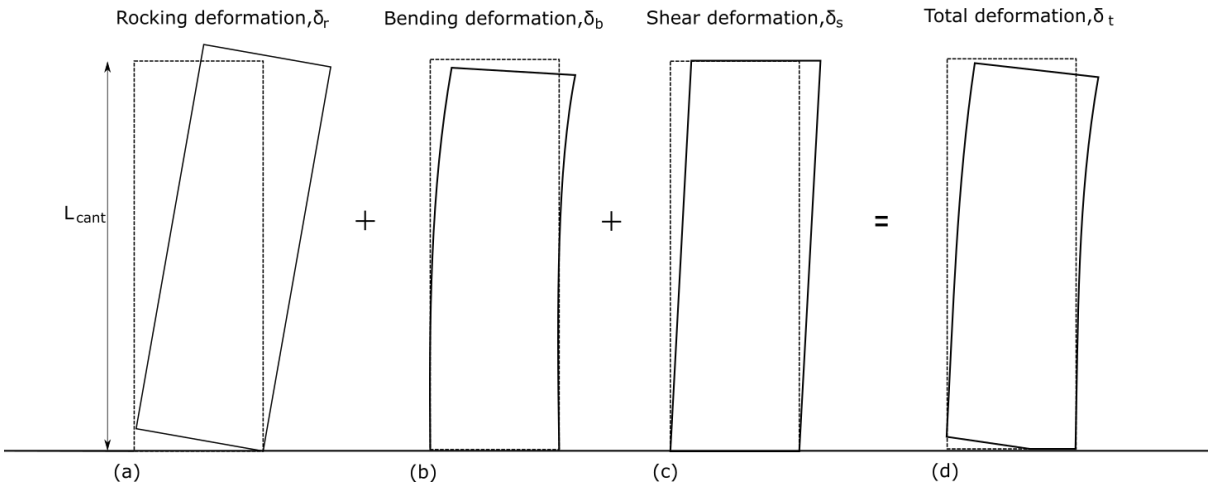


*Figure 7-4: Rocking wall deformation contributions: (a) rocking deformation, (b) bending deformation, (c) shear deformation, and (d) total deformation*

The total displacement, $\delta_T$, at the top of a wall can then be determined as:

$$\delta_T = \delta_r + \delta_b + \delta_s \tag{7-1}$$

where $\delta_r$ is discussed in Section 7.2.1, and $\delta_b$ and $\delta_s$ are discussed in Sections 7.2.2 and Section 7.2.3 respectively.

For a PT timber system, the recentering parameter, β, is generally used:

$$\beta = \frac{M_{pt}}{M_T}, where\ M_T = M_{pt} + M_s \tag{7-2}$$

Where $M_{pt}$ is the moment due to post-tensioning, $M_s$ is the moment provided by the dissipative elements (in this instance the UFPs, STS, and friction), and $M_T$ is the total moment. The strength of a PT wall is a combination of the post-tensioning and dissipative elements. Dissipative elements can range between yielding, friction, and/or viscous devices (Palermo et al., 2005). It is recommended to keep β ≥0.55 to minimize residual displacements (Pampanin et al., 2013; Smith et al., 2014).

### 7.2.1 Post-Tensioned Timber Wall Rocking Deformation

The rocking deformation, $\delta_r$, is determined for a given imposed rotation angle, $\theta_j$, as shown in Figure 7-5 as:

$$\delta_r = \theta_j L_{cant} \tag{7-3}$$

where $L_{cant}$ is the cantilever wall length.

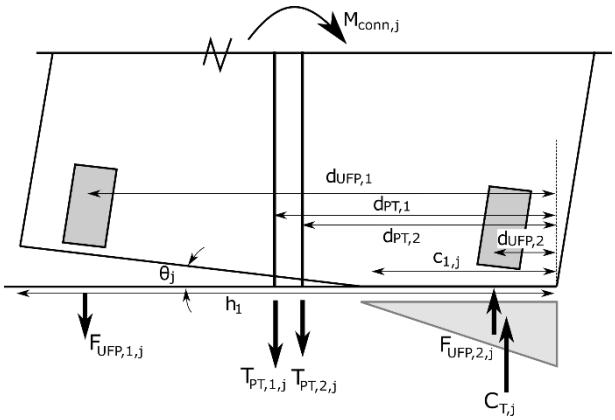


*Figure 7-5: Section analysis of a single post-tensioned wall*

The step-by-step procedure to satisfy equilibrium is summarized in the flowchart in Figure 7-6.

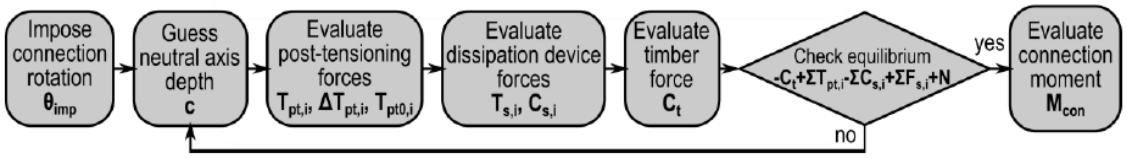


*Figure 7-6: MMBA step-by-step procedure summarized by Sarti* (2015)

Before gap opening, the cantilever wall is clamped to the foundation by the PT bars. With increasing initial post-tensioning force, the required overturning moment to initiate gap opening, called the decompression moment, will increase. The decompression moment, $M_{dec}$, is defined as:

$$M_{dec} = \frac{Z}{A_{eff}}(\sum T_{PT,o} + N) \quad (7\text{-}4)$$

Where:

$Z$ = section modulus of the CLT wall cross section which only considers the longitudinal CLT timber lamella

$A_{eff}$ = effective cross-sectional area of the CLT walls which only considers the longitudinal CLT timber lamella

$\sum T_{PT,o}$ = initial post-tensioning force acting on the wall section

$N$ = axial force from gravity loading

Before $M_{dec}$ is reached, the wall system can be treated as a fixed base cantilever system. Once $M_{dec}$ is reached, gap opening and imposed connection ration $\theta_j$ will occur at the base of the wall.

*Step 1: Impose connection rotation and estimate neutral axis depth*

Impose a connection rotation, $\theta_j$, considering the elastic deformations, and guess a neutral axis value $c_{1,j}$.

*Step 2: Evaluating post-tensioning forces*

The tendon elongation is determined by geometry due to gap opening with consideration for axial wall shortening as:

$$\Delta_{PT,i,j} = \theta_j\left(d_{PT,i} - c_{1,j}\right) - \frac{\left(\sum T_{PT,wi,j} - \sum T_{PT,o,wi}\right) l_{ub,i}}{E_o A_{eff,wi}} \quad (7\text{-}5)$$

Where

$\Delta_{PT,i,j}$ = elongation of the i-th post-tensioning bar for the j-th rotation increment

$d_{PT,i}$ = edge distance of the i-th post-tensioning bar (See Figure 7-5)

$\sum T_{PT,wi,j}$ = sum of post-tensioning bar force for the applicable wall for the j-th rotation increment

$\sum T_{PT,o,wi}$ = sum of the initial post-tensioning bar force for the applicable wall

$l_{ub,i}$ = unbonded length of the i-th post-tensioning bar

$E_o$ = timber elastic modulus

$A_{eff,wi}$ = effective area for the applicable wall

Kovacs (2016) also considered that the tendon elongation due the rotation of the CLT wall panel also has a component due to horizontal translation. This was not considered herein due to the relatively small drifts imposed and evaluated. It is worth noting that in Test CW-6 with peak drift of 2.3%, tendon elongation due to horizontal translation accounted for approximately 10% the total post-tensioning force. Therefore, if a PT wall system is designed for larger drifts tendon elongation due to horizontal translation should be considered. The incremental strain, $\Delta\epsilon_{pt,i,j}$, and force, $\Delta T_{pt,i,j}$, in the i-th post-tensioning bar for the given imposed connection rotation is then determined as:

$$\Delta\epsilon_{PT,i,j} = \frac{\Delta_{PT,i,j}}{l_{ub,i}} \quad (7\text{-}6)$$

$$\Delta T_{PT,i,j} = \Delta\epsilon_{PT,i,j} E_{PT} A_{PT,i} \quad (7\text{-}7)$$

Where:

$E_{PT}$ = post-tensioning steel elastic modulus

$A_{PT,i}$ = cross-section area of the i-th post-tensioning bar

Then, the total post-tensioning force, $T_{PT,i}$, can be evaluated:

$$T_{PT,i,j} = T_{PT,0,i} + \Delta T_{PT,i,j} \quad (7\text{-}8)$$

where:

$T_{PT,0,i}$ = initial post-tensioning force in the i-th bar

*Step 3: Evaluating UFP dissipaters forces*

Sarti et al. (2016) described that dissipative devices including tension/compression axial dissipaters (internal or external), or UPFs are commonly used for PT timber walls. To determine the force-displacement component behaviour of axial dissipaters, refer to the work by Sarti et al. (2016). UFPs can also be implemented at the base of PT SW timber systems. The recently completed Oregon State University Peavy Hall building employed UFPs at the PT CLT wall base (StructureCraft, n.d.). To determine the force-displacement behaviour of UFPs, refer to the work by Baird et al. (2014) and Kelly et al. (1972). Other devices such as dissipative steel angles (Smith et al., 2014) have also been implemented. Because UFPs were investigated in this research, they are presented in more detail; however, the imposed displacements are device independent. The imposed displacement due to gap opening at the wall base is found in a similar manner as the PT bars:

$$\Delta_{UFP,i,j} = \theta_j \left(d_{UFP,i} - c_{1,j}\right) \tag{7-9}$$

where

$\Delta_{UFP,i,j}$ = elongation of the i-th UFP element for the j-th rotation increment

$d_{UFP,i}$ = edge distance of the i-th UFP element (See Figure 7-5)

Analytical models to predict the behaviour of UFPs were first developed by Kelly et al. (1972). The UFP yield force, $F_{y,UFP}$, and yield moment, $M_{y,UFP}$, can be evaluated as:

$$F_{y,UFP} = \frac{2M_{y,UFP}}{D_u} \tag{7-10}$$

$$M_{y,UFP} = \frac{1}{4} b_u t_u f_{y,UFP} \tag{7-11}$$

where:

$D_u$ = average radius of the UFP

$b_u$ = the UFP width

$t_u$ = the UFP thickness

$f_{y,UFP}$ = the yield stress of the UFP steel

While Baird et al. (2014) carried out extensive numerical parametric modelling to fit the Ramberg-Osgood function for UFPs, in this study, simple elasto-plastic behaviour was assumed with acceptable performance, which will be presented in Chapter 8 and Chapter 9.

*Step 4: Evaluating the timber forces*

The compressive force in timber is evaluated by first determining the peak timber strain. Strain compatibility is determined following the MMBA. Some distinct differences exist with timber to adopt this method from concrete which were determined by Newcombe et al. (2008). The peak timber strain, $\varepsilon_t$, is determined as:

$$\varepsilon_{t,j} = c_1\left(\frac{3\theta_j}{L_{cant}} + \phi_{dec}\right) \quad (7\text{-}12)$$

Where:

$L_{cant}$ = wall cantilever length

$\phi_{dec}$ = decompression curvature = $\frac{M_{dec}}{E_{conn}I_{eff}}$

Where:

$M_{dec}$ = decompression moment as described by Pampanin et al. (2013)

$E_{conn}$ = timber connection elastic modulus = $0.83E_o$, derived by the CLT material testing presented in Section 7.4.1.1.

$I_{eff}$ = is the moment of inertia of the wall cross section considering only the longitudinal lamella

Then, the timber force, $C_{T,j}$, is determined assuming a triangular distribution as:

$$C_{T,j} = 0.5E_{conn}c_{1,j}b_{eff}\varepsilon_{t,j} \quad (7\text{-}13)$$

Where:

$b_{eff}$ = is the sum of the longitudinal board thickness only

It is important to note that Equation (7-13) and the MMBA analytical procedure for timber systems has primarily been validated with LVL walls. There are some distinct material property differences between CLT and LVL (See Chapter 6), and one key objective of this study was to refine the MMBA procedure for CLT wall systems. As such, the assumed triangular stress/strain distribution and peak timber strain need to be assessed with experimental results.

*Step 5: Check equilibrium and evaluate the connection moment*

Force equilibrium is then achieved by an iterative process from Step 1 to identify the location of the neutral axis of each wall. Then, the connection moment capacity can be evaluated and checked against

the moment demand. The force equilibrium and the moment equilibrium about the centroid of the timber compression force, are written as:

$$C_{T,i,j} - \sum T_{PT,i,j} - \sum F_{UFP,i,j} = 0 \tag{7-14}$$

$$M_{w,i,j} = \sum T_{PT,i,j}\left(d_{PT,i} - {}^{c_{1,j}}/_{3}\right) + \sum F_{UFP,i,j}\left(d_{UFP,i} - {}^{c_{1,j}}/_{3}\right) \tag{7-15}$$

### 7.2.2 Bending Deformation

The bending deformation, $\delta_{b,j}$, at the top of the wall for a given wall base rotation 'j' is calculated using the elastic formula for a fixed base cantilever as:

$$\delta_{b,j} = \frac{F_j L_{cant}^3}{3E_o I_{eff}} \tag{7-16}$$

Where:

$F_j$ = is the force at the top of the wall

$E_o I_{eff}$ = the elastic flexural stiffness of the CLT panel by considering the longitudinal lamella only (FPInnovations, 2019)

### 7.2.3 Shear Deformation

There are different methods in literature for calculating the in-plane shear deformation, $\delta_{s,j}$, of a CLT panel (Lukacs et al., 2019). In this instance, the shear stiffness method proposed by Schickhofer et al. (2010) was used which determines an effective shear modulus, $G_{eff}$, and the gross shear area, A as:

$$G_{eff}A = \frac{G_0 A}{1 + 6\left[0.32\left(\frac{t_b}{a}\right)^{-0.77}\right]\left(\frac{t_b}{a}\right)^2} \tag{7-17}$$

Where:

$t_b$ = average thickness the CLT lamella

$a$ = the average width of the CLT lamella.

Due to the ordered CLT, $G_{eff}A$ was approximately equal to 0.75GA as per the ProHolz guideline (Wallner-Novak et al., 2014). Then, the shear deformation for a given wall base rotation j' is determined as:

$$\delta_{s,j} = \frac{F_j L_{cant}}{G_{eff}A} \tag{7-18}$$

### 7.2.4 Pushover Analysis

The entire moment-rotation and force-displacement behaviour of a PT CLT single wall system can then be determined by incrementally increasing the imposed rotation angle, $\theta$, at the wall base.

## 7.3 COMPRESSION TOE BEHAVIOR AND COMPARISON TO MMBA

In order to accurately model the behaviour of a PT CLT wall system, the compressive behaviour at the wall base is critical to understand. In past research, the most common method for tracking the neutral axis depth at the base of a rocking timber wall is to linearly interpolate a number of single point measurements by LVDTs. If a detailed measurement of the rocking interface is desired, Particle Tracking Technology (PTT) has advantages over traditional LVDTs as the movement of a large number of particles can be tracked with digital cameras with high resolution. Figure 7-7 shows the PTT particles in the compression toe regions of the single CLT wall specimen whose global experimental results were presented in Chapter 6.

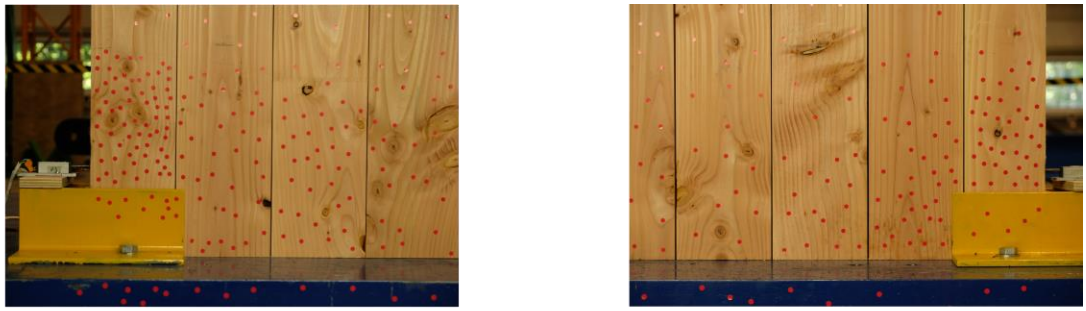

(a) (b)

*Figure 7-7: Photo of compression toes for (a) negative drift cycle, and (b) positive drift cycle*

PTT was utilized to determine the strain field within each compressive toe region over the lower 260mm wall height, along the entire compressive toe length. Figure 7-8 - Figure 7-11 give a summary of experimental testing strain results in comparison with the MMBA assumption at different drift levels. At each drift cycle, the scatter and the mean of timber strain are compared with the MMBA predictions (shown with grey lines) assuming a triangular distribution. The experimental neutral axis depth at each drift cycle is also shown on each graph with a solid red vertical line. In all instances, the MMBA over-predicted the neutral axis depth. CLT has significantly higher variability, which lead to highly non-linear wall base behaviour while the MMBA analogy is based on a monolithic and continuous element with no variability. This could contribute to the differences between the MMBA and experimental neutral axis results.

The results are given for both the positive and negative drift cycles, and significant differences were observed. It was also found that a higher concentration of knots existed on the negative drift cycle side (Figure 7-7a) compared to the positive drift side (Figure 7-7b). This could cause generally different compressive strains between positive and negative cycles at the same drift. Nonetheless, the variability in compressive strains over the 260mm wall base height highlighted the inherent variability

of timber and also increased variability of using non-edge glued visually graded lamella for the CLT. Based on the results from the 37 different measuring points presented in Figure 7-8 - Figure 7-11, it seemed that a linear strain distribution was appropriate, based on the mean experimental strains presented.

Further, at each drift cycle, and at each compressive toe, the peak average compressive strain was compared with the peak timber strain determined by the MMBA. A strain amplification factor $\phi_t$ is defined as the ratio between experimental strain and MMBA analytical strain. The $\phi_t$ factors from the drift cycles of each test are presented in Table 7-1 and an average value of 1.3 was found, based on a total of 37 analytical to experimental comparisons over the four tests. The significant differences in $\phi_t$ factors highlight the inherent variability on using sawn lumber as lamella. It should be noted that the $\phi_t$ factor of 1.3 was determined based on a limited number of experimental tests. Future work is needed to investigate different wall configurations, drift demands, timber species and engineered timber products.

*Table 7-1: Summary of timber strain amplification factors*

| Test | Negative Drift | Positive Drift | Average |
|---|---|---|---|
| SW-1 | 2.04 | 1.92 | 2.00 |
| SW-2 | 2.08 | 1.01 | 1.35 |
| SW-3 | 1.41 | 1.45 | 1.43 |
| SW-4 | 1.69 | 0.65 | 0.93 |
| Average | 1.75 | 1.06 | **1.3** |

It is suggested that the strain amplification factor $\phi_t$ be added to modify the previously presented Equation (7-13), which now becomes:

$$C_{T,j} = (0.5E_{conn}c_{1,j}b_{eff}\varepsilon_{t,j})\phi_t \quad (7\text{-}19)$$

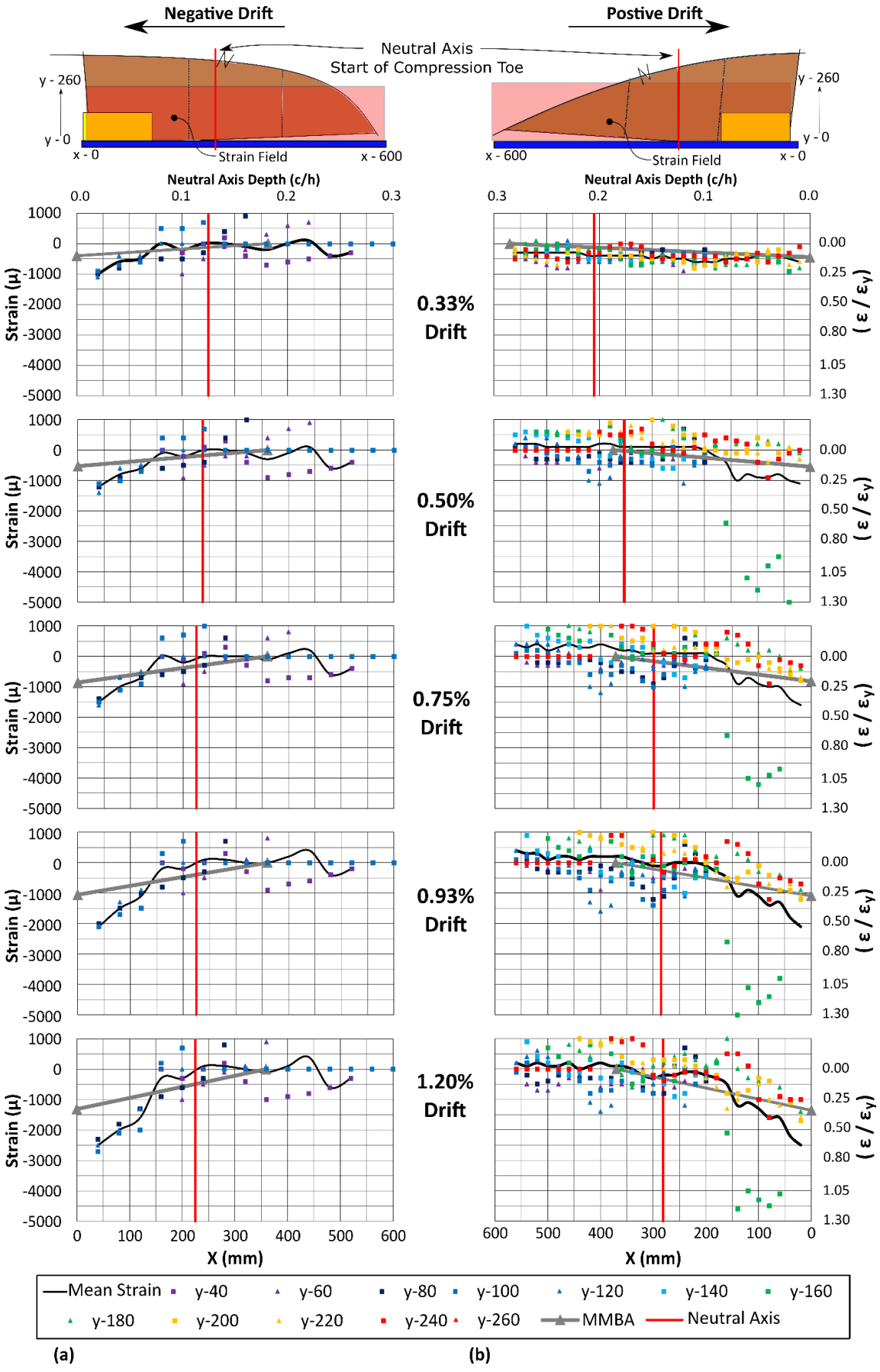


*Figure 7-8: Test SW-1 compression toe strain comparison to MMBA*

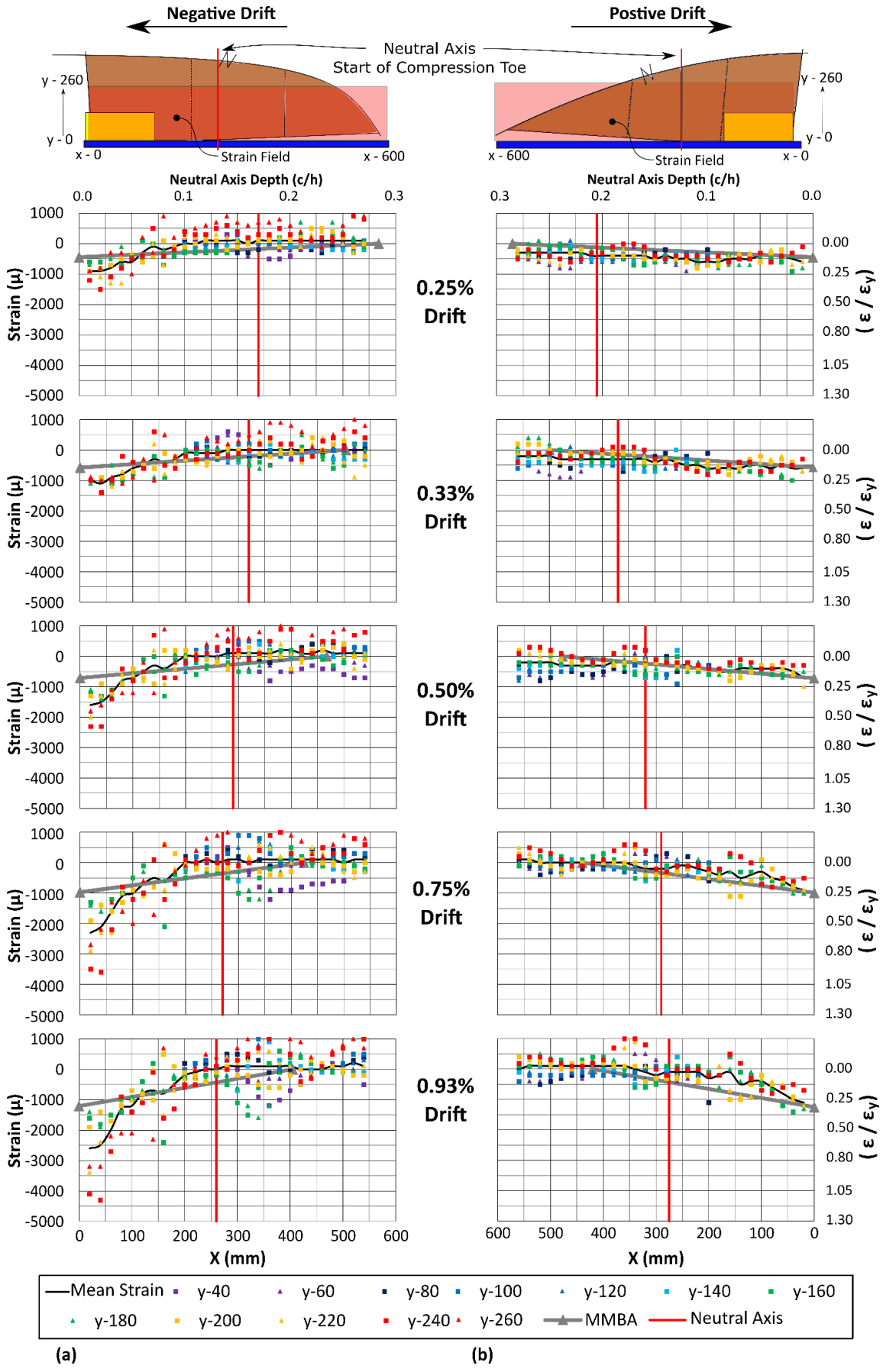


*Figure 7-9: Test SW-2 compression toe strain comparison to MMBA*

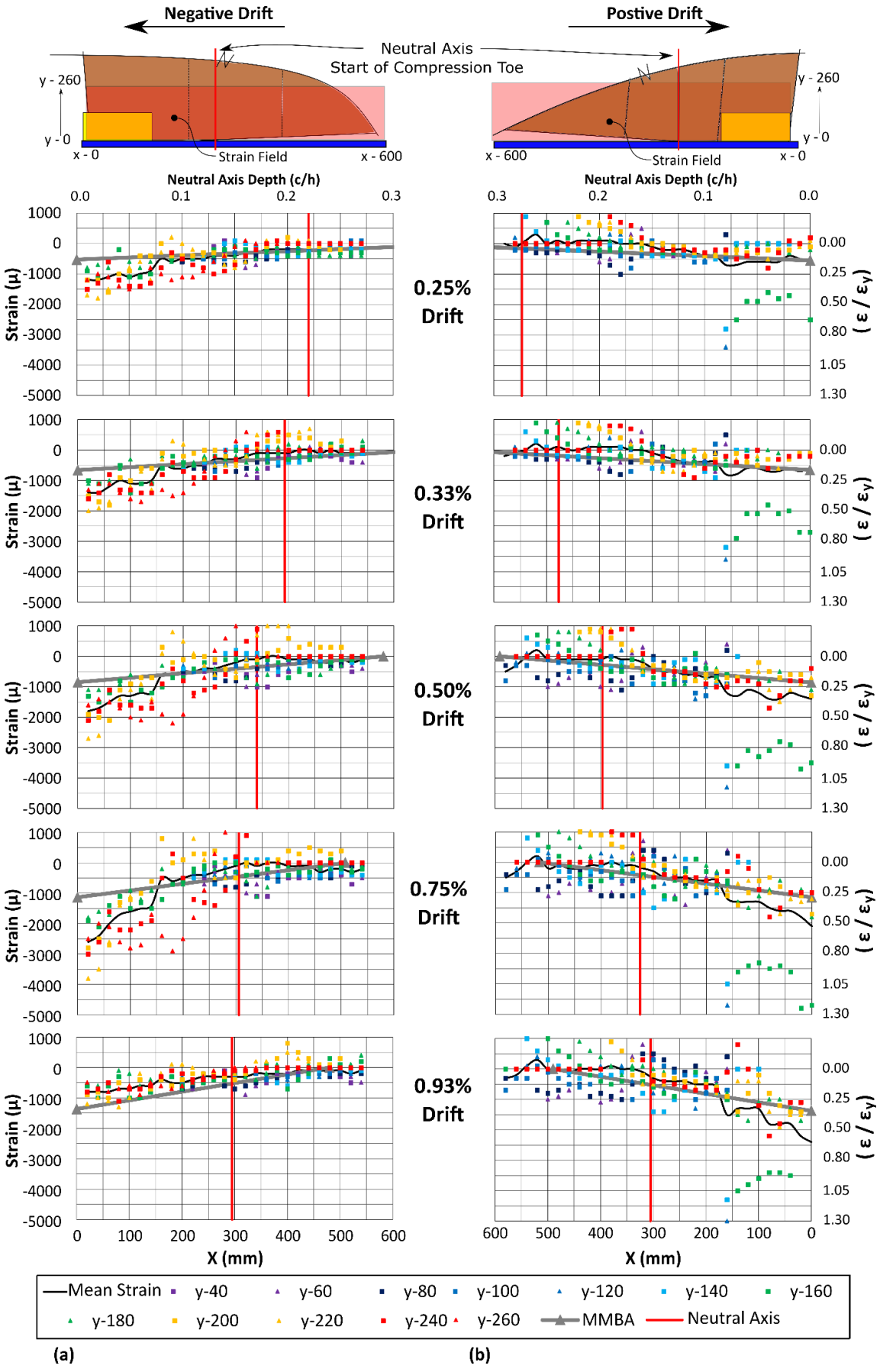


*Figure 7-10: Test SW-3 compression toe strain comparison to MMBA*

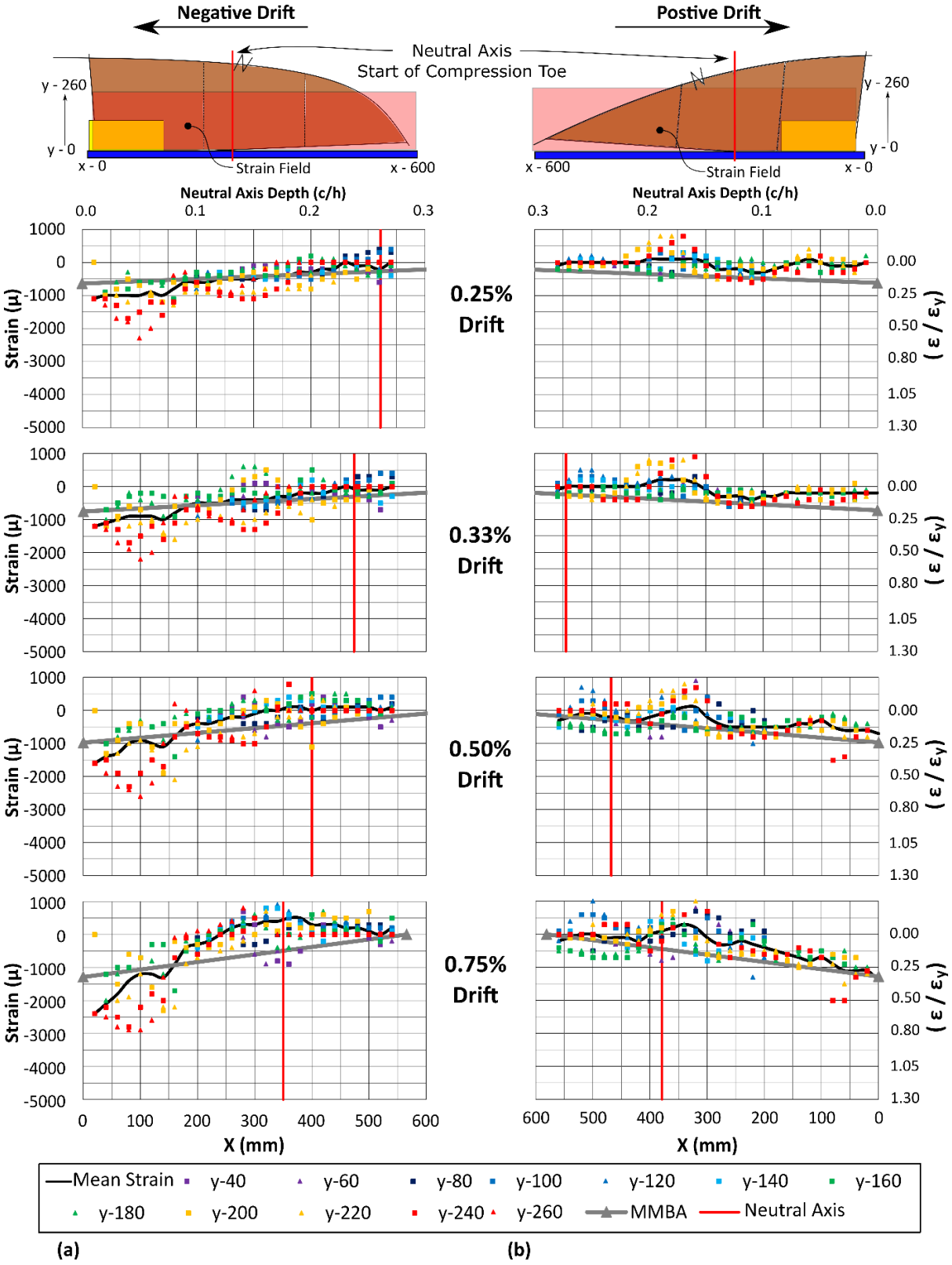


*Figure 7-11: Test SW-4 compression toe strain comparison to MMBA*

## 7.4 ANALYTICAL PARAMETRIC STUDY

A linear strain distribution and a strain amplification factor $\phi_t = 1.3$ as per Equation (7-19) were considered for the analytical parametric study. In addition, component testing on the CLT and PT bars was performed to assess their actual properties.

### 7.4.1 Material properties and input parameters

The component testing data were used as the input parameters for the existing MMBA model in Section 7.4.3 and 7.4.4.

#### *7.4.1.1 CLT compression tests for end effect calibration*

Compression testing as per EN 408 (2012) was employed to assess the CLT properties. The cross-section dimensions for the compression tests were 100mm x 175mm x 600mm high for CLT5 (5-layer) specimens and 70mm x 60mm x 360mm for CLT3 (3-layer) specimens. Past work by Newcombe et al. (2008) showed that the axial stiffness of a timber section is not constant throughout the specimen length. To account for the 'end effects' of timber under crushing loads, a reduced stiffness should be used following the adjustment factor, $k_{gap}$. For laminated veneer lumber (LVL) $k_{gap}$ = 0.7 was recommended for design (Pampanin et al., 2013). Figure 7-12 shows the test setup for the CLT5 and CLT3 specimens and CLT5 test results. Figure 7-12c shows the stress-strain curve when 'end effects' are considered (shown in grey) and when a gauge length is used (shown in black). The number of replicates for each CLT layup was five and the mean values are reported with coefficient of variation in parenthesis in Table 7-2. For the CLT5 specimen, the $k_{gap}$ factor was 0.83. And for the CLT3 specimens, the $k_{gap}$ factor was 0.71.

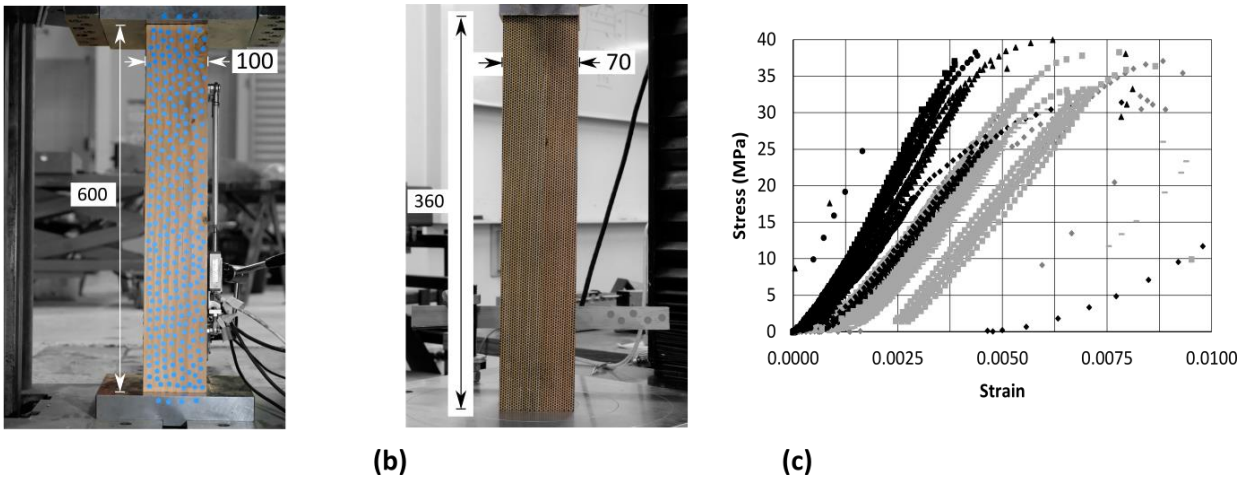


*Figure 7-12: CLT compression testing: (a) CLT5 specimen, (b) CLT3 specimen, and (c) stress-strain results*

*Table 7-2: CLT compression testing results*

| Layer thickness | Mean Density | $E_{0\text{-End}}$ | $E_0$ | $K_{gap}$ | $f_c$ |
|---|---|---|---|---|---|
| | Kg/m3 | MPa | MPa | | MPa |
| 45mm | 462 | 8,028 (4%) | 9,707 (13%) | 0.83 | 37 (9%) |
| 20mm | 539 | 9,489 (4%) | 13,435 (6%) | 0.71 | 54 (7%) |
| SG8 NZS 3603 (1993) | - | - | 8,000 | 0.7[1] | 18 |

Note:[1] $k_{gap}$ = 0.7 is as per Post-Tensioned Timber Buildings Design Guide (Pampanin et al., 2013)

#### *7.4.1.2 Post-tensioning bar tensile testing*

The post-tensioning bars were tested independently to verify their material properties. The tensile tests were performed on machined test pieces in a 1000kN Avery tensile test machine and followed the loading protocol as per BS EN ISO 6892-1 (2016). Figure 7-13 provides details of the machined specimen, test set-up and experimental results. Table 7-3 provides a summary of the mean results from three specimens with comparison to the properties provided by the supplier. The specimens were processed following BS EN ISO 6892-1 (2016) to determine the 0.1% and 0.2% proof stresses. The elastic modulus, $E_{PT}$, was determined by fitting a line to the linear portion of the stress-strain curve. The specimens were not tested to tensile failure in order to avoid damage to the test equipment. Once a load drop was observed at the onset of necking, the specimen was unloaded and its behaviour was recorded. The results showed mean $E_{PT}$ = 184 GPa, 8% greater than the provided $E_{PT}$ = 170 GPa (ETA-07/0046, 2018).

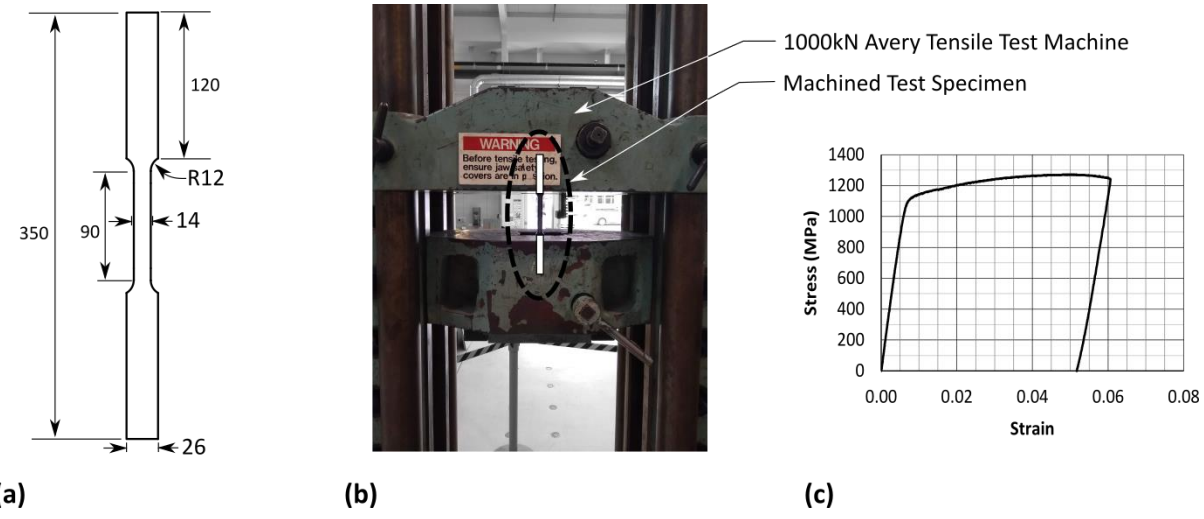


*Figure 7-13: Macalloy post-tensioning bar test*

*Table 7-3: Post-tensioning macalloy bar testing results*

| | Experimental | ETA (2018) |
|---|---|---|
| 0.1% Proof stress (MPa) | 1056 | 835 |
| 0.2% Proof stress (MPa) | 1093 | 865 |
| Ultimate tensile stress (MPa) | 1234 | 1030 |
| Elastic modulus (GPa) | 184 | 170 |

### 7.4.2 Experimental-analytical comparison using NZS3603 and Supplier Input Data

Experimental-analytical comparisons with Test SW-2 were first performed using readily available material properties from NZS 3603 and the material suppliers as well as the existing analytical models without considering $\phi_t$. Due to out-of-plane twisting on the positive push cycle (reported in Chapter 6), the comparison was only made to the negative drift cycles. Figure 7-14 shows the comparison, and at -0.93% drift, the analytical prediction error of the moment-rotation curve was within 15%.

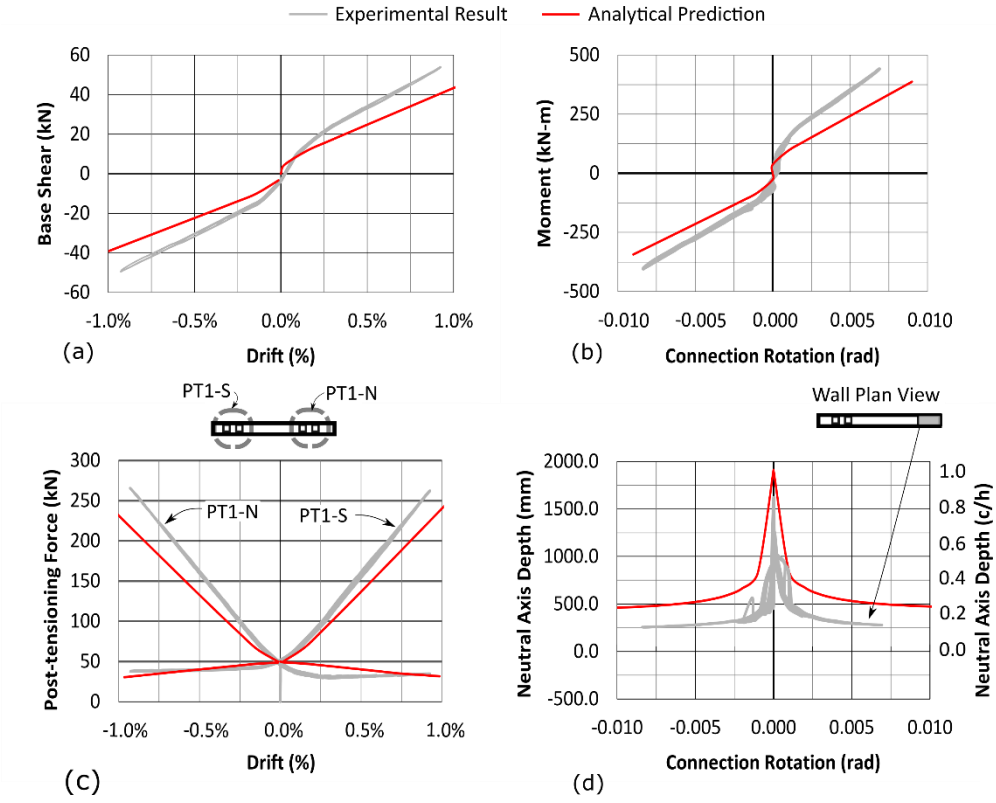


*Figure 7-14: SW-2 Comparison to analytical model with NZS 3603 (1993) and $k_{gap}$=0.7* (Pampanin et al., 2013)

### 7.4.3 Experimental-analytical comparison using component test data

Test SW-2 results were also compared to the analytical model using the material component testing data, i.e., $E_0$ = 9700 MPa, $k_{gap}$ = 0.83, and $E_{PT}$ = 184 GPa. Again, due to out-of-plane twisting on the positive push cycle, the comparison was only made to the negative drift cycles. Figure 7-15 shows significant improvements on the moment-rotation prediction along the negative drift cycle. Further, the post-tensioning force predictions agreed very well with the experimental results. The neutral axis was still over predicted, but the results were much closer to the experimental results. At 0.93% drift, analytical prediction error of the moment-rotation was within 10%.

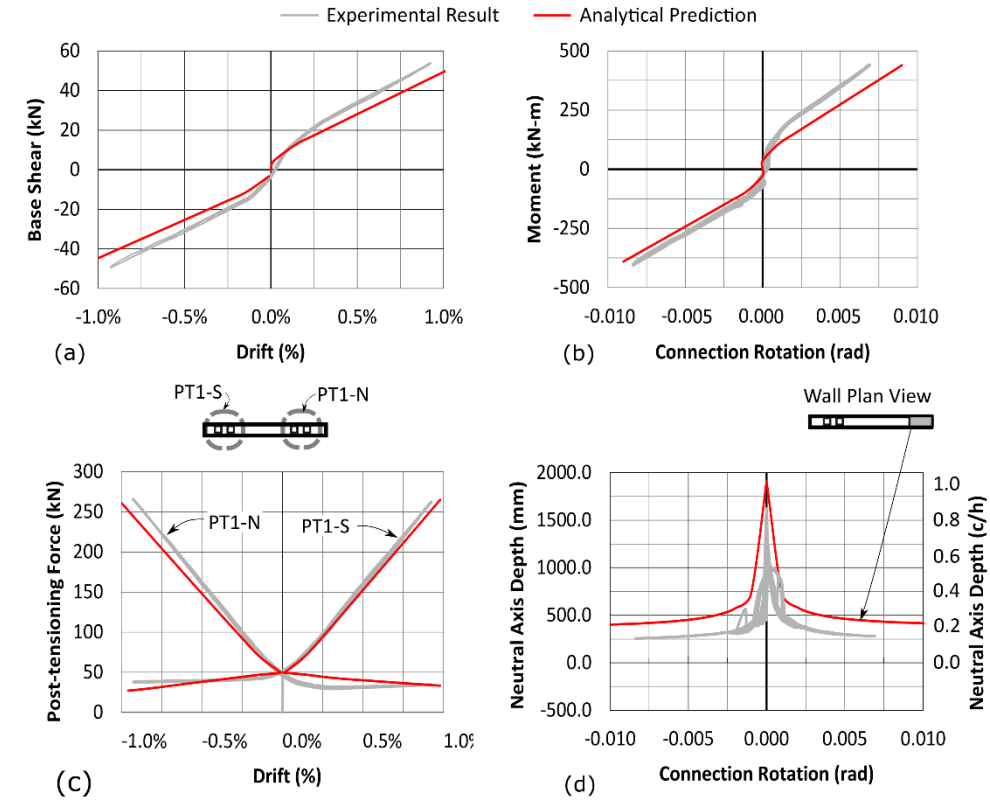


*Figure 7-15: SW-2 Comparison to analytical model with component input data*

### 7.4.4 Experimental-analytical comparison including strain amplification factor

In the final comparison, Test SW-2 was compared to the refined analytical model including $\phi_t = 1.3$ and incorporated the material component testing data. Again, due to out-of-plane twisting on the positive push cycle, the comparison was only made to the negative drift cycles. Figure 7-16 shows that the analytical prediction was further improved, and the neutral axis prediction was closer to the experimental results. The neutral axis was still slightly over predicted; however, it was acknowledged that there could be errors in how the neutral axis is determined based on experimental results. Work by Kovacs (2016) showed that there is error associated with linearly interpolating the results between a discrete number of linear variable displacement transducers (LVDTs). This is in part due to the fact that there is a curvature formed at the wall base and the fact that there is a slope change in the displacement when part of a wall shifts from uplifting to contacting the ground. The PTT results presented in (Chapter 6) also reflected this change of slope and disturbed region. At -0.93% drift, analytical prediction error of the moment-rotation curve was within 5%.

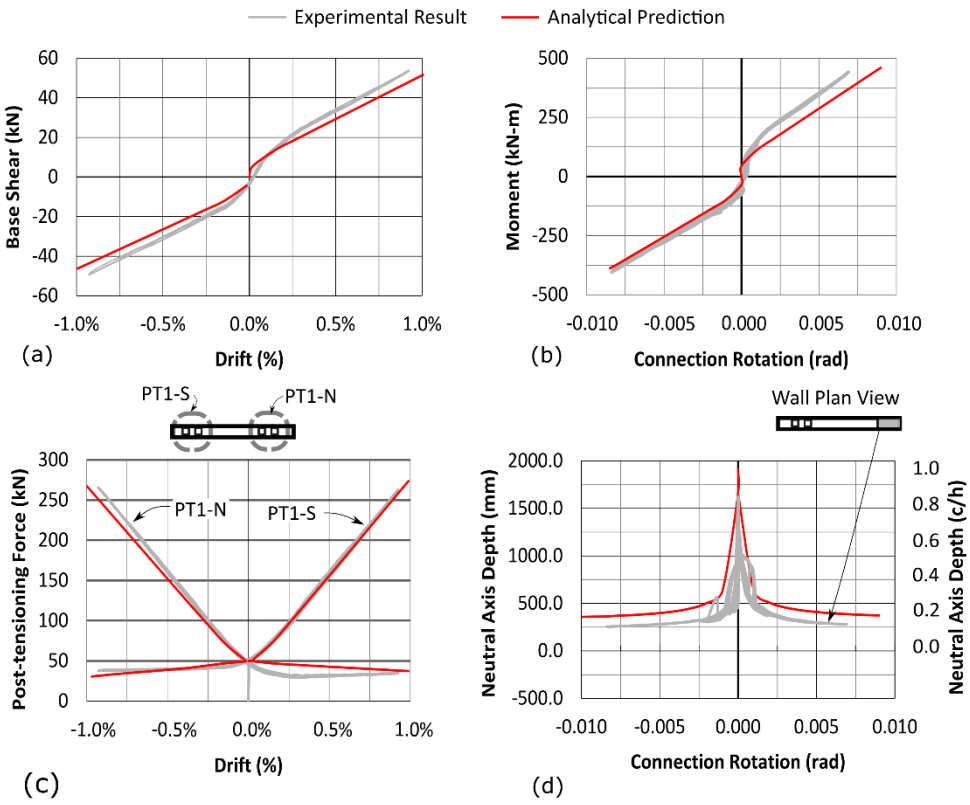


*Figure 7-16: SW-2 Comparison to analytical model with component input data and strain amplification factor of 1.3*

## 7.5 CONCLUSIONS

The Modified Monolithic Beam Analogy (MMBA) was verified for post-tensioned (PT) CLT wall systems. Particle Tracking Technology (PTT) was used to determine the compression strains within the toe of the PT CLT single walls (SW). The four SW experimental tests presented in Chapter 6 were investigated. The main conclusions are listed as follows:

- Triangular stress / strain distribution in the compression toe was verified when timber is within the elastic range. Further work should investigate the strain behaviour beyond timber yielding with PTT to investigate if the triangular distribution is still valid.
- The test results showed the MMBA could under-predict the peak strain response in the compression toe. Complex strain fields reflected the inherent cross-thickness inhomogeneity of CLT and the increased material variability when compared to LVL in past studies. Significant differences in peak strain occurred on each compressive toe of the wall (positive and negative drift cycles) which verified increased strain variability due to the material inhomogeneity.
- A strain amplification factor ($\phi_t$) of 1.3 was determined for the PT CLT wall systems based on the tests performed. When $\phi_t$ was considered, the analytical predictions agreed better with the experimental results. It should be noted that this amplification factor was derived from a limited number of experimental tests. Future work is needed to investigate different wall configurations, drift demands, timber species and engineered timber products. The $\phi_t$ is thus preliminarily recommended for CLT that is non-edge glued and the lamella are visual stress graded.
- At the system level, the moment-rotation behaviour was predicted with reasonable accuracy (within 15%) when readily available material properties and the existing MMBA method was applied. The prediction accuracy increased to within 10% and then 5% when material properties and then the strain amplification factor $\phi_t$ =1.3 was applied. By applying the actual material property values of $E_o$, $E_{PT}$, $k_{gap}$, and $\phi_t$ the prediction of the neutral axis and the peak strain was improved, which is also important for design.

## 7.6 REFERENCES

Baird, A., Smith, T., Palermo, A., & Pampanin, S. (2014). Experimental and numerical Study of U-shape Flexural Plate ( UFP ) dissipators. *NZSEE Conference*, 1–9.

CEN. (2012). *EN 408:2010+A1:2012*. European Committee for Standardization (CEN).

Computers and Structures. (2017). *SAP2000 v17.3*.

EN ISO 6892-1. (2016). *Metallic materials — Tensile testing Part 1 : Method of test at room*

*temperature*. European Committee for Standardization.

ETA-07/0046. (2018). *ETA-07/0046: Macalloy 1030 post tensioning system*. European Technical Approval.

FPInnovations. (2019). *CLT Handbook* (E. Karacabeyli & S. Gagnon (eds.)). FPInnovations.

Kelly, J. M., Skinner, R. I., & Heine, A. J. (1972). Mechanisms of energy absorption in special devices for use in earthquake resistant structures. *Bulletin of the New Zealand Society for Earthquake Engineering*, *5*(3), 63–73.

Kovacs, M. A. (2016). *Design of controlled rocking heavy timber walls for low-to-moderate seismic Hazard Regions*. Master Thesis - McMaster University.

Lukacs, I., Björnfot, A., & Tomasi, R. (2019). Strength and stiffness of cross-laminated timber (CLT) shear walls: State-of-the-art of analytical approaches. *Engineering Structures*, *178*(October 2018), 136–147. https://doi.org/10.1016/j.engstruct.2018.05.126

Nagashima, T., Tachibana, K., Yano, M., & Ohashi, Y. (2020). Design Method for Post-Tensioned timber Shear wall - triangular embedment and behaviour in elastic range. *AIJ*, *85*(770), 539–549. https://doi.org/10.1017/CBO9781107415324.004

Newcombe, M. P. (2011). *Seismic Design of Post-Tensioned Timber Frame and Wall Buildings: Vol. PhD Thesis*. University of Canterbury.

Newcombe, M. P., Pampanin, S., Buchanan, A., & Palermo, A. (2008). Section analysis and cyclic behavior of post-tensioned jointed ductile connections for multi-story timber buildings. *Journal of Earthquake Engineering*, *12*, 83–110. https://doi.org/10.1080/13632460801925632

Palermo, A. (2004). *Use of controlled rocking in the seismic design of bridges*. Technical University of Milan.

Palermo, A., Pampanin, S., Buchanan, A. H., & Newcombe, M. P. (2005). Seismic design of multi-storey buildings using laminated veneer lumber (LVL). *New Zealand Society for Earthquake Engineering Conference*.

Palermo, A., Pampanin, S., & Calvi, G. M. (2005). Concept and development of hybrid solutions for seismic resistant bridge systems. *Journal of Earthquake Engineering*, *9*(6), 899–921. https://doi.org/10.1080/13632460509350571

Pampanin, S., Nigel Priestley, M. J., & Sritharan, S. (2001). Analytical modelling of the seismic behaviour of precast concrete frames designed with ductile connections. *Journal of Earthquake Engineering*, *5*(3), 329–367. https://doi.org/10.1080/13632460109350397

Pampanin, S., Palermo, A., & Buchanan, A. (2013). *Post-Tensioned Timber Buildings - Design Guide Australia and New Zealand*. Structural Timber Innovation Company.

Sarti, F. (2015). *Seismic design of low-damage post-tensioned timber wall systems* (Issue PhD Thesis). University of Canterbury.

Sarti, F., Palermo, A., & Pampanin, S. (2016). Experimental calibration of parallel-to-grain strain penetration length for internal epoxied bars. *Construction and Building Materials*, *112*, 970–979. https://doi.org/10.1016/j.conbuildmat.2016.03.009

Schickhofer, G., Bogensperger, T., Moosbrugger, T., Augustin, M., Blaß, H. J., H, E., & et al. (2010). *BSPhandbuch, Holz- Massivbauweise in Brettsperrholz*. Technische Universitat Graz, Karlsruher Institut fur Technologie.

Smith, T., Pampanin, S., Di Cesare, A., Ponzo, F. C., Simonetti, M., Nigro, D., & Carradine, D. (2014). Shaking table testing of a multi-storey post-tensioned timber building. *NZSEE Conference*, *Figure 1*, 1–8.

Smith, T., Pampanin, S., & Fragiacomo, M. (2006). *LVL Rocking Shear Walls: With external dissipater attachment - 3rd professional year project report*.

Smith, T., Ponzo, F. C., Di Cesare, A., Pampanin, S., Carradine, D., Buchanan, A. H., & Nigro, D. (2014). Post-tensioned glulam beam-column joints with advanced damping systems: Testing and numerical analysis. *Journal of Earthquake Engineering*, *18*(1), 147–167. https://doi.org/10.1080/13632469.2013.835291

Standards New Zealand. (1993). *NZS 3603: Timber structures standard*. Standards New Zealand.

StructureCraft. (n.d.). *Oregon State University Peavy Hall*. Retrieved March 24, 2021, from https://structurecraft.com/projects/oregon-state-university-peavy-hall

Wallner-Novak, M., Koppelhuber, J., & Pock, K. (2014). *Cross-Laminated Timber structural design* (isbn 978-3). proHolz Austria. www.proholz.at

Wilson, A. W., Motter, C. J., Phillips, A. R., & Dolan, J. D. (2019). Modeling techniques for post-tensioned cross-laminated timber rocking walls. *Engineering Structures*, *195*(November 2018), 299–308. https://doi.org/10.1016/j.engstruct.2019.06.011

# 8 Analytical modelling of post-tensioned CLT double wall systems with STS vertical joints and UFP dissipaters

*Key Findings / Outputs:*

- The experimental results of five post-tensioned (PT) CLT double wall (DW) specimens were compared to analytical models.
- Particle tracking technology (PTT) results were used to confirm a linear and triangular stress/strain block within the compression toe.
- The modified monolithic beam analogy (MMBA) and a triangular strain distribution were verified for PT CLT double wall systems within the elastic timber range.
- The analytical model for PT DW systems was extended to capture the kinematic mode of combined single-coupled wall behaviour. To accurately estimate the bending deformation of the composite DW specimen, the 'Gamma Method' was employed.
- The proposed analytical model was able to predict Test DW-3 within 10%, in which both combined single-coupled wall (SCW) and coupled double wall (CDW) behaviour occurred. The model can also capture the instance (imposed base rotation angle) at which the kinematic behaviour changes from SCW to CDW.

## 8.1 INTRODUCTION

The main objective of Chapter 8 is to extend existing analytical models to well capture the response of post-tensioned (PT) double wall (DW) CLT systems. The existing analytical models for PT and non-PT DW timber wall systems are presented first, which consider both walls in contact with the foundation. If the relative connection strength and stiffness between the two wall panels is large enough, wall uplift could occur during the controlled rocking motion. In Section 8.2, the proposed extensions to the existing models are presented to capture different kinematic modes in the PT DW CLT systems, which include the wall uplift scenario. Section 8.3 briefly describes the relevant connection detailing and curve fitting processes employed to capture the highly nonlinear self-tapping screw (STS) joint slip behaviour. Section 8.4 compares the extended analytical models to the experimental results from Chapter 6.

### 8.1.1 Existing Analytical Models for Post-Tensioned CLT Wall Systems

Previous work on PT DW timber systems has primarily focussed on the DW system with U-Shaped Flexural Plates (UFPs) to form the in-plane joint between two walls. PT LVL DW systems with UFPs were experimentally tested by Iqbal et al. (2015) and incorporated in the Pres-Lam design guide (Pampanin et al., 2013). Since then, other experimental works have also focussed on UFPs as energy dissipating elements for PT DW timber systems (Chen et al., 2020; Ganey et al., 2017; Pei et al., 2019; Sun et al., 2020). There are also built examples such as the NMIT Arts & Media and Trimble Navigation buildings New Zealand and more recently the OSU Peavy Hall building in the United States (Granello et al., 2020).

Iqbal et al. (2015; 2018) experimentally tested PT LVL DW systems coupled with plywood and nails and developed an analytical model assuming a constant nail yield force equal to the design capacity for prediction at design drift. The model was able to adequately capture the moment-rotation response. If STS are implemented with different spatial insertion angles, the simplified constant yield force assumption will not be adequate to capture the highly nonlinear STS force-displacement (F-D) response. Further, if high composite action is desired where wall uplift occurs, the in-plane joint behaviour depending on the nonlinear F-D response of STS is critical to the system performance. Nonetheless, Iqbal et al. (2015) showed nailed plywood provides one cost effective method to provide strength and energy dissipation for PT DW systems. Through the work presented herein, the nonlinear curve fitting connection model presented by Foschi (1977) will be implemented to capture the STS F-D response.

### 8.1.2 Existing Analytical Models for Non-Post-Tensioned CLT Wall Systems

A survey on state-of-the-art analytical approaches for conventional CLT shear walls is presented by Lukacs et al. (2019). It was found few analytical models can capture the non-linear behaviour of CLT walls. Gavric et al. (2015) developed a non-linear analytical model for conventional single and double CLT shear walls with different levels of composite action between the panels. Figure 8-1 shows the model which can capture different kinematic modes where both walls are in contact with the foundation and also when only one wall is in contact with the foundation due to the high coupling action by the stiff in-plane joint. Some limitations with this model include: (a) the model assumes rocking occurs about its toe, while in reality there is a contact length (neutral axis depth) of wall with the foundation, (b) the model assumes a trilinear load-displacement curve for all connections which makes it susceptible to sudden load-drops at stiffness change instances, (c) the model does not account for composite action which will develop a composite elastic bending stiffness. The trilinear load-displacement connection behaviour is not suitable for PT wall systems coupled with STS at the in-plane joint and a more accurate model is required to capture the highly nonlinear behaviour of the STS connection. Through the work presented herein, the nonlinear curve fitting connection model presented by Foschi (1977) and the 'Gamma Method' to estimate the composite section bending stiffness are implemented.

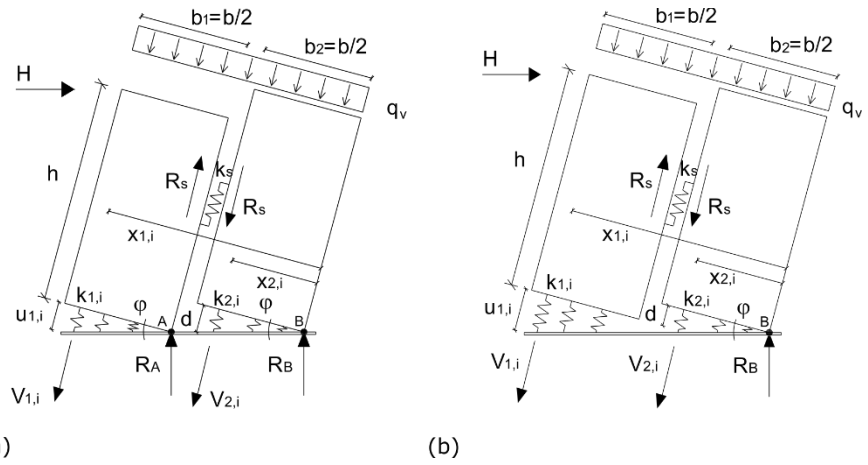


*Figure 8-1: Rocking deformation kinematic modes presented by Gavric et al. (2015): (a) coupled behaviour, and (b) combined single-coupled behaviour*

An elastic stiffness model for CLT platform construction presented by Shahnewaz et al. (2020) can capture the influence of orthogonal walls, and CLT floors above and below. Further, Shahnewaz et al. (2020) discussed the influence of friction between CLT wall panels. Friction is generally not considered in analytical models for CLT walls as under certain loading conditions, it cannot be relied upon (Izzi et al., 2018; Shahnewaz et al., 2020). Through this work, a friction component is implemented only for comparison to the quasi-static cyclic testing in which friction between CLT wall panels was present.

## 8.2 THEORY OF POST-TENSIONED TIMBER DOUBLE WALL SYSTEMS

The following is a continuation of the PT Pres-Lam theory presented in Chapter 7. A brief overview of the procedure will be presented. Then, the existing iterative procedure referred to as the Modified Monolithic Beam Analogy (MMBA) will be extended to capture the different possible kinematic modes in a PT DW system with nonlinear STS connections.

For a DW system, three different kinematic modes can occur as shown in Figure 8-2: coupled double wall (CDW) behaviour, combined single-coupled wall (SCW) behaviour, and single wall (SW) behaviour.

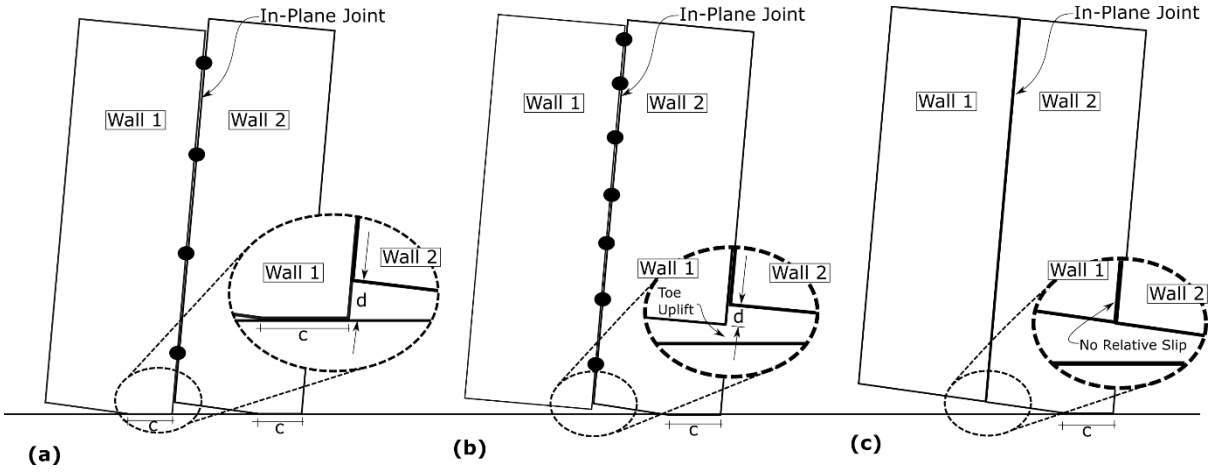


*Figure 8-2: Types of double wall kinematics: (a) coupled double wall behaviour, (b) combined single-coupled wall behaviour, and (c) single wall behaviour*

The step-by-step procedure to satisfy equilibrium is summarized in the following flowchart shown in Figure 8-3. In a DW system, the in-plane joint provides the coupling force. Depending on the relative strength and stiffness of the in-plane joint to the PT bars and the dissipative elements, a certain kinematic behaviour will occur. Thus, after evaluating the dissipative device forces, an additional step which evaluates the coupling force at the in-plane joint must be added. With the STS in-plane joint, this coupling force changes nonlinearly depending on the relative joint slip.

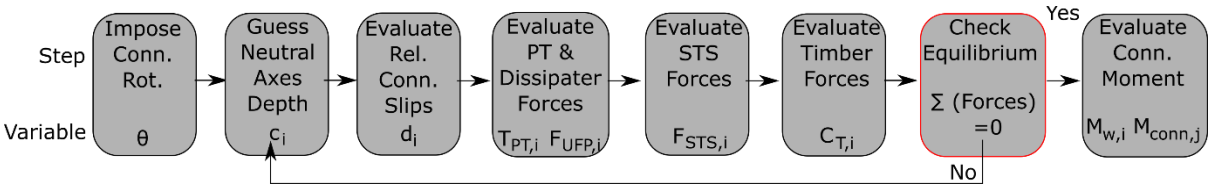


*Figure 8-3: MMBA step-by-step procedure adopted from Sarti* (2015) *with coupling STS force addition and relative connection slips*

In addition to evaluating the coupling force, the timber compression force for wall 'i', $C_{T,wi}$, is now evaluated considering the strain amplification factor, $\phi_t$, determined in Chapter 7 as:

$$C_{T,wi} = (0.5E_{conn}c_i b_{eff}\varepsilon_{t,i})\phi_t \quad (8\text{-}1)$$

where:

$E_{conn}$ = timber connection elastic modulus = $0.83E_o$, derived from the CLT material testing (See Chapter 7)

$c_i$ = neutral axis length for wall 'i'

$b_{eff}$ = is the sum of the longitudinal board widths only

$\varepsilon_{t,i}$ = wall 'i' timber strain determined through MMBA member compatibility

$\phi_t$ = 1.3 as determined in Chapter 7

The following sections describe the different analytical models for each possible DW kinematic mode when the doubled walls are connected with STS at the in-plane joint and UFP dissipater devices at the wall base. The analytical models are based on sectional analysis and the existing iterative MMBA procedure and therefore other connections and dissipative devices could be implemented if their associated force-displacement behaviour is known.

### 8.2.1 Coupled Double Wall (CDW) Theory

In the CDW kinematic behaviour, both Wall 1 and Wall 2 are in contact with the foundation, as shown in Figure 8-4.

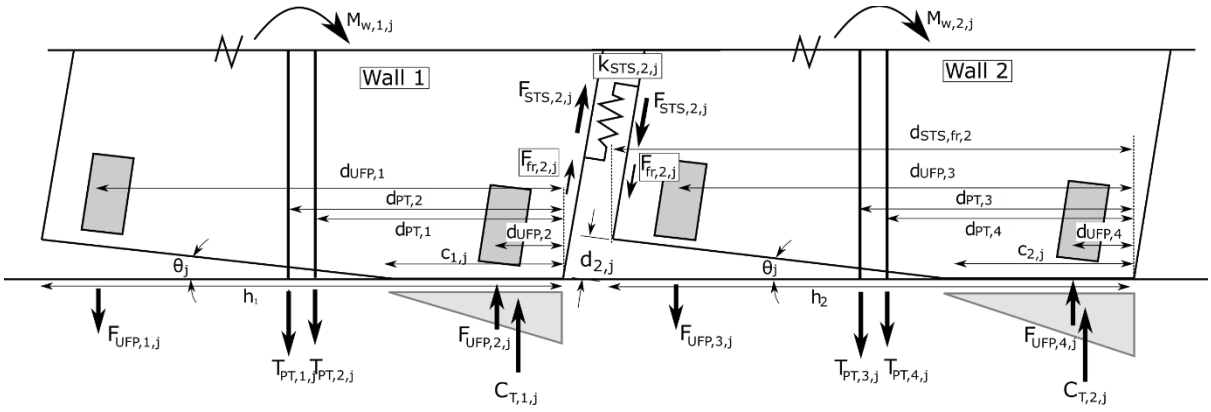


*Figure 8-4: Section analysis of post-tensioned double wall with UFPs and STS connectors under kinematic coupled double wall behaviour mode*

In order to evaluate the coupling force at the in-plane joint, the relative displacement, $d_{2,j}$, between the wall panels at the base is required and is approximated as:

$$d_{2,j} = \theta_j \cdot (h_2 - c_{2,j}) + \theta_j \cdot c_{1,j} \quad (8\text{-}2)$$

where:

$\theta_j$ = imposed base rotation angle for the 'j-th' increment

$c_{i,j}$ = neutral axis length for wall 'i' for the j-th rotation increment

$h_2$ = the length of Wall 2

Due to elastic deformations of the wall panels, the relative displacement, $d_{2,j}$, between Wall 1 and Wall 2 will increase along the height of the in-plane joint. However, for DW systems with low composite action, this can be neglected as reported in Chapter 6. Therefore, for the section analysis at the wall base, $d_{2,j}$ is considered as the uniform slip of the entire in-plane joint. The compressive displacement in Wall 1 ($\theta_j \cdot c_{1,j}$) is approximated and it will be compared to experimental results. Further, axial shortening is not accounted for in joint displacement as it is assumed to the same for Wall 1 and Wall 2. The coupling force provided by the STS joint, $F_{STS,2,j}$ can be determined as:

$$F_{STS,j} = n_{STS,2} k_{STS,2,j} d_{2,j} = K_{STS,2,j} d_{2,j} \quad (8\text{-}3)$$

where:

$n_{STS,2}$ = the number of STS along the in-plane joint

$k_{STS,2,j}$ = the stiffness of a single STS fastener for a given displacement, $d_{2,j}$

$K_{STS,2,j}$ = the total stiffness of the in-plane joint for a given displacement, $d_{2,j}$.

The load-displacement behaviour of laterally loaded STS, similar to any dowel-type fastener in timber, is highly non-linear. In order to accurately capture the nonlinear behaviour, numerous past research (Folz & Filiatrault, 2001; Li et al., 2009) has used an exponential function. In this research, the model originally proposed by Foschi (1974, 1977) was implemented as shown in Figure 8-5.

$$F_{Foschi} = sgn(\omega)(F_o + r_1 K_o|\omega|)\left(1 - exp\left(-\frac{K_o|\omega|}{F_o}\right)\right), |\omega| \leq |\omega_u| \quad (8\text{-}4)$$

$$F_{Foschi} = sgn(\omega)(F_u + r_2 K_o)(\omega - sgn(\omega)\omega_u), |\omega_u| < |\omega| \leq |\omega_f| \quad (8\text{-}5)$$

$$F_{Foschi} = 0, |\omega| > |\omega_f| \quad (8\text{-}6)$$

where:

$F_{\text{Foschi}}$ = Connector force as per Foschi model

$sgn(\omega)$ = signum function to extract the sign of the displacement, $\omega$

$\omega_u$ = displacement at maximum force

$\omega_f$ = final displacement

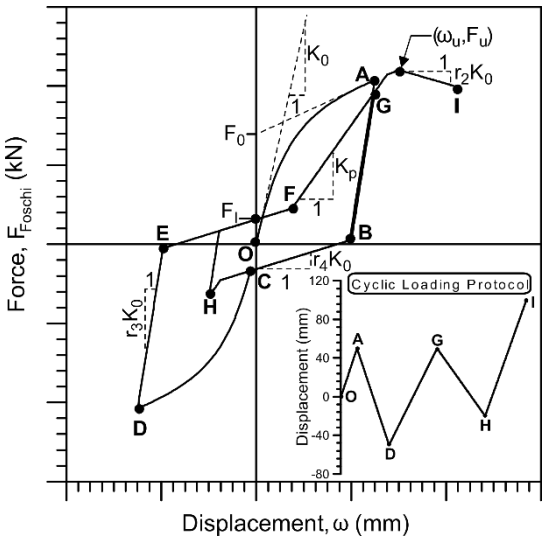


*Figure 8-5: Nail-slip model proposed by Foschi* (1977) *with figure from Folz & Filiatraut* (2001)

It was found that the simplified trilinear load-displacement curve to model connections as proposed by Gavric et al. (2015) was not appropriate in the instance of the SCW behaviour where connection stiffness is critical to determine. In Section 8.4.2, Test DW-2 will be compared to the analytical model using the simplified elasto-plastic connection behaviour as proposed by Iqbal et al. (2015).

With reference to Figure 8-4, the equilibrium for Wall 1 is determined as:

$$C_{T,1,j} + F_{fr,2,j} + F_{STS,2,j} + F_{UFP,2,j} - \sum T_{PT,i,j} - F_{UFP,1,j} = 0 \tag{8-7}$$

And the equilibrium for Wall 2 is determined as:

$$C_{T,2,j} - F_{fr,2,j} - F_{STS,2,j} - F_{UFP,3,j} - \sum T_{PT,i,j} + F_{UFP,4,j} = 0 \tag{8-8}$$

The neutral axis depth, $c_{1,j}$ and $c_{2,j}$, is then iterated until force equilibrium is achieved. Note, the friction term is generally neglected (Izzi et al., 2018; Shahnewaz et al., 2020) in analysing CLT structures. In this instance it is considered as it was required to predict the quasi-static experimental testing programme where friction was activated. The friction co-efficient was calibrated based on test DW-1 and them kept constant for the remaining double wall and core-wall tests. Once equilibrium is found the base connection moment can be determined for Wall 1 and Wall 2 with reference to Figure 8-4 as:

$$M_{w,1,j} = \sum T_{PT,i,j}\left(d_{PT,i} - {}^{c_{1,j}}/_{3}\right) + F_{fr,2,j}\left({}^{c_{1,j}}/_{3}\right) + F_{STS,2,j}\left({}^{c_{1,j}}/_{3}\right) + \sum F_{UFP,i,j}\left(d_{UFP,i} - {}^{c_{1,j}}/_{3}\right) \tag{8-9}$$

$$M_{w,2,j} = \sum T_{PT,i,j}\left(d_{PT,i} - {}^{c_{2,j}}/_{3}\right) + F_{fr,2,j}\left(d_{fr,2} - {}^{c_{2,j}}/_{3}\right) + F_{STS,2,j}\left(d_{STS,2} - {}^{c_{2,j}}/_{3}\right) + \sum F_{UFP,i,j}\left(d_{UFP,i} - {}^{c_{2,j}}/_{3}\right) \tag{8-10}$$

The friction and STS coupling forces can be assumed to be acting along the in-plane joint line. In reality, the STS will be placed with a minimum edge distance (3d = 24mm) from the panel edge but this small difference was neglected for simplification. The total base connection moment, $M_{conn}$, is then:

$$M_{conn,j} = M_{w,1,j} + M_{w,2,j} \tag{8-11}$$

Then, the elastic bending and shear deformations are determined as per Sections 8.2.4 and 8.2.5.

### 8.2.2 Combined Single-Coupled Wall (SCW) Theory

In the SCW kinematic behaviour, the coupling force and stiffness is large enough such that Wall 1 is not in contact with the ground, as shown in Figure 8-6. However, there is a relative slip, $d_{2,j}$, between Wall 1 and Wall 2 which is less than the uplift of Wall 2 at the in-plane joint.

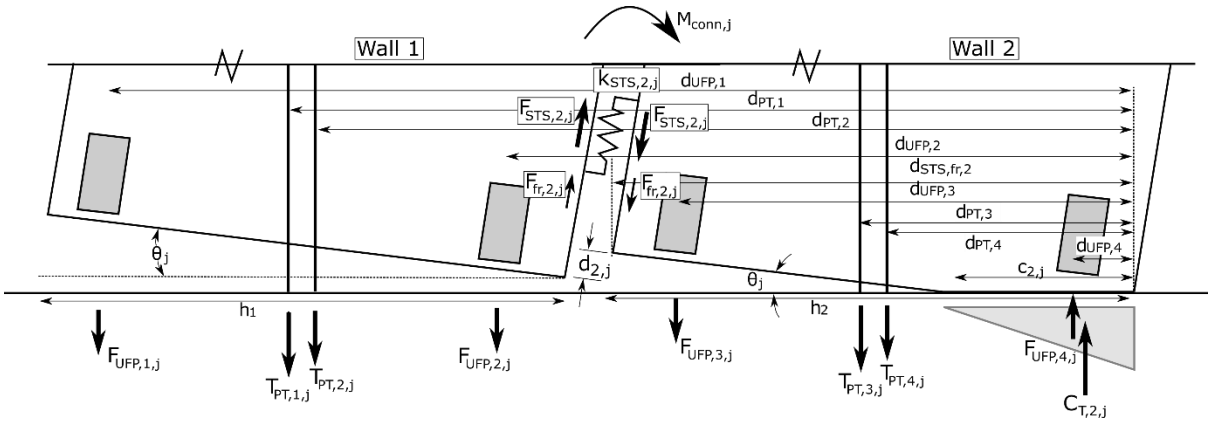


*Figure 8-6: Section analysis of post-tensioned double wall with UFPs and STS connectors under kinematic combined single-coupled wall behaviour mode*

In order to determine $d_{2,j}$, the vertical force equilibrium of Wall 1 is determined as a function of the stiffness of each component:

$$\sum k_{PT,W1,i,j}[(d_{PT,W1,i} - c_{2,j})\theta_j - d_{2,j}] + \sum k_{UFP,W1,i,j}[(d_{UFP,W1,i} - c_{2,j})\theta_j - d_{2,j}] + \sum T_{PT,0,w1} = K_{STS,2,j}d_{2,j} + F_{fr,2,j} \tag{8-12}$$

where:

$k_{PT,w1,i,j}$ = stiffness of the 'i-th' PT bar in Wall 1 for the 'j'-th rotation increment

$d_{PT,W1,i}$ = distance to the 'i-th' PT bar in Wall 1

$c_{2,j}$ = neutral axis length of Wall 2 for the 'j'-th rotation increment

$k_{UFP,W1,i,j}$ = stiffness of the 'i-th' UFP element in Wall 1 for the 'j'-th rotation increment

$d_{UFP,W1,i}$ = distance to the 'i-th' UFP element in Wall 1

$K_{STS,2,j}$ = total stiffness of the screwed in-plane joint for a given joint slip $d_{2,j}$ for the 'j'-th rotation increment

$F_{fr,2,j}$ = friction force along the in-plane joint for the 'j'-th rotation increment

Note that $K_{STS,2,j}$ is the stiffness at a given displacement $d_{2,j}$, which is changing in a non-linear manner as presented in Section 8.2.1. With reference to Figure 8-6, vertical force equilibrium of the two wall system can be determined as:

$$C_{T,2,j} - \sum T_{PT,W1i,j} - \sum T_{PT,W2,i,j} - F_{UFP,1,j} - F_{UFP,2,j} - F_{UFP,3,j} + F_{UFP,1,j} = 0 \quad (8\text{-}13)$$

where $T_{PT,W1,I,j}$ and $F_{UFP,I,j}$ are dependent on the relative wall displacement, $d_{2,j}$. $T_{PT,W1,I,j}$ is evaluated by first determining the tendon elongation for a given imposed rotation as:

$$\Delta_{PT,W1,i,j} = Elongation\ due\ to\ gap\ opening - Axial\ wall\ shortening - Relative\ connection\ slip\ (d_{2,j}) \quad (8\text{-}14)$$

$$\Delta_{PT,W1,ij} = \theta_j(d_{PT,W1,i} - c_{2,j}) - \left\{\frac{\sum(T_{PT,W1,i,j-1} - \sum T_{PT,W1,o})(L_{ub,i})}{E_0 A_{eff}}\right\} - d_2 \quad (8\text{-}15)$$

Where:

$\Delta_{PT,w1,i,j}$ = is the elongation of the 'i-th' PT bar for the j-th rotation increment

$\sum T_{PT,w1,o}$ = sum of the initial post-tensioning forces in Wall 1

$L_{ub,i}$ = the unbonded PT bar length

$E_0$ = the elastic modulus of the timber wall

$A_{eff}$ = the effective timber wall area which only considers the longitudinal layers of the CLT wall

Then, the strain and post-tensioning force increment of the 'i-th' PT bar is evaluated as presented in Chapter 7.

By rearranging Equation (8-12), an expression for the relative wall slip, $d_{2,j}$, can be determined for a given imposed wall rotation, $\theta_j$, and Wall 2 neutral axis depth, $c_{2,j}$.

$$d_{2,j} = \frac{\theta_j\{\sum k_{PT,W1,i,j}[(d_{PT,W1,i} - c_{2,j})] + \sum k_{UFP,W1,i,j-1}[(d_{UFP,W1,i} - c_{2,j})]\} - F_{fr,2,j} + \sum T_{PT,0,w1}}{(K_{STS,2,j-1} + \sum k_{PT,W1,i,j} + \sum k_{UFP,W1,i,j-1})} \quad (8\text{-}16)$$

Again, the friction component $F_{fr,2,j}$ can be neglected in design but is shown here for comparison to quasi-static experimental testing. Note that as with coupled wall behaviour, the axial shortening between both wall panels is considered to be equal for simplification and therefore is not considered in determining $d_{2,j}$. Then, by knowing $d_{2,j}$, the vertical force equilibrium shown in Equation (8-13) can

be determined with iteration for $c_{2,j}$. Equation (8-16) shows that as $K_{STS,2,j}$ decreases the relative connection slip, $d_{2,j}$, increases. The base connection moment, $M_{conn,j}$, can be evaluated as:

$$M_{conn,j} = \sum T_{PT,i,j}\left(d_{PT,i} - {}^{c_{2,j}}/_{3}\right) + \sum F_{UFP,i,j}\left(d_{UFP,i} - {}^{c_{2,j}}/_{3}\right) \quad (8\text{-}17)$$

Note, $F_{STS,2,j}$ does not explicitly appear in the Equation (8-17) but it has been accounted for when calculating the relative connection slip, $d_{2,j}$, in each contributing element from Wall 1 as demonstrated in Equation (8-15).

A combined SCW kinematic behaviour continues until Wall 1 toe touches the foundation, which is when $d_{2,j} = \theta_j \cdot (h_2 - c_{2,j})$. Once this occurs, the kinematic behaviour changes to CDW as described previously in Section 8.2.1.

Then, the elastic bending and shear deformations can be determined as per Sections 8.2.4 and 8.2.5. However, because the DW specimen is behaving in composite action the bending deformation will be determined using the 'Gamma Method' which is commonly used for composite sections connected with STS (Dietsch & Brandner, 2015; Symons et al., 2010).

### 8.2.3 Theoretical Full Composite Action Scenario

If there is no relative slip at the in-plane joint between Wall 1 and Wall 2, a SW kinematic behaviour occurs as shown in Figure 8-7.

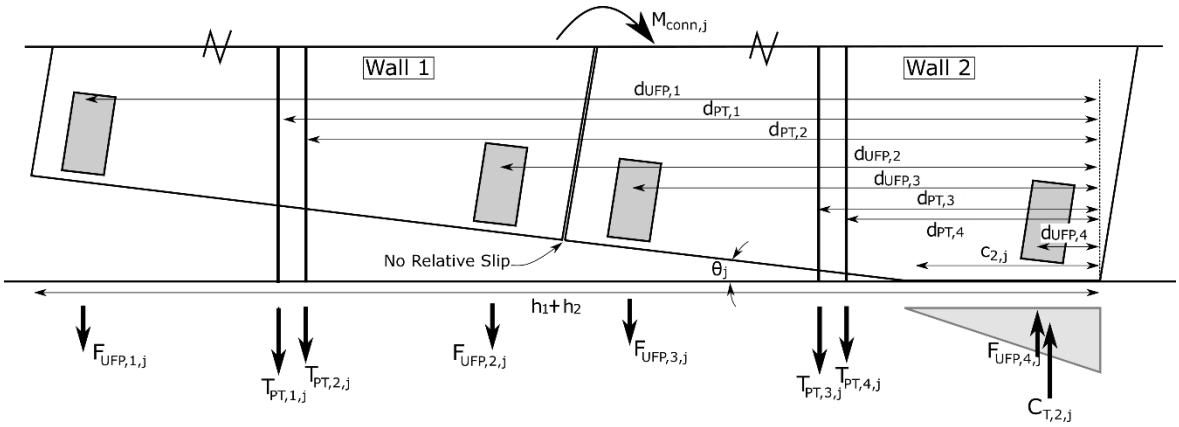


*Figure 8-7: Section analysis of post-tensioned double wall with UFPs and STS connectors under kinematic single wall behaviour mode*

In this instance, the wall length is now $h = h_1 + h_2$. To achieve no relative slip, $d_{2,j}$=0, $K_{STS,2,j} \rightarrow \infty$ in Equation (8-16) which is not possible in practice. However, by analysing the SW behaviour, theoretical upper bound and fully composite behaviour can be determined. Then, the partial composite action (CA) of the experimental double wall testing can be defined by comparing the test results with a

theoretical uncoupled and fully composite systems in a similar manner to that for composite beams (Gutkowski et al., 2008; Pault & Gutkowski, 1977)

$$\%CA_{\delta} = \frac{F_{Test,\delta} - F_{0\%,\delta}}{F_{100\%,\delta} - F_{0\%,\delta}} \tag{8-18}$$

where, for a given wall drift ($\delta$), $F_{0\%,\delta}$ is the theoretical force for a fully non-composite section, $F_{100\%,\delta}$ is the theoretical force for a fully composite section, and $F_{Test,\delta}$ is the measured force. This was used in Chapter 6 and shown in Figure 6-34 to quantify the partial composite action received during the experimental PT DW testing. Then, the elastic bending and shear deformations can be determined as per Sections 8.2.4 and 8.2.5.

### 8.2.4 Bending Deformation

The bending deformation, $\delta_b$, at the top of the wall for a given wall base rotation 'j' is calculated using the elastic formula for a fixed base cantilever as:

$$\delta_{b,j} = \frac{F_j L_{cant}^3}{3 E_o I_{eff,\gamma}} \tag{8-19}$$

Where:

$F_j$ = is the horizontal force at the top of the wall

$L_{cant}$ = is the cantilever wall height

$E_o I_{eff,\gamma}$ = the effective flexural stiffness of the CLT panel by considering the longitudinal layer only (FPInnovations, 2019). For coupled walls with composite action, the 'gamma method' in Eurocode 5 (CEN, 2014) is used to calculate the effective flexural stiffness, shown as follows:

$$E_t I_{eff,\gamma} = \sum_{i=1}^{2} (E_{t,o,i} I_{Eff,i} + \gamma_i E_{t,o,i} A_{eff,i} {a_i}^2), i = Wall\ 1\ and\ Wall\ 2 \tag{8-20}$$

where $\gamma$ is the gamma factor symbolizing the efficiency of the connection between the walls ($\gamma$ = 1 → rigid connection, $\gamma$ = 0 → no connection), $A_{eff}$ is the effective timber area which considers the layers loaded parallel to the grain, $a_i$ is the distance between the centroid of the composite section and geometric centre of element 'i'.

$$\gamma_i = \left[1 + \pi^2 E_{t,o,i} A_{eff,i} s_i / (k_{STS,2,j} {L_{eff}}^2)\right]^{-1} \tag{8-21}$$

where $s_i$ is the spacing of the STS and $s_i = n_{STS}/L_{cant}$, $k_{STS,2,j}$ is the stiffness of one individual STS connection at an assumed wall base rotation, $\theta_j$, and $L_{eff}$ is taken as twice the cantilever wall height.

Further,

$$a_2 = \frac{\gamma_1 E_{o,1} A_{eff,1}(h_1 + h_2)}{2\left(\sum_{i=1}^{2} \gamma_i E_{o,i} A_{eff,i}\right)} \tag{8-22}$$

where $h_1$ and $h_2$ are the length of the wall specimens. Because the walls are the same length, in this instance $a_1$=$a_2$=956mm.The calculated $E_o I_{eff,\gamma}$ can then be used with Equation (8-19) to determine the bending deformation, $\delta_b$, for the combined single-coupled wall system. Figure 8-8 shows the applicable symbols to utilize the gamma method in the double wall system.

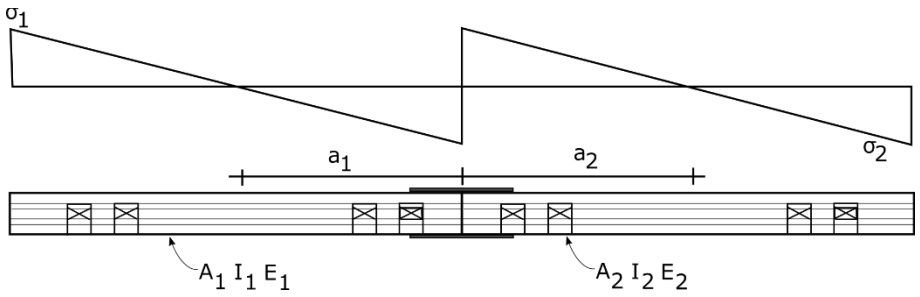


*Figure 8-8: Gamma method symbols for double wall system*

### 8.2.5 Shear Deformation

There are different methods in literature for calculating the in-plane shear deformation, $\delta_{s,j}$, of a CLT panel (Lukacs et al., 2019). In this instance, the shear stiffness method proposed by Schickhofer et al. (2010) was used which determines an effective shear modulus, $G_{eff}$, and the gross shear area, A as:

$$G_{eff}A = \frac{G_0 A}{1 + 6\left[0.32\left(\frac{t_b}{a}\right)^{-0.77}\right]\left(\frac{t_b}{a}\right)^2} \tag{8-23}$$

where:

$t_b$ = average thickness the CLT lamella

$a$ = the average width of the CLT lamella.

Due to the ordered CLT, $G_{eff}A$ was approximately equal to 0.75GA as per the ProHolz guideline (Wallner-Novak et al., 2014). Then, the shear deformation for a given wall base rotation 'j' is determined as:

$$\delta_{s,j} = \frac{F_j L_{cant}}{G_{eff}A} \tag{8-24}$$

### 8.2.6 Pushover Analysis

An iterative moment-rotation analysis to determine $M_{conn,j}$ followed by the elastic deformation calculations at each rotation angle can be carried out to determine the non-linear force-displacement curve for a PT DW system with dissipative devices and with varying levels of coupling / composite action at the in-plane joint. By using the non-linear curve fitting function by Foschi (1977), the analytical procedure can capture the full load-displacement curve of a PT DW system coupled with STS and capture the instance where the kinematic behaviour changes from combined SCW to CDW. Each wall base rotation step, $\Delta\theta$ shall be chosen small enough to ensure stable performance along the non-linear curve fitting function following the relationship presented in Equation (8-25).

$$\theta_{j+1} = \theta_j + \Delta\theta \tag{8-25}$$

Then, for each rotation $\theta_j$ the horizontal deflection at the top of the wall can be determined considering rocking, $\delta_r$, bending, $\delta_b$, and shear, $\delta_s$, deformation components as:

$$\delta_T = \delta_r + \delta_b + \delta_s \tag{8-26}$$

As mentioned in Section 8.2, depending on the relative strength and stiffness of the in-plane joint to the post-tensioning and dissipater elements, a certain kinematic mode will result. The flow chart shown in Figure 8-9 summarizes the step-by-step iterative procedure for the rocking deformation component.

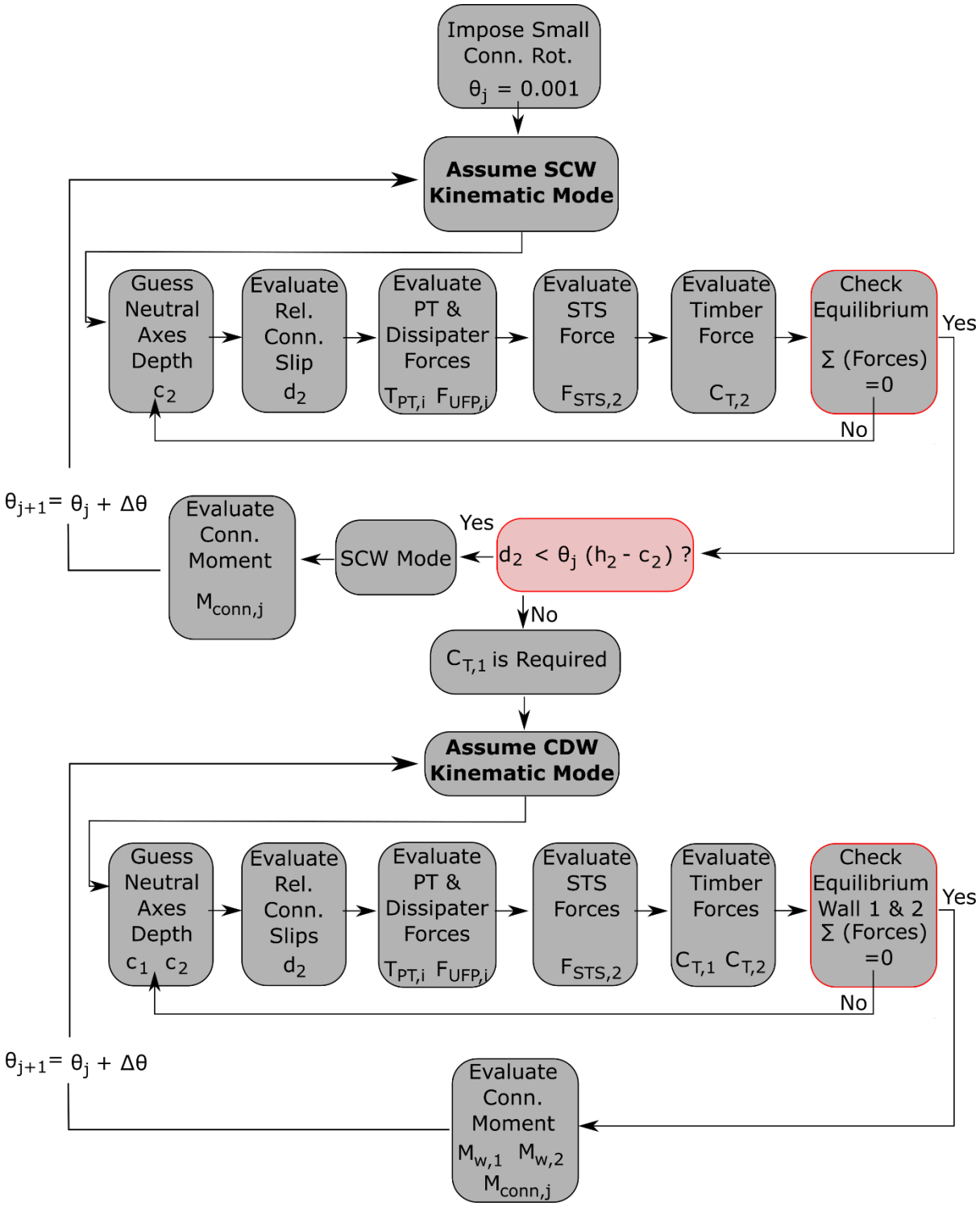


*Figure 8-9: Post-tensioned double wall analytical design iterative flowchart*

## 8.3 DOUBLE WALL TESTING SPECIMEN DETAILING

Some specific details from the DW testing reported in Chapter 6 are provided here for implementation in the presented analytical model.

### 8.3.1 Self-Tapping Screw Connection Detailing

$\phi$8x80mm partially threaded (PTH) STS were installed in pairs on each side of the in-plane joint with 17mm thick plywood as shown in Figure 8-10. The minimum spacing as per Eurocode 5 (CEN, 2014), $a_1$=10d, which was 80mm in this instance was followed.

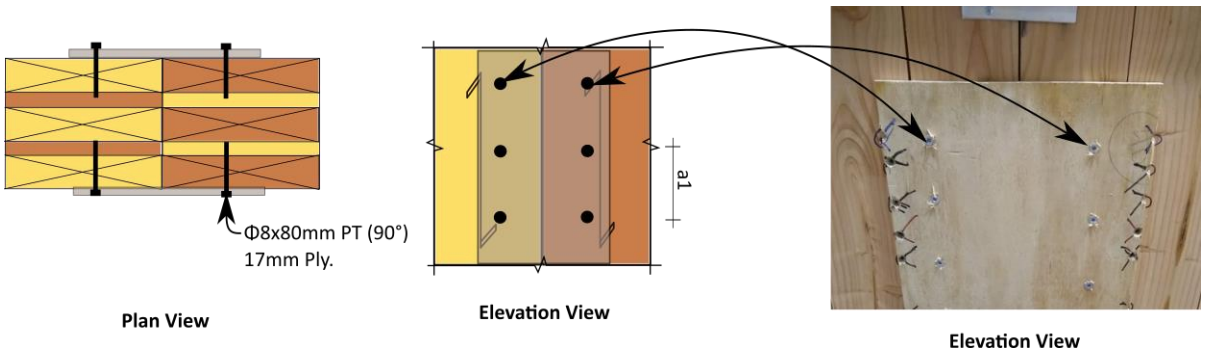


*Figure 8-10: In-plane joint details with self-tapping screws*

The STS connection tests were not performed as sufficent test data by Hossain (2019) existed for calibration of the nonlinear analytical model. Figure 8-11 shows the connection load-slip curves by Hossain (2019), the exponential load-slip model by Foschi (1977), and the fitted curve. Table 8-1 shows the curve fitting parameters required to fit the envelope curve OAI shown in Figure 8-11b.

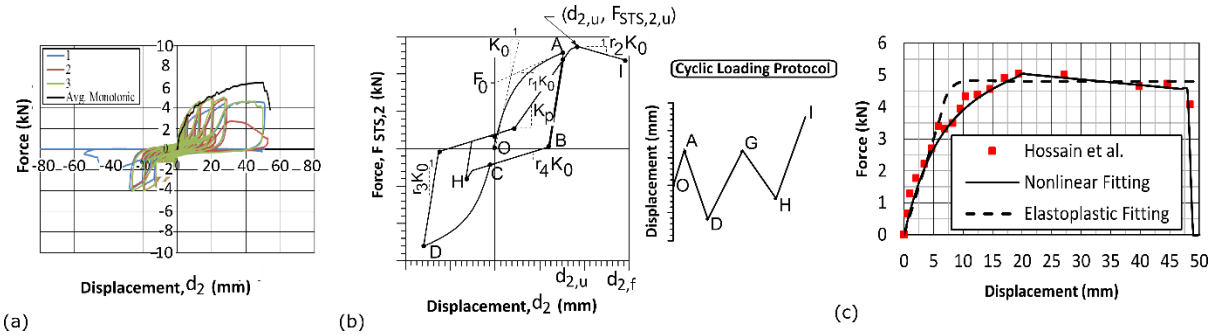


*Figure 8-11: (a) STS component testing by Hossain (2019), (b) nonlinear curve fitting model by Foschi (1977), and (c) curve fitting results*

*Table 8-1: Input parameters for non-linear curve fitting model*

| Initial Stiffness | Force Intercept | Stiffness reduction parameters | | Displacement at max. force | Displacement at final displacement | Max. force |
|---|---|---|---|---|---|---|
| (kN/mm) | (kN) | | | (mm) | (mm) | (kN) |
| $K_o$ | $F_o$ | $r_1$ | $r_2$ | $d_{2,u}$ | $d_{2,f}$ | $F_{STS,2,u}$ |
| 0.8 | 3.81 | 0.08 | -0.022 | 19.41 | 48.47 | 5.05 |

The number of STS pairs installed in Test DW-2, DW-3, and DW-4 was 32, 110, and 32 respectively which then amplified the curve fitting shown in Figure 8-11c for a single STS pair.

### 8.3.2 UFP Connection Detailing

The UFP connectors were tested separately in component testing to better evaluate their cyclic performance and the results were presented in Chapter 6, Section 6.3.6. The UFP pair were modelled as a bilinear elastic-plastic system with elastic stiffness of 5.5kN/mm and yield force of 71kN.

## 8.4 EXPERIMENTAL-ANALYTICAL COMPARISONS

A summary of experimental-analtycial comparisons of Wall 2 kinematics is presented in Table 8-2 as a percentage of total deformation. On average, the wall kinematics was predicted within 10% error for all the tests with different levels of coupling.

*Table 8-2: Wall 2 kinematics comparison*

| | | Experimental | | | Analytical | | |
|---|---|---|---|---|---|---|---|
| | Loading Direction | $\delta_r$ | $\delta_{sl}$ | $\delta_{b+sh}$ | $\delta_r$ | $\delta_{sl}$ | $\delta_{b+sh}$ |
| Test | | (%) | (%) | (%) | (%) | (%) | (%) |
| DW-1 | Positive | 82 | 3 | 15 | 80 | 0 | 20 |
| | Negative | - | - | - | 80 | 0 | 20 |
| DW-2 | Positive | 77 | 2 | 21 | 72 | 0 | 28 |
| | Negative | 86 | 2 | 12 | 78 | 0 | 22 |
| DW-3 | Positive | 70 | 5 | 25 | 61 | 0 | 39 |
| | Negative | 81 | 5 | 14 | 75 | 0 | 25 |
| DW-4 | Positive | 74 | 1 | 25 | 67 | 0 | 33 |
| | Negative | 85 | 2 | 15 | 75 | 0 | 25 |
| DW-5 | Positive | 77 | 1 | 22 | 76 | 0 | 24 |
| | Negative | 86 | 1 | 13 | 77 | 0 | 23 |

The input values for analytical models were taken from CLT and PT bar material testing presented in Chapter 7, Section 7.4.1 and UFP testing presented in Chapter 6, Section 6.3.6. The material input values were:

$E_0$ = 9700 MPa (8000MPa as per NZS 3603 (1993))

$k_{gap}$ = 0.83 (0.7 is recommended for LVL as per Pampanin et al. (2013))

$E_{PT}$ = 184 GPa (170GPa is catalogue value (ETA-07/0046, 2018))

$\phi_t$, = 1.3, timber strain amplification factor (derived from SW testing investigation in Chapter 7)

As with the SW anlaytical comparisons, all comparisons in the DW testing were made to the negative drift cycle as out-of-plane behaviour was minimized (see Chapter 6, Section 6.6.3).

### 8.4.1 Test DW-1

In Test DW-1, there was no connection between two wall panels and UFPs were not installed at the wall base. In this way, the contribution of friction during quasi-static testing could be quantified. Figure 8-12 shows the key experimental results with comparison to the analytical model which followed the coupled double wall kinematic mode.

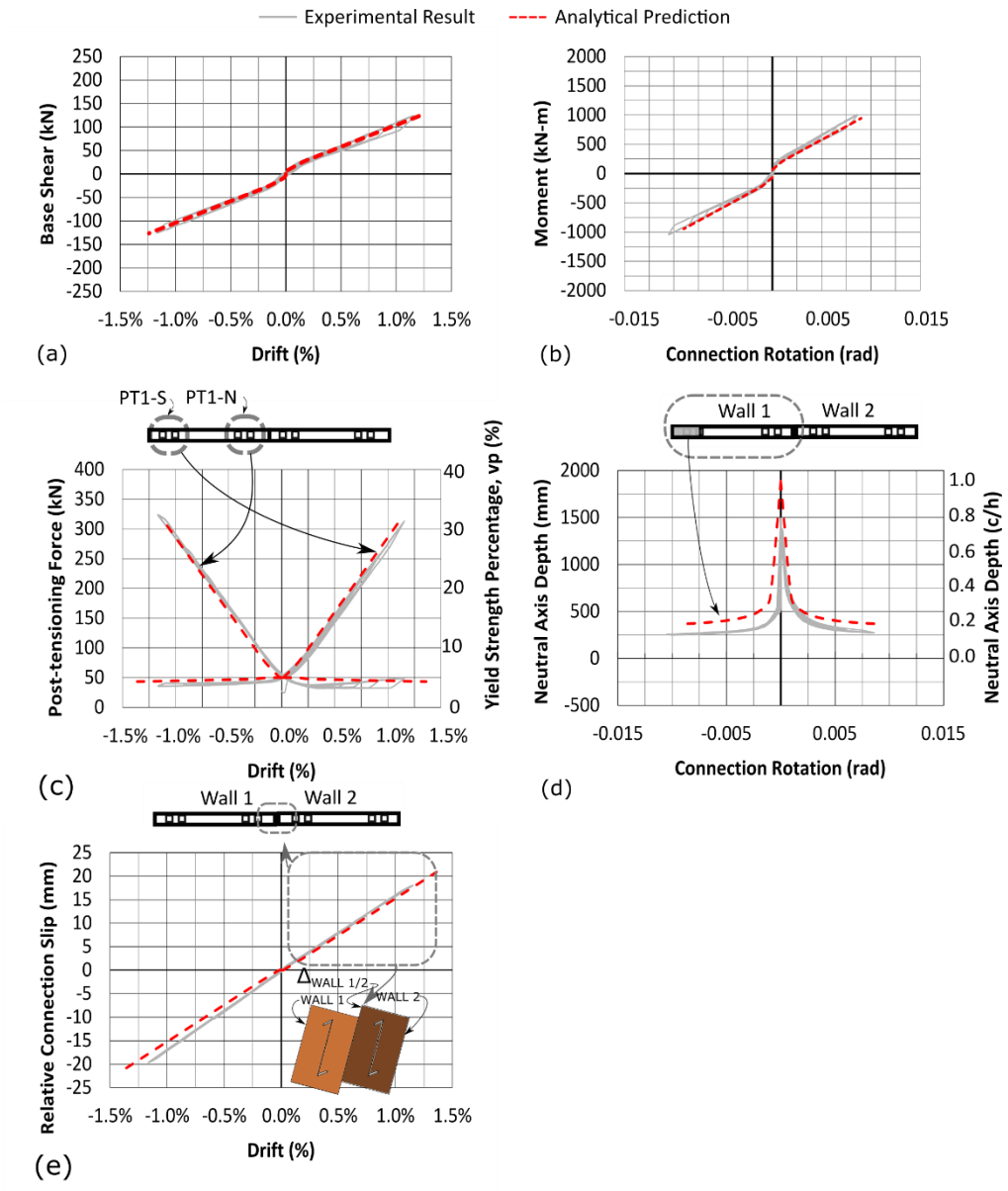


*Figure 8-12: Test DW-1 comparison to coupled double wall analytical model*

The coefficient of friction was found to be $\psi$=0.30 such that $F_{fr} = \psi F$, where F is the ram force. Note, the friction term is generally neglected (Izzi et al., 2018; Shahnewaz et al., 2020) in deflection

calculation and modelling of CLT structures. In this instance it is shown as it was required to predict the quasi-static experimental testing programme where friction was activated.

### 8.4.2 Test DW-2

In Test DW-2, 32 pairs of $\phi$8x80mm PTH STS were installed at 90° to the outer CLT face with 17mm thick plywood. Figure 8-13 shows the key experimental results with comparison to the analytical model which followed the coupled double wall kinematic mode. At low wall drifts (less than 0.25%), the system strength and stiffness are slightly under predicted which could in part be due to the increased friction which occurs at the onset of rocking motion as described by Moroder et al. (2018).

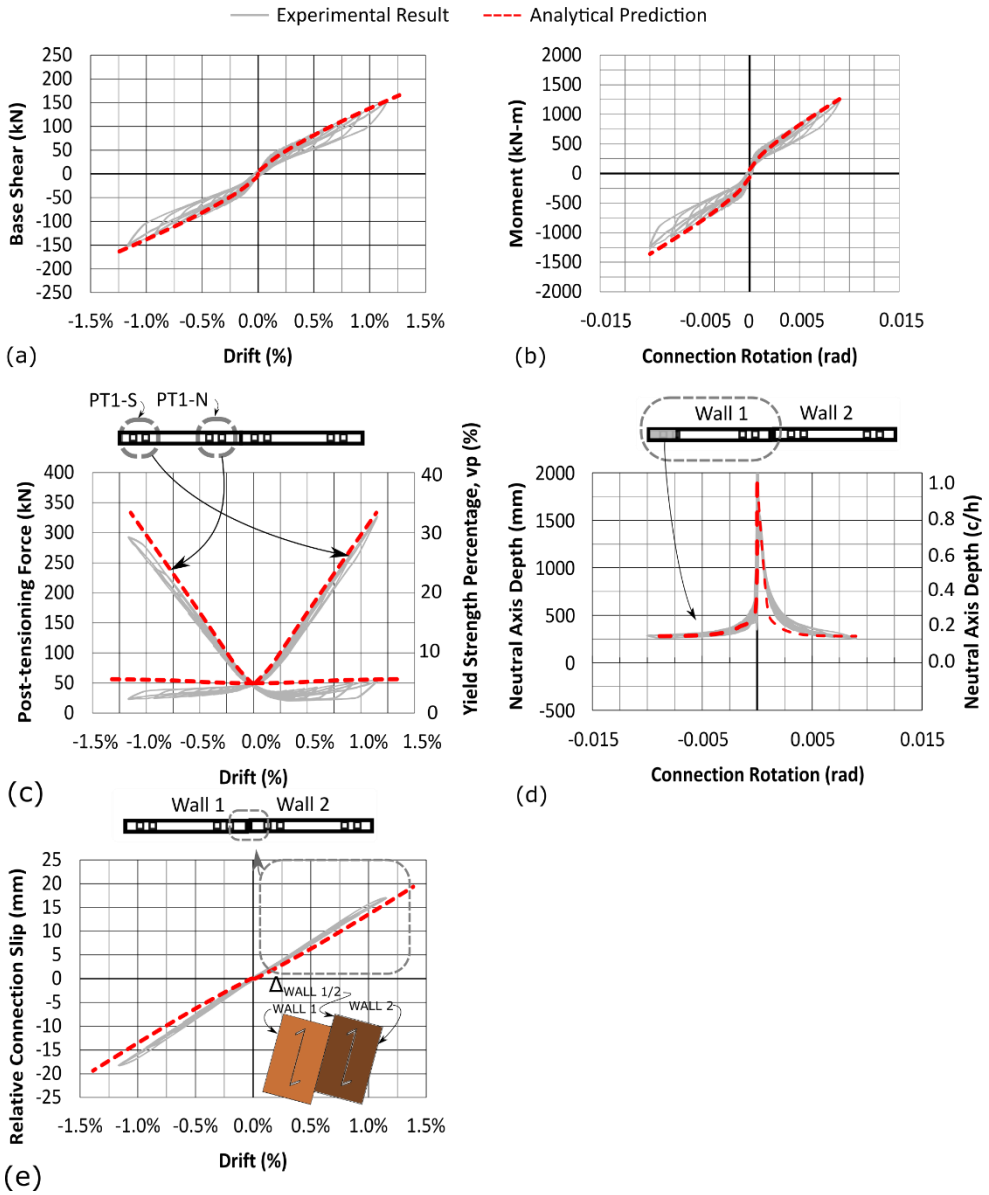


*Figure 8-13: Test DW-2 comparison to coupled double wall analytical model*

Iqbal et al. (2015) proposed an analytical model for PT double LVL walls coupled with nailed plywood sheets where the nail yielding force remains constant thus assuming an elasto-plastic behaviour.

Figure 8-14 and Figure 8-15 show the base shear – drift and moment rotation behaviour when an elasto-plastic behaviour is implemented in the coupled double wall analytical model instead of the exponential curve fitting function by Foschi (1977). In Figure 8-14, the test values from Hossain (2019) with elastic stiffness of 0.6kN/mm and maximum force of 4.4kN were used. In Figure 8-15, the values determined by Eurocode 5 (2014) with elastic stiffness of 2.7kN/mm and maximum force of 3.9kN were used. With experimental values by Hossain (2019), the analytical model slightly under predicted the results and at higher drifts (greater than 0.25%) there is good agreement. With Eurocode 5 (2014) input data, the significantly higher initial STS stiffness increases the system stiffness and slightly over predicts the experimental results at lower drifts (0.25%) and at higher drifts there is good agreement. It is well researched that the simplified analytical stiffness expression significantly over predicts the stiffness of STS connections (Brown et al., 2021; Hossain et al., 2018; Loss et al., 2018; Sullivan et al., 2018). The results show that the simplified elasto-plastic STS connector model implemented by Iqbal et al. (2015) could also be implemented for low composite action PT double wall systems when the CDW kinematic mode is observed.

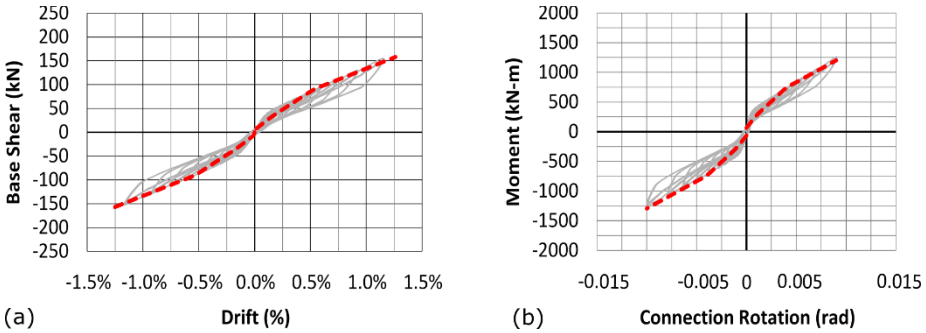


*Figure 8-14: Test DW-2 comparison to analytical using strength and stiffness values from Hossain (2019) and elasto-plastic STS connector model implemented by Iqbal et al. (2015)*

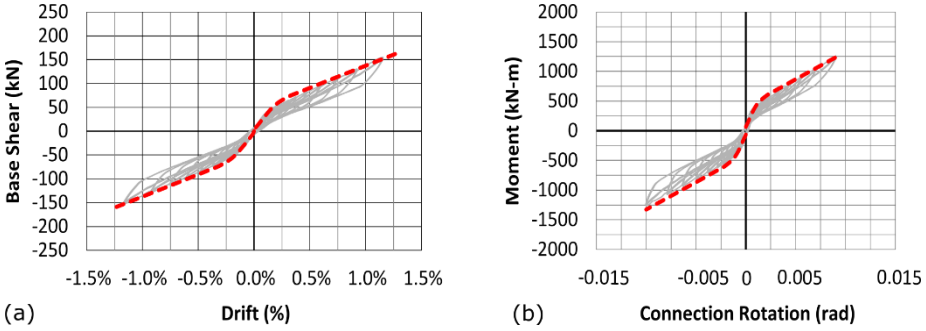


*Figure 8-15: Test DW-2 comparison to analytical using strength and stiffness values from Eurocode 5 (2014) and elasto-plastic STS connector model implemented by Iqbal et al. (2015)*

### 8.4.3 Test DW-3

In Test DW-3, 110 pairs of $\phi$8x80mm PTH STS were installed at 90° to the outer CLT face with 17mm thick plywood. During testing, wall uplift defined within the SCW kinematic behaviour was observed until the 0.93% drift cycle where the kinematic behaviour changed to CDW. Figure 8-16 shows the key experimental results with comparison to analytical models. The red solid line prediction curve is SCW behaviour and the red dashed curve is when CDW behaviour occurs.

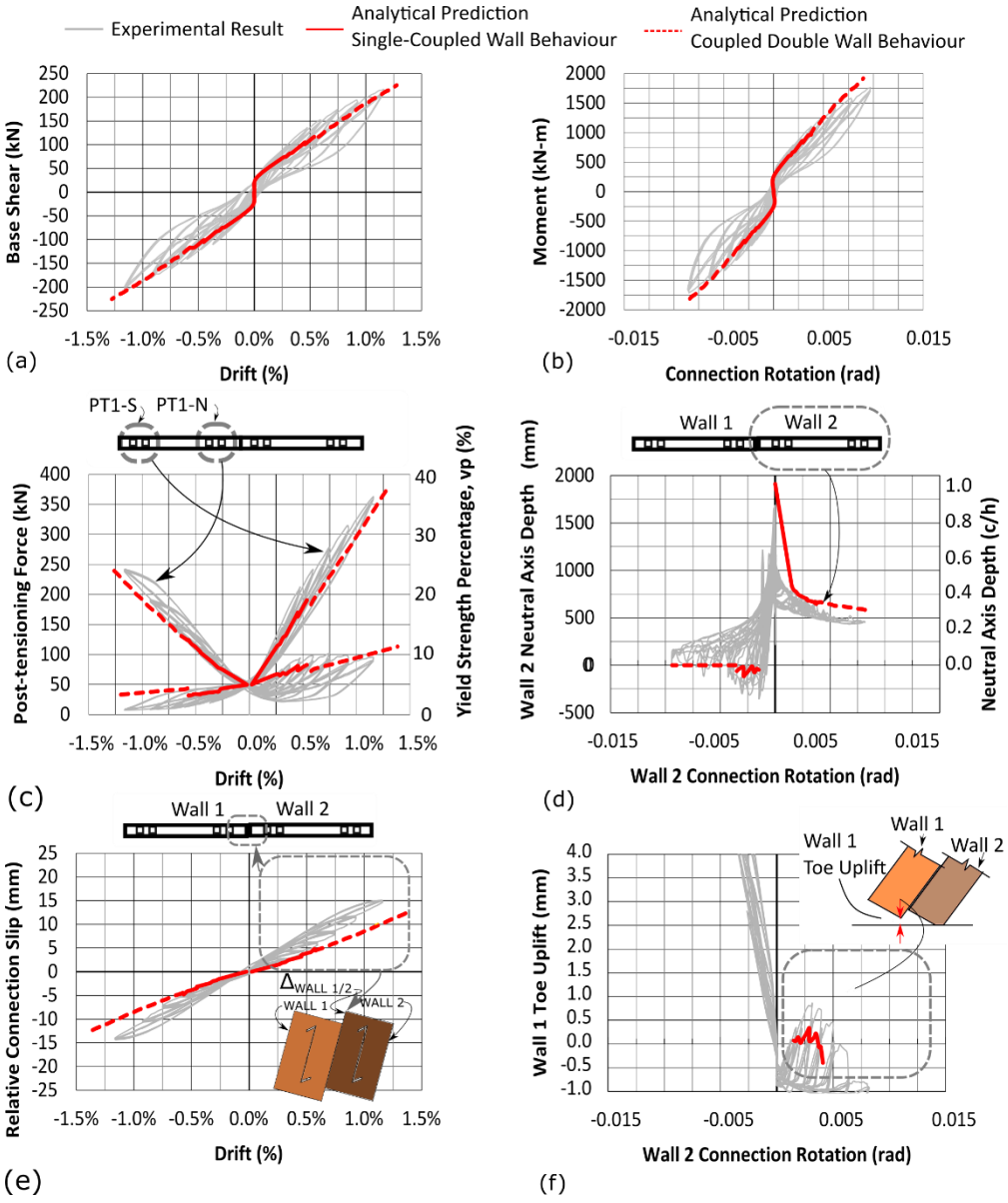


*Figure 8-16: Test DW-3 comparison to analytical model*

The CDW behaviour was triggered when Wall 1 toe touched the foundation, as shown in Figure 8-16f. The non-linear curve fitting model as per Foschi (1977) worked well to capture the gradually degrading stiffness of the in-plane joint with increased connection slip. The analytical model captured the Force-Drift and Moment-Rotation curve within 10% error at each drift level (see Figure 8-16a-b). Further, the "negative" neutral axis, which signifies wall uplift, was captured reasonably well with the model (see Figure 8-16d). The connection slip was slightly underestimated in the model during SCW behaviour (Figure 8-16e) and the increased experimental relative slip could be due to the large number of cycles that were performed at lower drifts whereas the STS data for calibration was from Hossain et al. (2019) which used a different loading protocol. Wall 1 toe uplift was captured well (with slightly lower uplift values) as shown in Figure 8-16f. When the analytical prediction intersects 0 at 0.004 rad, Wall 1 was in contact with the ground. This was also reflected by the neutral axis curve in Figure 8-16d.

### 8.4.4 Test DW-4

In Test DW-4, 32 pairs of $\phi$8x80mm PTH STS were installed at 90° to the outer CLT face with 17mm thick plywood at the in-plane joint. In addition, four pairs of UFPs were installed at the toe of each CLT wall base. Figure 8-17 shows the key experimental results with comparison to the analytical model which followed the CDW kinematic mode. A UFP yield force of 46kN and 71kN which was determined following analytical equations with a yield stress of 300MPa and by experimental results were investigated as shown in Figure 8-17b. Due to the low moment contribution from the UFPs the differences were negligible but the differences in UFP strength from using code yield stress values should be considered in design if UFPs provide significant moment contribution.

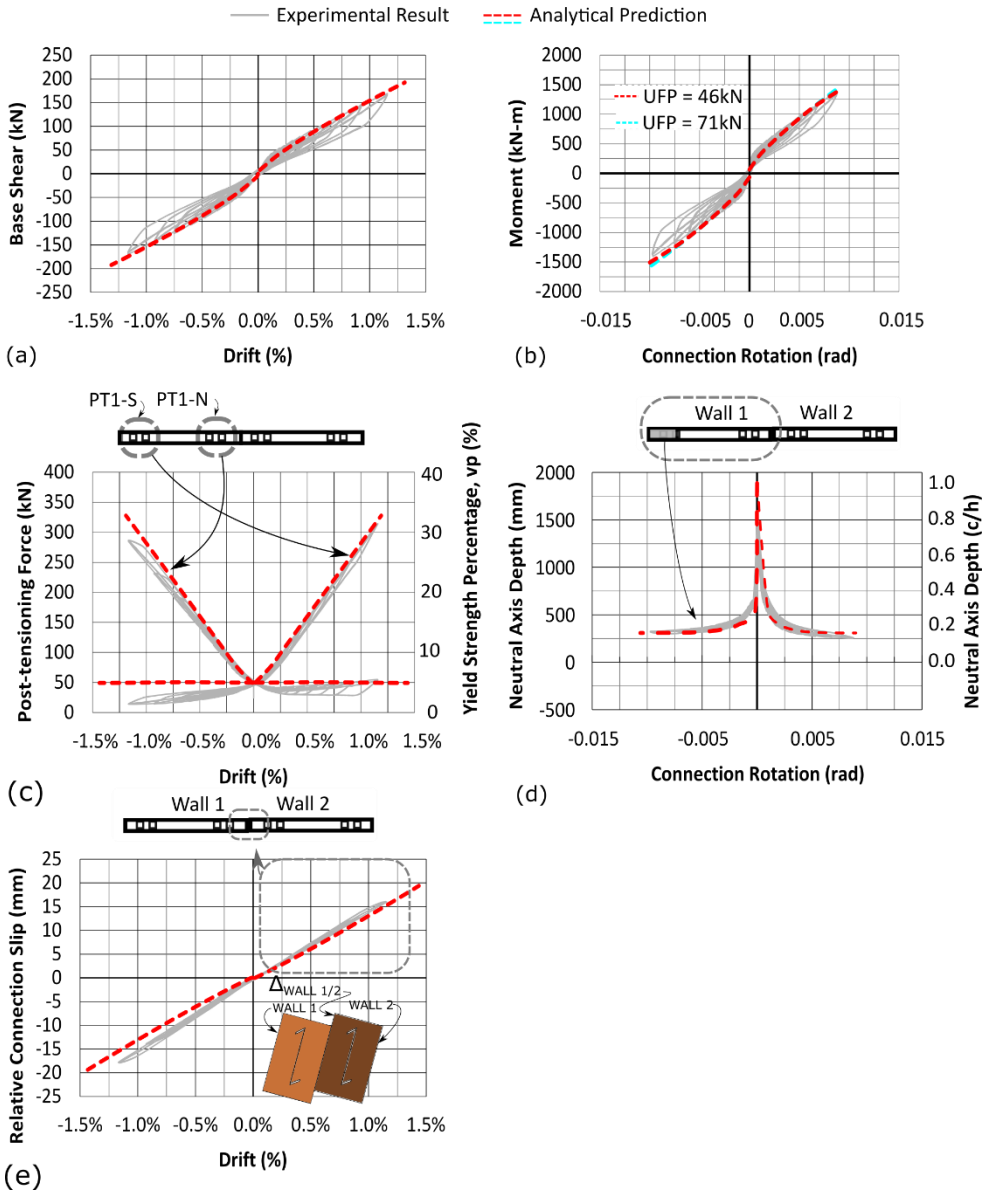


*Figure 8-17: Test DW-4 comparison to analytical model*

### 8.4.5 Test DW-5

In Test DW-5, four pairs of UFPs were installed at the toe of each CLT wall base and there was no STS connection at the in-plane joint. Figure 8-18 shows the key experimental results with comparison to the analytical model which followed the CDW kinematic mode.

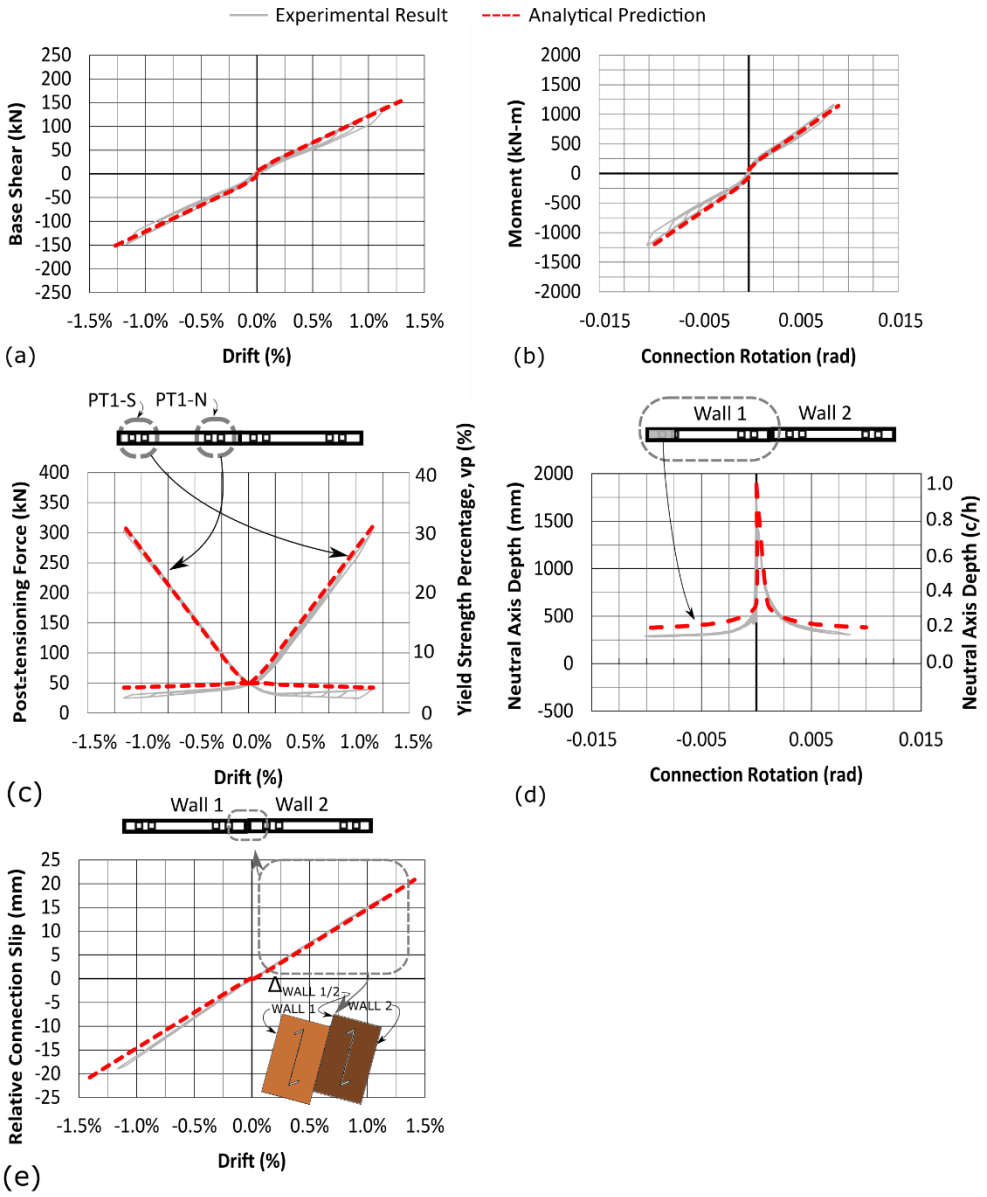


*Figure 8-18: Test DW-5 comparison to analytical model*

## 8.5 CONCLUSIONS

The experimental results from the post-tensioned (PT) double wall (DW) testing presented in Chapter 6 were compared to the proposed analytical model. Extensions were made to the existing iterative Modified Monolithic Beam Analogy (MMBA) analytical model to capture the performance of PT DW CLT systems coupled with self-tapping screws (STS) at the in-plane joint. The non-linear curve fitting function proposed by Foschi (1977) was employed to capture the entire load-displacement behaviour of the in-plane joint by STS. The main conclusions are listed as follows:

- The analytical model was extended to capture the kinematic mode of combined single-coupled wall (SCW) behaviour which is the case when one of the walls is uplifted without contacting the ground but there is relative slip between two walls.
- The analytical model was able to well capture the instance where the kinematic mode changes from SCW to coupled double wall (CDW), due to the strength and stiffness degradation of the STS connections at the in-plane joint. The analytical prediction error of the key test results was within 10% for DW-3 wall in which both SCW and CDW kinematic modes occurred.
- To accurately estimate the bending deformations of the composite double wall section, the 'Gamma Method' can be used.
- As the proposed analytical models are based on sectional analysis and the existing iterative MMBA procedure, other connections and dissipative devices could be implemented if their associated force-displacement behaviour is known.

## 8.6 REFERENCES

Brown, J. R., Li, M., Tannert, T., & Moroder, D. (2021). Experimental study on orthogonal joints in cross-laminated timber with self-tapping screws installed with mixed angles. *Engineering Structures*, *228*(February 2021), 111560. https://doi.org/10.1016/j.engstruct.2020.111560

CEN. (2014). Eurocode 5: Design of timber structures-Part 1-1: General-Common rules and rules for buildings. In *EN1995-1-1:2004-11 + AC2006-06 + A1:2008-06 + A2:2014-05 Eurocode 5*. European Committee for Standardization.

Chen, Z., Popovski, M., & Iqbal, A. (2020). Structural Performance of Post-Tensioned CLT Shear Walls with Energy Dissipators. *Journal of Structural Engineering*, *146*(4). https://doi.org/10.1061/(asce)st.1943-541x.0002569

Dietsch, P., & Brandner, R. (2015). Self-tapping screws and threaded rods as reinforcement for structural timber elements-A state-of-the-art report. *Construction and Building Materials*, *97*, 78–89. https://doi.org/10.1016/j.conbuildmat.2015.04.028

ETA-07/0046. (2018). *ETA-07/0046: Macalloy 1030 post tensioning system*. European Technical Approval.

Folz, B., & Filiatrault, A. (2001). Cyclic analysis of wood shear walls. *Journal of Structural Engineering*, *127*(04), 433–441.

Foschi, R. O. (1974). Load-slip characteristics of nails. *Wood Science*, *7*(1), 69–74.

Foschi, R. O. (1977). Analysis of wood diaphragms and trusses, Part 1: Diaphragms. *Canadian Journal of Civil Engineering*, *4*(3), 345–362.

FPInnovations. (2019). *CLT Handbook* (E. Karacabeyli & S. Gagnon (eds.); 2019 Editi). FPInnovations.

Ganey, R., Berman, J., Akbas, T., Loftus, S., Daniel Dolan, J., Sause, R., Ricles, J., Pei, S., Lindt, J. V. D., & Blomgren, H. E. (2017). Experimental investigation of self-centering Cross-Laminated Timber walls. *Journal of Structural Engineering*, *143*(10).

Gavric, I., Fragiacomo, M., & Ceccotti, A. (2015). Cyclic behavior of CLT wall systems: experimental tests and analytical prediction models. *Journal of Structural Engineering*, *141*(11), 4015034. https://doi.org/doi:10.1061/(ASCE)ST.1943-541X.0001246

Granello, G., Palermo, A., Pampanin, S., Pei, S., & Lindt, J. Van De. (2020). Pres-Lam Buildings : State-of-the-Art. *Journal of Structural Engineering*, *146*(6), 1–16. https://doi.org/10.1061/(ASCE)ST.1943-541X.0002603

Gutkowski, R., Brown, K., Shigidi, A., & Natterer, J. (2008). Laboratory tests of composite wood-concrete beams. *Construction and Building Materials*. https://doi.org/10.1016/j.conbuildmat.2007.03.013

Hossain, A. (2019). *Experimental Investigations of shear connection with STS for CLT Panels* (Issue Phd Thesis) [University of British Columbia]. https://doi.org/.1037//0033-2909.I26.1.78

Hossain, A., Popovski, M., & Tannert, T. (2018). Cross-laminated timber connections assembled with a combination of screws in withdrawal and screws in shear. *Engineering Structures*, *168*, 1–11. https://doi.org/10.1016/j.engstruct.2018.04.052

Iqbal, A, Pampanin, S., Palermo, A., & Buchanan, A. H. (2015). Performance and design of LVL walls coupled with UFP dissipaters. *Journal of Earthquake Engineering*, *19*(3), 383–409. https://doi.org/10.1080/13632469.2014.987406

Iqbal, A, Smith, T., Pampanin, S., Fragiacomo, M., Palermo, A., & Buchanan, A. H. (2015). Experimental performance and structural analysis of plywood-coupled LVL walls. *Journal of Structural Engineering*, *142*(2).

Iqbal, Asif, Fragiacomo, M., Pampanin, S., & Buchanan, A. (2018). Seismic resilience of plywood-coupled LVL wall panels. *Engineering Structures*, *167*, 750–759. https://doi.org/10.1016/j.engstruct.2017.09.053

Izzi, M., Casagrande, D., Bezzi, S., Pasca, D., Follesa, M., & Tomasi, R. (2018). Seismic behaviour of Cross-Laminated Timber structures: A state-of-the-art review. *Engineering Structures*, *170*, 42–52. https://doi.org/10.1016/j.engstruct.2018.05.060

Li, M., Lam, F., & Foschi, R. O. (2009). Seismic reliability analysis of diagonal-braced and structural-panel- sheathed wood shear walls. *Journal of Structural Engineering*, *135*(5), 587–596. https://doi.org/10.1061/(ASCE)ST.1943-541X.0000008

Loss, C., Hossain, A., & Tannert, T. (2018). Simple cross-laminated timber shear connections with spatially arranged screws. *Engineering Structures*, *173*, 340–356. https://doi.org/10.1016/j.engstruct.2018.07.004

Lukacs, I., Björnfot, A., & Tomasi, R. (2019). Strength and stiffness of cross-laminated timber (CLT) shear walls: State-of-the-art of analytical approaches. *Engineering Structures*, *178*(October 2018), 136–147. https://doi.org/10.1016/j.engstruct.2018.05.126

Moroder, D., Smith, T., Dunbar, A., Pampanin, S., & Buchanan, A. (2018). Seismic testing of post-tensioned Pres-Lam core walls using cross laminated timber. *Engineering Structures*, *167*, 639–654. https://doi.org/10.1016/j.engstruct.2018.02.075

Pampanin, S., Palermo, A., & Buchanan, A. (2013). *Post-Tensioned Timber Buildings - Design Guide Australia and New Zealand*. Structural Timber Innovation Company.

Pault, J., & Gutkowski, R. (1977). *Tests and analysis of composite action in glulam bridges', Structural Research report No. 17A* (No. 17A).

Pei, S., Van De Lindt, J. W., Barbosa, A. R., Berman, J. W., McDonnell, E., Daniel Dolan, J., Blomgren, H. E., Zimmerman, R. B., Huang, D., & Wichman, S. (2019). Experimental seismic response of a resilient 2-story mass-timber building with post-tensioned rocking walls. *Journal of Structural Engineering*, *145*(11), 1–15.

Sarti, F. (2015). *Seismic design of low-damage post-tensioned timber wall systems* (Issue PhD Thesis). University of Canterbury.

Schickhofer, G., Bogensperger, T., Moosbrugger, T., Augustin, M., Blaß, H. J., H, E., & et al. (2010). *BSPhandbuch, Holz- Massivbauweise in Brettsperrholz*. Technische Universitat Graz, Karlsruher Institut fur Technologie.

Shahnewaz, M., Popovski, M., & Tannert, T. (2020). Deflection of cross-laminated timber shear walls for platform-type construction. *Engineering Structures*, *221*(July), 111091. https://doi.org/10.1016/j.engstruct.2020.111091

Standards New Zealand. (1993). *NZS 3603: Timber structures standard*. Standards New Zealand.

Sullivan, K., Miller, T. H., & Gupta, R. (2018). Behavior of cross-laminated timber diaphragm connections with self-tapping screws. *Engineering Structures*, *168*, 505–524.

Sun, X., He, M., Li, Z., & Lam, F. (2020). Seismic performance of energy-dissipating post-tensioned CLT shear wall structures I: Shear wall modeling and design procedure. *Soil Dynamics and Earthquake Engineering*, *131*(January), 106022. https://doi.org/10.1016/j.soildyn.2019.106022

Symons, D., Persaud, R., & Stanislaus, H. (2010). Slip modulus of inclined screws in timber-concrete floors. *Proceedings of the Institution of Civil Engineers: Structures and Buildings*, *163*(4), 245–255. https://doi.org/10.1680/stbu.2010.163.4.245

Wallner-Novak, M., Koppelhuber, J., & Pock, K. (2014). *Cross-Laminated Timber structural design* (isbn 978-3). proHolz Austria. www.proholz.at

# 9 Analytical modelling of post-tensioned CLT core-wall systems primarily with screwed connectors

*Key Findings / Outputs:*

- An analytical model was developed to capture the base moment-rotation behaviour of a post-tensioned C-shaped CLT core-wall system comprising four CLT walls (two flange walls and two web walls) primarily connected by self-tapping screws (STS).
- The analytical model was able to capture three different kinematic modes along the strong axis of the core-wall: (1) low composite action where all four walls were in contact with the foundation, (2) medium composite action where flange wall uplift occurs on the tension side, (3) high composite action where flange and web wall uplift occurs on the tension side.
- The experimental results and analytical modelling results showed that the contribution from the compressive flange wall could be neglected under strong axis loading when the CLT walls were coupled together with STS.
- The analytical modelling results agreed well with the experimental results with prediction error less than 10%.

## 9.1 INTRODUCTION

The main objective of Chapter 9 is to develop an analytical model to capture the base moment-rotation behaviour of post-tensioned (PT) C-shaped core-wall CLT system. Currently, there is no analytical model to capture the base moment-rotation system behaviour of a PT timber core-wall system. The analytical model developed for the PT double wall (DW) systems is extended to include the contribution from orthogonal/flanged walls.

Section 9.2 provides the theory for PT core-wall systems. Section 9.3 briefly describes the relevant connection detailing and curve fitting processes employed and then Section 9.4 compares the analytical model predictions to the experimental results presented in Chapter 6.

## 9.2 THEORY OF POST-TENSIONED TIMBER CORE-WALL SYSTEMS

The core-wall analytical model is an extension of the PT Pres-Lam theory for single wall (SW) and DW systems presented in Chapter 7 and Chapter 8 respectively. As such, a brief overview of the procedure will be presented here. Then, the existing moment-rotation iterative procedure referred to as the Modified Monolithic Beam Analogy (MMBA) will be extended to capture different kinematic modes in a PT core-wall system with nonlinear self-tapping screws (STS) connections. For a PT core-wall system, four different kinematic modes can occur as summarized in Figure 9-1: low composite action (LCA) behaviour, medium composite action (MCA) behaviour, high composite action (HCA) behaviour and the theoretical rigid core-wall behaviour.

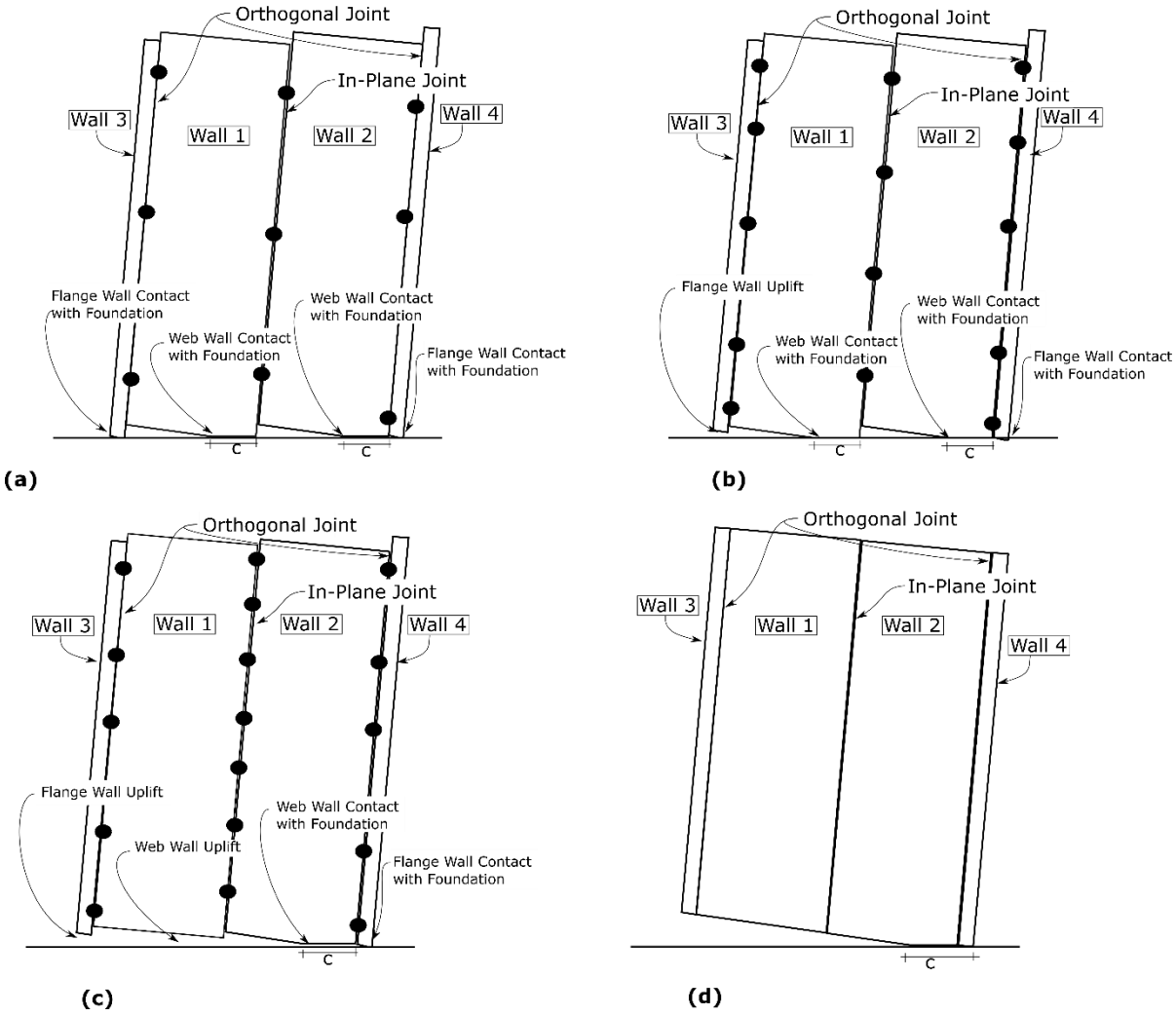


*Figure 9-1: Types of core-wall kinematics: (a) low composite action behaviour (all walls touching foundation), (b) medium composite action behaviour (flange wall uplift), (c) high composite action behaviour (flange and web wall uplift), and (d) theoretical rigid joint behaviour (no joint slip)*

### 9.2.1 General Design Considerations and Steps

The step-by-step general design procedure to satisfy equilibrium is summarized in the flowchart shown in Figure 9-2. The imposed connection rotation, $\theta_j$, is assumed to be the same for Wall 1 and Wall 2. In a core-wall system, there are coupling forces at the in-plane and orthogonal joints. Depending on the relative strength and stiffness of these joints to the PT and dissipater elements, a certain kinematic mode will result. Thus, after evaluating the dissipation device forces, an additional step to evaluate the coupling forces must be added. With the STS connections, these coupling forces will change nonlinearly depending on the joint slip.

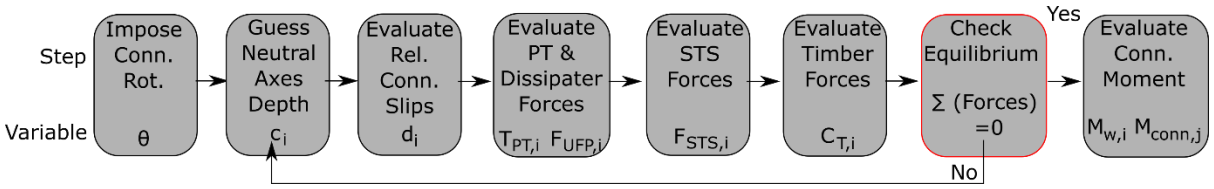


*Figure 9-2: MMBA step-by-step procedure adopted from Sarti* (2015) *with coupling STS force addition and relative connection slips*

### *9.2.1.1 Impose connection rotation and guess the neutral axis depth*

The first step is to impose base connection rotation, $\theta_j$, considering the elastic deformations and guess neutral axis depth for Wall 1 and Wall 2 respectively, $c_{1,j}$ and $c_{2,j}$.

### *9.2.1.2 Evaluating post-tensioning and UFP dissipater forces*

Depending on the kinematic behaviour, the change in displacement for the PT and UFP elements are determined and the relative slip between the walls needs to be considered as well.

#### 9.2.1.2.1 Low composite action (LCA) kinematic mode

The LCA mode is shown in Figure 9-3 with relative displacements $d_{2,j}$, $d_{3,j}$, and $d_{4,j}$.between each wall panel.

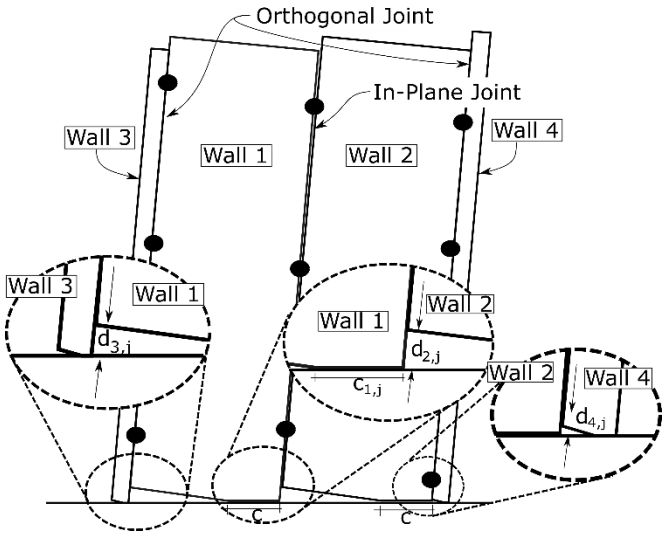


*Figure 9-3: LCA kinematic behaviour*

During the LCA mode shown in Figure 9-3a, the PT elongation is determined as:

$$\Delta_{PT,i,j} = \theta_j(d_{PT,i} - c_{i,j}) - \frac{(\sum T_{PT,wi,j-1} - \sum T_{PT,o,wi})l_{ub,i}}{E_o A_{eff,wi}} \quad (9\text{-}1)$$

Where

$\Delta_{PT,i,j}$ = elongation of the i-th PT bar for the j-th rotation increment

$d_{PT,i}$ = edge distance of the i-th PT bar (See applicable Figure 9-6 - Figure 9-8)

$\sum T_{PT,wi,j-1}$ = sum of post-tensioning bar forces for the applicable wall 'i' for the 'j-1th' rotation increment

$\sum T_{PT,o,wi}$ = sum of initial post-tensioning bars forces for the applicable wall

$l_{ub,i}$ = unbonded length of the i-th PT bar

$E_o$ = timber elastic modulus

$A_{eff,wi}$ = effective area for the applicable wall

The UFP elongation is determined as:

$$\Delta_{UFP,i,j} = \theta_j(d_{UFP,i} - c_{i,j}) \quad (9\text{-}2)$$

Where

$\Delta_{UFP,i,j}$ = elongation of the i-th UFP element for the j-th rotation increment

$d_{UFP,i}$ = edge distance of the i-th UFP element (See applicable Figure 9-6 - Figure 9-8)

#### 9.2.1.2.2 Medium composite action (MCA) kinematic mode (flange wall uplift scenario)

The MCA mode is shown in Figure 9-4 with relative displacements $d_{2,j}$, $d_{3,j}$, and $d_{4,j}$ between each wall panel.

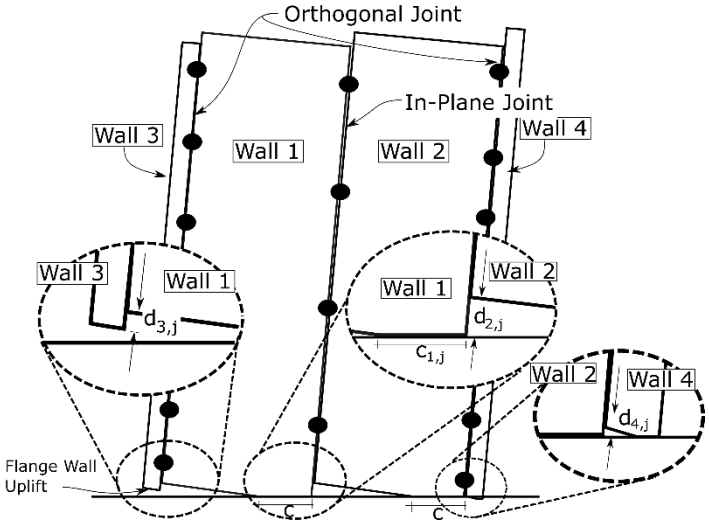


*Figure 9-4: MCA kinematic behaviour*

During the MCA mode shown in Figure 9-4, the imposed deformation on the Wall 1 and Wall 2 PT and UFP elements can be determined as per Equation (9-1) and (9-2). But the Wall 3 PT and UFP elongation is determined considering the joint slip $d_{3,j}$ between Wall 1 and Wall 3:

$$\Delta_{PT,W3,i,j} = \theta_j\left(d_{PT,W3,i} - c_{1,j}\right) - \frac{\left(\sum T_{PT,wi,j-1} - \sum T_{PT,o,wi}\right) l_{ub,i}}{E_o A_{eff,wi}} - d_{3,j} \quad (9\text{-}3)$$

$$\Delta_{UFP,W3,i,j} = \theta_j\left(d_{PT,W3,i} - c_{1,j}\right) - d_{3,j} \quad (9\text{-}4)$$

9.2.1.2.3 High composite action (HCA) kinematic mode (flange and web wall uplift scenario)

The HCA mode is shown in Figure 9-5 with relative displacements $d_{2,j}$, $d_{3,j}$, and $d_{4,j}$ between each wall panel.

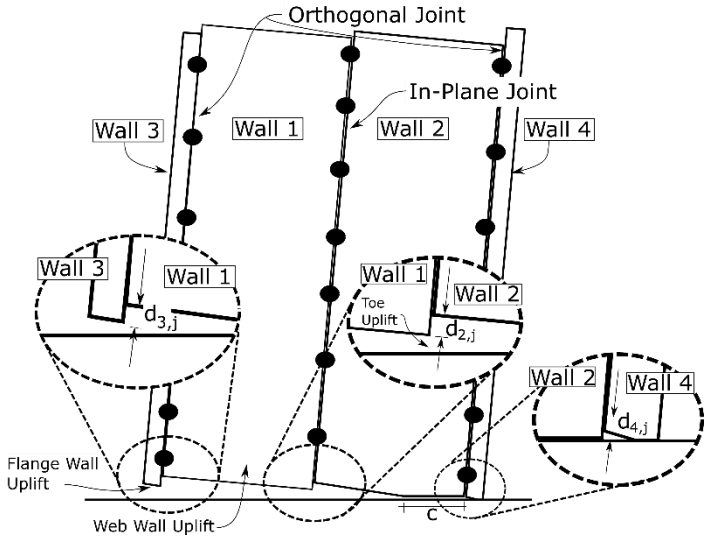


*Figure 9-5: HCA kinematic behaviour*

During the HCA mode shown in Figure 9-5, the Wall 3 PT and UFP elongation is determined as:

$$\Delta_{PT,W3,i,j} = \theta_j\left(d_{PT,W3,i} - c_{2,j}\right) - \frac{\left(\sum T_{PT,wi,j-1} - \sum T_{PT,o,wi}\right) l_{ub,i}}{E_o A_{eff,wi}} - d_{3,j} - d_{2,j} \quad (9\text{-}5)$$

$$\Delta_{UFP,W3,i,j} = \theta_j\left(d_{PT,W3,i,j} - c_{2,j}\right) - d_{3,j} - d_{2,j} \quad (9\text{-}6)$$

Wall 1 PT and UFP element imposed deformations are determined as:

$$\Delta_{PT,W1,i,j} = \theta_j\left(d_{PT,W1,i} - c_{2,j}\right) - \frac{\left(\sum T_{PT,wi,j-1} - \sum T_{PT,o,wi}\right) l_{ub,i}}{E_o A_{eff,wi}} - d_{2,j} \quad (9\text{-}7)$$

$$\Delta_{UFP,W1,i,j} = \theta_j\left(d_{PT,W1,i} - c_{2,j}\right) - d_{2,j} \quad (9\text{-}8)$$

Wall 2 PT and UFP elements imposed deformations can be determined as per Equation (9-1). However, for the HCA mode a 'pivot point' simplification will be presented and it decouples Wall 1 and Wall 2 and removes the unknown $d_{2,j}$ from Equation (9-5) and Equation (9-6).

Then, the PT bar strain, stress and forces can be evaluated as shown in Chapter 7, Section 7.2.1.

*9.2.1.3 Evaluating STS coupling forces*

The force-displacement behaviour of an STS is represented with the exponential curve fitting function proposed by Foschi (1974, 1977). As discussed in Chapter 8, the trilinear load-displacement connection behaviour is not suitable to PT wall systems coupled with STS at the in-plane joint and a more accurate model is required to capture the highly nonlinear behaviour of the STS connection. The exponential curve fitting function is required to capture the wall uplift scenarios under MCA and HCA kinematic modes. The relative joint slip, $d_{2,j}$, $d_{3,j}$, or $d_{4,j}$, for the joint of interest is determined depending on the kinematic modes which are presented in Section 9.2.2 - 9.2.4 and shown in Figure 9-1. The coupling force provided by the STS, $F_{STS}$, can be determined for each joint:

$$F_{STS,2,j} = n_{STS,2} k_{STS,2} d_{2,j} = K_{STS,2,j} d_{2,j} \quad (9\text{-}9)$$

$$F_{STS,3,j} = n_{STS,3} k_{STS,3} d_{3,j} = K_{STS,3,j} d_{3,j} \quad (9\text{-}10)$$

$$F_{STS,4,j} = n_{STS,4} k_{STS,4} d_{4,j} = K_{STS,4,j} d_{4,j} \quad (9\text{-}11)$$

where:

$K_{STS,2,j}, K_{STS,3,j}, and\ K_{STS,4,j}$ = the STS in-plane or orthogonal joint secant stiffness for a given displacement $d_{2,j}$, $d_{3,j}$, and $d_{4,j}$ for a j-th rotation increment

$k_{STS,2,j}, k_{STS,3,j}, and\ k_{STS,4,j}$ = the individual STS connection secant stiffness for a given displacement $d_{2,j}$, $d_{3,j}$, and $d_{4,j}$ for a j-th rotation increment

$n_{STS,2}, n_{STS,3}, and\ n_{STS,4}$ = the number of STS or effective number of STS along joints 2, 3 and 4 depending on the kinematic mode

$d_{2,j}, d_{3,j}, and\ d_{4,j}$ = the relative displacement between CLT walls as shown in Figure 9-6 - Figure 9-8 for a j-th base rotation increment.

*9.2.1.4 Evaluating the timber forces*

The timber forces are evaluated in the same manner presented in Chapter 7 and Chapter 8. Strain compatibility is determined following the MMBA adopted for timber (Newcombe et al., 2008; Palermo, 2004; Pampanin et al., 2001). Then, the timber force for each wall 'i', is determined assuming the verified triangular stress/strain distribution and strain amplification factor ($\phi_t$) as:

$$C_{T,wi,j} = 0.5 E_{conn} c_{i,j} b_{eff} \varepsilon_{t,i,j} \phi_t \quad (9\text{-}12)$$

Where:

$E_{conn}$ = timber connection elastic modulus = $0.83E_{t,o}$ as shown in material testing for CLT (See Chapter 7, Section 7.4.1)

$c_{i,j}$ = neutral axis length for wall 'i' for the 'j'-th rotation increment

$b_{eff}$ = is the sum of the longitudinal board widths only

$\varepsilon_{t,i,j}$ = timber strain determined through MMBA member compatibility for the 'j'-th rotation increment

$\phi_t$ = 1.33 as determined in Chapter 7

#### *9.2.1.5 Check equilibrium and evaluate the base connection moment*

Force equilibrium for each kinematic mode is then achieved by iterating the neutral axis depth of each wall. Then, the base connection moment can be evaluated. The specific force equilibrium for each core-wall kinematic mode is outlined in Sections 9.2.2-9.2.4

### 9.2.2 Low Composite Action (LCA) Kinematic Mode

In the core-wall system under LCA, all walls are in contact with the foundation as shown in Figure 9-6.

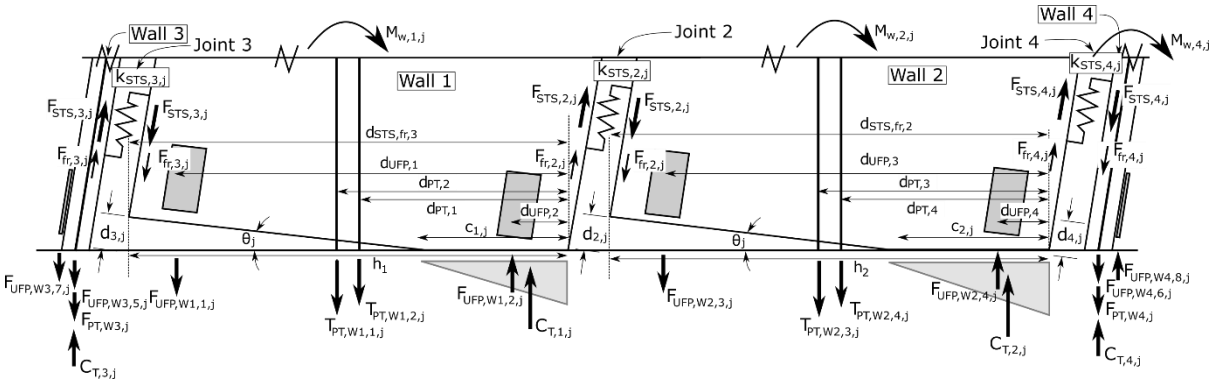


*Figure 9-6: Section analysis of post-tensioned core-wall under low composite action – all walls are in contact with foundation*

In order to evaluate the coupling force at the in-plane joint, the relative displacement, $d_{2,j}$, between the wall panels at the base is required and is approximated in the same manner as coupled double walls as:

$$d_{2,j} = \theta_j(h_2 - c_{2,j}) + \theta_j(c_{1,j}) \tag{9-13}$$

Where:

$\theta_j$ = imposed base rotation angle for the 'j'-th rotation increment

$c_{i,j}$ = neutral axis length for wall 'i' for the 'j'-th rotation increment

$h_2$ = the length of Wall 2

The orthogonal joint displacement, $d_{3,j}$ and $d_{4,j}$ is also required and is approximated as:

$$d_{3,j} = \theta_j(h_1 - c_{1,j}) \tag{9-14}$$

$$d_{4,j} = -\theta_j(c_{2,j}) \tag{9-15}$$

With reference to Figure 9-6, vertical force equilibrium equations for Wall 1 and Wall 2 are provided as follows:

$$C_{T,1,j} + F_{fr,2,j} - F_{fr,3,j} + F_{STS,2,j} - F_{STS,3,j} + F_{UFP,W1,2,j} - \sum T_{PT,w1,j} - F_{UFP,W1,1,j} = 0 \tag{9-16}$$

$$C_{T,2,j} - F_{fr,2,j} + F_{fr,4,j} - F_{STS,2,j} + F_{STS,4,j} - F_{UFP,W2,3,j} - \sum T_{PT,w2,j} + F_{UFP,W2,4,j} = 0 \tag{9-17}$$

The neutral axis is iterated until the force equilibrium is achieved. Note, the friction term is generally neglected (Izzi et al., 2018; Shahnewaz et al., 2020) in design and modelling of CLT structures. In this instance it is included as it was required to predict the quasi-static experimental testing programme where friction was activated. The friction terms are assumed to be equal in Equation (9-16) and (9-17) respectively. Then, once the force equilibrium is achieved, the base connection moment can be determined for Wall 1 and Wall 2 as:

$$\begin{aligned} M_{w,1,j} = {} & \sum T_{PT,i,j}\left(d_{PT,i} - {}^{c_{1,j}}/_{3}\right) + F_{STS,3,j}\left(d_{STS,3} - {}^{c_{1,j}}/_{3}\right) \\ & + F_{fr,3,j}\left(d_{fr,3} - {}^{c_{1,j}}/_{3}\right) + F_{fr,2,j}\left({}^{c_{1,j}}/_{3}\right) + F_{STS,2,j}\left({}^{c_{1,j}}/_{3}\right) \\ & + \sum F_{UFP,W1,i,j}\left(d_{UFP,i} - {}^{c_{1,j}}/_{3}\right) \end{aligned} \tag{9-18}$$

$$\begin{aligned} M_{w,2,j} = {} & \sum T_{PT,i,j}\left(d_{PT,i} - {}^{c_{2,j}}/_{3}\right) + F_{fr,2,j}\left(d_{fr,2} - {}^{c_{2,j}}/_{3}\right) \\ & + F_{STS,2,j}\left(d_{STS,2} - {}^{c_{2,j}}/_{3}\right) + F_{fr,4,j}\left({}^{c_{2,j}}/_{3}\right) + F_{STS,4,j}\left({}^{c_{2,j}}/_{3}\right) \\ & + \sum F_{UFP,W2,i,j}\left(d_{UFP,i} - {}^{c_{2,j}}/_{3}\right) \end{aligned} \tag{9-19}$$

The friction and STS coupling forces developed can be assumed to be acting vertically and along the in-plane joint line. In reality and design, the STS fasteners will be placed a minimum edge distance (3d = 24mm) from the in-plane joint but this small difference was neglected for simplification purposes.

The total base connection moment, $M_{conn,j}$, is then

$$M_{conn,j} = M_{w,1,j} + M_{w,2,j} \tag{9-20}$$

The base connection moment from Wall 4 about its weak axis was considered negligible. Then, the elastic bending and shear deformations can be determined as per Sections 9.2.8 and Section 9.2.9.

### 9.2.3 Medium Composite Action (MCA) Mode (Flange Wall Uplift Scenario)

In the core-wall system under MCA, there is flange uplift on the tension side while the two web walls are in contact with the foundation as shown in Figure 9-7.

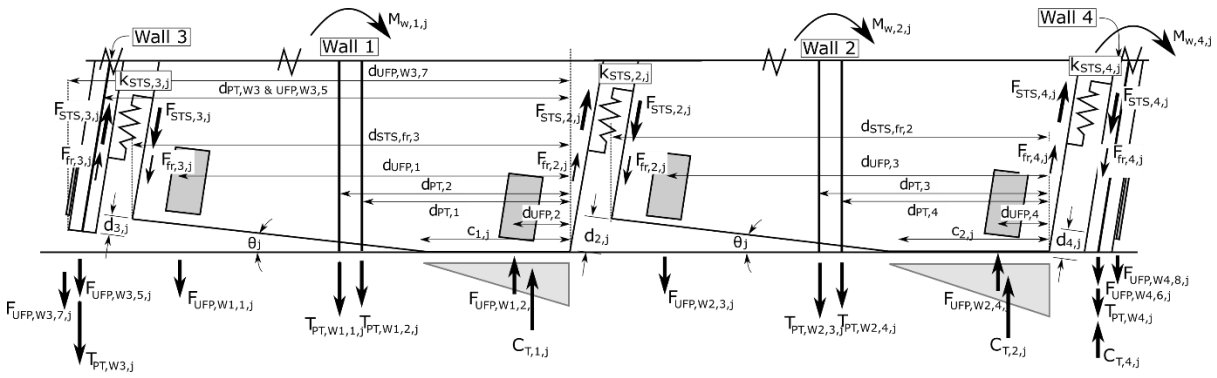


*Figure 9-7: Section analysis of post-tensioned core-wall under medium composite action – flange wall uplift occurs on the tension side*

In order to evaluate the coupling force at the in-plane joint, the relative displacement, $d_{2,j}$, between the wall panels at the base is required and is approximated in the same manner as the LCA kinematic mode as:

$$d_{2,j} = \theta_j(h_2 - c_{2,j}) + \theta_j(c_{1,j}) \tag{9-21}$$

The orthogonal joint displacement, $d_{4,j}$, is also approximated in the same manner to the LCA kinematic mode as:

$$d_{4,j} = -\theta_j(c_{2,j}) \tag{9-22}$$

In order to determine the orthogonal joint displacement, $d_{3,j}$, where the flange uplift occurs, the vertical force equilibrium of Wall 3 is determined as a function of the stiffness of each component as:

$$\sum k_{PT,W3,i,j}[(d_{PT,W3,i} - c_{1,j})\theta_j - d_{3,j}] + \sum k_{UFP,W3,i,j}[(d_{UFP,W3,i} - c_{1,j})\theta_j - d_{3,j}] \tag{9-23}$$

$$+ \sum T_{pt,0,w3} = K_{STS,3,j-1} d_{3,j} + F_{fr,3,j}$$

Where:

$k_{PT,W3,i,j}$ = stiffness of the 'i'-th PT Bar element for the 'j'-th rotation increment

$k_{UFP,W3,i,j}$ = stiffness of the 'i'-th UFP element for the 'j'-th rotation increment

Note that $k_{STS,3,j}$ is the secant stiffness at a given displacement, which is changing in a non-linear manner as presented in Chapter 8 Section 8.2. This method is an extension to the PT DW analytical model presented in Chapter 8 which was originally adopted from Gavric et al. (2015). As described in Chapter 7 Section 7.2.1, $K_{UFP,w3}$ was assumed to be elasto-plastic behaviour with zero stiffness after yielding which was determined an adequate assumption in Chapter 8. By rearranging Equation (9-23), an expression for the relative wall slip, $d_{3,j}$, can be determined for a given imposed wall rotation, $\theta_j$, and Wall 1 neutral axis depth, $c_1$, as:

$$d_{3,j} = \frac{\theta_j\{\sum k_{PT,W3,i,j}[(d_{PT,W3,i} - c_{1,j})] + \sum k_{UFP,W3,i,j-1}[(d_{UFP,W3,i} - c_{1,j})]\} - F_{fr,3,j} + \sum T_{pt,0,w3}}{(K_{STS,3,j-1} + \sum k_{PT,W3,i,j} + \sum k_{UFP,W3,i,j-1})} \quad (9\text{-}24)$$

With reference to Figure 9-7, vertical force equilibrium of Wall 1 and Wall 3 can be determined as:

$$C_{T,1,j} - \sum T_{PT,W1,i,j} - \sum F_{UFP,W1,i,j} - \sum T_{PT,W3,i,j} - \sum F_{UFP,W3,i,j} + F_{STS,2,j} + F_{Fr,2,j} = 0 \quad (9\text{-}25)$$

As with the LCA model, $F_{fr,i,j}$ should be neglected in design but it is considered here for comparison to quasi-static experimental testing. In order to solve for vertical force equilibrium (Equation (9-25)), the orthogonal joint connection slip, $d_{3,j}$, shown in Equation (9-24) is substituted in the appropriate components of Equation (9-25). Equation (9-24) shows that, as $K_{STS,3,j}$ decreases, the relative joint slip, $d_{3,j}$, increases. With reference to Figure 9-7, vertical force equilibrium of Wall 2 can be determined as:

$$C_{T,2,j} - \sum T_{PT,W2,i,j} - \sum F_{UFP,W2,i,j} - F_{STS,2,j} - F_{Fr,2,j} + F_{STS,4,j} + F_{Fr,4,j} = 0 \quad (9\text{-}26)$$

Then, once force equilibrium is found by iterating for $c_{1,j}$ and $c_{2,j}$ the base connection moment can be determined for Wall 1 and Wall 2 as:

$$M_{w,1,j} = \sum T_{PT,W1,i,j}\left(d_{PT,W1,i} - {}^{c_{1,j}}/_{3}\right) + \sum T_{PT,W3,i,j}\left(d_{PT,W3,i} - {}^{c_{1,j}}/_{3}\right) + \sum F_{UFP,W1,i,j}\left(d_{UFP,W1i} - {}^{c_{1,j}}/_{3}\right) + \sum F_{UFP,W3,i,j}\left(d_{UFP,W3i} - {}^{c_{1,j}}/_{3}\right) + F_{fr,2,j}\left({}^{c_{1,j}}/_{3}\right) + F_{STS,2,j}\left({}^{c_{1,j}}/_{3}\right) \quad (9\text{-}27)$$

$$M_{w,2,j} = \sum T_{PT,W2,i,j}\left(d_{PT,i} - {}^{c_{2,j}}/_{3}\right) + F_{fr,2,j}\left(d_{fr,2} - {}^{c_{2,j}}/_{3}\right) + F_{STS,2,j}\left(d_{STS,2} - {}^{c_{2,j}}/_{3}\right) + F_{fr,4,j}\left({}^{c_{2,j}}/_{3}\right) + F_{STS,4,j}\left({}^{c_{2,j}}/_{3}\right) + \sum F_{UFP,W2,i,j}\left(d_{UFP,W2,i} - {}^{c_{2,j}}/_{3}\right) \quad (9\text{-}28)$$

The friction and STS coupling forces developed can be assumed to be acting vertically and at the in-plane joint line as discussed in Section 9.2.2. The total base connection moment, $M_{conn,j}$, is then:

$$M_{conn,j} = M_{w,1,j} + M_{w,2,j} \quad (9\text{-}29)$$

The base connection moment from Wall 4 about its weak axis was considered negligible, and this will be verified in Test CW-2. A MCA core-wall kinematic behaviour occurs until Wall 3 touches the foundation, which occurs when $d_{3,j} = \theta_j(h_1 - c_{1,j})$. The kinematic behaviour then changes to LCA as previously derived in Section 9.2.2. The elastic bending and shear deformations can be determined as per Sections 9.2.8 and 9.2.9. However, because the core-wall is behaving in composite action the bending deformation will be determined using the 'Gamma Method' which is commonly used for composite sections connected with STS (Dietsch & Brandner, 2015; Symons et al., 2010).

### 9.2.4 High Composite Action (HCA) Mode (Flange and Web Wall Uplift Scenario)

In the core-wall system under HCA, both Flange Wall and Web Wall uplift occur on the tension side as shown in Figure 9-8.

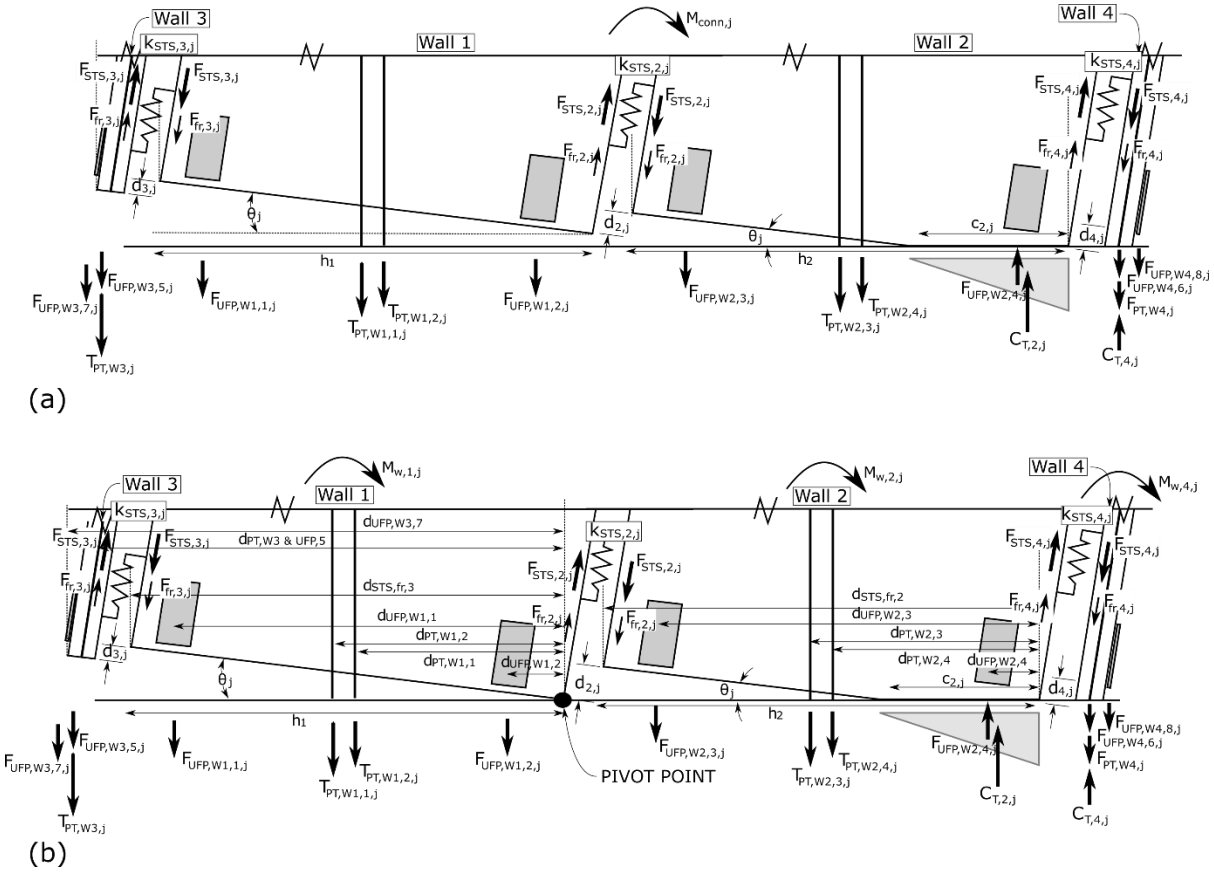


*Figure 9-8: Section analysis of post-tensioned core-wall under high composite action – flange and web wall uplift occurs on the tension side;.(a) displaced shape at core-wall base, and (b) simplified displaced shape at core-wall base with pivot point*

In order to evaluate this system, $d_{2,j}$, $d_{3,j}$, and $d_{4,j}$ must be solved concurrently with $c_{2,j}$. With four unknowns, a system with four equations can be developed considering vertical force equilibrium of Wall 3, Wall 1, Wall 2, and the entire four wall system. With reference to Figure 9-8a, vertical force equilibrium of Wall 3 can be determined as:

$$\sum T_{PT,W3,i,j} + \sum F_{UFP,W3,i,j} = F_{STS,3,j} + F_{Fr,3,j} \tag{9-30}$$

$$\sum \{k_{PT,W3,i,j}[(d_{PT,W3,i} + h_2 - c_{2,j})\theta_j - d_{2,j} - d_{3,j}]\} \tag{9-31}$$

$$+ \sum T_{PT,0,W3} + \sum \{k_{UFP,W3,i,j}[(d_{UFP,W3,i} + h_2 - c_{2,j})\theta_j - d_{2,j} - d_{3,j}]\}$$

$$= K_{STS,3,j-1} d_{3,j} + F_{fr,3,j}$$

Vertical force equilibrium of Wall 1 can be determined as:

$$\sum T_{PT,W1,i,j} + \sum F_{UFP,W1,i,j} + F_{STS,3,j} + F_{Fr,3,j} = F_{STS,2,j} + F_{Fr,2,j} \tag{9-32}$$

$$\sum \{k_{PT,W1,i,j}(d_{PT,W1,i} + h_2 - c_{2,j})\theta_j - d_{2,j}\} + \sum T_{PT,0,W1} \tag{9-33}$$

$$+ \sum \{k_{UFP,W1,i,j}(d_{UFP,W3,i} + h_2 - c_{2,j})\theta_j - d_{2,j}\} + K_{STS,3,j-1}d_{3,j}$$

$$+ F_{fr,3,j} = K_{STS,2,j-1}d_{2,j} + F_{fr,2,j}$$

Vertical force equilibrium of Wall 2 can be determined as:

$$\sum T_{PT,W2,i,j} + \sum F_{UFP,W2,i,j} + F_{STS,2,j} + F_{Fr,2,j} = C_{T,2,j} + F_{STS,4,j} + F_{Fr,4,j} \tag{9-34}$$

$$\sum \{k_{PT,W2,i,j}(d_{PT,W2,i} - c_{2,j})\theta_j\} + \sum T_{PT,0,W2} \tag{9-35}$$

$$+ \sum \{k_{UFP,W2,i,j}(d_{UFP,W3,i} - c_{2,j})\theta_j\} + K_{STS,2,j-1}d_{2,j} + F_{fr,2,j}$$

$$= K_{STS,4,j-1}d_{4,j} + F_{fr,4,j}$$

Global vertical force equilibrium can be determined as:

$$C_{T,2,j} + C_{T,4,j} - \sum T_{PT,i,j} - \sum F_{UFP,i,j} = 0 \tag{9-36}$$

Then, by rearranging the previous equations $d_{2,j}$, $d_{3,j}$, $d_{4,j}$, and $c_{2,j}$ can be determined for a given connection rotation, $\theta_j$. This system of four equations with four unknowns can be significantly simplified by imposing a 'pivot point' as shown in Figure 9-8b. In this way, the core-wall system can be decoupled at the in-plane joint. Now, similar to the MCA and LCA core-wall kinematic modes, $d_{2,j}$ can be approximated as:

$$d_{2,j} = \theta_j(h_2 - c_{2,j}) \tag{9-37}$$

as $c_{1,j} = 0$. Using this simplification, $d_{2,j}$, is slightly over estimated and this will be discussed in comparison with Test CW-6. The orthogonal joint displacement, $d_{4,j}$, is also approximated similar to the LCA and MCA kinematic modes as:

$$d_{4,j} = -\theta_j(c_{2,j}) \tag{9-38}$$

The orthogonal joint displacement, $d_{3,j}$, is determined in the same manner as the MCA kinematic mode following Equation (9-24), but with $c_{1,j} = 0$. Once force equilibrium is found by iterating for $c_{2,j}$ the connection moment can be determined for Wall 1 and Wall 2 as:

$$M_{w,1,j} = \sum T_{PT,W1,i,j}(d_{PT,W1,i}) + \sum T_{PT,W3,i,j}(d_{PT,W3,i}) \tag{9-39}$$

$$+\sum F_{UFP,W1,i,j}\left(d_{UFP,W1i}\right)+\sum F_{UFP,W3,i,j}\left(d_{UFP,W3i}\right)$$

$$M_{w,2,j}=\sum T_{PT,W2,i,j}\left(d_{PT,W2,i}-{}^{c_{2,j}}/_{3}\right)+F_{fr,2,j}\left(d_{fr,2}-{}^{c_{2,j}}/_{3}\right) \quad (9\text{-}40)$$

$$+F_{STS,2,j}\left(d_{STS,2}-{}^{c_{2,j}}/_{3}\right)+F_{fr,4,j}\left({}^{c_{2,j}}/_{3}\right)$$

$$+F_{STS,4,j}\left({}^{c_{2,j}}/_{3}\right)+\sum F_{UFP,W2,i,j}\left(d_{UFP,W2,i}-{}^{c_{2,j}}/_{3}\right)$$

as $c_1 = 0$. The total base connection moment, $M_{conn,j}$, is then

$$M_{conn,j}= M_{w,1,j}+ M_{w,2,j} \quad (9\text{-}41)$$

The connection moment from Wall 4 about its weak axis was considered negligible, and this will be verified in Test CW-6. The 'pivot point' assumption is checked for a given $\theta_j$ by verifying that:

$$\sum T_{PT,W3,i,j}+\sum F_{UFP,W3,i,j}+\sum T_{PT,W1,i,j}+\sum F_{UFP,W1,i,j}< F_{STS,2,j}+ F_{fr,2,j} \quad (9\text{-}42)$$

With increasing $\theta_j$ and joint displacement, the stiffness and coupling force of the STS at the in-plane joint will decrease until Wall 1 touches the foundation and a compression force $C_{T,1,j}$ is required for vertical force equilibrium. At this stage, the core-wall kinematic behaviour changes from HCA to MCA, and the connection moment can be evaluated as described in Section 9.2.3.

### 9.2.5 Theoretical 0% Composite Action Scenario

If it is assumed that there is no composite action between the wall panels, the strength and stiffness of the system can be determined as the sum of the moment capacity from Wall 1 and Wall 2.

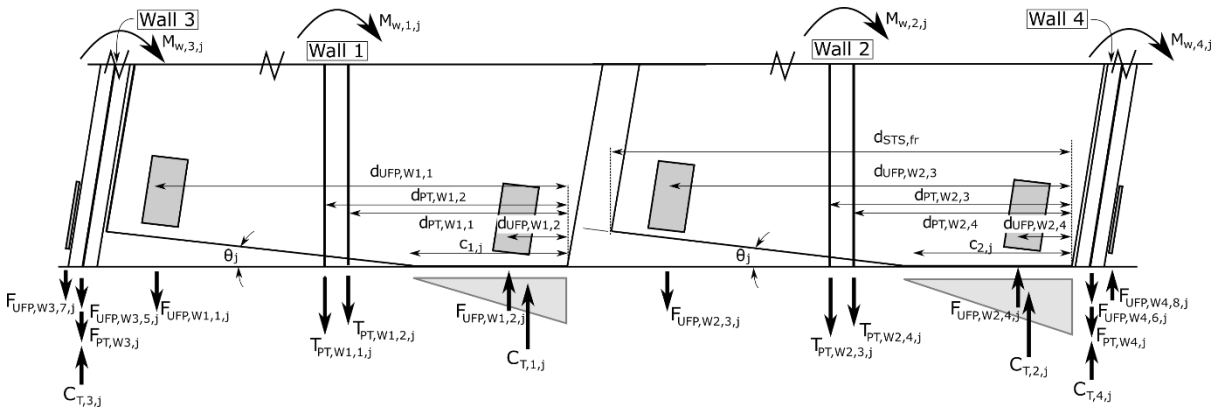


*Figure 9-9: Section analysis of theoretical 0% composite action core-wall scenario*

Then, once force equilibrium is found by iterating for $c_1$ and $c_2$ the connection moment can be determined for Wall 1 and Wall 2 as:

$$M_{w,1,j}=\sum T_{PT,W1,i,j}\left(d_{PT,W1,i}-{}^{c_{1,j}}/_{3}\right)+\sum F_{UFP,W1,i,j}\left(d_{UFP,W1i}-{}^{c_{1,j}}/_{3}\right) \quad (9\text{-}43)$$

$$M_{w,2,j} = \sum T_{PT,W2,i,j}\left(d_{PT,i} - {}^{c_{2,j}}/_{3}\right) + \sum F_{UFP,W2,i,j}\left(d_{UFP,W2,i} - {}^{c_{2,j}}/_{3}\right) \quad (9\text{-}44)$$

The total base connection moment, $M_{conn,j}$, is then:

$$M_{conn,j} = M_{w,1,j} + M_{w,2,j} \quad (9\text{-}45)$$

The theoretical 0% composite action scenario provides a lower bound for comparison to experimental results.

### 9.2.6 Theoretical 100% Rigid Composite Action Scenario

If it is assumed that there is no relative slip at the in-plane joint or orthogonal joints, a core-wall kinematic behaviour occurs as shown in Figure 9-10 and Figure 9-11.

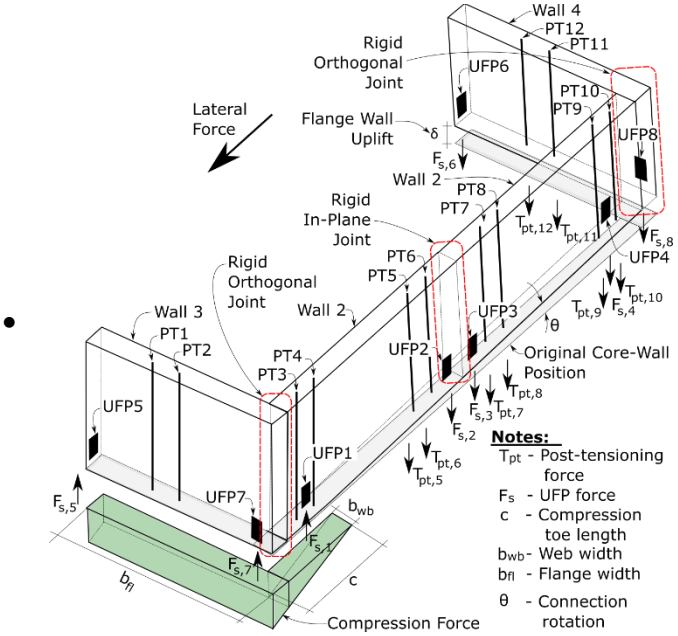


*Figure 9-10: Isometric view of theoretical 100% composite action core-wall scenario*

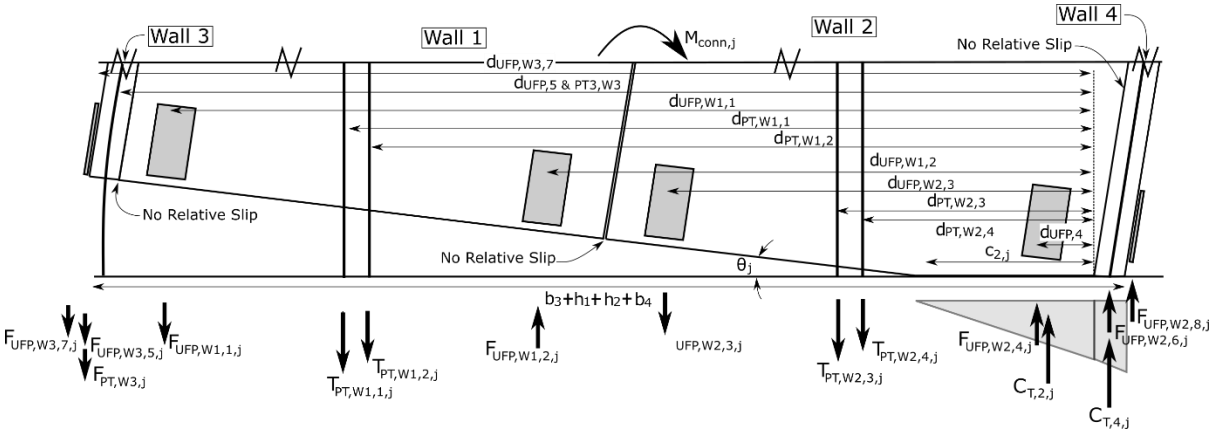


*Figure 9-11: Section analysis of theoretical 100% composite action core-wall scenario*

The wall height is now $h = b_3 + h_1 + h_2 + b_4$. The connection moment can be determined for core-wall system as:

$$M_{conn,j} = \sum T_{PT,i,j}\left(d_{PT,i} - {}^{c_{2,j}}/_{3}\right) + \sum F_{UFP,i,j}\left(d_{UFP,i} - {}^{c_{2,j}}/_{3}\right) \quad (9\text{-}46)$$

To achieve no relative slip, $d_2$, $d_3$, and $d_4 = 0$, $k_{STS} \rightarrow \infty$ which is not possible. However, by determining the theoretical single core-wall behaviour a theoretical upper bound and fully composite behaviour can be determined. Then, as with the double wall system the partial composite action (CA) of the experimental core-wall testing can be defined by comparing the test results with theoretical non-composite and fully composite systems in a similar manner to that for composite beams (Gutkowski et al., 2008; Pault & Gutkowski, 1977)

$$\%CA_{\delta} = \frac{F_{Test,\delta} - F_{0\%,\delta}}{F_{100\%,\delta} - F_{0\%,\delta}} \quad (9\text{-}47)$$

Where, for a given wall drift ($\delta$), $F_{0\%,\delta}$ is the theoretical force for a fully non-composite section, $F_{100\%,\delta}$ is the theoretical force for a fully composite section, and $F_{Test,\delta}$ is the measured force. In this way, the partial composite action of the core-wall system can be qualitatively assessed. This was used in Chapter 6 and shown in Figure 6-45 to quantify the partial composite action received during the experimental PT core-wall testing. Then, the elastic bending and shear deformations can be determined as per Sections 9.2.8 and 9.2.9.

### 9.2.7 Effect of Compression Flange Contribution

In the three aforementioned kinematic modes, the compression flange (Wall 4 in Figure 9-6- Figure 9-8) was assumed not to contribute the core-wall base connection moment along the core-wall strong axis. This assumption can be verified based on experimental findings with particle tracking technology (PTT) and analytically using the Winkler Spring Analogy (WSA).

Figure 9-12 compares the compressive strains between the Flange and Web Wall observed during three 1.5% drift cycles of Test CW-2. The instances in time where the Flange Wall was in 'uplift' or

'compression' are indicated by red vertical lines. During 'compression' loading step instances at ≈ 148.5 Figure 9-12a shows a clear trend of the Web Wall having compressive strains at its toe and the Flange Wall having either strains near 0 or tensile strains. As these Flange Wall strains are being measured at the orthogonal joint, it is assumed that the remainder of the Flange Wall will not have compressive strains. In contrast, during 'uplift' loading step instances at ≈ 146.5 Figure 9-12a shows a clear trend of the Web Wall having tensile strains and the Flange Wall having compressive strains. The compressive strain phenomena in the Flange Wall during uplift was due to the high PT compressive forces.

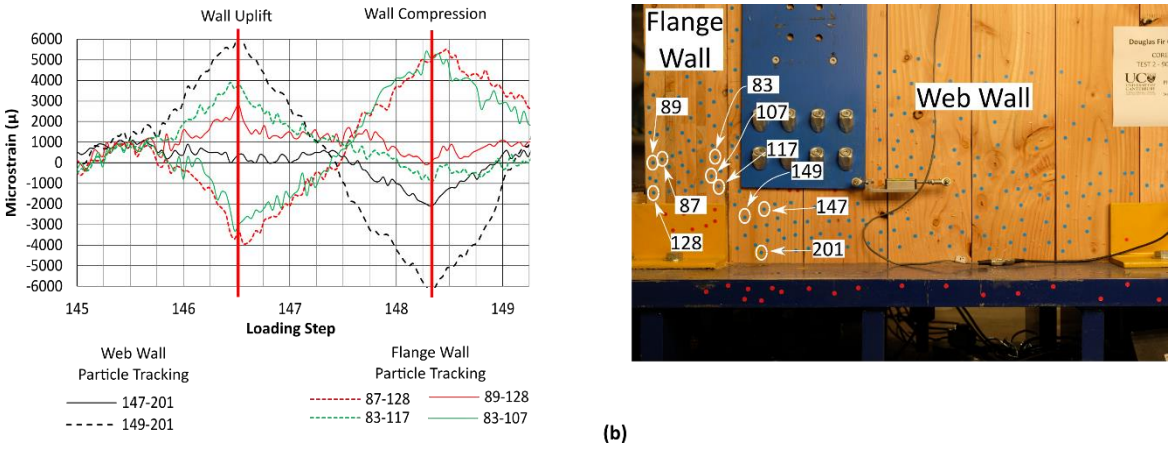


*Figure 9-12: Test CW-2: (a) compressive strain comparison of the Flange and Web Wall using Particle Tracking Technology, and (b) photo of experimental specimen*

Analytically, Figure 9-13 illustrates the assumed compressive component spring model at the base of the PT core-wall system with Flange and Web Wall elements. The stiffness of the timber parallel to grain, $K_{E,O,flange}$ and $K_{E,O,web}$ can be evaluated as:

$$K_{E,o,WSA} = \frac{E_{conn} A_{eff}}{L_{eff}} \tag{9-48}$$

Where:

$L_{eff}$ = the effective length of timber as shown in Figure 9-13

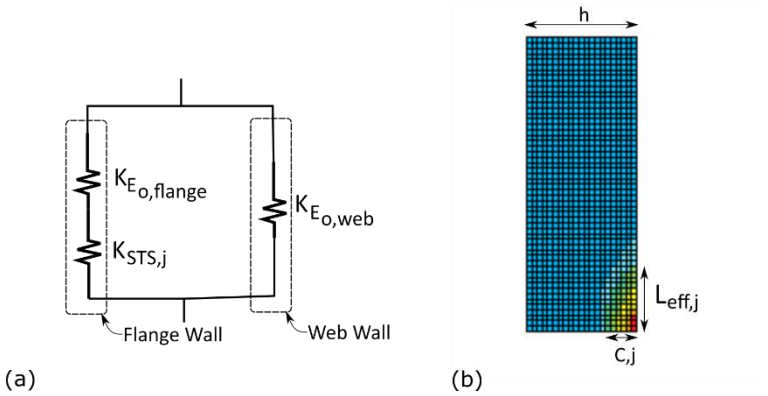


*Figure 9-13: Comparison of Web Wall and Flange Wall compressive stiffness using the Winkler Spring Analogy: (a) compressive spring model of Web and Flange Wall, and (b) numerical modelling of post-tensioned timber wall for WSA by Newcombe* (2015)

Through a parametric numerical study of PT LVL walls, Newcombe (2011, 2015) determined that $L_{eff}$ can be determined assuming a WSA with the relationship of:

$$L_{eff,j} = 120(\frac{h}{c_j} - 1) \tag{9-49}$$

While this was a limited parametric study and a different timber material (LVL) was used, using the WSA allows the relative stiffness of the Flange and Web Wall to be evaluated as per the spring model of Figure 9-13a. The Web and Flange Wall stiffness can be determined as:

$$K_{Web,j} = K_{E_{o,Web,j}} = \frac{E_{conn}A_{web,j}}{L_{eff,j}} \tag{9-50}$$

$$K_{E_{o,Flange,j}} = \frac{E_{conn}A_{Flange}}{L_{eff,j}} \tag{9-51}$$

Where:

$E_{conn}$ = timber connection elastic modulus = $0.83E_o$ as shown in material testing for CLT (See Chapter 7, Section 7.4.1)

$A_{web}$ = $c_{web,j} \cdot b_{eff}$ , where $c_{web,j}$ = the web wall neutral axis length for a given wall base rotation $\theta_j$

$b_{eff}$ = is the sum of the longitudinal board widths only

$A_{Flange}$ = $h_{Flange} \cdot b_{eff,Flange}$ , where $h_{Flange}$ = the Flange Wall length

$b_{eff,Flange}$ = 90mm and 45mm for Test CW-6 and CW-2 respectively and is based on experimental findings with PTT.

It was assumed that the $L_{eff,j}$ for the Flange Wall was the same as the Web Wall for comparative purposes. The stiffness of the orthogonal joint connection, $K_{STS,j}$ , is determined at each wall base rotation increment, $\theta_j$, as:

$$K_{STS,j} = K_{STS,4,j} \quad (9\text{-}52)$$

Where:

$K_{STS,4,j}$ = as per Section 9.2.1.3, Evaluating STS coupling forces, for a given $\theta_j$

Then, $K_{E_{0,Flange},j}$ and $K_{STS,4,i}$ are combined as two springs in series as shown in Figure 9-13.

$$K_{Flange,j} = \frac{K_{E_{0,Flange,j}} K_{STS,j}}{K_{E_{0,Flange,j}} + K_{STS,j}} \quad (9\text{-}53)$$

A comparison of Flange and Web Wall stiffness is provided in Table 9-1. In Test CW-6 which had the highest system stiffness and strength, before gap opening $K_{Flange}$ was 10% of $K_{Web}$. However, the relative stiffness decreased significantly and by 0.75% drift it was less than 3%. Therefore, experimental results by PTT and analytical spring models confirmed that the compression flange can be neglected and not considered to transfer compressive forces from strong axis loading.

*Table 9-1: Test CW-6 compression flange contribution comparison*

| $\theta$ | Drift | $c_{web}$ | $L_{eff}$ | $K_{web}$ | $K_{E,flange}$ | $K_{STS}$ | $K_{flange}$ | $K_{flange}$ / $K_{web}$ |
|---|---|---|---|---|---|---|---|---|
| (Rad) | (%) | (mm) | (mm) | (kN/m) | (kN/m) | (kN/m) | (kN/m) | (%) |
| 0 | 0.1 | 820 | 160 | 5.6E+06 | 6.7E+06 | 6.3E+05 | 5.7E+05 | 10.1 |
| 0.001 | 0.48 | 833 | 155 | 5.9E+06 | 6.8E+06 | 6.3E+05 | 5.7E+05 | 9.7 |
| 0.0015 | 0.65 | 964 | 118 | 9.0E+06 | 9.0E+06 | 3.3E+05 | 3.2E+05 | 3.6 |
| 0.002 | 0.78 | 919 | 130 | 7.8E+06 | 8.2E+06 | 2.4E+05 | 2.3E+05 | 3.0 |
| 0.0025 | 0.91 | 912 | 132 | 7.6E+06 | 8.1E+06 | 2.4E+05 | 2.3E+05 | 3.0 |
| 0.003 | 1.01 | 857 | 148 | 6.4E+06 | 7.2E+06 | 1.9E+05 | 1.8E+05 | 2.9 |
| 0.0035 | 1.11 | 831 | 156 | 5.9E+06 | 6.8E+06 | 1.5E+05 | 1.5E+05 | 2.5 |
| 0.004 | 1.15 | 879 | 141 | 6.9E+06 | 7.5E+06 | 1.5E+05 | 1.5E+05 | 2.2 |
| 0.0045 | 1.22 | 839 | 153 | 6.0E+06 | 6.9E+06 | 1.5E+05 | 1.5E+05 | 2.5 |
| 0.005 | 1.34 | 824 | 159 | 5.7E+06 | 6.7E+06 | 1.5E+05 | 1.5E+05 | 2.6 |
| 0.0055 | 1.44 | 821 | 159 | 5.7E+06 | 6.7E+06 | 1.2E+05 | 1.1E+05 | 2.0 |
| 0.006 | 1.56 | 822 | 159 | 5.7E+06 | 6.7E+06 | 1.2E+05 | 1.1E+05 | 2.0 |
| 0.0065 | 1.69 | 809 | 164 | 5.4E+06 | 6.5E+06 | 1.1E+05 | 1.1E+05 | 2.1 |
| 0.007 | 1.77 | 787 | 172 | 5.0E+06 | 6.2E+06 | 1.1E+05 | 1.1E+05 | 2.2 |
| 0.0075 | 1.83 | 753 | 185 | 4.5E+06 | 5.8E+06 | 1.1E+05 | 1.1E+05 | 2.5 |
| 0.008 | 2.08 | 720 | 199 | 4.0E+06 | 5.4E+06 | -7.7E+03 | -7.7E+03 | 0 |
| 0.0085 | 2.15 | 691 | 212 | 3.6E+06 | 5.0E+06 | -7.7E+03 | -7.7E+03 | 0 |
| 0.009 | 2.21 | 680 | 217 | 3.4E+06 | 4.9E+06 | -7.7E+03 | -7.7E+03 | 0 |
| 0.0095 | 2.24 | 640 | 239 | 3.0E+06 | 4.5E+06 | -7.7E+03 | -7.7E+03 | 0 |
| 0.01 | 2.31 | 630 | 244 | 2.8E+06 | 4.3E+06 | -7.7E+03 | -7.7E+03 | 0 |

### 9.2.8 Bending Deformation

The bending deformation, $\delta_{b,j}$, at the top of the wall is calculated using the elastic formula for a fixed base cantilever as:

$$\delta_{b,j} = \frac{F_j L_{cant}^3}{3 E_T I_{eff,\gamma}} \tag{9-54}$$

Where:

$F_j$ = force at the top of the wall

$L_{cant}$ = cantilever length of the wall

$E_T I_{eff,\gamma}$ = the elastic flexural stiffness of the CLT panel by considering the longitudinal layer only (FPInnovations, 2019) and the partial composite effective flexural stiffness by the 'gamma method', which is provided in Eurocode 5 (2014)

The core-wall system is decoupled at the in-plane joint and was assumed to be treated as two 'L-Shaped' mechanically joined sections as shown in Figure 9-14. This simplifying assumption was made because it was observed in experimental testing that there was significant relative in-plane joint slip. In addition, in Test DW-3 (see Chapter 8) the $\gamma$ factor was less than 10% due to the large in-plane joint displacement. In this instance:

$$E_T I_{eff,\gamma} = \sum_{i=1}^{2} (E_{T,i} I_{Eff,i} + \gamma_i E_{T,i} A_{T,eff,i} {a_i}^2) \tag{9-55}$$

Where $\gamma$ is the gamma factor symbolizing the efficiency of the connection ($\gamma$ = 1 → rigid connection, $\gamma$ = 0 → no connection), $A_{T,eff}$ is the effective timber area which considers the layers loaded parallel to the grain, $a_i$ is the distance between the centroid of the composite section and geometric centre of element 'i'. For the 'L-Shaped' section, the Flange Wall is i = 1 and the Web Wall is i = 2.

$$\gamma_2 = \left[1 + \pi^2 E_{T,2} A_{T,eff,2} s_2 / (K_{STS} {L_{eff}}^2)\right]^{-1} \tag{9-56}$$

where $s_2$ is the spacing of the STS and $s_2 = n_{STS}/L_{cant}$, $K_{STS}$ is the stiffness of the STS orthogonal joint connection at an assumed connection rotation, $\theta$, and $L_{eff}$ is taken as twice the cantilever wall length as per Eurocode 5 (2014). Further,

$$a_2 = \frac{\gamma_1 E_{T,1} A_{T,eff,1} (h_1 + t_{2,eff})}{2(\sum_{i=1}^{2} \gamma_i E_{T,i} A_{T,eff,i})} \tag{9-57}$$

where $h_1$ is the length of the web wall and $t_{2,eff}$ is the effective thickness of the flange wall (considering only longitudinal layers). By geometry $a_2 = \frac{h_2}{2} - a_1 + \frac{t_{1,eff}}{2}$. The calculated $E_T I_{eff,\gamma}$ can then be used with Eq. (9-54) to determine the bending deformation, $\delta_b$, for the core-wall system.

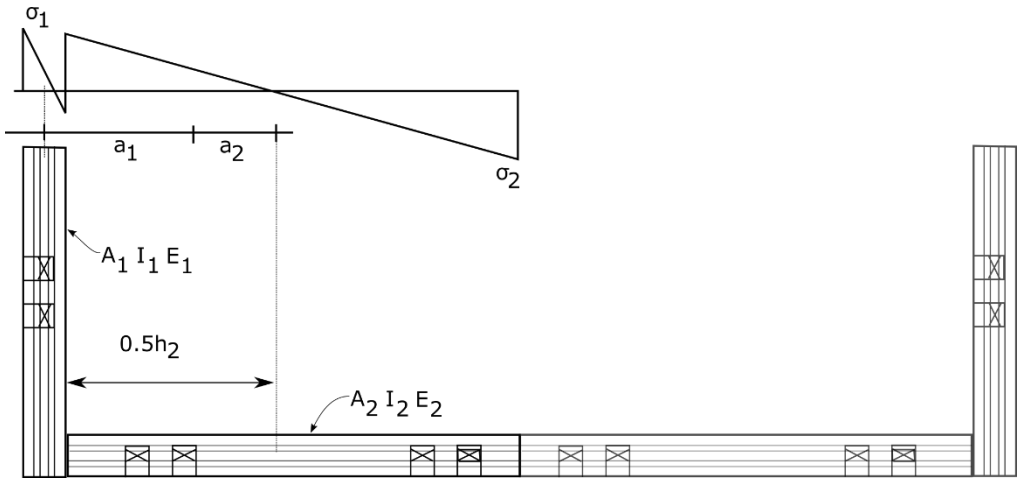


*Figure 9-14: Gamma method assumptions for core-wall system*

### 9.2.9 Shear Deformation

There are different methods in literature for calculating the in-plane shear deformation, $\delta_{s,j}$, of a CLT panel (Lukacs et al., 2019). In this instance, the shear stiffness method proposed by Schickhofer et al. (2010) was used which determines an effective shear modulus, $G_{eff}$, and the gross shear area, A as:

$$G_{eff}A = \frac{G_0 A}{1 + 6\left[0.32\left(\frac{t_b}{a}\right)^{-0.77}\right]\left(\frac{t_b}{a}\right)^2} \quad (9\text{-}58)$$

Where:

$t_b$ = average thickness the CLT lamella

$a$ = the average width of the CLT lamella.

For the core-wall system, only the Web Walls were considered for shear deformation. Due to the ordered CLT, $G_{eff}A$ was approximately equal to 0.75GA as per the ProHolz guideline (Wallner-Novak et al., 2014). Then, the shear deformation is determined as:

$$\delta_{s,j} = \frac{F_j L_{cant}}{G_{eff}A} \quad (9\text{-}59)$$

### 9.2.10 Pushover Analysis

An iterative moment-rotation analysis to determine $M_{conn,j}$ followed by elastic deformations at each rotation increment, 'j' can be carried out to determine the non-linear force-displacement curve for a PT core-wall system with dissipative devices and with varying levels of coupling / composite action at the in-plane and orthogonal joint. By using the non-linear curve fitting function by Foschi (1977), the analytical procedure can capture the full load-displacement curve of a PT core-wall system coupled

with STS and capture the instance where the kinematic behaviour changes from high composite action to medium composite action and then to low composite action. Each wall base rotation step, $\Delta\theta$ shall be chosen small enough to ensure stable performance along the non-linear curve fitting function following the relationship presented in Equation (9-60).

$$\theta_{j+1} = \theta_j + \Delta\theta \tag{9-60}$$

Then, for each rotation $\theta_j$ the horizontal deflection at the top of the wall can be determined considering rocking, $\delta_r$, bending, $\delta_b$, and shear, $\delta_s$, deformation components as:

$$\delta_T = \delta_r + \delta_b + \delta_s \tag{9-61}$$

As mentioned in Section 9.2.1, depending on the relative strength and stiffness of the orthogonal and in-plane joints to the PT and dissipater elements, a certain kinematic mode will result. The flow chart shown in Figure 9-15 summarizes the step-by-step iterative procedure for the rocking deformation component. First, a HCA kinematic mode can be assumed which then requires $c_1 = 0$ as shown in Figure 9-8. If the resulting Wall 1 vertical force equilibrium is less than zero (i.e., an upward acting timber compressive force in Wall 1 is required), then the HCA kinematic mode assumption was not correct and the system equilibrium is then determined under the MCA kinematic mode. Under MCA, the neutral axis for Wall 1 and Wall 2 is iterated with a new relative connection slip $d_2$, $d_3$, and $d_4$ until vertical force equilibrium is found for Wall 1 and Wall 2. Then, $d_3$ is compared against Wall 1 uplift. The core-wall system remains in MCA kinematic mode until $d_3 > Wall\ 1\ Uplift$ (see Figure 9-7). Then, the core-wall system changes to LCA kinematic mode.

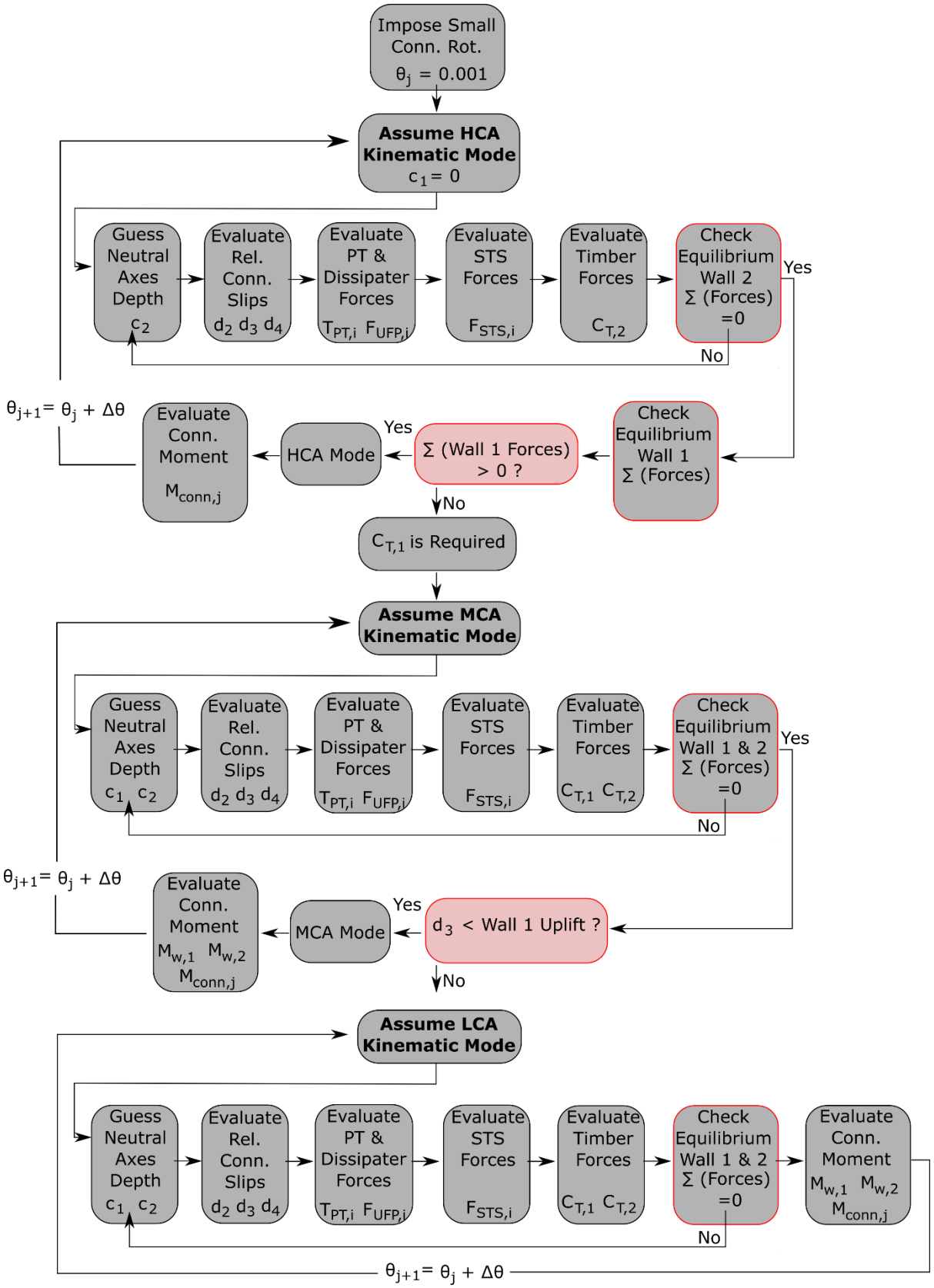


*Figure 9-15: Post-tensioned core-wall analytical design iterative flowchart*

## 9.3 CORE-WALL TESTING SPECIMEN DETAILING

Some specific details from the core-wall testing reported in Chapter 6 are provided here for implementation in the presented analytical model.

### 9.3.1 Selection of Core-Wall Test Programme

Table 9-2 shows the key details of the three selected tests from Chapter 6. For further details, refer to Chapter 6.

*Table 9-2: Selected tests of post-tensioned core-wall testing programme*

| Test | Initial Post-tensioning per bar (kN) | In-Plane Joint | | Orthogonal Joint | | | UFP |
|---|---|---|---|---|---|---|---|
| | | Screw | Screw Quantity | Screw | Screw Quantity | Screw Quantity | |
| | | | Wall 1/2 Joint | | Wall 1/3 Joint | Wall 2/4 Joint | |
| CW-2 | 75 (16%[1]) | 8x80 PTH (17mm Ply.) | 220(90°) | 8x350 FT | 83(90°) | 83(90°) | No |
| CW-3 | 75 (16%[1]) | Friction | n/a | Friction | n/a | n/a | No |
| CW-6 | 75 (16%[1]) | 8x160 FT, 8x80 PTH (22mm Ply.) | 248 (Inc.), 206 (90°) | 8x200 FT, 8x350 FT | 42 (ST), 36(SC), 78 (90°) | 34 (ST), 36(SC), 78 (90°) | Yes |

Note: [1] yield percentage of the post-tensioning bar [2] PTH – partially threaded STS, FT – fully threaded STS, ST – shear-tension STS, SC – shear-compression STS, Inc. – ST and SC STS in combination

### 9.3.2 Self-Tapping Screw Connection Detailing

#### *9.3.2.1 Test CW-2*

##### 9.3.2.1.1 In-plane joint

For the in-plane joint, the same detail as Test DW-3 was implemented for Test CW-2. $\phi$8x80mm PTH STS were installed in pairs on each side of the in-plane joint with 17mm thick plywood. The minimum spacing as per Eurocode 5 (CEN, 2014), a1=10d, which was 80mm in this instance was followed. Refer to Chapter 8, Section 8.3.1 for cailbration of component testing by Hossain (2019) to the nonlinear curve fitting model by Foschi (1977).

##### 9.3.2.1.2 Orthogonal joint

For the orthogonal joint, $\phi$8x350mm fully threaded (FT) STS were installed at 90°. As discussed in Chapter 4 FT STS installed at 90° engage significant rope effect. This is shown in Figure 9-16b which presents challenges for curve fitting. The experimental curve shows the large rope effect represented by the load increase after initial first peak load. The test was stopped at 20mm before failure occurred due to test setup limitations.

The Foschi (1977) model was calibrated over the first 10mm of joint slip as during Test CW-2, joint slip did not exceed this value. Table 9-3 shows the input parameters for the curve fitting model.

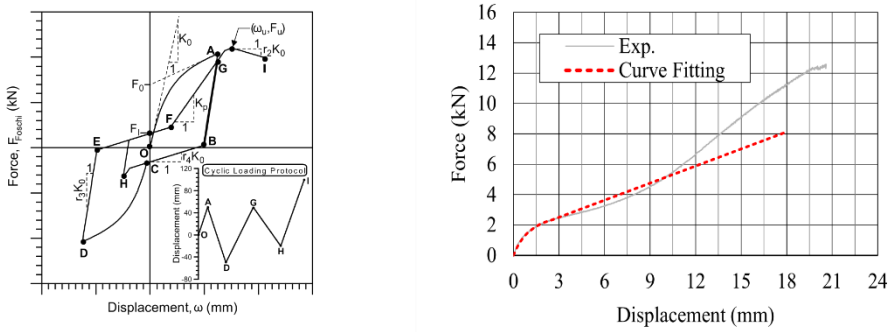


(a) (b)

*Figure 9-16: (a) non-linear curve fitting model by Foschi (1977), and (b) curve fitting results over 10mm connection displacement range*

*Table 9-3: Input parameters for non-linear curve fitting model of Test CW-2 orthogonal joint*

| Initial Stiffness | Force Intercept | Stiffness reduction parameters | | Displacement at max. force | Displacement at final displacement | Max. force |
|---|---|---|---|---|---|---|
| (kN/mm) | (kN) | | | (mm) | (mm) | (kN) |
| $K_o$ | $F_o$ | $r_1$ | $r_2$ | $\omega_u$ | $\omega_f$ | $F_u$ |
| 2.5 | 1.7 | 0.1 | 0.15 | 2.5 | 18 | 2.3 |

83 STS were installed at each orthogonal joint, and then n=83 was used to calibrate the single STS result from STS testing presented in Chapter 4.

### *9.3.2.2 Test CW-6*

During Test CW-6, experimental observations showed that the high composite action (Flange and Web Wall uplift) kinematic mode occurred. Experimental data showed that, at the instance the Web Wall made contact with the foundation, the shear force demand on the in-plane joint was approximately 1500kN. By equilibrium, Equation (9-42) shows that the sum of the post-tensioning and UFP forces from the uplifted Flange and Web Wall were greater than the coupling force provided by the in-plane STS joint at this instance.

Further, the test results showed that significant elastic deformation occurred (almost 40%), and that the deformation along the 8.6m joint height was not equal. The deformation was also restricted at the loading elevation which also created further differences along the joint line. Figure 9-17 shows the significant variation in joint slip along the entire wall height. The large-scale experimental core-wall results were important to understand how a STS connection will behave in a real situation. For example, in most STS connection testing the imposed joint movement is perfectly vertical. However, in a vertical joint between two CLT walls the relative joint slip is due to rocking and elastic

deformations. For these reasons, it was postulated that it may not be appropriate to consider the joint capacity as the capacity of a single STS multiplied by the number of STS along the joint line as was employed for previous DW and core-wall analytical models. In past analytical models, experimental observations showed that relatively similar deformation demands were imposed along the joint heights.

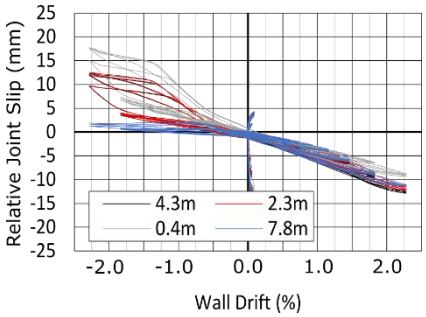


*Figure 9-17: Test CW-6 orthogonal joint slip variation over wall height*

Recently, Hossain et al. (2019) proposed equations to account for group effects for STS connections in CLT in an effort to provide design equations to represent that the load-carrying capacity of multiple STS is less than the sum of the individual STS in a row. Currently, the STS European Technical Approval (ETA) (ETA-12/0114, 2017) states that this group effect should be accounted for by considering an effective number of fasteners, $n_{ef}$, as per Eurocode (2014) as:

$$n_{ef} = n^{0.9^4}\sqrt{\frac{a_1}{13d}} \tag{9-62}$$

For Test CW-6, $n_{ef}$ was considered as per Equation (9-62). Figure 9-18 shows the specific details for the in-plane and orthogonal joint of Test CW-6 and the associated curve fitting processes will be described in the following sections.

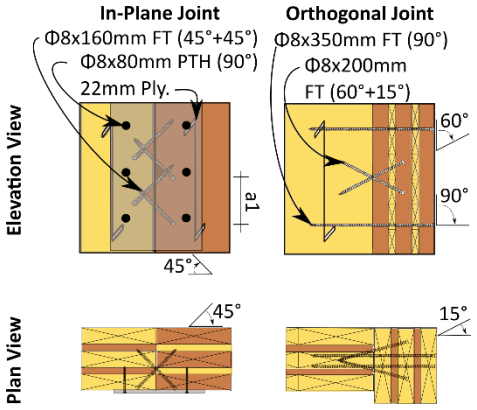


*Figure 9-18: STS details for Test CW-6 in-plane and orthogonal joint*

#### 9.3.2.2.1 In-plane joint

Test CW-6 in-plane joint employed a mixed angle installation with doubly inclined STS and STS installed with 22mm thick plywood at 90°. No experimental test details were available to match the connection detail implemented. Therefore, two different connection tests by Hossain (2019) were used. Figure 9-19 shows the two tests by Hossain (2019) which were combined. If group effects were not considered and then $n_{ef} = n$, the in-plane joint capacity would be approximately 2500kN at the instance when the Web Wall made contact with the foundation. However, as discussed in Section 9.3.2.2, the sum of the post-tensioning and UFP forces from the uplifted Flange and Web Wall was approximately 1500kN (see Equation (9-42)). Therefore, by equilibrium and experimental observations, it was determined that considering the joint capacity as a multiple of a single STS capacity multiplied by the number of STS of the joint ($n_{ef}$=n) was not appropriate. Group effects were assumed to have occurred, and for these reasons, $n_{ef}$ was considered as per Spax ETA (ETA-12/0114, 2017). Further, there were differences in the STS butt joint testing by Hossain et al. (2016) shown in Figure 9-19b and the Test CW-6 in-plane joint. The compound angle of the double inclined STS were less (53° instead of 60°) and the STS were slightly longer ($\phi$8x180mm long instead of $\phi$8x160mm long). Both of these differences would contribute to increased joint strength.

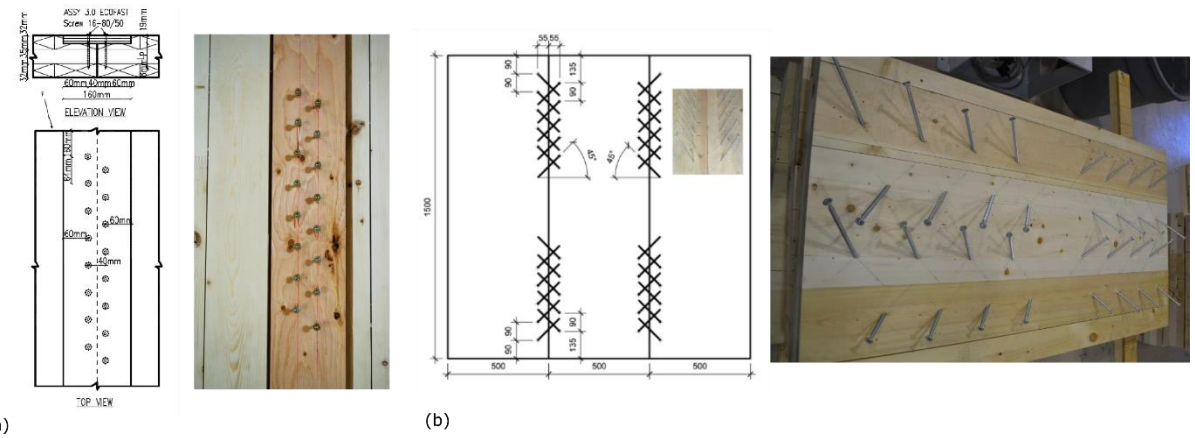


*Figure 9-19: (a) STS in-plane joint with plywood by Hossain* (2019)*, and (b) doubly inclined butt joint by Hossain et al.* (2019; 2016)

**Plywood with $\phi$8x80mm STS**

In testing by Hossain (2019), n = 8 and $a_1$ = 50mm. Therefore, as per Equation (9-62), $n_{ef}$ = 5.8. In Test CW-6, 22mm thick plywood sheets were placed at each floor level with n = 25 and $a_1$ = 100mm per level. Above level four, an additional 22mm thick plywood sheet with 3 STS were installed for a total of 103-$\phi$8x80mm PTH STS per joint side (206 STS total). As per Equation (9-62), $n_{ef}$ = 72. Then, the curve fitting Equations 8-4 – 8-6 shown as per Figure 8-11 and Table 8-1 was multiplied by $n_{ef}$ = 72.

**Doubly inclined $\phi$8x160mm FT STS**

In testing by Hossain et al. (2016), $\phi$8x180mm FT STS were installed at an angle of 45° to the joint line between the CLT panels and at an angle of 32.5° to the face of the panels. In Test CW-6, $\phi$8x160mm FT STS were installed at an angle of 45° to the joint line between the CLT panels and at an angle of 45° to the face of the panels. Though there were was some discrepancy between the connection test and core-wall Test CW-6, this was the most similar experimental information available and therefore it was used for curve fitting purposes. Further, Tomasi et al. (2010) has shown that the experimental performance between STS installed at angles between 30° - 45° is relatively similar so long as the same failure mode is achieved.

Hossain et al. (2016) installed STS in four groups of 10 fasteners, with n = 10 and $a_1$ = 90mm. Therefore, as per Equation (9-62), $n_{ef}$ = 7.5. In Test CW-6, the double-angled STS were installed in four groups, with n = 62 and $a_1$ = 62mm, which exceeded the code minimum of 5d. Therefore, as per Equation (9-62), $n_{ef}$ = 137 for the entire in-plane joint. Figure 9-20 and Table 9-4 summarize the curve fitting results for Test CW-6 in-plane joint.

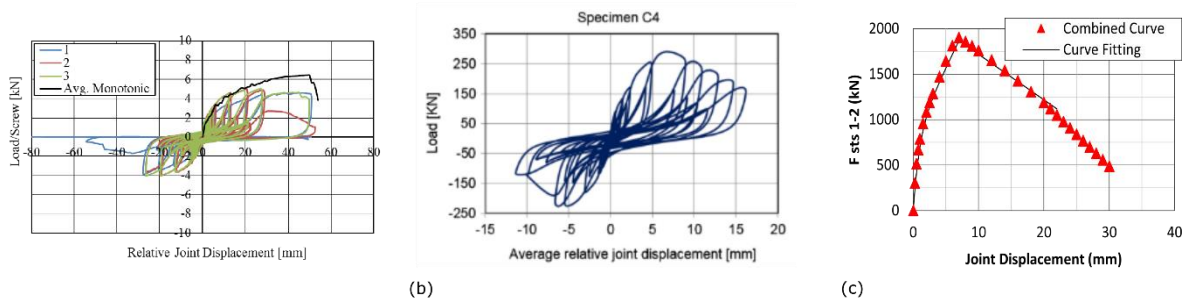


*Figure 9-20: (a) 90° STS connection with plywood* (Hossain, 2019),*(b) double-angled STS connection* (Hossain et al., 2016), *(c) superimposed in-plane joint curve for Test CW-6*

*Table 9-4: Input parameters for non-linear curve fitting model of Test CW-6 in-plane joint*

| Initial Stiffness | Force Intercept | Stiffness reduction parameters | | Displacement at max. force | Displacement at final displacement | Max. force |
|---|---|---|---|---|---|---|
| (kN/mm) | (kN) | | | (mm) | (mm) | (kN) |
| $K_o$ | $F_o$ | $r_1$ | $r_2$ | $\omega_u$ | $\omega_f$ | $F_u$ |
| 1000 | 818 | 0.15 | -0.05 | 7 | 30 | 1868 |

### 9.3.2.2.2 Orthogonal joint

Test CW-6 orthogonal joint employed a mixed angle installation in the same manner as the 16X+16S test series presented in Chapter 4. Therefore, the experimental results presented in Chapter 4 were used for calibration purposes. To be consistent with the in-plane joint and in acknowledgement that the deformation demands on the joint were not the same along the 8.6m joint height, $n_{ef}$ as per Spax ETA (ETA-12/0114, 2017) was implemented.

In the 16X+16S test series of Chapter 4, $\phi$8x350mm FT STS were installed at an angle of 90° to the outer CLT face and inclined $\phi$8x200mm FT STS were installed with a double angle of $\alpha$=30° and $\varepsilon$=15° as shown in Figure 9-21a. The STS were installed along 4 rows with n = 2 and $a_1$ = 80mm per row. Therefore, as per Equation (9-62), $n_{ef}$ = 28 while n=32 for the entire joint test. In Test CW-6, the STS were installed along 4 rows with n = 210 and $a_1$ = 210mm per row. Therefore, as per Equation (9-62), $n_{ef}$ = 129 while n=156 for the each joint. It is interesting to note that work by Tomasi et al. (2010) has shown that if $a_1$ >18d = 144mm, for STS $n_{ef}$ may not be applicable. However, to be consistent with the in-plane joint, $n_{ef}$ was implemented as deformation demand differences occurred along the 8.6m high joint line. It is important to note that the orthogonal joint underwent significantly less deformation demand and stayed within the ascending nonlinear branch of the curve fitting presented in Figure 9-21c.

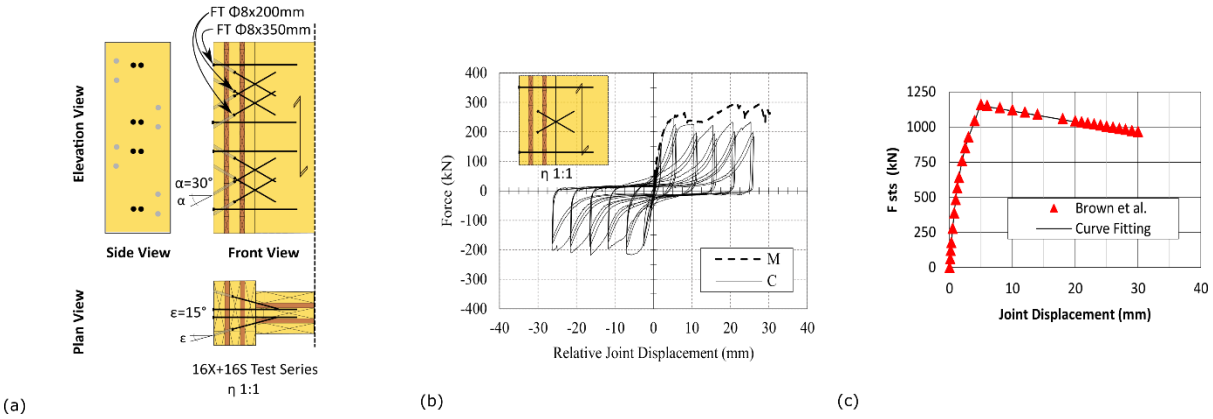


*Figure 9-21: (a) 16X+16S orthogonal joint connection test layout from Chapter 4, (b) Connection test experimental result from Chapter 4, and (c) curve fitting of orthogonal joint curve for Test CW-6*

*Table 9-5: Input parameters for non-linear curve fitting model of Test CW-6 orthogonal joint*

| Initial Stiffness | Force Intercept | Stiffness reduction parameters | | Displacement at max. force | Displacement at final displacement | Max. force |
|---|---|---|---|---|---|---|
| (kN/m) | (kN) | | | (mm) | (mm) | (kN) |
| $K_o$ | $F_o$ | $r_1$ | $r_2$ | $\omega_u$ | $\omega_f$ | $F_u$ |
| 645 | 831 | 0.1 | -0.012 | 5 | 31 | 1153 |

## 9.3.3 UFP connection detailing

The UFP connectors were tested separately in component testing to better evaluate their cyclic performance and the results were presented in Chapter 6, Section 6.3.6. The UFP pair were modelled as a bilinear elastic-plastic system with elastic stiffness of 5.5kN/mm and yield force of 71kN.

## 9.4 EXPERIMENTAL-ANALYTICAL COMPARISONS

The input values for analytical models were taken from CLT and PT bar material testing presented in Chapter 7, Section 7.4.1 and UFP testing presented in Chapter 6, Section 6.3.6. The material input values were:

$E_0$ = 9707 MPa (800MPa is as per NZS 3603 (1993))

$k_{gap}$ = 0.83 (0.7 is recommended for LVL as per Pampanin et al. (2013))

$E_{PT}$ = 184 GPa (170GPa is catalogue value (ETA-07/0046, 2018))

Peak timber strain amplification factor, $\phi_t$, = 1.33 (Derived from SW testing investigation in Chapter 7)

### 9.4.1 Test CW-3 – Low Composite Action (LCA) Kinematic Mode

In Test CW-3, there was no connection at the in-plane and orthogonal joints and no UFPs were installed. In this way the LCA kinematic mode could be evaluated. The comparison of key experimental results is shown in Figure 9-22. The experimental neutral axis was determined by linear interpolation between linear variable displacement transducers and there could be some error associated with the readings. Particle Tracking Technology was not used to determine the neutral axis but this provided increased accuracy and also capture the curvature at the wall based as described by Kovacs (2016).

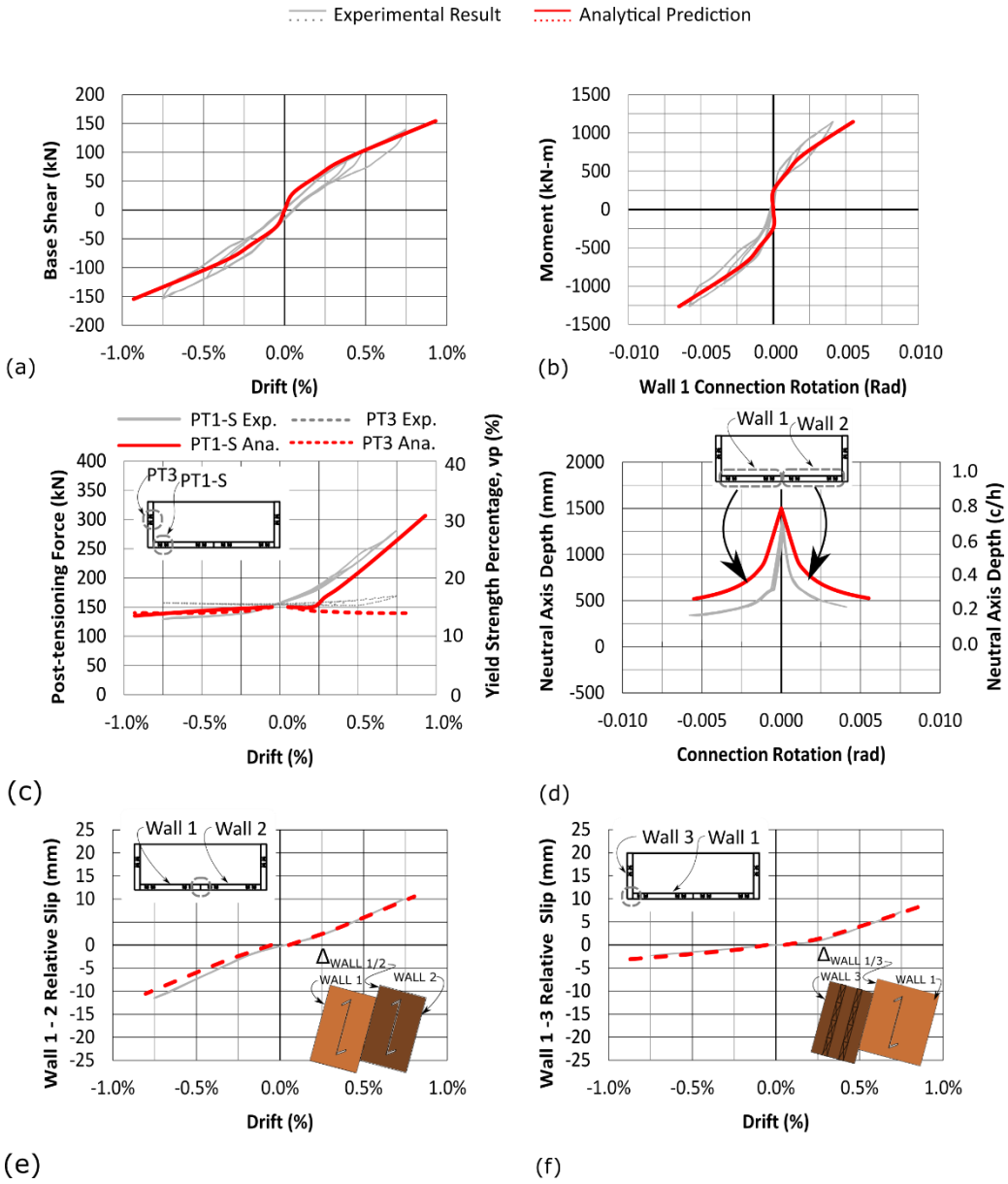


*Figure 9-22: Test CW-3 comparison to analytical model*

Test CW-3 validated that the friction co-efficient $\psi$=0.30 found in DW testing was appropriate. The moment-rotation curve was predicted with 5% at a base connection rotation of 0.006rad.

### 9.4.2 Test CW-2 – Medium Composite Action (MCA) Kinematic Mode

In Test CW-2, 90° STS were employed at the in-plane and orthogonal joint while no UFPs were installed at the wall base. In this way, the MCA kinematic mode could be evaluated. Figure 9-23 shows the key experimental results with comparison to the MCA analytical model where flange uplift on the tension side occurs.

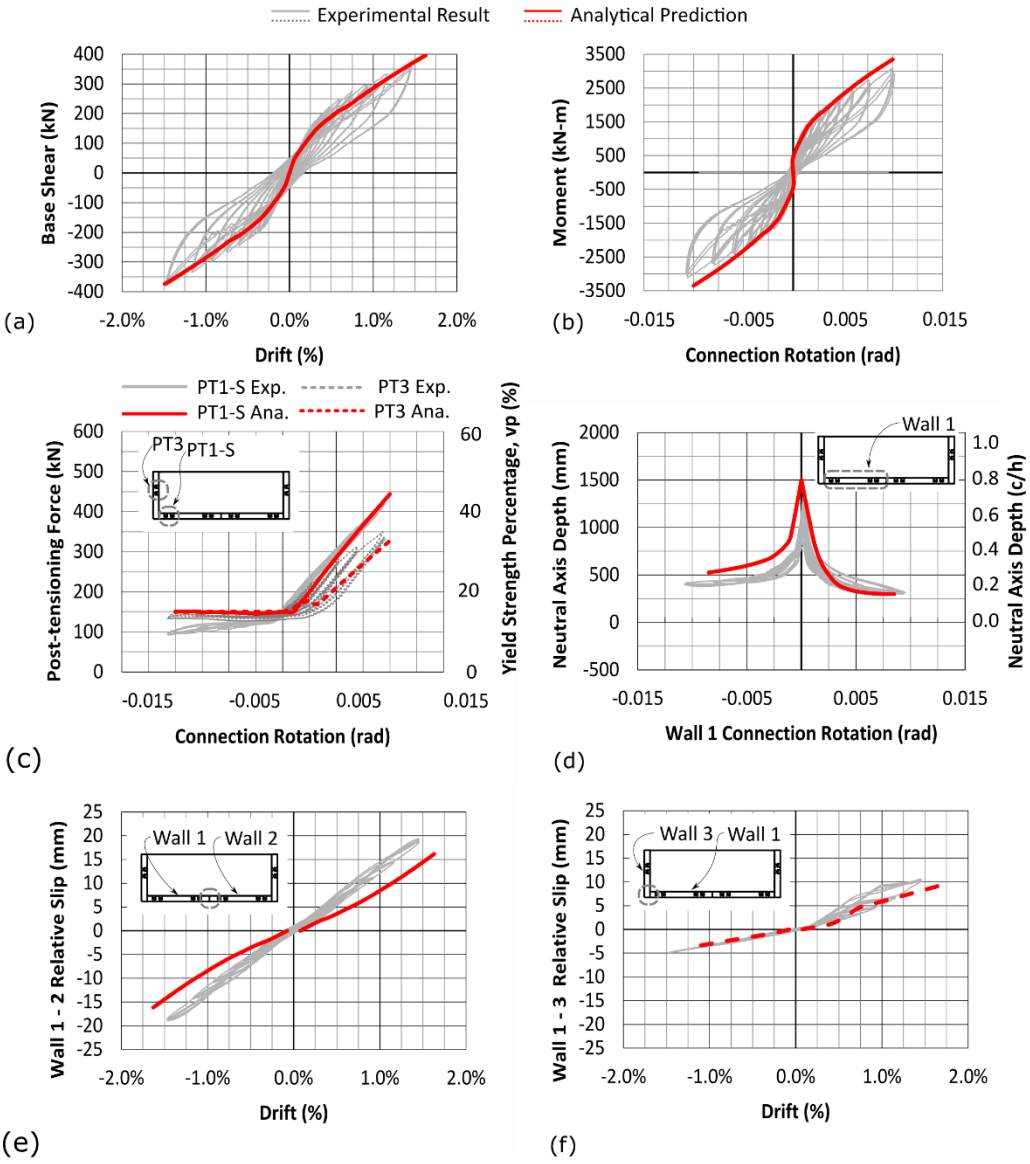


*Figure 9-23: Test CW-2 comparison to analytical model*

The moment-rotation curve was predicted within 5% at a base connection rotation of 0.0095rad such that $M_{Ana.}$ / $M_{Exp.}$ = 1.05. Figure 9-23c and Figure 9-23d show that the post-tensioning forces and neutral axis depth were predicted well. The connection moment of Wall 4 about its weak axis was found to be negligible. Taking the Wall 4 timber compressive force as located in the outer lamella (See Figure 6-55) and considering the Wall 4 post-tensioning forces and STS and friction forces due to $d_4$ joint displacement, Wall 4 peak connection moment was 74kN-m and less than 2.5% of the total connection moment. Therefore, considering the total moment as a contribution from the uplifted Flange Wall 3 and Web Walls 1 and 2 was found to be sufficient for design.

### 9.4.3 Test CW-6 – High Composite Action (HCA) Kinematic Mode – Mixed Angle STS

In Test CW-6, mixed angle STS were employed at the in-plane and orthogonal joint and UFPs were installed at the wall base. During testing, both the HCA and MCA kinematic modes occurred. Figure 9-24b and Figure 9-24d show the HCA (shown in Red Solid Line) and MCA (shown in Red Dash Line) analytical predictions which closely matched the experimental observations. In this instance, the approximation and application of $n_{ef}$ as per Spax ETA (ETA-12/0114, 2017) worked well to combine the individual test results by Hossain (2019) as presented in Section 9.3.2.2. Further work could replicate the in-plane joint STS configuration to more accurately apply curve fitting for analytical modelling.

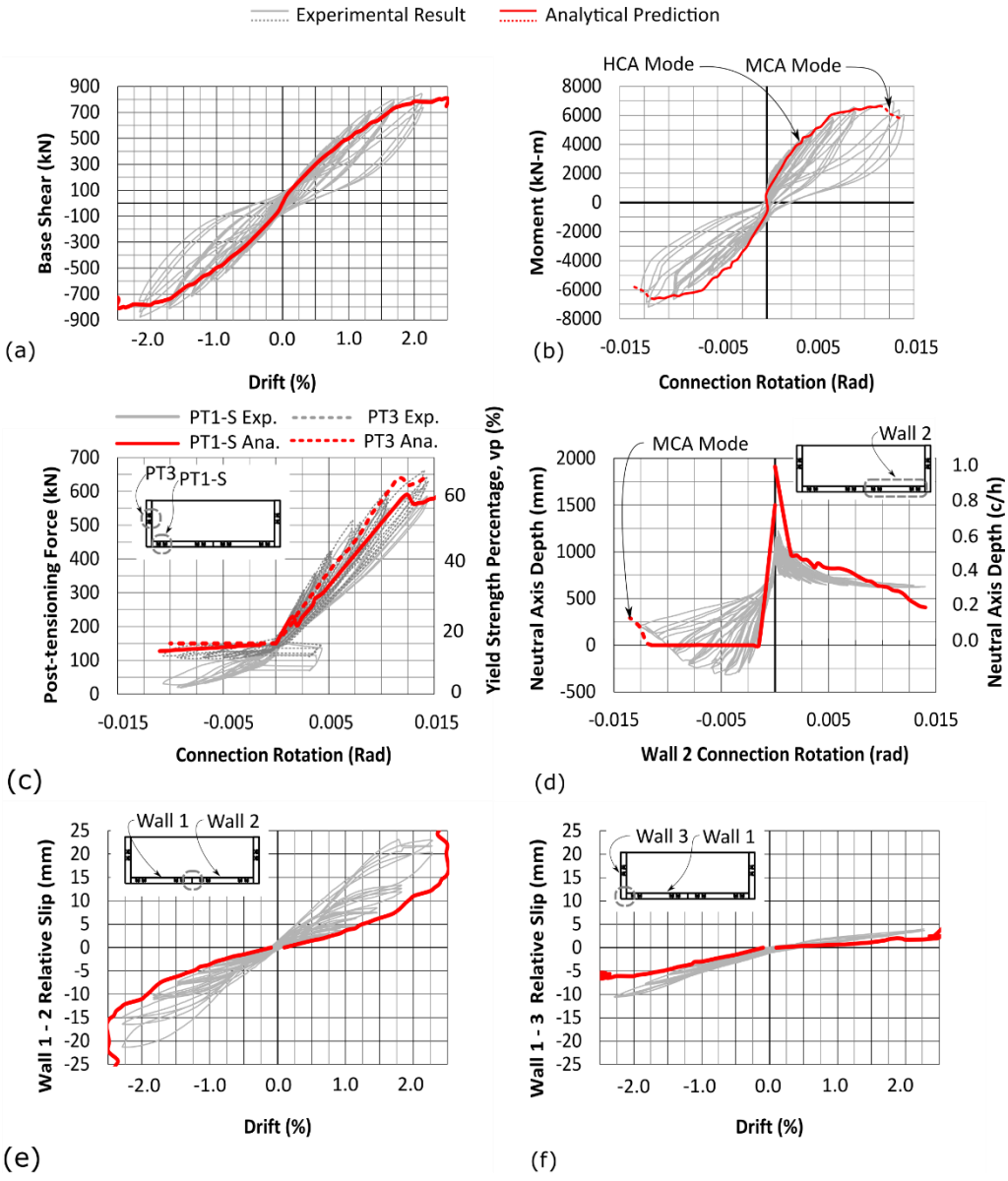


*Figure 9-24: Test CW-6 comparison to analytical model*

The peak moment was predicted within 10% such that $M_{Ana.} / M_{Exp.} = 0.92$. Figure 9-24c shows that the post-tensioning forces for the extreme Flange and Web Wall positions matched well, and Figure 9-24d shows that the 'pivot point' simplification (see Figure 9-8b) worked well in capturing the instance when the Flange Wall touched the ground. In Figure 9-24d, during negative rotation, the 'pivot point' method meant that $c_2 = 0$ until approximately -0.012rad. The in-plane joint relative slip, $d_2$, was slightly under-predicted and this was primarily due to the increased neutral axis prediction and approximated curve fitting employed. The compression flange relative slip, $d_4$, was slightly under-predicted and this was primarily due to the fact that Flange Wall 4 out-of-plane rotation was not considered. Further, axial shortening of the Web Wall was also not considered in approximating $d_4$. If axial wall shortening was considered, at 2.3% wall drift $d_4$ increased from -6.3mm to -7.0mm. It was therefore considered acceptable to not include axial shortening. The load drop in the analytical model was due to the failure of the in-plane joint, which was also the same governing failure mode observed in experimental testing. However, because the curve fitting of the in-plane joint was approximated based on two different STS connection tests by Hossain (2019), the differences as described previously occurred. The connection moment of Wall 4 about its weak axis was found to be negligible for Test CW-6 as well. Taking the Wall 4 timber compressive force as distributed over the entire flange wall width (See Figure 6-55) and considering the Wall 4 post-tensioning forces and STS and friction forces due to $d_4$ joint displacement, Wall 4 peak connection moment was approximately 120kN-m and less than 2.5% of the total connection moment. Therefore, considering the total moment as a contribution from the uplifted Flange Wall 3 and Web Walls 1 and 2 was found to be sufficient for design.

## 9.5 CONCLUSIONS

The experimental results from the post-tensioned (PT) core-wall testing presented in Chapter 6 were compared to the proposed analytical model. Extensions were made to the PT double wall (DW) analytical model presented in Chapter 8 to capture the four different kinematic modes possible in a four wall C-shaped PT core-wall system. The analytical prediction model employed the existing iterative Modified Monolithic Beam Analogy (MMBA). The non-linear curve fitting function proposed by Foschi (1977) was employed to capture the entire load-displacement behaviour of the STS connections at the in-plane and orthogonal joint. The main conclusions from this work were:

- An analytical model was developed to capture the moment-rotation behaviour of a PT C-shaped CLT core-wall system comprising four CLT walls primarily coupled together with self-tapping screws (STS).
- The analytical model extended the MMBA to consider a PT C-shaped core-wall system coupled with STS by using the non-linear curve fitting function proposed by Foschi (1977).

- The analytical model captured three different kinematic core-wall modes along its strong axis: (1) low composite action (LCA) where all four walls were in contact with the foundation, (2) medium composite action (MCA) where flange wall uplift occurred on the tension side, (3) high composite action (HCA) where flange and web wall uplift occurred on the tension side.
- It was determined by experimental results and analytical spring modelling that the compression flange should be neglected during strong axis loading when the CLT walls are coupled together with STS as its contribution was negligible.
- The analytical model was compared with experimental core-wall tests and the results were within 10%.
- To more accurately estimate the bending deformation of the composite double wall section, the 'Gamma Method' was employed.
- The proposed analytical model was able to predict key Test CW-6 within 10%, in which both HCA and MCA kinematic modes occurred. The model can also capture the instance (imposed base rotation angle) at which the kinematic behaviour changes using the 'pivot point' simplification.

## 9.6 REFERENCES

CEN. (2014). Eurocode 5: Design of timber structures-Part 1-1: General-Common rules and rules for buildings. In *EN1995-1-1:2004-11 + AC2006-06 + A1:2008-06 + A2:2014-05 Eurocode 5*. European Committee for Standardization.

Dietsch, P., & Brandner, R. (2015). Self-tapping screws and threaded rods as reinforcement for structural timber elements-A state-of-the-art report. *Construction and Building Materials*, *97*, 78–89. https://doi.org/10.1016/j.conbuildmat.2015.04.028

ETA-07/0046. (2018). *ETA-07/0046: Macalloy 1030 post tensioning system*. European Technical Approval.

ETA-12/0114. (2017). *SPAX self-tapping screws- screws for use in timber constructions* (Issue 305). ETA-Danmark A/S.

Foschi, R. O. (1974). Load-slip characteristics of nails. *Wood Science*, *7*(1), 69–74.

Foschi, R. O. (1977). Analysis of wood diaphragms and trusses, Part 1: Diaphragms. *Canadian Journal of Civil Engineering*, *4*(3), 345–362.

FPInnovations. (2019). *CLT Handbook* (E. Karacabeyli & S. Gagnon (eds.)). FPInnovations.

Gavric, I., Fragiacomo, M., & Ceccotti, A. (2015). Cyclic behavior of CLT wall systems: experimental tests and analytical prediction models. *Journal of Structural Engineering*, *141*(11), 4015034.

https://doi.org/doi:10.1061/(ASCE)ST.1943-541X.0001246

Gutkowski, R., Brown, K., Shigidi, A., & Natterer, J. (2008). Laboratory tests of composite wood-concrete beams. *Construction and Building Materials*. https://doi.org/10.1016/j.conbuildmat.2007.03.013

Hossain, A. (2019). *Experimental investigations of shear connection with STS for CLT panels* (Issue Phd Thesis) [University of British Columbia]. https://doi.org/.1037//0033-2909.I26.1.78

Hossain, A., Danzig, I., & Tannert, T. (2016). Cross-laminated timber shear connections with double-angled self-tapping screw assemblies. *Journal of Structural Engineering*, *142*(11).

Hossain, A., Popovski, M., & Tannert, T. (2019). Group Effects for Shear Connections with Self-Tapping Screws in CLT. *Journal of Structural Engineering (United States)*, *145*(8), 1–9. https://doi.org/10.1061/(ASCE)ST.1943-541X.0002357

Izzi, M., Casagrande, D., Bezzi, S., Pasca, D., Follesa, M., & Tomasi, R. (2018). Seismic behaviour of Cross-Laminated Timber structures: A state-of-the-art review. *Engineering Structures*, *170*, 42–52. https://doi.org/10.1016/j.engstruct.2018.05.060

Kovacs, M. A. (2016). *Design of controlled rocking heavy timber walls for low-to-moderate seismic Hazard Regions*. Master Thesis - McMaster University.

Lukacs, I., Björnfot, A., & Tomasi, R. (2019). Strength and stiffness of cross-laminated timber (CLT) shear walls: State-of-the-art of analytical approaches. *Engineering Structures*, *178*(October 2018), 136–147. https://doi.org/10.1016/j.engstruct.2018.05.126

Newcombe, M. P. (2011). *Seismic Design of Post-Tensioned Timber Frame and Wall Buildings: Vol. PhD Thesis*. University of Canterbury.

Newcombe, M. P. (2015). The connection response of rocking timber walls. *SESOCJournal*, *28*(1), 46–53.

Newcombe, M. P., Pampanin, S., Buchanan, A., & Palermo, A. (2008). Section analysis and cyclic behavior of post-tensioned jointed ductile connections for multi-story timber buildings. *Journal of Earthquake Engineering*, *12*, 83–110. https://doi.org/10.1080/13632460801925632

Palermo, A. (2004). *Use of controlled rocking in the seismic design of bridges*. Technical University of Milan.

Pampanin, S., Nigel Priestley, M. J., & Sritharan, S. (2001). Analytical modelling of the seismic behaviour of precast concrete frames designed with ductile connections. *Journal of Earthquake Engineering*, *5*(3), 329–367. https://doi.org/10.1080/13632460109350397

Pampanin, S., Palermo, A., & Buchanan, A. (2013). *Post-Tensioned Timber Buildings - Design Guide Australia and New Zealand*. Structural Timber Innovation Company.

Pault, J., & Gutkowski, R. (1977). *Tests and analysis of composite action in glulam bridges', Structural Research report No. 17A* (No. 17A).

Sarti, F. (2015). *Seismic design of low-damage post-tensioned timber wall systems* (Issue PhD Thesis). University of Canterbury.

Schickhofer, G., Bogensperger, T., Moosbrugger, T., Augustin, M., Blaß, H. J., H, E., & et al. (2010). *BSPhandbuch, Holz- Massivbauweise in Brettsperrholz*. Technische Universitat Graz, Karlsruher Institut fur Technologie.

Shahnewaz, M., Popovski, M., & Tannert, T. (2020). Deflection of cross-laminated timber shear walls for platform-type construction. *Engineering Structures*, *221*(July), 111091. https://doi.org/10.1016/j.engstruct.2020.111091

Standards New Zealand. (1993). *NZS 3603: Timber structures standard*. Standards New Zealand.

Symons, D., Persaud, R., & Stanislaus, H. (2010). Slip modulus of inclined screws in timber-concrete floors. *Proceedings of the Institution of Civil Engineers: Structures and Buildings*, *163*(4), 245–255. https://doi.org/10.1680/stbu.2010.163.4.245

Tomasi, R., Crosatti, A., & Piazza, M. (2010). Theoretical and experimental analysis of timber-to-timber joints connected with inclined screws. *Construction and Building Materials*, *24*(9), 1560–1571. https://doi.org/https://doi.org/10.1016/j.conbuildmat.2010.03.007

Wallner-Novak, M., Koppelhuber, J., & Pock, K. (2014). *Cross-Laminated Timber structural design* (isbn 978-3). proHolz Austria. www.proholz.at

# 10 Conclusions

## 10.1 GENERAL

The scope of this research was the investigation of CLT core-walls as a lateral load resisting system (LLRS) for taller CLT buildings. The research investigated three critical connection types for such a CLT core-wall system and then implemented a progressive three phase CLT shear wall testing programme which culminated with a four-storey 8.6m high C-shaped core-wall specimen.

The main objective of this research, which was to quantify the partial composite action of a CLT core-wall system based on its connection details, was achieved through experimental testing and then validated through analytical modelling. The experimental data collected throughout the research was implemented in the proposed analytical models to predict the load-drift response of a post-tensioned (PT) CLT core-wall system coupled together with self-tapping screw (STS) connections. The following provides a summary of each of the three main sections of the research: CLT connections, CLT shear wall testing, and analytical modelling of PT CLT shear wall systems.

## 10.2 SUMMARY OF CONTRIBUTIONS TO CLT CONNECTIONS

CLT core-wall systems will require high performance connections. As such, three chosen connection types were investigated in the research herein: dowelled hold-down connections, castellated shear connections for horizontal joints, and mixed angle STS connections for orthogonal vertical joints.

### 10.2.1 Dowelled CLT Hold-Down Connections with Increased Row Spacing and End Distance

The structural performance of CLT dowelled hold-down connections with one slotted-in steel plate was investigated. The work aimed to quantify the enhanced connection performance by increasing row spacing and end distance in the dowel layout compared with the standard spacing/end distance specified by design standards. The study was an extension of previous work by Ottenhaus et al. (2018) which primarily investigated brittle failure modes and mode cross-overs and postulated that increased fastener spacing would increase the connection performance.

A total of 47 hold-down specimens encompassing 3-layer (135mm thick), 5-layer (175mm thick), and 7-layer (275mm thick) CLT were subjected to monotonic and cyclic loading. In addition, 215 half hole dowel embedment tests were performed in New Zealand Douglas-Fir CLT according to ASTM D5764-97a (2013) in a load direction parallel and perpendicular to the outer CLT layer in order to derive 5$^{th}$ percentile values (CEN, 2016) and compare the results to the CLT handbook (Gagnon et al., 2011) embedment equation. It was found that increased dowel row spacing and end distance increased

connection displacement capacity and ductility by 35% and 20%, respectively; however, it did not affect the connection strength or stiffness. The maximum experimental overstrength was 1.7. With dowel embedment and dowel bending tests the theoretical component based overstrength, as developed by Ottenhaus et al. (2020), was 1.50. Eight of the 47 connection specimens were reinforced by inclined STS or by replacing the lower two dowels with threaded dowels with nut and washer. These reinforced specimens also had significantly increased displacement capacity and ductility by delaying the onset of brittle panel splitting failure.

### 10.2.2 Orthogonal Joints in CLT with Self-Tapping Screws Installed with Mixed Angles

In order to optimize orthogonal joint connections with mixed angled STS, a total of 59 specimens were tested in 9 different configurations and subjected to monotonic and cyclic loading. In addition, a total of 202 STS withdrawal tests were performed following EN 1382 (2016). The STS were installed in 5-layer (175mm thick) and 7-layer (275mm thick) CLT specimens with mixed angles, i.e. different installation angles between the STS axis and the plane of the CLT surface. Different ratios of STS installed inclined and STS installed at 90° to the CLT surface were investigated to determine an optimum ratio of STS for enhanced joint performance.

It was found that a ratio of two inclined STS to one 90° STS led to a significant increase in ductility and displacement capacity, approximately three times of the specimens using inclined STS only. Based on the STS withdrawal testing, the embedment length of the STS installed inclined on each side of the joint was limited to 12d to ensure gradual screw withdrawal as the governing failure mode. The primary failure modes were plastic timber embedment deformation and STS yielding. The strength and stiffness of the mixed angle STS joints were also affected by 90° STS.

Existing analytical models using the superposition of inclined STS and 90° STS were used to predict the connection strength. The average experimental overstrength was found to be 1.7 for most joint configurations. Existing stiffness models were found inaccurate. Existing expressions to estimate the axial withdrawal stiffness can vary up to 500% depending on the STS diameter and insertion length (Ringhofer, 2017), and the existing Eurocode 5 (2014) equation to estimate the stiffness of 90° STS was not appropriate. Further work is required to capture the joint stiffness of STS installed at spatial insertion angles to the timber grain.

### 10.2.3 CLT Shear Connections with Castellations and Angle Brackets

The strength and stiffness of CLT shear connections with mortise and tenon castellated joints was evaluated and compared to the CLT shear connections using commercial steel angle brackets. In this experimental study, a total of 29 castellated specimens and 6 angle bracket specimens were tested under monotonic loading to evaluate their structural performance. Four different castellation

geometries were tested in 5-layer (175mm thick) and 7-layer (275mm thick) CLT. The specimens using castellations and angle brackets were loaded parallel and perpendicular to the outer CLT layer.

It was found that the shear strength and stiffness of the castellated joints were 2.5 and 7 times greater than the specimens using the commercial angle brackets. The dominating failure modes in the castellation tests were a combination of longitudinal shear failure and rolling shear failure on the tenon side. The castellated joints did not experience a sudden load drop due to the cross-layer reinforcement. In all specimens, a relative displacement was observed between the CLT layers with the layers loaded parallel to grain having greater displacement than the layers loaded perpendicular to the grain. This observation affirmed that significant rolling shear load transfer occurred.

Based on an assumed deformed shape of the tenon both in-plane and in its cross-thickness between layers, a simplified component-based analytical model was developed to predict the strength of the castellated joints loaded parallel and perpendicular to grain of the CLT outer layers. The analytical model developed was similar to the stiffness-based load sharing approach by Zarnani & Quenneville (2014). Material testing was performed to validate the model against the component tests (informed values) and the readily available design values (code values). When informed material properties were used, the model was able to predict strength reasonably well with an average strength ratio of 0.92.

## 10.3 SUMMARY OF CONTRIBUTIONS TO EXPERIMENTAL TESTING OF POST-TENSIONED CLT SHEAR WALL SYSTEMS

A three phase CLT shear wall testing programme was executed to study the contribution of each component (wall and joint) to a CLT core-wall system under quasi-static uni-directional and bi-directional loading. A total of 17 wall tests were performed in the shear wall testing programme. The wall specimens were four storey and 8.6m high with a 2/3 scale factor. The five-layer (175mm thick) CLT wall panels were made out of New Zealand Douglas-Fir.

Four PT single wall (SW) specimens in Phase I were tested with varying initial post-tensioning forces. Five PT double wall (DW) specimens in Phase II had varying in-plane joint details with STS. In Phase III, 7 PT core-wall specimens and one conventional core-wall specimen were tested with varying in-plane and orthogonal joint details with STS, and under different loading protocols. U-shaped flexural plates (UFPs) were also implemented at the wall base in the PT DW and PT core-wall testing. Particle tracking technology (PTT) was implemented to better understand the base rocking interface behaviour and to monitor the UFP connection movement.

The experimental test results confirmed that significant system strength, stiffness, ductility and drift capacity can be achieved in a PT C-shaped CLT core-wall with minimal damage through careful connection detailing. The highest core-wall composite action of approximately two-thirds was achieved. The core-wall stiffness at SLS was greater than eight times a single wall for an approximate 3.5 times increase in wall area.

With SW testing, the Modified Monolithic Beam Analogy (MMBA) analytical model for PT CLT wall systems and a linear stress / strain distribution was verified by PTT. Significant differences in strength and stiffness were achieved in DW tests and in Test DW-3, a negative neutral axis occurred in one of the two walls which indicated wall uplift. This kinematic behaviour occurred due to the high stiffness and strength of the in-plane joint which provided high coupling effect. Mixed angle STS connections provided stable system performance at a core-wall drift of 2.3%, which was the stroke limit of the actuators. In Test CW-6 with mixed angle STS connections, a peak load of 845 kN (≈7,000kNm overturning moment at the core-wall base) was achieved. Mixed angle STS connections for the in-plane and orthogonal joints provided necessary displacement capacity and energy dissipation. The partial composite action of the core-wall system decreased with increasing core-wall drift and this behaviour was stable with STS installed either at 90° or mixed angles.

With PTT, it was found that the UFPs performed well in accommodating twisting and out-of-plane movement under bi-directional loading. The inclined STS connection detail for the UFPs could provide targeted vertical connection stiffness while providing some decoupling effect due to horizontal and out-of-plane wall movement. PTT captured the significant out-of-plane rotation of the compression Flange Wall during strong axis loading. Further, it was found that the compressive Flange Wall was not engaged due to the relatively less stiff STS connection between the Web and Flange Walls when compared to compression parallel to grain contact stiffness of the adjacent Web Wall.

The conventional core-wall test implemented 16 hold-downs which used either mild steel dowels with one slotted-in steel plate or mixed angle STS with steel side plates at the base of each wall and at the horizontal joint located at 5.5m wall height. The mixed angle STS hold-downs and mixed angle STS connection at the in-plane joint provided the primary energy dissipation mechanisms, and stable system performance was observed up to 1.8% wall drift. While the strength and stiffness of the conventional core-wall test was within the range of some PT core-wall tests, the PT core-wall proved superior in minimizing residual drift and having increased drift capacity.

Several tests were performed on the CLT wall specimens with only minor damage occurring at the compression toes of the CLT wall panels and in proximity of each STS even at high levels of drift. At the end of each test, all STS were removed and new STS were installed in a different location in an

efficient manner. No significant impairment to the connection behaviour was observed. This was one significant advantage in implementing STS connections along in-plane and orthogonal joints in terms of reparability.

## 10.4 SUMMARY OF CONTRIBUTIONS TO ANALYTICAL MODELLING OF POST-TENSIONED CLT SHEAR WALL SYSTEMS

Existing analytical models were verified for PT CLT SW systems. The test results showed that the MMBA could under predict the peak strain response in the compressive toe. A strain amplification factor, $\phi_t$, of 1.33 was determined based on 37 analytical-experimental comparisons from the four wall tests presented. This $\phi_t$ is recommended for PT CLT wall systems where CLT is non-edge glued and their lamella are not machine stress graded. Material property testing on CLT and PT bars was performed. When $\phi_t$ and the experimentally evaluated material properties were used, the PT SW experimental response was predicted within 5% error.

An analytical model was proposed to capture the response of PT DW systems with STS vertical joints and UFP dissipaters at the wall base. The analytical model could capture two unique kinematic modes and the instance (imposed wall base rotation angle) at which the kinematic behaviour changes. These kinematic modes were combined single-coupled wall (SCW) where only one wall is in contact with the foundation due to high strength and stiffness of the STS vertical in-plane joint and coupled double wall (CDW) in which both walls are in contact with the foundation. The nonlinear curve fitting connection model presented by Foschi (1977) was employed to capture the STS connection response. The 'Gamma Method' was used to estimate the bending stiffness of the composite wall section. The proposed analytical model was also able to predict Test DW-3 within 5% error, in which both the SCW and CDW kinematic behaviour occurred.

Finally, an analytical model was proposed to capture the base moment rotation behaviour of a PT C-shaped core-wall CLT system based on the STS orthogonal and in-plane vertical joint details and UFPs at the core-wall base. The proposed PT DW analytical model was extended to include the contribution of the orthogonal/Flange Walls. The analytical model could capture three unique kinematic modes: low composite action (LCA) where all four CLT walls are in contact with the foundation, medium composite action (MCA) where Flange Wall uplift occurs on the tension side, and high composite action (HCA) where Flange and Web Wall uplift occur on the tension side. Similar to the analytical PT DW system model, the nonlinear curve fitting connection model presented by Foschi (1977) to capture the STS connection response and the 'Gamma Method' to estimate the composite section bending stiffness were implemented. The compression Flange Wall was neglected during the strong axis

loading. The proposed analytical model was able to predict Test CW-6 within 10% error, in which both HCA and MCA kinematic behaviour occurred.

## 10.5 FUTURE RESEARCH

Suggestions for future research are presented as follows:

### 10.5.1 CLT Connection Testing

The connection research presented herein and most past related research has focused on connection ductility based on relatively smaller specimens (in comparison to full-scale building implementation) and defined a connection as ductile if its connection ductility ($\mu$) was greater than 6 (Smith et al., 2006). Future research should quantify what a given connection ductility means in terms of system ductility/drift capacity.

#### *10.5.1.1 Dowelled CLT hold-down connections*

The testing of dowelled hold-downs with one slotted-in steel plate showed that increased row spacing and fastener end distance increased connection displacement capacity and ductility while not having significant effect on connection strength and stiffness. Future work should investigate the influence of the number and slenderness of dowels, and further quantify the reinforcement effect by STS on the connection strength and stiffness. In CLT shear walls, hold-downs are located at the corner and base and due to their horizontal stiffness they will carry combined axial-shear loads. Future work should investigate the effect of biaxial loading on the hold-down performance. CLT connection performance under fire is also critical for implementation, and one common measure in practice is to use hidden / protected connections with sacrificial timber layers. As such, the performance of dowels whose lengths are less than the CLT wall thickness should be investigated. In the dowel embedment testing, only one of the four CLT layups (two three-layer, one five-layer, and one seven-layer) was qualified for the widely used CLT Handbook embedment equation. Further research should determine a more generally applicable CLT embedment strength formulation.

#### *10.5.1.2 Orthogonal joints in CLT with self-tapping screws*

Mixed angle STS connections for orthogonal joints provided increased displacement capacity and ductility under cyclic loading. Moreover, it was also found that relatively large $\phi$12mm STS could undergo significant yielding and dissipate energy while installed inclined or at 90° to the CLT face grain. It was postulated that STS slenderness ratio might be a more significant parameter than the fastener diameter to ensure significant joint displacement capacity and ductility. The impact of STS slenderness ratio on connection performance should be further investigated. In order to implement STS as ductile links in a CLT shear wall, their overstrength must be well understood. There are significant differences

between different STS suppliers to determine strength capacity especially in the instance of STS installed inclined. Further, depending on the spatial insertion angle of STS, the contribution of lateral dowel action to the total joint strength could be significant. Future research should work towards harmonizing calculation methods within STS product approvals to facilitate further implementation in practice. While current analytical strength models are sufficient to determine connection strength, they are not adequate to estimate connection stiffness. Connection stiffness is also critical to satisfy performance criteria. Future work should develop more accurate STS connection stiffness models which have physical meaning and account for the nonlinear connection behaviour. Of immediate importance is the development of an axial and lateral stiffness equation for STS wood-wood or steel-wood joints.

#### *10.5.1.3 CLT shear connections with castellated joints and angle brackets*

The testing of mortise and tenon castellated shear connections showed superior performance in terms of strength and stiffness when compared to commercial angle bracket connectors. However, as relatively small castellation joints were studied, most tenons did not contain lamination gaps. For n on-edge glued CLT, the presence of lamination gaps may affect the joint strength and cause brittle modes such as tension perpendicular to grain. Future experimental work should study different tenon geometries including tenon heights and then extend the proposed analytical component method to account for the influence of lamination gaps within a tenon. It was also found that the stiffness of commercial angle bracket connectors was significantly over-estimated by the existing Eurocode 5 equation. Further work is necessary to more accurately predict the stiffness of these angle brackets which are commonly employed in CLT structures.

### 10.5.2 CLT Shear Wall Systems

#### *10.5.2.1 Experimental investigations*

The PT SW, PT DW, PT core-wall and conventional core-wall test programme consisted of 17 wall tests. While the experimental study provided valuable information on the core-wall performance and its components (CLT walls and selected joints), the study was limited due to the same CLT wall specimens being studied and few STS joint configurations tested. Future work should investigate other common joint configurations with STS such as half-lap joints with STS at the in-plane and orthogonal joint. The experimental results showed that the in-plane joint dissipated significantly more energy than the orthogonal joint due to the increased shear flow demands. To capitalize and activate the partial composite action of the Flange Wall, mortise and tenon castellated orthogonal joints should be investigated which were shown in this research to provide one such strong and stiff non-energy dissipative connection.

Furthermore, the experimental testing was quasi-static and the actuator strokes ultimately limited wall drifts. Under dynamic loading scenarios, the influence of friction could be reassessed for applicability in design especially when using STS installed inclined that provide a clamping effect. The test set-up which implemented loading through contact bearing at the top of the CLT wall specimen was effective in studying a core-wall subassembly. In order to understand the behaviour of a core-wall subassembly in a building, diaphragm load transfer mechanisms should be investigated. This would also allow for a further investigation on torsion, which is relevant for the design of open sections such as C-shaped core-walls. Although stable system level performance was observed under bi-directional loading, further research is required to quantify the effects.

The conventional core-wall test demonstrated that when using hold-down connectors at the corners of each wall a comparable stiffness at serviceability limit state could be achieved. However, due to limited resources only one conventional core-wall specimen configuration was tested. As the conventional core-wall system is an extension of commonly constructed in-plane CLT shear walls, it could be more easily implemented in practice. Future work should investigate other high-performance and high energy dissipative hold-downs to optimize the conventional core-wall design. In particular the mixed angle STS hold-down with steel side plate showed high strength, stiffness and displacement capacity potential and research on this hold-down type is currently on-going at the University of Canterbury.

#### *10.5.2.2 Numerical investigations*

It has been shown in past research that higher mode effects can be significant in PT wall systems. Further numerical investigations could investigate higher mode effects for CLT core-wall systems, and also mitigation measures such as segmental rocking core-wall systems which has been previous investigated for in-plane PT wall systems (Pilon et al., 2019).

There is an ever increasing experimental connection database of STS CLT joints and it was shown in this work that connection data can be implemented in the proposed analytical model with sufficient accuracy. Numerical investigations with different STS configurations calibrated with experimental STS connection database could investigate the post-peak behaviour of PT CLT wall systems coupled with STS. These numerical simulations would not be limited by experimental lab restraints such as actuator stroke limits. While there are seemingly endless possibilities for the spatial insertion angle of STS in PT CLT Wall assemblies, the first subassembly modelling could investigate the most common cases, i.e., STS installed at 90° to the CLT face grain, under a suite of earthquake records to determine an appropriate hysteretic damping model. Then, a design approach such as direct displacement based design could be implemented. Applying methodologies such as FEMA P-695 (2009) to PT core-wall

systems would provide seismic design parameters in accordance with ASCE 7-10 (2010) following a force-based design approach (Sarti et al., 2017).

By using Particle Tracking Technology and the image processing software *Streams* (Nokes, 2019), the compressive strains at the base of a PT CLT wall were determined for the first time. Future numerical models could also compare experimental compressive strains to numerical modelling results.

#### *10.5.2.3 Analytical investigations*

The proposed analytical models were able to well capture the wall response with reasonable accuracy when compared to the experimental testing results. However, in most instances the experimental wall specimens were not tested to ultimate failure which would have occurred when the STS connections at the vertical joints failed. Future work should compare the proposed analytical models to experimental tests where PT wall systems with STS vertical joints were tested to failure.

In general, the proposed analytical models assumed a constant vertical joint slip along the height of the joint. This simplification was found to be adequate in all tests except one PT core-wall test (Test CW-6) where the highest partial composite action was observed. In Test CW-6, it was observed that significant vertical joint slip differences occurred along the CW joint height and in order to capture Test CW-6 response analytically, an effective number of fasteners, $n_{ef}$, was employed. While Hossain et al. (2019) has proposed $n_{ef}$ factors to determine strength and stiffness of common STS CLT-CLT joints, further experimental and numerical study is required to validate these expressions which are critical input parameters for the proposed analytical models. In taller CLT core-wall systems, it is postulated that significant vertical joint slip differences would occur due to wall elastic deformations and therefore future updates to the analytical models should propose factors such as $n_{ef}$ to account for this behaviour. Otherwise, the core-wall strength and stiffness will be overestimated.

## 10.6 REFERENCES

American Society for Civil Engineers and S.E. Institute. (2010). *Minimum design loads for building and other structures*. American Society of Civil Engineers, Structural Engineering Institute.

American Society for Testing and Materials. (2013). *ASTM D5764-97a - Standard test method for evaluating dowel-bearing strength of wood and wood-based prducts*.

CEN. (2014). Eurocode 5: Design of timber structures-Part 1-1: General-Common rules and rules for buildings. In *EN1995-1-1:2004-11 + AC2006-06 + A1:2008-06 + A2:2014-05 Eurocode 5*. European Committee for Standardization.

CEN. (2016). *EN 14358:2016 - Timber structures - Calculation and verification of characteristic values*.

European Committee for Standardization (CEN).

EN 1382. (2016). *Timber structures - test methods - withdrawal capacity of timber fasteners*. European Committee for Standardization (CEN).

FEMA. (2009). *Quantificantion of building seismic performance factors: FEMA P695*. Federal Emergency Management Agency.

Foschi, R. O. (1977). Analysis of wood diaphragms and trusses, Part 1: Diaphragms. *Canadian Journal of Civil Engineering*, *4*(3), 345–362.

Gagnon, S., Pirvu, C., & Fpinnovations. (2011). *CLT handbook: cross-laminated timber: Vol. SP-528E.;S* (Canadian, Issue Book, Whole). FPInnovations.

Hossain, A., Popovski, M., & Tannert, T. (2019). Group Effects for Shear Connections with Self-Tapping Screws in CLT. *Journal of Structural Engineering (United States)*, *145*(8), 1–9. https://doi.org/10.1061/(ASCE)ST.1943-541X.0002357

Nokes, R. (2019). *Streams 3.02: System Theory and Design*.

Ottenhaus, L., Li, M., & Smith, T. (2020). Analytical Derivation and Experimental Verification of Overstrength Factors of Dowel-type Timber Connections for Capacity Design. *Journal of Earthquake Engineering*, 1–15. https://doi.org/10.1080/13632469.2020.1781711

Ottenhaus, L. M., Li, M., Smith, T., & Quenneville, P. (2018). Overstrength of dowelled CLT connections under monotonic and cyclic loading. *Bulletin of Earthquake Engineering*, 1–21. https://doi.org/10.1007/s10518-017-0221-8

Pilon, D. S., Palermo, A., Sarti, F., & Salenikovich, A. (2019). Benefits of multiple rocking segments for CLT and LVL Pres-Lam wall systems. *Soil Dynamics and Earthquake Engineering*, *117*, 234–244. https://doi.org/10.1016/j.soildyn.2018.11.026

Quenneville, P., & Zarnani, P. (2014). Wood Block Tear-Out Resistance and Failure Modes of Timber Rivet Connections: A Stiffness-Based Approach. *Journal of Structural Engineering*, *140*(2), 4013055. https://doi.org/10.1061/(ASCE)ST.1943-541X.0000840

Ringhofer, A. (2017). Axially Loaded Self-Tapping Screws in Solid Timber and Laminated Timber Products. In *Graz University of Technology*. Timber Engineering & Technology, TET 5, Verlag der Technischen Universität Graz. https://doi.org/10.3217/978-3-85125-555-3

Sarti, F., Palermo, A., Pampanin, S., & Berman, J. (2017). Determination of the seismic performance factors for post-tensioned rocking timber wall systems. *Earthquake Engineering & Structural Dynamics*, *46*(2), 181–200. https://doi.org/10.1002/eqe.2784

Smith, I., Asiz, A., Snow, M., & Chui, Y. H. (2006). Possible Canadian / ISO Approach to Deriving Design Values From Test Data. *Proceedings of the CIB W18 Meeting Thirty-Nine*.